EFFECT OF VARYING HYSTERESIS MODELS AND DAMAGE MODELS ON DAMAGE ASSESSMENT OF R/C STRUCTURES UNDER STANDARD DESIGN LEVEL EARTHQUAKES OBTAINED USING A NEW SCALING METHOD

A thesis submitted in partial fulfilment
of the requirements for
the Degree of Ph.D of Civil Engineering
at the
University of Canterbury,
Christchurch, New Zealand

By
Ping DONG

University of Canterbury

2003

DEDICATION

This thesis is dedicated to my mother ZHANG Shanlan and father DONG Qingtang.

ABSTRACT

A seismic damage assessment of a real ductile framed structure of reinforced concrete requires not only realistic damage indices for members, storeys and the whole structure, but also a hysteresis rule simulating strength, stiffness and energy dissipation characteristics of the member hysteretic behaviour.

Many member damage indices and hysteresis models have been developed [Carr 1998]. Varying the member damage indices and the hysteresis models may result in significant variations in the predicted damage indices for storeys and structures subjected to design level earthquake excitations at ultimate limit state specified in New Zealand loading standard [NZS4203 1992]. This could greatly influence correct engineering decisions of a structural design engineer, hence the effect of varying member damage indices and hysteresis models on the damage indices for the storeys and structures should be identified.

To this purpose, three main aspects studied include the earthquake scaling, the relationship between the member curvature ductility and structural displacement ductility, and the effect of varying hysteresis models and member damage indices on the damage indices for the storeys and structures respectively.

Three structures, four earthquakes, eight hysteresis rules and four member damage indices were employed in this study for structural models, earthquake inputs, modelling the inelastic behaviour in members and member damage respectively.

The three reinforced concrete ductile frames are 6, 12 and 18 storeys respectively, designed according to the current New Zealand Standards [NZS4203 1992, NZS3101 1995] using the capacity design philosophy [Paulay 1992] with a structural displacement ductility of 5.0. The four different past earthquake excitations are Bucharest (1977-NS), El Centro (1940-NS), Northridge (Sylmar-949NW) and Kobe (1995-NS). The eight hysteresis models are the Elasto-Plastic, Bilinear, Modified Takeda (α=0.0, β=0.6), Degrading Bilinear (α=0.5), Clough, Modified Takeda (α=0.3, β=0.4), Q-Hyst (α=0.5) and Origin-Centred hysteresis models. The four member damage indices are the Park & Ang, Roufaiel & Meyer, Cosenza et al and

Banon & Veneziano. The storey and structural damage indices, quantifying the storey and structural damage measures respectively, were calculated as the energy weighted average of all the inelastic member damage indices in the storeys and overall structures respectively (Park & Ang method).

To have appropriate scaled earthquakes matching design-level requirements, six different scaling methods are used to scale the four earthquakes for the three structures. By comparing the maximum responses (the maximum base shears, inter-storey drifts and spectral accelerations), resulting from carrying out elastic dynamic time-history analyses to the scaled earthquakes with those at design level, a new procedure for earthquake scaling is proposed.

To check whether the member curvature ductility demand to the design level earthquakes is less than the member curvature ductility capacity, the relationship between the member curvature ductility and the structural displacement ductility was studied and identified by carrying out inelastic dynamic time-history analyses. For this purpose, the Carr & Tabuchi trend-line approach for defining the structural yield displacements was used.

By comparative studies of the storey and structural damage indices for a specified member damage index and a specified hysteresis model, the effect of varying the hysteresis models and member damage indices on the storey and overall structural damage indices, i.e. damage evaluations, are identified.

Finally a procedure for the seismic damage analyses of reinforced concrete ductile framed structures to design-level earthquake excitations is proposed, which is illustrated by computing storey and structural damage indices for evaluations of 6- and 12-storey structures responding to the El Centro (1940-NS) excitation.

ACKNOWLEDGEMENTS

The research work presented in this thesis was conducted at the Department of Civil Engineering, University of Canterbury, Christchurch, New Zealand. I am grateful to Canterbury University for the resources it provided, particularly to the academic and technical staffs of the department for their assistance.

I wish to express my sincerely deepest gratitude to my supervisor, Dr. Athol Carr for his wisdom, guidance and continuous encouragement throughout the Master of Engineering and the Ph.D studies. I also wish to extend my gratitude to Associate Professor Peter J. Moss who is the other supervisor of the Master of Engineering and the Ph.D studies for his wisdom, guidance and encouragement.

I also wish to express my sincere gratitude to Emeritus Professor Tom Paulay for his recommendations on the column sizes of the 12-storey structure and patient guidance on the Capacity Design Philosophy, and impressively funny jokes making questions easier to understand. His general review of the thesis and invaluable comments and suggestions are very much appreciated.

I am grateful to my whole family including my younger sister Yan DONG, brother Feng DONG and their own families for their encouragement, support and love, especially to my mum and dad for their taking care of my little daughter Nancy during my study when I had extreme personal difficulties. Many thanks are due to Nancy for her understandings when I should have been with her and her bright smile, lovely singing, and beautiful drawing and so on.

Many thanks are due to my colleagues, particularly to I. Satyarno, A.M. Rahman and X. Lin for the discussions, support, encouragement and friendship they provided.

Finally, sincere thanks to all those who have contributed to this work. Without your help this work could not be done.

CONTENTS

Chapter 4 Hysteretic Models for Reinforced Concrete Members

Chapter 5 Input Earthquake Excitations and Scaling Methods

LIST OF FIGURES

LIST OF TABLES

LIST OF SYMBOLS

a_0 Mass damping factor for the Rayleigh damping model

a_1 Stiffness damping factor for the Rayleigh damping model

a_n The spectral acceleration of the unscaled excitation for mode n

a_n^d Design spectral acceleration for mode n

$[a]$ Relationship matrix between the nodal displacement vector in the local coordinate system and the absolute nodal displacement vector

A Tributary loading area and member cross sectional area

A_g The total cross-sectional area of steel at the bottom face of a member section

A_g' The total cross-sectional area of steel at the top face of a member section

A_s The hoop cross-sectional area, and total area of steel cross section as shown in Fig. 4-11

b The effective width of bean flange, the width of the confined core, and width of a member section

b_w Width of web

c The distance between the neutral axis and the top extreme compressive concrete face

C_a^{design} Design acceleration coefficient

$C_h(T_1, \mu)$ Basic seismic hazard acceleration coefficient which accounts for different soil condition, structural ductility factor μ and fundamental period T_1

C_n^* Generalised damping for nth mode

$[C]$ Damping matrix

d The depth of the confined core, and steel bar diameter

d_n The spectral displacement of the unscaled excitation for mode n

d_n^d Design spectral displacement for mode n

d_m Previously attained maximum displacement

d_s Maximum inter-storey drift

d_{sy} Yield inter-storey drift

d_t Maximum top level displacement

d_{ty} Top level displacement at yield (structural yield displacement)

d_y Yielding displacement

dE Incremental dissipated hysteretic energy

$d\theta$ Increment of rotation

DI Damage index

DI_e Damage index for energy ductility

E Young's modulus of elasticity or earthquake load as specified

E_h Hysteretic energy dissipation index or dissipated energy

$E_{n(t)}$ Normalised dissipated energy

f Factor for slab effect on cast-in-place T or L beam member stiffness (=1.3~1.5 for interior T beams in this study), reflecting flange contribution to the stiffness in these beams

$f_c^{'}$ Concrete uniaxial cylinder strength

f_{cy} Concrete yielding strength

f_{cu} Concrete ultimate strength

f_{sy} Yielding strength of reinforcing steel

f_{su} Ultimate strength of reinforcing steel

F_c^{cy} The compressive force in the concrete the top concrete fibre strain reaches yielding

F_i Equivalent static lateral force at level i

F_t Equivalent static lateral force at top level

F_y Calculated yield strength shown in Fig. 6-5.

FDR Flexural damage ratio

$[f]_{2x2}$ The member 2 by 2 flexibility matrix

$[f]_{3x3}$ The 3 by 3 member flexibility matrix

$[f_c]$ The 2 by 2 flexibility matrix for a clear span member without considering rigid end block effect

g Gravity acceleration

G The dead load

h Height of a building, and depth of a member section

h_i Height of level i above the base of the structure

h_s Thickness of slab

h_t Height of the top level above the base of the structure

I Cross-section moment of inertia

ID^{design} The design maximum inter-storey drift over all levels

Ie The average effective member moments of inertia

Ig Moment of inertia for the gross section

k_{si} Plastic spring stiffness at member end i

k_{sj} Plastic spring stiffness at member end j

k_f Initial flexural stiffness

k_r Reduced secant stiffness at maximum displacement

k_u Secant stiffness at ultimate point

K_u The degraded unloading stiffness at maximum displacement d_m as shown in Fig. 9-1

K_0 Initial elastic stiffness

K_n^* Generalised stiffness for nth mode

$$k_{fi} = \begin{cases} \propto & \textit{Hinge is elastic} \\ 0 & \textit{Hinge is perfectly plastic} \\ \dfrac{EI}{l_p}\left(\dfrac{r_i}{1-r_i}\right) & \textit{Hinge is inelastic} \end{cases}$$ Equivalent inelastic flexural stiffness at member end i, where l_p is the plastic hinge length and r_i is the ratio of the inelastic to the elastic stiffness obtained from the moment-curvature hysteresis rule

$[K]$ Stiffness matrix

$[K]_{2x2}$ The member 2 by 2 stiffness matrix

$[K]_{3x3}$ The 3 by 3 member stiffness matrix

$[K]_{6x6}$ The 6 by 6 member stiffness matrix in the member local coordinate system

$[\hat{K}]_{6x6}$ The 6 by 6 member stiffness matrix in the global coordinate system

K_n^* Generalised stiffness for nth mode

l_p Plastic hinge length

L Member length

L_1 Rigid block length at left member end

L_2 Rigid block length at right member end

L_c Member length without considering rigid end blocks

L_n^* Effective mass for nth mode

L_{nv} The clear distance to next web

L_u Limit state factor for the ultimate limit state (=1.0)

L_x The span length of a beam

m Mass lumped at a node or joint

$\overline{m}$ Total uniform mass per unit length

$m'_{(x)}$ Total mass per unit member length

M_0 The yield moment at the axial compression force is zeor

M_{1b} The yield bending moments at the axial forces $(2/3)P_b$ where P_b is the axial compression force at response point b as shown in Fig. 4-10

M_{2b} The yield bending moments at the axial forces $(1/3)P_b$ where P_b isthe axial compression force at response point b as shown in Fig. 4-10

M_b The yield bending moment at response point b as shown in Fig. 4-10

M_n^* Generalised mass for nth mode

M_n^e The effective mass for mode n

M_t Plastic moment at time t

M_y Yield moment

M_u Ultimate moment

ΔM_i Incremental moment at member end i

ΔM_j Incremental moment at member end j

$[M]$ Mass matrix

P_b The axial compression force at response point b as shown in Fig. 4-10

P_{yc} The axial compression yield force as shown in Fig. 4-10

P_{yt} The axial tension yield force as shown in Fig. 4-10

Q $=\psi_a * Q_b$: is the reduced live load considering loading area

Q_b The basic live load (2.5kPa in this study)

Q_u $=0.4*Q=0.4*\psi_a*Q_b$: live load to be combined with either the wind or snow or earthquake forces which is equal to the reduced live load multiplied by combination factor 0.4

r_i The ratio of the inelastic to the elastic stiffness obtained from the moment-curvature hysteresis rule

$[r]$ Displacement vector of each degree-of-freedom due to unit displacement of the foundation

R Risk factor for a structure (=1.0 for category *IV* structure in this study)

R_n $=\frac{a_n^d}{a_n}$ or $\frac{d_n^d}{d_n}$ ratio of design acceleration or displacement to the acceleration or displacement of the unscaled excitation for mode *n*

R_p Ratio of post-yielding stiffness to initial elastic stiffness for reinforced concrete

S The hoop spacing

S_2 Bending moment at the left end of a member with considering rigid end block effect

S_3 Bending moment at the right end of a member with considering rigid end block effect

S_2^c Left member end bending moment for a member with length L_c

S_3^c Right member end bending moment for a member with length L_c

Sa_n^d The design acceleration for the single degree of freedom of natural period T_n

Sd_n^d The design displacement for the single degree of freedom of natural period T_n

SF The scaling factor

S_p Structural performance factor (=0.67 [4.2.4.1 NZS 4203 1992])

S_u the snow load for ultimate limit state

$\{S'\}$ Force vector in local coordinate system

$\{\hat{S}\}$ Force vector in global coordinate system

$\{S_c\}$ Bending moment vector for a clear span member without considering rigid end block effect

t The total number of levels

T_1 Fundamental period of free vibration

T_b^{cy} The tensile force in the bottom-face steel when the extreme compressive concrete fibre strain reaches yielding

T_t^{cy} The tensile force in the top-face steel when the extreme compressive concrete fibre strain reaches yielding

T_n Period of free vibration at mode n

$[T]$ Relationship matrix between the nodal displacement vectors in global and local coordinate systems

u_2^c Rotation at the left end of a member without considering rigid end block effect

u_3^c Rotation at the right end of a member without considering rigid end block effect

u_2 Rotation at the left end of a member with considering rigid end block effect

u_3 Rotation at the right end of a member with considering rigid end block effect

u_m Maximum response deformation under an earthquake shown in Fig. 6-5.

u_u Ultimate deformation capacity under monotonic loading shown in Fig. 6-5.

$\ddot{u}_g$ The ground acceleration

$\ddot{u}_t$ The ground acceleration at time t

$\{u\}$ Member relative displacement vector

$\{u'\}$ Member nodal displacement vector in the local coordinate system

$\{\hat{u}\}$ Member nodal displacement vector in the global coordinate system

$\{u\}$ Displacement vector

$\{\dot{u}\}$ Velocity vector

$\{\ddot{u}\}$ Acceleration vector

$\{\ddot{u}_g\}$ Ground acceleration induced acceleration vector

V Horizontal seismic base shear of a structure

V^{design} The design base shear

W Total seismic weight of a structure

W_i Seismic weight at level i

W_t Seismic weight at top level

W_u the wind load for ultimate limit state

x The difference between the bending moments at the left end of a member with and without considering rigid end block effect, as shown in Fig. 3-4

y The difference between the bending moments at the right end of a member with and without considering rigid end block effect, as shown in Fig. 3-4, and the distance between the neutral axis and the centre of the bottom tensile steel as shown in Fig. 4-9

$\bar{y}$ The distance between the neutral axis and the location of compressive concrete resultant forces

$\{Y\}$ The vector of the modal amplitudes

Z Zone factor (=0.8 for Christchurch)

α Unloading stiffness degradation parameter of hysteresis model or stress block factor

β Reloading stiffness degradation parameter of hysteresis model or experimental constant (=0.05 for reinforced concrete members) for Park and Ang damage model or stress block factor

α_1^{cy} and β_1^{cy} the stress-block factors when the extreme compressive concrete fibre strain reaches yielding

α_1^{m} and β_1^{m} the stress-block factors when the extreme compressive concrete fibre strain reaches the maximum strain ε_m

ε_t The extreme top compressive fibre strain

ε_t^{cy} The yielding strain in the extreme compressive concrete fibre

ε_t^{m} The maximum strain in the extreme compressive concrete fibre

ε_{cy} Concrete yielding strain

ε_{cu} Concrete ultimate strain

ε_{sy} Reinforcing steel yielding strain

ε_{su} Reinforcing steel ultimate strain

ϕ Member curvature

$\phi_{\max}$ Maximum curvature demand

ϕ_y Member yielding curvature demand

ϕ_n nth mode shape

$[\phi]$ Modal matrix in which each column is a mode shape

λ_n The artificial weighting factor for mode n for earthquake scaling

μ Displacement ductility

μ_e Energy ductility, defined $\mu_e = \dfrac{\int E_h}{M_y \phi_y} + 1$

$\mu_{e,u}$ Ultimate energy ductility capacity, $\mu_{e,u} \cong \mu_u$ and $\mu_{e,u} = \mu_u$ for an elastic-perfect plastic hysteresis model.

μ_m Maximum curvature ductility $\mu_{\max}$ or energy ductility μ_e

$\mu_{\max}$ Maximum curvature ductility demand

μ_s The storey ductility

μ_t The structural ductility

μ_u Ultimate curvature ductility capacity

μ_y Yield curvature ductility =1.0

θ The angle between the local and global coordinate systems

θ_u Ultimate rotation

θ_y Yield rotation

$\Delta\theta_i$ Incremental rotation at member end i

$\Delta\theta_j$ Incremental rotation at member end j

ρ $=2(b+d)A_s/(bds)$ where b, d are the width and depth of the confined core. A_s is the hoop cross-sectional area. s is the hoop spacing.

σ_b^{cy} The steel stress in the bottom face when the extreme compressive concrete fibre strain reaches yielding

σ_t^{cy} The steel stress in the top face when the extreme compressive concrete fibre strain reaches yielding

σ_b^{m} The steel stress in the bottom face when the extreme compressive concrete fibre strain reaches the maximum

σ_t^m The steel stress in the top face when the extreme compressive concrete fibre strain reaches the maximum

τ Time

ω_n Undamped natural circular frequency

ξ_n Damping ratio for *n*th mode

ψ_a Live load reduction factor considering tributary loading area

Δ Denotes an incremental part of quantity it precedes

$\dot{}$, $\ddot{}$ Denote the first and second differentials with respect to time

$\{\ \}$ Normally denotes a vector

$[\ ]$ Normally denotes a matrix

Chapter 1
Introduction

1-1 Introduction

The member curvature ductility, inter-storey displacement ductility and structural displacement ductility have been used as damage measures for members, storeys and overall structures respectively in most current seismic codes [IAEE 1996].

The philosophy for an earthquake resistant design of a building structure requires that the building should suffer repairable damage and avoid collapse when subjected to design level earthquakes at the ultimate limit state [NZS4203 1992]. To achieve this for a preliminary designed structure, say designed using the equivalent static method in this study, the structural displacement ductility demand in the structure should not exceed the structural displacement ductility capacity, which can be checked by carrying out a numerical integration time history analyses. This concept has been used for the last twenty-five years.

However, many more comprehensive damage models have been developed for reinforced concrete structures [Park 1985, Bracci 1989, Roufaiel 1987, Cosenza 1993, Chung 1987 and Banon 1982]. The damage in the members, storeys and overall structures are usually quantified by the corresponding damage indices. These damage indices are regarded as being more suitable for damage evaluations rather than the corresponding ductilities [Carr 1993]. Hence, for the preliminary designed structure, the overall structural damage index should be used as a damage measure rather than the structural displacement ductility.

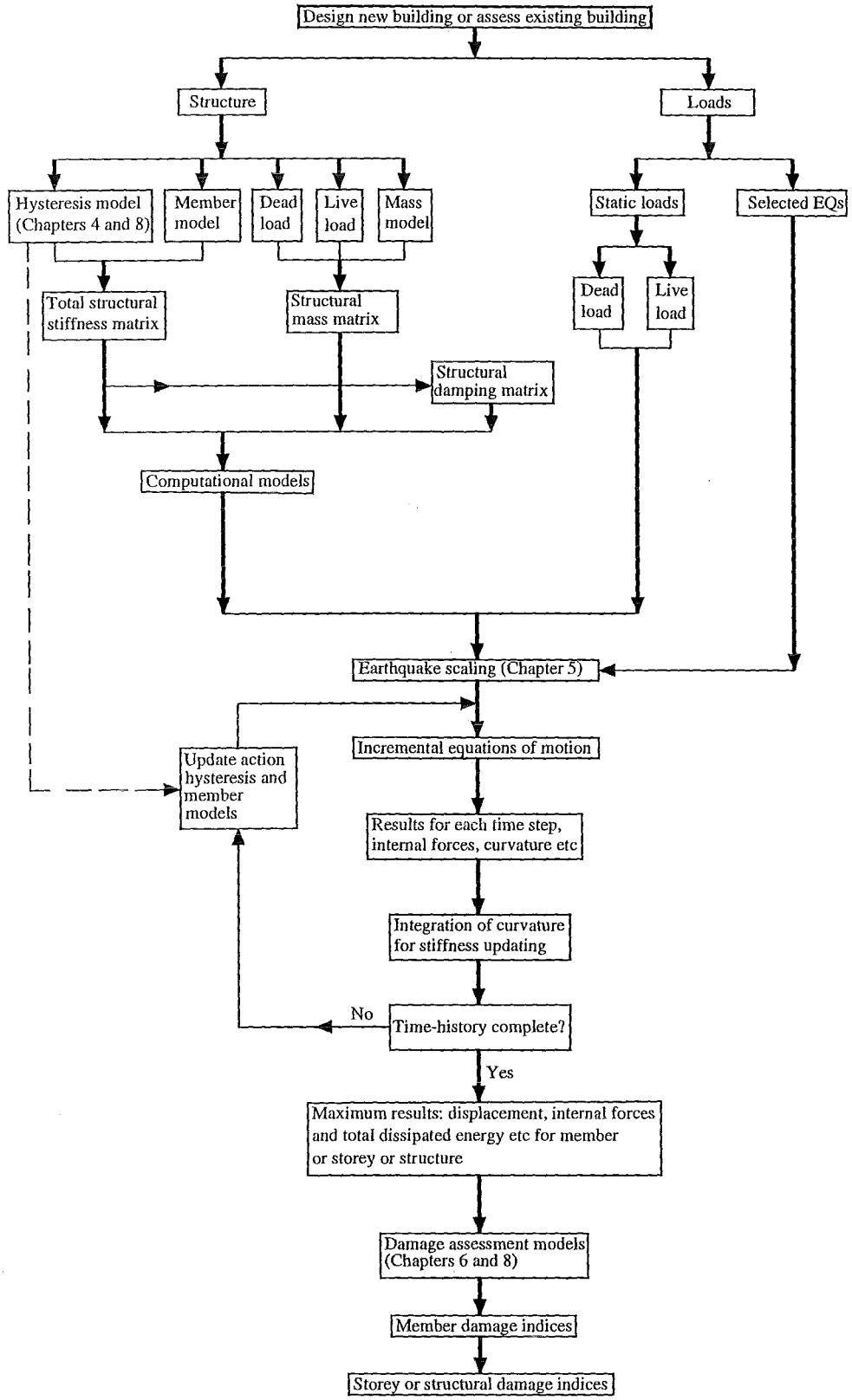

Fig. 1-1 Flow chart for damage assessment of reinforced concrete ductile- framed structure subjected to earthquake excitation using inelastic step-by-step time history method

A procedure for the seismic damage assessment, i.e. computing the damage indices, of a real ductile framed structure of reinforced concrete is very complex, as illustrated in Fig. 1-1, which requires not only modelling the mass, member hysteretic responses and damping for the generation of the structural mass, stiffness and damping matrices but also requires the acceleration assumption for each time step to solve the incremental dynamic equations for the displacements and the damage indices for the members, storeys and structures.

The member hysteretic responses can be simulated using a hysteresis model capable of capturing the strength, unloading and reloading stiffnesses, and energy dissipation characteristics of the members. Many hysteresis models have been developed. For instance, there are over thirty hysteresis models incorporated in the computer program RUAUMOKO [Carr 1998], ranging from the simple Elasto-plastic and Bilinear rules to complex rules that require over thirty parameters to keep track of the current stiffness.

The program RUAUMOKO on the Alpha Unix computer system of the Department of Civil Engineering, University of Canterbury was used for the two-dimensional inelastic dynamic analyses of the structures. In this program, several different options of member damage indices are available for reinforced concrete structures. The Park & Ang and Banon & Veneziano damage indices are related to the total dissipated energy and the maximum curvature ductility. The Bracci at al. and Roufaiel & Meyer damage indices are respectively related to the energy and secant stiffness of the members. The Cosenza damage index is a normalised ductility model.

Varying the member damage indices and the hysteresis models may result in significant variations in the predicted damage indices. This would greatly influence a structural design engineer when making an assessment of the likely damage in the preliminary design of a reinforced concrete structure for the design level earthquake excitations. Hence the effect of varying the member damage indices and hysteresis models on the computed damage indices for the structures and the storeys in the structures should be identified.

To this purpose, three reinforced concrete ductile framed structures of 6, 12 and 18 storeys were designed according to the current New Zealand seismic standards and structural design requirements [NZS4203 1992, NZS3101 1995] using the capacity design method [Paulay 1992] for the structural models. The Equivalent Static Method of the loading standard was used to design the structures with an assumed structural ductility of 5.0. Following the requirements of capacity design only the beams and the first storey columns are expected to respond nonlinearly in the idealised failure mechanism. The structures were assumed to be situated on an intermediate subsoil in Christchurch, New Zealand.

Four different earthquake excitations, i.e. Bucharest (1977-NS), El Centro (1940-NS), Northridge (Sylmar-949NW) and Kobe (1995-NS) were chosen and scaled to match the design level earthquakes as the earthquake inputs using an appropriate scaling method as presented in Chapter 5.

Shear failure and bar slippage are assumed to be suppressed due to the application of the current New Zealand seismic provisions and structural design requirements. The effect of shear deformation and bar slippage on the responses is small in new structures, hence only hysteresis models dominated by flexural actions are applied without considering pinching phenomenon in the member hysteretic performance. The shear-induced contribution to the member end rotation for the member stiffness matrix is assumed to be small and is therefore neglected.

The Elasto-Plastic, Bilinear, Modified Takeda (α=0.0, β=0.6), Degrading Bilinear (α=0.5), Clough, Modified Takeda (α=0.3, β=0.4) and Q-Hyst (α=0.5) models [Carr 1998] were used for modelling the member inelastic hysteretic responses, in addition to the use of the Origin-Centred model as it has the smallest hysteretic energy dissipation capacity and it is used to gauge the effect of loops with little energy dissipation.

Four member damage indices were used for the member damage measures. These were the Park & Ang, Roufaiel & Meyer, Cosenza et al. and Banon & Veneziano damage indices. The storey and overall structural damage indices were calculated as

the energy weighted average of the member damage indices in the storeys of the structure and the overall structure respectively (Park & Ang method) for each of the four different member damage indices.

A very large number of analyses varying the storey and overall structural ductilities and damage indices were carried out using the software program RUAUMOKO [Carr 1998], where the storey and structural ductilities were defined using the Carr & Tabuchi trend line approach [Carr 1993]. For instance, there were $3\times4\times8=96$ overall structural displacement ductilties computed for all three structures, four earthquakes and eight hysteresis models.

By comparing the computed storey and structural damage indices for a specified member damage index and a specified hysteresis model, the effect of varying the hysteresis models and member damage index choice on the computed storey and overall structural damage indices was observed.

1-2 Objectives of the Research

To have design-level earthquakes as earthquake inputs, a rational procedure for earthquake scaling should be identified.

As the four member damage indices are related to each other and are sensitive to the specified member ultimate curvature ductility [Carr 1993], the ratios of the member curvature ductilities to the structural displacement ductility should be found to see if the ultimate member curvature ductility capacity is greater than the response required for the design-level earthquakes.

In addition to these objectives, the main objectives of the research were to identify the effect of varying the hysteresis models and the member damage index choice on the weighted storey and structural damage indices and then propose a procedure to enable structural design engineers to carry out damage analyses during the preliminary design of structures to the current New Zealand design standards.

The objectives were to:

- find an appropriate earthquake scaling method and have the four earthquakes scaled to match the design-level earthquakes for each of the three structures.

- find the ratios of the member curvature ductilities to the structural displacement ductility at the design-level earthquakes and check if the member curvature ductility demand to the design-level earthquakes is less than the ultimate member curvature ductility capacity.

- investigate the effect of varying the choice of the hysteresis model on the storey and structural damage indices.

- investigate the effect of varying the member damage index choice on the storey and structural damage indices.

- develop a procedure so that structural design engineers can evaluate the storey and overall structural damage indices.

1-3 Scope and Outline of the Research

Before carrying out the elastic dynamic step-by-step integration time history analyses for the study of earthquake scaling methods in Chapter 5, the philosophy of capacity design and the three prototype structures, designed using the Equivalent Static Method of the New Zealand loading standard, are briefly described in Chapter 2.

The mathematical modelling, including the mass model, the member model and the damping model for the mass, stiffness and damping matrices respectively are presented in Chapter 3. In addition, the Newmark constant average acceleration model used for solving the incremental dynamic equations is described.

The stiffness properties and hysteretic characteristics of reinforced concrete members, and the hysteresis models used in this research are reviewed in Chapter 4. The hysteresis energy dissipation indices of these hysteresis models indicating their hysteresis energy dissipation capacity are also discussed in this chapter.

Much of the earlier work for Chapters 3 and 4 was obtained by the author for his Master of Engineering degree [Dong 1999] and the results are available in published books [Clough 1993, Chopra 1995, Carr 1998] but are also shown in this thesis for completeness.

To provide design-level earthquakes as required in the standards for the damage analyses, six different scaling methods were used to scale the four earthquakes for the three structures and these are presented in Chapter 5. By comparing the elastic maximum responses (maximum base shears, maximum inter-storey drifts and spectral accelerations) to the scaled earthquakes with those at the standard design level, a procedure for earthquake scaling is obtained. The method is based largely on the Equal Displacement Principle [Newmark 1960]. The scaling factors of the four excitations for the three structures are presented in Chapter 5.

In Chapter 6, the literature for the seismic damage indices for members, storeys and entire structures of reinforced concrete is reviewed.

To check whether or not the member curvature ductility capacity is greater than the seismic response requirements of the design-level earthquakes for the damage analysis studies, the four design-level earthquakes are used to excite the three structures for the eight different hysteresis models, which are discussed in Chapter 7. The storey and structural ductilities were defined using the Carr & Tabuchi [Carr 1993] trend line approach. The ratios of the ductilities for the members, storeys and structures are determined. In addition, the effect of varying the hysteresis models on the storey and overall structural ductilities are identified.

In Chapter 8, the four member damage indices are used to compute the storey and overall structural damage indices for the three structures subjected to the four design-

level earthquakes. The effect of varying the hysteresis models and member damage indices on the storey and structural damage indices are determined.

Recommended procedures for storey and overall structural damage indices or evaluations are presented in Chapter 9.

A summary of the results of the thesis, the conclusions and suggestions for further studies are presented in Chapter 10.

Chapter 2

Three Ductile Framed Structures of 6, 12 and 18 Storeys Used in the Research Work

2-1 Introduction

As has been mentioned earlier, three reinforced concrete ductile moment resisting frames of 6, 12 and 18 storeys were designed according to the current New Zealand Standards [NZS4203 1992, NZS3101 1995] using the capacity design method [Paulay 1992] for use as the prototype structural models. The floors were assumed to act as rigid diaphragms in their own planes. Hence all the nodes at each level were coupled to each other to give the same horizontal displacement. Due to the regularity of these structures over their heights and in their plans, torsional effects were not considered in the structural analyses. The foundations were assumed to be fixed without taking soil-structure interaction effects into account.

The design seismic base shear force of a structure is a function of the total seismic weight of the structure and the lateral design acceleration coefficient. The lateral design acceleration coefficient is a function of the basic seismic hazard acceleration coefficient, the structural performance factor, the risk factor, the zone factor, the limit state factor and the natural period of free vibration of the structure. The basic seismic hazard acceleration coefficient can be determined from the seismic acceleration spectrum for an assumed structure ductility, the fundamental period of free vibration of the structure and the site subsoil category.

The distributed seismic lateral force pattern is an inverted triangle. The lateral force is proportional to the seismic weight and the height of the level under consideration. A portion of the lateral load is concentrated at the top level to allow for high mode effects.

2-2 Philosophy of Capacity Design

The application of capacity design to ductile structures subjected to large earthquakes has been developed primarily in New Zealand over the last 25 years [Park 1975, Paulay 1977, Paulay 1979, Paulay 1980, Paulay 1988, Paulay 1992], where the capacity design method has been used extensively [NZS4203 1992, NZS3101 1995]. After some modification the philosophy has also been adopted in other countries [CSA 1984, TP 1987].

In the capacity design of a reinforced concrete framed structure for earthquake resistance, the ideal or expected energy-dissipating mechanism is clearly defined for resisting lateral forces, as shown in Fig. 2-1 for a 6-storey frame, for example. All beam-ends and the lower ends of the first storey columns of the structure subjected to design level or severe earthquakes are permitted to deform inelastically, where the inelastic displacement occurs in regions termed "plastic hinges". Hysteretic energy will be dissipated at these plastic hinges, while all columns except for a region at the lower ends of the first storey columns are assumed to remain elastic.

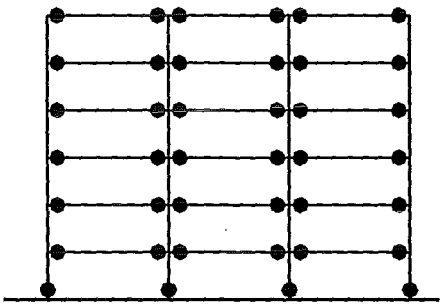

Fig. 2-1 Energy-dissipating mechanism for reinforced concrete frame designed using capacity design approach (note: black dots represent location of potential plastic hinge)

All the potential plastic hinge regions at the member ends are designed to have greater flexural yield strengths than that required by the design equivalent lateral earthquake forces, and are well detailed to provide sufficient inelastic deformation capacity or curvature ductility. This is done primarily by close-spaced and well-anchored transverse reinforcement. All shear or anchorage and instability failures of the members containing plastic hinges are suppressed by offering correspondingly larger strengths for these actions than that demanded by the flexural capacity of the plastic hinges at over-strength.

All columns are designed to respond elastically using the design bending moments derived from equilibrium at the beam-column joints at the over-strength of the plastic hinges. The dynamic or high mode effects on column response are taken into account by using dynamic magnification factors to enlarge the design bending moments for the column design. The design axial forces for the columns are the sum of the gravity loading and the shear forces transferred from the beams that are all assumed to be in an over-strength state. Different reduction factors are used for the beam-transferred shears for differing numbers of storeys above the column concerned.

2-3 Structural Models

Figs. 2-2 to 2-5 illustrate the typical plan, dimensions and member sizes of the three structures assumed to be situated on intermediate subsoil near the centre of Christchurch, New Zealand. The unreduced (basic) live load Q_b was 2.5 kPa for each floor except for the roof levels, where the assumed live load was zero. Full details of the input data used in the inelastic time-history and pushover analyses can be found in Appendix A.

The structural design ductility ranges from 4 to 6 for full ductile structures [NZS4203 1992]. Due to concerns that member curvature ductility demand will be greater than the capacity according the relationship between the curvature ductility and the overall structural displacement ductility (8:1) [Carr 1993], the structural displacement ductilities for these three interior frames were assumed to be 5 for the prototype designs rather than the standard limit of 6.

The frames were taken as typical three bay interior frames. It was assumed that the frames would be required to resist the component of the earthquake motion in the plane of the frame only. The component in the perpendicular direction was assumed to be taken by some other resisting system, for example by structural walls or by transverse frames.

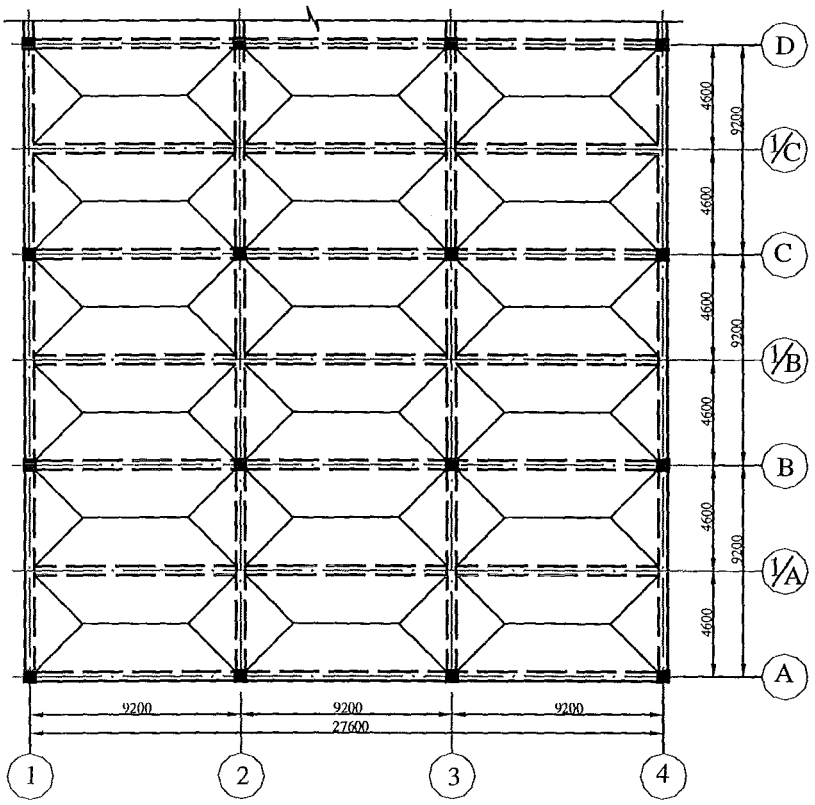

Note: a) All units are in millimetres but are not to scale.
b) Slab thickness is 160 mm throughout for every floor of the three structures.
c) $f_c^{'}$ = 30 MPa concrete was assumed for all members of the three structures.
d) All beams in the axes 1, 2, 3 and 4 are 900x400 (mm*mm).
e) The secondary beams in axes $1/A$, $1/B$ and $1/C$ are all 750x450 (mm*mm).

Fig. 2-2 Typical plan for the three structures

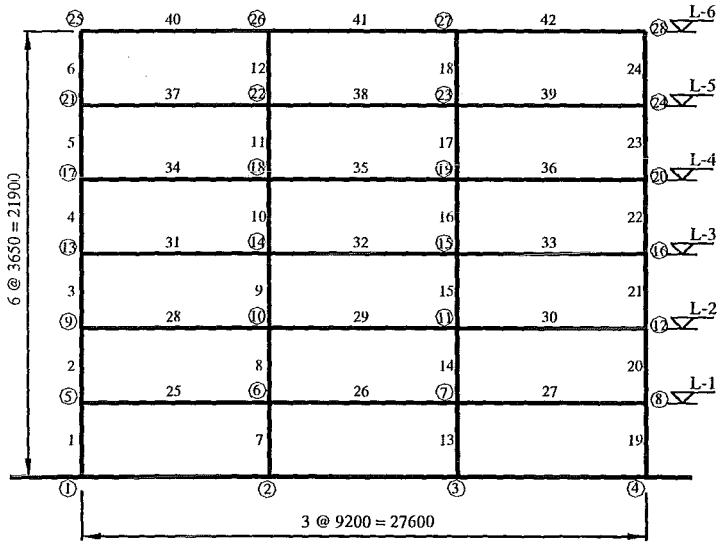

Fig. 2-3 Six storey three bay frame member and node numbering and level definition

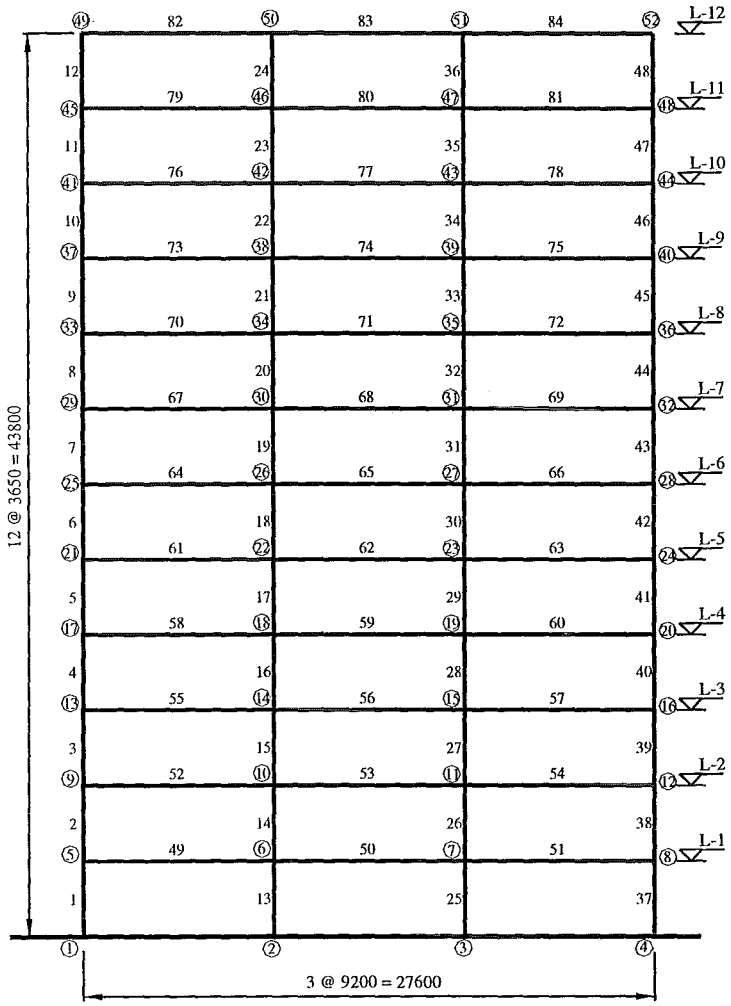

Fig. 2-4 Twelve storey three bay frame member and node numbering and level definition

Table 2-1 Member dimensions for the three frames

	6 Storey Frame		12 Storey Frame		18 Storey Frame	
MEMBERS	LEVEL	DIMENSIONS (mm)	LEVEL	DIMENSIONS (mm)	LEVEL	DIMENSIONS (mm)
Beams	1-3	900x400	1-6	900x400	1-6	1000x550
	4-6	850x400	7-9	850x400	7-9	950x550
			10-12	800x400	10-12	900x500
					13-15	850x500
					16-18	800x400
Exterior Columns	1-3	500x500	1-6	700x700	1-6	1000x650
	4-6	500x450	7-9	650x650	7-9	950x650
			10-12	600x600	10-12	850x650
					13-15	750x650
					16-18	650x650
Interior Columns	1-3	600x600	1-6	850x850	1-6	1000x1000
	4-6	550x500	7-9	750x750	7-9	950x950
			10-12	700x700	10-12	900x900
					13-15	850x850
					16-18	700x700

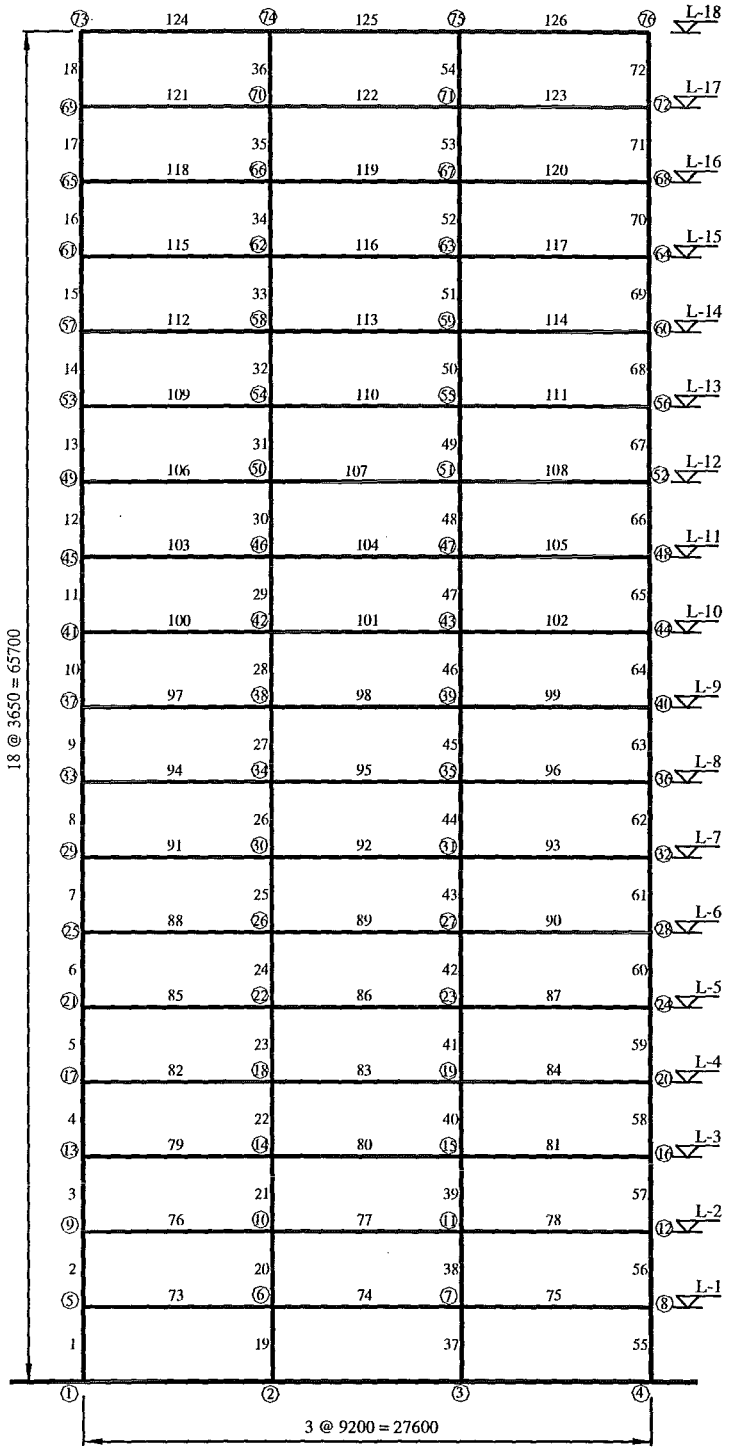

Fig. 2-5 Eighteen storey three bay frame member and node numbering and level definition

The load factors used in the design for each structure were in accordance with NZS4203: 1992, i.e.

$1.4G$

$1.2G+1.6Q$

$1.2G+Q_u+W_u$

$0.9G+W_u$

$1.2G+Q_u+1.2S_u$

$G+Q_u+E$

Where G: the dead load

$Q=\psi_a * Q_b$: is the reduced live load where Q_b is the basic live load and ψ_a area reduction factor is calculated by formula 2-1 shown below (=0.6 in this study)

$Q_u=0.4*Q=0.4*\psi_a * Q_b$: live load to be combined with either the wind or snow or earthquake forces which is equal to the reduced live load multiplied by combination factor 0.4.

W_u: the wind load.

S_u: the snow load.

E: the earthquake load.

$$\psi_a = 0.4 + \frac{2.7}{\sqrt{A}} \leq 1.0 \qquad \textbf{(2-1)}$$

where ψ_a is reduction factor. A is tributary floor area.

The reduction factor and combination factor for live load is 0.6 and 0.4 respectively. Hence the live load Q_u for seismic weights, lumped mass and fixed end forces of the beams used in the time history analyses is 0.24 of the basic live load Q_b.

The design fundamental periods of the structures were estimated by formula 2-2 [UBC 1991].

$$T_1 = 0.11 * h^{3/4} \qquad \textbf{(2-2)}$$

where h: height of building

Fig. 2-6 illustrates the basic seismic hazard acceleration coefficients for the assumed and computed fundamental periods of the structures considering the effects of rigid end blocks on the member stiffnesses. The design and the computed fundamental periods for the structures are shown in Table 2-2. In practical design, the fundamental period of a structure can be easily determined by running a computer analysis, such as RUAUMOKO, once the member sizes are assumed.

Table 2-2 Design and computed fundamental periods of the structures in seconds

6S		12S		18S	
Formula (2-2)	Computed	Formula (2-2)	Computed	Formula (2-2)	Computed
1.11	1.35	1.87	2.34	2.54	2.85

Note: Computed periods take into account the effect of rigid end blocks on member stiffnesses.

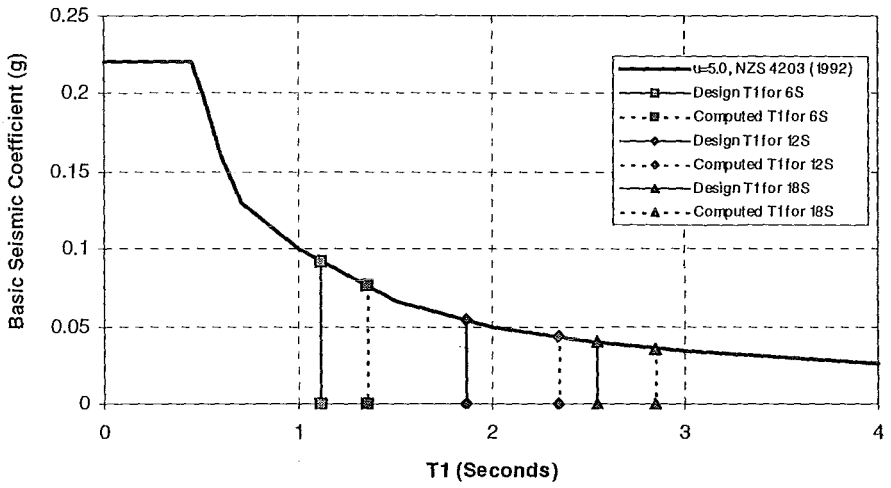

Fig. 2-6 Comparison basic seismic hazard acceleration coefficients for assumed design fundamental periods and computed fundamental periods (considering rigid end block effects) of the three structures for intermediate soil sites

For the ultimate limit state, the design lateral acceleration coefficient for the equivalent static method, C_a^{design}, is given by Eq. 2-3, but shall not be taken as less than 0.03 [NZS 4203: 1992].

$$C_a^{design} = C_h(T_1, \mu) S_p R Z L_u \geq 0.03 \qquad \textbf{(2-3)}$$

where $C_h(T_1,\mu)$: basic seismic hazard acceleration coefficient which accounts for different soil conditions, structural ductility factor μ and fundamental period T_1.

S_p structural performance factor (=0.67 [4.2.4.1 NZS 4203 1992]).

R risk factor for a structure (=1.0 for category *IV* structure used in this study).

Z zone factor (=0.8 for Christchurch).

L_u limit state factor for the ultimate limit state (=1.0).

Table 2-3 shows the design seismic weights, design lateral acceleration coefficients calculated using Eq. (2-3), and base shear forces for the three structures. Because the design lateral acceleration coefficients for the twelve and eighteen storey structures were 0.0289 and 0.0214 respectively, the minimum value, 0.03, was used in calculating the design base shear forces.

Table 2-3 Seismic weights, design lateral acceleration coefficients and base shears of the three structures where $V = C_a^{design} * W$

	6S	12S	18S
Seismic Weight, *W*(kN)	13207	27701	43167
C_a^{design}	0.05	0.03	0.03
Base Shear, *V*(kN)	658	831	1295

The average effective member moments of inertia *Ie* were calculated with the following assumptions as recommended by the New Zealand concrete design standard [NZS3101 1995] taking into account the effect of cracking on member stiffnesses.

Beams: $Ie = 0.35fIg$

Exterior columns: $Ie = 0.6Ig$

Interior columns: $Ie = 0.8Ig$

Where *Ig*: moment of inertia for the gross section.

f: factor for slab effect on cast-in-place T or L beam member stiffness (=1.3 to 1.5 for interior T beams in this study), reflecting the flange contribution to the stiffness in these beams.

The factor *f* is a function of two ratios. One is the ratio of the effective width of the beam flange to the web width. The other is the ratio of the slab thickness to the beam depth. Fig. 2-7 shows the chart from which the coefficient *f* can be obtained.

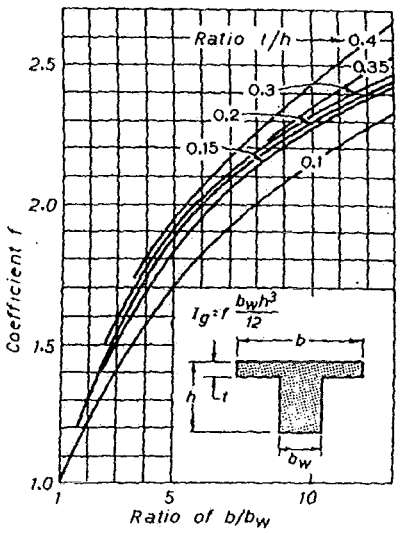

Fig. 2-7 Coefficient for moment of inertia of flanged sections [Paulay 1992]

The effective width of beam flange b shown in Fig. 2-8 is assumed to be the smallest of the following for the interior T beams.

(a) The web width plus eight times the slab thickness (bw+8hs).
(b) The web width plus half of the clear distance to the next web (bw+0.5Lny).
(c) One eighth of the span length of the beam (Lx/8).

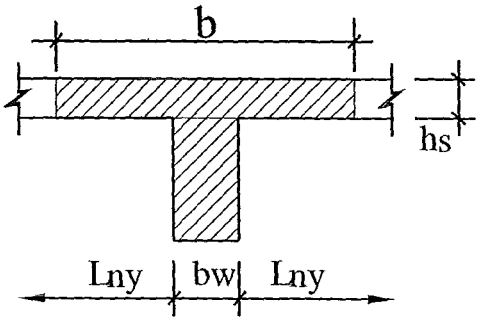

Fig. 2-8 Definition of the T beam properties

92% of the base shear was distributed to be the equivalent static lateral forces at each level, proportioned to the lumped weights and the heights at all levels, as shown in Eq. (2-4):

$$F_i = 0.92V \frac{W_i h_i}{\sum W_i h_i} \quad \text{for } i=1 \text{ to } t\text{-}1 \tag{2-4}$$

where t is the total number of levels

F_i: equivalent static lateral force at level i.

V: horizontal seismic base shear of a structure.

W_i: seismic weight at level i.

h_i: height of level i above the base of the structure.

At the top level of the structure, a remaining horizontal force of 0.08V is added to the value given by Eq. (2-4) and is assumed to consider the effects of higher modes, as shown in Eq. (2-5).

$$F_t = 0.92V \frac{W_t h_t}{\sum W_i h_i} + 0.08V \tag{2-5}$$

where F_t: equivalent static lateral force at top level.

W_t: seismic weight at top level.

h_t: height of the top level above the base of the structure.

It was found that the member sizes of the frames were dominated by the inter-storey drift limitations. The reinforcement of most members was determined by the requirements of the minimum reinforcement ratios. Hence the strengths of the members were larger than those required by the member internal forces of the frames induced by the required combinations of design forces. The objective of this research was to study the structure damage assessment of ductile-framed structures subjected to design earthquake loadings. The earthquake records used in this research should be appropriately scaled to match the requirement of the design standard.

Chapter 3
Mathematical Modelling and Computational Method

3-1 Introduction

A static pushover analysis requires only the elastic and inelastic member stiffnesses and the yield levels in the members i.e. the primary curve of the member moment curvature relationship. However the dynamic inelastic response analysis of ductile frames requires not only the primary curve but the full hysteresis models as well as the mass and the damping models so that the total corresponding structure matrices can be assembled for the equations of motion. An assumed relationship between the accelerations at the start and the end for each time step is also necessary in order to solve the incremental equilibrium equations.

Several different options were available for the modelling of the inelastic members, the mass and the damping, and for time-history integration in RUAUMOKO [Carr 1998]. The Giberson One-Component beam member model, the lumped mass model and the tangent Rayleigh or proportional damping model were chosen for the member, mass and damping models respectively in this research. The rigid end block length was assumed to be equal to half the appropriate member depth for all of the members [Jury 1978]. The plastic hinge length was taken as 70% of the overall section depth for the inelastic members. The hysteresis models and damage assessment models are discussed in Chapter 4 and Chapter 6 respectively.

The total structural stiffness matrix is assembled by the Direct Stiffness Method [Carr 1997A] with the elastic and the inelastic member stiffness matrices. Once the member stiffness was obtained from the Giberson one-component model, the stiffness matrices of all the members in the global coordinate system can be obtained using the principle of virtual displacements. Once the two coefficients for the Rayleigh damping model are computed by specifying the critical damping ratios at two modes, the total structural damping matrix can be obtained from the structural mass and

stiffness matrices. A 5% of critical damping ratio was assigned to the first and sixth mode, the first and twelfth mode, and the first and eighteenth mode for the 6, 12 and 18 storey structures respectively.

The Newmark Constant Average Acceleration model is used for the step-by-step integration analysis [Clough 1993, Chopra 1995, Carr 1998].

3-2 Giberson One-Component Beam Model

The ductile-framed structural models were designed according to the current New Zealand seismic provisions and structural design requirements. The seismic or static responses of all the members are expected to be dominated by their flexural deformations. The contributions of shear and bar slippage components to the member flexibility are small and are neglected in this research. Only the flexural deformations computed from the Giberson one-component model were considered in the members.

The Giberson One-component Model [Giberson 1969], shown in Fig. 3-2, has rigid-plastic rotational springs at the two member ends. All the inelastic deformation of a member is assumed to be concentrated at the member ends, and the central part of the beam is assumed to be elastic.

From the Giberson one-component model, the incremental flexure rotations at the member ends can be obtained from Eq. (3-1) in accordance with the sign conventions specified in RUAUMOKO as shown in Fig. 3-1.

Fig. 3–1 Positive Sign Conventions for Beams Specified in RUAUMOKO

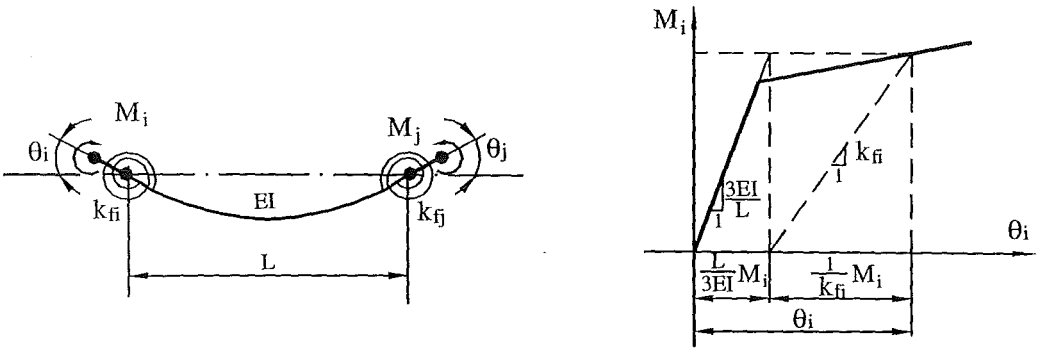

Fig. 3-2 Giberson One Component model and moment-rotation relation at member ends

$$\begin{Bmatrix} \Delta\theta_i \\ \Delta\theta_j \end{Bmatrix}_{flexure} = \textit{Elastic Flexure Rotation} + \textit{Plastic Flexural Spring Rotation}$$

$$= \frac{L}{6EI}\begin{bmatrix} 2 & 1 \\ 1 & 2 \end{bmatrix}\begin{Bmatrix} \Delta M_i \\ \Delta M_j \end{Bmatrix} + \begin{bmatrix} 1/k_{fi} & 0 \\ 0 & 1/k_{fj} \end{bmatrix}\begin{Bmatrix} \Delta M_i \\ \Delta M_j \end{Bmatrix}$$

$$= [f]_{2x2}\begin{Bmatrix} \Delta M_i \\ \Delta M_j \end{Bmatrix} \qquad \textbf{(3-1)}$$

where

$$k_{fi} = \begin{cases} \propto & \textit{Hinge is elastic} \\ 0 & \textit{Hinge is perfectly plastic} \\ \dfrac{EI}{l_p}\left(\dfrac{r_i}{1-r_i}\right) & \textit{Hinge is inelastic} \end{cases}$$

where r_i is the ratio of the inelastic to the elastic stiffness obtained from the moment-curvature hysteresis rule and l_p is the plastic hinge length. It was assumed that the plastic curvature is uniformly distributed along the plastic hinge length as shown in Fig. 3-3.

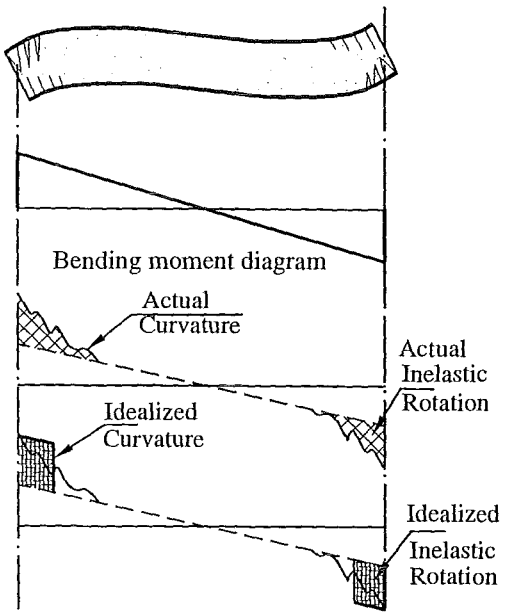

Fig. 3-3 Actual and Idealised Curvature Distribution

The member 2 by 2 flexibility matrix can be obtained from Eq. (3-1). Then the 2 by 2 stiffness matrix can be obtained by inverting the flexibility matrix.

$$[K]_{2\times2} = [f]^{-1}_{2\times2} \tag{3-2}$$

Eventually the 3 by 3 member stiffness matrix is determined from Eq. (3-3).

$$[K]_{3\times3} = \begin{bmatrix} \frac{AE}{L} & 0 \\ 0 & [K]_{2\times2} \end{bmatrix} \tag{3-3}$$

where *AE/L* is the axial stiffness of the beam or column member.

3-3 Rigid End-Blocks

Assumptions in respect of rigid or semi-rigid end-blocks of members can have a significant effect on the stiffness of a frame, its natural frequencies of free vibration and on the response of the structure to dynamic excitation. Some analyses have

indicated a decrease in the natural periods of the order of 10% to 20% when member rigid end-blocks were included [Carr 1994]. When a member connects into large joints, a rigid end-block effect should be considered for the analysis [Carr 1997B]. The natural periods decrease by 18%, 16% and 18 % respectively for the 6, 12 and 18 storey structures used in this research.

The variation of moment along each rigid end-block is linear as shown in Fig. 3-4. For an elastic member with length L_c:

$$\begin{Bmatrix} u_2^c \\ u_3^c \end{Bmatrix} = \frac{L_c}{6EI}\begin{bmatrix} 2 & 1 \\ 1 & 2 \end{bmatrix}\begin{Bmatrix} S_2^c \\ S_3^c \end{Bmatrix} = [f_c]\{S_c\} \tag{3-4}$$

where $[f_c] = \frac{L_c}{6EI}\begin{bmatrix} 2 & 1 \\ 1 & 2 \end{bmatrix}$ is the flexibility of an elastic member which may be replaced by the flexibility of any inelastic model such as the Giberson one-component model, or any other member models (the two component or the variable stiffness model [Carr 1998]).

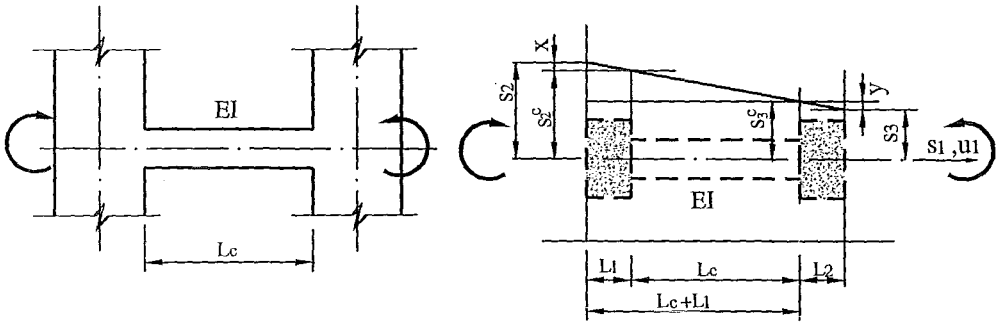

Fig. 3-4 Prototype and model for member with rigid end-block

From Fig. 3-4, the relationship between the member end forces and those at the ends of the rigid end-blocks can be derived:

$$\frac{x}{x + S_2^c - S_3^c} = \frac{L_1}{L_1 + L_c} \tag{3-5a}$$

$$\frac{y}{y+S_2^c-S_3^c}=\frac{L_2}{L_2+L_c} \tag{3-5b}$$

From Eqs. (3-5a,b), we have:

$$x=\frac{L_1}{L_c}\left(S_2^c-S_3^c\right) \tag{3-6a}$$

$$y=\frac{L_2}{L_c}\left(S_2^c-S_3^c\right) \tag{3-6b}$$

So we have

$$\begin{Bmatrix} S_2 \\ S_3 \end{Bmatrix}=\begin{Bmatrix} x+S_2^c \\ -y+S_3^c \end{Bmatrix}=\begin{bmatrix} 1+\frac{L_1}{L_c} & -\frac{L_1}{L_c} \\ -\frac{L_2}{L_c} & 1+\frac{L_2}{L_c} \end{bmatrix}\begin{Bmatrix} S_2^c \\ S_3^c \end{Bmatrix}=[b]\{S_c\} \tag{3-7a}$$

where $[b]=\begin{bmatrix} 1+\frac{L_1}{L_c} & -\frac{L_1}{L_c} \\ -\frac{L_2}{L_c} & 1+\frac{L_2}{L_c} \end{bmatrix}$

From Eq. (3-7a), we have

$$\{S_c\}=[b^{-1}]\{S\} \tag{3-7b}$$

From the principle of virtual work, we have

$$\begin{Bmatrix} S_1 \\ S_2 \end{Bmatrix}^T\begin{Bmatrix} u_2 \\ u_3 \end{Bmatrix}=\begin{Bmatrix} S_2^c \\ S_3^c \end{Bmatrix}^T\begin{Bmatrix} u_2^c \\ u_3^c \end{Bmatrix} \tag{3-8}$$

Substituting Eq. (3-7b) into Eq. (3-8) gives

$$\begin{Bmatrix} u_2 \\ u_3 \end{Bmatrix}=[b^{-1}]^T\begin{Bmatrix} u_2^c \\ u_3^c \end{Bmatrix} \tag{3-9}$$

Substituting Eq. (3-4) and (3-7b) into Eq. (3-9) gives finally

$$\begin{Bmatrix} u_2 \\ u_3 \end{Bmatrix}=[b^{-1}]^T[f_c][b^{-1}]\begin{Bmatrix} S_2 \\ S_3 \end{Bmatrix}=[f]\{S\} \tag{3-10}$$

where the flexibility of the member with rigid end-blocks is:

$$[f] = [b^{-1}]^T [f_c][b^{-1}] \tag{3-11}$$

Hence, the stiffness of the member with rigid end-blocks can be determined by inverting the flexibility matrix $[f]$.

3-4 Member Stiffness Matrix in Global Coordinate System

Once the stiffness matrix $[K]_{3x3}$ of a member is obtained by inverting the flexibility matrix $[f]_{3x3}$ determined using Eq. (3-2) or Eq. (3-11). The stiffness matrix $[K]_{3x3}$ can be transformed to be the $[K]_{6x6}$ in the member local coordinate system with the transformation matrix $[a]$ as shown in Eq. (3-13). Further the $[K]_{6x6}$ in the member local coordinate system will be transformed to be the $[\hat{K}]_{6x6}$ in the global coordinate system of the structure using the transformation matrix $[T]$ as shown in Eq. (3-15).

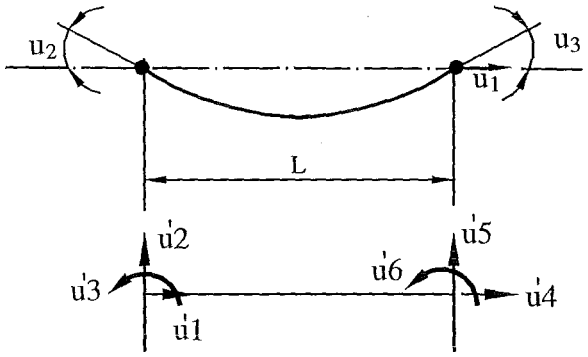

Fig. 3-5 The 6 nodal displacements in local coordinate system and the 3 relative displacements for deriving matrix $[a]$

Fig. 3-5 shows the 6 nodal displacements in local coordinate system and the 3 relative displacements. Considering small displacements in the member, the relative displacement vector $\{u\}$ can be expressed in terms of the nodal displacement vector $\{u'\}$ in the local coordinate system:

$$\begin{Bmatrix} u_1 \\ u_2 \\ u_3 \end{Bmatrix} = \begin{bmatrix} -1 & 0 & 0 & 1 & 0 & 0 \\ 0 & -1/L & -1 & 0 & 1/L & 0 \\ 0 & 1/L & 0 & 0 & -1/L & 1 \end{bmatrix} \begin{Bmatrix} u_1' \\ u_2' \\ u_3' \\ u_4' \\ u_5' \\ u_6' \end{Bmatrix} \qquad \textbf{(3-12a)}$$

$$\text{or } \{u\} = [a]\{u'\} \qquad \textbf{(3-12b)}$$

where the transformation matrix can be calculated from Eq. (3-13), being a function only of the member length.

$$[a] = \begin{bmatrix} -1 & 0 & 0 & 1 & 0 & 0 \\ 0 & -1/L & -1 & 0 & 1/L & 0 \\ 0 & 1/L & 0 & 0 & -1/L & 1 \end{bmatrix} \qquad \textbf{(3-13)}$$

Fig. 3-6 shows respectively the two nodal displacements vectors in the local and global coordinate system of a member. There is an angle θ between the two systems.

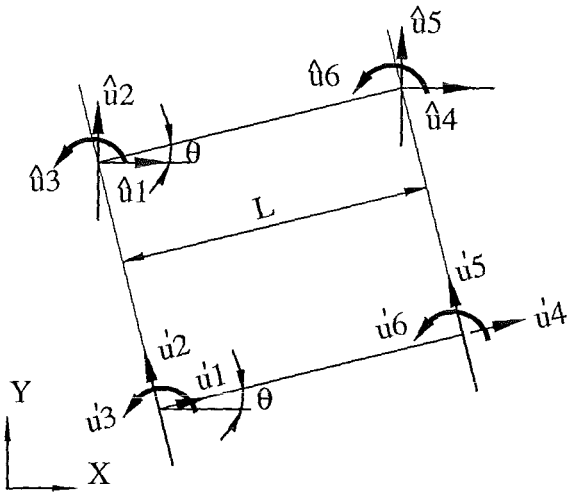

Fig. 3-6 Local and global coordinate systems of a member with angle θ for deriving the transformation matrix [*T*]

The six nodal displacements in the local system can be expressed in terms of the nodal displacements in the global system.

$$\begin{Bmatrix} u_1' \\ u_2' \\ u_3' \\ u_4' \\ u_5' \\ u_6' \end{Bmatrix} = \begin{bmatrix} \cos\theta & \sin\theta & 0 & 0 & 0 & 0 \\ -\sin\theta & \cos\theta & 0 & 0 & 0 & 0 \\ 0 & 0 & 1 & 0 & 0 & 0 \\ 0 & 0 & 0 & \cos\theta & \sin\theta & 0 \\ 0 & 0 & 0 & -\sin\theta & \cos\theta & 0 \\ 0 & 0 & 0 & 0 & 0 & 1 \end{bmatrix} \begin{Bmatrix} \hat{u}_1 \\ \hat{u}_2 \\ \hat{u}_3 \\ \hat{u}_4 \\ \hat{u}_5 \\ \hat{u}_6 \end{Bmatrix} \tag{3-14a}$$

$$\text{or } \{u'\} = [T]\{\hat{u}\} \tag{3-14b}$$

where the transformation matrix can be calculated from Eq. (3-15), being related only to the angle θ between the two system.

$$[T] = \begin{bmatrix} \cos\theta & \sin\theta & 0 & 0 & 0 & 0 \\ -\sin\theta & \cos\theta & 0 & 0 & 0 & 0 \\ 0 & 0 & 1 & 0 & 0 & 0 \\ 0 & 0 & 0 & \cos\theta & \sin\theta & 0 \\ 0 & 0 & 0 & -\sin\theta & \cos\theta & 0 \\ 0 & 0 & 0 & 0 & 0 & 1 \end{bmatrix} \tag{3-15}$$

From principle of virtual displacements, we have:

$$\{u'\}^T\{S'\} = \{u\}^T\{S\} \tag{3-16}$$

$$\{\hat{u}\}^T\{\hat{S}\} = \{u'\}^T\{S'\} \tag{3-17}$$

Substituting $\{u\} = [a]\{u'\}$ into Eq. (3-16) and $\{u'\} = [T]\{\hat{u}\}$ into Eq. (3-17) gives

$$\{S'\} = [a]^T\{S\} \tag{3-18}$$

$$\{\hat{S}\} = [T]^T\{S'\} \tag{3-19}$$

Substituting Eq. (3-18) into Eq. (3-19) gives

$$\{\hat{S}\} = [T]^T\,[a]^T\{S\} \tag{3-20}$$

Substituting $\{S\} = [K]_{3\times3}\{u\}$ and $\{u\} = [a][T]\{\hat{u}\}$ into Eq. (3-20) gives finally

$$\{\hat{S}\} = [T]^T\,[a]^T[K]_{3\times3}[a][T]\{\hat{u}\} \tag{3-21}$$

or $$\{\hat{S}\} = [\hat{K}]_{6\times6}\{\hat{u}\} \tag{3-22}$$

where the member's stiffness matrix in global coordinate system is

$$[\hat{K}]_{6\times6} = [T]^T [a]^T [K]_{3\times3} [a][T] \tag{3-23}$$

3-5 Lumped Mass Model

The lumped mass model assumes that the entire mass of a structure is concentrated at the beam-column joints. There are no inertial forces considered for the rotational degree of freedom at each node. The masses for the translational degrees of freedom of a member are lumped at the member ends, being expressed:

$$m = \frac{1}{2} * \int_0^L m'_{(x)} dx \tag{3-24}$$

where L member length

$m'_{(x)}$ total distributed mass per unit length

For the special case of a beam with a uniform mass per unit length $\overline{m}$, the translational masses will be

$$m = \frac{\overline{m}L}{2} \tag{3-25}$$

The lumped mass matrix of a uniform mass member with six degrees of freedom can be obtained from Eq. (3-26).

$$[M] = \begin{bmatrix} \frac{\overline{m}L}{2} & 0 & 0 & 0 & 0 & 0 \\ 0 & \frac{\overline{m}L}{2} & 0 & 0 & 0 & 0 \\ 0 & 0 & 0 & 0 & 0 & 0 \\ 0 & 0 & 0 & \frac{\overline{m}L}{2} & 0 & 0 \\ 0 & 0 & 0 & 0 & \frac{\overline{m}L}{2} & 0 \\ 0 & 0 & 0 & 0 & 0 & 0 \end{bmatrix} \tag{3-26}$$

The uniform weight per unit length $\overline{m}$ for the beams was assumed to be (Dead Load + 0.24*Basic Live Load) in this research as explained in Chapter 2.

3-6 Tangent Rayleigh or Proportional Damping Model

The damping forces are assumed to be partly proportional to the actual velocities of the degrees of freedom by taking the damping matrix to be partly proportional to the mass matrix of the structure. The damping forces are also assumed to be partly proportional to the relative velocities of the different degrees of freedom by taking the damping matrix to be partly proportional to the varying instantaneous stiffness matrix of the structure [Carr 1997C]. The damping matrix C is given by the expression

$$[C] = a_0[M] + a_1[K] \tag{3-27}$$

where $[M]$ and $[K]$ are the mass and tangent stiffness matrices respectively.

Considering the equations of motion of a structure of N degrees of freedom in the structure subjected to an earthquake excitation with the assumption that the rigid ground acceleration has no effect on the damping and elastic forces [Carr 1997D]:

$$[M]\{\ddot{u} + \ddot{u}_g\} + [C]\{\dot{u}\} + [K]\{u\} = \{0\} \tag{3-28}$$

where $\{\ddot{u}_g\} = \{r\}\ddot{u}_g$ **(3-29)**

$\{r\}$ is the displacement vector of each degree-of-freedom due to unit displacement of the foundation in the direction of the earthquake and $\ddot{u}_g$ is the ground acceleration.

Eq. (3-28) can be rearranged as

$$[M]\{\ddot{u}\} + [C]\{\dot{u}\} + [K]\{u\} = -[M]\{\ddot{u}_g\} = -[M]\{r\}\ddot{u}_g \tag{3-30}$$

where $[M]$, $[C]$ and $[K]$ are the mass, the damping and the stiffness matrices respectively, $\{\ddot{u}\}$, $\{\dot{u}\}$ and $\{u\}$ are the accelerations, the velocities and the displacements vectors of the structure respectively.

The displacements in each degree-of-freedom for an elastic response can be obtained as a combination of the mode shapes of free vibration:

$$\{u\} = [\phi]\{Y\} \tag{3-31}$$

where $\{Y\}$ is the vector of the modal amplitudes and $[\phi]$ is the modal matrix where each column of the matrix is a mode shape.

Substituting Eq. (3-31) into Eq. (3-29) and pre-multiply by $[\phi]^T$ gives

$$[M^*]\{\ddot{Y}\} + [C^*]\{\dot{Y}\} + [K^*]\{Y\} = -\{L^*\}\ddot{u}_{g(t)} \tag{3-32}$$

where

$$[\phi]^T[M][\phi] = [M^*]$$

$$[\phi]^T[C][\phi] = [C^*]$$

$$[\phi]^T[K][\phi] = [K^*]$$

$$[\phi]^T[M]\{r\} = \{L^*\}$$

From the properties of orthogonality, it can be shown that $[M^*]$ and $[K^*]$ are diagonal matrices with the diagonal elements called the generalised mass and generalised stiffness. In order to solve the equations, it is assumed that the properties of orthogonality are also valid for the damping matrix such that the generalised damping matrix $[C^*]$ is also diagonal.

$$M_n^* = \{\phi_n\}^T [M]\{\phi_n\}$$

$$C_n^* = \{\phi_n\}^T [C]\{\phi_n\}$$

$$K_n^* = \{\phi_n\}^T [K]\{\phi_n\}$$

and $$L_n^* = \{\phi_n\}^T [M]\{r\}$$

The N coupled equations of motion are uncoupled into N single degree of freedom systems. For each mode n:

$$M_n^* \ddot{Y}_n + C_n^* \ddot{Y}_n + K_n^* Y_n = -L_n^* \ddot{u}_{g(t)} \quad (n = 1,2,\cdots N) \tag{3-33}$$

For undamped free vibration, Eq. (3-3) is inverted to be:

$$[K_n^* - \omega_n^2 M_n^*]\{\phi_n\} = \{0\} \tag{3-33a}$$

hence $\omega_n^2 = \dfrac{K_n^*}{M_n^*}$ **(3-33b)**

By dividing through by M_n^*, Eq. (3-33) is rewritten as

$$\ddot{Y}_n + 2\xi_n \omega_n \ddot{Y}_n + \omega_n^2 Y_n = -\frac{L_n^*}{M_n^*} \ddot{u}_{g(t)} \tag{3-34}$$

and $\xi_n = \dfrac{C_n}{2M_n^* \omega_n} = \dfrac{C_n}{C_{cr}}$ **(3-35)**

which is the damping ratio or fraction of critical damping for the nth mode.

The critical damping coefficient is

$$C_{cr} = 2M_n^* \omega_n = 2\sqrt{K_n^* M_n^*} = \frac{2K_n^*}{\omega_n} \tag{3-36}$$

The modal damping ratio for mass proportional damping is [Chopra 1995]:

$$C_n^* = a_0 M_n^* \tag{3-37}$$

Substituting Eq.(3-35) into Eq. (3-37) gives

$$2\xi_n \omega_n M_n^* = a_0 M_n^* \text{ and } \xi_n = \frac{a_0}{2\omega_n} \tag{3-38}$$

The modal damping ratio for stiffness proportional damping is:

$$C_n^* = a_1 K_n^* \tag{3-39}$$

Substituting Eq.(3-35) and $K_n^* = \omega^2 M_n^*$ into Eq. (3-39) gives

$$2\xi_n \omega_n M_n^* = a_1 \omega_n^2 M_n^* \text{ and } \xi_n = \frac{a_1 \omega_n}{2} \tag{3-40}$$

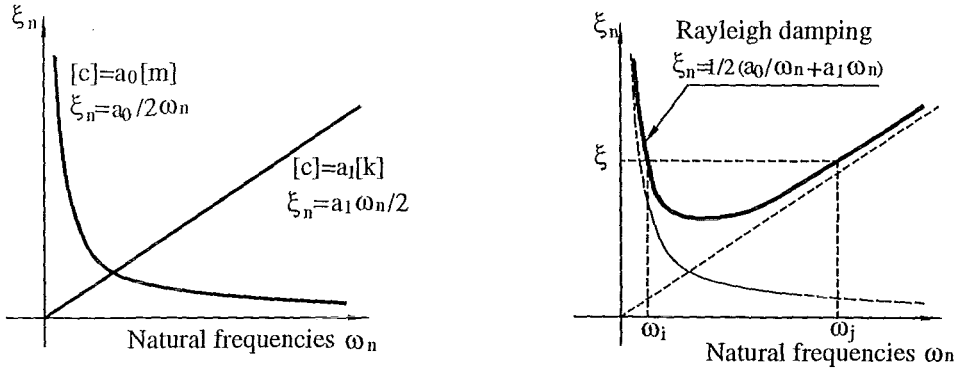

Fig. 3-7 Mass proportional damping, stiffness proportional damping and Rayleigh damping Models

For Rayleigh damping, which is assumed to be proportional to a combination of the mass and the stiffness matrices, the damping ratio is

$$\xi_n = \frac{1}{2}\left(\frac{a_0}{\omega_n} + a_1 \omega_n\right) \tag{3-41}$$

Assuming that ξ_i and ξ_j are the appropriate damping ratios for the *i*th mode at frequency ω_i and the *j*th mode at frequency ω_j, from Eq. (3-41)

$$\begin{Bmatrix} \xi_i \\ \xi_j \end{Bmatrix} = \frac{1}{2}\begin{bmatrix} 1/\omega_i & \omega_i \\ 1/\omega_j & \omega_j \end{bmatrix}\begin{Bmatrix} a_0 \\ a_1 \end{Bmatrix} \tag{3-42a}$$

$$\begin{Bmatrix} a_0 \\ a_1 \end{Bmatrix} = 2\frac{\omega_i \omega_j}{\omega_j^2 - \omega_i^2}\begin{bmatrix} \omega_j & -\omega_i \\ -1/\omega_j & 1/\omega_i \end{bmatrix}\begin{Bmatrix} \xi_i \\ \xi_j \end{Bmatrix} \tag{3-42b}$$

If the fraction of damping is the same at modes i and j, $\xi_i = \xi_j = \xi$, Eq. (3-42b) may be rewritten as

$$a_0 = \xi \frac{2\omega_i \omega_j}{\omega_i + \omega_j} \text{ and } a_1 = \xi \frac{2}{\omega_i + \omega_j} \tag{3-43}$$

Once the damping ratios at these two modes are given, the damping coefficients can be calculated from Eq. (3-42b) or Eq. (3-43). The structural Rayleigh damping matrix can be determined from Eq. (3-27). In the damping model used in these analyses the stiffness matrix used is the tangent stiffness matrix.

3-7 Newmark Constant Average Acceleration [Clough 1993, Chopra 1995, Carr 1998]

This unconditionally stable implicit method assumes that the acceleration variation during a time-step is a constant using the average of the values at the beginning and end of the time step. Hence, the incremental acceleration and velocity for that time-step can be expressed in terms of the acceleration and velocity at the beginning of the time-step, and the incremental displacement for the time-step. Substituting the incremental acceleration and the velocity into the equation of motion at the end of the time-step gives the final equation by which the incremental displacement can be solved.

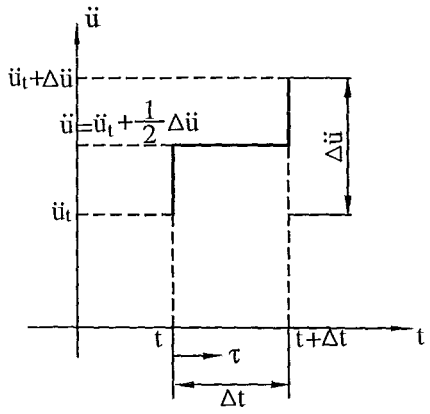

Fig. 3-8 Newmark Constant Average Acceleration Model

During the time-step from time t to time $t+\Delta t$ the acceleration is assumed to be a constant shown in Fig. 3-8, which is:

At time $t+\tau$: $(0<\tau<\Delta t)$

$$\{\ddot{u}_{t+\tau}\}=\{\ddot{u}_t\}+\frac{1}{2}\{\Delta\ddot{u}\} \tag{3-44}$$

Integrating Eq. (3-44) with respect to time over the time step Δt to get the increment in the velocity between time t and τ .

$$\{\Delta\dot{u}_{t+\tau}\}=\int^{+\tau}(\{\ddot{u}\}d_\tau)=\{\ddot{u}_t\}\tau+\frac{\{\Delta\ddot{u}\}}{2}\tau \tag{3-45}$$

The velocity at time $t+\tau$ is:

$$\{\dot{u}_{t+\tau}\}=\{\dot{u}_t\}+\{\Delta\dot{u}\}=\{\dot{u}_t\}+\{\ddot{u}_t\}\tau+\frac{\{\Delta\ddot{u}\}}{2}\tau \tag{3-46}$$

Integrating Eq. (3-46) with respect to time over the time step Δt to get the increment in the displacement.

$$\{\Delta u\}=\int^{+\Delta t}\left(\{\dot{u}_t\}+\{\ddot{u}_t\}\tau+\frac{\{\Delta\ddot{u}\}}{2}\tau\right)d_\tau=\{\dot{u}_t\}\Delta t+\frac{\{\ddot{u}_t\}}{2}(\Delta t)^2+\frac{\{\Delta\ddot{u}\}}{4}(\Delta t)^2 \tag{3-47}$$

From Eq. (3-47):

$$\{\Delta\ddot{u}\}=\frac{4}{(\Delta t)^2}\{\Delta u\}-\frac{4\{\dot{u}_t\}}{\Delta t}-2\{\ddot{u}_t\} \tag{3-48}$$

Substituting Eq. (3-48) into Eq. (3-45) to get the incremental velocity.

$$\{\Delta\dot{u}\}=\frac{2}{\Delta t}\{\Delta u\}-2\{\dot{u}_t\} \tag{3-49}$$

Substituting

$$\{\ddot{u}_{t+\Delta t}\}=\{\ddot{u}_t\}+\{\Delta\ddot{u}\} \tag{3-50}$$

$$\{\dot{u}_{t+\Delta t}\}=\{\dot{u}_t\}+\{\Delta\dot{u}\} \tag{3-51}$$

$$\{u_{t+\Delta t}\}=\{u_t\}+\{\Delta u\} \tag{3-52}$$

into the equation of motion at time $t+\Delta t$:

$$[M]\{\ddot{u}_{t+\Delta t}\}+[C]\{\dot{u}_{t+\Delta t}\}+[K]\{u_{t+\Delta t}\}=\{P_{t+\Delta t}\} \quad \textbf{(3-53)}$$

gives

$$[M](\{\ddot{u}_t\}+\{\Delta\ddot{u}\})+[C](\{\dot{u}_t\}+\{\Delta\dot{u}\})+[K_s](\{u_t\}+\{\Delta u\})=\{P_{t+\Delta t}\} \quad \textbf{(3-54)}$$

where the stiffness term may be rewritten as

$$[K_{t+\Delta t}](\{u_t\}+\{\Delta u\})=[K_t]\{u_t\}+[K_T]\{\Delta u\}=\{F^t_{Elastic}\}+[K_T]\{\Delta u\} \quad \textbf{(3-55)}$$

where $[K_t]$ represents the secant stiffness matrix at time t and the elastic forces are the nodal equivalent of the member forces at time t and the matrix $[K_T]$ is the current tangent stiffness matrix.

Similarly, the damping term may be rewritten in terms of the nodal damping forces and the current tangent damping matrix and the incremental of the velocities.

$$[C_{t+\Delta t}](\{\dot{u}_t\}+\{\Delta\dot{u}\})=[C_t]\{\dot{u}_t\}+[C_T]\{\Delta\dot{u}\}=\{F^t_{Damping}\}+[C_T]\{\Delta\dot{u}\} \quad \textbf{(3-56)}$$

where the damping forces are those at time t and the matrix $[C_T]$ is the current tangent damping matrix.

This means that Eq. (3-54) may be rewritten in the form

$$[M]\{\Delta\ddot{u}\}+[C_T]\{\Delta\dot{u}\}+[K_T]\{\Delta u\}=\{P_{t+\Delta t}\}-[M]\{\ddot{u}_t\}-\{F_{(t)Damping}\}-\{F_{(t)Elastic}\} \quad \textbf{(3-57)}$$

Substituting Eqs. (3-48) and (3-49) into Eq. (3-57) gives eventually

$$\left[\frac{4}{(\Delta t)^2}[M]+\frac{2}{\Delta t}[C_T]+[K_T]\right]\{\Delta u\}=\{P_{t+\Delta t}\}+[M]\left\{\ddot{u}_t+\frac{4}{\Delta t}\dot{u}_t\right\}$$
$$+2[C_T]\{\dot{u}_t\}-\{F_{Damping}\}-\{F_{Elastic}\} \quad \textbf{(3-58)}$$

If the damping matrix is constant, i.e. does not change with time, Eq. (3-58) may be simplified to give the following Eq. (3-59):

$$\left[\frac{4}{(\Delta t)^2}[M]+\frac{2}{\Delta t}[C_T]+[K_T]\right]\{\Delta u\}=\{P_{t+\Delta t}\}+[M]\left\{\ddot{u}_t+\frac{4}{\Delta t}\dot{u}_t\right\}$$
$$+\{F_{Damping}\}-\{F_{Elastic}\} \qquad \textbf{(3-59)}$$

This equation may be solved for the incremental displacements. The displacement, velocity and acceleration vectors can now be updated from Eqs. (3-48) to (3-52) and the member forces at time $t_{t+\Delta t}$ computed giving the elastic force vector and the damping force vector at the new time-step. After updating the damping and stiffness matrices, the above sequence is repeated for the next time-step.

Chapter 4
Hysteresis Models for Reinforced Concrete Members

4-1 Introduction

When carrying out a dynamic inelastic analysis for design or assessment of a building structure, the large earthquake excitations that the structure may be subjected to during its lifetime are unknown. In other words, realistic dynamic loading histories for the structural components are not available. Hence the hysteresis characteristics of the members undergoing realistic dynamic loading histories are not available. However, a static test for simulated earthquake loading histories can be more easily conducted. It has been found that the strain rate is small when a member undergoes seismic inelastic response and the effect on the response is also small [Otani 1980]. The hysteresis characteristics observed in the tests can be applied to represent the dynamic hysteresis characteristics of the members under large earthquake excitations.

The hysteresis behaviour observed in a static tests shows stiffness degradation, strength decay and any pinching phenomenon that the member experiences. The hysteresis models should be capable of simulating any or all of these hysteresis characteristics if they are to capture the real hysteretic behaviour of the members in the structure.

Many hysteresis models have been developed to represent the inelastic behaviour of individual members of reinforced concrete structures under earthquake excitation. For instance, in the computer program RUAUMOKO [Carr 1998], there are over thirty different hysteresis models incorporated, ranging from the simple Elasto-Plastic and Bilinear rules to complex rules that require over thirty parameters to keep track of their current stiffness.

The main hysteresis models for reinforced concrete members can be generally divided into five groups. The first group is the stiffness non-degrading models, such as the Elasto-Plastic and the Bilinear models.

The second group is the stiffness degrading models, i.e. the Clough model [Clough 1966], the degrading Bilinear model, the Takeda model [Takeda 1970], the modified Takeda model, the Riddell and Newmark model [Riddell 1972], the Q-Hyst model [Saiidi 1979], the Imbeault and Nielsen model [Imbeault 1973], and the degrading trilinear model [Magdy 1987].

The third group is the axial force-moment interaction models, the Takayanagi and Schnobrich model [Takayanagi 1976], the Saatcioglu et al. model [Saatcioglu 1980, Saatcioglu 1983] and the Keshavarzian and Schnobrich models [Keshavarzian 1985].

The fourth group is the shear model, such as the Banon, Biggs, and Irvine model [Banon 1981], the Takayanagi and Schnobrich model [Takayanagi 1976], Takayanagi model [Takayanagi 1979], Kabeyasawa et al. [Kabeyasawa 1982] and the Ozcebe and Saatcioglu model [Ozcebe 1989].

The last group is for bar-slip models, the Otani [Otani 1974], Soleimani [Soleimani 1979], the Fillipou model [Fillipou 1983], the Morita and Kaku model [Morita 1984] and the Alsiwat and Saatcioglu model [Alsiwat 1990].

The pinching phenomenon is directly related to shear cracking and bar slippage. Due to the current New Zealand seismic provisions and structural design requirements, and the capacity design method used for the design of the structural models, the responses of the components are expected to be dominated by their flexural behaviour. Shear failures and bar slippage can be suppressed. Further, the effect of interaction of flexural-shear and flexural-bar slippage on the moment-curvature response of properly designed members is small. The pinching phenomenon in the moment-curvature hysteretic response can therefore be dismissed, leaving only the flexurally dominant hysteresis model requirements that are used in this research. If the model is to be used later for research into the behaviour of older structures, this assumption would have to be reassessed.

The hysteresis energy dissipation indices (E_h) [Otani 1981] are very important parameters that quantify the hysteretic energy dissipation capacities for different hysteresis models. Significant variations in member curvature ductilities were observed due to large or small variations in hysteretic energy dissipation indices [Dong 1999]. Hence different hysteresis models with both large and small variations in the hysteretic energy dissipation indices are chosen in this study.

This chapter will cover the study of the stiffness properties, hysteretic characteristics, primary curves, and the flexural dominated hysteresis models and their hysteretic energy dissipation indices, together with the models chosen in this study, for typical reinforced concrete members.

4-2 Stiffness Properties of Reinforced Concrete Members

4-2.1 Strain Rate Effect

There are two reasons that lead to the use of a static force-deformation relationship in a dynamic inelastic analysis. One is that it is technically difficult to conduct dynamic tests under different dynamic loading histories that the real structural components are likely to be subjected to during a large earthquake shaking as the different loading histories are unknown at present. A static test for hysteresis behaviour can be more easily conducted. The other reason is that the strain rate effect on the stiffness is small.

The speed of loading can affect the stiffness and strength of various materials. The investigations on member test results [Otani 1980] show that:

(a) High strain rates increase the initial yield resistance (strength), but cause only a small difference in both stiffness and resistance in subsequent cycles at the same displacement amplitudes.

(b) The strain rate effect on the resistance diminishes with increased deformation in the strain-hardening range of deformation.

(c) No substantial changes were observed in the ductility and the overall energy absorption capacity.

The strain rates in structural members subjected to earthquake force decreases with increasing inelastic deformation, the highest strain rate effect occurs at a low stress levels in the elastic stage. Cracking and yielding of the member reduces the stiffness, elongating the period of the structure's oscillation as the inelastic deformation increases. So the strain rate is gradually diminished. Therefore, the strain rate is small when the members undergo seismic inelastic response and the effect on the response is also small. Therefore, the static hysteresis behaviour observed in a laboratory test can be applied in an inelastic dynamic analysis of reinforced concrete structures [Otani 1980].

Takeda [Takeda 1970] also indicated that a realistic conceptual model for predicting the dynamic response of a reinforced concrete system should be based on a static force-displacement relationship which reflects the changes in stiffness for the loading and unloading as a function of the previous loading history.

4-2.2 Flexural Characteristics From Laboratory Tests

The flexural deformation index (average curvature) is obtained from longitudinal strain measurements at two levels over the depth of a member cross section assuming that a plane section remains plane. This flexural deformation index does not represent the flexural deformation in a strict sense because a plane section does not remain plane in a region where a significant shear deformation occurs. However, the index is useful for a qualitative understanding of the flexural deformation characteristics.

A typical moment-flexural deformation index curve obtained from a simply supported beam test [Celebi 1973] is shown in Fig. 4-1. The stiffness during loading gradually decreases with loading, forming what is referred to as a fat hysteresis loop, absorbing a large amount of hysteretic energy. The hysteresis loops remain almost identical for several loading cycles at the same displacement amplitude beyond

yielding. Therefore, vibration energy can be efficiently dissipated through flexural hysteresis loops without a reduction in resistance.

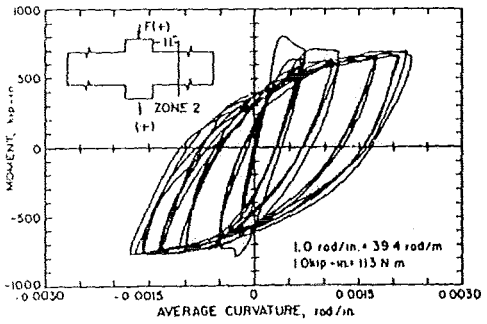

Fig. 4-1 **Flexural Deformation Characteristics [Celebi 1973]**

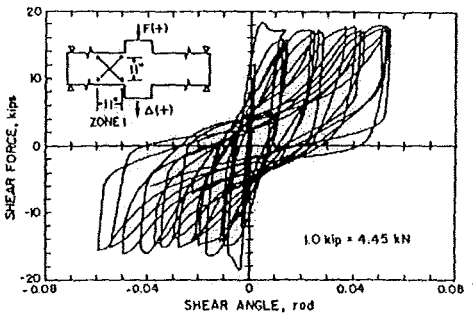

Fig. 4-2 **Shear Deformation Characteristics [Celebi 1973]**

4-2.3 Shear Characteristics

In a manner similar to the flexural deformation index, a shear deformation index is defined from strain measurements in the two diagonal directions. Again, this index does not represent the true shear deformation because of the effect of flexural deformation.

A typical lateral load-shear deformation index curve [Celebi 1973] is shown in Fig. 4-2. Unlike the behaviour that occurs in flexure, the stiffness gradually increases within reloading branches, exhibiting a "pinching" in the curve. The hysteretic energy dissipation is smaller. The "pinching" phenomenon in the hysteresis loops gets more significant with an increase in the number of load reversals, resulting in a smaller stiffness at the same peak displacement in each repeated loading cycle. The pinching in the force-deformation curve is obviously less desirable. However, it is hard to eliminate this undesirable effect when a high shear force exists on the section.

The shear span to effective depth ratio of the member is the most significant parameter in the pinching phenomenon. Decreasing the shear span to depth ratio causes a more pronounced pinching in hysteresis loops and a faster degradation of the hysteretic energy-dissipating capacity. Considerable improvements in delaying and reducing the degrading effects can be accomplished by using closely spaced ties in

the reinforcement in the hinge regions. The presence of a compressive axial force tends to retard the decrease in stiffness and resistance with increasing cycles of inelastic deformation.

4-2.4 Bar Slip and Bond Deterioration

In testing a beam-column subassembly, Bertero and Liu [Bertero 1975, Liu 2001] reported a significant rotation at a beam end caused by the slippage (pullout) of the beam's main longitudinal reinforcement within the beam-column joint, shown in Fig. 4-3. The general shape of the moment-bar slip rotation curve demonstrates a pronounced pinching of a hysteresis loop. The contribution of bar slip to total deformation cannot be neglected, especially in a short or deep stiff member. This phenomenon is very important as the modelling of older structures where plain round longitudinal reinforcement may be present.

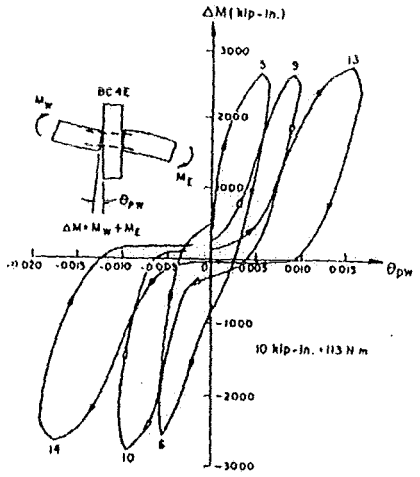

Fig. 4-3 Rotation Due to Bar Slip [Bertero 1975, Liu 2001]

4-3 Hysteretic Characteristics of Reinforced Concrete Members

Reinforced concrete members under inelastic deformation reversals exhibit characteristic features which should be essentially captured in a hysteretic model for the successful representation of the inelastic response of the members.

4-3.1 Stiffness Degradation

Unlike perfectly elasto-plastic materials, reinforced concrete members show stiffness degradation under inelastic load reversals. Degradation of stiffness occurs during reloading and unloading. Once the moment reaches or exceeds the yielding moment M_y in one direction, for instance, the reloading stiffness of all subsequent cycles will degrade because of the cracks caused by the previous inelastic excursion as well as a reduced stiffness of the longitudinal reinforcement due to the Bauschinger effect. The unloading stiffness will be smaller than the initial stiffness $(EI)_e$. Laboratory experiments [Ma 1976] indicated that this softening is more pronounced if the prior inelastic excursion is greater. The greater the degree of inelastic deformation with an increase in the number of inelastic excursions, the greater is the stiffness degradation.

4-3.2 Strength Decay

Reinforced concrete members exhibit progressive loss of strength under cycles of relatively high-level inelastic deformation. The monotonic strength of such members cannot be attained under reversed cyclic loading. Fig. 4-4 illustrates strength decay in a test specimen [Saatcioglu 1989]. The degree of strength decay depends on many parameters including the governing deformation mode, the confinement of the concrete, the shear strength, the history of loading and the level of axial load.

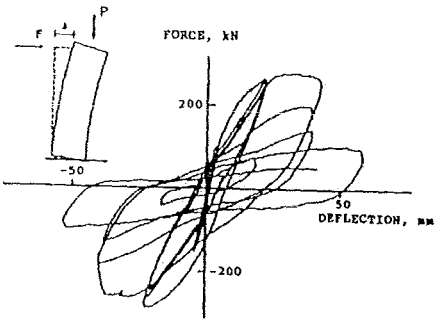

Fig. 4-4 Strength Decay Under Cyclic Loading [Saatcioglu 1989]

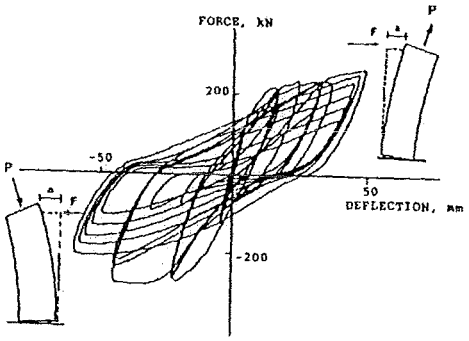

Fig. 4-5 Effect of Variable Axial Force on Hysteretic Behaviour [Saatcioglu 1989]

4-3.3 Axial Force Effects

Substantial levels of axial force variation can be induced in the columns of a framed structure. A variable axial force during the response produces a significant change in the hysteresis loops. Fig. 4-5 illustrates the behaviour of a column specimen subjected to simultaneous axial load and lateral load reversals [Saatcioglu 1989]. It is observed that the presence of axial compression reduces ductility and accelerates strength decay.

4-3.4 Pinching of Hysteresis Loops

Hysteresis loops of reinforced concrete members generally show a marked change in slope during reloading. This change in slope is associated with opening and closing of cracks caused by previous inelastic deformations. Following significant cracking by a load in one direction, a reversed loading in the opposite direction undergoes little initial resistance until the cracks close. Subsequently, the cracked surfaces come into full contact, increasing load resistance. This phenomenon is reflected in the force-deformation relationship as a change in slope during reloading, and is called "pinching" of the hysteresis loops. If the cracks are inclined shear cracks, some sliding occurs between the cracked surfaces before they come in full contact. Also if cracking is associated with bar slip, more deformation takes place in the opposite direction while the reinforcement is slipping back to its previous position before the cracks are closed and full resistance is attained. Therefore, the pinching action is more prevalent in shear force-shear distortion and bond-slip relationships. Fig. 4-3 illustrates pinching action.

4-4 Primary Curve for Reinforced Concrete Members

A primary curve can be obtained by modelling the force-deformation relationship under monotonic loading, providing an envelope to the hysteretic loops. The primary curve may be called a "skeleton," or "backbone" curve. It can be used to define the strength boundary for modelling. This primary curve usually consists of either two or three distinct segments. The two segment primary curve is of a bi-linear relationship

where the first line segment represents the average effective elastic stiffness from zero up to yielding, used in this research work. The average effective elastic stiffness can be obtained from the initial stiffness multiplied by reduction factors for taking the effect of cracking on the member stiffness into account [NZS3101 1995]. The reduction factors are the same as those used in the static analyses for the design of structural models, as shown below:

Beams:	$Ie = 0.35fIg$
Exterior columns:	$Ie = 0.6Ig$
Interior columns:	$Ie = 0.8Ig$

Where Ie: the effective moment of inertia of the section.

Ig: gross moment of inertia of the section.

f: factor for slab effect on beam member stiffness, = 1.3 to 1.5 in this study.

Primary curves used for hysteretic modelling are generally in the form of moment-curvature, moment-rotation, shear force-shear deformation, reinforcement bond-slip, or force-displacement relationships. Sometimes the primary curve can be of three segments. The first segment represents the initial stiffness up to cracking, the second one represents the cracked stiffness up to yielding, and the third one represents the post-yielding stiffness up to the onset of strength decay. Fig. 4-6 illustrates idealisation of a primary moment-curvature relationship. If one is modelling a pristine laboratory member the tri-linear backbone may be important but in general design one may assume that the structure has already been subjected to smaller earthquakes, wind and other environmental loads prior to being subjected to the design level earthquake. Hence a bi-linear model for the backbone may be taken as adequate.

Members under increasing inelastic deformation may exhibit strength decay. In this case, the envelope of the strength-inelastic excursion number relationship has a descending branch. The strength decay was not considered in the modelling for the moment-curvature relationship used in this study. The post yielding stiffness was assumed to be 2.5% of the initial stiffness for all the chosen hysteresis models [Jury 1978].

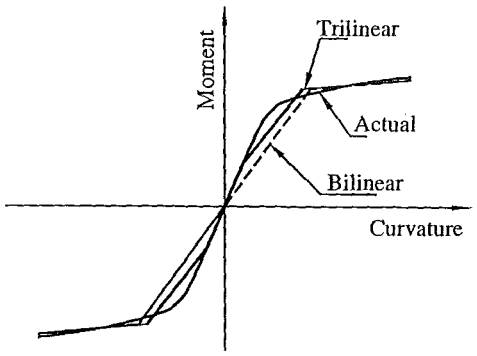

Fig. 4-6 Idealisation of Primary Curve

4-4.1 Primary Moment-Curvature Curve for Reinforced Concrete Members

Based on the assumption that plane sections remain plane even after cracking of the concrete and assuming appropriate stress-strain curves for the reinforcing steel and the concrete, the primary moment-curvature relationship (for monotonically increasing moment) of a beam section can be derived using the method of stress-block factors [Collins 1997]. This method was used in this study.

4-4.1.1 Stress-Strain Representation of Reinforcing Steel and Concrete

The primary stress-strain relationship curve of the reinforcing steel is idealised as a bilinear curve, shown in Fig 4-7. The primary stress-strain relationship curve of the concrete is modelled as a trilinear curve, shown in Fig. 4-8.

The ultimate strength of concrete f_{cu} and associated strain ε_{cu} are functions of the uniaxial cylinder strength $f_c^{'}$ and the amount of confinement steel ρ [Magdy 1987]:

$$f_{cu} = (1+10\rho)f_c^{'} \;;\quad \varepsilon_{cu} = (1+10\rho)\varepsilon_0 \qquad \textbf{(4-1)}$$

where $\rho = 2(b+d)A_s/(bds)$

b, d are the width and depth of the confined core.

A_s the hoop cross-sectional area

s the hoop spacing

The loading branch is represented by a bilinear curve in such a way that the area under the curve is the same as the area under the parabola proposed by Park [Park 1972]. The slope of the first straight line is equal to the initial stiffness of the parabola:

$$f_{cy} = \frac{2}{3} f_{cu}\,; \quad \varepsilon_{cy} = \frac{1}{3}\varepsilon_{cu} \tag{4-2}$$

The coordinate of the cut-off point of the unloading branch can be chosen empirically as:

$$f_m = 0.2 f_{cu}\,; \quad \varepsilon_m = (2 + 600\rho)\varepsilon_{cu} \tag{4-3}$$

Experimental data suggests that concrete members will start to degrade sharply during subsequent load cycles after once reaching the 'ultimate' strain ε_m. This strain may be regarded as the indicator of member failure because the member will sustain only a few load cycles with decreasing strength amplitudes after reaching the critical value ε_m.

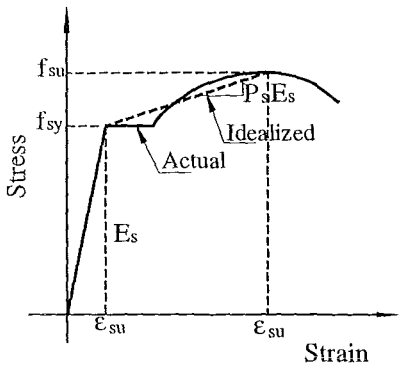

Fig. 4-7 Stress-Strain Law for Reinforcing Steel [Park 1972]

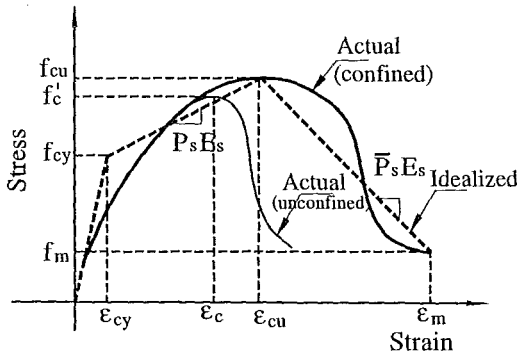

Fig. 4-8 Stress-Strain Law for concrete [Park 1972]

4-4.1.2 Stress-Block Factors Method [Collins 1997]

For a given compressive stress distribution of a rectangular cross section, the stress-block factors α_1 and β_1 as shown in Fig. 4-9 are determined so that the magnitude and location of the resultant forces are the same for the equivalent uniform stress distribution and the actual stress distribution. It requires that:

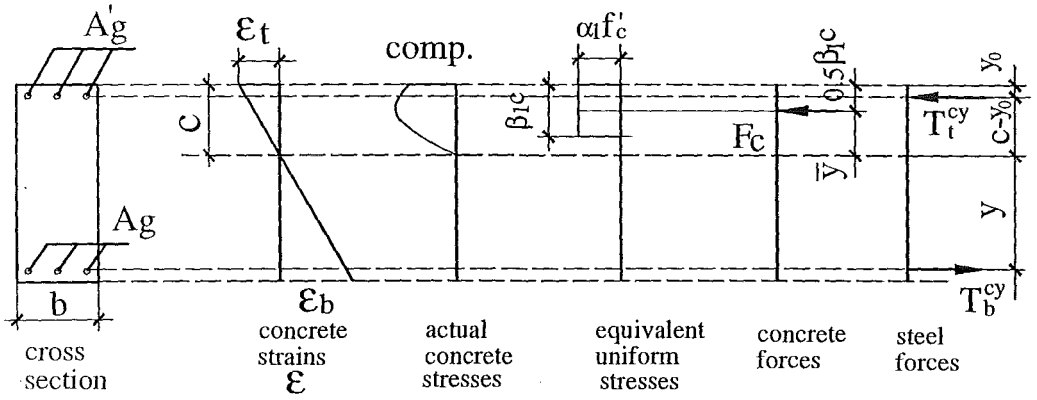

Fig. 4-9 Stress-Block Factors [Collins 1997]

$$\int_0^c f_c b d_y = \alpha_1 f_{cu} \beta_1 c b \tag{4-4}$$

For a parabolic stress-strain curve and a constant width, b, Eq. (4-4) reduces to

$$\alpha_1 \beta_1 = \frac{\varepsilon_t}{\varepsilon_{cu}} - \frac{1}{3}\left(\frac{\varepsilon_t}{\varepsilon_{cu}}\right)^2 \tag{4-5}$$

The requirement that the location of the resultant forces remain the same is

$$\bar{y} = \frac{\int_0^c f_c b y d_y}{\int_0^c f_c b d_y} = c - 0.5\beta_1 c = c(1 - 0.5\beta_1) \tag{4-6}$$

where $\bar{y}$ is measured from the neutral axis (see Fig. 4-8).

For a parabolic stress-strain curve and a constant beam width, b, Eq. (4-6) reduces to

$$\beta_1 = \frac{4 - \left(\varepsilon_t / \varepsilon_{cu}\right)}{6 - 2\left(\varepsilon_t / \varepsilon_{cu}\right)} \tag{4-7}$$

where ε_t and ε_{cu} are the extreme compressive fibre strain and ultimate concrete strain respectively. To determine the primary moment-curvature curve, ε_t should be replaced by the yield strain ε_{cy} and the maximum strain ε_m respectively for the yield moment M_y and the maximum moment M_m, in addition to using the corresponding curvatures.

4-4.1.3 Determination of Curvature and Moment for the Primary Curve

To determine the yielding curvature and moment as well as maximum curvature and moment, a value of ε_b, the concrete strain of extreme tension fibre should be chosen and determined by trial and error, so that it results in zero axial load at equilibrium. The cracking curvature and moment can be similarly derived for the first segment of a trilinear backbone.

The first step is to determine the stress-block factors corresponding to the extreme compressive concrete strain ε_t, which may be, ε_{cy} or ε_m using Eq. (4-5) and Eq. (4-7).

$$\alpha_1^{cy} * \beta_1^{cy} = \frac{\varepsilon_{cy}}{\varepsilon_{cu}} - \frac{1}{3}\left(\frac{\varepsilon_{cy}}{\varepsilon_{cu}}\right)^2; \qquad \beta_1^{cy} = \frac{4 - \left(\varepsilon_{cy} / \varepsilon_{cu}\right)}{6 - 2\left(\varepsilon_{cy} / \varepsilon_{cu}\right)} \tag{4-8}$$

$$\alpha_1^{m} * \beta_1^{m} = \frac{\varepsilon_{cy}}{\varepsilon_{cu}} - \frac{1}{3}\left(\frac{\varepsilon_{m}}{\varepsilon_{cu}}\right)^2; \qquad \beta_1^{m} = \frac{4 - \left(\varepsilon_{m} / \varepsilon_{cu}\right)}{6 - 2\left(\varepsilon_{m} / \varepsilon_{cu}\right)} \tag{4-9}$$

where α_1^{cy} and β_1^{cy} are the stress-block factors when $\varepsilon_t = \varepsilon_{cy}$

α_1^{m} and β_1^{m} are the stress-block factors when $\varepsilon_t = \varepsilon_m$

The second step is to find ε_b^{cy} and $\varepsilon_b{}^m$ so that the axial force N=0. ε_b^{cy} and $\varepsilon_b{}^m$ are the concrete strains of extreme tension fibres corresponding to ε_{cy} and ε_m. In this step, the strain-stress relationship of the reinforcing steel is that shown in Fig. (4-6). N=*0* requires that

$$T_b^{cy} - T_t^{cy} - F_c^{cy} = 0 \tag{4-10}$$

$$T_b^{m} - T_t^{m} - F_c^{m} = 0 \tag{4-11}$$

or

$$A_g * \sigma_b^{cy} - \left(\alpha_1^{cy} * \beta_1^{cy} * f_{cu} * C_{cy} + A_g{}' * \sigma_t^{cy}\right) = 0 \tag{4-12}$$

$$A_g * \sigma_b^{m} - \left(\alpha_1^{m} * \beta_1^{m} * f_{cu} * C_m + A_g{}' * \sigma_t^{m}\right) = 0 \tag{4-13}$$

where T_b^{cy}, T_t^{cy} and F_c^{cy} are the tensile force in the bottom-face steel, the compressive force in the top face steel and the compressive force in the concrete respectively

A_g and $A_g^{'}$ are the total cross-sectional areas of steel at the bottom and the top-faces respectively

σ_b^{cy}, σ_t^{cy}, σ_b^m and σ_t^m are the steel stresses in the bottom and top-faces for $\varepsilon_t = \varepsilon_{cy}$ and $\varepsilon_t = \varepsilon_m$ respectively

The last step is to determine the curvatures and moments corresponding to the strain distributions. The curvatures are

$$\Phi_y = \frac{\varepsilon_t^{cy}}{c_{cy}} \tag{4-14}$$

$$\Phi_m = \frac{\varepsilon_t^m}{c_m} \tag{4-15}$$

Where ε_t^{cy} and ε_t^m are yielding and maximum strain in the extreme compressive concrete fibre. The moments are

$$M_y = T_b^{cy} * y_{cy} - T_t^{cy} * \left(C_{cy} - y_0\right) - F_c^{cy} * \bar{y}_{cy} \tag{4-16}$$

$$M_m = T_b^m * y_m - T_t^m * \left(C_m - y_0\right) - F_c^m * \bar{y}_m \tag{4-17}$$

where the symbols refer to Fig. 4-9 and the superscripts or subscripts, *cy* and *m* represent states of the yielding and maximum strain in the extreme compressive concrete fibre respectively. The primary curvature-moment curve is determined by the four equations (4-14), (4-15), (4-16) and (4-17).

4-4.2 Axial Force-Bending Moment Yield Interaction Surface for First Storey Columns

The first storey columns of structures during a large seismic response are expected to yield as required by the energy-dissipation mechanism as discussed in section 2-2 of Chapter 2. Unlike the beam members whose yield bending moments are not affected by the axial forces, the varying axial forces in those columns have a great effect on the column yield bending moments. In order to track the yield bending moments for the

columns, a cubic relationship between the axial force and yield bending moment is assumed in RUAUMOKO [Carr 1998]. There are seven items required for modelling this cubic relationship illustrated in Fig. 4-10.

P_{yc} is the axial compression yield force at M=0.0. P_b and M_b are respectively the axial compression force and yield bending moment at response point b, which is the end of straight line as shown in Fig. 4-10. M_{1b} and M_{2b} are the yield bending moments at the axial forces $(2/3)P_b$ and $(1/3)P_b$ respectively. M_0 is the yield moment at P=0.0. P_{yt} is the axial tension yield force. There is a cubic curve used from M_0 to M_b and straight lines from P_{yc} to P_b and from M_0 to P_{yt}.

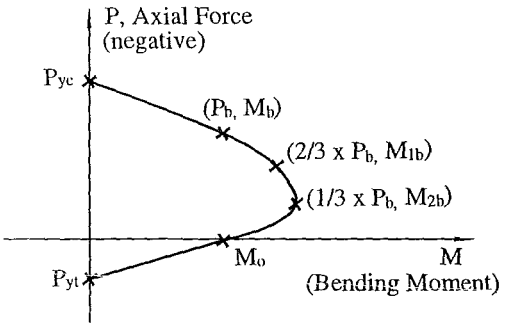

Fig. 4-10 Concrete beam-column yield interaction surface

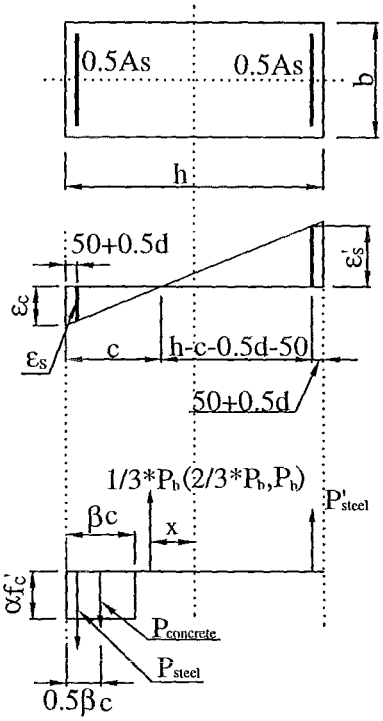

Fig. 4-11 Strain distribution for axial force and bending moment interaction for columns

Fig. 4-11 shows the strain distribution of the concrete and steel for the column section subjected to eccentrically axial force for the case where the concrete cover is 50mm and d is the bar diameter. P_{yc}, P_{yt} and M_0 can be calculated directly from Eq. (4-18), (4-19) and (4-20) respectively.

$$P_{yc} = \left(A_g - A_s\right) * f_c^{'} + A_s * f_y \quad \textbf{(4-18)}$$

$$P_{yt} = A_s * f_y \quad \textbf{(4-19)}$$

$$M_o = 0.5 * A_s * f_y * d \quad \textbf{(4-20)}$$

where d is the internal arm lever.

In this study, the axial force is assumed to lie in the range from zero to that at the balance point. Therefore P_b will be taken as the balance point axial force and the straight line interaction relationship outside the range of interest is insignificant. The ultimate concrete strain and steel yield strain are assumed to be 0.003 and 0.0015 respectively for the calculation of P_b and M_b at the balance response point used in this study, as shown in Fig. 4-12. The value of c can be calculated from Eq. (4-21).

$$c = \frac{1}{3} * (2h - d - 100) \quad \textbf{(4-21)}$$

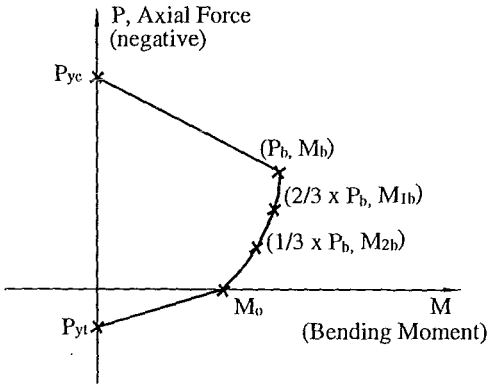

Fig. 4-12 Concrete beam-column yield interaction surface used in this study

When the compressive strain in the steel reaches the yield strain, the forces in the compressive and tensional steel balance each other. From equilibrium in the axial forces, the axial force at the balance response point can be obtained as:

$$P_b = \alpha * f_c^{'} * b * \beta * c \quad \textbf{(4-22)}$$

According the equilibrium in the bending moments, the bending moment at the balance response point can be obtained as:

$$M_{2b} = P_b * x$$

$$= A_s * f_y * (0.5h - 0.5d - 50) + \alpha * f_c^{'} * \beta * c * b * (0.5h - 0.5\beta * c) \quad \textbf{(4-23)}$$

When evaluating the strength of yielding moments for reinforced concrete members, the stress block factors α and β are all 0.85 for $f_c^{'} \leq 55MPa$ as specified in clause 8.3.1.7 [NZS 3101 1995].

For the calculation of M_{1b} and M_{2b}, the following steps are required. First try ε_c to satisfy the equilibrium in axial forces, while checking the steel strain in compression to see whether it reaches the yield point by using Eq. (4-24) and Eq. (4-25) in determining the compressive steel force.

$$c = \frac{\varepsilon_c * (h - 0.5d - 50)}{\varepsilon_c + 0.0015} \tag{4-24}$$

$$\varepsilon_s = \frac{\varepsilon_c * (c - 0.5d - 50)}{c} \tag{4-25}$$

The concrete force in compression is a function of the concrete strain at the extreme fibre and c which can be determined using the stress-block factor method discussed earlier. The steel force in compression can be determined by Eq. (4-26) for $\varepsilon_s \geq 0.0015$ or Eq. (4-27) for $\varepsilon_s < 0.0015$.

$$P_{steel} = 0.5A_s * f_y \tag{4-26}$$

$$P_{steel} = 0.5A_s * E_s * \varepsilon_s \tag{4-27}$$

When the equilibrium of axial forces is satisfied by the trial and error method for $(2/3)P_b$ and $(1/3)P_b$, the yielding bending moments for the two response points then can be obtained from the equilibrium of bending moments.

If $\varepsilon_s \geq 0.0015$

$$M_{1b} \ or \ M_{2b}$$

$$= A_s * f_y * (0.5h - 0.5d - 50) + \alpha * f_c^{'} * \beta * c * b * (0.5h - 0.5\beta * c) \tag{4-28}$$

If $\varepsilon_s < 0.0015$

$$M_{1b} \ or \ M_{2b}$$

$$= 0.5A_s (E_s * \varepsilon_s + f_y)(0.5h - 0.5d - 50) + \alpha * f_c^{'} * \beta * c * b(0.5h - 0.5\beta * c) \tag{4-29}$$

4-5 Hysteresis Models for Flexure Dominated Members

4-5.1 Elasto-Plastic and Bilinear Models

The Elasto-Plastic hysteresis model, shown in Fig. 4-13, is intended for perfectly elasto-plastic materials. The backbone consists of a bi-linear curve. The response point moves on the elastic stiffness line just like any other model in the elastic stage before reaching the yield stress. Once it reaches the yield load, the member is assumed to have zero stiffness until unloading begins. The member stiffness during unloading and reloading beyond the elastic range is the same as the initial elastic stiffness.

The primary curve of the Bilinear model, shown in Fig. 4-14, also consists of two segments as in the Elasto-Plastic model. The only difference between the Bilinear and Elasto-Plastic models is the slopes of the second segments. The stiffness after yielding of the bilinear model is based on the strain hardening characteristics of the reinforcing steel and concrete.

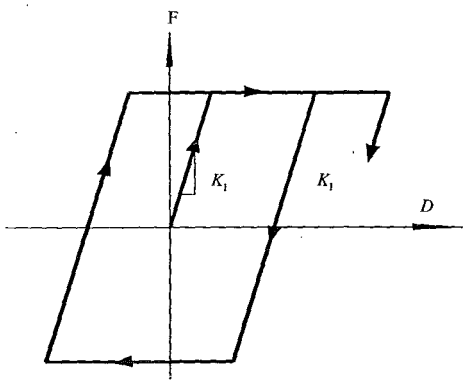

Fig. 4-13 Elasto-Plastic Model

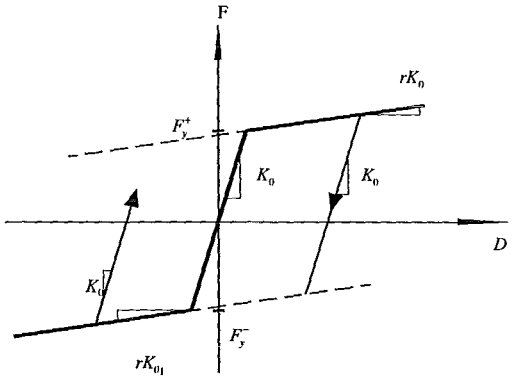

Fig. 4-14 Bilinear Model

These two models do not represent the degradation of unloading and reloading stiffnesses due to inelastic deformation, which is a characteristic feature of reinforced concrete. The energy dissipation during small amplitudes is also not modelled. These two models are not appropriate for a refined nonlinear analysis of a reinforced concrete framed structure.

4-5.2 Degrading Bilinear Model

This model is similar to the Bilinear rule except that the loading and unloading stiffnesses degrade with the previous maximum displacement [Nielsen 1971], shown in Fig. 4-15. The degraded stiffness can be defined by:

$$K_u = K_0\left(\frac{d_y}{d_m}\right)^{\alpha} \tag{4-30}$$

where α: unloading stiffness degrading parameter ($0 < \alpha < 1$).

K_0: initial elastic stiffness

d_y: yielding displacement

d_m: previously attained maximum displacement in any direction

The unloading stiffness will remain constant until the response displacement amplitude exceeds the previous maximum displacement in either direction. If the value of α is chosen to be zero, the unloading stiffness will not degrade with yielding and the degrading bilinear model reverts to the bilinear model. A smaller value of α tends to produce a larger residual displacement. Like the Elasto-Plastic and Bilinear models this model does not dissipate hysteretic energy until yield occurs.

4-5.3 Clough Degrading Stiffness Model [Clough 1966]

This rule, shown in Fig. 4-16, was the first degrading stiffness rule to represent reinforced concrete member hysteretic behaviour. The rule is the same as the modified Takeda rule (see below) when the parameters α and β are both equal to zero. The unloading stiffness after yielding is kept equal to the initial elastic stiffness. The response point during reloading moves toward the previous maximum response point.

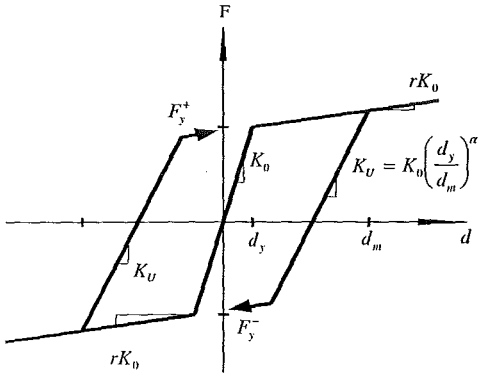

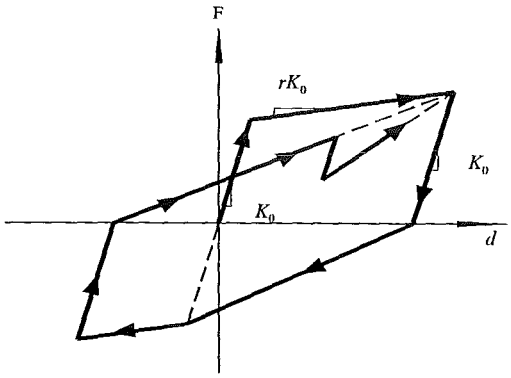

Fig. 4-15 Degrading Bilinear Model [Nielsen 1971] **Fig. 4-16 Clough Degrading Model [Clough 1966]**

The Clough model has two areas of deficiency. On one hand, the model does not consider the degradation of the unloading stiffness, which is one of the characteristic features of reinforced concrete members. On the other hand, the model may over-estimate the softening of the reloading stiffness for the subsequent cycles of small inelastic excursion after a large inelastic excursion. However, in a global sense, when considering both the unloading and reloading paths an effective cyclic reduction of stiffness is observed.

4-5.4 Modified Takeda Model

This rule modified by Otani in 1974 [Otani 1974] and shown in Fig. 4-17, has two stiffness degrading factors α and β. The unloading stiffness after yielding is $(d_y / d_m)^\alpha$ times the initial elastic stiffness k_o, which is similar to the approach used by Emori and Schnobrich [Emori 1978]. The response point during reloading moves toward the point whose displacement is $(d_m - \beta * d_\rho)$, where d_m is the displacement of the previously maximum inelastic response point. Alpha usually ranges from 0.0 to 0.5, while beta is from 0.0 to 0.6. An alternative that is modelled on the Drain-2D program [Kanaan 1973] for the unloading stiffness is available in the program RUAUMOKO [Carr 1998].

Increasing α decreases the unloading stiffness and increasing β increases the reloading stiffness.

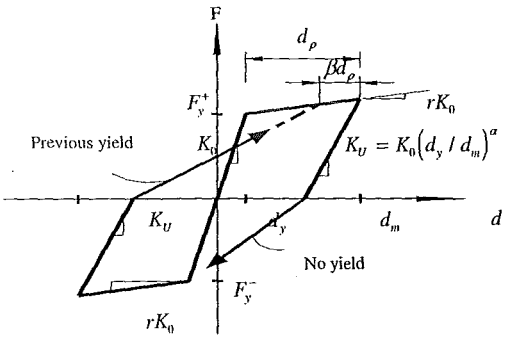

Fig. 4-17 Modified Takeda Model [Otani 1974]

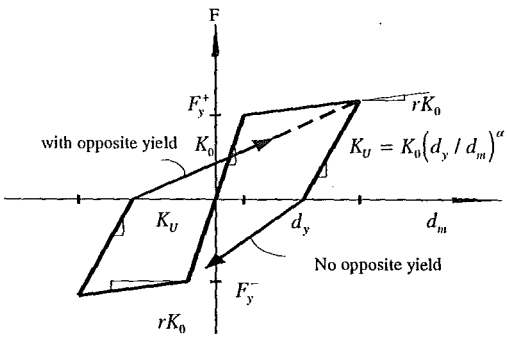

Fig. 4-18 Q-HYST Degrading Model [Saiidi 1979]

4-5.5 Q-Hyst Model

Saiidi and Sozen presented this rule [Saiidi 1979], shown in Fig. 4-18, is the same as the Modified Takeda rule with the parameter β set to 0.0.

4-5.6 Origin-Centred Bilinear Model

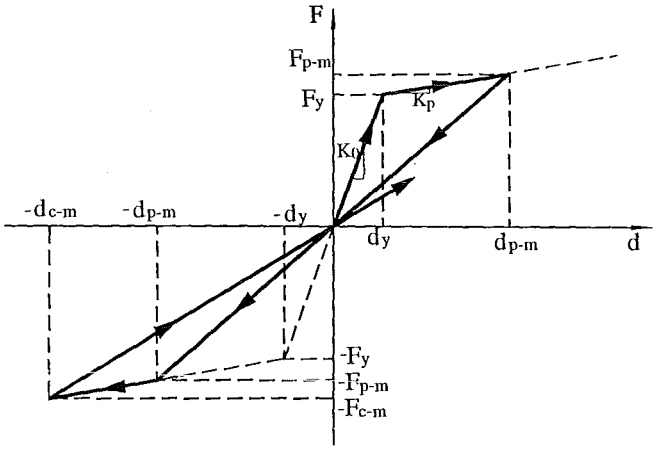

Fig. 4-19 Origin-Centred Bilinear Model [Carr 1998]

Fig. 4-19 shows the Origin Centred model. Once the inelastic displacement occurs, the response point for the unloading and reloading will pass through the origin. The unloading and reloading stiffness will be the same and stay constant until a larger inelastic displacement occurs in either the positive or negative direction. Cycles of smaller inelastic displacements than the previous maximum displacement do not

dissipate hysteretic energy. This is why the model is sometimes also called a non-linear elastic model, though this is not strictly an elastic model.

This hysteresis model cannot reflect the characteristics for concrete member hysteretic responses. However due to the fact that the hysteretic energy dissipation capacity of this model is the minimum of all these considered above, it is used in the study for interest to see what are the differences in the structural responses between this model and the other hysteresis models.

4-6 Hysteretic Energy Dissipation Index (E_h)

The hysteretic energy dissipation capacity of a member can be expressed by a hysteretic energy dissipation index (E_h), which can be obtained from Eq. (4-31) with the hysteresis model for the member [Otani 1981]. The index (E_h) is defined to be the amount of hysteretic energy dissipated Δw per cycle during a displacement cycle of equal amplitudes in the positive and negative directions divided by $2\pi F_m d_m$, where $2\pi F_m d_m$ is the critical viscous damping energy of an equivalent elastic member of stiffness $k_{eq=} F_m / d_m$.

$$E_h = \Delta w / 2\pi F_m d_m \qquad \textbf{(4-31)}$$

where F_m is the resistance at the peak displacement d_m, shown in Fig. 4-20. The value of the index is equal to the equivalent viscous damping ratio of a linearly elastic system which is capable of dissipating energy Δw in one cycle under "resonant steady-state" oscillation.

The force F could be concentrated force and bending moment. The displacement d could be deflection, rotation and curvature. In this research work, all forces and displacements related to hysteresis models refer to bending moment and curvature.

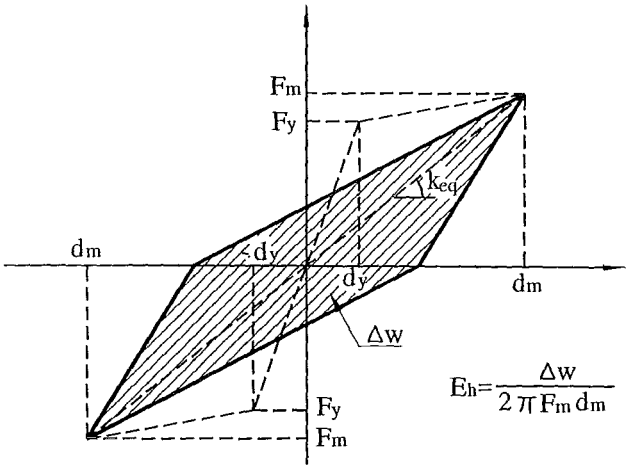

Fig. 4-20 Hysteretic energy dissipation index [Otani 1981]

The hysteretic energy dissipation index of the Elasto-Plastic Model is given by:

$$E_h = \frac{2*(\mu-1)}{\pi*\mu} \tag{4-32}$$

where $\mu = d_m / d_y$ is the ductility factor (ratio of maximum displacement to the initial yield displacement). The equation is only valid if μ>1.0.

The index of the Elasto-Plastic model is a function only of the ductility factor μ. Fig. 4-21 shows the relationship between the hysteretic energy dissipation index and the ductility factor.

The hysteretic energy dissipation index of the Degrading Bilinear model is given by [Otani 1981]:

$$E_h = \frac{2(1-R_p)\{\mu-\mu^{\alpha}(1-R_p+\mu R_p)\}}{\pi\mu(1-R_p+\mu R_p)(1-R_p\mu^{\alpha})} \tag{4-33}$$

where

R_p ratio of post-yielding stiffness to initial elastic stiffness

α unloading stiffness degradation parameter

μ ductility factor (ratio of maximum displacement to the initial yield displacement)

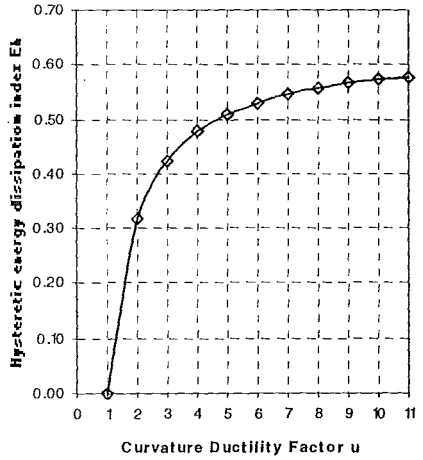

Fig. 4-21 Hysteretic energy dissipation index of the Elasto-Plastic model

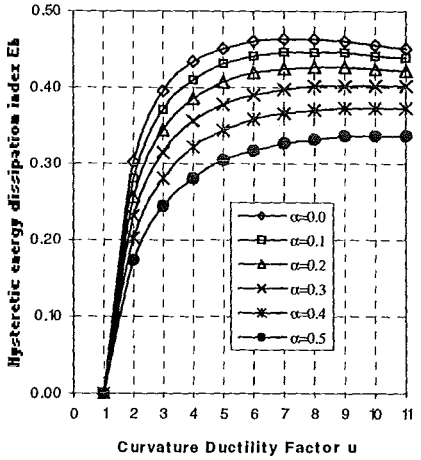

Fig. 4-22 Hysteretic energy dissipation index of the Degrading Bilinear model (R_p=0.025)

The equation is valid only when the ductility factor is greater than unity. Fig. 4-22 shows the relationship between the hysteretic energy dissipation index and the ductility factor for R_p=0.025. The index increases rapidly when the ductility factor increases from 1 to 4. For a given ductility factor, the index decreases with the increase of the unloading stiffness degradation parameter. The hysteretic energy dissipation index of the regular Bilinear model can be obtained from the (4-33) by substituting α=0 shown in Eq. (4-34).

$$E_h = \frac{2(1-R_p)\{\mu-(1-R_p+\mu R_p)\}}{\pi\mu(1-R_p+\mu R_p)(1-R_p)} \tag{4-34}$$

The hysteretic energy dissipation index of the Clough model is derived from Eq. (4-37) by letting $\alpha=\beta$ =0.0:

$$E_h = \frac{1}{\pi} * \frac{(\mu-(1-R_p+\mu R_p))}{\mu} \tag{4-35}$$

The hysteretic energy dissipation index of the Q-Hyst model is derived from Eq. (4-37) by letting β =0.0:

$$E_h = \frac{1}{\pi} * \frac{(\mu-(1-R_p+\mu R_p)*\mu^{\alpha})}{\mu} \tag{4-36}$$

Fig. 4-23 and 4-24 show the relationship between the hysteretic energy dissipation index and the ductility factor for R_p=0.025 for the Clough and Q-Hyst model respectively.

The hysteretic energy dissipation index of the Modified Takeda model is given by [Appendix B]:

$$E_h = \frac{1}{2\pi}\left\{2-\left[R_p(\beta-2)(\mu-1)-2\right]\mu^{\alpha-1}+\frac{2\beta(\mu-1)R_p}{1+R_p(\mu-1)}+\beta\left(1-\frac{1}{\mu}\right)\right\} \qquad \textbf{(4-37)}$$

where R_p ratio of post-yielding stiffness to initial elastic stiffness

α unloading stiffness degradation parameter

β reloading stiffness degradation parameter

μ ductility factor (ratio of maximum displacement to the initial yield displacement)

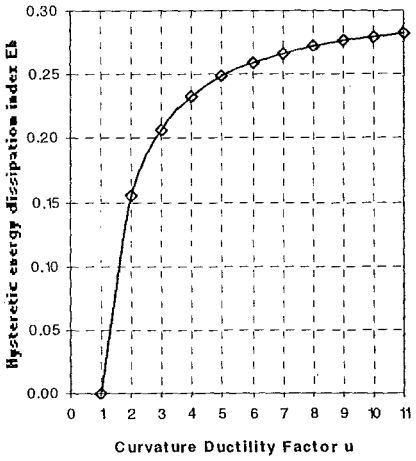

Fig. 4-23 Hysteretic energy dissipation Index of the Clough model

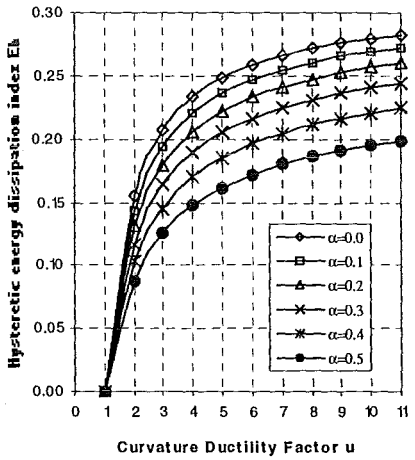

Fig. 4-24 Hysteretic energy dissipation index of the Q-Hyst model (Rp=0.025)

The energy index is a function of the unloading and reloading stiffness degradation parameters, the ratio of post-yielding stiffness to the initial elastic stiffness and the curvature ductility factor. The hysteretic energy dissipation index formula for the Clough and the Q-Hyst models can both be obtained from Eq. (4-37), which are special cases of the modified Takeda model using appropriate choices of parameters. Eq. (4-36) for the Q-Hyst model is the same as Eq. (4-37) with β=0.0. Letting α=β=0.0 leads to Eq. (4-35) for the Clough model.

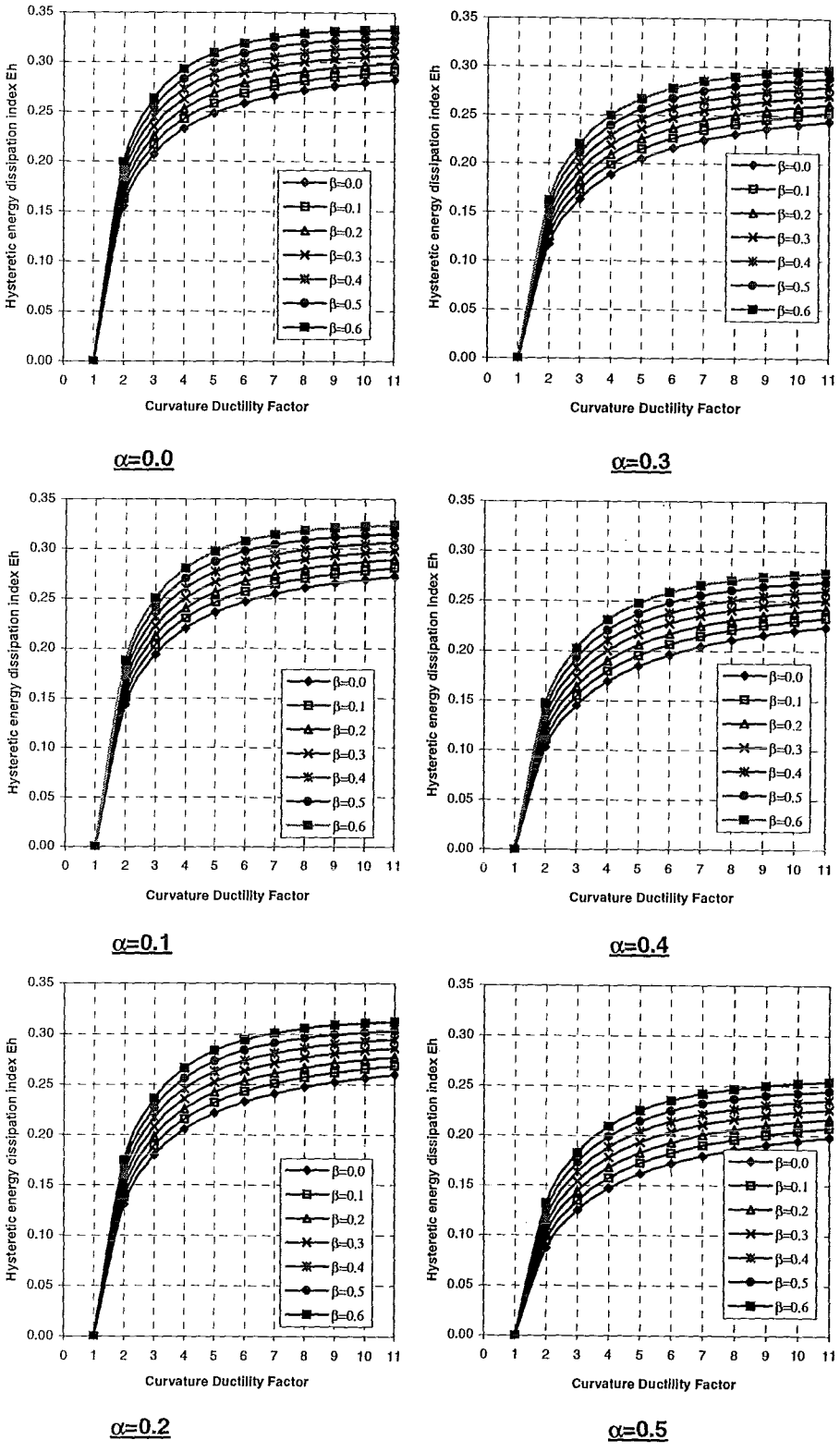

Fig. 4-25 Hysteretic energy dissipation index of the modified Takeda model with constant α (Rp=0.025)

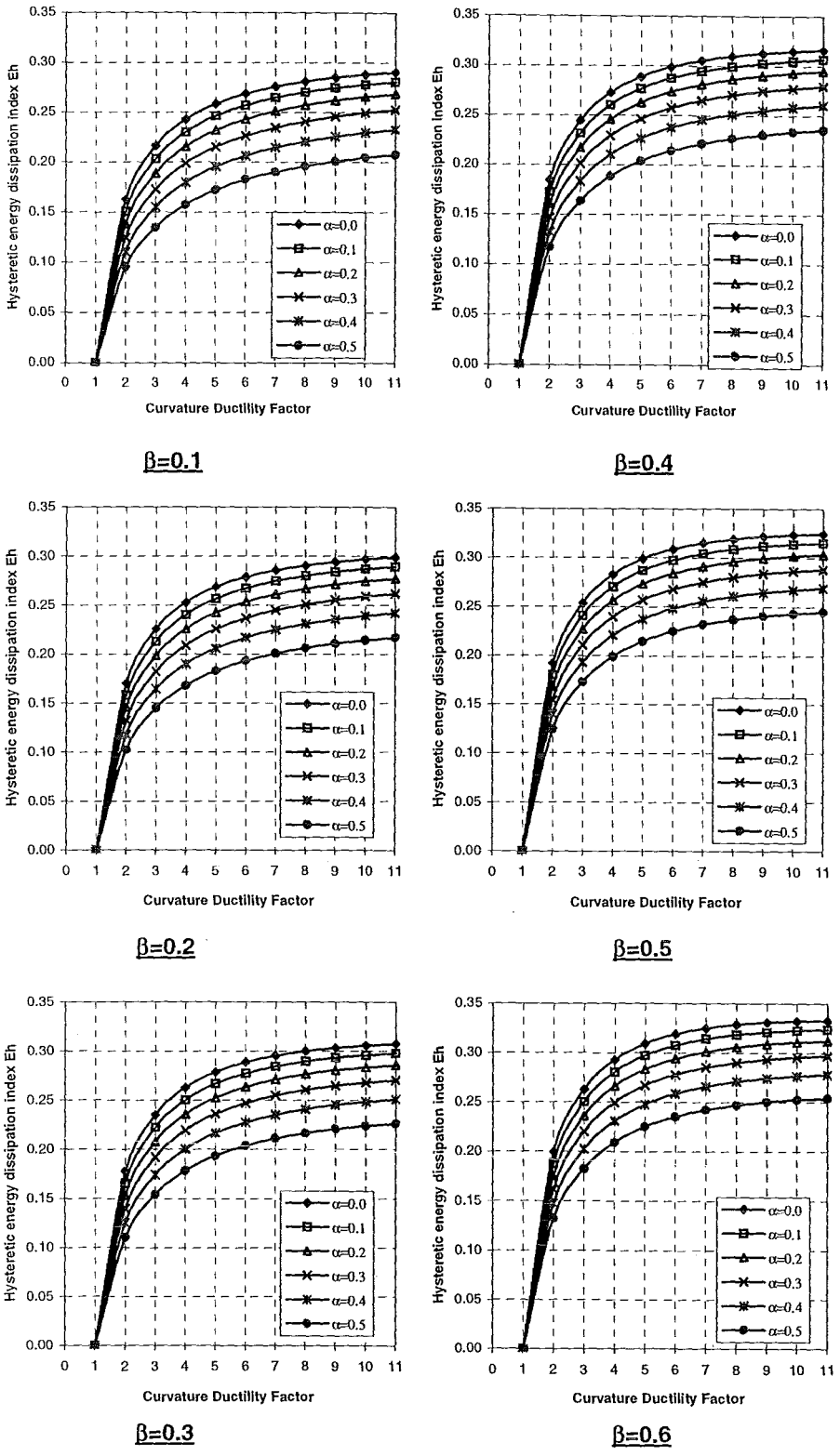

Fig. 4-26 Hysteretic energy dissipation index of the modified Takeda model with constant β (Rp=0.025)

Figs. 4-25 and 4-26 show the relationship between the hysteretic energy dissipation index to the curvature ductility factor with R_p=0.025 for constant α and β respectively. It is observed that for a constant α the index increases with an increase of β, while for a constant β the index increases with a decrease of α. The variation rate of the index due to β variation with constant α is smaller than that due to α variation with constant β.

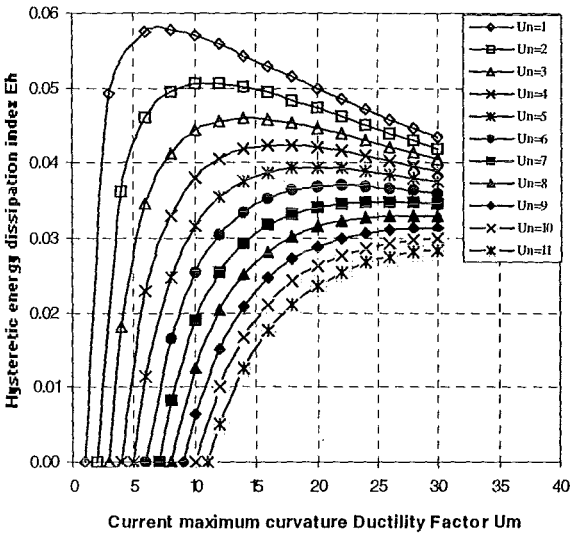

Fig. 4-27 Hysteretic energy dissipation index of the Origin Centred bilinear model (*Rp=0.025*) for different constant μ_n

The hysteretic energy dissipation index of the Origin-Centred bilinear model is given in Appendix C as:

$$E_h = \frac{1}{4\pi}\left[\frac{1+R_p(\mu_n-1)}{1+R_p(\mu_m-1)} - \frac{\mu_n}{\mu_m}\right] \qquad \textbf{(4-38)}$$

where R_p ratio of post-yielding stiffness to initial elastic stiffness

$\mu_n \geq 1.0$, ductility factor for the previous maximum curvature

$\mu_m \geq u_n$, ductility factor for the current maximum curvature

The energy index is a function of the ratio of post-yielding stiffness to the initial elastic stiffness, the previous and the currently maximum curvature ductility factors. There will be no energy dissipation when the currently maximum curvature ductility factor is equal or less than the previous maximum curvature ductility. This is also shown in Fig. 4-27 and Table 4-1.

Table 4-1 Hysteretic Energy Dissipation Indices of the Origin-Centred Bilinear Model for Different Constant Previous Max. Ductility μ_n (R_p=0.025)

μ_m	μ_n =1	μ_n =2	μ_n =3	μ_n =4	μ_n =5	μ_n =6	μ_n =7	μ_n =8	μ_n =9	μ_n =10	μ_n =11
1	0	0	0	0	0	0	0	0	0	0	0
2	-	0	0	0	0	0	0	0	0	0	0
3	0.0493	-	0	0	0	0	0	0	0	0	0
4	-	0.0361	0.0180	0	0	0	0	0	0	0	0
5	-	-	-	-	0	0	0	0	0	0	0
6	0.0575	0.0460	0.0345	0.0230	0.0115	0	0	0	0	0	0
7	-	-	-	-	-	-	0	0	0	0	0
8	0.0578	0.0495	0.0413	0.0330	0.0248	0.0165	0.0083	0	0	0	0
9	-	-	-	-	-	-	-	-	0	0	0
10	0.0570	0.0507	0.0443	0.0380	0.0317	0.0253	0.0190	0.0127	0.0063	0	0
11	-	-	-	-	-	-	-	-	-	-	0
12	0.0558	0.0507	0.0456	0.0406	0.0355	0.0304	0.0254	0.0203	0.0152	0.0101	0.0051
14	0.0544	0.0502	0.0460	0.0418	0.0376	0.0335	0.0293	0.0251	0.0209	0.0167	0.0125
16	0.0529	0.0494	0.0458	0.0423	0.0388	0.0353	0.0317	0.0282	0.0247	0.0212	0.0176
18	0.0514	0.0484	0.0454	0.0423	0.0393	0.0363	0.0333	0.0302	0.0272	0.0242	0.0212
20	0.0500	0.0473	0.0447	0.0421	0.0395	0.0368	0.0342	0.0316	0.0289	0.0263	0.0237
22	0.0486	0.0463	0.0439	0.0416	0.0393	0.0370	0.0347	0.0324	0.0301	0.0278	0.0254
24	0.0472	0.0452	0.0431	0.0411	0.0390	0.0369	0.0349	0.0328	0.0308	0.0287	0.0267
26	0.0459	0.0441	0.0422	0.0404	0.0386	0.0367	0.0349	0.0331	0.0312	0.0294	0.0275
28	0.0447	0.0430	0.0414	0.0397	0.0380	0.0364	0.0347	0.0331	0.0314	0.0298	0.0281
30	0.0435	0.0420	0.0405	0.0390	0.0375	0.0360	0.0345	0.0330	0.0315	0.0300	0.0285

Note: "-" shows values not computed.

It is observed from Fig. 4-27 that the larger the previous maximum curvature ductility, the smaller the hysteretic energy dissipation index is for a constant value μ_m. For a smaller constant value μ_n, say μ_n<7.0, the E_h curves increase sharply for the lower values μ_m and then goes down with a descending path that is flatter for a larger μ_n. For a larger constant value μ_n, say μ_n>7.0, the E_h curves increase sharply for the lower values μ_m and then stay relatively unchanged.

Table 4-2 shows the hysteretic energy dissipation indices of the Elasto-Plastic, Bilinear and Clough models for curvature ductility factor μ=5. Table 4-3 shows the indices of the Degrading Bilinear model for μ=5. Table 4-3 shows the indices of the Modified Takeda model for the different combinations of α and β for μ=5. The values of indices in the first column in Table 4-4 when β=0.0 for the Modified Takeda model are also the indices of the Q-Hyst model.

Table 4-2 Hysteretic Energy Dissipation Indices of the Three Hysteresis Models (μ=5)

No.	Model Name	α	β	R_p	E_h
1	Elasto-Plastic	-	-	0.00	0.509
2	Bilinear	-	-	0.025	0.451
3	Clough	-	-	0.025	0.248

Table 4-3 Hysteretic Energy Dissipation Indices of the Degrading Bilinear Model (μ=5 and Rp=0.025)

α=0.0	*α=0.1*	*α=0.2*	*α=0.3*	*α=0.4*	*α=0.5*
0.451	0.431	0.407	0.378	0.344	0.304

Table 4-4 Hysteretic Energy Dissipation Indices of the Modified Takeda models (μ=5 and R_p=0.025)

α \ β	*0.0*	*0.1*	*0.2*	*0.3*	*0.4*	*0.5*	*0.6*
0.0	0.248	0.258	0.269	0.278	0.289	0.299	0.309
0.1	0.236	0.246	0.257	0.267	0.277	0.287	0.297
0.2	0.222	0.232	0.242	0.253	0.263	0.273	0.283
0.3	0.205	0.215	0.226	0.236	0.246	0.257	0.267
0.4	0.185	0.196	0.206	0.216	0.227	0.237	0.248
0.5	0.162	0.172	0.183	0.193	0.204	0.215	0.225

4-7 Hysteresis Models Used in This Research Work

In order to limit the number of hysteresis models used, eight hysteresis models were chosen in this research work as shown in Table 4-5. This was in an attempt to cover the different kinds of hysteresis models for flexure dominated reinforced concrete members and the variety in hysteretic energy dissipation indices. The Elasto-Plastic and Bilinear models are used for comparison, as they were the models used in many earlier studies on the earthquake response of reinforced concrete structures [Jury 1978]. Due to the Modified Takeda model can model the unloading and reloading

stiffness degradation that best fit the tested hysteretic behaviour, two set of α and β were chosen for check of sensitivity of varying α and β to the results.

Table 4-5 Hysteretic Energy Dissipation Indices of the Eight Hysteresis Models (μ_n =5)

No.	*Model Name*	α	β	R_p	E_h	Note
1	Elasto-Plastic	-	-	0.00	0.509	-
2	Bilinear	-	-	0.025	0.451	-
3	Modified Takeda	0	0.6	0.025	0.309	-
4	Degrading Bilinear	0.5	-	0.025	0.304	-
5	Clough	-	-	0.025	0.248	-
6	Modified Takeda	0.3	0.4	0.025	0.246	-
7	Q-Hyst	0.5	-	0.025	0.162	-
8	Origin-Centred	-	-	0.025	0.058	μ_n =1.0 *and* μ_m =8.0

4-8 Conclusions

The strain rate effect on the stiffness of members is small. The hysteresis force-deformation relationship observed from the static tests in the laboratory can be applied in the inelastic analysis of reinforced concrete structures subjected to extreme earthquake shaking. The primary curve of the moment-curvature relationship can be determined using the stress-block factors method.

Reinforced concrete members under inelastic deformation reversals may show characteristics such as shear cracking and bar-slippage related pinching, unloading and reloading stiffness degradation, and axial force effects for columns etc. The modelling for member inelastic behaviour should be able to capture any of these characteristics that are required to match the realistic hysteresis responses of the member.

The hysteretic energy dissipation capacity of flexure dominated hysteresis models: the Elasto-Plastic, Bilinear, Clough, Degrading Bilinear, Q-Hyst and the modified Takeda, and Origin-Centred model were studied. For a ratio of post-yielding stiffness to the initial elastic stiffness of R_p=0.025, the Origin-Centred model has the smallest magnitude of hysteretic energy dissipation index of all the models used in this study while the energy dissipation indices of the Elasto-Plastic and Bilinear models have the largest magnitude of all the hysteresis models considered in this study.

Chapter 5
Input Earthquake Excitations and Scaling Methods

5-1 Introduction

5-1.1 Term Definitions

For convenience some terms used in this chapter for design and maximum response of the 6-, 12- and 18-storey structures should be defined first of all, as shown below.

The design base shear:

The design base shear of the elastic structures ($\mu = 1.0$) for an intermediate soil site [NZS4203 1992].

The design inter-storey drift:

The maximum value of the inter-storey drifts for each level obtained using the SRSS method with the design displacement spectrum derived from the design acceleration spectrum of the current New Zealand loading standard [NZS4203 1992] as shown in Eq. 5-2.

The maximum base shear:

The largest absolute value obtained during the time history of the base shear available from an elastic dynamic time-history analysis.

The maximum inter-storey drift:

The largest absolute value observed over all stories in the structure during the time histories from an elastic dynamic time-history analysis.

5-1.2 Introduction

Four different natural earthquake records, i.e. Bucharest (1977-NS), El Centro (1940-NS), Northridge (Sylmar-949NW) and Kobe (1995-NS) were chosen for earthquake inputs for the inelastic time-history analyses, as presented in Chapters 7 and 8.

The four natural earthquake records should be scaled so as to match the intensity at design level implied in the current standard [NZS4203 1992] before being used as earthquake inputs for the inelastic time-history analyses. The objectives of the study of this chapter were to obtain scaling factors for these four earthquake records for each of the three structures and to generate a general means for earthquake scaling.

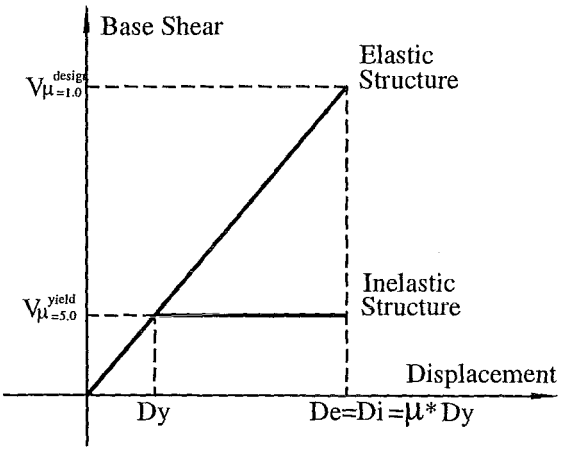

Fig. 5-1 Equal displacement principle for a ductile structure of ductility μ=5.0

According to the Equal Displacement Principle [Newmark 1960] as shown in Fig. 5-1, for long period structures, the inelastic structure has a similar magnitude of maximum displacement to that of an identical structure that is constrained to remain linearly elastic. This implies that for long period structures, the standard design level earthquakes of the inelastic structure for inelastic time history analyses should be those that are able to produce the maximum response values, which are similar to the standard design level base shear and the standard design level displacements (inter-storey drift) for this elastic structure. The maximum base shear and the maximum displacements, which are related to the inter-storey drifts of the elastic structure, are used to assess the intensity of an excitation for the inelastic structure and should match the corresponding design responses for the scaled earthquakes.

Clause 4.10.2 in NZS4203: 1992 requires that "scaling should be such that over the period range of interest for the structure being analysed, the 5% damped spectrum of the earthquake record does not differ significantly from the design spectrum for the limit state being considered". This implies that the maximum base shear of the elastic structure under the ideally scaled earthquake records should match the design base shear associated with the design acceleration spectra.

There are two ways for the maximum base shear to satisfy the design requirement in base shear for the scaled earthquakes, in general, as discussed in the later section 5-6. One is to have the maximum base shear match the design value directly. The other is to match the design base shear by matching the design spectral accelerations for the first few modes of free-vibration, which dominate the maximum base shear of the structure.

The potential problem is that the maximum base shear obtained from the scaled earthquakes for all current scaling methods as shown in the following section 5-2 may not be able to match standard design base shear as expected.

Furthermore, for these current scaling methods, although when the design base shear is matched, for example, the maximum inter-storey drift for the scaled earthquakes may be very much smaller than design inter-storey drift for a structure when subjected to some certain types of earthquake. For a case where all earthquake records chosen as earthquake inputs for the inelastic dynamic analyses are one of these types of earthquake, all predicted maximum inter-storey drifts would be very much smaller than the design inter-storey drift. This would lead to unsafe predictions when compared to those earthquakes for which both the maximum base shear and maximum inter-storey drift are not less than the corresponding design values for these same earthquake scaling methods. This is dependent on the earthquake type. Therefore for an appropriate earthquake scaling method, both the maximum base shear and maximum inter-storey drift to the scaled earthquakes may be required to be close to, and to be not less than, the corresponding design values.

In order to have an appropriate earthquake scaling method, six different scaling methods that are outlined in the later section 5-6 of this chapter are applied to scale the four earthquakes for the three structures. By comparing the maximum responses (the maximum base shears, inter-storey drifts and spectral accelerations) to the scaled earthquakes with the corresponding design requirements, a procedure for earthquake scaling is found, leading to the scaling factors of the four excitations for the three structures.

The design acceleration spectrum for an intermediate soil site is available in the loading standard [NZS4203 1992] for design base shears. The design displacement spectrum is not given in the standard and is derived on the relationship between the spectral acceleration and the spectral displacement for a single degree of freedom system for the calculation of the design inter-storey drifts of the three structures.

5-2 Review of Current Earthquake Scaling Methods

The scaling methods were not given in either the New Zealand Standard [NZS4203 1992] or the codes for any other country around the world [Regulation 1996].

Moss and Carr [Moss 1999] summarised four kinds of scaling methods most widely used for earthquake scaling, which are listed below:

(1) Scale the peak acceleration to about 0.4 to 0.5g.
(2) Scale the record so as to match the design spectrum at the first mode period of free vibration of the structure.
(3) Scale the record so as to match the design spectrum in a range of period of free vibration of interest.
(4) Scale the record to match the design spectrum at all frequencies.
(5) Artificial record produced by using software programme SIMOKE [Carr 1998].

Pradono [Pradono 1998] used the spectrum scaling method at the first mode period and Lin [Lin 1999] used the frequency scaling method in their research works. For the frequency scaling method, an unscaled earthquake record is transformed into the frequency domain and the response at every frequency is scaled so that the record matches the design spectrum without changing the phase characteristics. The scaled record is then transformed back into the time domain. All the artificial records produced using either the frequency scaling method or the software SIMOKE are not natural earthquakes. There are no natural earthquake records which will match the code spectra over the whole natural period range as the code spectra are designed to encompass large earthquakes a great distance away from the site and small earthquakes close to the site. The former will give greater accelerations in the long natural period range and the latter greater accelerations in the shorter natural period range. Any generated earthquake that matched the whole code spectrum is therefore unrealistic.

Charng [Charng 1998] used three different scaling methods belonging to kinds 2 and 3 above. By comparing the maximum base shears of structures under the scaled excitations with the corresponding design base shears, appropriate scaling factors were determined producing maximum base shears closer to the design ones. The three scaling methods are shown below:

(1) Scaled at the fundamental period of free vibration of the structures.

(2) An average of scale factors for the fundamental, second and third modal periods of free vibration of the structures.

(3) Weighted average of scale factors for the fundamental (weight 2), second (weight 1) and third (weight 1) modal periods of free vibration of the structures.

Satyarno [Satyarno 2000] scaled the maximum base shear of a structure under a natural earthquake record to match the design base shear of the structure directly. This scaling method is one of the design-response scaling methods. The draft of Australia/New Zealand Standard [AS/NZS 1170] introduces the record scale factor k1 and the family scale factor k2, trying to scale earthquakes so as to match the target or design spectra of period range of interests. A similar scaling method that tries to match design spectra is found in FEMA [FEMA356 2000], which belongs to the design-spectrum scaling as discussed in section 5-6.

There is a potential problem in all of the scaling methods used by the researchers discussed above. All of these methods have not been checked to make sure that the maximum base shears of the structures excited by these scaled earthquakes are able to match the design base shears.

5-3 Design Response Spectra

The design acceleration spectrum was calculated from Eq. (5-1), which was 80% of the basic seismic hazard acceleration coefficient for the assumed site for this study in Christchurch, New Zealand.

$$C_{a(T)}^{design} = C_{(T,\mu=1.0)} * Sp * R * Z * Lu$$
$$= 0.8 * C_{(T,\mu=1.0)} \qquad \textbf{(5-1)}$$

where $C_{a(T)}^{design}$ design spectral acceleration coefficient.

$C_{(T,\mu=1.0)}$ basic seismic hazard acceleration coefficient for intermediate soil site and $\mu=1.0$ (elastic).

Sp =1.0 structure performance factor for elastic time history analysis [C4.6.2.7, C4.6.2.8 and C4.6.2.9 NZS4203: 1992]

R =1.0 risk factor for building category IV [C4.6.2.4 NZS4203: 1992]

Z =0.8 for Christchurch, zone factor

Lu =1.0 limit state factor

The basic seismic hazard acceleration coefficient spectra for rock, intermediate and flexible soil sites were given in NZS4203: 1992, as shown in Fig. 5-2. Only the one for the intermediate soil site and ductility $\mu=1.0$ was used in this chapter for the design acceleration spectrum.

5-4 Assumptions Used for the Elastic Time-History Analysis

In order to obtain the maximum responses (base shear and inter-storey drift) of the three structures under the four earthquakes scaled by using the six scaling methods, elastic time-history analyses were carried out using RUAUMOKO [Carr 1998]. The assumptions and mathematical modelling used were:

(1) The floors were assumed to be rigid in their own planes. All the nodes at each level were coupled so that each had the same horizontal displacement.

(2) The foundations were assumed to be fixed without taking any soil-structure interaction effects into account.

(3) A lumped mass model was used.

(4) Large displacement option was selected. Effects of large displacements allowing for the P-Delta effects on member flexibility and the nodal coordinates was considered and updated in every time step automatically in the software.

(5) Initial stiffness Rayleigh damping model was used to represent the damping in the structure. The 5% critical viscous damping ratio, which is assumed for most standard design spectra, was assigned to the first and sixth, the first and twelfth, the first and eighteenth modes for the 6, 12 and 18 storey structures respectively.

(6) Newmark constant average acceleration model (β=0.25) was used for the time-history integration of the response.

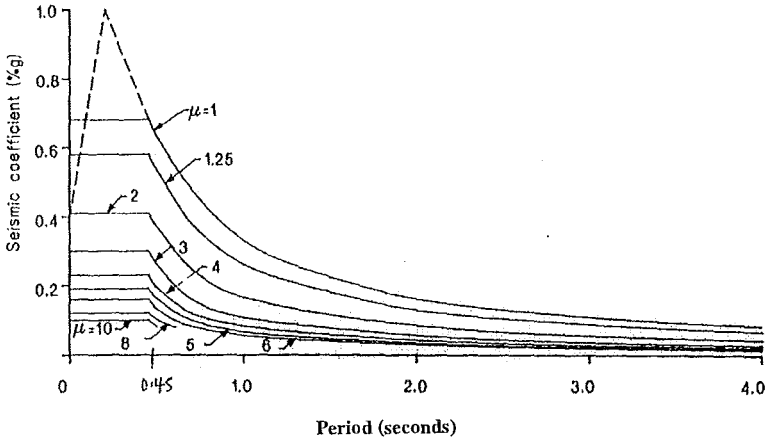

(a) For rock or very stiff soil sites

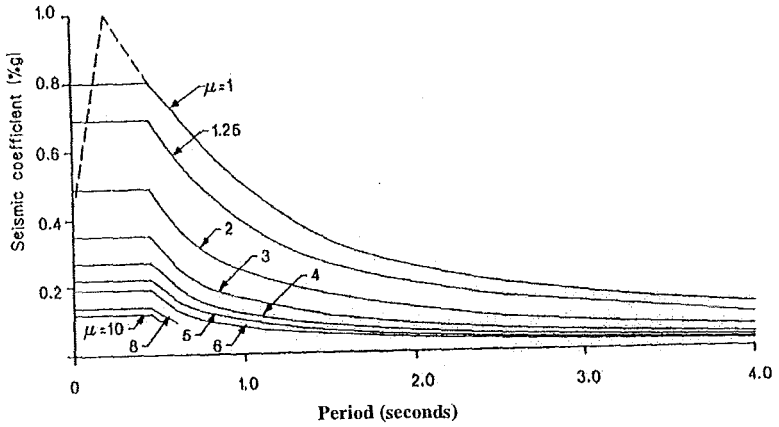

(b) For intermediate soil sites

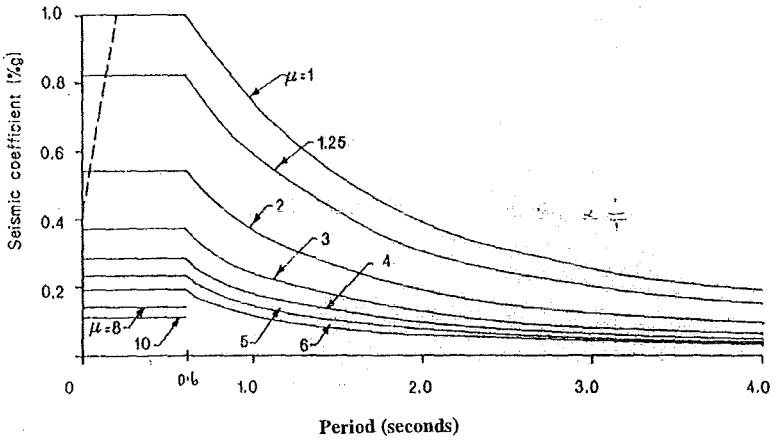

(c) For flexible or deep soil sites

Fig. 5-2 Basic seismic hazard acceleration coefficient spectra for three different soil sites [NZ4203 1992]

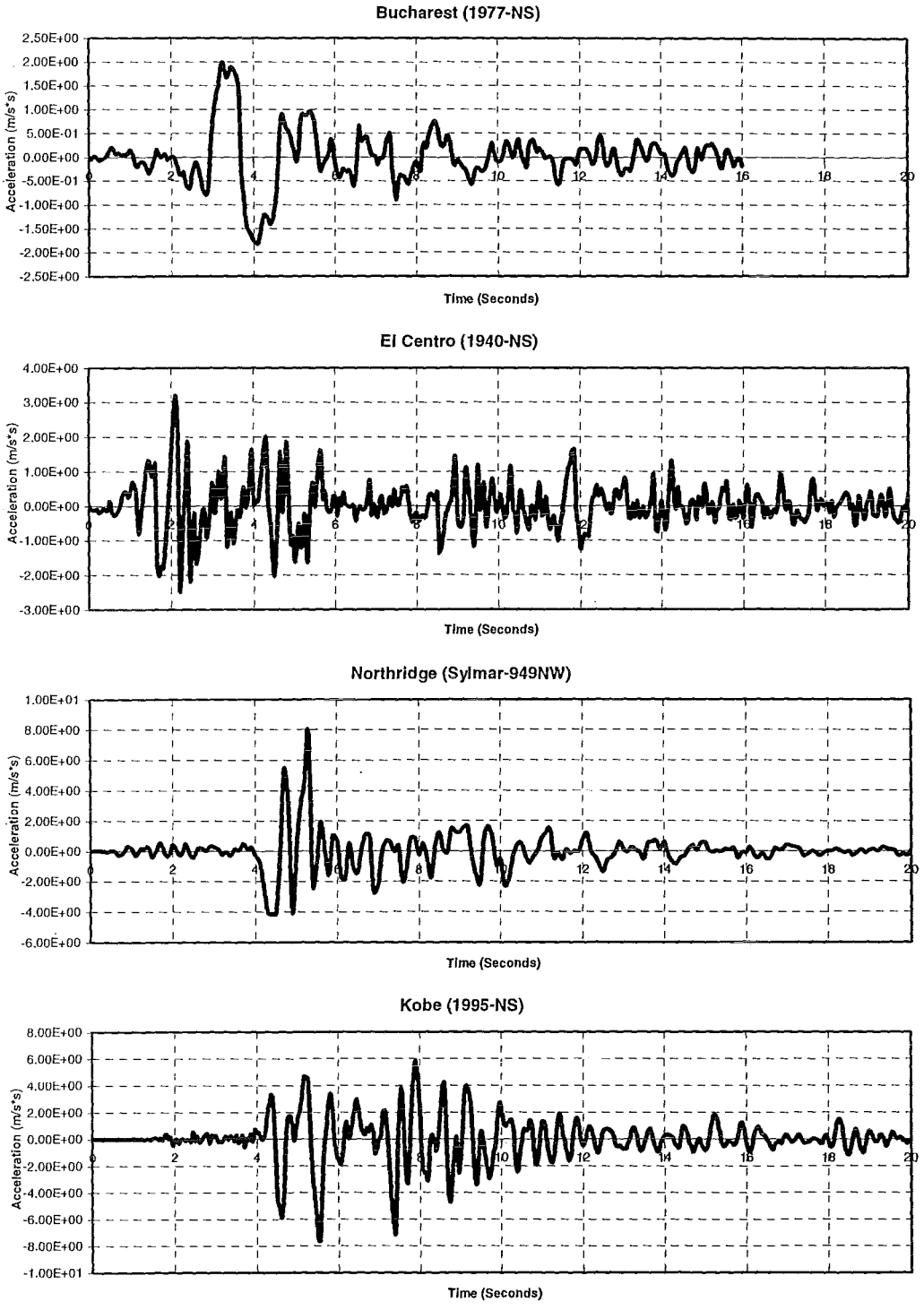

Fig. 5-3 The accelerograms for the four unscaled earthquake excitations

5-5 The Four Unscaled Earthquake Excitations

A peak acceleration-to-velocity (*A/V*) ratio of an earthquake excitation is a very important parameter. The *A/V* ratio is closely correlated with the energy content of the record in the frequency domain. High *A/V* ratio records, in general, have larger input energy in the short-period range and vice versa for low *A/V* records [Tso 1993]. Four different earthquake excitations with different durations of excitation were used in this research as shown in Table 5-1. The *A/V* ratios for the Bucharest (1977-NS), El Centro (1940-NS), Northridge (Sylmar-949NW) and Kobe (1995-NS) are 0.29g, 0.92g, 0.71g and 0.91g respectively with (1/Second) unit, trying to cover the different characteristics of earthquake records.

Table 5-1 General description of the four earthquake records

No.	Earthquake	Site	Date	Component	PGA (m/s^2)	PGV (m/s)	Ratio A/V (1/Second)	Duration (Seconds)
1	Romania	Bucharest	4/3/1977	N-S	0.21g	0.73	0.29g	16
2	Imperial Valley California	El Centro	18/5/1940	N-S	0.35g	0.38	0.92g	20
3	Northridge	Sylmar	17/1/1994	949-NW	0.80g	1.12	0.71g	20
4	Kobe, Japan	MA, observatory	17/01/1995	N-S	0.84g	0.92	0.91g	20

Fig. 5-3 shows the accelerograms for the four unscaled earthquake excitations, i.e. Bucharest (1977-NS), El Centro (1940-NS), Northridge (Sylmar-949NW) and Kobe (1995-NS). Figs. 5-4.a.b.c show the design elastic acceleration and displacement spectra, the 5% damped acceleration, and displacement, and velocity spectra for the four unscaled excitations.

The design elastic spectral acceleration was 80% of the basic hazard seismic coefficient from Eq. (5-1). The basic hazard seismic coefficient spectrum in NZS 4203 and the design acceleration spectrum are shown in Fig. 5-4d.

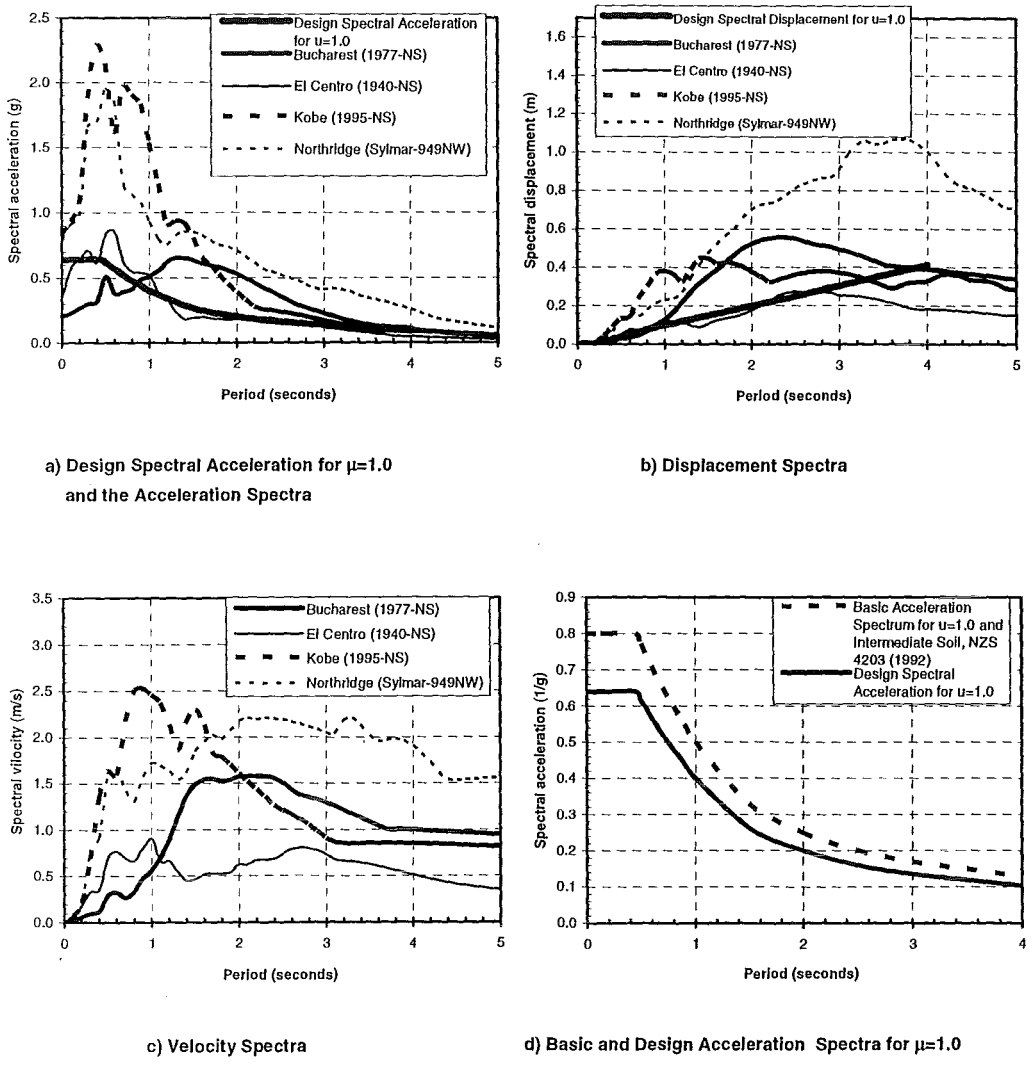

Fig. 5-4 Basic and design spectral acceleration for μ=1.0 and the 5% damped acceleration, displacement and velocity spectra for the four unscaled earthquake excitations, for Z=0.8 located in Christchurch

The design 5% damped elastic spectral displacements were derived from the Eq. (5-2) shown below based on the assumption of 5% damping in the spectral response for a single degree of freedom system.

$$Sd_n^d = \frac{(T_n)^2}{4\pi^2} * Sa_n^d \qquad \textbf{(5-2)}$$

where Sd_n^d and Sa_n^d is the design spectral displacement and acceleration for the single degree of freedom of natural period T_n. Table 5-2 shows the basic spectral

acceleration for an intermediate soil [NZS4203 1992], design spectral acceleration and displacement for the different natural periods of free vibration for zone factor 0.80 for Christchurch.

Fig. 5-5 shows the design response spectra, and the 5% damped spectral responses from the first six modes of the three structures for the four unscaled earthquake excitations.

Table 5-2 Basic and design spectral acceleration, and design spectral displacement from NZS4203 [NZS4203 1992]

T (seconds)	0.00	0.13	0.20	0.45	0.50	0.60	0.70	0.80	0.90	1.00	1.50	2.00	2.50	3.00
Basic spectral acceleration (g)	0.80	0.80	0.80	0.80	0.77	0.71	0.65	0.60	0.55	0.50	0.33	0.25	0.20	0.17
Design spectral acceleration (g)	0.64	0.64	0.64	0.64	0.62	0.57	0.52	0.48	0.44	0.40	0.26	0.20	0.16	0.14
Design spectral displacement (10^{-3}m)	0	3	6	32	38	51	63	76	89	99	148	199	249	304

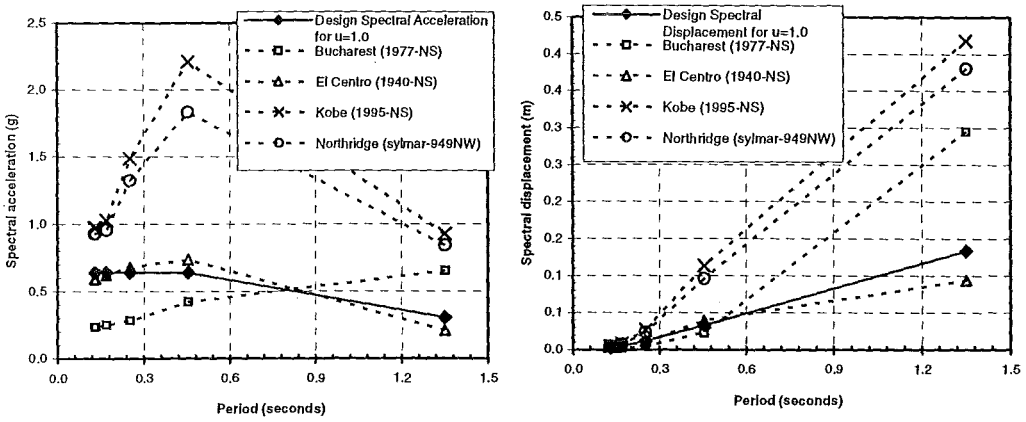

6-Storey Structure

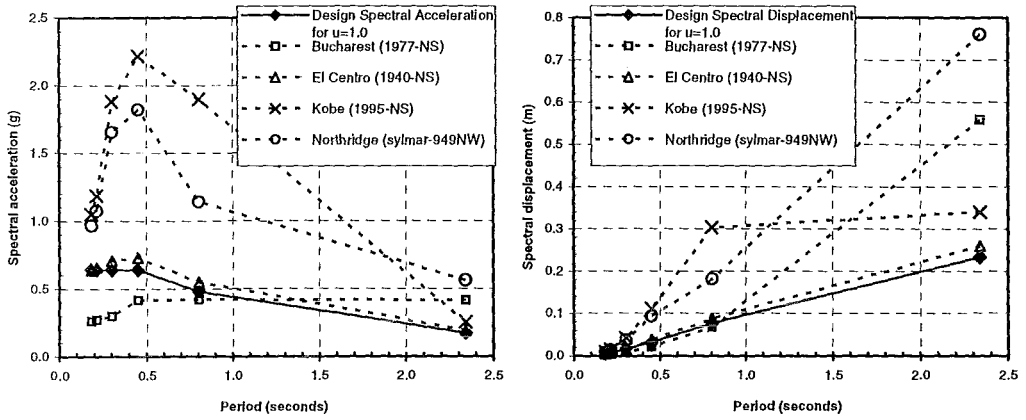

12-Storey Structure

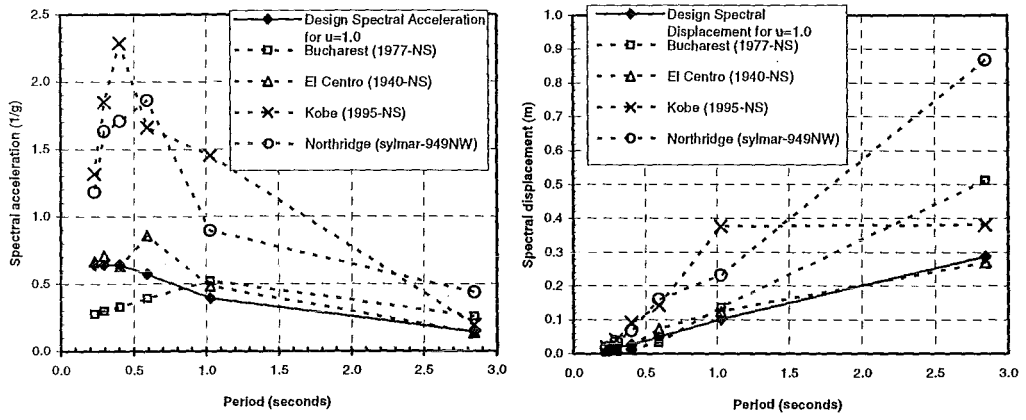

18-Storey Structure

Fig. 5-5 Design and 5% damped spectral responses for the first six modes of the three structures for the four unscaled earthquake excitations

5-6 The Design-Spectra Scaling, Design-Response Scaling and the Six Different Scaling Methods Used

The scaling factor for a design-spectra-based scaling method can be obtained from the weighted average of the acceleration or the displacement ratios for the first few significant modes in order to make the spectral accelerations or displacements for the scaled excitation as close as possible to the corresponding design values. The weighting factors represent the influence for the mode under consideration. The scaling factor can be calculated from the following equation;

$$SF = \sum_{n=1}^{N} \lambda_n R_n \quad n = 1, 2, \ldots, N \tag{5-3}$$

where SF is the scaling factor considering the first N modes

λ_n is the artificial weighting factor for mode n

$R_n = \frac{a_n^d}{a_n}$ or $\frac{d_n^d}{d_n}$ ratio of design acceleration or displacement to the acceleration or displacement of the unscaled excitation for mode n

If one assumes the weighting factor is $\lambda_n = T_n \Big/ \sum_{n=1}^{N} T_n$ and $\lambda_n = M_n^e \Big/ \sum_{n=1}^{N} M_n^e$ respectively where T_n and M_n^e are the natural period of free vibration and the effective mass respectively for mode n, then Eq. (5-3) can be re-arranged to be Eq. (5-4) and Eq. (5-5) respectively for the period and the effective mass weighted average scaling methods considering the first N modes:

$$SF = \frac{\sum_{n=1}^{N} R_n T_n}{\sum_{n=1}^{N} T_n} \tag{5-4}$$

$$SF = \frac{\sum_{n=1}^{N} R_n M_n^e}{\sum_{n=1}^{N} M_n^e} \tag{5-5}$$

The effective mass for mode n is determined by Eq. (5-6).

$$M_n^e = \frac{(L_n^*)^2}{M_n^*} \tag{5-6}$$

where $M_n^* = \{\phi_n\}^T [M]\{\phi_n\}$ and $L_n^* = \{\phi_n\}^T [M]\{r\}$. $\{\phi_n\}$ is the nth mode shape. $[M]$ is the mass matrix. $\{r\}$ is the displacement vector of the structure due to a unit ground displacement in the direction of the earthquake excitation.

The four different scaling methods of weighted average acceleration or displacement ratios used in the study can be obtained from the Eqs. (5-3), (5-4) and (5-5) as shown in Eq. (5-7). Method 1 is obtained from Eq. (5-3) considering only the first mode. Method 2 is derived from Eq. (5-3) by assigning arbitrary weighting factors 92%, 5% and 3% for the first three modes. Using the first three modes of free vibration in Eqs. (5-4) and (5-5) leads to method 3 and method 4 respectively.

Method 1: $SF = R_1$ **(5-7a)**

Method 2: $SF = 0.92R_1 + 0.05R_2 + 0.03R_3$ **(5-7b)**

Method 3: $SF = \frac{T_1R_1 + T_2R_2 + T_3R_3}{T_1 + T_2 + T_3}$ **(5-7c)**

Method 4: $SF = \frac{M_1^eR_1 + M_2^eR_2 + M_3^eR_3}{M_1^e + M_2^e + M_3^e}$ **(5-7d)**

The design-response scaling factor is the ratio of the design response values to the maximum elastic response values for a structure under an unscaled excitation. The responses may be the maximum inter-storey drift or the maximum base shear. The base-shear and interstorey-drift scaling methods were used in this study, which are expressed by Eqs. (5-8a) and (5-8b) respectively.

Method 5: $SF = \frac{V^{design}}{V}$ **(5-8a)**

Method 6: $SF = \frac{ID^{design}}{ID}$ **(5-8b)**

Where V^{design} and ID^{design} is the design base shear and design maximum interstorey drift over all levels respectively, V and ID is the maximum base shear and the maximum inter-storey drift produced by an unscaled earthquake excitation.

Because the three ductile framed structures were designed using the equivalent static method with ductility μ=5.0, the design base shear forces were determined by this method, being equal to the design spectral accelerations multiplied by the structure seismic weights, shown in Eq. (5-9).

$$\begin{aligned} V_{u=1.0}^{design} &= C_{a(T)}^{design} * W \\ &= C_{(T,\mu=1.0)} * Sp * R * Z * Lu * W \\ &= 0.8 * C_{(T_1,\mu=1.0)} * W \end{aligned} \qquad \textbf{(5-9)}$$

where $C_{a(T)}^{design}$ design spectral acceleration coefficient obtained from Eq. 5-1 where $Sp * R * Z * Lu = 0.8$

$C_{(T_1,\mu=1.0)}$ the basic acceleration coefficient for $\mu=1.0$

W total seismic weight of structure

The design inter-storey drift was obtained by combining the inter-storey drifts for the first few modes of interests calculated from the design spectral displacements and the mode shapes as shown in Eq. (5-10). The simple combination method, square root of sum of squares (SRSS) is often used for response combination in reinforced concrete framed structures. This is due to the frequency characteristics for the structures. In a two-dimensional structure no two lateral frequencies are close, and therefore no strong correlation between modal responses is likely. The SRSS method implies no correlation between the responses of the different modes; further, the maximum of each mode is independent of the maximum in other modes. The natural frequencies of free vibration of such frames increase roughly in the ratios of 1:3:5:7:9 etc. in a uniform moment resisting frame undergoing a shear-type sway deformation [Carr 1994].

$$ID_n = \sqrt{\left(\sum_{i=1}^{N} \left(ID_i^n\right)^2\right)}, \qquad \textbf{(5-10a)}$$

where ID_i^n is the inter-storey drift at level n for mode i (i=1, 2, 3, ...N)

ID_n is inter-storey drift for level n (n=1, 2, 3, ...6. =1, 2, 3, ...12. and =1, 2, 3, ...18 for the 6, 12 and 18 storey structure respectively)

$$ID^{design} = Max\{ID_1, ID_2, ID_3 ..... ID_n\} \qquad \textbf{(5-10b)}$$

where n=6, 12 and 18 for the three structures.

ID^{design} is the design inter-storey drift for a structure.

5-7 Scaling Factors for Spectral Acceleration Ratios and for Spectral Displacement Ratios

The scaling factor for the design-spectra scaling, i.e. the weighted average of acceleration or displacement ratios is a function of the ratios and the weighting factors. Those ratios are the design spectral responses (accelerations and displacements) to the corresponding spectral responses to the unscaled earthquakes. The assumed weighting factors for each method are constant. Hence the scaling factor is dominated by the ratios only.

Tables 5-3, 5-4 and Figs. 5-6a.b.c show the ratios of design spectral acceleration and displacement to the 5% damped spectral response values for the first six modes of the three structures under the four unscaled excitations. It was observed that the spectral acceleration and displacement ratios were very close. That indicated that the scaling factors for both the spectral acceleration and displacement ratios would be similar for all of the methods 1, 2, 3 and 4. Hence only the scaling factors for the spectral acceleration ratios were used in this study.

Table 5-3 The ratios of the design spectral acceleration to the 5% damped spectral one of the four unscaled excitations for the first six modes of the three structures

Periods (Seconds)		Design Spectral Acceleration for μ =1.0 (g)	Spectral acceleration (g)				Ratio of design acceleration to spectral acceleration of the unscaled excitation			
			Bucharest (1977-NS)	El Centro (1940-NS)	Kobe (1995-NS)	Northridge (sylmar-949NW)	Sa/Bucharest (1977-NS)	Sa/El Centro (1940-NS)	Sa/Kobe (1995-NS)	Sa/Northridge (sylmar-949NW)
6S	T1=1.35	0.30	0.65	0.21	0.93	0.84	0.47	1.46	0.33	0.36
	T2=0.45	0.64	0.42	0.74	2.21	1.83	1.51	0.87	0.29	0.35
	T3=0.25	0.64	0.28	0.68	1.49	1.33	2.27	0.94	0.43	0.48
	T4=0.17	0.64	0.25	0.62	1.03	0.96	2.53	1.03	0.62	0.67
	T5=0.13	0.64	0.24	0.59	0.98	0.93	2.69	1.08	0.66	0.69
	T6=0.13	0.64	0.24	0.59	0.97	0.93	2.71	1.09	0.66	0.69
12S	T1=2.34	0.17	0.41	0.19	0.25	0.56	0.42	0.90	0.68	0.31
	T2=0.80	0.48	0.42	0.55	1.90	1.14	1.15	0.87	0.25	0.42
	T3=0.45	0.64	0.41	0.73	2.22	1.82	1.54	0.88	0.29	0.35
	T4=0.30	0.64	0.30	0.71	1.88	1.66	2.14	0.91	0.34	0.39
	T5=0.21	0.64	0.27	0.66	1.19	1.07	2.37	0.98	0.54	0.60
	T6=0.18	0.64	0.26	0.63	1.05	0.97	2.47	1.01	0.61	0.66
18S	T1=2.85	0.14	0.26	0.14	0.19	0.43	0.56	1.06	0.74	0.33
	T2=1.03	0.39	0.52	0.48	1.45	0.89	0.75	0.81	0.27	0.44
	T3=0.59	0.57	0.39	0.86	1.66	1.86	1.46	0.67	0.34	0.31
	T4=0.40	0.64	0.33	0.62	2.28	1.71	1.97	1.02	0.28	0.38
	T5=0.30	0.64	0.30	0.71	1.85	1.63	2.16	0.91	0.35	0.39
	T6=0.23	0.64	0.28	0.67	1.32	1.18	2.32	0.96	0.49	0.54

Table 5-4 The ratios of the design spectral displacement to the 5% damped spectral one of the four unscaled excitations for the first six modes of the three structures

Periods (Seconds)		Design spectral displacement for μ =1.0 (m)	Spectral displacement (m)				Ratio of design displacement to spectral displacement of the unscaled excitation			
			Bucharest (1977-NS)	El Centro (1940-NS)	Kobe (1995-NS)	Northridge (sylmar-949NW)	Sd/Bucharest (1977-NS)	Sd/El Centro (1940-NS)	Sd/Kobe (1995-NS)	Sd/Northridge (sylmar-949NW)
6S	T1=1.35	0.133	0.295	0.093	0.418	0.380	0.45	1.43	0.32	0.35
	T2=0.45	0.033	0.023	0.039	0.113	0.096	1.43	0.84	0.29	0.34
	T3=0.25	0.012	0.005	0.011	0.027	0.024	2.49	1.04	0.44	0.50
	T4=0.17	0.005	0.002	0.005	0.008	0.007	2.39	0.97	0.59	0.64
	T5=0.13	0.003	0.001	0.003	0.005	0.005	2.29	0.93	0.56	0.60
	T6=0.13	0.003	0.001	0.003	0.005	0.004	2.31	0.94	0.57	0.60
12S	T1=2.34	0.233	0.558	0.259	0.340	0.760	0.42	0.90	0.68	0.31
	T2=0.80	0.077	0.067	0.088	0.303	0.182	1.15	0.88	0.25	0.42
	T3=0.45	0.032	0.022	0.038	0.112	0.094	1.46	0.85	0.29	0.34
	T4=0.30	0.017	0.007	0.016	0.043	0.037	2.50	1.06	0.40	0.45
	T5=0.21	0.008	0.003	0.008	0.015	0.014	2.45	1.01	0.52	0.58
	T6=0.18	0.006	0.002	0.006	0.009	0.009	2.41	0.98	0.59	0.65
18S	T1=2.85	0.287	0.512	0.270	0.381	0.867	0.56	1.07	0.75	0.33
	T2=1.03	0.102	0.137	0.125	0.376	0.232	0.74	0.82	0.27	0.44
	T3=0.59	0.050	0.034	0.074	0.143	0.161	1.48	0.67	0.35	0.31
	T4=0.40	0.027	0.013	0.025	0.092	0.069	2.06	1.08	0.30	0.40
	T5=0.30	0.016	0.006	0.015	0.041	0.036	2.51	1.06	0.40	0.46
	T6=0.23	0.010	0.004	0.009	0.020	0.018	2.47	1.02	0.47	0.53

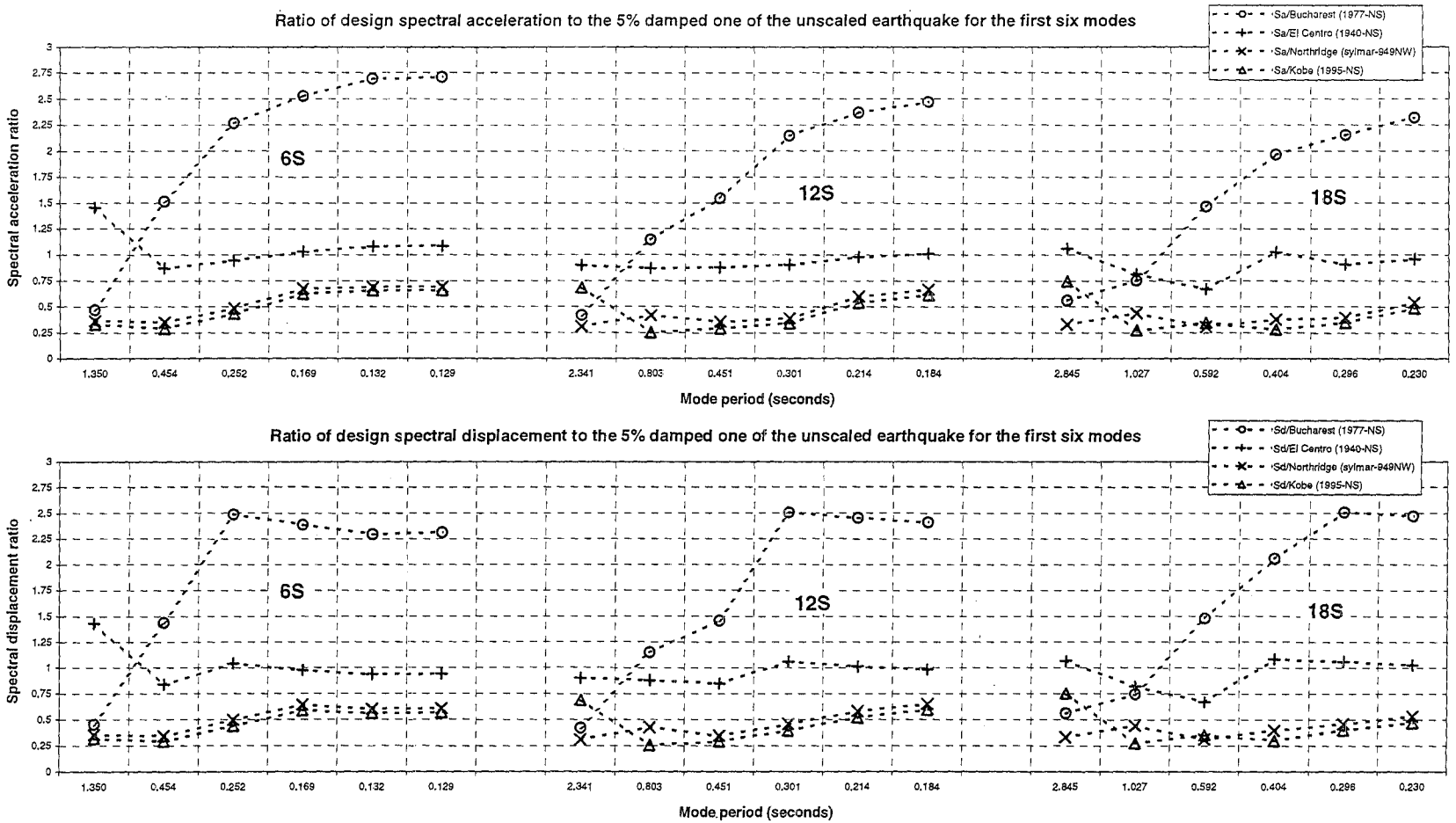

Fig. 5-6 Ratios of the design spectral acceleration to the 5% damped spectral ones, and the ratios of the design spectral displacements to the 5% damped spectral ones of the four unscaled earthquakes for the first modes of the three structures

5-8 Scaling Factors to the Six Different Scaling Methods for the Three Structures under the Four Earthquake Excitations

All values used in the six different scaling methods were determined. By carrying out elastic dynamic analyses for the three structures subjected to the natural earthquake records, natural periods of free vibration and effective masses in addition to the maximum base shears and interstorey drifts were obtained. The acceleration response spectra of the natural earthquakes were available by running the program SPECTRA, which is a module within in RUAUMOKO [Carr 1998]. The design base shears were determined by Eq. (5-9) of the Equivalent Static Method. The design inter-storey drifts were derived by using the SRSS modal combination method with the design spectral displacements.

From Table 5-5 showing the period and effective mass weighting factors for the first three modes of the three structures, the period weighting factors for the three structures were similar for the first three modes. This is because the ratios of those natural periods of free vibration for uniform moment resisting frames are roughly the same 1: (1/3): (1/5).

Table 5-5 Period and effective mass weighting factors for the first three modes of the three structures for method 3 and method 4

			6S	12S	18S
Period Weighting Factor	Period	T_1	1.35	2.34	2.85
		T_2	0.45	0.80	1.03
		T_3	0.25	0.45	0.59
	$T_1+T_2+T_3$		2.06	3.60	4.46
	Weighting Factor	$T_1/(T_1+T_2+T_3)$	**0.66**	**0.65**	**0.64**
		$T_2/(T_1+T_2+T_3)$	**0.22**	**0.22**	**0.23**
		$T_3/(T_1+T_2+T_3)$	**0.12**	**0.13**	**0.13**
Effective Mass Weighting Factor	Effective mass	M_1^r	1108	2272	3263
		M_2^r	141	310	555
		M_3^r	45	113	183
	$M_1^r+M_2^r+M_3^r$		1294	2695	4001
	Weighting Factor	$M_1^r/(M_1^r+M_2^r+M_3^r)$	**0.86**	**0.84**	**0.82**
		$M_2^r/(M_1^r+M_2^r+M_3^r)$	**0.11**	**0.12**	**0.14**
		$M_3^r/(M_1^r+M_2^r+M_3^r)$	**0.03**	**0.04**	**0.05**

Table 5-6 shows the design base shears and the maximum base shears, design inter-storey drifts and the maximum inter-storey drifts for the three structures under the four unscaled excitations.

Table 5-6 Design and maximum base shears and design and maximum inter-storey drifts for the three structures under the four unscaled earthquake excitations

	Design BS (kN)	Maximum BS (kN)				Design SRSS ID (m)	Maximum ID (m)			
		Bucharest (1977-NS)	El Centro (1940-NS)	Kobe (1995-NS)	Northridge (sylmar-949NW)		Bucharest (1977-NS)	El Centro (1940-NS)	Kobe (1995-NS)	Northridge (sylmar-949NW)
6S	4025.5	7900.0	3023.1	13250.0	6329.8	0.033	0.085	0.030	0.135	0.064
12S	4784.5	9420.4	6041.5	9418.6	9810.3	0.039	0.082	0.052	0.099	0.072
18S	6191.9	9459.7	7227.8	10503.0	12060.0	0.043	0.055	0.041	0.082	0.061

Table 5-7 shown in the following two pages presents the first four and five mode shapes for the 6-, and 12-, 18-storey structure respectively. The design spectral displacement, inter-storey drift for each mode and final combined inter-storey drifts are also shown in this table. The sum of the effective masses for the modes used for the 6-, 12- and 18-storey frames was respectively 99%, 97% and 96% of their total masses.

Table 5-8 and Fig. 5-7 shows the scaling factors from the six different scaling methods for the three structures and the four unscaled earthquake excitations.

Table 5-8 Scaling factors to the six scaling methods for the three structures under the four excitations

Method	6S				12S				18S			
	Bucharest (1977-NS)	El Centro (1940-NS)	Kobe (1995-NS)	Northridge (Sylmar-949NW)	Bucharest (1977-NS)	El Centro (1940-NS)	Kobe (1995-NS)	Northridge (Sylmar-949NW)	Bucharest (1977-NS)	El Centro (1940-NS)	Kobe (1995-NS)	Northridge (Sylmar-949NW)
R1	0.47	1.46	0.33	0.36	0.42	0.90	0.68	0.31	0.56	1.06	0.74	0.33
0.92R1	0.57	1.41	0.33	0.36	0.49	0.90	0.65	0.31	0.60	1.03	0.71	0.34
PW	0.92	1.26	0.33	0.37	0.72	0.89	0.54	0.34	0.72	0.95	0.58	0.35
EMW	0.64	1.37	0.33	0.36	0.55	0.90	0.62	0.32	0.63	1.01	0.66	0.34
BS	0.51	1.33	0.30	0.64	0.51	0.79	0.51	0.49	0.65	0.86	0.60	0.51
ID	0.39	1.08	0.25	0.52	0.47	0.75	0.40	0.54	0.78	1.06	0.53	0.70

Note: **R1** - first mode method. **0.92R1** - first three modes with arbitrary weighting factors 0.92, 0.05 and 0.03.
PW - period weighted average of the first three modes. **EMW** - effective mass weighted average of the first three modes.
BS – base shear method. **ID** – inter-storey drift method.

Table 5-7 Calculation of the design inter-storey drifts for 6, 12 and 18storey structures using SRSS method

	Mode-shape					Design spectral displacement (m)					Design displacement for each mode (m)					Design interstorey drift (m)					Iinterstorey drift (m)
Level No.	mode-1	mode-2	mode-3	mode-4	mode-5	mode-1	mode-2	mode-3	mode-4	mode-5	mode-1	mode-2	mode-3	mode-4	mode-5	mode-1	mode-2	mode-3	mode-4	mode-5	SRSS
6	1.000	1.000	-0.864	0.683		0.133	0.033	0.012	0.005		0.133	0.033	-0.010	0.003		0.010	0.019	-0.014	0.008		0.027
5	0.925	0.435	0.368	-0.938		0.133	0.033	0.012	0.005		0.123	0.014	0.004	-0.004		0.019	0.026	-0.007	-0.004		**0.033**
4	0.785	-0.352	1.000	-0.172		0.133	0.033	0.012	0.005		0.105	-0.012	0.012	-0.001		0.025	0.018	0.009	-0.006		0.033
3	0.598	-0.909	0.195	1.000		0.133	0.033	0.012	0.005		0.080	-0.030	0.002	0.005		0.026	0.001	0.011	0.005		0.029
2	0.401	-0.947	-0.759	-0.101		0.133	0.033	0.012	0.005		0.053	-0.031	-0.009	0.000		0.029	-0.013	0.000	0.004		0.032
1	0.185	-0.545	-0.783	-0.988		0.133	0.033	0.012	0.005		0.025	-0.018	-0.009	-0.005		0.025	-0.018	-0.009	-0.005		0.032
12	1.000	1.000	1.000	1.000	-0.919	0.233	0.077	0.032	0.017	0.008	0.233	0.077	0.032	0.017	-0.007	0.007	0.016	0.017	0.016	-0.011	0.031
11	0.970	0.795	0.473	0.045	0.428	0.233	0.077	0.032	0.017	0.008	0.226	0.061	0.015	0.001	0.003	0.011	0.025	0.023	0.015	-0.004	**0.039**
10	0.921	0.470	-0.224	-0.836	1.000	0.233	0.077	0.032	0.017	0.008	0.215	0.036	-0.007	-0.014	0.008	0.015	0.030	0.018	0.001	0.007	0.038
9	0.855	0.085	-0.766	-0.921	0.147	0.233	0.077	0.032	0.017	0.008	0.199	0.007	-0.025	-0.016	0.001	0.018	0.028	0.005	-0.012	0.008	0.036
8	0.777	-0.277	-0.914	-0.231	-0.840	0.233	0.077	0.032	0.017	0.008	0.181	-0.021	-0.030	-0.004	-0.007	0.021	0.024	-0.008	-0.015	-0.001	0.036
7	0.686	-0.587	-0.671	0.630	-0.764	0.233	0.077	0.032	0.017	0.008	0.160	-0.045	-0.022	0.011	-0.006	0.023	0.015	-0.016	-0.006	-0.008	0.033
6	0.588	-0.787	-0.170	0.964	0.212	0.233	0.077	0.032	0.017	0.008	0.137	-0.060	-0.006	0.016	0.002	0.023	0.005	-0.017	0.006	-0.005	0.030
5	0.490	-0.858	0.342	0.593	0.861	0.233	0.077	0.032	0.017	0.008	0.114	-0.066	0.011	0.010	0.007	0.024	-0.003	-0.012	0.013	0.002	0.030
4	0.386	-0.816	0.724	-0.154	0.596	0.233	0.077	0.032	0.017	0.008	0.090	-0.063	0.023	-0.003	0.005	0.025	-0.011	-0.004	0.011	0.007	0.031
3	0.277	-0.669	0.848	-0.797	-0.299	0.233	0.077	0.032	0.017	0.008	0.064	-0.051	0.027	-0.013	-0.002	0.026	-0.018	0.006	0.002	0.005	0.032
2	0.166	-0.439	0.677	-0.923	-0.893	0.233	0.077	0.032	0.017	0.008	0.039	-0.034	0.022	-0.016	-0.007	0.024	-0.020	0.012	-0.007	-0.002	0.034
1	0.064	-0.178	0.305	-0.491	-0.608	0.233	0.077	0.032	0.017	0.008	0.015	-0.014	0.010	-0.008	-0.005	0.015	-0.014	0.010	-0.008	-0.005	0.024

Table 5-8 continues

Note: the effective mass for the first four modes for 6storey structure and for the first five modes for 12storey structure is 99% and 97% respectively of their total mass.

Table 5-7 continued

	Mode-shape					Design spectral displacement (m)					Design displacement for each mode (m)					Design interstorey drift (m)					Iinterstorey drift (m)
Level No.	mode-1	mode-2	mode-3	mode-4	mode-5	mode-1	mode-2	mode-3	mode-4	mode-5	mode-1	mode-2	mode-3	mode-4	mode-5	mode-1	mode-2	mode-3	mode-4	mode-5	SRSS
18	1.000	1.000	1.000	1.000	1.000	0.287	0.102	0.050	0.027	0.016	0.287	0.102	0.050	0.027	0.016	0.007	0.014	0.017	0.017	0.016	0.032
17	0.976	0.864	0.665	0.379	0.043	0.287	0.102	0.050	0.027	0.016	0.280	0.088	0.033	0.010	0.001	0.011	0.022	0.025	0.021	0.014	**0.043**
16	0.939	0.649	0.173	-0.378	-0.830	0.287	0.102	0.050	0.027	0.016	0.270	0.066	0.009	-0.010	-0.014	0.013	0.026	0.024	0.013	0.001	0.040
15	0.893	0.390	-0.313	-0.854	-0.917	0.287	0.102	0.050	0.027	0.016	0.256	0.040	-0.016	-0.023	-0.015	0.015	0.026	0.016	0.000	-0.010	0.035
14	0.842	0.139	-0.642	-0.860	-0.314	0.287	0.102	0.050	0.027	0.016	0.242	0.014	-0.032	-0.024	-0.005	0.017	0.026	0.009	-0.009	-0.013	0.036
13	0.784	-0.114	-0.820	-0.518	0.467	0.287	0.102	0.050	0.027	0.016	0.225	-0.012	-0.041	-0.014	0.008	0.018	0.023	0.000	-0.015	-0.007	0.034
12	0.722	-0.341	-0.814	0.010	0.909	0.287	0.102	0.050	0.027	0.016	0.207	-0.035	-0.041	0.000	0.015	0.018	0.019	-0.008	-0.013	0.002	0.031
11	0.657	-0.524	-0.647	0.495	0.773	0.287	0.102	0.050	0.027	0.016	0.189	-0.054	-0.032	0.014	0.013	0.019	0.014	-0.014	-0.008	0.009	0.031
10	0.590	-0.666	-0.367	0.795	0.206	0.287	0.102	0.050	0.027	0.016	0.169	-0.068	-0.018	0.022	0.003	0.019	0.009	-0.016	0.000	0.010	0.029
9	0.523	-0.754	-0.044	0.812	-0.437	0.287	0.102	0.050	0.027	0.016	0.150	-0.077	-0.002	0.022	-0.007	0.019	0.004	-0.015	0.007	0.006	0.026
8	0.458	-0.789	0.257	0.573	-0.808	0.287	0.102	0.050	0.027	0.016	0.132	-0.081	0.013	0.016	-0.013	0.019	-0.001	-0.013	0.011	0.000	0.025
7	0.393	-0.779	0.510	0.173	-0.786	0.287	0.102	0.050	0.027	0.016	0.113	-0.080	0.025	0.005	-0.013	0.018	-0.005	-0.008	0.012	-0.006	0.025
6	0.329	-0.728	0.675	-0.255	-0.402	0.287	0.102	0.050	0.027	0.016	0.094	-0.074	0.034	-0.007	-0.007	0.018	-0.009	-0.003	0.009	-0.009	0.024
5	0.268	-0.644	0.735	-0.590	0.139	0.287	0.102	0.050	0.027	0.016	0.077	-0.066	0.037	-0.016	0.002	0.018	-0.012	0.002	0.005	-0.008	0.023
4	0.206	-0.530	0.697	-0.766	0.615	0.287	0.102	0.050	0.027	0.016	0.059	-0.054	0.035	-0.021	0.010	0.018	-0.014	0.006	-0.001	-0.004	0.024
3	0.145	-0.391	0.567	-0.745	0.831	0.287	0.102	0.050	0.027	0.016	0.042	-0.040	0.028	-0.020	0.014	0.017	-0.016	0.010	-0.006	0.002	0.026
2	0.085	-0.239	0.369	-0.539	0.705	0.287	0.102	0.050	0.027	0.016	0.024	-0.024	0.018	-0.015	0.011	0.015	-0.015	0.011	-0.008	0.006	0.026
1	0.032	-0.093	0.148	-0.230	0.327	0.287	0.102	0.050	0.027	0.016	0.009	-0.009	0.007	-0.006	0.005	0.009	-0.009	0.007	-0.006	0.005	0.017

Note: the effective mass for the modes used for the inter-storey drift of 18-storey structure is 96% of the total mass.

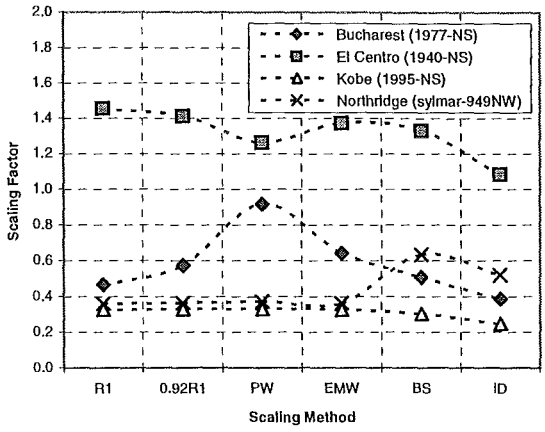

(a) 6 Storey Structure

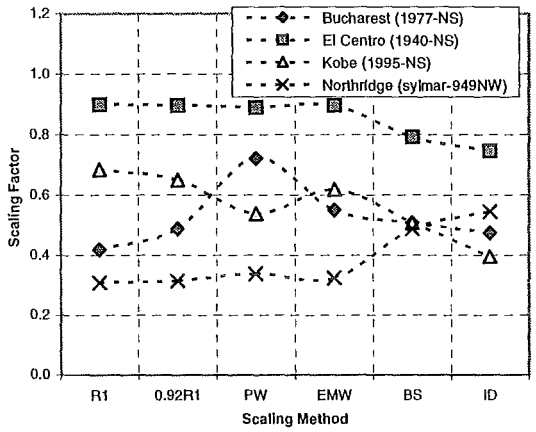

(b) 12 Storey Structure

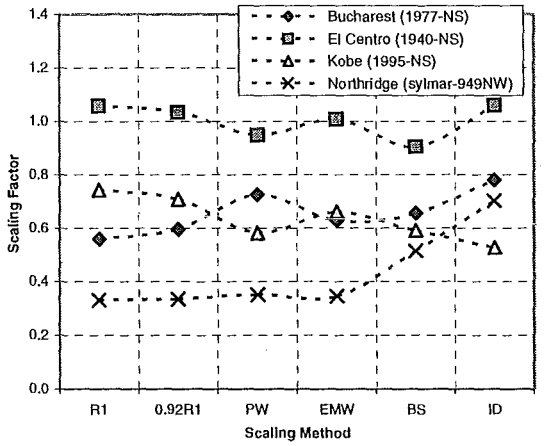

(c) 18 Storey Structure

Fig. 5-7 Scaling factors versus the six different scaling methods for the three structures subjected to the four earthquakes

Note: **R1** - first mode method. **0.92R1** - first three modes with arbitrary weighting factors 0.92, 0.05 and 0.03.
PW - period weighted average of the first three modes. **EMW** - effective mass weighted average of the first three modes.
BS – base shear method. **ID** – inter-storey drift method.

5-9 Maximum Elastic Responses of the Three Structures Under the Scaled Earthquake Excitations

5-9.1 Maximum Base Shears

Maximum base shears of the three structures to the records obtained using the six different scaling methods for the four earthquake excitations are shown in Figs. 5-8a to 5-8c.

It can be seen from Figs. 5-8a to 5-8c that for the base shear scaling method to each of the three structures, the four dotted lines showing the maximum base shears for the four earthquakes converge to the solid line representing the design base shear. In another word, the maximum base shears for the base shear scaling method are very similar to the design base shears. This is independent of the characteristics of the excitations and the natural periods of free-vibration of structures. Hence the base shear scaling method can be used for earthquake scaling when design base shear is required to be matched.

For the 6 and 12 storey structures as shown in Figs. 5-8a,b, the period weighted scaling method (PW) present very large base shears relative to the design level base shears for the Bucharest (1977-NS) excitation. However for all three structures as shown in Figs. 5-8a,b,c, the four design-spectra scaling methods, symbolised as R1, 0.92R1, PW and EMW, present very much smaller base shears than the design values when subjected to the Northridge (Sylmar-949NW) excitation. This indicates that, for any period structure, these four scaling methods may produce significantly small base shears and this is dependent on the characteristics of earthquake excitations. Hence these four scaling methods may not be reliable for earthquake scaling when design base shear is required to be matched.

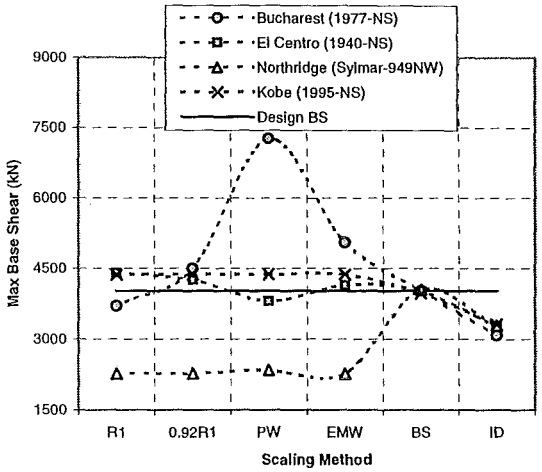

(a) 6 Storey Structure

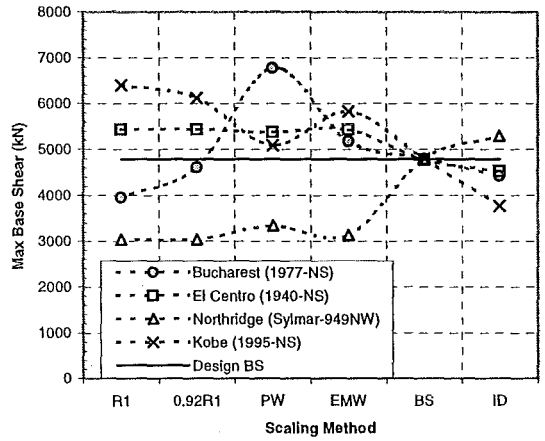

(b) 12 Storey Structure

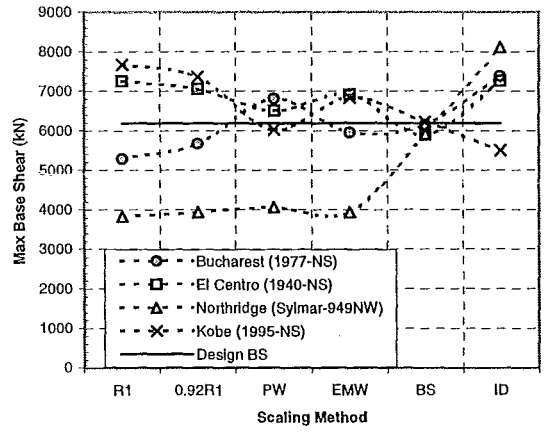

(c) 18 Storey Structure

Fig. 5-8 Maximum base shears of the three structures for the four different earthquake excitations scaled by using the six different scaling methods

For the 6 storey structure under all the four earthquakes, the inter-storey drift (ID) scaling method presents significantly smaller base shears when compared with the design value, as shown in Fig. 5-8a. This means that for a relatively short period structure the application of this scaling method always leads to significantly lower base shears than the design base shears. This method should not be used for earthquake scaling for these short period structures when design base shears are required to be matched.

For the 12 and 18 storey structure when applying the inter-storey drift (ID) scaling method as shown in Figs. 5-8b,c, the maximum base shears for the Kobe (1995-NS) earthquake are significantly smaller than the corresponding design base shears. This means that the maximum base shears for the inter-storey drift (ID) scaling method depend on the characteristics of earthquake excitations. This scaling method should not be used for earthquake scaling when design base shears are required to be matched for the 12 and 18 storey structures, say medium and long period structures.

5-9.2 Maximum Inter-storey Drifts

The distributions of the inter-storey drift versus the six different scaling methods for the 6, 12 and 18 storey structures under the four different earthquakes are shown in Figs. 5-9 to 5-11 respectively, in which solid lines represent the design inter-storey drifts obtained by combining the design spectral displacements with the SRSS method as discussed in 5-6. It is observed that the distributions of the inter-storey drift are different for different earthquakes for each of the three structures. The numbers of levels where the maximum interstorey drifts occurred for the three structures under the four different earthquakes are different and are listed in Table 5-9.

Table 5-9 Numbers of levels where the maximum interstorey drifts occurred for the three structures under the four earthquakes

	Bucharest (1977-NS)	El Centro (1940-NS)	Northridge (Sylmar-949NW)	Kobe (1995-NS)
6S	2	4	2	2
12S	3	8	2	10
18S	11	13	11	14

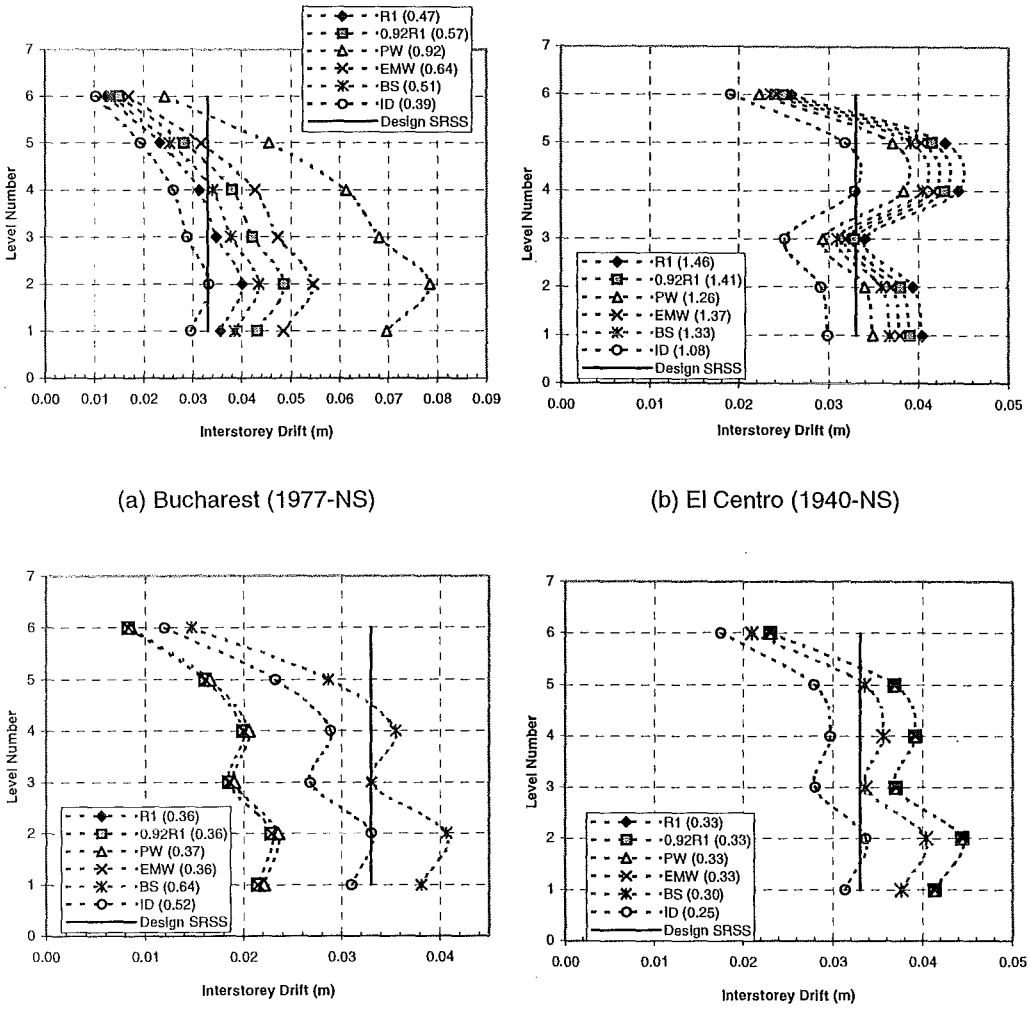

Fig. 5-9 Distribution of maximum inter-storey drift versus the six different scaling methods for 6-storey structure under the four different earthquakes

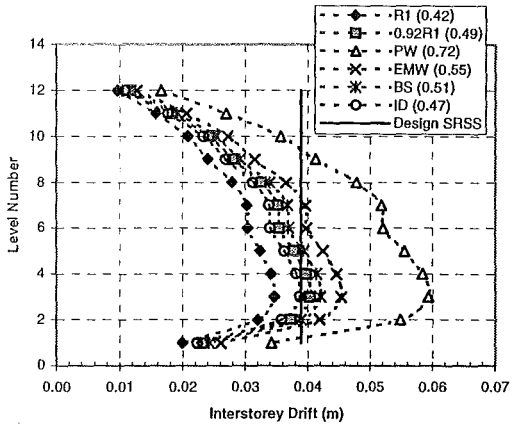

(a) Bucharest (1977-NS)

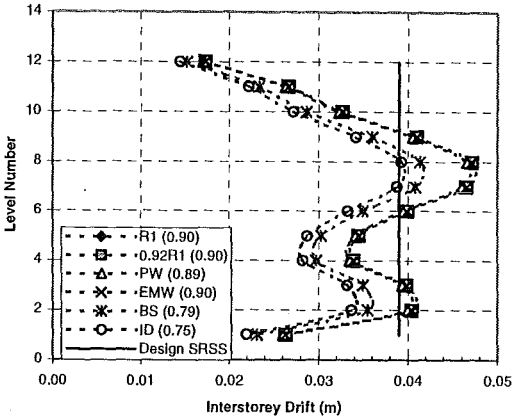

(b) El Centro (1940-NS)

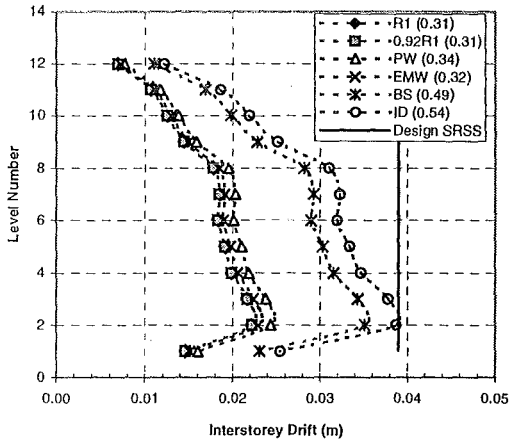

(c) Northridge (Sylmar-949NW)

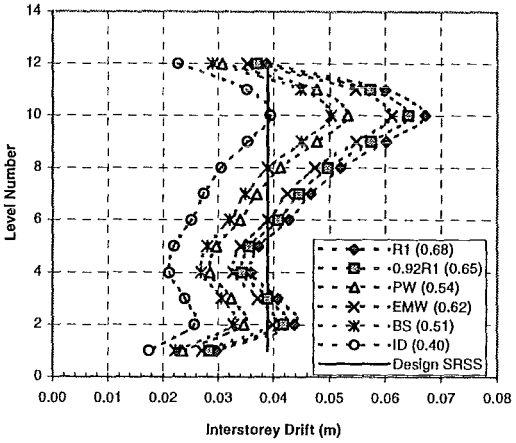

(d) Kobe (1995-NS)

Fig. 5-10 Distribution of maximum inter-storey drift versus the six different scaling methods for 12-storey structure under the four different earthquakes

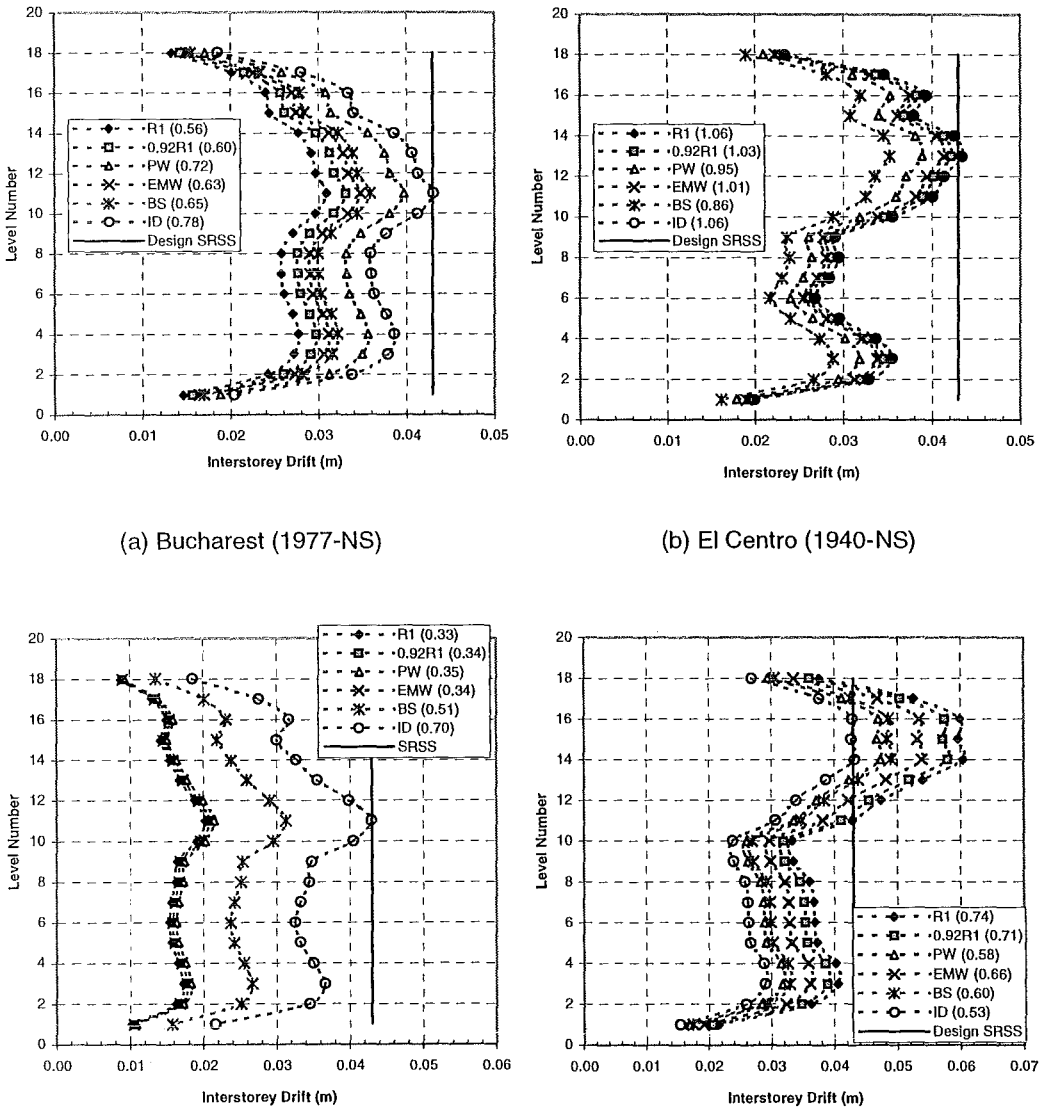

Fig. 5-11 Distribution of maximum inter-storey drift versus the six different scaling methods for 18-storey structure under the four different earthquakes

It can be seen that in Figs. 5-9 to 5-11, when each of the three structures is subjected to each of the four different earthquakes, the inter-storey drift scaling method presents the same maximum inter-storey drift as the corresponding design inter-storey drift represented using solid lines. This relationship is independent of the characteristics of the earthquakes and the structures. Hence this scaling method can be applied for earthquake scaling when design inter-storey drift is required to be matched for a natural earthquake.

It's found in Fig. 5-9 that, for the 6-storey structure under all of the four different earthquakes, the base shear scaling method presents larger maximum inter-storey drifts than design values. As discussed in the previous Section 5-9.1, this base shear scaling method is able to match the design base shear. This implies that this base shear scaling method is able to provide strong enough earthquakes for which both the maximum base shear and the maximum inter-storey drift are not smaller than the corresponding design values. This base shear scaling method is regarded as an optimum way and therefore should be used for earthquake scaling for the 6-storey structure, say a short period structure.

It is found from Fig. 5-10c that for the 12-storey structure when subjected to the Northridge (Sylmar-949NW) excitation, the base shear scaling method produces significantly smaller maximum inter-storey drift than the design inter-storey drift. Similarly for the 18-storey structure when subjected to the Bucharest (1977-NS), El Centro (1940-NS) and Northridge (Sylmar-949NW) earthquakes as shown in Figs. 5-11a.b.c, this base shear scaling method presents significantly smaller maximum inter-storey drifts relative to the design inter-storey drift. This indicates that for the 12- and 18-storey structures, the base shear scaling method may produce significantly smaller inter-storey drifts than design values and this is earthquake type dependent. Hence, this base shear scaling method should not be used for earthquake scaling when the design inter-storey drifts are required to be matched for the 12- and 18-storey structures, say, medium and long period structures.

Compared with the design inter-storey drifts, for the 6- and 12-storey structures as shown in Figs. 5-9c and 5-10c, the four design-spectra (R1, 0.92R1, PW and EMW) scaling methods produce very much smaller maximum inter-storey drifts than the

design inter-storey drifts when subjected to the Northridge (Sylmar-949NW) excitation. Similarly, it is found in Figs. 5-11a,c that for the 18-storey structure, these four design-spectra scaling methods present significantly smaller maximum inter-storey drifts than the design value for the Bucharest (1977-NS) and Northridge (Sylmar-949NW) excitations. This indicates that for all the three structures, the four design-spectra (R1, 0.92R1, PW and EMW) scaling methods are not able to match the design inter-storey drifts, depending on the characteristics of earthquakes, and therefore should not be used for earthquake scaling when design inter-storey drift is required to be matched.

5-10 5% Damped Spectral Accelerations and Displacements of the First Six Modes of the Three Structures Versus the Six Different Scaling Methods for the Four Earthquakes

In Fig. 5-12 to Fig. 5-15, the 5% damped spectral accelerations and displacements for the first six modes of the three structures for the six different scaling methods for the four different earthquakes are presented.

For the 6-storey structure under the Northridge (Sylmar-949NW) excitation shown in Fig. 5-14a, the spectral accelerations of the first three modes for the base shear and inter-storey drift scaling methods were large relative to the design values. For the 12-storey structure, larger spectral accelerations than the design values were observed for the first four modes when using the base shear and inter-storey drift scaling methods, as shown in Fig. 5-14b. Larger spectral accelerations of the first five modes for the same two scaling methods were found for the 18-storey structure in Fig. 5-14c.

For the 18-storey structure under the Kobe (1995-NS) excitation shown in Fig. 5-15c, the spectral accelerations for the base shear and inter-storey scaling methods were very similar for the first mode, and significantly larger relative to the design values for modes 2 to 5.

The maximum base shears and inter-storey drifts are dominated by the first few modes, say the first 3, 4 and 5 modes for the 6-, 12- and 18-storey structures respectively. The earthquake records for these cases discussed in the previous two

paragraphs, for which the spectral accelerations for the first 3, 4 or 5 modes were similar or smaller than the design values, will produce smaller base shears and inter-storey drifts relative to those at the required design level. Further, in the case of the frequency scaling method, which produces very similar spectral accelerations to the design values, the maximum base shears and inter-storey drifts under the scaled earthquake records would be significantly smaller than those at design level. This indicates that the use of the frequency scaling method will lead to records of low intensity producing small values of the maximum base shears and inter-storey drifts compared with the design requirements for certain type of earthquakes for all the three structures.

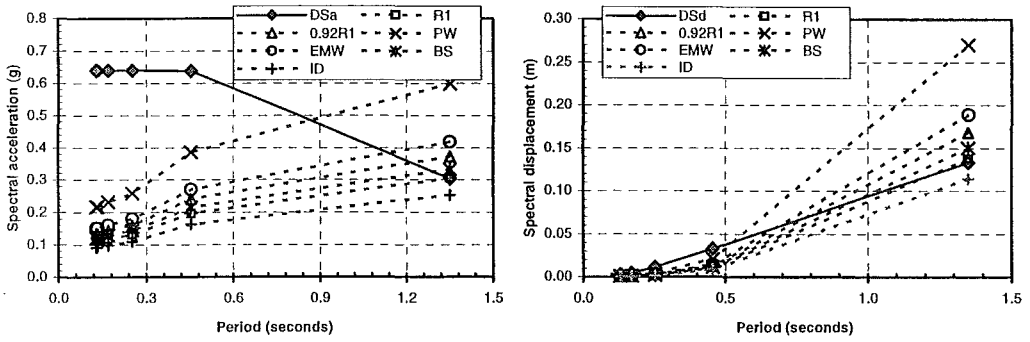

(a) 6 Storey Structure

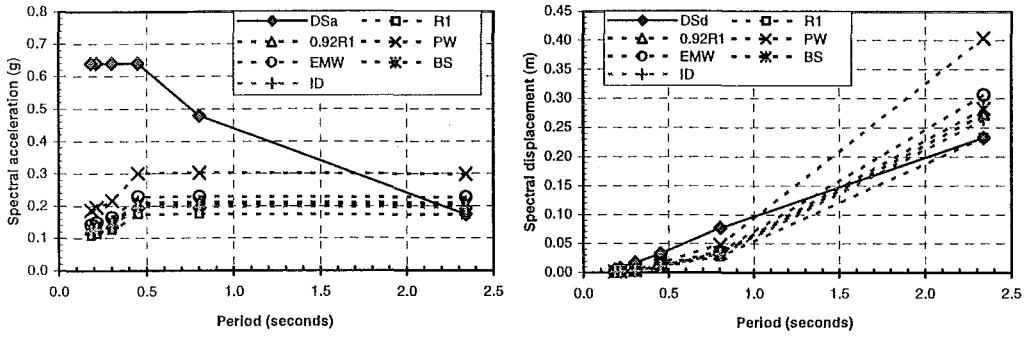

(b) 12 Storey Structure

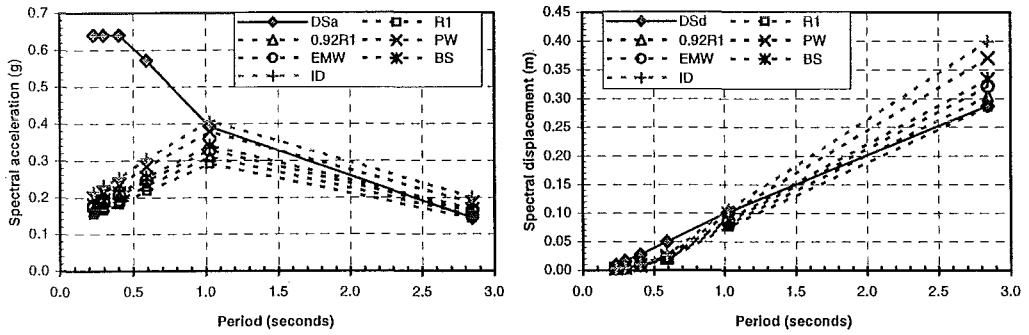

(c) 18 Storey Structure

Fig. 5-12 5% damped spectral responses of the first six modes of the three structures for **Bucharest (1977-NS)** earthquake scaled by using the six different scaling methods

Note: **DSa** – design special acceleration
R1 - first mode method.
0.92R1 - first three modes with arbitrary weighting factors 0.92, 0.05 and 0.03.
PW - period weighted average of the first three modes.
EMW - effective mass weighted average of the first three modes.
BS – base shear method.
ID – inter-storey drift method.

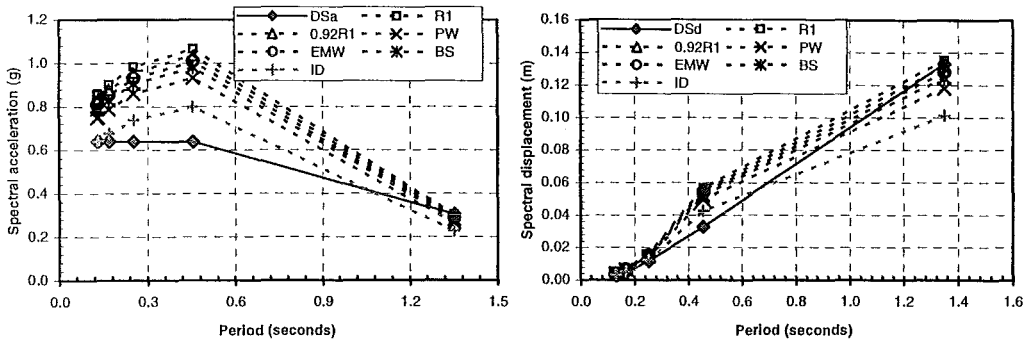

(a) 6 Storey Structure

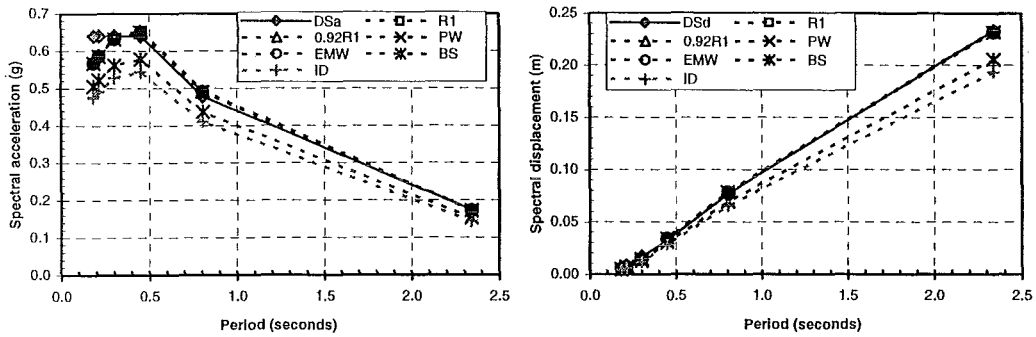

(b) 12 Storey Structure

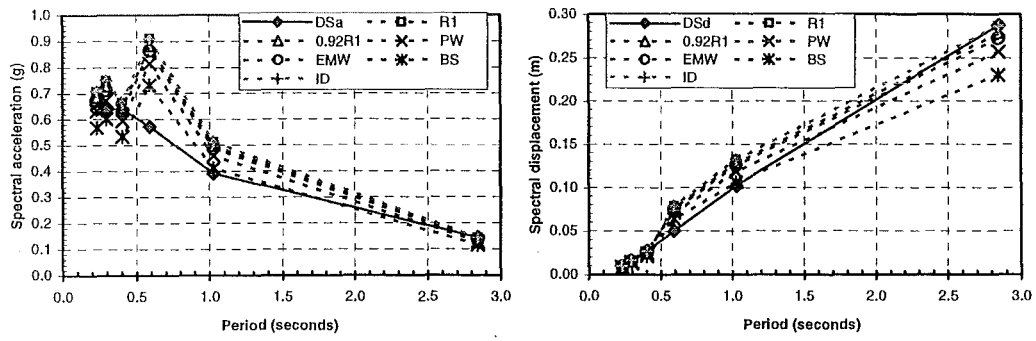

(c) 18 Storey Structure

Fig. 5-13 5% damped spectral responses of the first six modes of the three structures for **El Centro (1940-NS)** earthquake scaled by using the six different scaling methods

Note: **DSa** – design special acceleration
R1 - first mode method.
0.92R1 - first three modes with arbitrary weighting factors 0.92, 0.05 and 0.03.
PW - period weighted average of the first three modes.
EMW - effective mass weighted average of the first three modes.
BS – base shear method.
ID – inter-storey drift method.

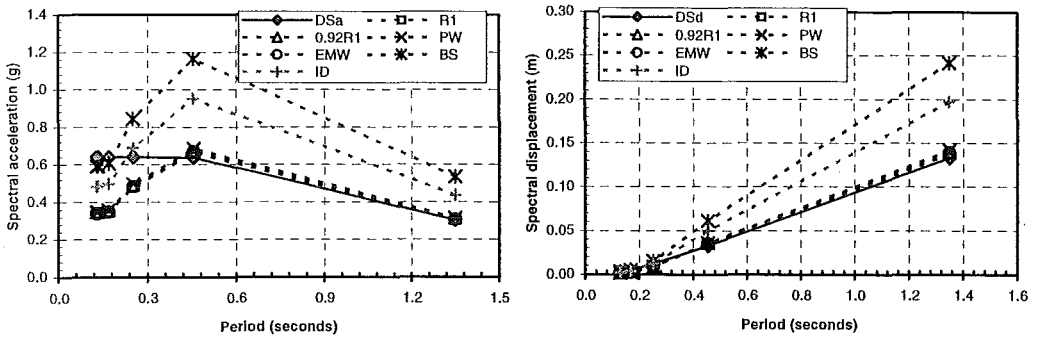

(a) 6 Storey Structure

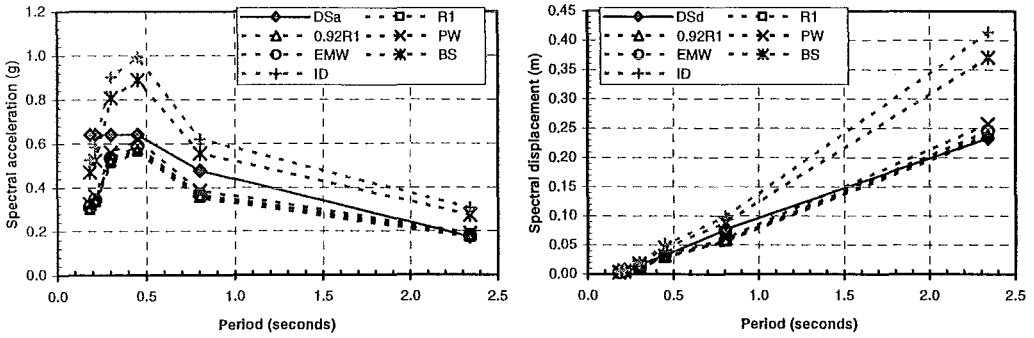

(b) 12 Storey Structure

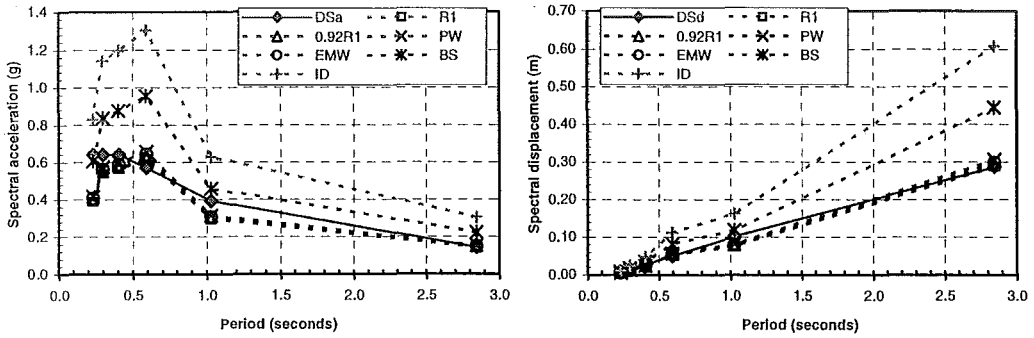

(c) 18 Storey Structure

Fig. 5-14 5% damped spectral responses of the first six modes of the three structures for **Northridge (Sylmar-949NW)** earthquake scaled by using the six different scaling methods

Note: **DSa** – design special acceleration
R1 - first mode method.
0.92R1 - first three modes with arbitrary weighting factors 0.92, 0.05 and 0.03.
PW - period weighted average of the first three modes.
EMW - effective mass weighted average of the first three modes.
BS – base shear method.
ID – inter-storey drift method.

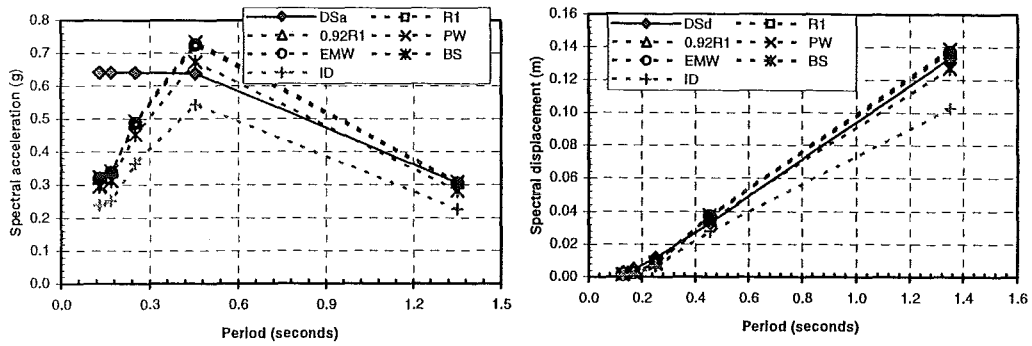

(a) 6 Storey Structure

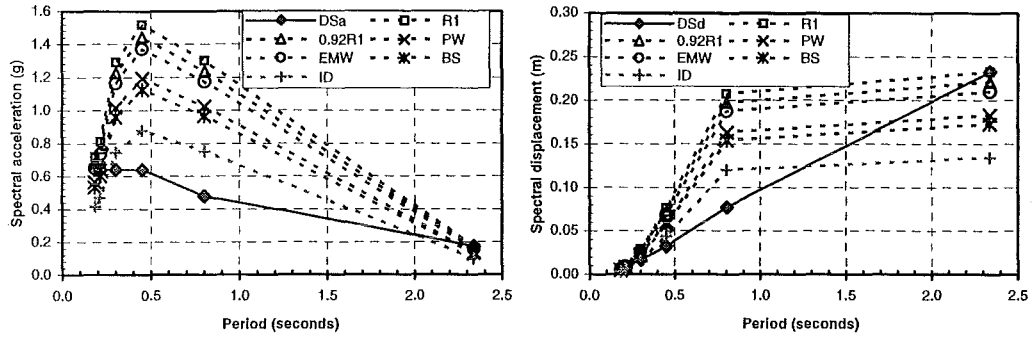

(b) 12 Storey Structure

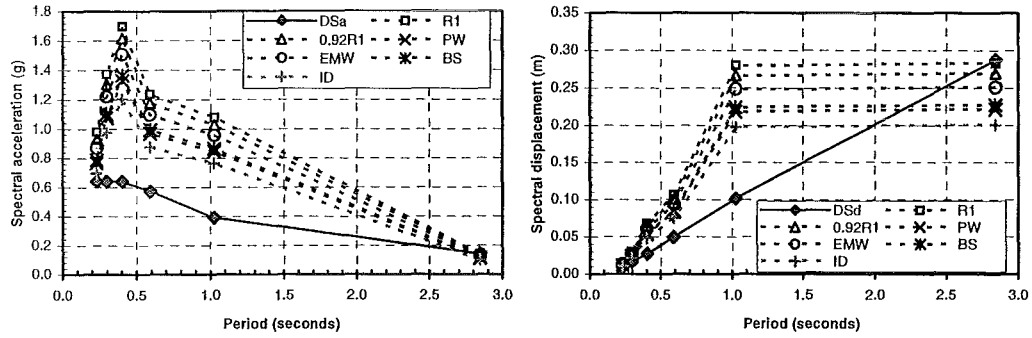

(c) 18 Storey Structure

Fig. 5-15 5% damped spectral responses of the first six modes of the three structures for **Kobe (1995-NS)** earthquake scaled by using the six different scaling methods

Note: **DSa** – design special acceleration
R1 - first mode method.
0.92R1 - first three modes with arbitrary weighting factors 0.92, 0.05 and 0.03.
PW - period weighted average of the first three modes.
EMW - effective mass weighted average of the first three modes.
BS – base shear method.
ID – inter-storey drift method.

5-11 Comparing the Base Shear, Inter-storey Drift and Roof Level Displacement for the SRSS Method with the Corresponding Maximum Responses Computed from the Time-History Analysis to the Same Scaled Earthquake Records

The 5% damped spectral accelerations and displacements of the scaled records for the four different earthquakes obtained using the six different scaling methods were computed on the software program SPECTRA [Carr 1998], as shown in Figs. 5-12 to 5-15. The base shears, inter-storey drifts and roof level displacements for the SRSS method can be obtained from these spectral responses. The maximum base shear, inter-storey drift and roof level displacements to those scaled earthquake records from time history analysis were available by running RUAUMOKO [Carr 1998]. In order to study the validity of the SRSS combination method, the ratios of the response values for SRSS to the maximum response values from the time-history analysis were calculated and presented in Figs. 5-16.a.b.c and Table 5-10.

In Figs. 5-16a.b.c, the ratios versus the scaling methods for each of the four earthquakes were approximately constant for the three structures. This means that, for a structure under all the records scaled using the six different scaling methods for a same natural earthquake, the variation between the response values predicted by using the SRSS method and dynamic time-history analysis are constant. The scaling factors do not affect this relationship, which depends only on the characteristics of the natural earthquake.

In Figs. 5-16b.c., the base shear ratios for the 12-storey structure under the Bucharest (1977-NS) excitation, the base shear and roof level displacement ratios for the 18 storey structure under the Kobe (1995-NS) were very close to 1.0. This means that only for these three cases can the SRSS method predict similar response values to those resulting from the elastic time-history analyses.

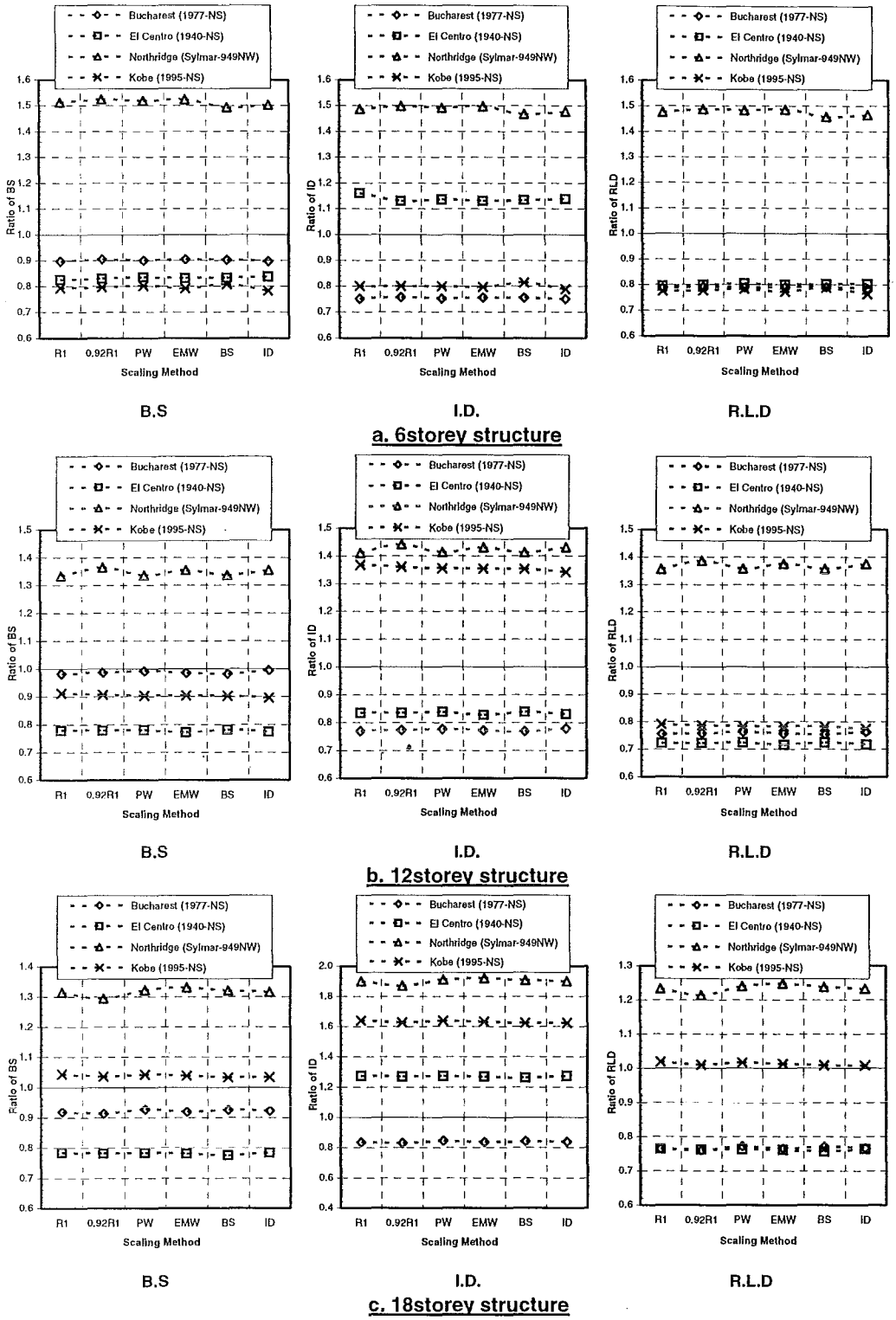

Fig. 5-16 Ratios of roof level displacement, inter-storey drift and base shear obtained by combining the 5% damped spectral responses with SRSS method to the computed correspondingly maximum responses V.S. the records for the six different scaling methods for the three structures under the four different earthquakes

Note: B.S. – base shear. **I.D.** – inter-storey drift. **R.L.D.** – roof level displacement

Table 5-10 Ratios of the base shear, inter-storey drift and roof level displacement obtained by combining the 5% damped spectral responses with SRSS method to the computed correspondingly maximum responses V.S. the six different scaling methods for the three structures under the four different earthquakes

		Bucharest (1977-NS)						El Centro (1940-NS)						Northridge (Sylmar-949NW)						Kobe (1995-NS)					
		R1	0.92R1	PW	EMW	BS	ID	R1	0.92R1	PW	EMW	BS	ID	R1	0.92R1	PW	EMW	BS	ID	R1	0.92R1	PW	EMW	BS	ID
6S	B.S.	0.90	0.90	0.90	0.90	0.90	0.90	0.83	0.83	0.84	0.83	0.83	0.84	1.51	1.52	1.52	1.52	1.49	1.50	0.79	0.80	0.80	0.79	0.81	0.78
	I.D.	0.75	0.76	0.75	0.76	0.76	0.75	1.16	1.13	1.14	1.13	1.13	1.14	1.49	1.50	1.49	1.50	1.47	1.48	0.80	0.80	0.80	0.80	0.81	0.79
	RLD	0.79	0.79	0.79	0.79	0.79	0.79	0.79	0.80	0.80	0.80	0.80	0.81	1.48	1.49	1.48	1.49	1.46	1.47	0.77	0.78	0.78	0.77	0.79	0.76
12S	B.S.	0.98	0.99	0.99	0.99	0.98	0.99	0.78	0.78	0.78	0.77	0.78	0.77	1.34	1.36	1.34	1.35	1.34	1.35	0.91	0.91	0.90	0.90	0.90	0.90
	I.D.	0.77	0.77	0.78	0.77	0.77	0.78	0.84	0.84	0.84	0.83	0.84	0.83	1.41	1.44	1.41	1.43	1.41	1.43	1.37	1.36	1.35	1.35	1.35	1.34
	RLD	0.76	0.76	0.76	0.76	0.75	0.76	0.72	0.72	0.72	0.72	0.73	0.72	1.36	1.39	1.36	1.38	1.36	1.38	0.79	0.79	0.78	0.78	0.78	0.78
18S	B.S.	0.92	0.91	0.93	0.92	0.93	0.92	0.78	0.78	0.78	0.78	0.78	0.78	1.31	1.29	1.32	1.33	1.32	1.32	1.04	1.04	1.04	1.04	1.03	1.03
	I.D.	0.84	0.83	0.84	0.84	0.84	0.84	1.27	1.27	1.27	1.27	1.26	1.27	1.90	1.87	1.91	1.92	1.91	1.90	1.64	1.63	1.64	1.63	1.62	1.62
	RLD	0.76	0.76	0.77	0.77	0.77	0.77	0.76	0.76	0.76	0.76	0.76	0.76	1.23	1.21	1.24	1.25	1.24	1.23	1.02	1.01	1.02	1.01	1.01	1.01

Note: B.S. – base shear; I.D. – inter-storey drift; R.L.D. – roof level displacement.

It is observed in Figs. 5-16a.b.c, for the Northridge (Sylmar-949NW) earthquake, the base shear, inter-storey drift and roof level displacement ratios were approximately 1.5, 1.5 and 1.5 respectively for the 6 storey structure, 1.35, 1.4 and 1.4 respectively for the 12 storey structure, and 1.3, 1.9 and 1.25 respectively for the 18 storey structure. This means that, for the Northridge (Sylmar-949NW) earthquake, the response values (base shear, inter-storey drift and roof level displacement) predicted using the SRSS method were all larger than the corresponding values from the time-history analysis for all the three structures. The maximum ratio, 1.9 for the inter-storey drift response in the 18 storey structure means that the maximum interstorey drift of the 18 storey structure for the SRSS method was approximately twice that of the time-history analysis. This implies that for some types of earthquake, the SRSS method may predict a very large overestimation of the structural responses relative to that for the time-history analysis.

However, for the 6-storey structure, both the base shear and roof level displacement ratios for the Kobe (1995-NS) earthquake were 0.8, and the inter-storey drift ratio to the El Centro (1940-NS) earthquake was 0.75. Similarly for the 12-storey structure, the base shear and roof level displacement ratios to the El Centro (1940-NS) earthquake were 0.8 and 0.7 respectively, and the inter-storey drift ratio to the Bucharest (1977-NS) earthquake was 0.8. Finally for the 18-storey structure, the base shear ratio to the El Centro (1940-NS) earthquake and the inter-storey drift ratio to the Bucharest (1977-NS) earthquake were the same 0.8, the roof level displacement ratio to both the El Centro (1940-NS) and Bucharest (1977-NS) earthquakes were 0.76. This indicates that for those cases the SRSS combination method predicted significantly smaller response values relative to that of the elastic time-history analysis.

The application of the SRSS method may lead to significant variation in the structural responses compared with the responses from the time-history analysis for certain types of structure and earthquake. Hence the SRSS modal combination method may not be appropriate for a rigorous engineering analysis.

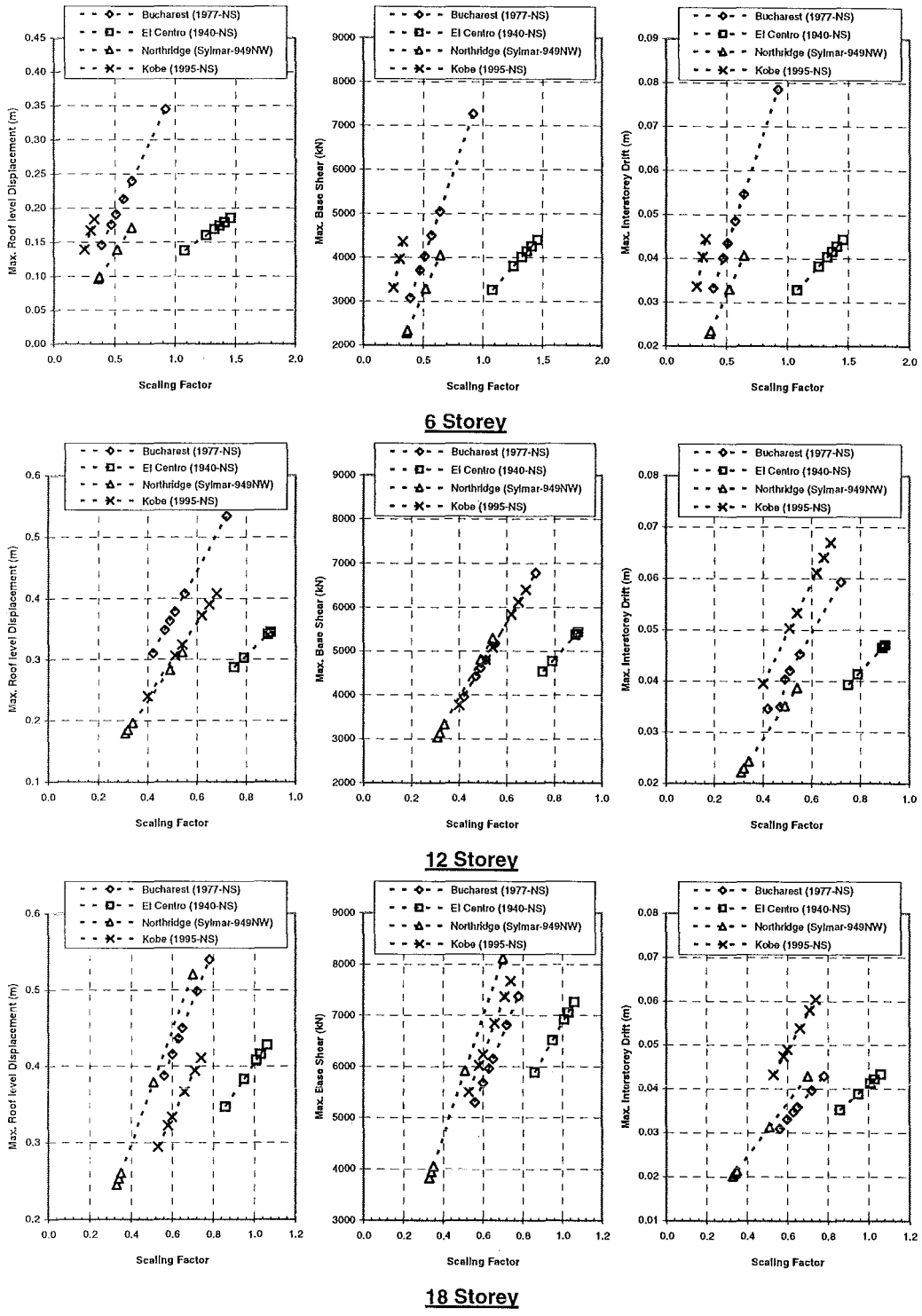

Fig. 5-17 Relationship between the maximum elastic responses and the scaling factors for the three structures under the four excitations

5-12 Relationships between the Maximum Elastic Responses and the Scaling Factors

Fig. 5-17 shows the relationships between the maximum roof level displacement, base shear, inter-storey drift and the scaling factors for the three structures under the four earthquakes scaled using the six scaling methods. Each one of the four earthquakes has six excitations for the six scaling factors obtained from the six scaling methods. That means 24 excitations are imposed on each of the three structures. There is a strong linear relationship between the maximum roof level displacement, base shear, inter-storey drift and scaling factors for the three structures, as expected.

5-13 Recommended Procedure for Earthquake Scaling and Scaling Factors Chosen for Inelastic Time-History Analysis

For short period structures, the earthquake scaling is governed by base shear for which the inter-storey drift is less than standard limit. For long period structures, usually inter-storey drift governs the scaling. A new method using whichever of the base shear or inter-storey drift governs, is required to match what is implied in New Zealand Standard [NZS4203 1992]. From the above study, none of the earlier scaling methods meet this requirement.

According to the proceeding sections of this chapter, the base shear scaling method and the inter-storey drift scaling method are reliable for earthquake scaling when the design base shear and the design inter-storey drift is required to be matched respectively.

In order to have an appropriate scaling method for which both the maximum base shear and maximum inter-storey drift to the scaled earthquakes are as close as to and are not less than the corresponding design values, which are implied in New Zealand Standard [NZS4203 1992] as expressed by either Eq. (5-11) or Eq. (5-12), either the base shear scaling method or the inter-storey drift scaling method whichever giving the larger scaling factor should be used for earthquake scaling, based on the linear relationships between the maximum elastic responses and scaling factors.

$$V_{SF=1.0} > V^{design} \text{ and } ID_{SF=1.0} = ID_{SRSS}^{design\ spectra} \tag{5-11}$$

$$V_{SF=1.0} = V^{design} \text{ and } ID_{SF=1.0} > ID_{SRSS}^{design\ spectra} \quad \textbf{(5-12)}$$

where $ID_{SRSS}^{design\ spectra}$: design inter-storey drift from SRSS of the spectral displacements.

V^{design} : design base shear determined by using equivalent static method.

$ID_{SF=1.0}$: the maximum inter-storey drift for natural earthquake excitation.

$V_{SF=1.0}$: the maximum base shear for natural earthquake excitation.

A seven-step procedure for earthquake scaling is recommended:

Step 1:

Carry out a modal frequency analysis to obtain the natural periods of free vibration and the mode shapes for the first few modes. The sum of the effective mass for the modes to be combined should exceed 90% of the total mass.

Step 2:

If the natural periods of the structures are less than 1.35 seconds, the scaling factor SF may be determined using the base shear scaling method shown in Eq. 5-13. Otherwise proceed to step 3.

$$SF = \frac{V^{design}}{V_{SF=1.0}} \quad \textbf{(5-13)}$$

where V^{design} : design base shear determined by using equivalent static method.

$V_{SF=1.0}$: the maximum base shear for natural earthquake excitation.

Step 3:

Calculate the design spectral displacements for the chosen first few modes with the design displacement spectrum.

Step 4:

Compute the design spectra SRSS inter-storey drift using the design spectral displacements and the mode shapes for the first few modes.

Step 5:

Calculate the design base shear of the elastic structure ($\mu = 1.0$) using equivalent static method used in this study.

Step 6:

Carry out dynamic elastic time-history analysis for the structure under consideration subjected to the natural earthquake to obtain the maximum inter-storey drift and the maximum base shear.

Step 7:

Determination of the scaling factor *SF* shown in Eq (5-12) below.

$$SF = max\left\{\frac{ID_{SRSS}^{design\ spectra}}{ID_{SF=1.0}},\ \frac{V^{design}}{V_{SF=1.0}}\right\} \qquad \textbf{(5-12)}$$

where $ID_{SRSS}^{design\ spectra}$: design inter-storey drift from SRSS of the spectral displacements.

V^{design} : design base shear determined by using equivalent static method.

$ID_{SF=1.0}$: the maximum inter-storey drift from elastic time-history analysis for natural earthquake excitation.

$V_{SF=1.0}$: the maximum base shear from elastic time-history analysis for natural earthquake excitation.

The scaling factors for the three structures under the four earthquakes to be used for the inelastic time-history analysis are chosen and listed in Table 5-11 according to the recommended scaling procedure.

Table 5-11 Scaling factors for the three structures under the four excitations used for inelastic time-history analysis

	Bucharest (1977-NS)	El Centro (1940-NS)	Northridge (Sylmar-949NW)	Kobe (1995-NS)
6S	0.51	1.33	0.64	0.30
12S	0.51	0.79	0.54	0.51
18S	0.78	1.06	0.70	0.60

5-14 Summary and Conclusions

The first period, the arbitrary weighting factor, the period weighted and the effective mass weighted scaling methods symbolised as R1, 0.92R1, PW and EMW respectively trying to match the design acceleration spectra, the base shear scaling and the inter-storey drift scaling methods trying to match the design base shear and design inter-storey drift respectively were used for check to see whether these scaling methods are reliable for earthquake scaling by comparing the maximum base shears, the maximum inter-storey drifts and the 5% damped spectral responses (accelerations and displacements) with the corresponding design values implied in the New Zealand loading standard.

By comparing the maximum responses (roof level displacement, inter-storey drift and base shear), which were calculated using the SRSS modal combination method, with those resulting from the elastic time-history analyses, the validity of the SRSS method is checked.

From the above study, the following conclusions may be drawn:

(1) The application of any scaling method attempting to match the scaled record to the design acceleration spectra may lead to large variations between the maximum base shear and the design base shear. This design-acceleration-spectra scaling method and the frequency scaling method are not recommended when design base shear is required to be matched implied in the current New Zealand loading standard [NSZ4203 1992].
(2) The base shear scaling method is reliable for earthquake scaling when design base shear is required to be matched.
(3) The inter-storey drift scaling method is reliable for earthquake scaling when design inter-storey drift is required to be matched.
(4) The base shear scaling method is recommended to be used for earthquake scaling for short period structures, such as the 6 storey structure used in this study.

(5) A general earthquake scaling procedure has been proposed, for which both the maximum base shear and maximum inter-storey drift to the scaled earthquakes are as close as to and are not less than the corresponding design values.

(6) A set of scaling factors for the four different earthquakes for the inelastic dynamic time history analysis of the three structures to be used later in this research work is obtained according to the general earthquake scaling procedure.

(7) The SRSS combination method may predict very large variations in base shear, roof level displacement and maximum inter-storey drift when compared with that obtained from the elastic dynamic time-history analysis for certain types of earthquake. This method may not be a good match for rigorous engineering analysis.

Chapter 6
Seismic Damage Assessment Models

6-1 Introduction

Ductile moment resisting framed structures of reinforced concrete designed using the capacity design philosophy allow energy to be dissipated at any of the beam ends at any level and the bases of the first storey columns by using inelastic hysteretic behaviour. The degree of seismic damage for the members, the storeys, or the whole structure can be predicted or evaluated by using damage models in order to either adjust the preliminary structural design under the design level earthquake, make an engineering decision to demolish or repair an existing structure after an extreme or moderate earthquake excitation, or to assess the potential damage to a structure in a future earthquake. The degrees of damage are usually quantified using damage indices. In the past, many analyses have just used the member ductility factors as a crude measure of damage potential.

A realistic damage index for seismic damage assessment requires capturing not only the maximum response value, say member curvature ductility or storey displacement and structural displacement ductility that are used in most of the current seismic codes [IAEE 1996], but also the total dissipated energy [Park 1985]. Fig. 6-1 shows two different inelastic displacement (curvature) histories of the same maximum response value experienced by one member. The degrees of damage implied for the two curvature time histories will be the same if only the maximum curvature ductility is used as the measure of damage. This method ignores the effect of the accumulatively dissipated hysteretic energy or the number of inelastic excursions on the accumulated damage in the member. However, it is obvious that the displacement (curvature) history *b* will result in larger accumulated dissipated energy and much more damage in the member than that for history *a*.

Damage models for reinforced concrete members are generally divided into five main categories. They are maximum ductility, normalised energy [Bracci 1989], ductility

and energy [Banon 1982, Park 1985], a modified version of Miner's Hypothesis [Chung 1987], and a stiffness degraded method [Roufaiel 1987]. All these damage models and the corresponding storey and overall structure damage models will be summarised in this chapter.

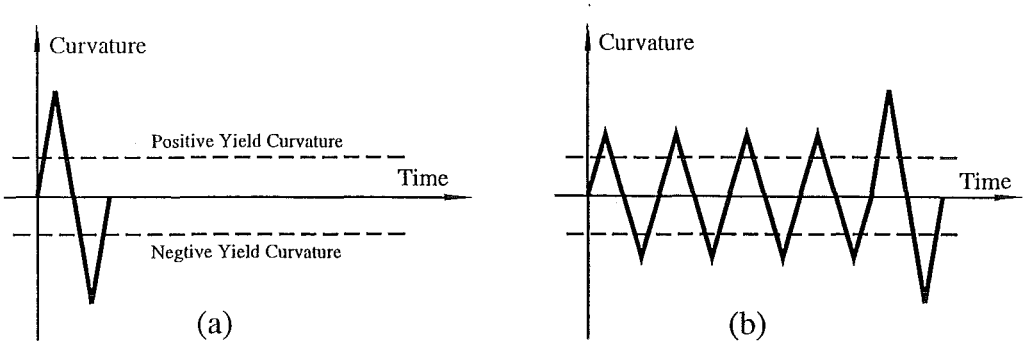

Fig. 6-1 Two different inelastic displacement (curvature) histories

The global damage index may take three forms, the weighted average of the local member damage indices, the weighted average of all the storey damage indices, and the softening global damage index. Damage in a structure always results in softening of the structure leading to a variation in the stiffnesses or natural periods of free vibration. The softening global damage index can be defined as a function of stiffness related parameters, such as the stiffness and the natural periods of free vibration of the undamaged and damaged structure. The softening global damage indices will be summarised in this chapter for future use in RUAUMOKO though they are not used in this study.

6-2 Member, Storey and Whole Structure Ductility

Member ductility can be expressed as a function of either rotation or curvature at the member end. The member curvature ductility is defined as a ratio of maximum curvature to the yield curvature. The yield curvature can be obtained from the static moment-curvature relationship.

$$\mu_{\max} = \frac{\phi_{\max}}{\phi_y} \tag{6-1}$$

where $\mu_{\max}$: maximum member curvature ductility

$\phi_{\max}$: maximum curvature at the member end

ϕ_y : yield curvature

The storey ductility, μ_s, is defined as the ratio of the maximum inter-storey drift to the yield interstorey drift which can be determined using a pushover analysis or by the Carr & Tabuchi approach [Carr 1993]:

$$\mu_s = \frac{d_s}{d_{sy}} \tag{6-2}$$

where d_s : maximum inter-storey drift

d_{sy} : yield inter-storey drift

The structural ductility, μ_t, is defined as the ratio of the maximum top-level displacement to the yield top-level displacement.

$$\mu_t = \frac{d_t}{d_{ty}} \tag{6-3}$$

where d_t : maximum top level displacement

d_{ty} : top level displacement at yield

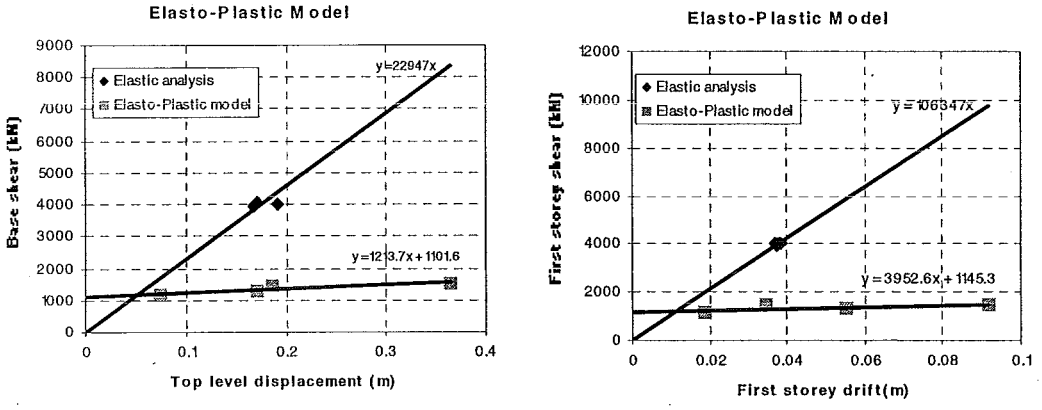

Fig. 6-2 The elastic and inelastic response trend lines for the overall structure and the first storey respectively predicted using the Elasto-Plastic model for the 6 storey structure and the four scaled earthquake excitations

The yield displacements for the storey and the structure can be determined from a pushover analysis using a prescribed loading pattern [Carr 1998]. In this study, an approach proposed by Carr [Carr 1993] is used to define the storey or overall structure yield point. The structural yield point is defined as the intersection point of two trend lines representing the relationship between the maximum base shear and the top level displacement for the elastic and inelastic responses respectively. Each trend line is based upon the responses resulting from the dynamic time history analysis for the four different excitations chosen in Chapter 5. The yield point for a storey is defined in a similar way using the inter-storey shears and the inter-storey drifts.

Fig. 6-2 presents the elastic and inelastic response trend lines for the overall structure and the first storey respectively, predicted using the elasto-plastic model for the 6-storey structure as an example.

6-3 Local Damage Index for Reinforced Concrete Structures

6-3.1 Banon and Veneziano Local Damage Model

Banon et al [Banon 1982] developed a local damage model using probabilistic concepts based on cyclic load tests of large-scale reinforced concrete elements, which is a function of a flexural damage ratio and a normalised dissipated energy.

The flexural stiffness ratio:

$$FDR = \frac{k_f}{k_r} \tag{6-4}$$

where FDR: flexural damage ratio

k_f: initial flexural stiffness

k_r: reduced secant stiffness at maximum displacement

The normalised dissipated energy:

$$E_{n(t)} = \frac{\int M_{(t)} d\theta}{0.5 * M_y \theta_y} \tag{6-5}$$

where $E_{n(t)}$: normalised dissipated energy

$\int_0 M_{(t)} d\theta$: dissipated energy

M_y: yield moment

θ_y: yield rotation

M_t: plastic moment at time t

$d\theta$: increment of rotation

The values of FDR and $E_{n(t)}$, designated as D_1 and D_2 respectively, are considered to be variables for the local damage model. By transforming the damage variables D_1, D_2 into $D_1^* = D_1 - 1$ and $D_2^* = b * D_2^r$ where b=1.1 and r=0.38 respectively, the member damage index is expressed as:

$$DI = \frac{\sqrt{(D_1^*)^2 + (D_2^*)^2}}{Numerator \ \ for \ \ monotonic \ \ loading \ \ to \ \ ultimate}$$

$$= \frac{\sqrt{\left(\frac{k_f}{k_r} - 1\right)^2 + \left[1.1\left(\frac{2E_h}{M_y \theta_y}\right)^{0.38}\right]^2}}{Numerator \ \ for \ \ monotonic \ \ loading \ \ to \ \ ultimate} \qquad \textbf{(6-6)}$$

where E_h is the total dissipated energy and the numerator for monotonic loading to ultimate is defined by Eq. (6-7a):

$$Numerator = \sqrt{\left(\frac{k_f}{k_u} - 1\right)^2 + \left[1.1\left(\frac{2E_h^u}{M_y \theta_y}\right)^{0.38}\right]^2} \qquad \textbf{(6-7a)}$$

where $E_h^u = 0.5 M_y \theta_y + M_y(\theta_u - \theta_y) + 0.5(M_u - M_y)(\theta_u - \theta_y)$ **(6-7b)**

M_y: yield moment

M_u: ultimate moment

θ_y: yield rotation

θ_u: ultimate rotation

k_f : initial stiffness

k_u : secant stiffness at ultimate point

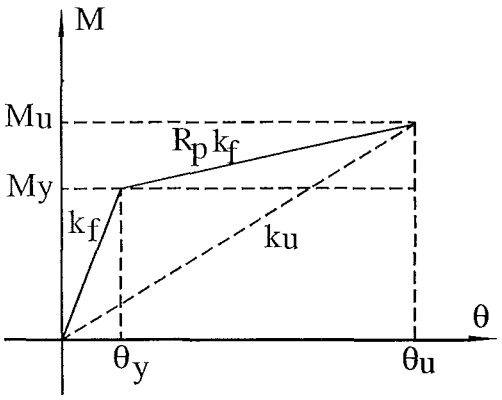

Fig. 6-3 Terms for the numerator for monotonic loading to ultimate for Banon local damage index

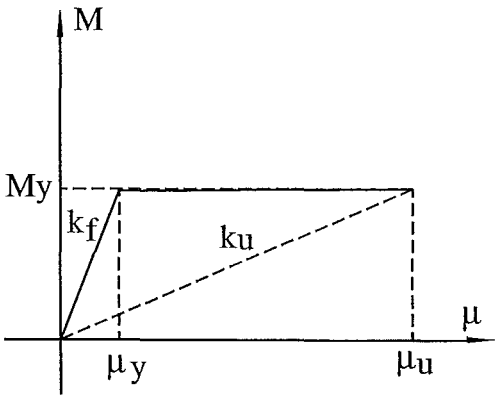

Fig. 6-4 Terms for the numerator for monotonic loading to ultimate for Banon local damage index used in RUAUMOKO ($M_u = M_y$)

An equivalent form of Eq. (6-8) is used in RUAUMOKO [Carr 1998] assuming the post yield stiffness is zero:

$$DI = \frac{\sqrt{\left(\frac{\mu_{\max}}{\mu_y} - 1\right)^2 + \left[1.1\left(\frac{2E_h}{M_y \mu_y}\right)^{0.38}\right]^2}}{Numerator\ \ for\ \ monotonic\ \ loading\ \ to\ \ ultimate}$$

$$= \frac{\sqrt{(\mu_{\max} - 1)^2 + \left[1.1\left(\frac{2E_h}{M_y}\right)^{0.38}\right]^2}}{Numerator\ \ for\ \ monotonic\ \ loading\ \ to\ \ ultimate} \qquad \textbf{(6-8)}$$

where $\mu_{\max}$: maximum curvature ductility

μ_y : yield curvature ductility =1.0

E_h : dissipated energy

M_y : yield bending moment

$$Numerator = \sqrt{(\mu_u - 1)^2 + \left[1.1(2\mu_u - 1)^{0.38}\right]^2}$$

μ_u : ultimate curvature ductility

6-3.2 Park and Ang's Local Damage Index

Park and Ang's local damage index is a linear combination of the maximum deformation and the total dissipated energy caused by repeated cyclic loading [Park 1985]. The index is expressed as follows:

$$DI = \frac{u_m}{u_u} + \frac{\beta}{F_y * u_u} \int dE \qquad \textbf{(6-9)}$$

where: u_m : maximum response deformation under an earthquake shown in Fig. 6-5.

u_u : ultimate deformation capacity under monotonic loading shown in Fig. 6-5.

F_y : calculated yield strength shown in Fig. 6-5.

dE : incremental dissipated hysteretic energy.

$\int dE$: total dissipated energy.

β : experimental constant (=0.05 for reinforced concrete members).

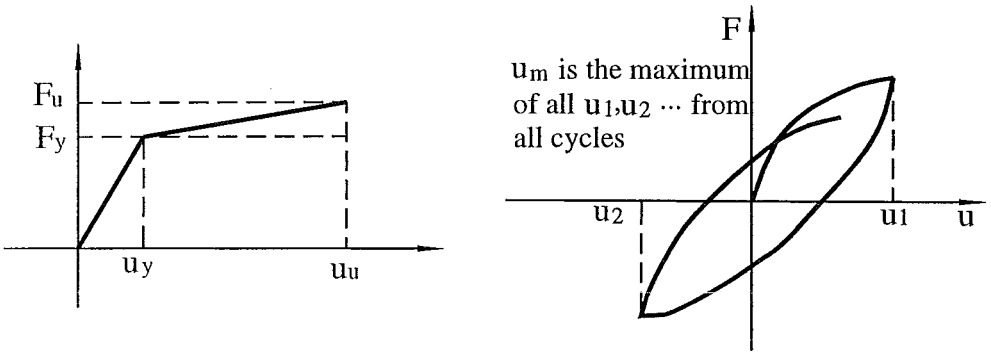

Fig. 6-5 Definition of F_y, u_u and u_m in Park and Ang's damage index

The first term in Eq. (6-10) represents the damage due to maximum deformation experienced during seismic loading, and the second term reflects the influence of the total absorbed hysteretic energy on the local or member damage. This contribution of energy component that is number of cycles related could be very significant even β =0.05, as shown in Appendix K.

The constant parameter β is found experimentally. According to Park et al., β was determined using a regression equation obtained from experimental results with 400 reinforced concrete columns and beams. The value of β obtained by Park et al. [Park 1985B] was 0.05 for reinforced concrete members, and this is used in this study.

For reinforced concrete structures, an equivalent form of the Park and Ang damage index is used [Carr 1998]. The damage index for the plastic hinge locations at the ends of a member is defined as follows:

$$DI_{mem} = \frac{\phi_m}{\phi_u} + \frac{\beta}{M_y * \phi_u} \int dE \qquad \textbf{(6-10)}$$

where: ϕ_m : maximum positive or negative curvature.

ϕ_u : ultimate curvature capacity under monotonic loading.

M_y : calculated yield moment.

$\int dE$: total dissipated energy.

β : experimental constant model parameter (=0.05 in this study).

The ultimate curvature ductility of a member under monotonic loading has a strong influence on the member damage index and is an indicator of the curvature deformation capacity. Hence it is very important to accurately evaluate the ultimate curvature ductility capacity. The curvature ductility for reinforced concrete members depends strongly on the confinement detailing in the plastic hinge region of the member.

6-3.3 Roufaiel and Meyer Local Damage Index

Roufaiel and Meyer [Roufaiel 1987] proposed a damage index for reinforced concrete members.

$$DI = \max\left\{DI^+,\ DI^-\right\} \qquad \textbf{(6-11)}$$

where
$$DI^{+} = \frac{\frac{\phi_m^{+}}{M_m^{+}} - \frac{\phi_y^{+}}{M_y^{+}}}{\frac{\phi_u^{+}}{M_u^{+}} - \frac{\phi_y^{+}}{M_y^{+}}} \qquad \textbf{(6-12)}$$

$$DI^{-} = \frac{\frac{\phi_m^{-}}{M_m^{-}} - \frac{\phi_y^{-}}{M_y^{-}}}{\frac{\phi_u^{-}}{M_u^{-}} - \frac{\phi_y^{-}}{M_y^{-}}} \qquad \textbf{(6-13)}$$

This damage index is a function of the secant stiffnesses at the yield point M_y/ϕ_y, the maximum response point M_{max}/ϕ_{max} and the ultimate point M_u/ϕ_u as shown in Fig. 6-6. Superscripts + and – denote the loading direction.

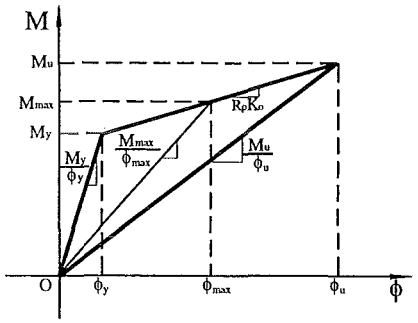

Fig. 6-6 Definition of Roufaiel and Meyer damage index

The value *DI=0.0* indicates that the yield moment of a member has not been exceeded, the member is in the elastic stage and damage in the member is nonexistent. At the other extreme, if failure or ultimate curvature ϕ_u has been reached, then *DI=1.0*.

This damage model is also based on the assumption that a shear failure, bar slippage or any other potentially premature local failure is eliminated. This can be assumed by use of the capacity design method and the reinforcement detailing required in the New Zealand Standards [NZS4203 1992, NZS3101 1995]. However, this may not be assumed for pre-1980s designed structures in New Zealand in New Zealand for structures designed before the 1980s when capacity design principle were not in use.

6-3.4 Chung, Meyer and Shinozuka's Local Damage Index

Chung et al. [Chung 1987] proposed a damage index that combines a modified version of Miner's Hypothesis for positive and negative inelastic deformation respectively. This index is given by the following expression:

$$DI = \sum_i \sum_j \left(\alpha_{ij}^{+} \frac{n_{ij}^{+}}{N_i^{+}} + \alpha_{ij}^{-} \frac{n_{ij}^{-}}{N_i^{-}} \right) \qquad \textbf{(6-14)}$$

where i: indicator of different displacement or curvature levels.

j: indicator of cycle number for a given curvature level i.

$N_i = \dfrac{M_{i1} - M_{fi}}{\Delta M_i}$: number of cycles at curvature level i to cause failure.

M_{i1}: moment for the first cycle at curvature level i.

M_{fi}: moment to cause member failure at curvature level i.

ΔM_i: strength drop for every cycle at curvature level i.

n_{ij}: j-th cycle at curvature level i actually applied.

α_{ij}: damage accelerator for j-th cycle at curvature level i.

+, -: indicator of loading sense.

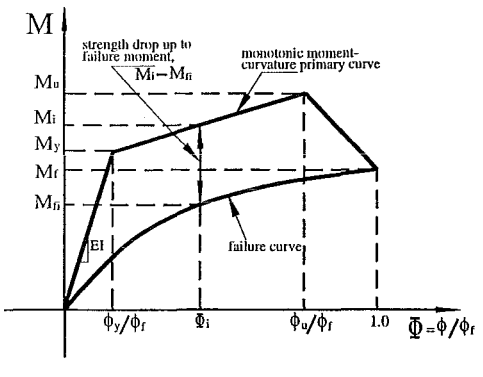

Fig. 6-7 **Definition of terms for the fatigue failure curve for positive loading sense for Chung et al damage model**

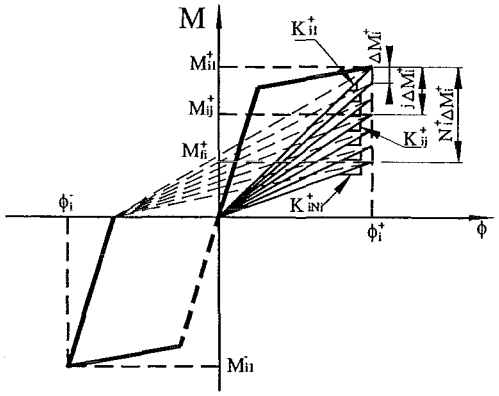

Fig. 6-8 **Definition of terms for the positive damage accelerator for Chung et al damage model**

The inelastic cycles considered for contribution to the local damage are those cycles whose displacements or curvatures are larger than those at yield, i.e. the $\phi_i > \phi_y$. This implies that all the amplitudes that are smaller than the yield amplitudes during the inelastic stage in addition to those in the elastic range, are not considered for the local damage assessment. The energy dissipated by those small inelastic amplitudes does not affect the damage index in this model.

The failure moment for different curvature levels is a function of the failure moment for monotonic loading and ratio of the response curvature to the failure curvature for monotonic loading. This failure curve is plotted in Fig. 6-7 and defined as:

$$M_{fi} = M_f \frac{2\Phi_i}{\Phi_i + 1.0} \tag{6-15}$$

where M_{fi}: failure moment for a given curvature level ϕ_i.

M_f: failure moment for monotonic loading.

$\Phi_i = \frac{\phi_i}{\phi_f}$: curvature ratio.

ϕ_f: failure curvature for monotonic loading.

The effect of the loading sequence (loading history) is taken into account by a damage accelerator, α_{ij}, which for positive moment loading is defined as:

$$\alpha_{ij}^{+} = \frac{K_{ij}^{+}}{\overline{K}_i^{+}} * \frac{\phi_i^{+} + \phi_{i-1}^{+}}{2\phi_i^{+}}$$

$$= \frac{M_{ij}^{+}}{\left[M_{i1}^{+} - 0.5\left(N_i^{+} - 1\right)\Delta M_i^{+}\right]} * \frac{\phi_i^{+} + \phi_{i-1}^{+}}{2\phi_i^{+}} \tag{6-16}$$

where K_{ij}^{+}: secant stiffness for j-th cycle at curvature level i, $j=1,2,3\ldots N$.

$\overline{K}_i^{+} = \frac{K_{i1}^{+} + K_{i2}^{+} + \ldots K_{iN}^{+}}{N}$: average of secant stiffness of all the cycles at curvature level i.

K_{i1}^{+}: secant stiffness for the first cycle at curvature level i.

K_{iN}^{+} : secant stiffness for the cycle to cause member failure at curvature level i.

ΔM_i : strength drop for every cycle at curvature level i.

ϕ_i^+ : curvature at level i.

ϕ_{i-1}^+ : curvature for most recent cycle of ϕ_i^+.

The definitions of terms in Eqs. (6-15) and (6-16) are also shown in Figs. 6-7 and 6-8.

For a constant-amplitude (curvature) loading cycles, the energy dissipated during a single cycle decreases for successive cycles due to the decrease in stiffness and the strength degradation, as shown in Fig. 6-8. That means the damage increments also decrease. The first load cycle will cause more damage than the following cycles. The damage accelerator decreases as the loading cycles proceed. This is indicated by introducing the stiffness ratio into the damage accelerator shown in Eq. (6-16).

As shown in Fig. 6-9, even though the second cycle in both cases involves the same curvature level, the dissipated energy or damage incurred for the two cycles is different, because the damage due to the preceding cycles is different. This effect of difference in inter-cycle curvature on the damage accelerator is reflected in the ratio $\frac{\phi_i^+ + \phi_{i-1}^+}{2\phi_i^+}$.

The effect of loading history on the damage evaluation is taken into account by the positive and negative damage accelerators in this model, which is not seen in the other models available at the current time.

Because the values of the total number of cycles causing member failure for different curvature levels N_i^+ and N_i^- as well as the strength drop for each cycle ΔM_i to level i are not available currently from laboratory tests, this damage model cannot be readily used at the present time.

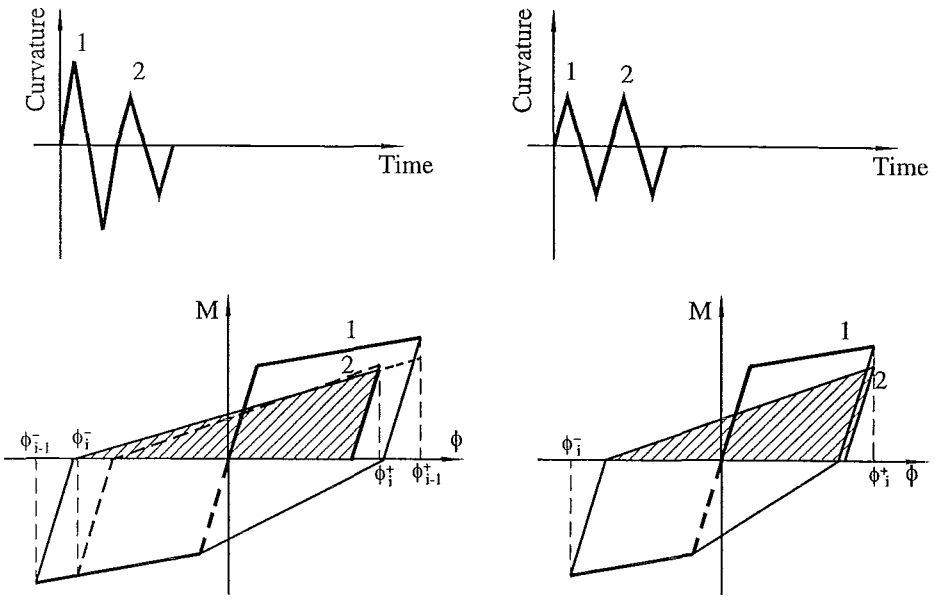

Fig. 6-9 Two displacement (curvature) histories and their moment-curvature responses for damage accelerator

6-3.5 Bracci et al.'s Local Damage Index

6-3.5.1 Concept of Bracci et al.'s Local Damage Index

Bracci et al. [Bracci 1989] proposed a damage index in terms of the ratio of the damage consumption (D_c) to the damage potential (D_p) of a component. The index is expressed in Eq. (6-17).

$$DI = \frac{D_c}{D_p} \tag{6-17}$$

The damage potential is the total energy capacity of the component to sustain damage. The damage potential is defined as the total area between the monotonic load-deformation curve $f_m(\phi)$ and the low cycle fatigue failure envelope $f_f(\phi)$, as shown in Fig. 6-10a. The low cycle fatigue constitutes failure after repeated cycling at a given amplitude of deformation. The fatigue failure envelope is obtained by connecting all failure points of inelastic fatigue testing at different deformation levels. This is an opposite extreme loading case to the monotonic loading.

$$D_p = \int_{-\phi_u}^{+\phi_u} [f_m(\phi) - f_f(\phi)] d\phi \qquad \textbf{(6-18)}$$

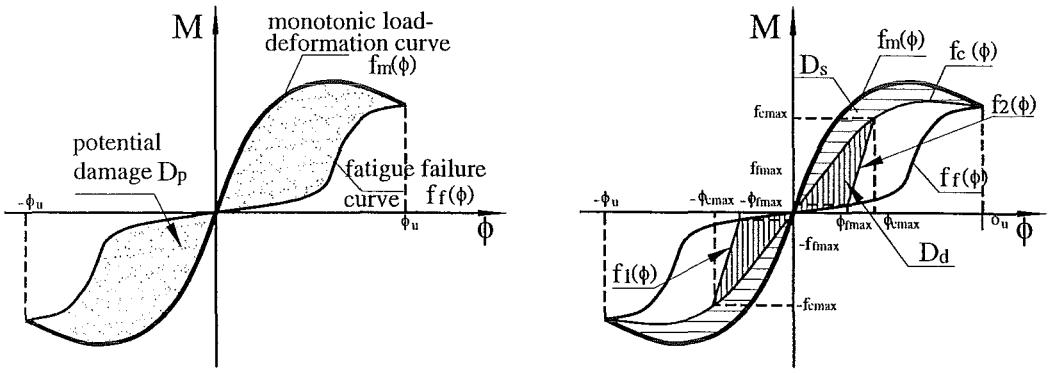

Fig. 6-10 Definition of D_p, D_s and D_d for Bracci damage model

The damage consumption or energy consumption consists of the strength damage and the deformation damage expressed in Eq. (6-19).

$$D_c = D_s + D_d \qquad \textbf{(6-19)}$$

Strength damage, D_s, is caused by strength deterioration due to the dynamic inelastic cyclic loading, which is defined as the area between the monotonic load-deformation (primary) curve $f_m(\phi)$ and the strength-damaged curve $f_c(\phi)$, as shown in Fig. 6-9b and Eq. (6-20).

$$D_s = \int_{-\phi_u}^{+\phi_u} [f_m(\phi) - f_c(\phi)] d\phi \qquad \textbf{(6-20)}$$

The deformation damage, D_d, is due to the irrecoverable permanent deformation illustrated in Fig. 6-10b. It is defined as the area bounded by the strength-damaged curve, $f_c(\phi)$, unloading curves, $f_1(\phi)$ and $f_2(\phi)$, and the fatigue failure envelope, $f_f(\phi)$. The unloading curves are the two assumed linear lines for the unloading responses of the member from the maximum curvature points in the positive and negative directions, which are related to the residual curvature or the unloading

stiffness parameter in the hysteresis rules. The deformation damage is expressed in Eq. (6-21).

$$D_d = \int_{-\phi_{c\max}}^{+\phi_{c\max}} [f_c(\phi) - f_f(\phi)]d\phi - \int_{\phi_{f\max}}^{\phi_{c\max}} [f_2(\phi) - f_f(\phi)]d\phi$$
$$- \int_{-\phi_{c\max}}^{-\phi_{f\max}} [f_1(\phi) - f_f(\phi)]d\phi \qquad (6\text{-}21)$$

where

$f_c(\phi)$ strength-damaged curve

$f_f(\phi)$ fatigue failure curve

$f_1(\phi)$ unloading curve from the maximum curvature point in negative direction

$f_2(\phi)$ unloading curve from the maximum curvature point in positive direction

$\phi_{c\max}$ the maximum curvature in positive direction

$-\phi_{c\max}$ the maximum curvature in negative direction

$\phi_{f\max}$ the curvature for the intersection point of the positive unloading curve and the fatigue failure curve

$-\phi_{f\max}$ the curvature for the intersection point of the negative unloading curve and the fatigue failure curve

Because it is too difficult to obtain the experimental low cycle inelastic fatigue failure curve, $f_f(\phi)$, Bracci et al. proposed two kinds of assumed fatigue function curve for reinforced concrete members. The two functionals are the transposed form of the monotonic primary curve and the simple straight line shown in Fig. 6-11 for the bilinear hysteresis model.

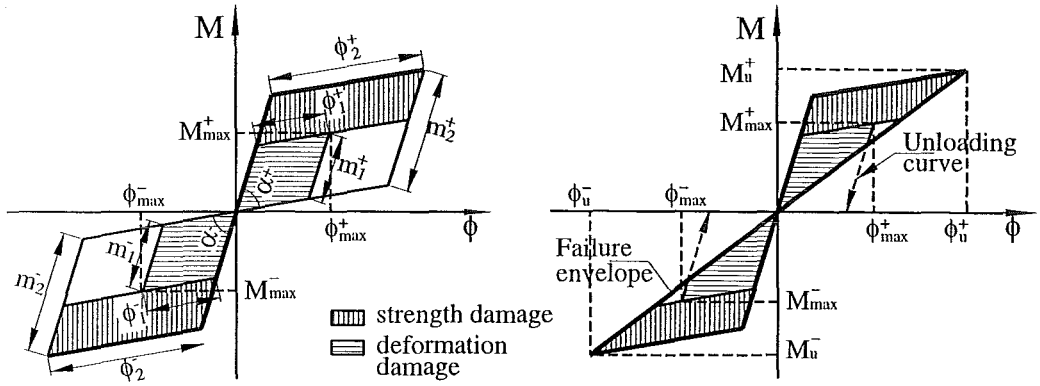

a) Transposed form of monotonic primary curve **b) Simple straight line**

Fig. 6-11 Two assumptions for fatigue failure curve of Bracci damage model for reinforced concrete members with Bilinear hysteresis model

From Fig. 6-10a and the transposed failure curve, the following expressions are derived:

$$D_s = (m_2^+ - m_1^+)\phi_2^+ \sin\alpha^+ + (m_2^- - m_1^-)\phi_2^- \sin\alpha^- \quad \textbf{(6-22)}$$

$$D_d = (m_1^+)\phi_1^+ \sin\alpha^+ + (m_1^-)\phi_1^- \sin\alpha^- \quad \textbf{(6-23)}$$

$$D_p = (m_2^+)\phi_2^+ \sin\alpha^+ + (m_2^-)\phi_2^- \sin\alpha^- \quad \textbf{(6-24)}$$

If the yielding and ultimate moments, initial and post-yielding stiffness in one direction are assumed to be same as in the reverse direction, then $m_1^+ = m_1^-$, $m_2^+ = m_2^-$, $\phi_1^+ = \phi_1^-$, $\phi_2^+ = \phi_2^-$ and $\alpha^+ = \alpha^-$. The damage index for one end of the member is:

$$DI = \frac{D_s + D_d}{D_p}$$

$$= \frac{(m_2 - m_1)\phi_2 \sin\alpha + (m_2 - m_1)\phi_2 \sin\alpha + m_1\phi_1 \sin\alpha + m_1\phi_1 \sin\alpha}{m_2\phi_2 \sin\alpha + m_2\phi_2 \sin\alpha}$$

$$= \frac{2(m_2 - m_1)\phi_2 + 2m_1\phi_1}{2m_2\phi_2}$$

$$= \frac{(m_2 - m_1)\phi_2 + m_1\phi_1}{m_2\phi_2}$$

$$= \frac{m_2 - m_1}{m_2} + \frac{m_1\phi_1}{m_2\phi_2}$$

$$= D_1 + D_2 - D_1 D_2 \qquad \textbf{(6-25)}$$

where $D_1 = \dfrac{\phi_1}{\phi_2} = \dfrac{\phi_{\max}}{\phi_u}$

$$D_2 = \frac{m_2 - m_1}{m_2} = \frac{\Delta M}{M_y}$$

From Eq. (6-25), it is found that the damage index is a function of the irrecoverable permanent deformation $\dfrac{\phi_{\max}}{\phi_u}$ and the strength damage $\dfrac{\Delta M}{M_y}$, but has nothing to do with the angle α between the initial stiffness straight line and the post yield stiffness straight line, as shown in Fig. 6-11a. This angle is the assumed post yield stiffness for a specified initial stiffness of a member.

6-3.5.2 Bracci Local Damage Index with Straight-Line Fatigue Failure Curve Assumption

The assumed straight-line fatigue failure curves which are the lines connecting the origin and the ultimate response points for the Bracci local damage indices of the modified Takeda and origin-centred bilinear hysteresis models are shown in Fig. 6-12. In these examples, the post-yielding branches of the primary curves are assumed to have no strength degradation in the hysteresis models.

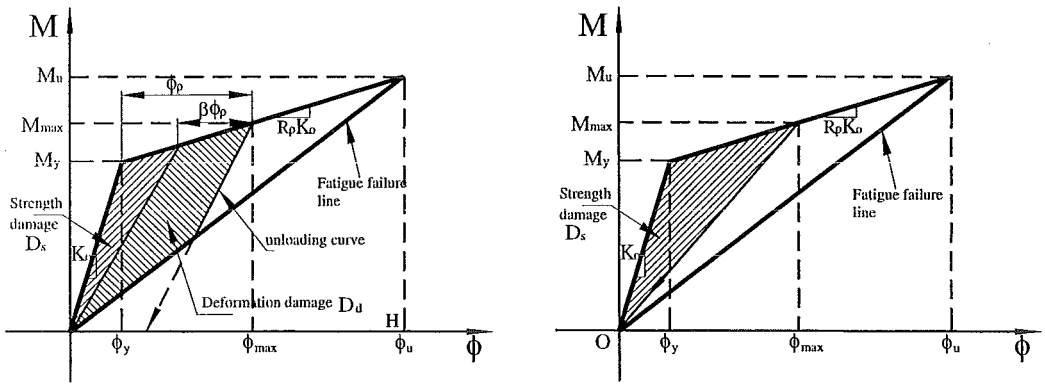

a) For modified Takeda model **b) For Origin-centred bilinear model**

Fig. 6-12 Bacci damage index for modified Takeda and origin-centred bilinear models with assumed straight line for fatigue failure curve

Fig. 6-12a shows the strength and deformation damage for the modified Takeda model. The reloading stiffness parameter β can influence the strength damage D_s, but not affect the sum of the strength and deformation damage, i.e. the total hatched area. This is also reflected in Eq. (6-26) for the damage index DI. The derivations for Eq. (6-26) are given in Appendix D.

$$DI = \frac{(\mu_{\max}-1)(2R_p-\mu_{\max}^{-\alpha})-\mu_u^{-1}(1-R_p)+\phi_y(\mu_u^{-1}-\mu_{\max}^{-1})-\mu_{\max}^2 R_p \mu_u^{-1}+1}{(\mu_u-1)[R_p+(1-R_p)\mu_u^{-1}-\mu_{\max}^{-\alpha}]} \quad \textbf{(6-26)}$$

where ϕ_y: yielding curvature

R_p: ratio of post-yielding stiffness to initial stiffness

$\mu_{\max}$: maximum curvature ductility demand

μ_u: ultimate curvature ductility capacity

α: unloading stiffness parameter for Emori type model [Emori 1978].

Eq. (6-26) is also valid for the Q-Hyst [Saiidi 1979] and degrading bilinear models [Nielsen 1971].

If $R_p = \alpha = 0.00$, the Bracci damage index for the Elasto-plastic model is derived from Eq. (6-26) and is expressed as:

$$DI = \frac{2+(\phi_y-1)\mu_u^{-1}-\mu_{\max}+\phi_y\mu_{\max}^{-1}}{(\mu_u-1)(\mu_u^{-1}-1)} \quad \textbf{(6-27)}$$

If $\alpha = 0.00$, Eq. (6-27) gives the damage index for the Bilinear and Clough hysteresis models [Clough 1966]:

$$DI = \frac{(\mu_{\max}-1)(2R_p-1)-\mu_u^{-1}(1-R_p)+\phi_y(\mu_u^{-1}-\mu_{\max}^{-1})-\mu_{\max}^2 R_p \mu_u^{-1}+1}{(\mu_u-1)[R_p+(1-R_p)\mu_u^{-1}-1]} \quad \textbf{(6-28)}$$

The strength damage and the assumed straight fatigue failure line for the Origin-centred bilinear model are shown in Fig. 6-12b. There is no irrecoverable permanent

deformation damage because the unloading curve is assumed to pass through the origin. This will give a smaller damage index than that predicted with any other hysteresis model.

The Bracci damage model for the Origin-centred bilinear hysteresis model is expressed by Eq. (6-29) where the derivation is given in Appendix D.

$$DI = \frac{\phi_{\max} - \phi_y}{\phi_u - \phi_y} = \frac{\mu_{\max} - 1}{\mu_u - 1} \tag{6-29}$$

where ϕ_y, $\phi_{\max}$, ϕ_u are the yield, maximum and ultimate curvatures respectively and $\mu_{\max}$, μ_u are the maximum and ultimate curvature ductilities respectively.

6-3.5.3 Bracci Local Damage Index with Transposed Bilinear Fatigue Failure Curve Assumption

The transposed bilinear fatigue failure curve for the Bracci local damage index consists of two straight lines that are parallel to the two segments of the bilinear primary curve, as shown in Fig. 6-13.

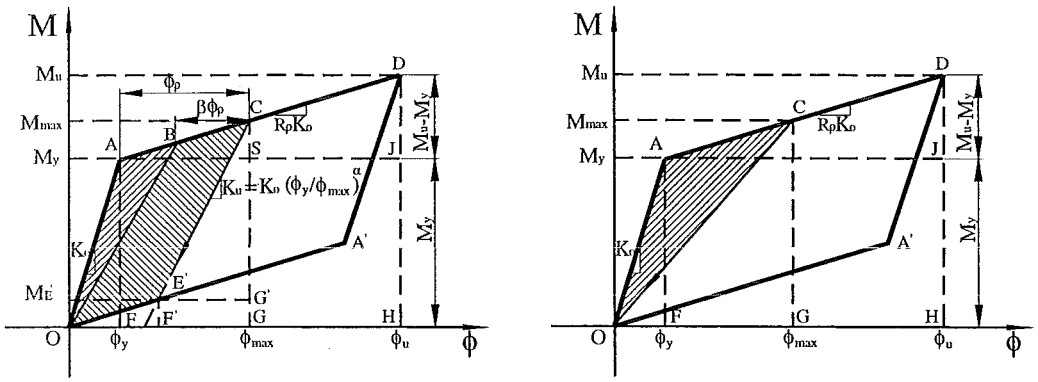

a) For modified Takeda model

b) For Origin-centred bilinear model

Fig. 6-13 Bracci damage index for modified Takeda and origin-centred bilinear hysteresis models with assumed transposed bilinear fatigue failure curve

The reloading stiffness parameter β for the modified Takeda model does not affect the total hatched area $A_{OACE'}$ that is the sum of the strength damage and the deformation

damage, as shown in Fig. 6-13a. This is also reflected in Eq. (6-30) for the Bracci damage index for the modified Takeda hysteresis model with the transposed bilinear fatigue failure assumption. The derivation of this damage index is given in Appendix E.

$$DI = \frac{R_p \mu_{\max} - \mu_{\max}^{1-\alpha} + 0.5\mu_{\max}^{-\alpha} - R_p + 0.5}{\left(R_p - \mu_{\max}^{-\alpha}\right)\left(\mu_u - 1\right)} \tag{6-30}$$

where R_p: ratio of post-yield stiffness to the initial stiffness

α: unloading stiffness parameter

$\mu_{\max}$: maximum curvature ductility (demand)

μ_u: ultimate curvature ductility (capacity)

Eq. (6-30) is valid for the Degrading Bilinear and Q-Hyst hysteresis models. For the Elasto-Plastic, Bilinear and Clough models, the Bracci damage indices are determined by Eq. (6-31) derived from Eq. (6-30) as shown in Appendix E.

$$DI = \frac{\mu_{\max} - 1}{\mu_u - 1} \tag{6-31}$$

For the Origin-centred bilinear hysteresis model, the Bracci damage index is derived in Appendix E and is shown in Eq. (6-32) below:

$$DI = \frac{0.5\left(\mu_{\max} - 1\right)}{\mu_u - 1} \tag{6-32}$$

6-3.6 Cosenza, Manfredi and Ramaseo Local Damage Index

Cosenza et al [Cosenza 1993] proposed a normalised functional as a damage index, as shown in Eq. (6-33):

$$DI = \begin{cases} 0 & when \quad \mu \le 1 \\ \left(\dfrac{\mu_m - 1}{\mu_u - 1}\right)^{\alpha} & when \quad 1 < \mu \le \mu_u, \ \alpha > 0 \\ 1 & when \quad \mu > \mu_u \end{cases} \tag{6-33}$$

where μ_m: maximum curvature ductility $\mu_{\max}$ determined by Eq. (6-34) or energy ductility μ_e defined by Eq. (6-36).

μ_u: ultimate curvature ductility or ultimate energy ductility (capacity).

For the maximum curvature ductility:

$$\mu_{\max} = \frac{\phi_{\max}}{\phi_y} \tag{6-34}$$

where $\mu_{\max}$: maximum curvature ductility

$\phi_{\max}$: maximum curvature demand

ϕ_y: yield curvature

Considering $\alpha = 1.0$, from Eq. (6-33), the damage index for the curvature ductility is obtained as:

$$DI = \frac{\mu_{\max} - 1}{\mu_u - 1} \tag{6-35}$$

where $\mu_{\max}$: maximum curvature ductility

μ_u: ultimate monotonic curvature ductility capacity

The energy ductility is:

$$\mu_e = \frac{\int E_h}{M_y \phi_y} + 1 \tag{6-36}$$

Replacing the curvature ductility in Eq. (6-35) by the energy ductility that is defined by Eq. (6-36), the corresponding normalised damage index is defined as:

$$DI_e = \frac{\mu_e - 1}{\mu_{e,u} - 1} \tag{6-37}$$

where DI_e: damage index for energy ductility

μ_e: energy ductility, defined by Eq. (6-36)

$\mu_{e,u}$: ultimate energy ductility capacity, $\mu_{e,u} \cong \mu_u$ and $\mu_{e,u} = \mu_u$ for an elastic-perfect plastic hysteresis model.

The damage index expressed in Eq. (6-35) that is a function of curvature ductility is used in this study.

Six different member damage indices are summarised in this section. Unfortunately the Chung et al's damage model cannot be used in a practical analysis due to the difficulty in defining the total number of cycles causing member failure for different curvature levels, and the strength drop for each fatigue cycle from laboratory tests, even though the effect of loading sequence on the damage evaluation is taken into account in this model.

The Bracci et al. member damage index was not available in RUAUMOKO. Hence, the four member damage indices incorporated in RUAUMOKO i.e. the Banon & Veneziano, Park & Ang, Roufaiel & Mayer and the Cosena et al. were used for the member damage evaluation in this study.

6-4 The Storey Damage Index and the Whole Structure or Global Damage Index

The damage index for a storey or a whole structure is used to quantify the degree of damage to the storey or to the overall structure. A storey is defined as all the beams at the level under consideration and all the columns just below that level.

The damage index for the storey can be obtained by calculating a weighted average of the local damage indices at all the inelastic member ends in this storey. Park and Ang [Park 1985A] proposed a damage index for the storeys in which the dissipated energy is used in calculating the weighting factors for every member end. However the important factor of yield in the columns is not taken into account in this model when carrying out the storey damage analysis for the first storey of a framed structure

designed using the capacity design method. Hence a new damage model for the storey may be studied in the future as recommended in Chapter 10.

There are three ways for computing the global damage index. The first one is to calculate a weighted average of the local damage indices at member ends over the whole structure. The second is to calculate a weighted average of the damage indices for all storeys. The last method is by considering some variation in the overall characteristics of the structure such as the lower modal periods of free-vibration and is called the softening global damage index.

The damaged structure always shows degradation in stiffness when compared with the undamaged structure. This implies a variation in the natural periods of free vibration in every time step during the earthquake. The history of the degree of damage for the overall structure can be expressed by the history of variation in the stiffness [Mork 1992, Nielsen 1992]] or period of free-vibration [DiPasquale 1990] etc. The maximum damage index in this history can be regarded as the overall damage index.

6-4.1 Park and Ang Global Damage Index

Park and Ang [Park 1985A] proposed a global damage index defined as a weighted average of the local damage indices for all components of a structure. The weighting factor for each end of a member is proportional to the dissipated energy at the corresponding end in the element. The global damage index DI_g is given by Eq. (6-38):

$$DI_g = \sum_{i=1}^{n} (\lambda_i * DI_i) \qquad \textbf{(6-38a)}$$

where $\lambda_i = \dfrac{E_i}{\sum_{i=1}^{n} E_i}$ **(6-38b)**

n: number of member ends of whole structure where the local damage index is computed.

E_i : dissipated energy at end i of a member.

The storey-level damage index is also obtained from Eq. (6-38). The only difference is that the number of member ends is limited to these in the storey under consideration.

According to the damage assessment carried out by Park and Ang [Park 1985A] for a prototype structure, the global structural damage index is interpreted as follows:

$DI_g \leq 0.4$	Repairable damage
$DI_g > 0.4$	Damage beyond repair
$DI_g \geq 1.0$	Total collapse

6-4.2 Roufaiel and Meyer's Global Damage Index

Roufaiel and Meyer [Roufaiel 1987] proposed a global damage index expressed in terms of displacements at the roof level of a structure. Because the maximum roof displacement is directly related to the variation in fundamental frequency of the structure due to the earthquake damage, this global damage index is also expressed as a function of the undamaged and damaged fundamental frequencies of the structure as shown in Eq. (6-39). This kind of global damage index related to the change in the natural periods of the overall structure is called a softening damage index.

$$DI_g = \frac{d_m - d_y}{d_f - d_y} \tag{6-39}$$

where d_m : maximum roof displacement under earthquake excitation.

$d_y = 0.06H$: roof displacement at which the first member of the structure reaches the yield moment [Roufaiel 1987].

H : the structure height.

d_f : roof displacement at which the structure is assumed to fail.

The yield displacement at the roof level d_y is assumed to be the displacement when the first member reaches a yielding response for the first mode. This is valid for a single degree of freedom structure exactly. This is also reasonably valued for a very short period structure as the responses of the very short period structure, say the base shear and roof level displacement relationship curve, are dominated by the first mode and the effect of higher modes on the structural responses is small and not considered.

The fundamental frequency of the earthquake-damaged structure, ω can be computed with the initial stiffnesses for elastic members and the tangent stiffnesses for those inelastic members at the time-step in which the structure reaches the maximum roof level displacement. It is easy to define this time-step once one has the time-history of the roof level displacement say in DYNAPLOT [Carr 1998], and further, the tangent stiffnesses of the inelastic members for this time-step saved in the computer analysis.

The damage due to accumulated energy dissipated by the hysteretic response in members is not reflected in this global damage index.

6-4.3 Chung, Meyer and Chinozuka Global Damage Index

Chung et al [Chung 1987] used the damage index for each storey to define the global damage index. The storey damage index is defined as a weighted average of the local damage indices of all elements in the storey. The weighting factor for each member end is directly proportional to the dissipated energy at this end. This storey damage index is the same as the Park and Ang's storey damage index expressed as follows:

$$DI_{sk} = \frac{\sum_{i=1}^{n} DI_i^k * E_i^k}{\sum_{i=1}^{n} E_i^k} \qquad \textbf{(6-40)}$$

where DI_i^k: local damage index at member end i on storey k.

E_i^k: dissipated energy at member end i on storey k.

n: number of member ends at which the local damage is computed for storey k.

The distribution of the weighting factors over the height of the structure for each storey is assumed to be linear triangular function of the storey number with the maximum at the base. Hence the global damage index DI_g is a weighted average of the storey damage indices and is obtained from the following Eq. (6-41):

$$DI_g = \sum_{k=1}^{N} DI_{sk} * \lambda_k \qquad \textbf{(6-41)}$$

where $\lambda_k = \dfrac{N+1-k}{N}$: weighting factor for storey k starting from bottom.

N: number of storeys.

6-4.4 Bracci et al's Global Damage Index

Bracci et al [Bracci 1989] proposed a global damage index obtained by combining all the component damage indices using a self-weight procedure. The weighting factor for each component, λ_i, is a function of the member importance factors w_i and the member damage indices as shown in Eq. (6-42):

$$\lambda_i = \frac{w_i * DI_i^{m_i}}{\sum_{i=1}^{n} w_i * DI_i^{m_i}} \qquad \textbf{(6-42)}$$

where $w_i = \dfrac{(Total\ \ tributary\ \ gravity\ \ load)_i}{(Total\ \ tributary\ \ gravity\ \ load)_{all\ members}}$

DI_i: damage index for component i

m_i: control weighting factor for component i

n: number of components

The larger value of the exponent for member i, say m_i>1.0, the smaller the weighting factor for this member will be because the damage index of the member is less than 1.0. The weighting factor for m_i=1.0 is:

$$\lambda_i = \frac{w_i * DI_i}{\sum_{i=1}^{n} w_i * DI_i} \tag{6-43}$$

The importance factor w_i is the ratio of the gravity load supported by component i to the total tributary gravity load supported by all the inelastic members. Therefore, columns will be weighted more than beams and columns in lower storey levels will have greater importance than columns in upper storey levels. However, for the capacity-designed reinforced concrete ductile framed structures used in this study, only the first storey columns are assumed to respond inelastically and the columns in upper storeys will be assumed to be in an elastic state during earthquake loading. Hence only the first storey columns are affected and assigned a much larger weighting factor than the factors for the beams as the beams carry only loads from their contributory floor areas.

The Bracci et al's global damage index is then determined from Eq. (6-44):

$$DI_g = \frac{\sum_{i=1}^{n} w_i * (DI_i)^2}{\sum_{i=1}^{n} w_i * DI_i} \tag{6-44}$$

Bracci et al proposed four damage limit states to represent the damage of the structure for the Bracci damage index based on the transposed bilinear fatigue failure curve assumption as follows:

$DI \leq 0.33$	Serviceable state
$0.33 < DI \leq 0.66$	Repairable state
$0.6 < DI \leq 1.0$	Irrepairable state
$DI > 1.0$	Collapse state

6-4.5 DiPasquale and Cakmak Softening Global Damage Index

DiPasquale and Cakmak [DiPasquale 1990] proposed a softening damage index for the overall damage evaluation of a whole structure, which is a function of the maximum softening index, DI_m and the cumulative softening index, DI_E as shown below:

$$DI_{DiPasquale} = f(DI_m,\ DI_E) \tag{6-45}$$

The simple form of this function is a linear combination:

$$DI_{DiPasquale} = DI_m + \beta * DI_E \tag{6-46}$$

where β = combination factor

$$DI_m = \max_{i=1,n} \frac{(\Delta T_o)_i}{(T_o)_{initial}} \tag{6-47}$$

$$DI_E = \sum_{i=1}^{n} \frac{(\Delta T_o)_i}{(T_o)_{initial}} \frac{S_i}{(T_o)_i} \tag{6-48}$$

and where $(\Delta T_o)_i = (T_o)_i - (T_o)_{initial}$ is the difference between the equivalent fundamental period at time step i and the initial fundamental period of the structure. S_i is the time step length at the $i-th$ step. n is the total number of time steps.

The equivalent fundamental period at time step i, $(T_0)_i$, can be computed with the initial stiffnesses for the elastic members (the upper storey columns) and with the inelastic tangent stiffnesses for those inelastic members for each time step. When the equivalent fundamental period for some time step is equal to the initial period, $(\Delta T_o)_i = (T_o)_i - (T_o)_{initial} = 0.0$. This means that this time step is in the elastic range and has no contribution to the cumulative softening damage index.

According to DiPasquale and Cakmak [DiPasquale 1990], the maximum softening index, DI_m has a very strong correlation with the maximum ductility experienced by the structure, while the cumulative damage index, DI_E is very strongly correlated with the dissipated energy. That means that the DiPasquale and Cakmak damage

index can reflect the effects of both the maximum response and the time-dependent dissipated energy on the damage assessment.

The advantage of this global damage index is that no yield point of the whole structure is required. However, the equivalent tangent fundamental periods at each time step must be computed in order to evaluate the cumulative softening damage index. For a large structure this is computationally very expensive.

6-4.6 Mork Softening Global Damage Index

The softening damage indices discussed already provide very little information about the distribution of damage over the height of the structure. At each time-step during the analysis with the varying of the tangent stiffnesses of the members, there are equivalent modes of free-vibration for the whole structure irrespective of whether it is an elastic or inelastic state. At each time-step, the damage in the upper and lower parts of the structure shows itself mainly as the stiffness degradation for the equivalent first and second modes. The time-histories of the variations in the structural stiffnesses for the first and second modes can reflect the damage histories in the upper and lower parts of the structure respectively. The minimum stiffnesses for the first and second modes among all of those for each time-step during the earthquake can indicate the maximum damage in the upper and lower parts of the structure. This requires a modal analysis at each time-step. Again this is computativelly expensive for a large structure.

Mork [Mork 1992] proposed a global damage model based on the damage indices corresponding with the first two modes of free vibration in order to measure the degree of damage in the lower and upper parts of the structure respectively, as shown in the following two equations.

$$DI_1 = 1 - \sqrt{\frac{k_{1,\min}}{k_{1,0}}} \qquad \textbf{(6-49a)}$$

$$DI_2 = 1 - \sqrt{\frac{k_{2,\min}}{k_{2,0}}} \qquad \textbf{(6-49b)}$$

where DI_1: maximum softening index corresponding to the first mode

DI_2: maximum softening index corresponding to the second mode

$k_{1,o}$: initial stiffness of the undamaged structure for the first mode which

$k_{2,o}$: initial stiffness of the undamaged structure for the second mode

$k_{1,\min}$: minimum degraded stiffness among all the time steps during earthquake excitation for the first mode

$k_{2,\min}$: minimum degraded stiffness among all the time steps during earthquake excitation for the second mode

The initial stiffnesses of the undamaged structure for the first and second modes, and the minimum degraded stiffnesses among all time steps during the earthquake excitation for the first and second modes can be determined using the Eq. (6-50a) and Eq. (6-50b) respectively.

$$k_{n,o}=\{\phi_{n,o}\}^T[K_o]\{\phi_{n,o}\} \quad (n=1, 2) \qquad \textbf{(6-50a)}$$

$$k_{n,\min}=min\left[\{\phi_{n,t1}\}^T[K_{t1}]\{\phi_{n,t1}\},\ \{\phi_{n,t2}\}^T[K_{t2}]\{\phi_{n,t2}\}\ \ldots\ \{\phi_{n,tN}\}^T[K_{tN}]\{\phi_{n,tN}\}\right] \qquad \textbf{(6-50b)}$$

where n: $(=1, 2)$ mode number

N: total number of time-steps

$\{\phi_{n,o}\}$: n-th mode shape for undamaged structure

$[K_o]$: stiffness matrix for undamaged structure

$\{\phi_{n,t1}\}, \{\phi_{n,t2}\} \ldots \{\phi_{n,tN}\}$: n-th mode shape for the first, second,...last time-step

$[K_{t1}], [K_{t2}] \ldots [K_{tN}]$: tangent stiffness matrix for the first, second,...last time-step

The values of DI_1 and DI_2 is in the range of 0.0 to 1.0, where 0.0 and 1.0 correspond to the elastic response and total collapse respectively.

This method would be difficult to use in a large dynamic analysis. The data is not available at each time step and the extra computation at each step would increase the computation time per-step very significantly.

6-4.7 Nielsen et al's Softening Global Damage Index

Nielsen et al [Nielsen 1992] proposed contours for the overall softening index, DI_m, which is a function of the maximum softening indices for the first and second modes and can be determined in the $DI_1 - DI_2$ by using the following relationship:

$$DI_2 = 1 - \sqrt{\frac{1}{4\lambda}} * \sqrt{\frac{DI^2 - 2DI*(1-DI_1)^2}{DI-(1-DI_1)^2}},\ 0 \le DI_1 \le DI_{1,\max} \qquad \textbf{(6-51)}$$

where $\lambda = \dfrac{k_{2,o}}{k_{1,o}}$ **(6-52)**

$k_{1,o}$: initial stiffness of the undamaged structure for the first mode

$k_{2,o}$: initial stiffness of the undamaged structure for the second mode

$$DI = (1-DI_m)^2 * \left(1 + 2\lambda - \sqrt{1+4\lambda^2}\right) \qquad \textbf{(6-53)}$$

$$DI_{1,\max} = 1 - \sqrt{\frac{4\lambda * DI - DI^2}{4\lambda - 2*DI}} \qquad \textbf{(6-54)}$$

DI_1: the maximum softening index corresponding to the first mode determined by Eq. (6-49a)

DI_2: the maximum softening index corresponding to the second mode determined by Eq. (6-49b)

$k_{1,\min}$: minimum degraded tangent stiffness among all the time steps during earthquake excitation for the first mode determined by Eq. (6-50b)

$k_{2,\min}$: minimum degraded tangent stiffness among all the time steps during earthquake excitation for the second mode determined by Eq. (6-50b)

Seven global damage indices have been summarised in this section. They are the Park & Ang, Roufaiel & Meyer, Chung et al, Bracci et al and the three softening global

damage indices. These softening global damage indices include the DiPasquale & Cakmak, Mork and the Nielsen et al damage indices.

The Roufaiel & Meyer global damage index is a short period structure oriented damage index. The Chung et al global damage index is a weighted average of the storey damage indices. The Bracci et al global damage index is a gravity load and local damage index self-weighted average of all member damage indices.

The three softening global damage indices require a large amount of extra computing work, i.e. the equivalent modal response analyses for each time-step. This seems that these three global damage indices cannot be used for practical analysis, especially for a large structure. Therefore they were not used for the global damage evaluation in this study.

6-5 Damage Indices for Storeys and Overall Structures Used in This Study

As mentioned earlier, four member damage indices were used in this study. They are the Banon & Veneziano, Park & Ang, Roufaiel & Mayer and the Cosena et al. models.

Banon [Banon 1982] and Cosenza [Cosenza 1993] did not present global damage indices for the storey and structure together with their member indices. A damage index for an overall structure for the Roufaiel & Mayer member damage model was proposed but was a short period structure oriented method [Roufaiel 1987]. Hence, the damage indices for storeys and overall structures proposed by Park and Ang [Park 1985A] were used in this study for all of the four member damage models, which are the energy weighted average of the inelastic member damage indices in a storey and in the whole structure.

6-6 Local and Global Damage Indices for Member, Storey and Overall Structure Used in This Study

In order to study the effect of varying member damage indices on the structural damage indices and limit the workload, only four different member damage indices were used and these are listed in Table 6-1. The four member damage indices include one ductility-related model i.e. the Cosenza et al., two ductility-dissipated energy models, i.e. the Banon & Veneziano, Park & Ang and one flexibility degraded model of Roufaiel & Meyer.

The storey damage indices and overall structural damage index for all of the four different member damage indices were computed using the Park & Ang weighting method, which is the energy-weighted average of the inelastic member damage indices in a storey or a whole structure, as shown in Table 6-1.

Table 6-1 Four different member damage indices and the damage indices for storey and whole structure used in this research work

No	Name	Member *DI*	Storey *DI*	Structure *DI*	Interpretation of DI_g
1	Banon and Veneziano	$\frac{\sqrt{(\mu_m-1)^2+\left[1.1\left(\frac{2E_h}{M_y}\right)^{0.38}\right]^2}}{\textit{Numerator for monotonic loading to ultimate}}$	$DI_g=\sum_{i=1}^{n}(\lambda_i * DI_i)$ where $\lambda_i=\frac{E_i}{\sum_{i=1}^{n}E_i}$ E_i: dissipated energy at member end i.		
2	Park and Ang	$DI=\frac{\mu_m}{\mu_u}+\frac{\beta}{F_y * \mu_u}\int dE$			$DI_g \le 0.4$ Repairable damage $DI_g > 0.4$ Damage beyond repair $DI_g \ge 1.0$ Total collapse
3	Roufaiel and Meyer	$DI=\max\{DI^+,\ DI^-\}$ $DI^+=\frac{\frac{\phi_m^+}{M_m^+}-\frac{\phi_y^+}{M_y^+}}{\frac{\phi_u^+}{M_u^+}-\frac{\phi_y^+}{M_y^+}}$			
4	Cosenza et al.	$DI_u=\frac{\mu_{\max}-1}{\mu_u-1}$			

Chapter 7
The Structural Ductility

7-1 Introduction

The four different member damage indices of Park & Ang, Roufaiel & Meyer, Cosenza et al. and Banon & Veneziano are used in evaluating seismic damage degree of the three prototype structures, which is to be described in Chapter 8. These member damage indices are sensitive to the member ultimate curvature ductility [Carr 1993]. The relationship between the member curvature ductility and the overall structural displacement ductility should be investigated to see if the ultimate member curvature ductility capacity is larger than the response demand required by the design-level earthquakes with a design structural ductility of 5.0.

In this chapter, four design-level scaled earthquakes, i.e. Bucharest (1977-NS), El Centro (1940-NS), Northridge (Sylmar-941NW) and Kobe (1995-NS) as discussed in Chapter 5 were used as the earthquake inputs to the three prototype frames designed to the current New Zealand Standards discussed in Chapter 2. The eight hysteresis models i.e. the Elasto-Plastic, Bilinear, Modified Takeda (α=0.0, β=0.6), Degrading Bilinear (α=0.5), Clough, Modified Takeda (α=0.3, β=0.4), Q-Hyst (α=0.5) and the Origin-Centred hysteresis model discussed in Chapter 4 were used in modelling the member inelastic behaviour for the inelastic dynamic analyses.

Two techniques are currently available for defining a storey or an overall structural yield displacement. These are the Carr & Tabuchi trend-line approach [Carr 1993] and the pushover method in RUAUMOKO [Carr 1998, Satyarno 2000]. As the Carr & Tabuchi trend-line approach presents a realistic force displacement relationship rather than the pushover analysis, which predominantly considers only the first mode, this method was used in defining the storey displacement ductility and structural displacement ductility in this study. The pushover method was used only for the comparison study of the yield displacements between these two techniques.

By comparing the ductilities of the storeys and the overall structures predicted using the eight hysteresis models for the four earthquake excitations, the effect of varying the hysteresis models on the computed storey displacement ductility and the structural displacement ductility was found.

Finally the relationships between the maximum member curvature ductilities in the structure and the overall structural displacement ductility were identified.

7-2 Comparison of the Overall Structural and Storey Yield Displacements for the Pushover and Carr & Tabuchi Approaches

7-2.1 Overall Structural and Storey Yield Displacements for the Pushover Method

The seismic standard equivalent static or first mode loading pattern [NZS4203: 1992] was used in the pushover analysis for the overall structural yield displacements and yield displacements at level-1. 92% of the base shear was distributed to be the equivalent static lateral forces at each level, which are proportional to the total weights and the heights at levels under consideration. An additional force of 8% of the base shear was added at the top level. The normalised loading patterns for the three structures are shown in Table 7-1 and Fig. 7-1. The load is ramped up linearly and the non-linear response of the structure is obtained.

In order to take effect of higher modes on a yield point at an upper storey of the structure, the lateral translational displacements at the lower levels should be constrained and all upper levels remain free [Satyarno 2000]. The lateral loading patterns for the upper storeys were the same as those for the overall structural yield points but the lateral loadings were zero at all levels with constrained lateral displacements.

Table 7-1 Normalised NZS4203 loading pattern, overall structural and storey yield displacements (m) of the three structures for pushover method

		Normalised NZS4203 Loading Pattern			Yield Displacements (m)		
		6S	12S	18S	6S	12S	18S
Overall Structure					0.058	0.100	0.150
Storey	L-18			1.000			0.0115
	17			0.565			0.012
	16			0.531			0.01
	15			0.507			0.0085
	14			0.473			0.0085
	13			0.440			0.0077
	12		1.000	0.415		0.0115	0.0075
	11		0.657	0.382		0.0115	0.008
	10		0.596	0.348		0.01	0.007
	9		0.542	0.319		0.009	0.0067
	8		0.482	0.280		0.009	0.007
	7		0.422	0.246		0.008	0.0062
	6	1.000	0.373	0.213	0.0155	0.008	0.0065
	5	0.728	0.307	0.179	0.0135	0.008	0.0065
	4	0.583	0.247	0.145	0.0125	0.008	0.007
	3	0.442	0.187	0.106	0.01	0.008	0.0067
	2	0.296	0.127	0.072	0.01	0.008	0.0067
	1	0.146	0.060	0.034	0.01	0.008	0.0065

The base shear versus roof-level displacement curves and the storey shear versus storey deformation curves for the overall structure and the storey yield displacements respectively were obtained by carrying out a pushover analysis with RUAUMOKO [Carr 1998]. The curves and their equivalent bilinear models for the overall structural displacements are shown in Figs. 7-1(a) to 7-1(c), while those for the storey yield points are shown in Figs. F-1 to F-6 of Appendix F. The overall structure and storey yield displacements of the three structures for the pushover analysis presented in Table 7-1 were used to determine the difference between the two techniques for the yield displacements as discussed in section 7-2.3.

As only the back-bone part of the moment-curvature relationship is used in the monotonic pushover analysis there are no difference among any of the eight hysteresis models as all models in this thesis have the same back-bone moment-curvature relationship.

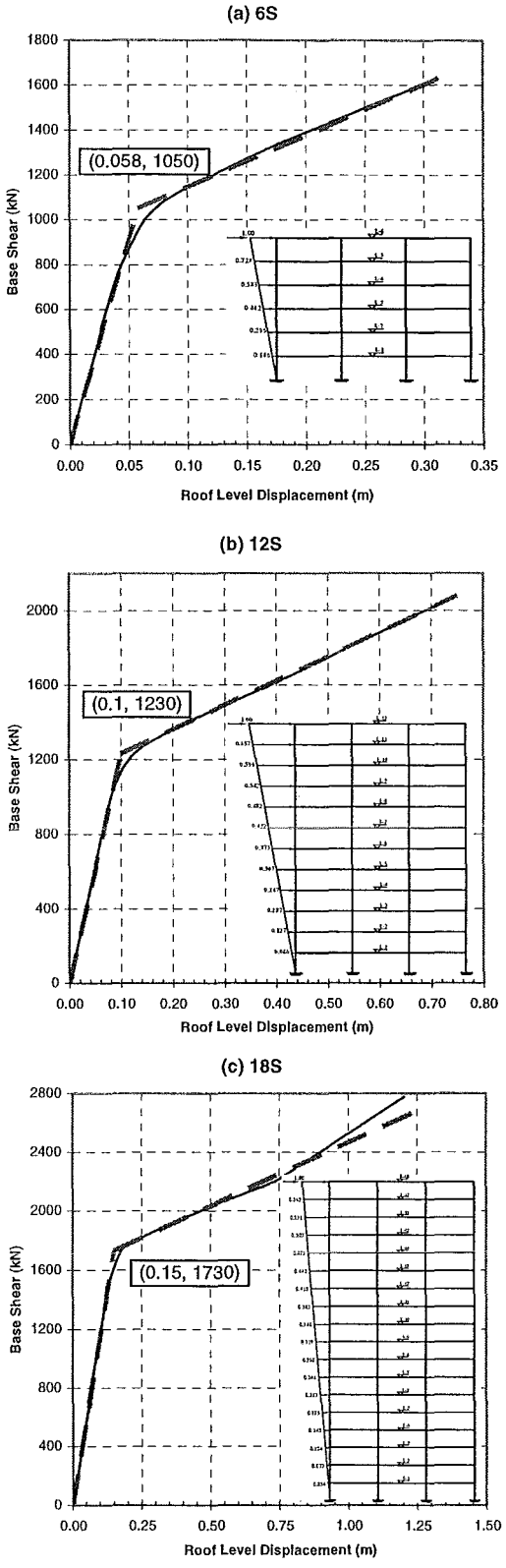

Fig. 7-1 Bases shear versus roof level displacement curves, and NZS4203 lateral loading patterns for overall structural yield displacements of the 6-, 12- and 18-storey structures using the pushover method

7-2.2 Overall Structural and Storey Yield Points for Carr & Tabuchi Method

Carr & Tabuchi [Carr 1993] proposed an approach for defining overall structural yield points and storey yield points of structures. The overall structural yield points are defined as the intersection point of two trend lines representing the relationship between the maximum base shear and the roof-level displacement for the elastic and inelastic responses respectively.

In this chapter, the four different scaled earthquake excitations discussed in Chapter 5 were used. The scale factors for the four earthquakes for the three structures of 6, 12 and 18 storeys, obtained in Chapter 5 and listed in Table 5-11, were used in the elastic and inelastic time-history analyses.

For each structure of 6, 12 and 18 storeys, four response points (base shear versus top-level displacement) were obtained for the four different earthquakes for the elastic and inelastic analyses respectively. The elastic trend line is a best fit though the four elastic response points and the origin while the inelastic trend line is a best fit linear relationship though the four inelastic response points. The intersection point of these two trend lines is defined as the overall structural yield point.

The storey yield points are defined in a similar way. The response points are based on the interstorey shears and interstorey drifts rather than the base shears and roof-level displacements which are used for the overall structural yield points.

Varying the hysteresis models in the inelastic dynamic time-history analysis will result in variations in the forces (base shear, interstorey shear) and the displacements (roof-level displacement, interstorey drifts) [Dong 1999]. This will affect the slope of the trend lines though the inelastic response points and lead to a variation in the yield points for both the storeys and the overall structure. Consequently the storey and structural ductilities will be affected by the variations in both the yield displacements as well as the inelastic displacement responses.

In order to identify the effect of varying the hysteresis models on the yield displacements, the eight hysteresis models discussed in Chapter 4 were again used in

this chapter. These were the Elasto-Plastic, Bilinear, Modified Takeda (α=0.0, β=0.6), Degrading Bilinear (α=0.5), Clough, Modified Takeda (α=0.3, β=0.4), Q-Hyst (α=0.5) and Origin-Centred models, covering a wide range of hysteretic energy dissipation capacities.

Table 7-2 shows the overall structural yield displacements of the three structures for the eight hysteresis models. It is found from Table 7-2 that the overall structural yield displacements are approximately *N/120(m)*, *N/100(m)* and *N/100(m)* for the 6, 12 and 18 storey structures where *N* are the number of the storeys for all the hysteresis models except for the Origin-Centred hysteresis model.

Table 7-2 Overall structural yield displacements (m) of the three structures for the eight hysteresis models for Carr & Tabuchi approach

	Elasto-Plastic	Bilinear	Modified Takeda (α=0.0, β=0.6)	Degrading Bilinear (α=0.5)	Clough	Modified Takeda (α=0.3, β=0.4)	Q-Hyst (α=0.5)	Origin-Centred
6S	0.0507	0.0448	0.0475	0.0506	0.0481	0.0489	0.0468	0.0587
12S	0.1309	0.1338	0.1227	0.1249	0.1220	0.1231	0.1226	0.1273
18S	0.1833	0.1861	0.1722	0.1737	0.1722	0.1718	0.1713	0.2216

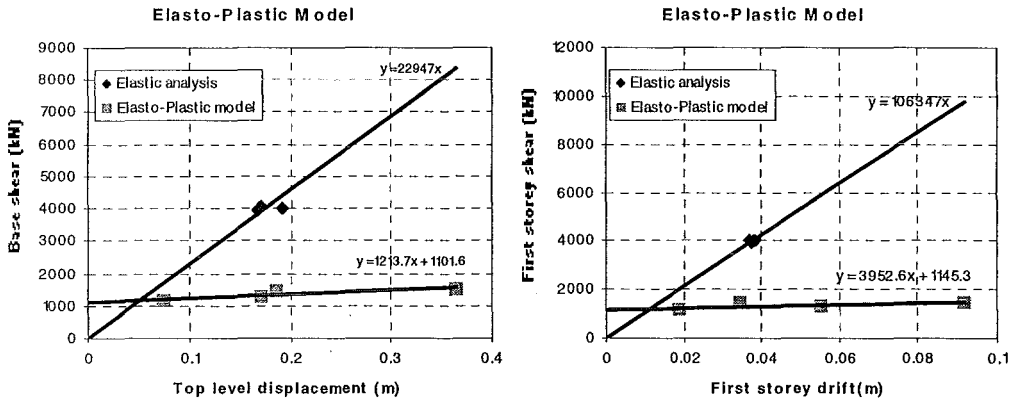

Fig. 7-2 The elastic and inelastic response trend lines for the overall structure and the first storey respectively predicted using the Elasto-Plastic model for the 6 storey structure under the four scaled earthquake excitations

As an example, Fig. 7-2 presents the elastic and inelastic response trend lines for the overall structure and for the first storey respectively using the Elasto-Plastic hysteresis model for the 6 storey structure. All the figures for the overall structure and storey

yield points for the three structures using the eight hysteresis models are presented in Figs. G-1 to G-39 in Appendix G.

Table 7-3 shows the storey yield displacements of the three structures for the eight hysteresis models. It is observed that the storey yield displacements at level 6 of the 6 storey structure for the Modified Takeda (α=0.0, β=0.6) and Clough models, and the storey yield displacement at level-17 of the 18 storey structure for the Degrading Bilinear (α=0.5) model were negative. This is due to the fact that the linear functions of the trend lines for these inelastic response points gave an intersection point in the negative quadrant rather than in the positive quadrant, as shown in Figs. G-7 and G-38.

From Fig. G-20 in Appendix G, it is observed that the inelastic trend lines at level-12 of the 12 storey structure for the Elasto-Plastic and the Bilinear hysteresis models were of larger slopes or stiffnesses than the stiffnesses of the corresponding elastic trend lines. This was not expected. For these reasons all storey yield displacements in bold as shown in Table 7-3 are treated as not reliable and are therefore not considered in this study.

Table 7-3 Storey yield displacements (m) of the three structures for Carr & Tabuchi approach

		L-1	L-2	L-3	L-4	L-5	L-6	L-7	L-8	L-9	L-10	L-11	L-12	L-13	L-14	L-15	L-16	L-17	L-18
6S	Elasto-Plastic	0.0112	0.0127	0.0124	0.0135	0.0134	0.0048												
	Bilinear	0.0103	0.0120	0.0114	0.0118	0.0103	0.0070												
	Modified Takeda (α=0.0, β=0.6)	0.0108	0.0123	0.0119	0.0119	0.0107	-0.0005												
	Degrading Bilinear (α=0.5)	0.0109	0.0120	0.0114	0.0121	0.0105	0.0064												
	Clough	0.0107	0.0126	0.0122	0.0118	0.0107	-0.0059												
	Modified Takeda (α=0.3, β=0.4)	0.0109	0.0127	0.0120	0.0117	0.0116	0.0045												
	Q-Hyst (α=0.5)	0.0106	0.0127	0.0125	0.0119	0.0112	0.0052												
	Origin-Centred	0.0120	0.0113	0.0114	0.0098	0.0100	0.0068												
12S	Elasto-Plastic	0.0094	0.0125	0.0129	0.0121	0.0122	0.0115	0.0125	0.0148	0.0115	0.0104	0.0071	0.0130						
	Bilinear	0.0095	0.0123	0.0126	0.0123	0.0122	0.0112	0.0127	0.0159	0.0116	0.0108	0.0081	0.6598						
	Modified Takeda (α=0.0, β=0.6)	0.0089	0.0130	0.0126	0.0110	0.0119	0.0105	0.0128	0.0130	0.0118	0.0091	0.0099	0.0074						
	Degrading Bilinear (α=0.5)	0.0091	0.0133	0.0137	0.0121	0.0124	0.0117	0.0148	0.0157	0.0113	0.0116	0.0069	0.0083						
	Clough	0.0088	0.0129	0.0125	0.0110	0.0114	0.0109	0.0127	0.0131	0.0117	0.0100	0.0096	0.0071						
	Modified Takeda (α=0.3, β=0.4)	0.0089	0.0130	0.0127	0.0110	0.0117	0.0111	0.0130	0.0130	0.0123	0.0105	0.0096	0.0072						
	Q-Hyst (α=0.5)	0.0089	0.0131	0.0131	0.0112	0.0118	0.0108	0.0130	0.0128	0.0121	0.0095	0.0088	0.0080						
	Origin-Centred	0.0086	0.0136	0.0142	0.0127	0.0109	0.0104	0.0143	0.0058	0.0052	0.0086	0.0072	0.0073						
18S	Elasto-Plastic	0.0079	0.0111	0.0118	0.0120	0.0110	0.0105	0.0111	0.0115	0.0114	0.0117	0.0135	0.0128	0.0141	0.0166	0.0175	0.0184	0.0115	0.0115
	Bilinear	0.0080	0.0113	0.0117	0.0120	0.0110	0.0106	0.0111	0.0116	0.0113	0.0116	0.0134	0.0128	0.0137	0.0137	0.0158	0.0165	0.0160	0.0116
	Modified Takeda (α=0.0, β=0.6)	0.0074	0.0113	0.0110	0.0119	0.0110	0.0109	0.0111	0.0116	0.0114	0.0113	0.0124	0.0129	0.0128	0.0135	0.0145	0.0161	0.0127	0.0097
	Degrading Bilinear (α=0.5)	0.0075	0.0115	0.0117	0.0120	0.0110	0.0120	0.0122	0.0120	0.0116	0.0135	0.0129	0.0138	0.0133	0.0173	0.0197	0.0183	-0.0092	0.0109
	Clough	0.0074	0.0113	0.0111	0.0118	0.0110	0.0108	0.0112	0.0115	0.0113	0.0107	0.0116	0.0127	0.0128	0.0128	0.0145	0.0165	0.0131	0.0097
	Modified Takeda (α=0.3, β=0.4)	0.0073	0.0112	0.0115	0.0120	0.0108	0.0113	0.0116	0.0116	0.0111	0.0116	0.0117	0.0138	0.0124	0.0134	0.0145	0.0182	0.0141	0.0098
	Q-Hyst (α=0.5)	0.0071	0.0110	0.0116	0.0120	0.0109	0.0113	0.0119	0.0115	0.0110	0.0112	0.0112	0.0131	0.0125	0.0141	0.0127	0.0170	0.0150	0.0104
	Origin-Centred	0.0058	0.0095	0.0098	0.0117	0.0117	0.010	0.0111	0.0115	0.0115	0.0121	0.0125	0.0114	0.0099	0.0043	0.0072	0.0120	0.0132	0.0115

7-2.3 Effect of Varying Hysteresis Models for the Carr & Tabuchi Method, and of Altering the Carr & Tabuchi and the Pushover Methods on the Storey and Overall Structural Yield Displacements

The distributions of storey yield displacements for the Carr & Tabuchi method using each of the eight hysteresis models and for the pushover method are illustrated in Fig. 7-3(a). The distributions of the ratios of the storey yield displacements for each of the eight hysteresis models for the Carr & Tabuchi method and for the pushover method to the averages of those for the four hysteresis models, i.e. the Modified Takeda (α=0, β=0.6), Clough, Modified Takeda (α=0.3, β=0.4) and Q-Hyst (α=0.5) for the Carr & Tabuchi method are shown in Fig. 7-3(b).

It can be seen from Figs. 7-3(a),(b) that the four hysteresis models, the Modified Takeda (α=0, β=0.6), Clough, Modified Takeda (α=0.3, β=0.4) and Q-Hyst (α=0.5) predict very similar storey yield displacements for each of the three structures when using the Carr & Tabuchi method. This is independent of the fundamental periods of free vibration of the structures and is indicated by the ratios of the storey yield displacements for each of the four hysteresis models to the averages of those for the four hysteresis models. The ratios are in the ranges of 0.79 to 1.01, 0.96 to 1.01, 0.93 to 1.05 and 0.99 to 1.07 for the four hysteresis models respectively for the 6 storey structure as an example, as shown in Table 7-4, in which those for the 12 and 18 storey structures are also shown.

Table 7-4 Ratios of storey yield displacements for the Carr & Tabuchi method using each of the eight hysteresis model and for the pushover method to the averages of those for the four hysteresis models for the Carr & Tabuchi method

		6S	12S	18S
Carr & Tabuchi Method	Elasto-Plastic	1.00 ~ 1.21	0.75 ~ 1.14	0.84 ~ 1.24
	Bilinear	0.93 ~ 1.43	0.86 ~ 1.23	0.95 ~ 1.17
	Modified Takeda (α=0, β=0.6)	**0.97 ~ 1.01**	**0.93 ~ 1.04**	**0.92 ~ 1.06**
	Degrading Bilinear (α=0.5)	0.94 ~ 1.32	0.73 ~ 1.21	1.00 ~ 1.40
	Clough	**0.96 ~ 1.01**	**0.95 ~ 1.02**	**0.95 ~ 1.03**
	Modified Takeda (α=0.3, β=0.4)	**0.93 ~ 1.05**	**0.97 ~ 1.07**	**0.98 ~ 1.07**
	Q-Hyst (α=0.5)	**0.99 ~ 1.07**	**0.93 ~ 1.08**	**0.90 ~ 1.10**
	Origin-Centred	0.83 ~ 1.39	0.44 ~ 1.15	0.32 ~ 1.16
Pushover Method		0.79 ~ 3.19	0.62 ~ 1.55	0.54 ~ 1.16

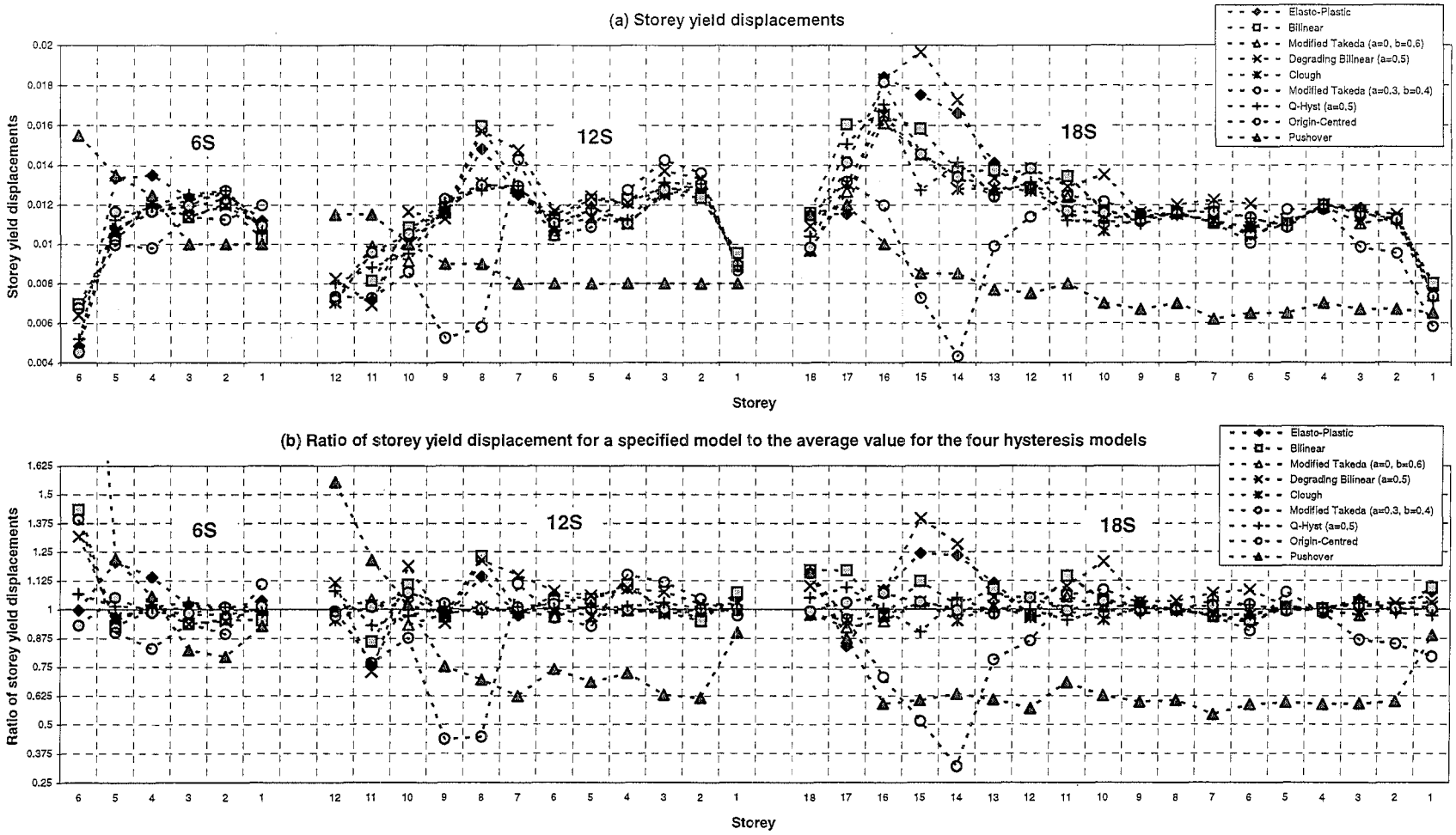

Fig. 7-3 (a) Storey yield displacement distribution for the Carr & Tabuchi method using each of the eight hysteresis models and for the pushover method
(b) Ratio of storey yield displacement for the Carr & Tabuchi method using each of the eight hysteresis models and the pushover to the average value for the four hysteresis model for the Carr & Tabuchi method

It is found from Fig. 7-3(b) that the Elasto-Plastic, Bilinear and the Degrading Bilinear (α=0.5) models predict significant larger storey yield displacements in the upper storeys of the three structures. The ratios of the storey yield displacements for each of the Elasto-Plastic, Bilinear and Degrading Bilinear (α=0.5) models to the averages of those for the four other hysteresis models for the 6 storey structure as an example, are in the ranges of 1.00 to 1.21, 0.93 to 1.43 and 0.94 to 1.32 respectively shown in Table 7-4.

In the upper parts of the three structures, the Origin-Centred model predicts significantly smaller yield displacements when compared to the averages of those for the other four hysteresis models. The ratios of the storey yield displacements for this model to those averages are in the ranges of 0.83 to 1.39, 0.44 to 1.15 and 0.32 to 1.16 for the 6, 12 and 18 storey structures respectively shown in Table 7-5.

When compared to the averages of the storey yield displacements for the four hysteresis models for the Carr & Tabuchi method, significant larger and smaller yield displacements for the pushover method are found in the upper and lower storeys respectively for the 6 and 12 storey structures, while significantly smaller values are found in every storey for the 18 storey structure, as shown in Fig. 7-3. The ratios of the yield displacements for the pushover method to those average values range from 0.79 to 3.19, 0.62 to 1.55 and 0.54 to 1.16 for the 6, 12 and 18 storey structures respectively.

The overall structural yield displacements of the three structures for the Carr & Tabuchi approach using each of the eight hysteresis models, and for the pushover method are illustrated in Fig. 7-4.

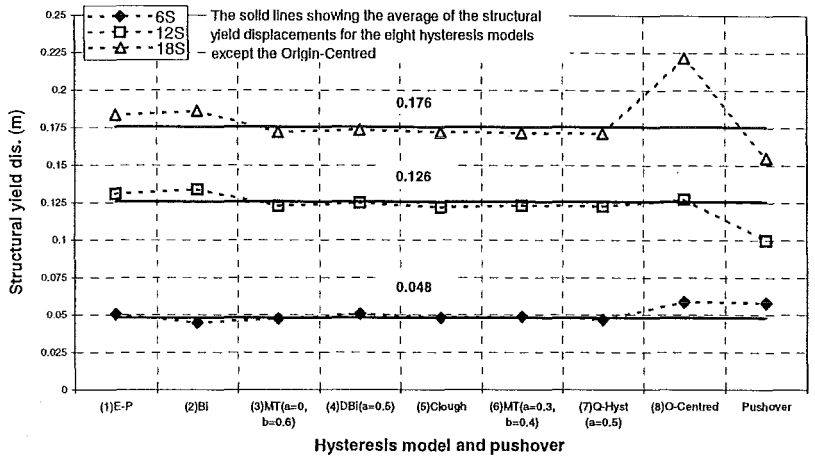

Fig. 7-4 The overall structural yield displacements for the Carr & Tabuchi approach using the eight hysteresis models and for the pushover method

It is found from Fig. 7-4 that all the hysteresis models except the Origin-Centred model predict similar structural yield displacements for the three structures for the Carr & Tabuchi method. The ratios of the yield displacements for the seven hysteresis models to the averages of those for the seven hysteresis models range from 0.93 to 1.05, 0.97 to 1.06 and 0.97 to 1.06 for the 6, 12 and 18 storey structures respectively as shown in Table 7-5 and Fig. 7-5.

However the Origin-Centred hysteresis model predicts much larger overall structural yield displacements when compared to those predicted using the other hysteresis models for the 6 and 18 storey structures. The ratios of the yield displacement for this model to the averages of those for the seven hysteresis models are 1.22 and 1.26 for the 6 and 18 storey structures respectively as shown in Table 7-5.

Table 7-5 Ratios of the structural yield displacements for the Carr & Tabuchi method using each of the eight hysteresis models and for the pushover to the averages of those for the seven hysteresis models of the eight except the Origin-Centred model

	E-P	Bi	MT(α=0, β=0.6)	DBi(α=0.5)	Clough	MT(α=0.3, β=0.4)	Q-Hyst (α=0.5)	O-Centred	Pushover
6S	1.05	0.93	0.99	1.05	1.00	1.01	0.97	1.22	1.20
12S	1.04	1.06	0.98	0.99	0.97	0.98	0.98	1.01	0.80
18S	1.04	1.06	0.98	0.99	0.98	0.98	0.97	1.26	0.88

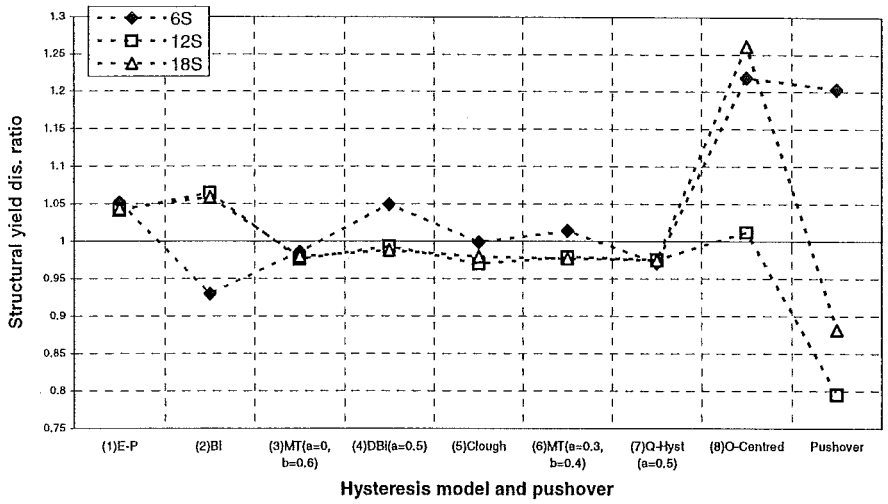

Fig. 7-5 Ratios of the structural yield displacements for the Carr & Tabuchi method using each of the eight hysteresis models and for the pushover to the averages of those for the seven hysteresis models of the eight except the Origin-Centred model

It is observed from Fig. 7-5 that the pushover method predicts a significantly larger structural yield displacement for the 6 storey structure, and significantly smaller values for the 12 and 18 storey structures when compared to the averages of those for the seven hysteresis models for the Carr & Tabuchi method. The ratios of the yield displacements for the pushover method to the averages are 1.20, 0.8 and 0.88 for the 6, 12 and 18 storey structures respectively as shown in Table 7-5.

From the previous studies it is found that the responses in terms of the storey and structural yield displacements predicted using the Origin-Centred model may vary very significantly when compared to those for the other seven hysteresis models. This may be due to the fact that this model has the minimum hysteretic energy dissipation capacity of all the eight hysteresis models and the unloading and reloading characteristics do not match what has been observed by any static test for reinforced concrete members in a laboratory. Hence this model is unrealistic for use for inelastic dynamic analyses and is not used in the following studies.

7-3 Effect of Varying Hysteresis Models on the Storey Ductility for the Carr & Tabuchi Method

The distribution of the storey displacement ductility for each of the seven hysteresis models for the three framed structures under the four earthquakes are shown in Figs. 7-6(a) to 7-8(a). It is found from these figures that for each of the three structures, three hysteresis models, i.e. the Modified Takeda (α=0.0, β=0.6), Clough and Modified Takeda (α=0.3, β=0.4) predict very similar storey ductilities in every storey for all four earthquakes.

The average values of storey ductilities predicted using these above three hysteresis models for each level were computed and were then compared to those predicted using each of the seven hysteresis models. The ratios of storey ductilities for each of the seven hysteresis models to these average values for each level of the three structures are illustrated in Figs. 7-6(b) to 7-8(b). Table 7-6 shows the ranges of the storey ductility ratios of all the levels for each of the three structures under the four earthquakes for each of the seven hysteresis models.

Table 7-6 Ratios of storey displacement ductilities for each of the seven hysteresis models to the averages of those for the three hysteresis models i.e. the Modified Takeda (α=0.0, β=0.6), Clough and Modified Takeda (α=0.3, β=0.4) models for the three structures under the four earthquakes

		E-P	Bi	MT (α=0, β=0.6)	DBi (α=0.5)	Clough	MT (α=0.3, β=0.4)	Q-Hyst (α=0.5)
6S	Bucharest	0.58~1.07	0.77~1.06	1.00~1.08	0.70~1.11	0.98~1.09	0.83~1.01	0.88~1.05
	El Centro	0.66~1.20	0.68~1.21	0.88~1.03	0.99~1.64	0.96~1.09	0.94~1.03	0.94~1.23
	Northridge	0.84~1.05	0.58~0.84	0.95~1.00	0.66~1.09	0.98~1.02	0.98~1.07	0.92~1.34
	Kobe	0.81~1.09	0.74~1.26	0.94~1.02	0.82~1.25	0.96~1.03	0.97~1.04	0.91~1.12
12S	Bucharest	0.84~1.37	0.82~1.18	0.97~1.04	0.85~1.43	0.96~1.03	0.98~1.03	0.91~1.16
	El Centro	0.71~1.38	0.71~1.18	0.94~1.08	0.80~1.42	0.98~1.09	0.92~1.04	0.79~1.24
	Northridge	0.72~1.30	0.59~1.14	0.91~1.05	0.78~1.78	0.97~1.01	0.97~1.12	0.91~1.26
	Kobe	0.42~1.17	0.42~1.04	0.93~1.02	0.87~1.31	0.96~1.04	0.96~1.05	1.03~1.28
18S	Bucharest	0.90~1.30	0.82~1.04	0.94~1.02	0.85~1.19	0.95~1.03	0.97~1.10	0.96~1.48
	El Centro	0.79~1.55	0.80~1.37	0.90~1.01	0.88~1.64	0.98~1.06	0.99~1.09	0.98~1.49
	Northridge	0.58~2.05	0.75~1.65	0.93~1.06	0.75~1.35	0.95~1.08	0.86~1.11	0.66~2.22
	Kobe	0.59~1.33	0.55~1.27	0.93~1.04	0.91~1.37	0.88~1.02	0.97~1.08	0.99~1.53

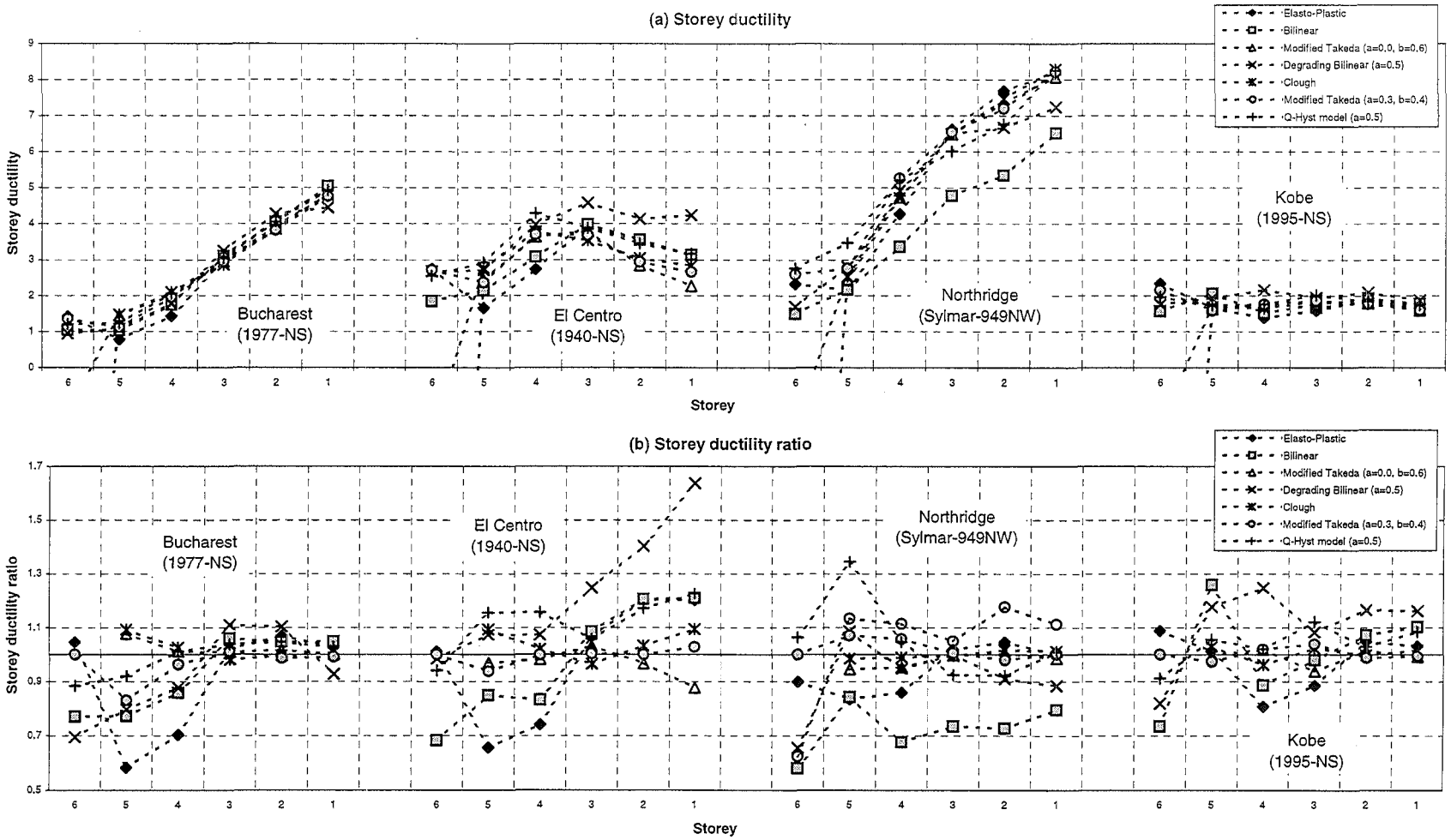

Fig. 7-6 (a) The maximum storey ductility for each of the seven hysteresis models for the 6S under the four excitations using the Carr & Tabuchi method
(b) The ratio of the storey ductility for each of the seven hysteresis models to the averages of those for the three hysteresis models for the 6S

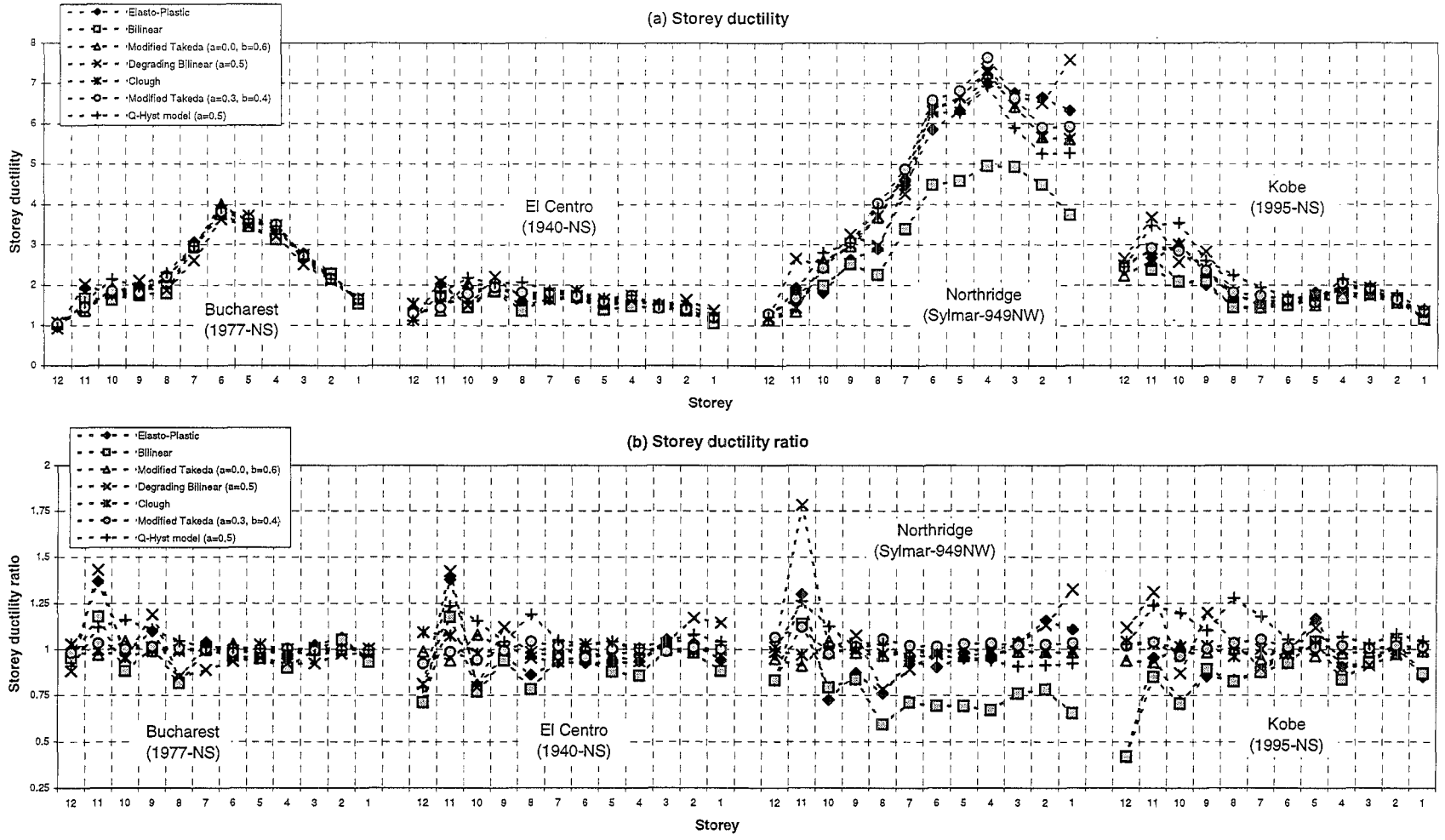

Fig. 7-7 (a) The maximum storey ductility for each of the seven hysteresis models for the 12S under the four excitations using the Carr & Tabuchi method
(b) The ratio of the storey ductility for each of the seven hysteresis models to the averages of those for the three hysteresis models for the 12S

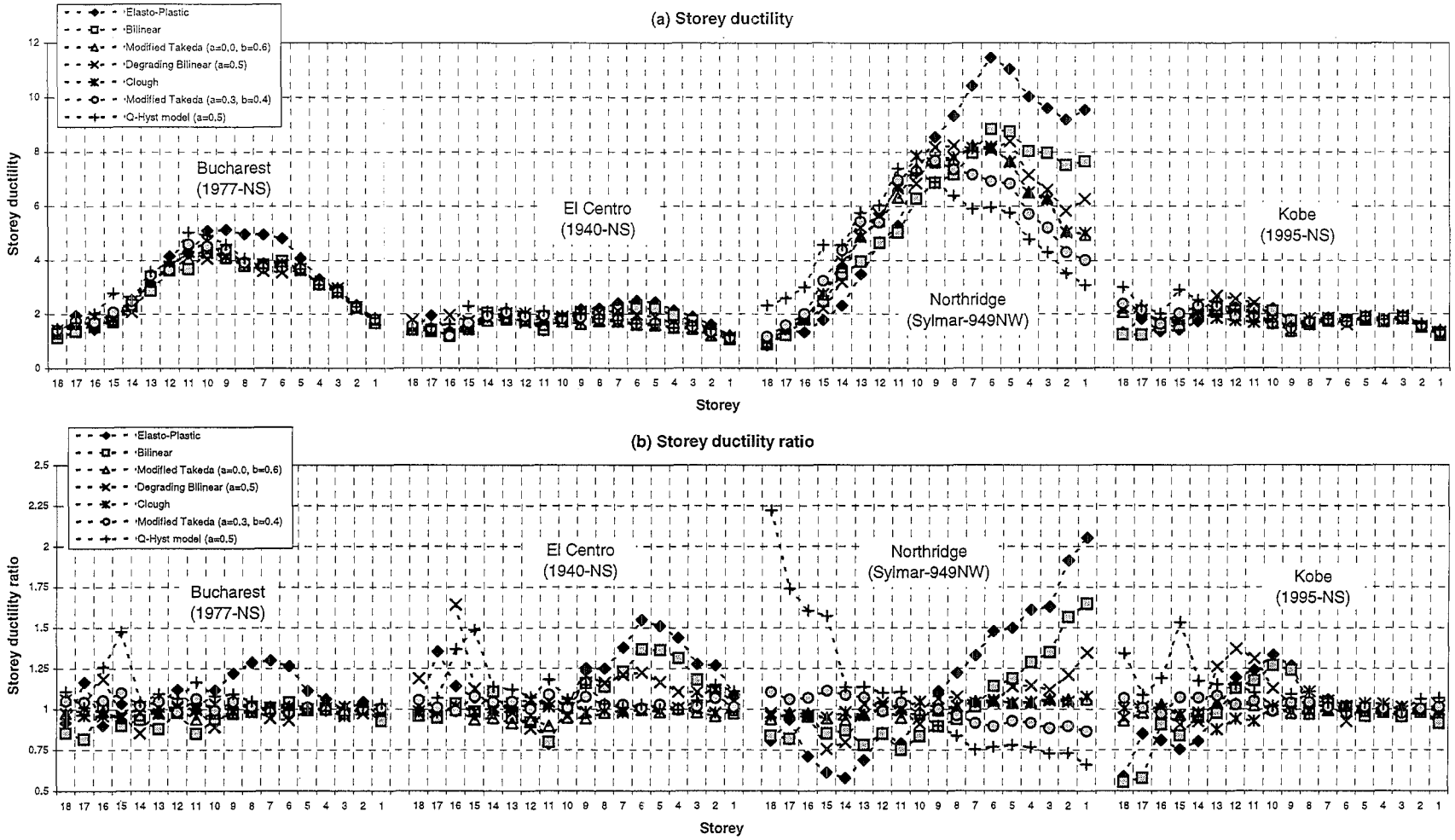

Fig. 7-8 (a) The maximum storey ductility for each of the seven hysteresis models for the 18S under the four excitations using the Carr & Tabuchi method
(b) The ratio of the storey ductility for each of the seven hysteresis models to the averages of those for the three hysteresis models for the 18S

It is found from Figs. 7-6 to 7-8 that compared to the averages of the storey ductilities for the three hysteresis models, the Elasto-Plastic hysteresis model predicts significantly smaller values in storeys 4 and 5 for the 6 storey structure when subjected to the Bucharest (1977-NS) and El Centro (1940-NS) earthquakes, and in the upper storeys for each of the 12 and 18 storey structures under the Northridge (Sylmar-949NW) and Kobe (1995-NS) earthquakes. The ratios of the storey ductilities for the Elasto-Plastic hysteresis model to the averages are 0.58 to 1.07 for the 6 storey structure under the Bucharest (1977-NS) earthquake, for an example, as shown in Table 7-6.

The Bilinear hysteresis model predicts significantly smaller storey ductilities at each level, in general, for the 6 and 12 storey structures, and in the upper storeys for the 18 storey structure under the Northridge (Sylmar-949NW) earthquake. The ratios of the storey ductilities for the Bilinear model to the average values range from 0.58 to 0.84 for those corresponding storeys as shown in Table 7-6.

The Degrading Bilinear model (α=0.5) predicts significantly smaller storey ductilities in storeys 4 to 6 for the 6 storey structure under the Bucharest (1977-NS) earthquake, as shown in Fig. 7-6(b).

However, the Q-Hyst (α=0.5) model produces larger storey ductilities, in general, except in the lower storeys for the 18 storey structure when subjected to the Northridge (Sylmar-949NW) earthquake where insignificantly smaller storey ductilities are predicted using this model when compared to the averages of those for the three hysteresis models.

7-4 Effect of Varying Hysteresis Models on the Overall Structural Ductility

Fig. 7-9(a) presents overall structural ductilities of the three framed structures under the four scaled earthquakes predicted using each of the seven hysteresis models for the Carr & Tabuchi method, and the averages of those for the hysteresis models excepting the Elasto-Plastic and Bilinear models. Fig. 7-9(b) shows the ratios of the overall structural ductility for each of the seven hysteresis models to the averages for the three structures under the four scaled earthquakes.

It's found from Fig. 7-9(a) that the structural displacement ductility demand is over 5.0 for the 6- and 18-storey structures when subjected to Northridge (Sylmar-949NW) earthquake. This means damage in these two structures is larger than that expected from the scaling methods which are attempting to match the design standard. This is not surprising considering the 'near field' effects exhibited by this earthquake record. The new draft standard [AS/NZS 1170] is attempting to take this effect into account.

Table 7-7 Ratio of the structural ductilities for each of the seven hysteresis models to the averages of those for the hysteresis models except the Elasto-Plastic and Bilinear

		E-P	Bi	MT(α=0, β=0.6)	DBi (α=0.5)	Clough	MT(α=0.3, β=0.4)	Q-Hyst (α=0.5)
6S	Bucharest	0.98	1.06	1.00	0.95	0.99	0.98	1.09
	El Centro	0.93	1.00	0.95	1.11	0.94	0.91	1.09
	Northridge	1.02	**0.79**	1.01	0.90	1.02	1.02	1.04
	Kobe	**0.73**	0.86	0.95	0.93	1.00	0.99	1.12
12S	Bucharest	0.95	0.92	1.00	0.98	1.01	1.00	1.00
	El Centro	**0.68**	**0.68**	0.97	0.94	1.02	0.99	1.09
	Northridge	0.92	**0.65**	0.97	1.07	0.98	1.02	0.96
	Kobe	0.86	0.76	0.97	0.91	1.00	1.02	1.10
18S	Bucharest	**1.30**	0.94	1.00	0.99	1.00	1.00	1.01
	El Centro	0.93	0.91	0.94	1.00	0.98	1.04	1.04
	Northridge	1.12	0.94	1.00	1.09	1.00	0.98	0.93
	Kobe	1.07	1.02	0.98	1.14	0.91	0.98	0.99

It is observed from Fig. 7-9(b) that the variation in the ratios of the overall structural ductilities for the five hysteresis models, i.e. the Modified Takeda (α=0, β=0.6), Degrading Bilinear (α=0.5), Clough, Modified Takeda (α=0.3, β=0.4) and Q-Hyst (α=0.5) models are very small, ranging from 0.91 to 1.11, 0.91 to 1.10 and 0.94 to 1.14 of the averages for the 6, 12 and 18 storey structure respectively under the four scaled earthquake excitations, as shown in Table 7-7. This indicates that these five hysteresis models predict similar overall structural ductilities. This is independent of

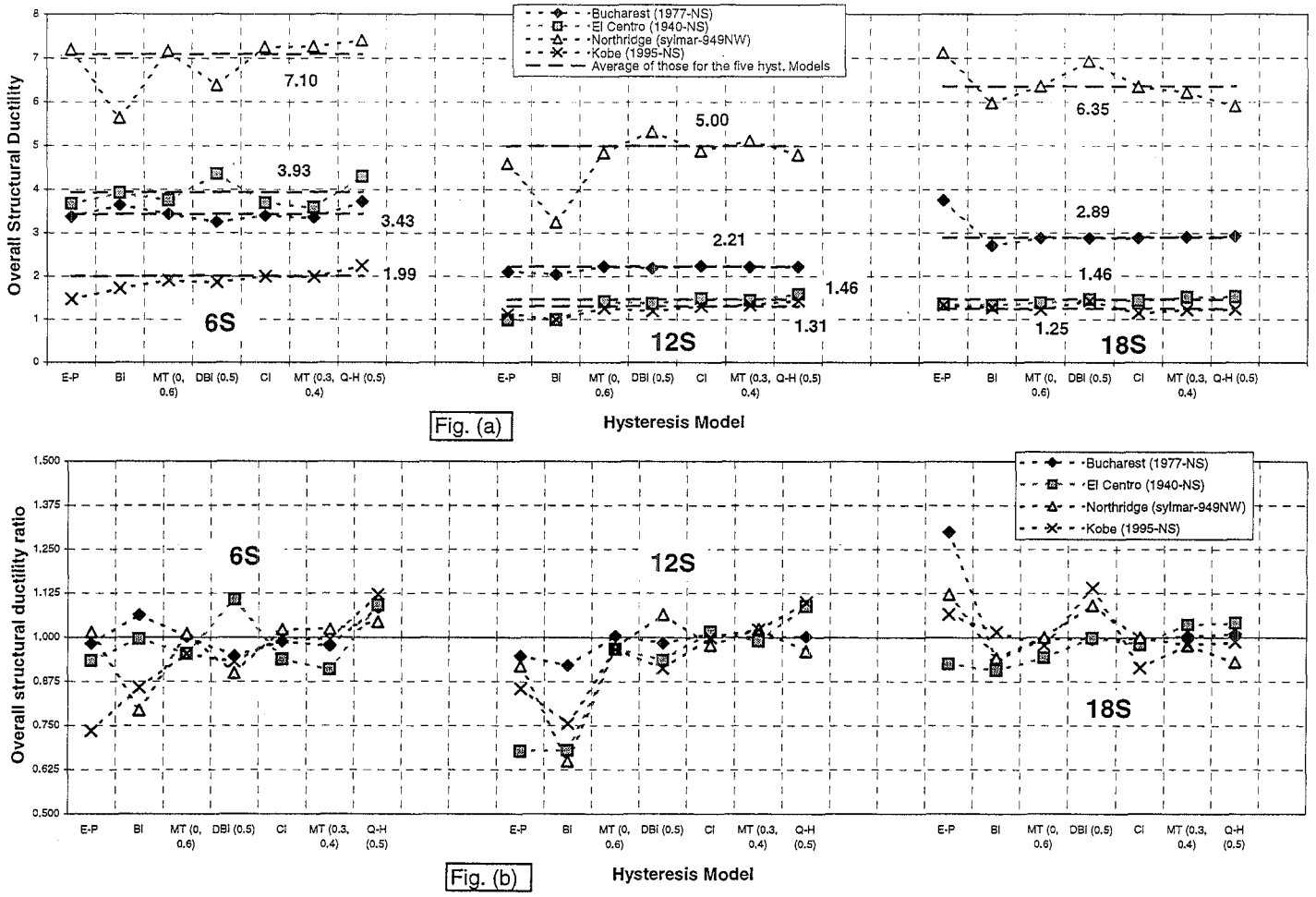

Fig. 7-9 (a) Overall structural ductilities of the three frames under the four scaled earthquakes for each of the seven hysteresis models
(b) The ratio of the overall structural ductility for each of the seven hysteresis models to the averages of those for the five hysteresis models rather than the Elasto-Plastic and Bilinear models

the characteristics of the earthquakes and the fundamental periods of free vibration of the structures concerned.

It is found from Fig. 7-9(b) that when compared to the averages of the overall structural ductilities for the five hysteresis models, the Elasto-Plastic hysteresis model predicts significant smaller values for the 6 storey structure under the Kobe (1995-NS) earthquake, and for the 12 storey structure under the El Centro (1940-NS) earthquake. The Bilinear model predicts significantly smaller values for the 6 storey structure under the Northridge (Sylmar-949NW) earthquake, and for the 12 storey structure under the El Centro (1940-NS) and Northridge (Sylmar-949NW) earthquakes.

The ratios of the structural ductilities for the Elastio-Plastic model to those averages are 0.73 and 0.68 for the 6 storey structure under the Kobe (1995-NS) earthquake, and for the 12 storey structure under the El Centro (1940-NS) earthquake respectively, as shown in Table 7-7. The ratios of the structural ductilities for the Bilinear model to those averages are 0.79 for the 6 storey structure under the Northridge (Sylmar-949NW) earthquake, and are 0.68 and 0.65 for the 12 storey structure under the El Centro (1940-NS) and Northridge (Sylmar-949NW) earthquakes respectively.

However, the Elasto-Plastic model predicts a significantly larger structural ductility than the averages for the five other hysteresis models for the 18 storey structure when subjected to the Bucharest (1977-NS) earthquake. The ratio of the structural ductility for the Elasto-Plastic model to the averages is 1.30 as shown in Table 7-7. This is earthquake dependent.

7-5 Relationship Between the Member Curvature, Storey Displacement and Structural Displacement Ductilities

7-5.1 Relationship Between Beam Member Curvature Ductility and Storey Displacement Ductility

The relationships between the maximum beam member curvature ductility and the maximum storey displacement ductility for each storey from the Carr & Tabuchi method predicted using the seven hysteresis models for the three structures under the four earthquakes are shown in Figs. 7-10 to 7-12

It can be seen from Figs. 7-10 to 7-12 that there is a very strong and stable linear relationship between the maximum member curvature ductility and the maximum storey displacement ductility. The ratios of the maximum member ductility to the maximum storey ductility are approximately 4, 3 and 3 for the 6, 12 and 18 storey structures respectively. The characteristics of the excitation and varying the hysteresis models do not significantly affect this relationship.

The maximum member ductility, storey ductility and the ratios of the maximum member ductility to the maximum storey ductility covering the four earthquakes are shown in Table 7-8.

Table 7-8 The maximum member ductility, storey ductility and the ratios of the maximum member ductility to the maximum storey ductility covering the four earthquakes

	Hysteresis model	Max. member ductility	Max. storey ductility	Ratio (Mem. duct./Storey duct.)
6S	Elasto-Plastic	23.56	8.19	2.88
	Bilinear	22.75	6.51	3.59
	Modified Takeda (α=0.0, β=0.6)	31.17	8.07	4.56
	Degrading Bilinear (α=0.5)	28.09	7.23	3.95
	Clough	30.84	8.29	4.25
	Modified Takeda (α=0.3, β=0.4)	30.81	8.22	4.24
	Q-Hyst model (α=0.5)	30.47	8.26	4.73
12S	Elasto-Plastic	15.10	7.02	3.15
	Bilinear	15.98	4.95	4.02
	Modified Takeda (α=0.0, β=0.6)	19.65	7.25	3.58
	Degrading Bilinear (α=0.5)	27.49	7.57	5.09
	Clough	19.76	7.26	3.55
	Modified Takeda (α=0.3, β=0.4)	20.60	7.63	5.48
	Q-Hyst model (α=0.5)	21.32	6.93	3.88
18S	Elasto-Plastic	20.28	11.46	3.41
	Bilinear	21.12	8.85	4.55
	Modified Takeda (α=0.0, β=0.6)	20.26	8.23	3.98
	Degrading Bilinear (α=0.5)	26.80	8.40	5.15
	Clough	20.35	8.18	4.85
	Modified Takeda (α=0.3, β=0.4)	22.16	7.69	4.39
	Q-Hyst model (α=0.5)	27.51	7.39	5.03

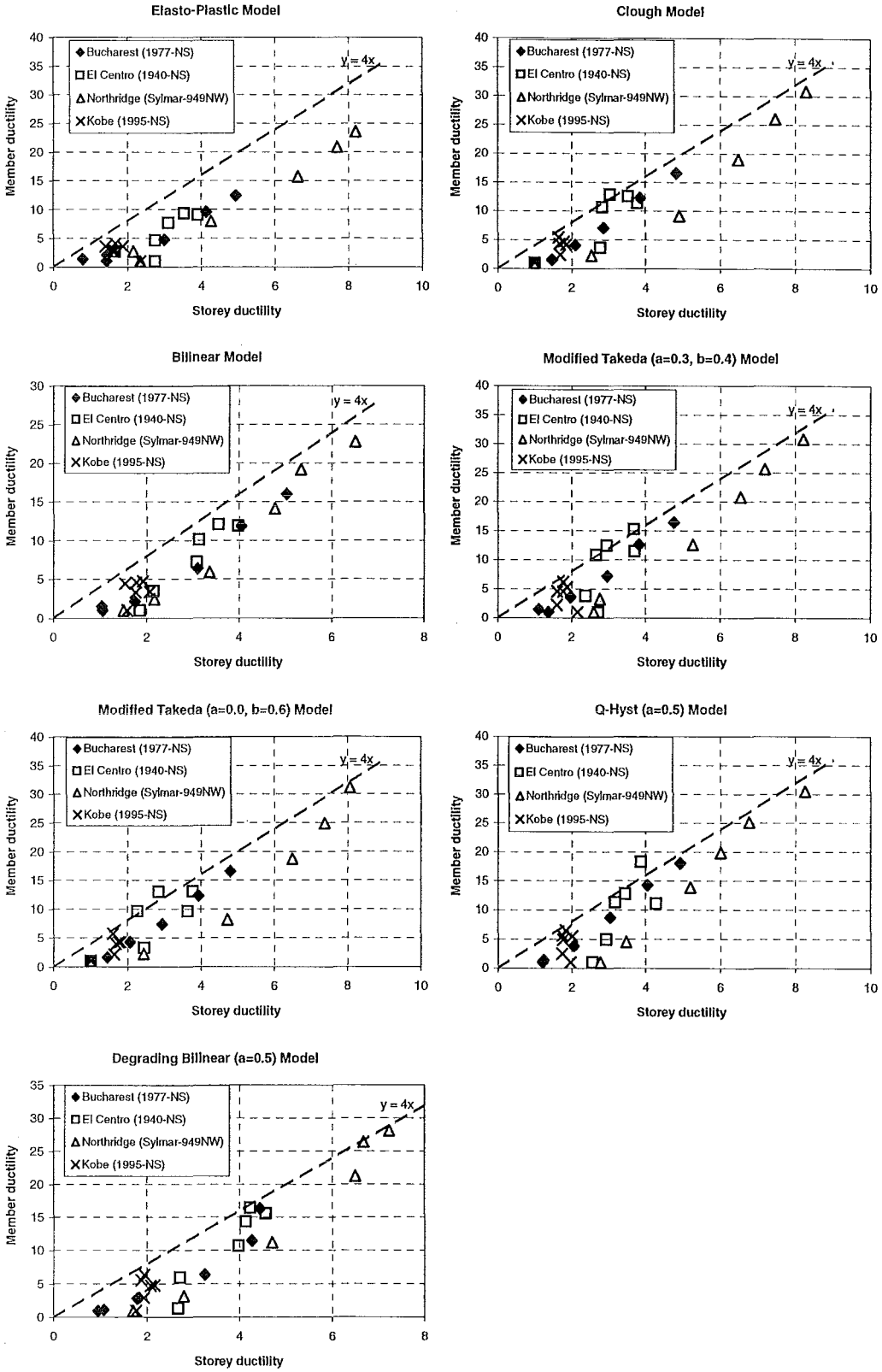

Fig. 7-10 Relationship between maximum beam member ductility and the storey ductility for **6 storey structure** for the Carr & Tabuchi method using the seven hysteresis models under the four excitations

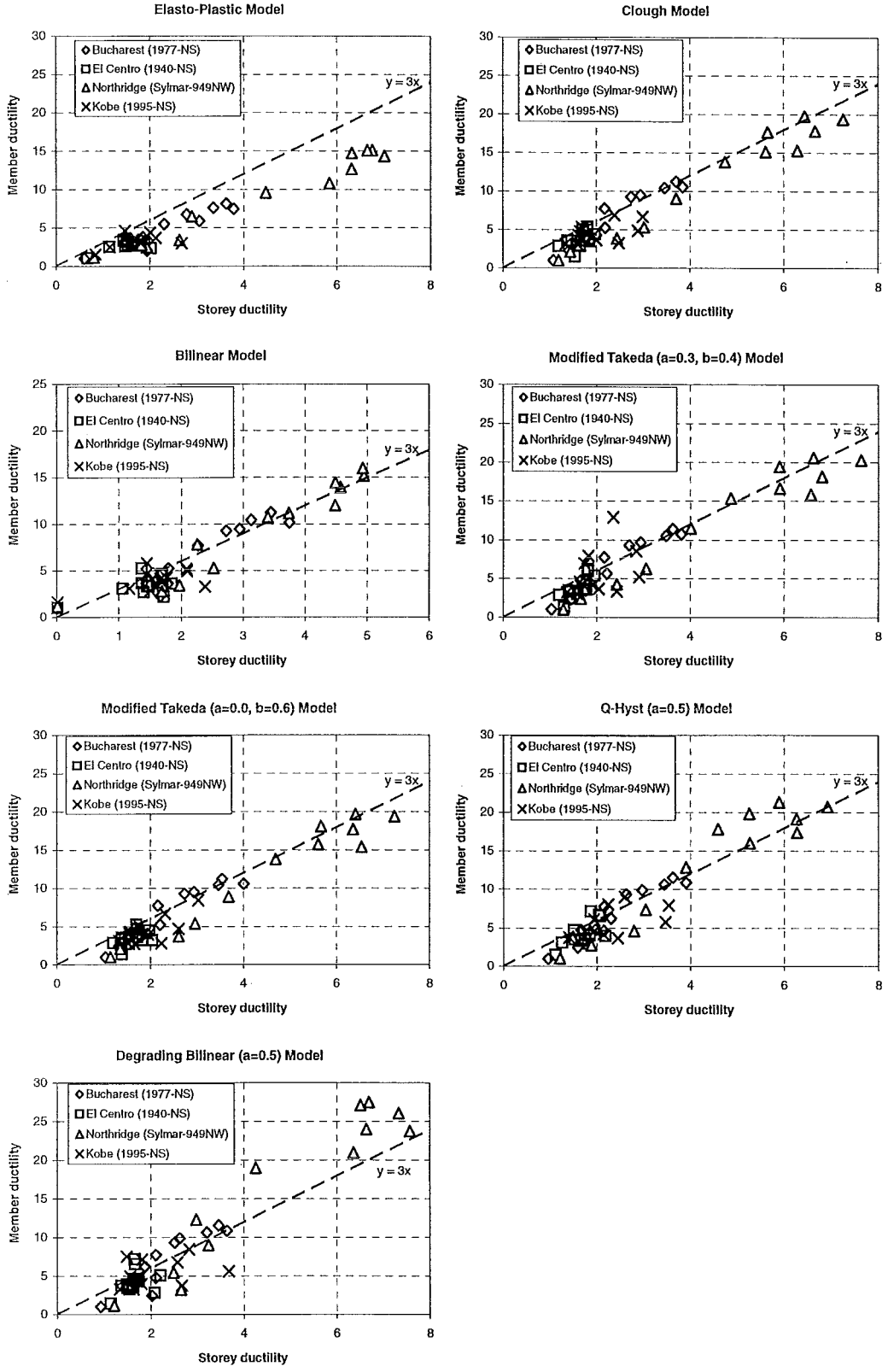

Fig. 7-11 Relationship between maximum beam member ductility and the storey ductility for **12 storey structure** for the Carr & Tabuchi method using the seven hysteresis models under the four excitations

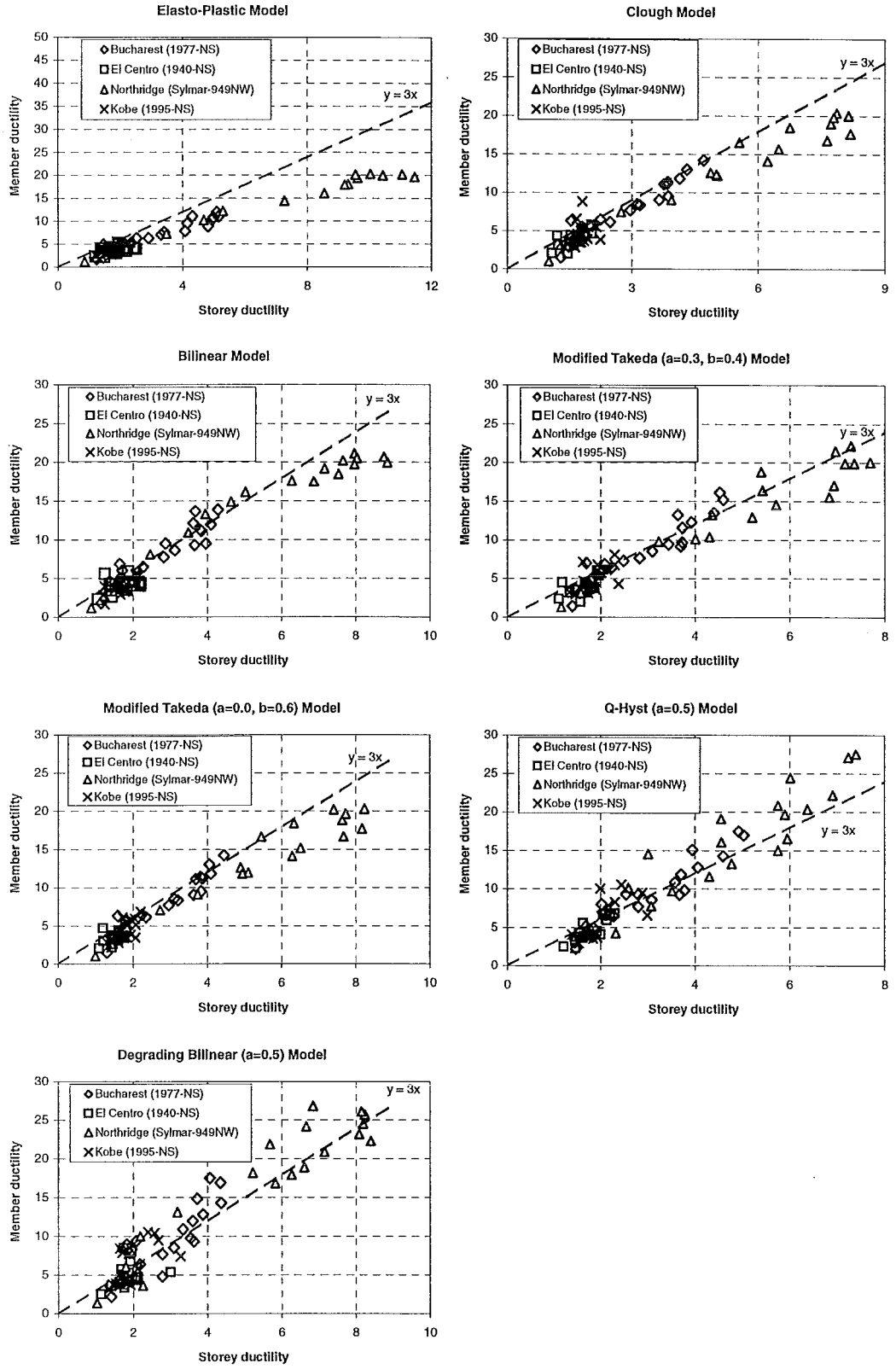

Fig. 7-12 Relationship between maximum beam member ductility and the storey ductility for **18 storey structure** for the Carr & Tabuchi method using the seven hysteresis models under the four excitations

7-5.2 Relationship Between Storey Ductility and Overall Structural Ductility

Fig. 7-13 shows the maximum ratios of the storey ductility to the structural ductility for the Carr & Tabuchi method using each of the seven hysteresis models other than the Origin-Centred model for the three framed structures under the four different earthquakes.

It is found from Fig.7-13 that the different choices of the different seven hysteresis models do not significantly affect the ratios of the storey ductility to the structural ductility for each of the four earthquakes for the three structures. However, the ratios are much dependent on the characteristics of the excitations. The maximum ratios are seen for the Bucharest (1977-NS) for the 6 storey structure and for the Kobe (1995-NS) earthquakes for the 12 and 18 storey structures.

The average of the ratios of the maximum storey ductility to the maximum structural ductility predicted using these hysteresis models for all three structures are shown in Table 7-9. The average values of the ratios for the 6 storey structure, for an example, are 1.40, 1.03, 1.13 and 1.12 for the Bucharest (1977-NS), El Centro (1940-NS), Northridge (Sylmar-949NW) and Kobe (1995-NS) earthquakes respectively. The maximum ratios of the average values are 1.40, 2.46 and 1.92 for the 6, 12 and 18 storey structures respectively covering the four earthquakes, which are to be used to obtain the required beam member ductilities.

Table 7-9 Ratios of the maximum storey ductility to the structural ductility

		Elasto-Plastic	Bilinear	MTakeda (α=0, β=0.6)	Degrading Bilinear (α=0.5)	Clough	MTakeda (α=0.3, β=0.4)	Q-Hyst (α=0.5)	Average	Max. of Average Values
6S	Bucharest	1.47	1.38	1.40	1.37	1.43	1.42	1.33	1.40	1.40
	El Centro	1.06	1.02	1.01	1.05	1.02	1.03	1.00	1.03	
	Northridge	1.14	1.16	1.12	1.13	1.14	1.13	1.11	1.13	
	Kobe	1.60	1.21	0.95	1.16	0.92	1.09	0.90	1.12	
12S	Bucharest	1.80	1.84	1.80	1.67	1.72	1.72	1.76	1.76	2.46
	El Centro	2.04	1.87	1.45	1.62	1.33	1.35	1.38	1.58	
	Northridge	1.53	1.52	1.50	1.42	1.49	1.49	1.44	1.48	
	Kobe	2.39	2.41	2.40	3.08	2.29	2.18	2.46	2.46	
18S	Bucharest	1.36	1.58	1.54	1.51	1.63	1.58	1.72	1.56	1.92
	El Centro	1.84	1.63	1.27	1.43	1.42	1.36	1.51	1.49	
	Northridge	1.61	1.48	1.30	1.21	1.29	1.24	1.25	1.34	
	Kobe	1.71	1.70	1.81	1.88	1.96	1.95	2.43	1.92	

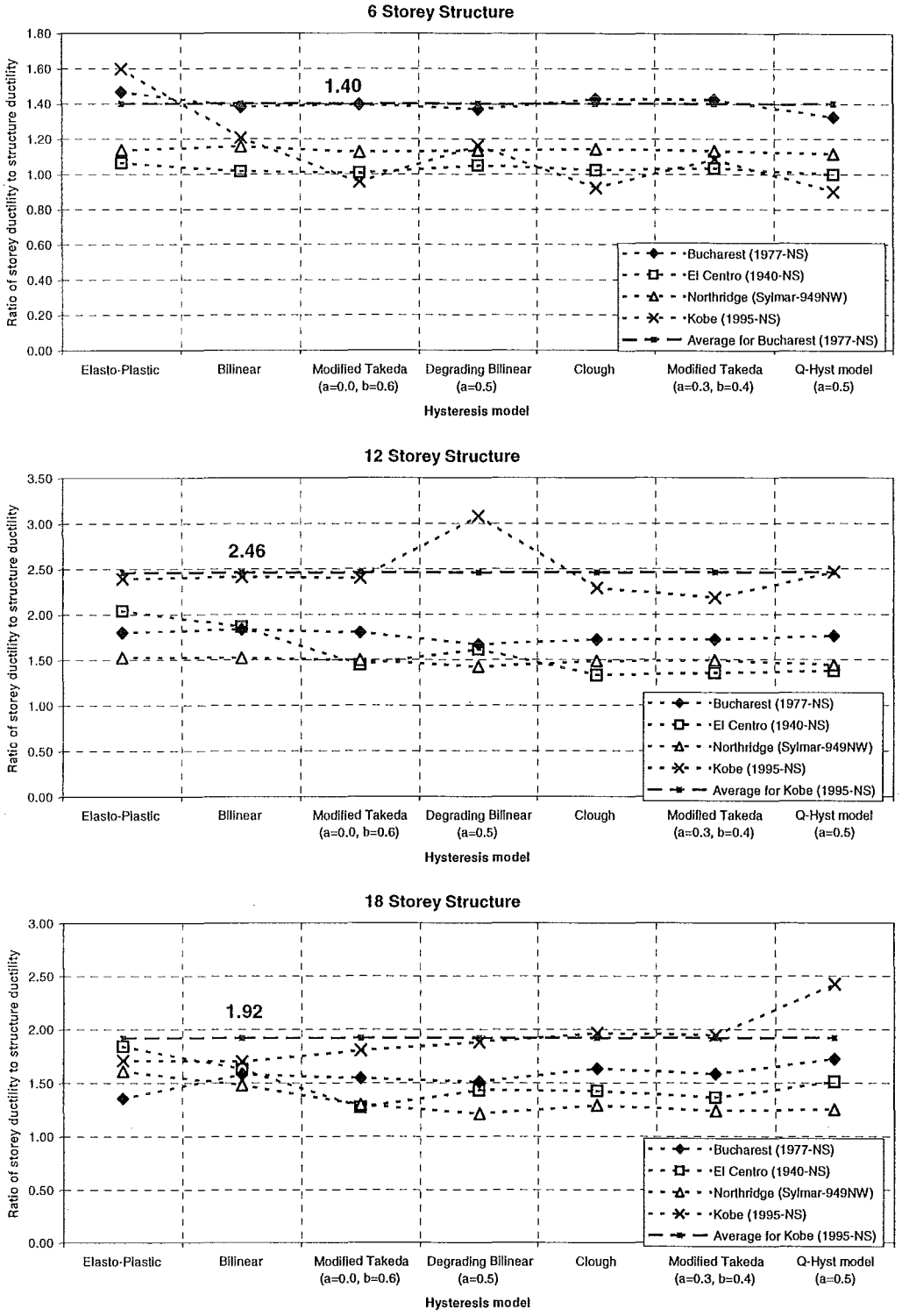

Fig. 7-13 The maximum ratios of the storey ductility to the structural ductility for the hysteresis models except the Origin-Centred model for the three framed structures under the four earthquakes

It is observed from Fig.7-13 that the ratios of the storey ductility to the structural ductility for the three structures under a specified earthquake are greatest for the 12-storey frame and least for the 6-storey structure. This is why the ratios of the member ductility to the structural ductility for the 12 storey structure are larger than that for the 18 storey structure with the same ratios of the member ductility to the storey ductility for these two structures shown in Table 7-10. This will be discussed in the following section 7-5.3.

7-5.3 Relationship between Member Curvature Ductility and Overall Structural Displacement Ductility, and Required Member Ductility

The ratios of the member ductility to the structural ductility are equal to the ratios of the member ductility to the storey ductility multiplied by the ratio of the storey ductility to the structural ductility. Table 7-10 shows the ratios of the maximum beam curvature ductility to the maximum structural displacement ductility and the required member ductility for design structural ductility 5.0.

Table 7-10 Ratios of the maximum beam curvature ductility to maximum structural displacement ductility, and required beam curvature ductility for structural ductility 5

	Ratios of beam member duct. to storey duct.	Ratios of storey duct. to structural duct.	Ratios of member duct. to structural duct.	Structural ductility	Required member ductility
6S	4.0	1.40	5.60	5.0	21~28
12S	3.0	2.46	7.38	5.0	22~37
18S	3.0	1.92	5.76	5.0	20~29

The ranges of the ratios of the beam member curvature ductility to the structural displacement ductility are 4.12 to 5.60, 4.44 to 7.38 and 4.02 to 5.76 for the 6-, 12- and 18-storey structures respectively. The beam curvature ductilities required by the inelastic responses at the design level earthquakes are obtained by multiplying these ratios with the design structural ductility of 5.0, being in the ranges of 21 to 28, 22 to 37 and 20 to 29 for the 6, 12 and 18 storey framed structures respectively. The required beam curvature ductilities found by Carr and Tabuchi [Carr 1993] are 32 which is larger by 15% than those for the 6 and 18 storey structures, and smaller by approximately 15% than those for the 12 storey structure used in the present study.

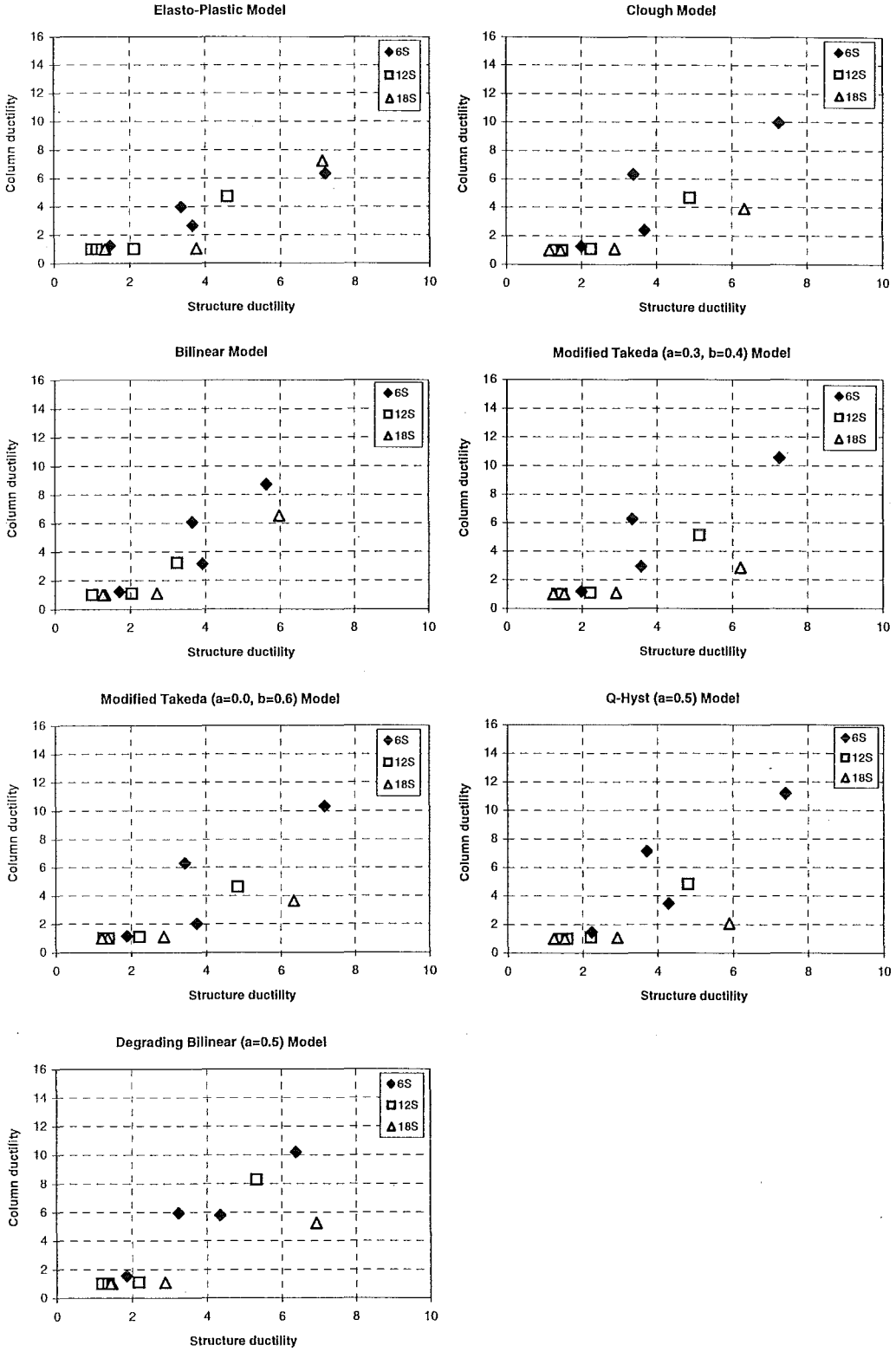

Fig. 7-14 Relationship between the maximum column curvature ductility in the first storey and the maximum structural displacement ductilities for the three framed structures under the four excitations predicted for the Carr & Tabuchi method using the seven hysteresis models

Fig 7-14 illustrates the relationship between the maximum column curvature ductility in the first storeys and the maximum structural displacement ductilities of the three structures under the four earthquakes. The column ductilities were up to approximately 1.4 times the structural displacement ductility. Hence the required column curvature ductility for the three structures is of the order of 7.

7-6 Summary and Conclusions

In this chapter three framed structures of 6, 12 and 18 storeys, designed according to the current New Zealand Codes using a design structural ductility of 5.0 as discussed in Chapter 2, were modelled and excited by the four design level scaled excitations to determine their inelastic dynamic responses. The excitations were the Bucharest (1977-NS), El Centro (1940-NS), Northridge (Sylmar-949NW) and Kobe (1995-NS) accelerograms discussed in Chapter 5. The inelastic responses studied consisted of the storey and overall structural yield displacements, and the storey and overall structural ductilities.

Seven hysteresis models, the Elasto-Plastic, Bilinear, Modified Takeda (α=0.0, β=0.6), Degrading Bilinear (α=0.5), Clough, Modified Takeda (α=0.3, β=0.4), Q-Hyst (α=0.5) were used for the studies on the yield displacements, ductilities for the storeys and structures. The Origin-Centred model was used only for the studies on the storey and structural yield displacements.

The relationship between the member curvature ductility, storey and the overall structural displacement ductility was obtained based on that predicted for the Carr & Tabuchi approach using all the hysteresis models except the Origin-Centred model. Further, the required member curvature ductilities based on the relationship between the member curvature ductilities and structural displacement ductilities were determined.

From the above study the following conclusions for this chapter may be drawn:

(1) Significant variation in both the storey and overall structural yield displacements caused by the different choices of the Carr & Tabuchi approach and the pushover analyses for the three structures are found. The Carr & Tabuchi method is recommended because the inelastic responses result from inelastic dynamic analyses, whereas a pushover analysis is based on a static lateral load analysis.

(2) Four of the hysteresis models, the Modified Takeda (α=0.0, β=0.6), Clough, Modified Takeda (α=0.3, β=0.4) and Q-Hyst (α=0.5) predict similar storey yield displacements. All the hysteresis models, except the Origin-Centred model, predict similar overall structural yield displacements.

Three hysteresis models, the Modified Takeda (α=0.0, β=0.6), Clough and Modified Takeda (α=0.3, β=0.4) predict very similar storey displacement ductilities, which are independent of the fundamental periods of free vibration and the characteristics of the earthquakes. The Elasto-Plastic, Bilinear, Degrading Bilinear (α=0.5) and Q-Hyst (α=0.5) models predict significantly smaller storey ductilities than those for the other hysteresis models when subjected to certain types of earthquakes.

All the different hysteresis models, except the Elasto-Plastic and Bilinear models, predict similar structural displacement ductilities. The Elasto-Plastic and Bilinear models predict significantly smaller structural ductilities than the others for certain types of earthquakes.

(4) The ratios of the beam curvature ductility to the structural displacement ductility are up to 5.6, 7.38 and 5.76 for the 6, 12 and 18 storey structures respectively. The required beam curvature ductility ranges were 21 to 28, 22 to 37 and 20 to 29 for the 6, 12 and 18 storey structures respectively.

(5) The ratio of the column curvature ductility in the first storey to the structural displacement ductility is about 1.4 for all three structures. Therefore, the required column curvature ductility is approximately 7.0 for a design structural ductility of 5.0.

Chapter 8
Seismic Damage Assessment of Reinforced Concrete Ductile Framed Structures

8-1 Introduction

In evaluating seismic damage in a reinforced concrete ductile framed structure, the damage indices for the structure and storeys are regarded as more rational indicators than the structure and storey displacement ductilities. Though the structural and storey displacement ductilities are strongly related to the overall damage in the structure and storeys, they cannot reflect the contribution of the dissipated energy due to inelastic cyclic behaviour and the stiffness deterioration etc. in members to the overall damage in the structure and in its storeys.

Many hysteresis models and member damage indices have been developed as discussed in Chapters 4 and 6 respectively. Varying the hysteresis models in modelling member inelastic behaviour when conducting a dynamic inelastic time history analysis for the overall structural damage assessment will affect the structural responses in terms of the maximum member curvature ductility, member dissipated energy and stiffness degradation. Hence varying the member damage indices and the hysteresis models may lead to significant variations in the computed damage indices for the structure and storeys. As a result, this could influence an engineer in making engineering judgements of the performance of the structure under earthquake excitation at a standard required design level (ultimate limit state).

In order to identify the effects of varying the member damage indices and hysteresis models on the storey and structural damage indices, four different member damage indices and seven hysteresis models were used in modelling the member damage and member inelastic behaviour for the storey and structural damage indices of the three framed structures discussed in Chapter 2 when subjected to the four scaled earthquake excitations.

The four member damage indices used are the Park & Ang, Banon & Veneziano, Roufaiel & Meyer and Cosenza et al. damage indices as discussed in Chapter 6.

The seven hysteresis models used in this study are the Elasto-Plastic, Bilinear, Modified Takeda (α=0.0, β=0.6), Degrading Bilinear (α=0.5), Clough, Modified Takeda (α=0.3, β=0.4) and Q-Hyst (α=0.5) and are discussed in Chapter 4. Four design-level scaled earthquake excitations at the ultimate limit state, i.e. the Bucharest (1977-NS), El Centro (1940-NS), Northridge (Sylmar-949NW) and Kobe (1995-NS) excitations as discussed in Chapter 5 were used as the earthquake inputs.

The energy weighted average (Park & Ang) method was used for the calculation of the storey and structural damage indices, as discussed in Chapter 6. From the inelastic step-by-step integration time-history analyses, the member damage indices for every inelastic member end were obtained. The storey and the structural damage indices were then calculated as the energy weighted average of all the inelastic member ends in a storey and in the whole structure respectively.

The effect of varying member damage indices and hysteresis models on the storey and structural damage indices was identified by comparative studies, leading to a recommendation as to the choice of a member damage index and hysteresis model for evaluating of the storey and structural damage analyses for ductile reinforced concrete framed structures.

8-2 Ultimate Member Curvature Ductility for Member Damage Indices

From Chapter 7, the ranges of ratios of the beam curvature ductility to the structural displacement ductility are 4.12 to 5.60, 4.40 to 7.38 and 4.02 to 5.76 for the 6, 12 and 18 storey structures respectively. The required beam curvature ductilities are obtained by multiplying these ratios with the design structural ductility of 5.0, giving member curvature ductility ranges of 21 to 28, 22 to 38 and 20 to 29 for the 6, 12 and 18 storey structures respectively. The beam members were carefully designed and detailed

according to the current New Zealand codes and should be able to sustain curvature ductilities of up to 30, and therefore just meet the required member ductility demands.

The ratio of the column ductility in the first storeys to the structural displacement ductility is approximately 1.4. Hence the required column ductility for the three structures is 7 for a design structure ductility of 5.0. However, it is very difficult to determine the curvature ductility capacity for columns as the capacities are strongly dependent on the magnitude of the axial forces, which vary during the earthquake excitations. This issue should be investigated in future studies.

Based on a conservative point of view, a column ductility of 15, which is smaller than the 20 used in the input data for the Jury frames [Jury 1978], was used as the ultimate column curvature ductility for all the columns in the first storeys of the three structures as part of the input data for the member damage indices.

8-3 Storey Damage Analysis of the Three Ductile Framed structures

8-3.1 Effect of Varying Hysteresis Models on the Storey Damage Indices

Figs. H-1 to H-6 in Appendix H show the distributions of storey damage indices calculated as the energy weighted average of all the member damage indices in the storeys of the three structures for the four earthquakes, predicted using each of the seven hysteresis models for the four different member damage indices.

It is observed from Figs. H-1 to H-6 that, in general, for each of the three structures under each of the four earthquake excitations, neither varying the seven hysteresis models nor varying the four member damage indices significantly affects the distribution of the storey damage indices. The distribution of the storey damage indices up the height of a structure is, however, earthquake dependent, as expected.

It can be seen from Figs. H-1 and H-6 that for the three structures, three hysteresis models, i.e. the Modified Takeda (α=0, β=0.6), Clough and the Modified Takeda

(α=0.3, β=0.4) show similar storey damage indices. This is independent of the type of earthquake and the member damage indices.

In order to compare the variation in the storey damage indices caused by using different hysteresis models, the average values of storey damage indices for the three hysteresis models, the Modified Takeda (α=0, β=0.6), Clough and the Modified Takeda (α=0.3, β=0.4), were calculated for each level of each of the three structures. Then the ratios of the storey damage indices for each of the seven hysteresis models to these corresponding average values were calculated for the three structures, and are illustrated in Figs. H-7 to H-12. The ranges of those ratios from level-1 up to the top level of the three structures are presented in Table 8-1 for each of the seven hysteresis models.

It's found from Figs. H-7 to H-10 that when compared to the averages of those for the three hysteresis models, the Elasto-Plastic hysteresis model predicted significantly smaller storey damage indices for the 6- and 12-storey structures and this result is independent of the type of earthquake and member damage index. The storey damage indices for this model is of the order of 0.7 and 0.4 times these of the corresponding averages for the Park & Ang and Roufaiel & Meyer member damage indices respectively, as an example. This hysteresis model predicted either significantly smaller storey damage indices, or significantly larger and smaller values in the lower and upper storeys respectively for the 18 storey structure, as shown in Figs. H-11, 12 and this is dependent of the type of earthquake.

It is observed from Figs. H-8(a) and H-10(a) that for the 6 and 12 storey structures when subjected to the Northridge (Sylmar-949NW) earthquakes, the Bilinear hysteresis model predicted significantly smaller storey damage indices than the averages for the other three hysteresis models. The storey damage indices for this hysteresis model are approximately 75% of those of the other three hysteresis models. This model also predicted significantly smaller and larger storey damage indices in the upper and middle heights of the 18 storey structure for the Kobe (1995-NS) earthquake as shown in Fig. H-12(b).

Table 8-1

Ranges of ratios of storey damage indices predicted using each of the seven hysteresis models to the average values of those for the three hysteresis models, the Modified Takeda (α=0.0,β=0.6), Clough and Modified Takeda (α=0.3,β=0.4) models for the three structures under the four earthquakes

		6S				12S				18S			
		Park & Ang	Roufaiel & Meyer	Cosenza et al	Banon & Venerziano	Park & Ang	Roufaiel & Meyer	Cosenza et al	Banon & Venerziano	Park & Ang	Roufaiel & Meyer	Cosenza et al	Banon & Venerziano
Bucharest (1977-NS)	Elasto-Plastic	0.53~0.88	0.21~0.55	0.34~0.69	0.47~0.89	0.65~0.90	0.41~0.51	0.60~0.82	0.66~0.96	0.77~0.98	0.46~0.66	0.91~0.98	0.79~0.99
	Bilinear	0.59~1.00	0.44~1.00	0.43~1.03	0.54~1.04	0.95~1.06	0.95~1.13	0.94~1.13	0.89~1.07	0.97~1.15	0.97~1.19	0.97~1.21	0.97~1.14
	M-T (α=0.0,β=0.6)	0.98~1.04	0.98~1.12	0.98~1.12	0.98~1.07	0.94~1.00	0.93~1.00	0.92~1.00	0.94~1.01	0.93~1.00	0.92~1.00	0.91~1.00	0.93~1.00
	DBi (α=0.5)	0.76~1.03	0.19~1.01	0.19~1.01	0.68~1.02	0.98~1.21	0.99~1.27	0.99~1.29	0.95~1.19	0.98~1.46	1.00~1.44	1.00~1.52	0.96~1.48
	Clough	0.97~1.02	0.97~1.03	0.96~1.03	0.97~1.04	0.94~1.00	0.93~1.00	0.92~1.00	0.94~1.02	0.93~1.00	0.92~1.00	0.91~1.00	0.92~1.00
	M-T (α=0.3,β=0.4)	0.94~1.05	0.87~1.05	0.88~1.06	0.91~1.05	1.00~1.11	1.00~1.14	1.00~1.15	0.97~1.11	1.00~1.15	1.00~1.16	1.00~1.18	0.99~1.15
	Q-Hyst (α=0.5)	0.91~1.13	0.71~1.17	0.74~1.21	0.82~1.13	1.00~1.23	1.00~1.27	1.00~1.30	0.97~1.23	0.99~1.48	0.99~1.48	0.99~1.57	0.98~1.50
El Centro (1940-NS)	Elasto-Plastic	0.55~0.86	0.33~0.60	0.48~0.87	0.60~0.88	0.59~0.97	0.32~0.58	0.51~0.96	0.63~0.96	0.78~1.39	0.40~1.00	0.64~1.65	0.82~1.28
	Bilinear	0.84~1.11	0.84~1.15	0.79~1.17	0.85~1.09	0.77~1.15	0.75~1.18	0.73~1.18	0.78~1.14	0.89~1.48	0.84~1.81	0.83~1.84	0.97~1.38
	M-T (α=0.0,β=0.6)	0.83~0.98	0.78~0.97	0.76~0.97	0.88~0.98	0.93~1.02	0.92~1.03	0.90~1.03	0.93~1.04	0.88~1.04	0.85~1.07	0.84~1.07	0.92~1.03
	DBi (α=0.5)	1.05~1.58	1.09~1.68	1.10~1.90	1.05~1.54	1.00~1.48	1.03~1.65	1.04~1.71	0.84~1.35	1.08~1.97	1.14~2.37	1.16~2.47	0.87~1.67
	Clough	0.98~1.16	0.98~1.21	0.97~1.23	0.98~1.08	0.96~1.07	0.94~1.12	0.94~1.12	0.96~1.04	0.95~1.03	0.89~1.06	0.88~1.06	0.96~1.01
	M-T (α=0.3,β=0.4)	1.01~1.13	1.01~1.13	1.00~1.16	1.01~1.12	0.91~1.11	0.86~1.12	0.85~1.14	0.93~1.08	1.00~1.14	1.02~1.19	1.01~1.21	0.99~1.10
	Q-Hyst (α=0.5)	1.10~1.20	1.11~1.21	1.13~1.22	1.10~1.18	1.02~1.33	1.03~1.40	1.03~1.44	1.00~1.24	1.08~1.49	1.13~1.59	1.13~1.67	0.97~1.35
Northridge (Sylmar-949NW)	Elasto-Plastic	0.73~1.08	0.50~0.71	0.71~1.14	0.72~1.08	0.63~1.25	0.34~0.92	0.55~1.54	0.65~1.21	0.54~1.94	0.28~1.67	0.43~2.20	0.54~2.02
	Bilinear	0.62~0.98	0.62~0.97	0.58~0.97	0.61~0.96	0.71~1.42	0.72~1.86	0.67~1.89	0.70~1.37	0.83~1.81	0.86~1.80	0.82~2.03	0.83~1.87
	M-T (α=0.0,β=0.6)	0.87~0.99	0.83~1.00	0.82~0.99	0.87~0.99	0.92~1.00	0.89~1.00	0.89~1.00	0.92~1.00	0.84~1.04	0.77~1.04	0.76~1.05	0.84~1.05
	DBi (α=0.5)	0.93~1.23	0.96~1.38	0.94~1.40	0.93~1.23	1.16~1.60	1.16~2.00	1.20~2.06	1.16~1.57	1.15~1.51	1.15~1.59	1.19~1.65	1.15~1.54
	Clough	0.92~1.01	0.86~1.00	0.86~1.00	0.91~1.00	0.95~1.00	0.93~1.00	0.94~1.00	0.95~1.00	0.90~1.11	0.91~1.11	0.89~1.13	0.90~1.11
	M-T (α=0.3,β=0.4)	1.01~1.19	1.01~1.30	1.02~1.32	1.02~1.20	1.01~1.13	1.01~1.14	1.01~1.15	1.01~1.13	0.85~1.22	0.85~1.29	0.82~1.30	0.84~1.21
	Q-Hyst (α=0.5)	1.01~1.77	1.01~2.20	1.01~2.30	1.01~1.90	1.01~1.26	1.02~1.40	1.02~1.41	1.01~1.24	0.67~3.56	0.66~4.86	0.60~5.53	0.65~3.50
Kobe (1995-NS)	Elasto-Plastic	0.68~1.30	0.36~0.98	0.58~1.63	0.75~1.06	0.53~1.05	0.29~0.64	0.45~1.06	0.61~0.98	0.44~1.33	0.15~0.92	0.25~1.54	0.37~1.13
	Bilinear	0.79~1.56	0.69~2.10	0.68~2.14	0.91~1.30	0.67~1.15	0.64~1.17	0.62~1.18	0.75~1.10	0.45~1.60	0.27~1.88	0.26~1.96	0.36~1.35
	M-T (α=0.0,β=0.6)	0.95~1.01	0.93~1.01	0.94~1.01	0.96~1.03	0.83~1.02	0.80~1.05	0.78~1.06	0.90~1.04	0.85~1.05	0.81~1.10	0.80~1.10	0.89~1.03
	DBi (α=0.5)	1.02~1.39	1.10~1.58	1.10~1.62	0.97~1.26	1.03~1.41	1.03~1.59	1.03~1.63	1.01~1.28	1.02~1.90	1.06~2.07	1.06~2.29	0.94~1.68
	Clough	0.96~1.03	0.95~1.06	0.95~1.06	0.98~1.00	0.90~1.01	0.89~1.03	0.86~1.03	0.92~1.01	0.87~1.05	0.85~1.05	0.84~1.06	0.90~1.06
	M-T (α=0.3,β=0.4)	0.99~1.08	1.00~1.10	1.00~1.11	0.97~1.06	0.99~1.21	0.98~1.27	0.97~1.31	0.99~1.16	0.99~1.18	0.99~1.23	1.00~1.25	0.98~1.12
	Q-Hyst (α=0.5)	1.04~1.20	1.09~1.25	1.10~1.27	0.99~1.13	1.08~1.28	1.12~1.36	1.13~1.39	0.99~1.20	1.02~1.70	1.03~1.88	1.04~1.99	0.98~1.55

Both the Elasto-Plastic and the Bilinear hysteresis models predicted significantly smaller storey damage indices relative to those average values for the three hysteresis models for the 6 and 12 storey structures. This may be explained by the fact that these two hysteresis models show much greater hysteretic energy dissipation capacity when compared with the other hysteresis models. For the 18 storey structure, significant larger and smaller storey damage indices in the lower and upper storeys were predicted using these two hysteresis models and this is possibly due to the effect of higher modes that have greater significance than in the 6 and 12 storey structures. This is also dependent of the type of earthquake.

It's found from Figs. H-7 to H-12 that, in general, the Degrading Bilinear (α=0.5) and the Q-Hyst (α=0.5) models predicted significantly larger storey damage indices than those averages for the above three hysteresis models for the three structures. The storey damage indices for these two hysteresis models are up to twice of those averages, as shown in Table 8-1. This is possibly because the degraded unloading stiffness and the degraded reloading stiffness remain the same for a same maximum previous inelastic curvature for the Degrading Bilinear (α=0.5), and the Q-Hyst (α=0.5) model has the smallest energy dissipation capacity.

8-3.2 Effect of Varying the Different Member Damage Indices on the Storey Damage Indices

Figs. H-13 to H-24 in Appendix H show the distributions of storey damage indices for the three structures under the four earthquakes, predicted using each of the seven different hysteresis models, for the four different member damage indices.

It can be seen clearly from Figs. H-13 to H-24 that for each of the seven hysteresis models, varying the choice of member damage indices does not affect the distributions of the storey damage indices. This is independent of the fundamental periods of free vibration of the structures and the type of earthquake, as expected. It is found from these figures that the Cosenza et al member damage index produces the smallest storey damage indices.

In order to identify the variation in the storey damage indices caused by using different member damage indices, the ratios of storey damage indices at each level predicted using each of the Roufaiel & Meyer, Park & Ang and Banon & Veneziano member damage indices to those predicted using the Cosenza et al. member damage index for the three structures under the four earthquakes were calculated and their distributions were illustrated in Figs. H-25 to H-45. Table 8-2 shows the ranges of those ratios covering level-1 up to the top level for the three structures.

It is found from Figs. H-25 to H-36 that when using the Elasto-Plastic hysteresis model for modelling the member inelastic hysteretic responses, the Park & Ang and Banon & Veneziano member damage indices predicted very similar storey damage indices, as did the Roufaiel & Meyer and the Cosenza et al. member damage indices. Meanwhile, the storey damage indices for the Park & Ang and Banon & Veneziano member damage indices were significant larger than those for the Roufaiel & Meyer and Cosenza et al. member damage indices. This is for all three structures under all four earthquakes.

It is observed from Figs. H-25 to H-36 that when using all the hysteresis models except the Elasto-Plastic model, in general, the Roufaiel & Meyer and Cosenza et al. member damage indices provided the greatest and smallest storey damage indices respectively. The storey damage indices predicted using the Park & Ang and Banon & Veneziano member damage indices are similar. This is for all three structures under all four earthquakes and is possibly due to the factor that both member damage indices are more directly related to the dissipated energy than is the Roufaiel & Meyer and Cosenza et al member damage indices.

Table 8-3 shows the maximum ratios of the storey damage indices for each of the Roufaiel & Meyer, the Park & Ang and Banon & Veneziano member damage indices to those for the Cosenza et al. member damage index for the three structures. The storey damage indices predicted using the Roufaiel & Meyer, the Park & Ang and Banon & Veneziano member damage indices are up to 1.40 to 1.60 times those for the Cosenza et al. member damage index for certain types of earthquakes.

Table 8-2 Ranges of ratios of storey damage indices for the Park & Ang, Roufaiel & Meyer and Banon & Veneziano member damage indices to those for the Cosenza et al member damage index for the three structures under the four earthquakes

		6S			12S			18S		
		Roufaiel	Park	Banon	Roufaiel	Park	Banon	Roufaiel	Park	Banon
Bucharest (1977-NS)	Elasto-Plastic	1.00~1.01	1.18~4.41	1.09~3.82	1.00~1.01	1.18~2.15	1.10~1.88	1.00~1.00	1.11~2.41	1.04~2.14
	Bilinear	1.29~1.68	1.15~3.06	1.05~2.70	1.41~1.68	1.14~1.82	1.06~1.51	1.36~1.70	1.12~2.46	1.04~2.19
	M-Takeda (α=0,β=0.6)	1.28~1.73	1.16~2.94	1.05~2.56	1.41~1.67	1.13~1.93	1.05~1.63	1.36~1.69	1.11~3.58	1.04~3.24
	Degrading Bilinear (α=0.5)	1.28~1.67	1.19~1.60	1.07~1.30	1.41~1.67	1.12~1.77	1.04~1.32	1.29~1.69	1.08~1.89	1.02~1.51
	Clough	1.28~1.75	1.17~3.15	1.06~2.75	1.41~1.67	1.13~1.93	1.05~1.63	1.36~1.68	1.11~3.54	1.04~3.23
	M-Takeda (α=0.3,β=0.4)	1.26~1.71	1.18~3.42	1.07~2.79	1.41~1.66	1.13~1.90	1.05~1.50	1.32~1.74	1.09~3.59	1.02~3.10
	Q-Hyst (α=0.5)	1.23~1.66	1.16~3.88	1.05~2.99	1.40~1.66	1.13~1.85	1.05~1.44	1.29~1.67	1.09~1.93	1.02~1.57
El Centro (1940-NS)	Elasto-Plastic	1.00~1.02	1.24~1.67	1.15~1.73	1.00~1.01	1.54~1.93	1.58~2.16	1.00~1.01	1.30~1.88	1.24~2.11
	Bilinear	1.39~1.65	1.23~1.52	1.12~1.58	1.58~1.67	1.38~1.88	1.37~2.11	1.56~1.68	1.34~1.82	1.29~1.90
	M-Takeda (α=0,β=0.6)	1.39~1.65	1.21~1.65	1.11~1.94	1.58~1.74	1.37~4.22	1.43~3.54	1.60~1.72	1.43~2.14	1.45~2.26
	Degrading Bilinear (α=0.5)	1.29~1.57	1.12~1.31	1.04~1.24	1.52~1.72	1.30~3.80	1.25~2.70	1.48~1.66	1.21~1.65	1.13~1.46
	Clough	1.38~1.60	1.20~1.43	1.10~1.49	1.58~1.77	1.41~3.34	1.43~2.89	1.57~1.73	1.35~2.38	1.38~2.37
	M-Takeda (α=0.3,β=0.4)	1.36~1.63	1.18~1.53	1.08~1.76	1.55~1.78	1.35~4.69	1.36~3.70	1.56~1.70	1.31~1.18	1.26~2.22
	Q-Hyst (α=0.5)	1.31~1.61	1.16~1.49	1.07~1.61	1.52~1.70	1.31~3.27	1.25~2.59	1.53~1.68	1.26~1.90	1.18~1.95
Northridge (Sylmar-949NW)	Elasto-Plastic	1.00~1.01	1.07~1.59	1.01~1.30	1.00~1.01	1.09~1.77	1.02~1.54	1.00~1.03	1.06~2.17	1.01~2.01
	Bilinear	1.19~1.67	1.08~1.70	1.01~1.36	1.31~1.66	1.10~1.58	1.03~1.35	1.19~1.67	1.06~1.78	1.01~1.60
	M-Takeda (α=0,β=0.6)	1.10~1.69	1.07~1.83	1.00~1.48	1.23~1.68	1.08~2.17	1.01~1.87	1.22~1.68	1.07~2.02	1.01~1.92
	Degrading Bilinear (α=0.5)	1.12~1.64	1.06~1.48	1.00~1.20	1.12~1.63	1.05~1.52	1.00~1.22	1.12~1.63	1.05~1.47	1.00~1.25
	Clough	1.10~1.66	1.07~1.79	1.00~1.45	1.24~1.68	1.08~2.17	1.01~1.87	1.22~1.67	1.07~1.83	1.01~1.70
	M-Takeda (α=0.3,β=0.4)	1.09~1.64	1.07~1.51	1.00~1.24	1.23~1.70	1.07~1.98	1.01~1.58	1.21~1.65	1.07~1.62	1.01~1.50
	Q-Hyst (α=0.5)	1.09~1.60	1.06~1.29	1.00~1.13	1.21~1.67	1.07~1.78	1.01~1.42	1.13~1.61	1.06~1.36	1.00~1.19
Kobe (1995-NS)	Elasto-Plastic	1.00~1.02	1.50~1.60	1.55~2.09	1.00~1.01	1.53~3.39	1.70~2.76	1.00~1.02	1.37~2.61	1.35~2.26
	Bilinear	1.59~1.66	1.44~1.45	1.46~2.07	1.56~1.70	1.47~3.38	1.54~2.68	1.57~1.68	1.37~2.54	1.32~2.10
	M-Takeda (α=0,β=0.6)	1.59~1.68	1.39~2.06	1.48~2.10	1.52~1.67	1.36~1.75	1.32~2.14	1.55~1.66	1.34~1.71	1.34~1.99
	Degrading Bilinear (α=0.5)	1.54~1.66	1.29~1.60	1.22~1.48	1.48~1.65	1.30~1.59	1.23~1.81	1.44~1.66	1.18~1.59	1.10~1.74
	Clough	1.59~1.70	1.40~1.93	1.45~1.92	1.53~1.65	1.32~1.67	1.28~1.94	1.55~1.68	1.36~1.80	1.34~2.12
	M-Takeda (α=0.3,β=0.4)	1.58~1.71	1.39~2.01	1.39~2.10	1.45~1.65	1.29~1.64	1.23~1.86	1.51~1.66	1.31~1.66	1.27~1.94
	Q-Hyst (α=0.5)	1.56~1.67	1.30~1.89	1.24~1.89	1.49~1.65	1.24~1.57	1.17~1.73	1.45~1.66	1.22~1.62	1.15~1.75

Table 8-3 **The maximum ratios of the storey damage indices for each of the Roufaiel & Meyer, Park & Ang and Banon & Veneziano member damage indices to those for the Cosenza et al. member damage index**

6S			12S			18S		
Roufairl /Cosenza	Park /Cosenza	Banon /Cosenza	Roufairl /Cosenza	Park /Cosenza	Banon /Cosenza	Roufairl /Cosenza	Park /Cosenza	Banon /Cosenza
1.60	1.40		1.60	1.50		1.60	1.40	

8-4 Overall Structural Damage Analysis of the Three Ductile Framed Structures

8-4.1 Effect of Varying Hysteresis Models on the Overall Structural Damage Indices

Figs. H-37 to H-39 show the overall structural damage indices for the seven hysteresis models calculated using the energy weighted (Park & Ang) method for the three structures.

It is observed from Figs. H-37 to H-39 that three hysteresis models, the Modified Takeda (α=0, β=0.6), Clough and Modified Takeda (α=0.3, β=0.4) hysteresis models predict similar structural damage indices. This is for all three structures, all four member damage indices and all four earthquake excitations.

In order to identify the variation in the structural damage indices from the different hysteresis models, the averages of those predicted using three hysteresis models, the Modified Takeda (α=0, β=0.6), Clough and Modified Takeda (α=0.3, β=0.4) hysteresis models were calculated for the three structures subjected to the four scaled earthquakes. These averages were then compared for each of the seven hysteresis models. The ratios of the structural damage indices are shown in Table 8-4.

For the 6 and 12 storey structures, the Elasto-Plastic hysteresis model predicts significantly smaller structural damage indices when compared to the averages of those for the three hysteresis models, the Modified Takeda (α=0, β=0.6), Clough and Modified Takeda (α=0.3, β=0.4) as illustrated in Figs. H-37, 38. This is for all four member damage indices and all four earthquakes. The structural damage index for

this hysteresis model is approximately 70% of the average for the 6 storey structure when subjected to the Bucharest (1977-NS) earthquake for an example, as shown in Table 8-4.

It is found from Table 8-4 that for the 12 storey structure under the Northridge (Sylmar-949NW) earthquake, the ratios of the structural damage indices for the Bilinear hysteresis model to the three hysteresis model averages are 0.77, 0.80, 0.75 and 0.77 for the Park & Ang, Roufaiel & Meyer, Cosenza et al. and Banon & Veneziano member damage indices respectively. This indicates that the Bilinear model predicts significantly smaller structural damage indices than those for the base three hysteresis models.

It is found from Fig. 8-39(b)(d) that for the 18 storey structure subjected to the El Centro (1940-NS) and Kobe (1995-NS) earthquakes, the Degrading Bilinear (α=0.5) hysteresis model predicts significantly larger structural damage indices than those averages for the Modified Takeda (α=0.0, β=0.6), Clough and Modified Takeda (α=0.3, β=0.4) models.

Table 8-4 Ratios of structural damage indices for each of the seven hysteresis models to the averages of those for the Modified Takeda (α=0, β=0.6), Clough and Modified Takeda (α=0.3, β=0.4) hysteresis models

		6S				12S				18S			
		Park	Roufaiel	Cosenza	Banon	Park	Roufaiel	Cosenza	Banon	Park	Roufaiel	Cosenza	Banon
Bucharest (1977-NS)	E-P	**0.72**	**0.55**	**0.72**	**0.73**	**0.75**	**0.43**	**0.72**	**0.75**	0.86	0.59	0.84	0.86
	Bi	0.95	0.98	0.98	0.95	1.03	1.03	1.03	1.03	1.02	1.01	1.01	1.02
	M-T (0, 0.6)	**0.97**	**0.98**	**0.97**	**0.97**	**0.99**	**0.99**	**0.99**	**1.00**	**0.97**	**0.97**	**0.97**	**0.97**
	DBi(0.5)	1.01	1.00	1.00	1.00	1.02	1.03	1.03	1.02	1.12	1.11	1.14	1.12
	Cl	**0.97**	**0.97**	**0.97**	**0.97**	**1.00**	**1.00**	**0.99**	**1.00**	**0.97**	**0.97**	**0.97**	**0.97**
	M-T (0.3,0.4)	**1.06**	**1.05**	**1.06**	**1.06**	**1.01**	**1.01**	**1.01**	**1.01**	**1.06**	**1.05**	**1.06**	**1.06**
	Q-Hyst (0.5)	1.14	1.13	1.16	1.14	1.02	1.02	1.03	1.02	1.12	1.11	1.14	1.13
El Centro (1940-NS)	E-P	**0.77**	**0.53**	**0.75**	**0.78**	**0.76**	**0.36**	**0.67**	**0.80**	1.01	0.63	1.02	0.98
	Bi	0.99	1.00	0.99	0.98	0.94	0.93	0.92	0.96	1.14	1.17	1.18	1.12
	M-T (0, 0.6)	**0.96**	**0.95**	**0.94**	**0.97**	**0.95**	**0.95**	**0.94**	**0.97**	**0.94**	**0.93**	**0.92**	**0.97**
	DBi(0.5)	1.23	1.28	1.35	1.22	1.21	1.28	1.31	1.15	**1.44**	**1.54**	**1.61**	**1.33**
	Cl	**1.00**	**1.01**	**1.00**	**1.00**	**0.98**	**0.98**	**0.98**	**0.98**	**0.99**	**0.99**	**0.98**	**0.99**
	M-T (0.3,0.4)	**1.04**	**1.05**	**1.06**	**1.04**	**1.06**	**1.07**	**1.08**	**1.05**	**1.07**	**1.09**	**1.10**	**1.04**
	Q-Hyst (0.5)	1.12	1.13	1.17	1.11	1.22	1.27	1.30	1.15	1.21	1.28	1.31	1.14
Northridge (Sylmar-949NW)	E-P	**0.76**	**0.66**	**0.76**	**0.76**	**0.77**	**0.52**	**0.75**	**0.76**	1.11	0.89	1.13	1.12
	Bi	0.78	0.83	0.76	0.77	**0.77**	**0.80**	**0.75**	**0.77**	1.15	1.12	1.16	1.15
	M-T (0, 0.6)	**0.98**	**0.99**	**0.98**	**0.98**	**0.99**	**0.99**	**0.98**	**0.99**	**0.99**	**0.99**	**0.99**	**0.99**
	DBi(0.5)	0.99	1.00	0.99	0.99	**1.37**	**1.28**	**1.42**	**1.39**	1.27	1.21	1.31	1.29
	Cl	**0.99**	**0.99**	**0.99**	**0.99**	**0.98**	**0.98**	**0.98**	**0.98**	**1.00**	**1.00**	**1.00**	**1.00**
	M-T (0.3,0.4)	**1.02**	**1.02**	**1.02**	**1.02**	**1.03**	**1.03**	**1.04**	**1.03**	**1.01**	**1.01**	**1.01**	**1.01**
	Q-Hyst (0.5)	1.01	1.01	1.01	1.01	1.05	1.05	1.06	1.05	1.09	1.07	1.10	1.10
Kobe (1995-NS)	E-P	**0.79**	**0.45**	**0.72**	**0.83**	**0.72**	**0.36**	**0.64**	**0.81**	0.82	0.49	0.78	0.87
	Bi	0.95	0.92	0.91	0.98	0.96	0.89	0.87	1.00	1.00	0.97	0.96	1.03
	M-T (0, 0.6)	**0.98**	**0.98**	**0.98**	**1.00**	**0.93**	**0.92**	**0.91**	**0.96**	**0.98**	**0.97**	**0.97**	**0.99**
	DBi(0.5)	1.18	1.23	1.25	1.12	1.22	1.23	1.26	1.16	**1.47**	**1.54**	**1.63**	**1.35**
	Cl	**0.99**	**0.98**	**0.98**	**0.99**	**0.95**	**0.95**	**0.94**	**0.96**	**0.96**	**0.95**	**0.94**	**0.97**
	M-T (0.3,0.4)	**1.03**	**1.04**	**1.04**	**1.01**	**1.11**	**1.13**	**1.15**	**1.08**	**1.06**	**1.08**	**1.09**	**1.04**
	Q-Hyst (0.5)	1.11	1.16	1.18	1.05	1.18	1.23	1.26	1.12	1.25	1.31	1.36	1.18

For all three structures as shown in Figs. H-37 to H-39, the Q-Hyst (α=0.5) model may predict significantly larger structural damage indices than those of the three hysteresis model averages. This is earthquake type dependent. For the Park & Ang and Banon & Veneziano member damage indices, the maximum ratio of the structural damage index by the Q-Hyst (α=0.5) model to the average can be as high as 1.25. The ratio for the Roufaiel & Meyer and Cosenza et al. member damage indices can be up to 1.36, as shown in Table 8-4

8-4.2 Effect of Varying Different Member Damage Indices on the Overall Structural Damage Indices

It is found from Figs. H-37 to H-39 that for all three structures, the Park & Ang and Banon & Veneziano member damage indices predicted similar structural damage indices. This is independent of the hysteresis models and earthquakes types.

The averages of the structural damage indices predicted using the Park & Ang and Banon & Veneziano member damage indices were calculated and were compared to those predicted using each of the four member damage indices. The ratios of the structural damage indices for each of the four damage indices to these corresponding averages are presented in Table 8-5.

It is observed from Figs. H-37 to H-39 that when using the Elasto-Plastic hysteresis model, the structural damage indices predicted using the Roufaiel & Meyer and Cosenza et al. member damage indices are similar, but are significant larger than those for the Park & Ang and Banon & Veneziano member damage indices for the three structures when subjected to the El Centro (1977-NS) and Kobe (1995-NS) earthquakes, i.e. certain types of earthquakes.

It can be seen from Figs. H-37 to H-39 that for the other hysteresis models, except the Elasto-Plastic model, the Roufaiel & Meyer and the Cosenza et al. predict the greatest and the smallest structural damage indices of the four member damage indices. The Park & Ang and Banon & Veneziano member damage indices predict similar values. This is for all the three structures and all the four earthquakes.

Table 8-5 Ratios of structural damage indices for each of the four member damage indices to the averages of those for the Park & Ang and Banon & Veneziano member damage indices

		6S				12S				18S			
		Park	Roufaiel	Cosenza	Banon	Park	Roufaiel	Cosenza	Banon	Park	Roufaiel	Cosenza	Banon
Bucharest (1977-NS)	E-P	1.04	0.88	0.87	0.96	1.04	0.85	0.85	0.96	1.04	0.90	0.90	0.96
	Bi	1.04	1.19	0.89	0.96	1.04	**1.47**	0.88	0.96	1.04	1.29	0.91	0.96
	M-T (0, 0.6)	1.05	1.16	0.87	0.95	1.04	**1.48**	0.89	0.96	1.04	1.30	0.91	0.96
	DBi(0.5)	1.05	1.15	0.87	0.95	1.04	**1.49**	0.90	0.96	1.04	1.28	0.93	0.96
	CI	1.04	1.16	0.87	0.96	1.04	**1.48**	0.89	0.96	1.04	1.30	0.91	0.96
	M-T (0.3,0.4)	1.05	1.14	0.87	0.95	1.04	**1.48**	0.89	0.96	1.04	1.29	0.92	0.96
	Q-Hyst (0.5)	1.05	1.14	0.89	0.95	1.04	**1.48**	0.89	0.96	1.04	1.28	0.93	0.96
El Centro (1940-NS)	E-P	1.03	0.79	0.79	0.97	0.95	0.57	0.57	1.05	1.00	0.69	0.69	1.00
	Bi	1.04	1.17	0.82	0.96	0.97	1.18	**0.63**	1.03	0.99	1.12	**0.70**	1.01
	M-T (0, 0.6)	1.04	1.13	0.79	0.96	0.97	1.19	**0.64**	1.03	0.97	1.05	**0.64**	1.03
	DBi(0.5)	1.04	1.20	0.90	0.96	1.01	1.31	**0.73**	0.99	1.02	1.20	**0.78**	0.98
	CI	1.04	1.16	0.82	0.96	0.98	1.20	**0.65**	1.02	0.98	1.08	**0.67**	1.02
	M-T (0.3,0.4)	1.04	1.16	0.83	0.96	0.99	1.23	**0.67**	1.01	1.00	1.12	**0.70**	1.00
	Q-Hyst (0.5)	1.04	1.17	0.85	0.96	1.01	1.30	**0.72**	0.99	1.02	1.18	**0.75**	0.98
Northridge (Sylmar-949NW)	E-P	1.03	0.96	0.95	0.97	1.04	0.92	0.92	0.96	1.03	0.96	0.96	0.97
	Bi	1.04	1.17	0.95	0.96	1.04	**1.42**	0.91	0.96	1.03	1.17	0.96	0.97
	M-T (0, 0.6)	1.03	1.11	0.96	0.97	1.04	**1.36**	0.93	0.96	1.03	1.21	0.94	0.97
	DBi(0.5)	1.03	1.11	0.96	0.97	1.03	**1.26**	0.96	0.97	1.03	1.14	0.97	0.97
	CI	1.03	1.10	0.96	0.97	1.04	**1.36**	0.93	0.96	1.03	1.21	0.95	0.97
	M-T (0.3,0.4)	1.03	1.10	0.96	0.97	1.04	**1.35**	0.94	0.96	1.03	1.20	0.95	0.97
	Q-Hyst (0.5)	1.03	1.10	0.96	0.97	1.04	**1.35**	0.94	0.96	1.03	1.18	0.96	0.97
Kobe (1995-NS)	E-P	0.96	0.61	0.61	1.04	0.92	0.58	0.58	1.08	0.96	0.63	0.62	1.04
	Bi	0.97	1.05	0.65	1.03	0.96	1.12	0.61	1.04	0.97	1.02	0.64	1.03
	M-T (0, 0.6)	0.98	1.09	0.68	1.02	0.97	1.20	0.66	1.03	0.98	1.06	0.66	1.02
	DBi(0.5)	1.01	1.17	0.75	0.99	1.01	1.28	0.72	0.99	1.02	1.17	0.78	0.98
	CI	0.98	1.09	0.68	1.02	0.98	1.23	0.67	1.02	0.98	1.05	0.66	1.02
	M-T (0.3,0.4)	0.99	1.12	0.70	1.01	1.00	1.27	0.72	1.00	0.99	1.10	0.70	1.01
	Q-Hyst (0.5)	1.01	1.18	0.75	0.99	1.01	1.32	0.75	0.99	1.01	1.16	0.76	0.99

For the 12 storey structure under the Bucharest (1977-NS) and Northridge (Sylmar-949NW) earthquakes as shown in Figs. H-38(a), (c), the Roufaiel & Meyer member damage index predicts significantly larger structural damage indices than those for the Park & Ang and Banon & Veneziano member damage indices. The ratios of structural damage indices for the Roufaiel & Meyer to the averages of the Park & Ang and Banon & Veneziano member damage indices range approximately from 1.30 to 1.50, as shown in Table 8-5.

It is found from Figs. H-38(b), 39(b) that for the 12 and 18 storey structures subjected to the El Centro (1940-NS) earthquake, the Cosenza et al. member damage index predicts significantly smaller structural damage indices relative to the averages of those for the Park & Ang and Banon & Veneziano member damage indices. The structural damage index for this member index is of the order of 64% of the averages of the Park & Ang and Banon & Veneziano member damage indices, as shown in Table 8-5.

8-5 The Relationship between Structural Damage Index and the Structural Displacement Ductility

Figs. H-40 to H-43 illustrate the relationship between the structural damage indices and the overall structural displacement ductilities using each of the four member damage indices. It is found from these figures that there is a linear relationship between the structural damage indices and the structural displacement ductilities for each of the seven hysteresis models. This relationship may alter for long durations of strong shaking due to larger number of cycles of inelastic behaviour giving larger accumulated energy dissipation to the structural damage index.

The ratios of the trend lines are approximately 0.1 for all the seven hysteresis models except for the Elasto-Plastic hysteresis model where the slope is less than 0.1. This is applicable for all four member damage indices.

8-6 Discussion of the Design Structural Displacement Ductility

When the design structural displacement ductility of 5.0 is researched, the structural damage index is 0.50 for Park & Ang damage model, according to the relationship between the structural ductility and the structural damage index as discussed in section 8-5 for the three structures designed using structural displacement ductility 5.0. However, due to the design of the 12- and 18-storey structures are controlled by the minimum acceleration of 0.03 as shown in Chapter 2, for which the equivalent design structural ductilities are 4.75 and 3.57 for the 12- and 18-storey structure respectively rather than the ductility of 5.0. The equivalent structural displacement ductility, as an example, for the 12-storey structure is determined as $\mu_{equ} = 5.0 * \frac{0.0214}{0.03} = 3.57$ where 0.0214 is the spectral acceleration coefficient for structural displacement ductility 5.0, as shown in Chapter 2. Hence the corresponding design structural displacement ductilities are 4.75 and 3.57 for the 12- and 18-storey structure respectively to the structural damage index 0.5 when subjected to the standard level earthquakes, as shown in Table 8-7.

In order to study the seismic structural damage in the three structures designed using other structural displacement ductility rather than 5.0 when subjected to the standard level earthquakes, the member strength of the three structures designed using structural displacement ductility 5.0 is increased by 25% to obtain structures designed using design structural displacement ductilities of 4.0, 3.8 and 2.58 for the 6-, 12- and 18-storey structure respectively. The strength is decreased by 17% to have the three structures designed using structural displacement ductilities of 6.0, 5.72 and 4.30 for the 6-, 12- and 18-storey structure respectively. The structural damage indices of Park & Ang for all these modified structures are carried out under the four scaled earthquakes and shown in Table 8-6.

Table 8-6 Structural damage index (Park & Ang) of the three structures of increased strength by 25% and of decreased strength by 17%

		Structural displacement ductility	$DI_{struc.}$				
			Bucharest (1977-NS)	El Centro (1940-NS)	Northridge (Sylmar-949NW)	Kobe (1995-NS)	Max.
25%	6S	4.0	0.43	0.30	**0.47**	0.15	**0.47**
	12S	3.8	0.20	0.15	**0.37**	0.21	**0.37**
	18S	2.85	0.27	0.15	**0.42**	0.20	**0.42**
17%	6S	6.0	0.58	0.52	**0.77**	0.23	**0.77**
	12S	5.72	0.36	0.20	**0.74**	0.30	**0.74**
	18S	4.30	0.41	0.20	**0.67**	0.29	**0.67**

According to the ranges of ratios of the member curvature ductility to the structural displacement ductility are 4.12 to 5.60, 4.44 to 7.38 and 4.02 to 5.76 for the 6-, 12- and 18-storey structures respectively as discussed in section 7-5.3 in Chapter 7. Table 8-7 shows the maximum structural displacement ductilities among those for the four standard design level earthquakes, and their corresponding structural damage indices and member curvature ductility demand.

Table 8-7 Design structural displacement ductility, structural damage index and member curvature ductility demand under standard level earthquakes

	6S			12S			18S		
μ_{design}	4.0	5.0	**6.0**	3.80	4.75	**5.72**	2.85	3.57	**4.30**
$DI_{struc.}$	0.47	0.50	**0.77**	0.37	0.50	**0.74**	0.42	0.50	**0.67**
Mem. Curv. demand	16~22	21~28	**25~34**	17~28	21~35	**25~42**	11~16	14~21	**17~25**

Fig. 8-1 shows the structural damage indices versus the design structural displacement ductilities when subjected to the standard level earthquakes.

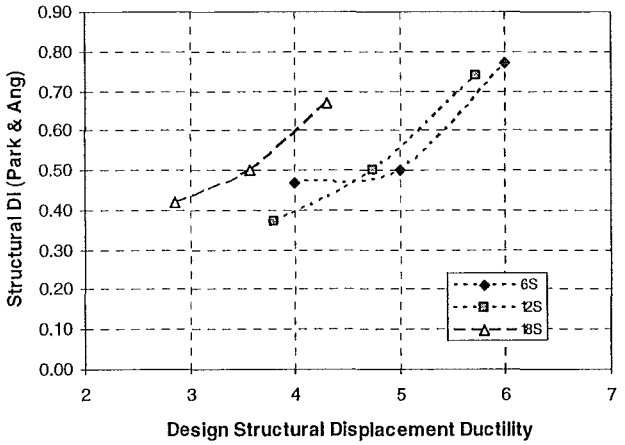

Fig. 8-1 The structural damage indices versus the design structural displacement ductilities for the three structures under standard level earthquakes

When talking about the earthquake returning period of 450 years for structural design [NZS4203 1992], the design structural displacement ductilities could not exceed values for which the corresponding structural damage indices are 0.40 indicating the repairable damage limit, according to Park & Ang [Park 1985]. Otherwise structural damage beyond economic repair will be expected under the design standard level earthquakes. The choice of design structural displacement ductility 5.0 and 6.0 for which the corresponding structural damage indices are larger than 0.5, as shown in Fig. 8-1, will possibly lead to greater damage than that implied by the design standard.

The recommended design structural displacement ductilities are 4.0 and 3.0 for the 12- and 18-storey structure respectively, for which the corresponding structural damage indices are approximately 4.0 under the design standard level earthquakes. For the 6-storey structures, the recommended design displacement ductility should be smaller than 4.0.

8-7 Recommended Hysteresis Model and Member Damage Index for Damage Assessment

8-7.1 Member Damage Index

The Park & Ang structural damage index may be used in evaluating overall structural damage when the structural displacement ductility is around the design structural ductility.

Because the damage indices for the members, storeys and structures for the Park & Ang damage model, and the interpretation of the overall structural damage indices for the degree of damage is available and because it is the only damage index calibrated from laboratory tests [Park 1985], the Park & Ang damage model is to be recommended for computing the damage indices until experimentally verified interpretations of the other structural damage indices are available.

8-7.2 Recommended Hysteresis Model

Table 8-8 shows the unloading and reloading stiffness degrading parameters for the Clough, Q-Hyst (α=0.5) and the two Modified Takeda models used in this study. The Clough and Q-Hyst (α=0.5) models are the variations of the Modified Takeda model as is discussed in Chapter 4.

Table 8-8 The unloading and reloading stiffness degrading parameters for the four hysteresis models

	α	β
Clough	0.0	0.0
Modified Takeda	0.3	0.4
Modified Takeda	0.0	0.6
Q-Hyst	0.5	0.0

From the earlier studies, the Clough, Modified Takeda (α=0.3, β=0.4) and Modified Takeda (α=0.0, β=0.6) predict similar damage indices for the storeys and structures. This implies that varying the unloading stiffness degradation parameters α from 0.0 to 0.3 or the reloading stiffness degradation parameters β from 0.0 to 0.6 does not

significantly affect the predicted storey and structural damage indices for the Modified Takeda hysteresis model.

When compared to the other three hysteresis models, the Q-Hyst (α=0.5) hysteresis model predicts approximately 25% larger overall structural damage indices for the Park & Ang and Banon & Veneziano damage indices, and 40% larger overall structural damage indices for the Roufaiel & Meyer and Cosenza et al models, as shown in Table 8-4. This shows that the unloading stiffness degradation parameters α larger than 0.30 leads to larger overall structural damage indices. In other words, the overall structural damage index is more sensitive to the unloading stiffness degradation parameter α than the reloading stiffness degradation parameter β.

Considering that the Modified Takeda hysteresis model is able to use different unloading and reloading stiffness degrading parameters, and better represents realistically the hysteretic behaviour of reinforced concrete members, this hysteresis model is recommended for use in damage evaluations. The main problem is to identify the unloading and reloading stiffness degradation parameters α and β, especially the unloading stiffness degradation parameter α due to its greater sensitivity in the overall structural damage prediction.

The unloading and reloading stiffness degradation parameters α and β can be identified by comparing with experimental hysteresis loops for the same or similar members to those in the structures under evaluation as shown in section 9-2 in chapter 9.

8-8 Summary and Conclusions

In this chapter, the effect of varying hysteresis models and member damage indices on the predicted damage indices for the storeys and structures is studied and is identified. The sensitivity of the unloading and reloading stiffness degradation parameters α and β on the predicted overall structural damage indices is examined for the Modified Takeda model.

From these studies, the following conclusions are drawn:

(1) The three hysteresis models, i.e. the Modified Takeda (α=0, β=0.6), Clough and Modified Takeda (α=0.3, β=0.4) hysteresis models predict very similar damage indices for both the storeys and structures. This is independent of the fundamental periods of free vibration of the structures, the earthquake type and the different member damage indices.

Compared with these three hysteresis models, the Elasto-Plastic and Bilinear models predict significantly smaller damage indices for the storeys and structures. However, the Degrading Bilinear (α=0.5) and Q-Hyst (α=0.5) models predict significantly larger damage indices. This result is earthquake type dependent for a given structure.

(2) For using each of the seven hysteresis models except the Elasto-Plastic model, the Park & Any and Banon & Veneziano member damage indices predict similar storey and structural damage indices. This is for all three structures and all four earthquake excitations.

When compared with the Park & Ang and Banon & Veneziano member damage indices, the Roufaiel & Meyer and the Cosenza et al. member damage indices predict significantly larger and smaller damage indices respectively for the storeys and structures depending on the earthquake type.

(3) The Modified Takeda hysteresis model and the Park & Ang damage model are recommended when carrying out inelastic time history analysis for computing damage indices for members, storeys and structures.

(4) Varying the unloading stiffness degradation parameters α from 0.0 to 0.3 and the reloading stiffness degradation parameters β from 0.0 to 0.6 does not significantly affect the predicted storey and structural damage indices for the Modified Takeda hysteresis model. The larger the unloading stiffness degradation parameters α ($0.3<\alpha<0.5$), the larger the predicted overall structural damage indices. This is earthquake type dependent. For the Park &

Ang and Banon & Veneziano member damage indices, the maximum variation in the structural damage index by increasing the unloading stiffness degradation parameters α ($0.3<\alpha<0.5$) can be up to 1.25. The ratio for the Roufaiel & Meyer and Cosenza et al. member damage indices can be up to 1.40.

(5) If economic repairable damage in a structure was expected under design standard level earthquakes, any structural displacement ductility that is larger than 5.0, would not be recommended for use in capacity design of a structure.

Chapter 9
Recommended Procedure for Seismic Damage Assessment and Examples Illustrating the Use of the Procedure

9-1 Introductions

Based on the results mentioned in the preceding chapters, a procedure for seismic damage assessment is recommended for a rational damage analysis for reinforced concrete ductile framed structures.

9-2 Recommended Procedure for Seismic Damage Assessment:

A procedure for seismic damage assessment is recommended as follows:

Step 1: For pre 1970's structures where bond failure and shear crack related pinching of the hysteresis loops is evident. The hysteresis model should be chosen to represent accurately the behaviour of typical reinforced concrete members of the time such as that done by Liu [Liu 2001], and it is also noted strength degradation of the loops may need to be modelled.

For post 1970's structures, if the hysteretic loops from laboratory tests for the members or similar members of structures to be analysed are unavailable, the Modified Takeda (α=0.5, β=0.0), i.e. the Q-Hyst (α=0.5) hysteresis model may be used for the damage evaluation.

For post 1970's structure where typical hysteresis loops are available it is suggested that the Modified Takeda model be used. The equivalent unloading and reloading stiffness degradation parameters α and β should be determined for the experimental hysteretic loops of the similar members, as shown in Eqs. (9-1) and (9-2).

$$\alpha = \frac{\ln \frac{K_u}{K_0}}{\ln \frac{d_y}{d_m}} \tag{9-1}$$

$$\beta = \frac{\beta d_p}{d_p} \tag{9-2}$$

where K_o and K_u are the initial and degraded unloading stiffness at maximum displacement d_m respectively. d_y is the yield displacement. $d_p = d_m - d_y$ and βd_p refer to Fig. 9-1.

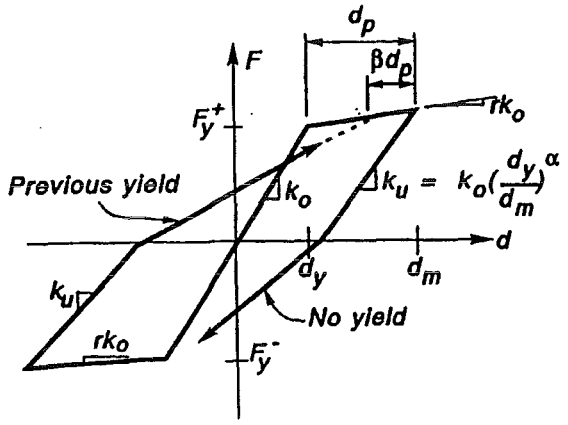

Fig. 9-1 Modified TAKEDA hysteresis rule [Otani 1974]

Step 3: Conduct the damage analyses using appropriate hysteresis model and the Park & Ang damage model for the ductile reinforced concrete framed structures subjected to the chosen earthquake excitations.

9-3 Examples of Damage Evaluation Using the Jury 6 and 12 Storey Framed Structures and the El Centro (1940-NS) Earthquake Excitation:

9-3.1 Structural Models, Mathematical Models

The analytic structural models for the examples of damage evaluation are a six-storey and a twelve-storey framed structures of reinforced concrete of two-bay designed by Jury [Jury 1977]. The dimensions and member sizes for these two frames are given in Figs. 9-2 and 9-3 respectively and for the full data are given in Appendix I and Appendix J respectively.

The lumped mass model is used for the mass modelling. The tangent stiffness Rayleigh damping is used for the damping model. The Giberson one component model is used for the member modelling. 5% critical damping ratios is assigned to the first and sixth modes

and to the first and tenth modes of free vibration for the damping model for the 6 and 12 storey Jury frames. The earthquake record of the El Centro 1940, North-South accelerogram shown in Fig. 5-3 and discussed in Chapter 5 is used for the earthquake excitation.

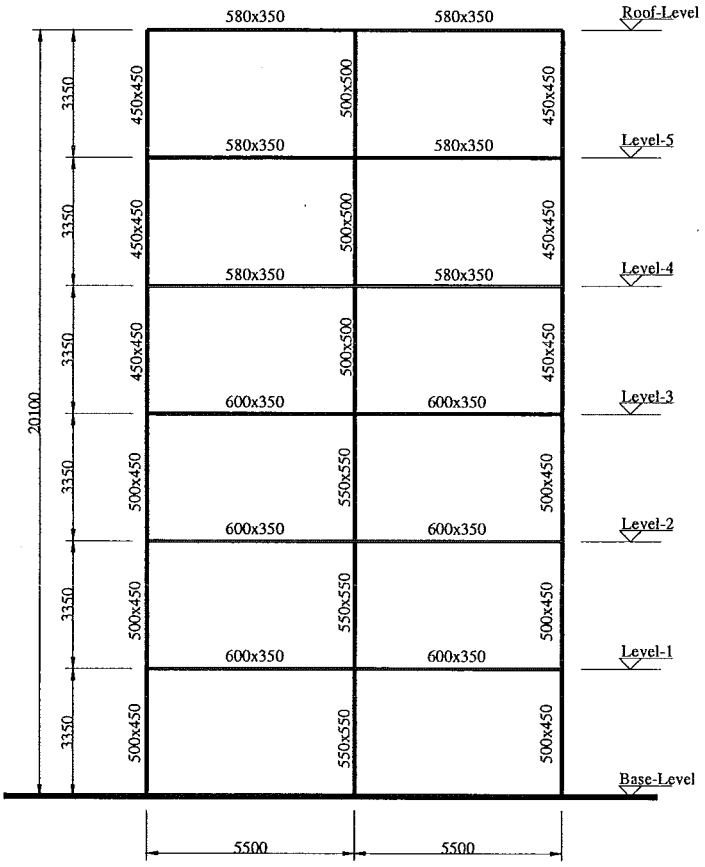

Fig. 9-2 Jury two-bay six-storey ductile-framed structure of reinforced concrete
(Note: all units are in millimetres)

The equation of motion is solved using the Newmark Constant Average Acceleration Method ($\beta = 1/4$) [Clough 1993]. This method has the advantage of being unconditionally stable and has no amplitude error.

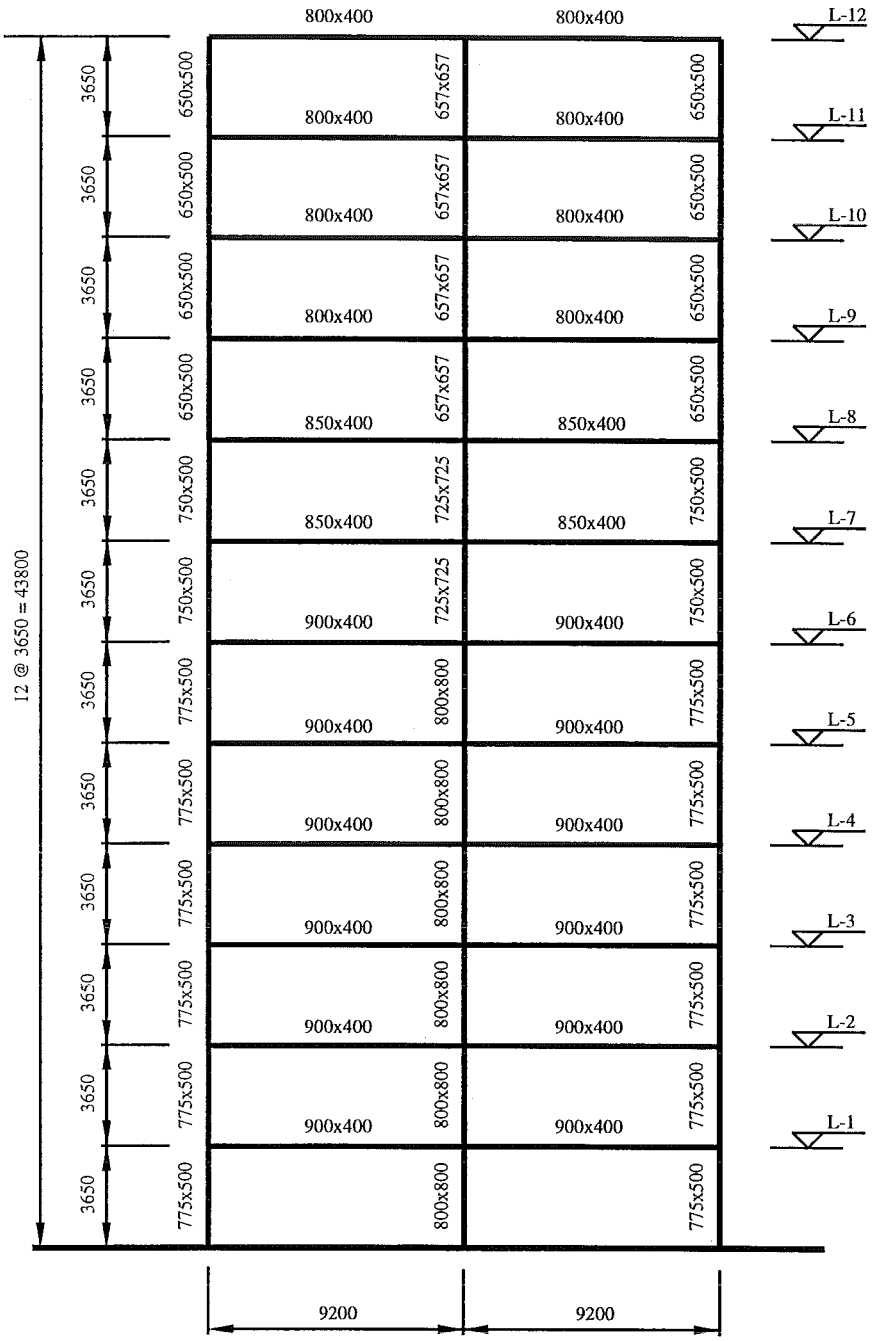

Fig. 9-3 Jury two-bay twelve-storey ductile-framed structure of reinforced concrete
(Note: all units are in millimetres)

9-3.2 Damage Evaluations for the Jury 6 Storey Frame

Carry out earthquake scaling according to the procedure presented in section 5-13 of Chapter 5:

Step 1:

The structural periods and effective masses for the first two modes are computed from a modal response analyses listed in Table 9-1. The mass for the two modes is 92% of the total and is larger than 90% required by NZS4203: 1992.

Table 9-1 Structural periods and effective mass of Jury 6 storey structure

	Mode-1	Mode-2	Note
Period (Seconds)	0.987	0.332	
Effective Mass (kN)	232.9	340.6	92% > 90%

Step 2:

The fundamental period of 0.987 seconds is less than 1.35 seconds, hence the base shear scaling method is applied for calculating the scaling factor.

Design base shear:

The base shear, which the structure is required to resist by the standard [NZS4203 1992], can be determined using structural ductility 1.0 and assuming that the structure is situated on an intermediate soil site in Christchurch:

$$C_{a(T)}^{design} = C_{(T,\mu=1.0)} * Sp * R * Z * Lu$$
$$= C_{(T=0.987,\mu=1.0)} * 0.8$$
$$= 0.5065 * 0.8 = 0.4052$$

where $C_{a(T)}^{design}$ design spectral acceleration coefficient.

$C_{(T,\mu=1.0)}$ (=0.5065) basic seismic hazard acceleration coefficient for intermediate soil site and μ=1.0

Sp (=1.0) structure performance factor for elastic time history analysis [C4.6.2.7, C4.6.2.8 and C4.6.2.9 NZS4203: 1992]

R =1.0 risk factor for building category IV [C4.6.2.4 NZS4203: 1992]

Z =0.8, zone factor for Christchurch

Lu =1.0 limit state factor

The seismic weight of the structure is 2908kN [Jury 1978]. Hence the design base shear is 0.4052*2908=1178.3kN.

Elastic base shear to the initial earthquake obtained by running an elastic dynamic analysis: 1324.5kN.

Earthquake scaling factor = (design base shear)/(elastic base shear)

=1178.3/1324.5= 0.89

Storey and structural damage analyses:

Using the Modified Takeda (α=0.5, β=0.0) hysteresis model and Park & Ang damage model, the inelastic dynamic step-by-step integration time-history is carried out.

The storey damage index distribution is shown in Fig. 9-4. It is can be seen from this figure that the maximum storey damage occurs in storeys 5, and all of the storey damage indices are small.

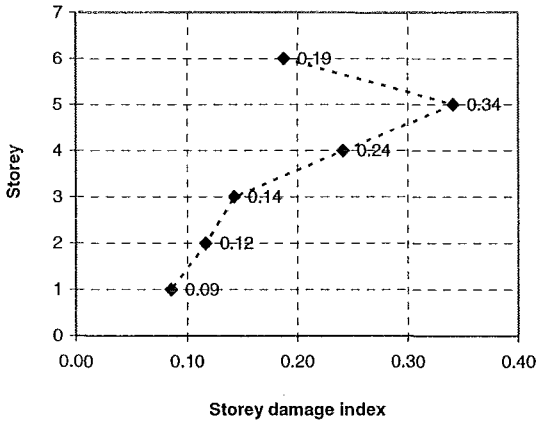

Fig. 9-4 Storey damage index distribution of Jury 6-storey frame

The overall structural damage index is 0.21 that is much less than 0.4, showing that the structure, as designed, will have a low level of damage and does not require any remedial action.

9-3.3 Damage Evaluations for the Jury 12 Storey Frame

Carry out earthquake scaling according to the procedure presented in section 5-13 of Chapter 5:

Step 1:

The structural periods and effective masses for the first three modes are computed from a modal response analyses listed in Table 9-2. The mass for the three modes is 94% of the total and is larger than 90% required by NZS4203: 1992.

Table 9-2 Structural periods and effective mass of Jury 12 storey structure

	Mode-1	Mode-2	Mode-3	Note
Period (Seconds)	1.94	0.68	0.38	
Effective Mass (kN)	1531	230	74	94% > 90%

Step 2:

The fundamental period of 1.94 seconds is larger than 1.35 seconds, hence go to Step 3.

Step 3:

Calculate the design spectral displacements for the first three modes using the design displacement spectrum as shown in Table 5-2 assuming a zone factor 0.8 for Christchurch.

Table 9-3 Design spectral displacements for the first three modes of the Jury 12 storey structure

	Mode-1	Mode-2	Mode-3
Period (Seconds)	1.94	0.68	0.38
Design Spectral Displacement (10^{-3}m)	193	64	33

Step 4:

Compute the design spectra SRSS inter-storey drift using the design spectral displacements and mode shapes.

Table 9-4 The first three mode shapes and lateral displacement at each level of the Jury 12 storey structure

	Mode Shapes			Lateral Displacement (m)	Interstorey Drift (m)
	mode-1	mode-2	mode-3		
12	1.000	1.000	-0.986	0.206	0.013
11	0.963	0.784	-0.449	0.193	0.016
10	0.906	0.449	0.270	0.177	0.015
9	0.832	0.045	0.846	0.163	0.014
8	0.745	-0.339	1.000	0.149	0.014
7	0.656	-0.627	0.722	0.135	0.014
6	0.562	-0.813	0.193	0.120	0.013
5	0.469	-0.881	-0.356	0.107	0.014
4	0.372	-0.842	-0.778	0.093	0.018
3	0.270	-0.702	-0.936	0.075	0.024
2	0.168	-0.480	-0.780	0.052	**0.029**
1	0.070	-0.212	-0.381	0.023	0.023

The maximum design inter-storey drift is 0.029m.

Step 5:

Design base shear:

The base shear, which the structure is required to resist by the code [NZS4203 1992], can be determined using structural ductility 1.0 and assuming that the structure is situated on an intermediate soil site in Christchurch:

$$C_{a(T)}^{design} = C_{(T,\mu=1.0)} * Sp * R * Z * Lu$$

$$= C_{(T=1.94,\mu=1.0)} * 0.8$$

$$= 0.26 * 0.8 = 0.21$$

where $C_{a(T)}^{design}$ design spectral acceleration coefficient.

$C_{(T,\mu=1.0)}$ (=0.5065) basic seismic hazard acceleration coefficient for intermediate soil site and μ=1.0

Sp (=1.0) structure performance factor for elastic time history analysis [C4.6.2.7, C4.6.2.8 and C4.6.2.9 NZS4203: 1992]

R =1.0 risk factor for building category IV [C4.6.2.4 NZS4203: 1992]

Z =0.8, zone factor for Christchurch

Lu =1.0 limit state factor

The seismic weight of the structure is 18312kN [Jury 1978]. Hence the design base shear is 0.21*18312kN=3845.52kN.

Step 6:

The maximum base shear and maximum inter-storey drift of the 12 storey structure for the initial El Centro (1940-NS) is 4253.4kN and 0.035m respectively.

Step 7:

Determine the scaling factor *SF* by the following equation:

$$SF = max\left\{\frac{ID_{SRSS}^{design\ spectra}}{ID_{SF=1.0}},\ \frac{V^{design}}{V_{SF=1.0}}\right\} = max\left\{\frac{0.029}{0.035},\ \frac{3845.52}{4253.4}\right\}$$

$$= max\left\{\frac{0.029}{0.035},\ \frac{3845.52}{4253.4}\right\} = max\{0.83,\ 0.90\} = 0.90$$

where $ID_{SRSS}^{design\ spectra}$: SRSS design inter-storey drift using the spectral displacements.

V^{design} : design base shear determined by using equivalent static method.

$ID_{SF=1.0}$: the maximum inter-storey drift for unscaled earthquake excitation.

$V_{SF=1.0}$: the maximum base shear from the unscaled earthquake excitation.

Storey and structural damage analyses:

Using the Modified Takeda (α=0.5, β=0.0) hysteresis model and Park & Ang damage model, the inelastic dynamic step-by-step integration time-history is carried out.

The storey damage index distribution is shown in Fig. 9-5. It is can be seen from this figure that the maximum storey damage occurs in storey 11, and all of the storey damage indices are small.

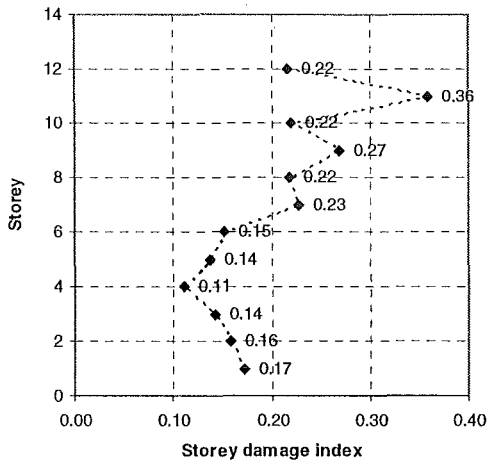

Fig. 9-5 Storey damage index distribution of Jury 12-storey frame

The overall structural damage index is 0.20, which is much less than 0.4, showing that the structure, as designed, will have a low level of damage and therefore does not require any remedial action.

9-4 Summary and Conclusions:

In this chapter, a procedure for storey and structural damage evaluation of reinforced concrete ductile-framed structure is outlined. This procedure is applied to two framed structures of 6 and 12 storeys to demonstrate how it may be applied in practice.

Chapter 10
Summary, Conclusions, Contributions and Recommendations for Future Research

10-1 Summary

The member curvature ductility, inter-storey displacement ductility and structural displacement ductility have been used as damage measures for the members, storeys and overall structures respectively in most of the current seismic codes [IAEE 1996] for the last twenty-five years. However, many more comprehensive damage models have been developed for reinforced concrete structures, some of which are able to take the accumulated damage and dissipated energy into account in addition to the maximum displacement. The damage in the members, storeys and overall structures are usually quantified by the corresponding damage indices. These damage indices are regarded as being more suitable for the damage evaluations rather than the corresponding ductilities [Park 1985, Carr 1993 and Satyarno 2000].

This research has set out to find a rational procedure for carrying out structural damage evaluations using structural damage indices for ductile framed structures of reinforced concrete designed to the current New Zealand Standards [NZS4203 1992, NZS3101 1995] when subjected to code level earthquakes at the ultimate limit state. To this purpose, three main aspects, i.e. the earthquake scaling, the relationship between the member curvature ductility and structural displacement ductility, and the effect of varying hysteresis models and member damage indices on the structural damage index were studied by carrying out elastic and inelastic time-history analyses employing three fully ductile structures, four different earthquakes, seven different hysteresis rules and four different member damage indices.

The three reinforced concrete ductile framed structures of 6, 12 and 18 storeys used for the structural models were designed to the current New Zealand seismic standards and structural design requirements [NZS4203 1992, NZS3101 1995] with an assumed

structural ductility of 5.0. The four different earthquake excitations used were the Bucharest (1977-NS), El Centro (1940-NS), Northridge (Sylmar-949NW) and Kobe (1995-NS) earthquake records for earthquake input motions. The seven different hysteresis models used were the Elasto-Plastic, Bilinear, Modified Takeda (α=0.0, β=0.6), Degrading Bilinear (α=0.5), Clough, Modified Takeda (α=0.3, β=0.4) and Q-Hyst (α=0.5) [Carr 1998] for modelling the member inelastic hysteretic responses. The four member damage indices were the Park & Ang, Roufaiel & Meyer, Cosenza et al and Banon & Veneziano damage indices for the member damage measures [Park 1985, Roufaiel 1987, Cosenza 1993 and Banon 1982].

In order to have code required design level earthquakes at the ultimate limit state, six different scaling methods were used to scale the four different earthquakes for the three ductile reinforced concrete framed structures. By comparing the maximum response demand (maximum base shears, maximum inter-storey drifts and 5% damped spectra) with the corresponding responses at design level for the four earthquakes for each of the six scaling methods, a general scaling method has been obtained.

To check whether the ultimate member curvature ductility capacity is greater than the required member curvature ductilities for the structures under the design-level earthquake excitations, the relationships between the member curvature ductilities and the structural displacement ductility were studied.

The effect of varying the hysteresis models and member damage indices on the computed damage indices for storeys and structures were studied.

As a preliminary to the studies indicated for the three main aspects, Chapters 2, 3 and 4 discuss the mathematical modelling (including the mass model, the member stiffness model and the damping model for the mass, stiffness and damping matrices) and analysis options used in this project. The seismic damage indices for members, storeys and entire structures of reinforced concrete are reviewed in Chapter 6.

10-2 Conclusions:

From the above studies, the following main conclusions may be drawn:

10-2.1 Earthquake Scaling

(1) The application of any scaling method attempting to match the scaled record to the design acceleration spectra may lead to large variations between the maximum base shear and the design base shear. The design-acceleration-spectra scaling method and the frequency scaling method are not recommended when the design base shear is required to be matched as is implied in the current New Zealand loading standard [NSZ4203 1992].

(2) The base shear scaling method is reliable for earthquake scaling when the design base shear is required to be matched.

(3) The inter-storey drift scaling method is reliable for earthquake scaling when the design inter-storey drift is required to be matched.

(4) The base shear scaling method is recommended to be used for earthquake scaling for short period structures, such as the 6 storey structure used in this study.

(5) A general earthquake scaling procedure has been proposed, for which both the maximum base shear and the maximum inter-storey drift from the scaled earthquakes are as close as possible to, and are not less than, the corresponding design values.

10-2.2 Relationship between the Member Curvature Ductilities and the Structural Displacement Ductility

(6) The observed ranges of the ratios between the member curvature ductility and the structural displacement ductility were 4.12 to 5.60, and 4.02 to 5.76 for short and long period structures respectively, such as the 6-, and 18-storey structures respectively. Those ratios for medium period structure range from 4.44 to 7.38, such as for the 12-storey structure.

10-2.3 The Effect of Varying the Hysteresis Models and Member Damage Indices on the Computed Damage Indices for Storeys and Structures

(7) Three hysteresis models, i.e. the Modified Takeda (α=0, β=0.6), Clough and Modified Takeda (α=0.3, β=0.4) hysteresis models predict similar damage indices for the storeys and structures. This is independent of the fundamental periods of free vibration of the structures, the earthquake type and the member damage indices.

Compared to these three hysteresis models, the Elasto-Plastic and Bilinear models predict significantly smaller damage indices for the storeys and structures. However, the Degrading Bilinear (α=0.5) and Q-Hyst (α=0.5) models predict significantly larger values. This is earthquake type dependent for a given structure.

(8) When using any of the seven hysteresis models except the Elasto-Plastic model, the Park & Ang and Banon & Veneziano member damage indices predict similar storey and structural damage indices. This is for all three structures and all four earthquake excitations.

When compared with the Park & Ang and Banon & Veneziano member damage indices, the Roufaiel & Meyer and the Cosenza et al member damage indices are significantly larger and smaller respectively for both the storeys and the structures. This result depends on the earthquake.

(9) Varying the unloading stiffness degradation parameters α from 0.0 to 0.3 or the reloading stiffness degradation parameters β from 0.0 to 0.6 does not significantly affect the predicted storey and structural damage indices for the Modified Takeda hysteresis model.

The larger the unloading stiffness degradation parameters α ($0.3<\alpha<0.5$), the larger the predicted overall structural damage indices. This is dependent of earthquake characteristics. For the Park & Ang and Banon & Veneziano member damage indices, the maximum variation in the structural damage index by

increasing the unloading stiffness degradation parameters α ($0.3<\alpha<0.5$) can be up to 1.25. The ratio for the Roufaiel & Meyer and Cosenza et al. member damage indices can be up to 1.40. Increasing the unloading stiffness degradation parameters α ($0.3<\alpha<0.5$) may cause significant increasing in the structural damage indices. Hence it should be much more careful to determine the unloading stiffness parameter α ($0.3<\alpha<0.5$) than to determine the reloading stiffness degradation parameter β.

(10) The Modified Takeda hysteresis model and the Park & Ang damage model are the recommended procedures when carrying out an inelastic time history analysis for a damage assessment. A rational procedure for the damage evaluation of reinforced concrete ductile-framed structure is recommended in Chapter 8.

10-2.4 The Design Structural Displacement Ductility

(11) If economic repairable damage in a structure was expected under design standard level earthquakes, any structural displacement ductility, which is larger than 4.0, are not recommended for use in capacity design.

10-3 Main Contributions Obtained from This Research:

The first and main contribution is the seismic damage analysis using damage indices, which have not been used for practical damage evaluation in an overall structure, rather than using just the structural displacement ductility. A rational procedure of damage evaluation for existing or newly designed structures using damage indices which are able to take the accumulated damage and dissipated energy into account in addition to the maximum displacement ductility, is developed for reinforced concrete ductile framed structures, especially for those designed to the current New Zealand standards [NSZ4203 1992, NZS3101 1995].

The second contribution is the earthquake scaling. It has been found that the scaling method attempting to match the scaled record to the design acceleration spectra as set out in the current New Zealand loading code [NSZ4203 1992] is not reliable when the

design base shear is to be matched, as is implied in the code. The frequency scaling method, widely used by consulting engineers in New Zealand, is also not reliable for scaling earthquakes to match the design base shear. However, the base shear scaling method, as discussed in Chapter 5, is able to exactly match the design base shear. This method can be used when the design base shear is the quantity required to be matched.

Furthermore, a general earthquake scaling procedure, which is more rational than the base shear scaling method, is proposed, in which both the maximum base shear and maximum inter-storey drift from the scaled earthquake is as close as possible to, and are not less, than the corresponding design values. This procedure is able to avoid the possible case in the base shear scaling method where all maximum base shears for all scaled earthquakes match the design base shear but all maximum inter-storey drifts for the scaled earthquakes are very much smaller than the design inter-storey drift.

The last contribution is that if economic repairable damage is required as what implied by New Zealand Standard [4203 1992] under design standard level earthquakes, the design structural displacement ductility is recommended as not to exceed 4.0, which is much smaller than 5.0 or 6.0 presented in the standard and used by practical consulting engineers.

10-4 Recommendations for Future Research:

As in any other research project, the results are based on the assumptions and structural modellings used for the computations. The following topics in both analytical modelling and in experimental evaluation should be considered for future study:

10-4.1 Topics in Analytical Modelling

(1) The interior frames were used to resist lateral earthquake loads. This kind of earthquake resistant structural system becomes less and less in New Zealand. The perimeter frames of same beam sizes, which are used to resist seismic loads, may

be used as structural models in future study to see the probable different results between the two different systems.

(2) The contribution of joint flexibility and bar slip to the member flexibility, which was not considered in this study due to that no models were available, may significantly affect the results and should be incorporated in future study once those models are available. The bar slippage and shear cracking related pinching phenomenon should be incorporated in the modelling.

(3) The plastic hinge length used in this study is taken as 70% of the member depth. This was used for the input data in the Jury frames in earlier research in the Department of Civil Engineering, University of Canterbury as well as in many other research analyses. The sensitivity to varying the plastic hinge length on the computed damage indices for both the storeys and the structure should be identified.

(4) The inelastic dynamic responses, i.e. the secant stiffnesses, the dissipated energy and the maximum curvature or ductilities of the members in the structure, will be affected by different choices of damping model. The effects of varying the damping model on the responses and the structural damage indices needs to be studied.

(5) For a storey damage index, such as in the first or lowest storeys in this study, the damage in the columns may take a much larger importance or weighting than damage in the beams. The storey damage index may be dominated by either the energy weighted average of all member damage indices in this storey or the maximum column damage index, which may be expressed in Eq. (10-1). This is not considered in the Park & Ang damage index for the storeys.

$$DI^{Storey} = \max\left\{DI^{Storey}_{Park\ \&\ Ang}, DI^{Columns}\right\} \qquad \textbf{(10-1)}$$

For an overall structural damage index, the damage in columns may deserve a larger weight than that of the beams. The overall structural damage index may be dominated by either the energy weighted average of all member damage indices

in the whole structure or the maximum storey damage index, which may be expressed in Eq. (10-2). This is not considered in the Park & Ang damage index for whole structures.

$$DI^{Structure} = \max\left\{DI^{Structure}_{Park\ \&\ Ang}, DI^{Max.\ Storey}\right\} \qquad \textbf{(10-2)}$$

The effects of different weightings between the different types of members in the structure on the structural damage index need to be investigated.

(6) Different structural forms, such as structural walls and frame-wall hybrid structures, and the effect of different foundation systems, such as a base-isolation or soil-structure interaction needs to be incorporated in future studies. In this thesis, only pure framed structures ignoring soil-structure interaction effects were considered.

(7) An energy weighted overall structural damage index model needs to be incorporated into analysis software, such as RUAUMOKO [Carr 1998].

10-4.2 Topics Related to Experimental Investigation

(8) Laboratory tests of beam-columns, designed to the current New Zealand and other seismic codes need to be subjected to simulated earthquake cyclic loadings to obtain bending moment – curvature hysteretic behaviour in beam and column members to assess the equivalent unloading and reloading stiffnesses, the α and β parameters for the Modified Takeda model. It may be more realistic member hysteresis models will result from these studies.

(9) Laboratory tests of beam-columns, designed to the current New Zealand and other design codes and subjected to simulated earthquake cyclic loadings need to be carried out to obtain the ultimate curvature ductility capacity of beam and column members so that the ultimate limit parameters can be found for the damage index models.

(10) Laboratory tests need to be done to determine realistic estimates of the effective plastic hinge length for members designed according to the current New Zealand and other concrete design codes, so that reliable estimates can be made for the curvatures in the members.

(11) Laboratory tests of beam-columns, designed to the current New Zealand and other seismic codes need to be subjected to simulated earthquake cyclic loadings to correlate Park & Ang damage index with the tested damage. The $\beta = 0.05$ used in Park & Ang member damage model may be validated or different value may be identified for the modern standards designed members

(12) Experimental work needs to be done to enable correlation of the Banon & Veneziano, Park & Ang, Roufaiel & Meyer, and Cosenza et al. member damage indices to the observed damage in the members and this enable the user of the analytical assessment to decide whether the computed damage is insignificant, repairable, and beyond economical restoration.

REFERENCES

[Alsiwat 1990] Alsiwat, J., and Saatcioglu, M., 1990 "Ahysteretic Model for Reinforcement Extension and Slip in Concrete Structures", Research Report, Department of Civil Engineering, University of Ottawa, Ottawa, Canada.

[AS/NZS 1170] Draft of Australia/New Zealand 1170.4 Standards, "Earthquake Loading", Draft Number: DR PPCD 8. Wellington, New Zealand.

[Bertero 1975] Bertero, V.V., and Popov, E.P., 1975, "Hysteretic Behaviour of Ductile Moment Resisting Reinforced Concrete Frame Components", Report No. EERC-75-16, University of California at Berkeley.

[Banon 1981] Banon, H. and Biggs, J. M. and Irvine, H. M., September 1981 "Seismic Damage in Reinforced Concrete Frames", Journal of the Structural Division, ASCE, Vol. 107, No. ST9, pp. 1713-1729.

[Banon 1982] Banon, H. and Veneziano, D., 1982 "Seismic Safety of Reinforced Concrete Members and Structures", Earthquake Engineering and Structural Dynamics, Vol. 10, pp. 179-193.

[Bracci 1989] Bracci, J. M., Reinhorn, A. M., Mander, J. B. and Kunnath, S. K., 1989 "Deterministic Model for Seismic Damage Evaluation of Reinforced Concrete Structures", Technical Report NCEER-89-0033, National Centre for Earthquake Engineering Research, State University of New York at Buffalo.

[Carr 1993] Carr, A. J., and Tabuchi, M., June 1993, "The structural Ductility and the Damage Index for Reinforced Concrete Structure under Seismic Excitation", Proceedings of the Second European Conference on Structural Dynamics: EURODYN'93, Trondheim, Norway, Vol. 1, pp169-176.

[Carr 1994] Carr, A. J., "Dynamic Analysis of Structures", Bulletin of the New Zealand National Society for Earthquake Engineering, Vol. 27, No. 2, June 1994, pp.129-146.

[Carr 1997A] Carr, A. J., 1997 "Direct Stiffness Method", Hand out for the Master course of structural dynamic analysis, Department of Civil Engineering, University of Canterbury.

[Carr 1997B] Carr, A. J., 1997 "Matrix Structural Analysis", Hand out for the Master course of structural dynamic analysis, Department of Civil Engineering, University of Canterbury.

[Carr 1997C] Carr, A. J., 1997 "Inelastic Time-History Analyses", Hand out for the Master course of structural dynamic analysis, Department of Civil Engineering, University of Canterbury.

[Carr 1997D] Carr, A. J., 1997 "Response to Earthquake Loading", Hand out for the Master course of structural dynamic analysis, Department of Civil Engineering, University of Canterbury.

[Carr 1998] Carr, A. J., 1998 "User's Manual of RUAUMOKO, the Maori God of Volcanoes and Earthquakes", Department of Civil Engineering, University of Canterbury.

[Celebi 1973] Celebi, M., and Penzien, 1973, "Experimental Investigation into the Seismic Behaviour of Critical Regions of Reinforced Components as Influenced by Moment and Shear", Report No. EERC 73-4, University of California at Berkeley.

[Charng 1998] Charng, Peng-Hsiang, "Base Isolation for Multistorey Building Structures", A thesis submitted in partial fulfilment of the requirements for the degree of Doctor of Philosophy in the Department of Civil Engineering, University of Canterbury, at Christchurch, New Zealand.

[Chung 1987] Chung, Y. S., Meyer, C. and Shinozuka, M., 1987 "Seismic Damage Assessment of Reinforced Concrete Members", Technical Report NCEER-87-0022, National Centre for Earthquake Engineering Research, State University of New York at Buffalo.

[Chopra 1995] Chopra Anil K., 1995, "Dynamics of Structures: Theory and Applications to Earthquake Engineering", Prentice Hall, Englewood Cliffs, New Jersey.

[Clough 1993] Clough, R.W., and Penzien, J, 1993, "Dynamics of Structures", Second Edition, McGraw-Hill Book Co., New York.

[Clough 1965] Clough, R.W., Benuska, K. L. and Wilson, E. L. 1966, "Inelastic Earthquake Response of Tall Buildings", Proceedings of the third World Conference on Earthquake Engineering, Wellington, New Zealand, Vol. 2, pp. 68-89.

[Clough 1966] Clough, R.W., 1966, "Effect of Stiffness Degradation on Earthquake Ductility Requirements", Structural and Materials Research, Structural Engineering Laboratory, University of California, Berkeley, Report 66-16.

[Collins 1997] Collins, M.P., and Mitchell, D., 1997, "Prestressed Concrete Structures", Response Publications, Canada.

[Cosenza 1993] Cosenza, E., Manfredi, G. and Ramasco, R., 1993, "The Use of Damage Functionals in Earthquake Engineering: A Comparison Between Different Models", Earthquake Engineering and Structural Dynamics, Vol. 22, pp. 855-868.

[CSA 1984] "Design of Concrete Structures for Buildings", A National Standard of Canada, CAN-A23.3-M84, Canadian Standard Association, 1984.

[DiPasqale 1990] DiPasqale, E., and Cakmak, A. S., 1990, "Seismic Damage Assessment Using Linear Models", Soil Dynamics and Earthquake Engineering, Vol. 9, No. 4, pp. 194-215.

[Dong 1999] Dong P. 1999, "Effect of Different Choice of Hysteresis Models on the Responses of Framed Structures of Reinforced Concrete Subjected to Earthquake Excitations", thesis presented to the University of Canterbury, at Christchurch, New Zealand, in partial fulfilment of the requirements for the degree of Master.

[Emori 1978] Emori, K. and Schnobrich, W.C., 1978, "Analysis of Reinforced Concrete Frame-Wall Structures for Strong Motion Earthquakes", Structural Research Series, No. 434, Civil Engineering Studies, University of Illinois, Urbana, Illinois.

[FEMA356 2000] FEMA 356, November 2000, "Prestandard and Commentary for the Seismic Rehabilitation of Buildings", Federal Emergency Management Agency, Washington D.C..

[Filippou 1983] Filippou, F.C., Popov, E.P., and Bertero, V.V., November 1983, "Modelling of Reinforced Concrete Joints Under Cyclic Excitations", Journal of Structural Engineering, ASCE, Vol. 109, No. 11, pp. 2666-2684.

[Giberson 1969] Giberson, M.F., 1969, "Two nonlinear beams with definitions of ductility", Journal of the Structural Division, ASCE, Vol. 95, No. ST2, pp. 137-157.

[IAEE 1996] International Association for Earthquake Engineering, 1996, "Regulations for Seismic Design", A world List.

[Imbeault 1973] Imbeault, F.A., and Nielsen, N.N., 1973, "Effect of Degrading Stiffness on the Response of Multistorey Frames Subjected to Earthquake", Proceedings of the Fifth World Conference on Earthquake Engineering, Rome, Italy.

[Jury 1978] Jury, R. D., February 1978, "Seismic Load Demands on Columns of Reinforced Concrete Multi-storey Frames", M.E. Report 78-12, Department of Civil Engineering, University of Canterbury.

[Kabeyasawa 1982] Kabeyasawa, H., Shioara, H., Otani, S. and Aoyama, H., 1982, "Analysis of the Full Scale Seven-Storey Reinforced Concrete Test Structures: Test PSD3", Proceedings, Third Joint Technical Coordinating Committee, U.S.-Japan Cooperative Earthquake Research Program, Building Research Institute, Tsukuba, Japan.

[Kanaan 1973] Kanaan, A.E. and Powell, G.H., 1973, "General Purpose Computer Program for Inelastic Dynamic Response of Plane Structures", Report No. EERC 73-6, University of California at Berkeley.

[Kasiraj 1969] Kasiraj, I. and Yao, J. T. P., 1969, "Fatigue Damage in Seismic Structures", Journal of the Structural Division, ASCE, Vol. 95, No. ST7, pp. 1341-1360.

[Keshavarzian 1985] Keshavarzian, M. and Schobrich, W. C., 1985, "Inelastic Analysis of Coupled Shear Walls", Earthquake Engineering and Structural Dynamics, Vol. 13, pp. 427-448.

[Krawinkler 1983] Krawinkler, H. and Zohrei, M., 1983, "Cumulative Damage in Steel Structure Subjected to Earthquake Ground Motions", Computers and Structures, Vol. 16, No. 1-4, pp. 531-541.

[Lin 1999] Lin, Xi, 1999, "Analysis and Design of Building Structures with Supplemental Lead Dampers under Earthquake and Wind Loads", a thesis presented to the University of Canterbury, at Christchurch, New Zealand, in partial fulfilment of the requirements for the degree of Doctor of Philosophy.

[Liu 2001] Liu, Aizhen, 2001, "Seismic Assessment and Retrofic of Pre-1970s Reinforced Concrete Frame Structures", a thesis presented to the University of Canterbury, at Christchurch, New Zealand, in partial fulfilment of the requirements for the degree of Doctor of Philosophy.

[Ma 1976] Ma, S.M., Bertero, V.V., and Popov, E.P., 1976, "Experimental and Analytical Studies of the Hysteretic Behaviour of Reinforced Concrete Rectangular and T-beams", Report No. EERC 76-2, University of California at Berkeley.

[Magdy 1987] Magdy, S. L., Roufaiel and Meyer, C., March 1987, "Analytical Modelling of Hysteretic Behaviour of R/C Frames", Journal of the Structural Division, ASCE, Vol. 113, No. ST3, pp. 429-444.

[Morita 1984] Morita, S. and Kaku, T., 1984, "Slippage of Reinforcement in Beam-Column Joint of Reinforced Concrete Frames", Proceedings of the Eighth World Conference on Earthquake Engineering, San Francisco, U.S.A., Vol. 6, pp. 477-484.

[Mork 1992] Mork, K. J., 1992, "Stochastic Analysis of Reinforced Concrete Frames Under Seismic Excitation", Soil Dynamics and Earthquake Engineering, Vol. 11, No. 3, pp. 145-161.

[Moss 1992] Moss, P. J. and Carr A. J., 1992, "Earthquake Scaling Methods", Unpublished Materials, Department of Civil Engineering, University of Canterbury.

[Newmark 1960] Newmark, N. M. and Veletsos, A. S., 1960, "Effect of Behaviour of Simple Systems to Earthquake Motion", Proceedings of the Second World Conference on Earthquake Engineering, Tokyo, 11-18, July pp. 895-912.

[Nielsen 1971] Nielsen, N. N. and Imbeault, F. A., 1971, "Validity of Various Hysteretic Systems", Proceedings of the Third Japan National Conference on Earthquake Engineering, pp. 707-714.

[Nielsen 1992] Nielsen, S. R. K., Koyluoglu, H. U., and Cakmak, A. S., 1992, "One and Two-Dimensional Maximum Softening Damage Indicators for Reinforced Concrete Structures Under Seismic Excitation", Soil Dynamics and Earthquake Engineering, Vol. 11, No. 4, pp. 435-443.

[NZS4203 1992] Standards New Zealand, 1992, "Code of Practice for General Design and Design Loadings for Buildings-Loadings Standard", Wellington, New Zealand.

[NZS3101 1995] Standards New Zealand, 1995, "Concrete Structures Standard", Wellington, New Zealand.

[Otani 1974] Otani, Shunsuke, 1974, "SAKE, A Computer Program for Inelastic Response of R/C Frames to Earthquake", Report UILU-Eng-74-2029, Civil Engineering Studies, University of Illinois at Urbana-Champaign, Nov.

[Otani 1980] Otani, Shunsuke, 1980, "Nonlinear Dynamic Analysis of R/C Building Structures", Canadian Journal of Civil Engineering, Vol. 7, pp. 333-344.

[Otani 1981] Otani, Shunsuke, 1981, "Hysteresis Models of Reinforced Concrete for Earthquake Response Analysis", Journal of the Faculty of Engineering, University of Tokeyo, Vol XXXVI, No. 2.

[Ozcebe 1989] Ozcebe, G., and Saatcioglu, M., January 1989, "Hysteretic Shear Model for Reinforced Concrete Members", Journal of the Structural Engineering, ASCE, Vol. 115, No. 1, pp. 132-148.

[Park 1972] Park, R., Kent, D. C. and Sampson, R. A., July 1972, "Reinforced Concrete Members with Cyclic Loading", Journal of the Structural Division, ASCE, Vol. 98, No. ST7, pp. 1341-1360.

[Park 1975] Park, R. and Paulay T., 1975, "Reinforced Concrete Structures", John Wiley & Sons, New York.

[Park 1985A] Park, Y-J and Ang, A. H-S. 1985, "Mechanical Seismic Damage Model for Reinforced Concrete", ASCE Vol. 111, No. 4, April, pp. 722-739.

[Park 1985B] Park, Y-J, Ang, A. H-S. and Wen, Y. K., 1985, "Seismic Damage Analysis of Reinforced Concrete Buildings", ASCE Vol. 111, No. 4, April, pp. 740-757.

[Paulay 1977] Paulay T., June 1977, "Seismic Design of Ductile Moment Resisting Reinforced Concrete Frames, Columns: Evaluation of Actions", Bulletin of the New Zealand Society for Earthquake Engineering, Vol. 10, No. 2, 85-94.

[Paulay 1979] Paulay T., June 1979, "Capacity Design of Earthquake Resisting Ductile Multistorey Reinforced Concrete Frames", Proceeding of the 3rd Canadian Conference on Earthquake Engineering, Montreal, Vol. 2, pp. 917-948.

[Paulay 1980] Paulay T., 1980, "Deterministic Design Procedure for Ductile Frames in Seismic Areas", ACI Publication SP-63, American Concrete Institute, Detroit, pp. 357-381

[Paulay 1988] Paulay T., September 1988, "Seismic Design in Reinforced Concrete: the State of the Art in New Zealand", Bulletin of the New Zealand Society for Earthquake Engineering, Vol. 25, No. 1, pp57-69

[Paulay 1992] Paulay T. and Priestley M. J. N., 1992, "Seismic Design of Reinforced Concrete and Masonry Buildings", John Wiley & Sons, New York.

[Pradono 1998] Pradono, Mulyo Harris, "Dynamic Amplification of Static Design Forces at Flexural Overstrength of Coupled-Wall Structures", A thesis submitted in partial fulfilment of the requirements for the degree of Master in the Department of Civil Engineering, University of Canterbury, at Christchurch, New Zealand.

[Regulation 1996] International Association for Earthquake Engineering, 1996, "Regulations for Seismic Design", A world List.

[Riddell 1972] Riddell, R. and Newmark, N.M., 1972, "Statistical Analysis of the Response of Nonlinear Systems Subjected to Earthquakes", Structural Research Series No. 468, Civil Engineering Studies, University of Illinois, Urbana.

[Roufaiel 1987] Roufaiel, M. S. L. and Meyer, C., 1987, "Reliability of Concrete Frames Damaged by Earthquakes", ASCE Vol. 113, No. 3, ST3, pp. 445-457.

[Roufaiel 1987] Roufaiel, M. S. L. and Meyer, C., 1987, "Analytical Modelling of Hysteretic Behaviour of R/C Frames", ASCE Vol. 113, No. 3, March, pp. 429-457.

[Saatcioglu 1980] Saatcioglu, M., Derecho, A. T. and Corley, W. G., 1980, "Coupled Walls in Earthquake Resistant Buildings – Modelling Techniques and Dynamic Analysis", Report to NSF, Construction Technology Laboratories, Portland Cement Association Skokie, Illinois, 117 pp.

[Saatcioglu 1983] Saatcioglu, M., Derecho, A. T. and Corley, W. G., 1983, "Modelling Hysteretic Behavior of Coupled Walls for Dynamic Analysis", Earthquake Engineering and Structural Dynamic, Vol. 11, pp. 711-726.

[Saatcioglu 1989] Saatcioglu, M. and Ozcebe, G., 1989, "Response of Reinforced Concrete Columns to Simulated Seismic Loading", ACI Structural Journal, Vol. 86, No. 1, January-February, pp. 3-12.

[Saiidi 1979] Saiidi, M., and Sozen, M. A., Nov. 1979, "Simple and Complex Models for Nonlinear Seismic Response of Reinforced Concrete Structures", Structural Research Series No. 465, Civil Engineering Studies, University of Illinois, Urbana, Illinois.

[Saiidi 1982] Saiidi, M., May 1982, "Hysteresis Models for Reinforced Concrete", Journal of the Structural Division, ASCE, Vol. 108, No. ST5, pp. 1077-1087.

[Satyarno 2000] Satyarno, Iman, "Adaptive Pushover Analysis for the Seismic Assessment of Old Reinforced Concrete Buildings", A thesis submitted in partial fulfilment of the requirements for the degree of Doctor of Philosophy in the Department of Civil Engineering, University of Canterbury, at Christchurch, New Zealand.

[Sharpe 1974] Sharpe, Richard, 1974, "The Seismic Response of Inelastic Structures", thesis presented to the University of Canterbury, at Christchurch, New Zealand, in partial fulfilment of the requirements for the degree of Doctor of Philosophy.

[Takayanagi 1976] Takayanagi, T., and Schnobrich W. C., 1976, "Computed Behavior of Reinforced Concrete Coupled Shear Walls", Structural Research Series No. 434, Civil Engineering Studies, University of Illinois, Urbana, Illinois.

[Takayanagi 1979] Takayanagi, T., Derecho, A. T. and Corley W. G., 1979, "Analysis of Inelastic Shear Deformation Effects in Reinforced Concrete Structural Wall Systems", Nonlinear Design of Concrete Structures, Proceedings of the CSCE-ASCE-ACI-CEB International Symposium, University of Waterloo, Ontario, pp. 545-579.

[Takeda 1970] Takeda, T., Sozen, M. A. and Nielsen N. N., December 1970, "Reinforced Concrete Response to Simulated Earthquakes", Journal of the Structural Division, ASCE, Vol.96, No. ST12, pp. 2557-2573.

[Toshikatsu 1994] Toshikatsu, Ichinose and Katsuki Takiguchi, August 1974, "Experimental Verification of Beam Models for RC", Journal of the Structural Division, ASCE, Vol.120, No. 8, pp. 2261-2279.

[TP 1987] "Seismic Design of Concrete Structures", Technical Press, New York, 1987, 298p.

[Tso 1993] Tso, W. K., Zhu, T. J. and Heidebrecht, A. C., 1993, "Engineering Implication of Ground Motion A/V Ratio", Soil Dynamic Earthquake Engineering, Vol. 11, pp. 133-144.

[UBC 1991] Uniform Building Code, International Conference of Building Officials, whittier, California, 1991.

APPENDIX A
The three structural models

Six-Storey Three-Bay Reinforced Concrete Frame

General Data

Design Fundamental Period	=	1.11	seconds
Computed Fundamental Period with Rigid End Block Effect	=	1.35	seconds
Computed Fundamental Period without Rigid End Block Effect	=	1.652	seconds
Seismic Coefficient for Lateral Force	=	0.05	
Total Frame Weight	=	13207	kN
Design Base Shear	=	658	kN
Modulus of Elasticity, E	=	25.1	GPa
Shear Modulus, G	=	10.5	GPa
Concrete Compressive Strength, f'c	=	30.0	MPa
Floor Slab Thickness	=	160	mm

Section Properties

Member	Levels	Axial Area (m^2)	Shear Area (m^2)	Moment of Inertia (m^4)	Plastic Hinge Length (m)
Beams	1-3	0.336	0.252	0.012760	0.630
	4-6	0.322	0.238	0.010750	0.595
External Columns	0-3	0.200	0.150	0.003125	0.350*
	3-6	0.180	0.167	0.002813	-
Internal Columns	0-3	0.324	0.270	0.008640	0.42*
	3-6	0.248	0.206	0.005546	-

* Those values are only used for the first storey columns.

Length of Rigid End Block (m)

Beams: (symmetric values were used.)

Level	*Left Bay*		*Middle Bay*
	Left End	*Right End*	*Left End*
1-3	0.25	0.30	0.30
4-6	0.25	0.275	0.275

Columns:

Level	*Exterior and Interior Columns*	
	End-1	*End-2*
1	0.00	0.45
2-3	0.45	0.45
4	0.45	0.425
5-6	0.425	0.425

Additional Data

Bay Width	=	9.2	metres
Storey Height	=	3.65	metres
Total Structure Height	=	21.9	metres
Column Interaction Type	=	Concrete Beam-Column Yield Interaction (See Fig. A –1)	

Yield Interaction Data for First Storey Column: for definition of term see Fig. A–1

Column	*Pyc (kN)*	*Pb (kN)*	*Mb (kNm)*	*M1b (kNm)*	*M2b (kNm)*	*Mo (kNm)*	*Pyt (kN)*
Exterior	-8050	-3165	513	447	302	115	611
Interior	-11594	-4664	898	789	536	210	882

Beam Yield Data

Level	*Left End Positive*	*Left End Negative*	*Right End Positive*	*Right End Negative*
1-3	364	-586	364	-586
4-6	321	-519	321	-519

Note: All the numbers are in *kNm*.
The three beams at each level have the same yield data.

Beam Initial Fixed End Moments and Shears

Level	*Moment (kNm) Left End*	*Moment (kNm) Right End*	*Shear (kN) Left End*	*Shear (kN) Right End*
1-3	-214	-214	-122	122
4-5	-210	-210	-120	120
6	-193	-193	-110	110

Note: Fig. A–2 depicts the positive sign conventions used in RUAUMOKO.

Column Initial Fixed End Self Weight Vertical Load

Level	*Exterior Column (kN)*	*Interior Column (kN)*
1-3	-11	-16
4-6	-10	-12

Static Nodal Loads and Nodal Lumped Weights

Level	*Lumped Nodal Weight (kN)*		*Static Nodal Loads (kN)*	
	Exterior Node	*Interior Node*	*Exterior Node*	*Interior Node*
1-3	422	738	-287	-462
4-5	418	728	-287	-462
6	366	632	-271	-430

Note: a) Based on Dead Load + 0.24*Live Load.
b) The nodal loads correspond to the gravity load carried by the frame apart from the member loads.
c) Nodal weight is converted to mass internally in the program.

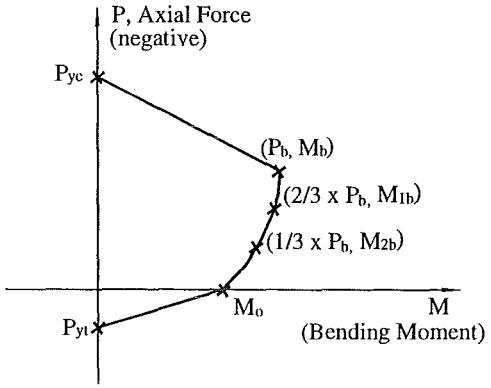

Fig. A-1 Concrete beam-column yield interaction surface used in this study

(Note: The interaction is symmetric about the *M=0.0* axis.)

Fig. A-1 shows the concrete beam-column yield interaction surface. P_{yc} is the axial compression yield force at M=0.0. P_b and M_b are respectively the axial compression force and yield bending moment at balance point b as used in this study. M_{1b} and M_{2b} are the yield bending moments at (2/3)* P_b and (1/3)* P_b respectively. M_0 is the yield moment at *P*=0.0. P_{yt} is the axial tension yield force.

Fig. A–2 Positive Sign Conventions for Beams Specified in RUAUMOKO

Fig. A-2 depicts the positive sign conventions specified in RUAUMOKO. M_i and M_j is the initial fixed-end moments at left and right beam ends respectively. V_i and V_j are the initial fixed-end shear forces at left and right beam ends respectively.

Twelve-Storey Three-Bay Reinforced Concrete Frame

General Data

Design Fundamental Period	=	1.89	seconds
Computed Fundamental Period With Rigid End Block Effect	=	2.341	seconds
Computed Fundamental Period without Rigid End Block Effect	=	2.769	seconds
Seismic Coefficient For Lateral Force	=	0.03	
Total Frame Weight	=	27701	kN
Design Base Shear	=	831	kN
Modulus of Elasticity, E	=	25.1	GPa
Shear Modulus, G	=	10.5	GPa
Concrete Compressive Strength, f'c	=	30.0	MPa
Floor Slab Thickness	=	160	mm

Section Properties

Member	Levels	Axial Area (m^2)	Shear Area (m^2)	Moment of Inertia (m^4)	Plastic Hinge Length (m)
Beams	1-6	0.336	0.252	0.012760	0.630
	7-9	0.322	0.238	0.010750	0.595
	10-12	0.308	0.224	0.009020	0.560
External Columns	1-6	0.392	0.327	0.012010	0.490*
	7-9	0.338	0.282	0.008925	-
	10-12	0.288	0.240	0.006480	-
Internal Columns	1-6	0.650	0.542	0.034800	0.595*
	7-9	0.506	0.422	0.021090	-
	10-1	0.441	0.368	0.016010	-

* Those values are only used for the first storey columns.

Length of Rigid End Block (m)

Beams: (symmetric values were used.)

Level	*Left Bay*		*Middle Bay*
	Left End	*Right End*	*Left End*
1-6	0.35	0.425	0.425
7-9	0.325	0.375	0.375
10-12	0.300	0.350	0.350

Columns:

Level	*Exterior and Interior Columns*	
	End-1	*End-2*
1	0.00	0.45
2-6	0.45	0.45
7	0.45	0.425
8-9	0.425	0.425
10	0.425	0.40
11-12	0.40	0.40

Additional Data

Bay Width	=	9.2	metres
Storey Height	=	3.65	metres
Total Structure Height	=	43.8	metres
Column Interaction Type	=	Concrete Beam-Column Yield Interaction (See Fig. A–1)	

Yield Interaction Data for First Storey Column: for definition of term see Fig. A–1

Column	*Pyc (kN)*	P_b *(kN)*	M_b *(kNm)*	M_{1b} *(kNm)*	M_{2b} *(kNm)*	*Mo (kNm)*	*Pyt (kN)*
Exterior	-15806	-6413	1444	1273	872	351	1229
Interior	-23222	-9629	2574	2282	1562	621	1719

Beam Yield Data

Level	*Left End Positive*	*Left End Negative*	*Right End Positive*	*Right End Negative*
1-6	441	-697	441	-697
7-9	318	-583	318	-582
10-12	278	-462	278	-462

Note: All the numbers are in *kNm*.
The three beams at each level have the same yield data.

Beam Initial Fixed End Moments and Shears

Level	*Moment (kNm) Left End*	*Moment (kNm) Right End*	*Shear (kN) Left End*	*Shear (kN) Right End*
1-6	-214	-214	-122	122
7-9	-210	-210	-120	120
10-11	-207	-207	-118	118
12	-189	-189	-108	108

Note: Fig. A–2 depicts the positive sign conventions used in RUAUMOKO.

Column Initial Fixed End Self Weight Vertical Load

Level	*Exterior Column (kN)*	*Interior Column (kN)*
1-6	-21	-32
7-9	-19	-25
10-12	-16	-21

Static Nodal Loads and Nodal Lumped Weights

Level	*Lumped Nodal Weight (kN)*		*Static Nodal Loads (kN)*	
	Exterior Node	*Interior Node*	*Exterior Node*	*Interior Node*
1-6	442	768	-287	-462
7-9	434	753	-287	-462
10-11	427	745	-287	-462
12	369	639	-271	-430

Note: a) Based on Dead Load + 0.24*Live Load.
b) The nodal loads correspond to the gravity load carried by the frame apart from the member loads.
c) Nodal weight is converted to mass internally in the program.

Eighteen-Storey Three-Bay Reinforced Concrete Frame

General Data

Design Fundamental Period	=	2.54	seconds
Computed Fundamental Period With Rigid End Block Effect	=	2.845	seconds
Computed Fundamental Period without Rigid End Block Effect	=	3.448	seconds
Seismic Coefficient For Lateral Force	=	0.03	
Total Frame Weight	=	43167	kN
Design Base Shear	=	1295	kN
Modulus of Elasticity, E	=	25.1	GPa
Shear Modulus, G	=	10.5	GPa
Concrete Compressive Strength, f'c	=	30.0	MPa
Floor Slab Thickness	=	160	mm

Section Properties

Member	*Levels*	*Axial Area (m^2)*	*Shear Area (m^2)*	*Moment of Inertia (m^4)*	*Plastic Hinge Length (m)*
Beams	1-6	0.4522	0.3850	0.02085	0.700
	7-9	0.4330	0.3658	0.01788	0.665
	10-12	0.3878	0.3150	0.01414	0.630
	13-15	0.3703	0.2975	0.01191	0.595
	16-18	0.3080	0.2240	0.00902	0.560
External Columns	1-6	0.5200	0.4333	0.03250	0.700*
	7-9	0.4940	0.4117	0.02786	-
	10-12	0.4420	0.3683	0.01996	-
	13-15	0.3900	0.3250	0.01371	-
	16-18	0.3380	0.2817	0.00893	-
Internal Columns	1-6	0.9000	0.7500	0.06667	0.700*
	7-9	0.8123	0.6769	0.05430	-
	10-12	0.7290	0.6075	0.04374	-
	13-15	0.6503	0.5419	0.03480	-
	16-18	0.4410	0.3675	0.01601	-

*Those values are only used for the first storey columns.

Length of Rigid End Block (m)

Beams: (symmetric values were used.)

Level	*Left Bay*		*Middle Bay*
	Left End	*Right End*	*Left End*
1-6	0.50	0.50	0.50
7-9	0.475	0.475	0.475
10-12	0.425	0.450	0.450
13-15	0.375	0.425	0.425
16-18	0.325	0.35	0.35

Columns:

Level	*Exterior and Interior Columns*	
	End-1	*End-2*
1	0.00	0.50
2-6	0.50	0.50
7	0.50	0.475
8-9	0.475	0.475
10	0.475	0.450
11-12	0.450	0.450
13	0.450	0.425
14-15	0.425	0.425
16	0.425	0.40
17-18	0.40	0.40

Additional Data

Bay Width = 9.2 metres
Storey Height = 3.65 metres
Total Structure Height = 65.7 metres
Column Interaction Type = Concrete Beam-Column Yield Interaction (See Fig. A–1)

Yield Interaction Data for First Storey Column: for definition of term see Fig. A–1

Column	*Pyc (kN)*	*P_b (kN)*	*M_b (kNm)*	*M_{1b} (kNm)*	*M_{2b} (kNm)*	*Mo (kNm)*	*Pyt (kN)*
Exterior	-21237	-8773	2902	2606	1836	838	1930
Interior	-32171	-13496	4224	3766	2592	1047	2413

Beam Yield Data

Level	*Left End Positive*	*Left End Negative*	*Right End Positive*	*Right End Negative*
1	642	-1006	642	-1006
2-6	811	-1006	811	-1006
7-9	643	-895	643	-895
10-12	463	-770	463	-770
13-15	400	-640	400	-640
16-18	279	-470	279	-470

Note: All the numbers are in *kNm*.
The three beams at each level have the same yield data.

Beam Initial Fixed End Moments and Shears

Level	*Moment (kNm) Left End*	*Moment (kNm) Right End*	*Shear (kNm) Left End*	*Shear (kNm) Right End*
1-6	-242	-242	-141	141
7-9	-237	-237	-138	138
10-12	-226	-226	-130	130
13-15	-222	-222	-128	128
16-17	-207	-207	-118	118
18	-189	-189	-108	108

Note: Fig. A–2 depicts the positive sign conventions used in RUAUMOKO.

Column Initial Fixed End Self Weight Vertical Load

Level	*Exterior Column (kN)*	*Interior Column (kN)*
1-6	-28	-44
7-9	-27	-40
10-12	-24	-35
13-15	-21	-32
16-18	-19	-21

Static Nodal Loads and Nodal Lumped Weights

Level	*Lumped Nodal Weight (kN)*		*Static Nodal Loads (kN)*	
	Exterior Node	*Interior Node*	*Exterior Node*	*Interior Node*
1-6	451	771	-287	-462
7-9	447	761	-287	-462
10-12	436	748	-287	-462
13-15	429	738	-287	-462
16-17	416	711	-287	-462
18	372	638	-271	-430

Note: a) Based on Dead Load + 0.24*Live Load.
b) The nodal loads correspond to the gravity load carried by the frame apart from the member loads.
c) Nodal weight is converted to mass internally in the program.

APPENDIX B.

Derivation of the hysteretic energy dissipation index of the Modified Takeda model

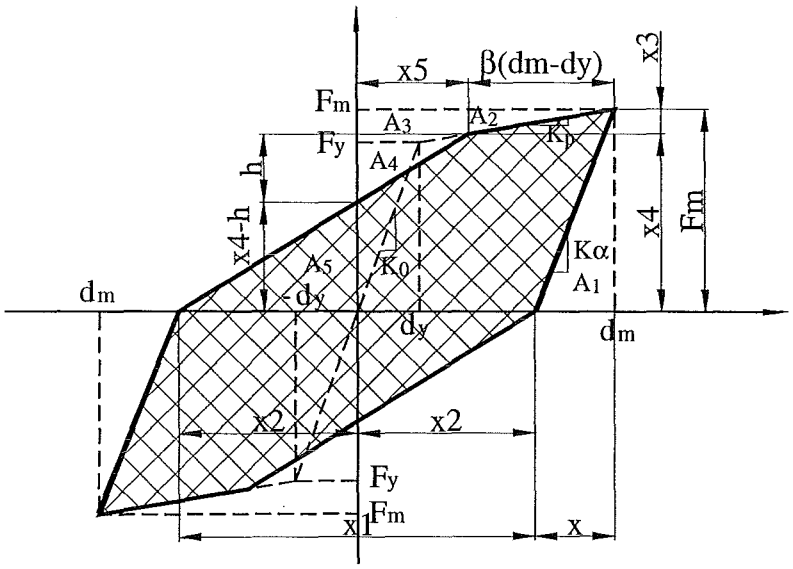

Fig. B-1 The hysteretic energy dissipation index of the modified Takeda model

Given the unloading stiffness of Emori type

$$K_\alpha = K_0\left(\frac{d_y}{d_m}\right)^\alpha = \frac{F_y}{d_y}\left(\frac{d_y}{d_m}\right)^\alpha \tag{B-1}$$

Substituting $K_\alpha = \frac{F_m}{x}$ into Eq. (B-1) yields

$$\frac{F_m}{x} = \frac{F_y}{d_y \mu^\alpha} \text{ or } x = \frac{F_m d_y \mu^\alpha}{F_y} \tag{B-2}$$

Substituting $d_y = \frac{d_m}{\mu}$ into Eq. (B-2) yields finally

$$x = \frac{F_m d_m \mu^{\alpha-1}}{F_y} \tag{B-3}$$

From $\frac{x_3}{\beta(d_m - d_y)} = R_p \frac{F_y}{d_y}$, x_3 is given by

$$x_3 = \beta(d_m - d_y) R_p \frac{F_y}{d_y} \tag{B-4}$$

From Fig. B-1:

$$x_4 = F_m - x_3 \tag{B-5}$$

$$x_2 = d_m - x_3 \tag{B-6}$$

$$x_5 = d_m - \beta(d_m - d_y) \tag{B-7}$$

From the rectangles A4 and A5:

$$\frac{h}{x_4 - h} = \frac{x_5}{x_2} \text{ or } h = \frac{x_4 x_5}{x_2 + x_5} \tag{B-8}$$

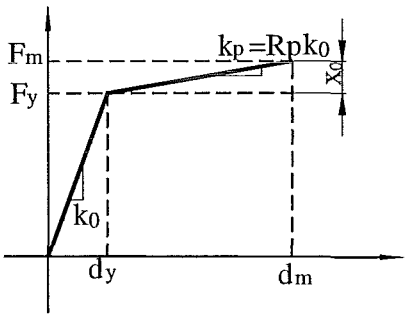

Fig. B-2 Derivation of $\frac{F_m}{F_y} = 1 + R_p(\mu - 1)$

From Fig. B-2:

$$x_0 = K_p(d_m - d_y) = R_p K_0(d_m - d_y) = R_p \frac{F_y}{d_y}(d_m - d_y) \tag{B-9}$$

Substituting Eq. (B-9) into $F_m = F_y + X_0$ yields

$$F_m = F_m + x_0 = F_y + R_p \frac{F_y}{d_y}(d_m - d_y) = F_y\left[1 + R_p\left(\frac{d_m}{d_y} - 1\right)\right] \tag{B-10a}$$

or

$$\frac{F_m}{F_y} = 1 + R_p(\mu - 1) \tag{B-10b}$$

The hatched area in Fig. B-1, $A_{hatched}$ can be determined by Eq. (B-11)

$$A_{hatched} = 2(F_m d_m - A_1 - A_2 - A_3 - A_4) + 2A_5 \tag{B-11}$$

Substituting Eq.s (B-5, 6, 7 and 8) into Eq. (B-11) yields

$$
\begin{aligned}
A_{hatched} &= 2\left(F_m d_m - A_1 - A_2 - A_3 - A_4\right) + 2A_5 \\
&= 2\left[F_m d_m - \frac{1}{2}xF_m - \frac{1}{2}x_3\beta\left(d_m - d_y\right) - x_3 x_5 \frac{1}{2}x_5 h\right] + 2 * \frac{1}{2}x_2\left(x_4 - h\right) \\
&= 2F_m d_m - xF_m - x_3\beta\left(d_m - d_y\right) - 2x_3 x_5 - x_5 h + x_2\left(x_4 - h\right) \\
&= 2F_m d_m - xF_m - x_3\beta\left(d_m - d_y\right) - 2x_3 x_5 - \left(x_5 + x_2\right)h + x_2 x_4 \\
&= 2F_m d_m - xF_m - x_3\beta\left(d_m - d_y\right) - 2x_3 x_5 - \left(x_5 + x_2\right)\frac{x_4 x_5}{x_2 + x_5} + x_2 x_4 \\
&= 2F_m d_m - xF_m - x_3\beta\left(d_m - d_y\right) - 2x_3 x_5 + x_4\left(x_2 - x_5\right) \\
&= 2F_m d_m - xF_m - x_3\beta\left(d_m - d_y\right) - 2x_3 x_5 + \left(F_m - x_3\right)\left(d_m - x - x_5\right) \\
&= 2F_m d_m - xF_m - x_3\beta\left(d_m - d_y\right) - 2x_3 x_5 + F_m d_m - F_m x - F_m x_5 - x_3 d_m + x_3 x + x_3 x_5 \\
&= 3F_m d_m - 2xF_m - x_3\beta\left(d_m - d_y\right) - x_3 x_5 - F_m x_5 - x_3 d_m + x_3 x \\
&= 3F_m d_m - 2xF_m - F_m x_5 + \left[x - \beta\left(d_m - d_y\right) - x_5 - d_m\right]x_3
\end{aligned}
\qquad \text{(B-12)}
$$

Substituting Eq.(B-3) and Eq. (B-4) yields

$$
\begin{aligned}
A_{hatched} &= 3F_m d_m - 2F_m \frac{F_m d_m \mu^{\alpha-1}}{F_y} - F_m\left[d_m - \beta\left(d_m - d_y\right)\right] \\
&\quad + \left[\frac{F_m d_m \mu^{\alpha-1}}{F_y} - \beta\left(d_m - d_y\right) - d_m + \beta\left(d_m - d_y\right) - d_m\right]x_3 \\
&= 3F_m d_m - 2F_m \frac{F_m d_m \mu^{\alpha-1}}{F_y} - F_m d_m + F_m\beta\left(d_m - d_y\right) \\
&\quad + \left(\frac{F_m d_m \mu^{\alpha-1}}{F_m} - 2d_m\right)\beta\left(d_m - d_y\right)R_p\frac{F_y}{d_y} \\
&= 2F_m d_m - 2F_m \frac{F_m d_m \mu^{\alpha-1}}{F_y} + F_m\beta\left(d_m - d_y\right) \\
&\quad + \frac{F_m d_m \mu^{\alpha-1}}{F_y}\beta\left(d_m - d_y\right)R_p\frac{F_y}{d_y} - 2d_m\beta\left(d_m - d_y\right)R_p\frac{F_y}{d_y} \\
&= 2F_m d_m - 2F_m \frac{F_m d_m \mu^{\alpha-1}}{F_y} + F_m\beta\left(d_m - d_y\right) \\
&\quad + F_m d_m \mu^{\alpha-1}\beta R_p\left(\mu - 1\right) - 2d_m\beta\left(\mu - 1\right)R_p F_y
\end{aligned}
\qquad \text{(B-13)}
$$

Substituting Eq. (B-13) into Eq. (B-14) gives the hysteretic energy dissipation index of the modified Takeda model.

$$E_h = \frac{A_{hatched}}{2\pi F_m d_m} \tag{B-14}$$

$$E_h = \frac{A_{hatched}}{2\pi F_m d_m}$$

$$= \frac{1}{2\pi}\left[2 - \frac{2F_m \mu^{\alpha-1}}{F_y} + \beta\left(1-\frac{1}{\mu}\right) + \mu^{\alpha-1}\beta R_p(\mu-1) - 2\beta(\mu-1)R_p\frac{F_y}{F_m}\right] \tag{B-15}$$

Substituting Eq. (B-10b) into Eq. (B-15) finally yields

$$E_h = \frac{1}{2\pi}\left\{2 + \left[\beta R_p(\mu-1) - 2\left(1+R_p(\mu-1)\right)\right]\mu^{\alpha-1} - \frac{2\beta(\mu-1)R_p}{1+R_p(\mu-1)} + \beta\left(1-\frac{1}{\mu}\right)\right\}$$

$$= \frac{1}{2\pi}\left\{2 + \left[(\beta-2)R_p(\mu-1) - 2\right]\mu^{\alpha-1} - \frac{2\beta(\mu-1)R_p}{1+R_p(\mu-1)} + \beta\left(1-\frac{1}{\mu}\right)\right\} \tag{B-16}$$

The hysteretic energy dissipation index of the modified Takeda model is determined by Eq. (B-16).

APPENDIX C
Derivation of the hysteretic energy dissipation index of the Origin-Centred bi-linear model

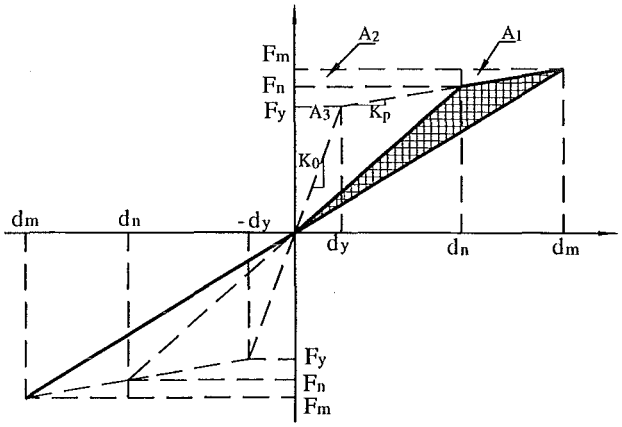

Fig. C-1 The hysteretic energy dissipation index of the Origin-Centred bi-linear model

From Fig. C-1:

$$A_{hatched} = 0.5F_m d_n - (A_1 + A_2 + A_3) \tag{C-1}$$

Substituting

$$A_1 = 0.5(F_m - F_n)(d_m - d_n)$$

$$A_2 = (F_m - F_n)d_n$$

$$A_3 = 0.5F_n d_n$$

into Eq. (C-1) yields:

$$\begin{aligned} A_{hatched} &= 0.5F_m d_n - (A_1 + A_2 + A_3) \\ &= 0.5(F_m - F_n)(d_m - d_n) + (F_m - F_n)d_n + 0.5F_n d_n \\ &= 0.5F_m d_m - 0.5F_m d_m + 0.5F_m d_n + 0.5F_n d_m - 0.5F_n d_n - F_m d_n + F_n d_n - 0.5F_n d_n \\ &= 0.5(F_n d_m - F_m d_n) \end{aligned} \tag{C-2}$$

hence the hysteresis energy dissipation index is given by Eq. (C-3).

$$E_h = \frac{A_{hatched}}{2\pi F_m d_m}$$

$$= \frac{0.5(F_n d_m - F_m d_n)}{2\pi F_m d_m} = \frac{1}{4\pi}\left(\frac{F_n}{F_m} - \frac{d_n}{d_m}\right) \tag{C-4}.$$

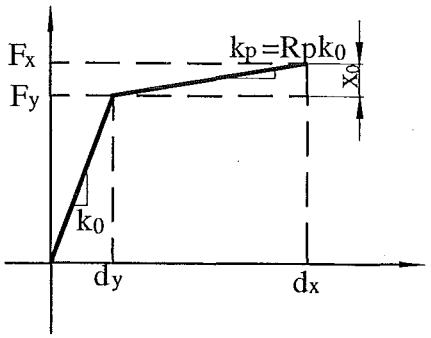

Fig. C-2 Derivation of $\frac{F_x}{F_y} = 1 + R_p(\mu_x - 1)$

From Fig. C-2:

$$x_0 = K_p(d_x - d_y) = R_p K_0(d_x - d_y) = R_p \frac{F_y}{d_y}(d_x - d_y) \tag{C-5}$$

Substituting Eq. (C-5) into $F_x=F_y+X_0$ yields

$$F_x = F_y + x_0 = F_y + R_p \frac{F_y}{d_y}(d_x - d_y) = F_y\left[1 + R_p\left(\frac{d_x}{d_y} - 1\right)\right] \tag{C-6a}$$

or

$$\frac{F_x}{F_y} = 1 + R_p(\mu_x - 1) \tag{C-6b}$$

For response points (F_n, d_n) and (F_m, d_m) from Eq. (b-6b):

$$\frac{F_n}{F_y} = 1 + R_p(\mu_n - 1) \tag{C-7}$$

$$\frac{F_m}{F_y} = 1 + R_p(\mu_m - 1) \tag{C-8}$$

Hence from Eq. (C-7) and (C-8):

$$\frac{F_n}{F_m} = \frac{1 + R_p(\mu_n - 1)}{1 + R_p(\mu_m - 1)} \tag{C-9}$$

From $d_n = \mu_n d_y$ and $d_m = \mu_m d_y$:

$$\frac{d_n}{d_y} = \frac{\mu_n}{\mu_m} \tag{C-10}$$

Substituting Eq. (C-9) and (C-10) into Eq. (C-4) yields finally:

$$E_h = \frac{A_{hatched}}{2\pi F_m d_m} = \frac{1}{4\pi}\left(\frac{F_n}{F_m} - \frac{d_n}{d_m}\right) = \frac{1}{4\pi}\left[\frac{1 + R_p(\mu_n - 1)}{1 + R_p(\mu_m - 1)} - \frac{\mu_n}{\mu_m}\right] \tag{C-11}$$

APPENDIX D

Derivation of the Bracci damage index for modified Takeda and Origin-centred hysteresis models with straight line of fatigue failure assumption

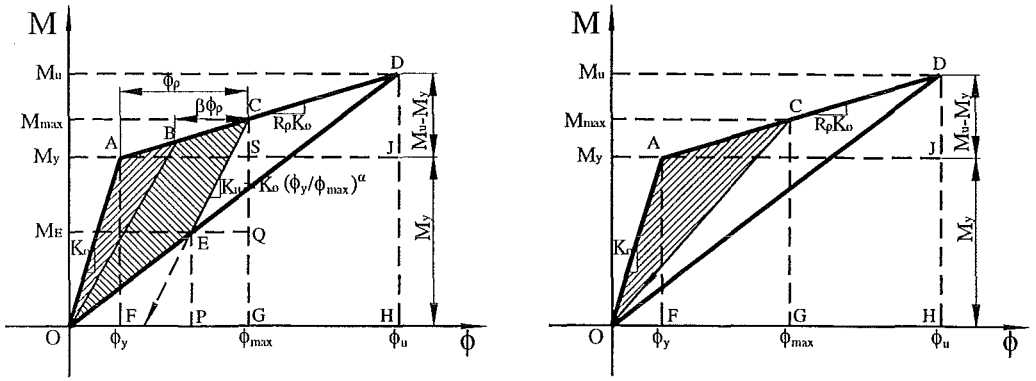

a) Modified Takeda model

b) Origin-centred model

Fig. D-1 The Bracci damage index for modified Takeda and Origin-Centred hysteresis models with straight line of fatigue failure assumption

For modified Takeda hysteresis model.

The damage potential is the triangle area A_{OAD} shown in Fig. D-1:

$$
\begin{aligned}
D_p &= A_{OAD} = A_{ADHO} - A_{ODH} \\
&= A_{OAF} + A_{ADJ} + A_{AJHF} - A_{ODH} \\
&= 0.5\phi_y^2 K_o + 0.5(\phi_u - \phi_y)^2 R_p K_o + \phi_u \phi_y K_o - \phi_y^2 K_o - 0.5\phi_u \phi_y K_o - 0.5\phi_u(\phi_u - \phi_y) R_p K_o \\
&= 0.5\phi_u \phi_y K_o - 0.5\phi_y^2 K_o + 0.5\left[(\phi_u^2 - 2\phi_u \phi_y + \phi_y^2) R_p K_o - \phi_u^2 R_p K_o + \phi_u \phi_y R_p K_o\right] \\
&= 0.5(\phi_u \phi_y K_o - \phi_y^2 K_o + \phi_u^2 R_p K_o - 2\phi_u \phi_y R_p K_o + \phi_y^2 R_p K_o - \phi_u^2 R_p K_o + \phi_u \phi_y R_p K_o) \\
&= 0.5(\phi_u \phi_y K_o - \phi_y^2 K_o - \phi_u \phi_y R_p K_o + \phi_y^2 R_p K_o) \\
&= 0.5\phi_y K_o\left[(1 - R_p)\phi_u - (1 - R_p)\phi_y\right] \\
&= 0.5(1 - R_p) K_o \phi_y (\phi_u - \phi_y) \\
&= 0.5(1 - R_p) K_o \phi_y^2 (\mu_u - 1)
\end{aligned}
\qquad \text{(D-1)}
$$

where ϕ_y yielding curvature.

ϕ_u ultimate curvature capacity.

K_o initial stiffness.

R_p ratio of post yielding stiffness to initial stiffness.

μ_u ultimate curvature ductility capacity.

The coordinate for point E should be derived for calculation of the hatched area, i.e sum of the strength and deformation damage. The function for line EC is expressed by Eq. (D-2):

$$M = K_u(\phi - \phi_o) \tag{D-2}$$

Substitute $K_u = K_o(\phi_y / \phi_{\max})^{\alpha}$ and point C ($M_{\max}$, $\phi_{\max}$) into Eq. (D-2):

$$K_u = \frac{M_{\max}}{\phi_{\max} - \phi_o} = K_o(\phi_y / \phi_{\max})^{\alpha}$$

$$\phi_{\max} - \phi_o = \frac{M_{\max}}{K_o(\phi_y / \phi_{\max})^{\alpha}}$$

$$\phi_o = \phi_{\max} - \frac{M_{\max}}{K_o(\phi_y / \phi_{\max})^{\alpha}} \tag{D-3}$$

The function for line OD is expressed by Eq. (D-4):

$$M = \frac{M_u}{\phi_u}\phi \tag{D-4}$$

The coordinate for point E is obtained by substituting Eq. (D-4) into Eq. (D-2):

$$\frac{M_u}{\phi_u}\phi_E = K_o(\phi_y / \phi_{\max})^{\alpha}\left(\phi_E - \phi_{\max} + \frac{M_{\max}}{K_o(\phi_y / \phi_{\max})^{\alpha}}\right)$$

$$\phi_E\left[\frac{M_u}{\phi_u} - K_o(\phi_y / \phi_{\max})^{\alpha}\right] = M_{\max} - K_o\phi_{\max}(\phi_y / \phi_{\max})^{\alpha}$$

$$\phi_E = \frac{M_{\max} - K_o\phi_{\max}(\phi_y / \phi_{\max})^{\alpha}}{(M_u / \phi_u) - K_o(\phi_y / \phi_{\max})^{\alpha}} = \frac{K_o\phi_y + R_pK_o(\mu_{\max}\phi_y - \phi_y) - K_o\phi_y\mu_{\max}\mu_{\max}^{-\alpha}}{(M_u / \phi_u) - K_o\mu_{\max}^{-\alpha}}$$

$$= \frac{K_o\phi_y[1 + R_p(\mu_{\max} - 1)] - K_o\phi_y\mu_{\max}^{1-\alpha}}{(M_u / \phi_u) - K_o\mu_{\max}^{-\alpha}}$$

$$= \frac{K_o\phi_y[1 + R_p(\mu_{\max} - 1) - \mu_{\max}^{1-\alpha}]}{(M_u / \phi_u) - K_o\mu_{\max}^{-\alpha}} \tag{D-5}$$

From Fig. D-1:

$$M_u = K_o\phi_y + (\phi_u - \phi_y)R_pK_o = K_o\phi_y + \phi_uR_pK - \phi_yR_pK$$

So

$$\frac{M_u}{\phi_u} = K_o\phi_u^{-1} + R_pK_o - \phi_u^{-1}R_pK_o = K_o[R_p + (1 - R_p)\mu_u^{-1}] \tag{D-6}$$

Substituting Eq. (D-6) into Eq. (D-5):

$$\phi_E = \frac{K_o\phi_y\left[1+R_p\left(\mu_{\max}-1\right)-\mu_{\max}^{1-\alpha}\right]}{K_o\left[R_p+\left(1-R_p\right)\mu_u^{-1}-\mu_{\max}^{-\alpha}\right]} = \frac{\phi_y\left[1+R_p\left(\mu_{\max}-1\right)-\mu_{\max}^{1-\alpha}\right]}{\left[R_p+\left(1-R_p\right)\mu_u^{-1}-\mu_{\max}^{-\alpha}\right]} \tag{D-7}$$

Once the ϕ_E is determined, the M_E can be defined using Eq. (D-4).

It was found from Eqs. (D-5) and (D-6) that once the ultimate response (M_u, ϕ_u) is defined, the response at point E is a function of the maximum response ductility u, initial stiffness K_o, post yielding stiffness parameter R_p and the unloading stiffness degradation parameter α.

The strength and deformation damage is the hatched triangle area, ABO and the quadrilateral area BCEO respectively shown in Fig. D-1a. The sum of the strength and deformation damage is derived as follows:

$$\begin{aligned} D_s + D_d &= A_{ACEO} \\ &= A_{ACGO} - A_{CEQ} - A_{OEP} - A_{EQGP} \end{aligned} \tag{D-8}$$

where $A_{ACGO} = A_{ACS} + A_{ASGF} + A_{AOF}$

$$\begin{aligned} &= 0.5\left(\phi_{\max}-\phi_y\right)\left(M_{\max}-M_y\right)+\left(\phi_{\max}-\phi_y\right)M_y+0.5\phi_y M_y \\ &= 0.5\left(\phi_{\max}-\phi_y\right)^2 R_p K_o+\left(\phi_{\max}-\phi_y\right)\phi_y K_o+0.5\phi_y^2 K_o \end{aligned} \tag{D-9}$$

$$A_{CEQ} = 0.5\left(\phi_{\max}-\phi_E\right)\left(M_{\max}-M_E\right)$$

$$= 0.5\left(\phi_{\max}M_{\max}-\phi_{\max}M_E-\phi_E M_{\max}+\phi_E M_E\right)$$

$$\because \quad M_{\max} = M_y+\left(\phi_{\max}-\phi_y\right)R_p K_o = \phi_y K_o+\phi_{\max}R_p K_o-\phi_y R_p K_o$$

$$\therefore \quad A_{CEQ} = 0.5\left(\phi_{\max}-\phi_E\right)\left(\phi_y K_o+\phi_{\max}R_p K_o-\phi_y R_p K_o-M_E\right) \tag{D-10}$$

$$A_{OEP} = 0.5\phi_E M_E \tag{D-11}$$

$$A_{EQGP} = \left(\phi_{\max}-\phi_E\right)M_E \tag{D-12}$$

Substituting Eqs. (D-9) to (D-12) into Eq. (D-8):

$$
\begin{aligned}
& D_s + D_d \\
= \; & 0.5(\phi_{\max} - \phi_y)^2 R_p K_o + (\phi_{\max} - \phi_y)\phi_y K_o + 0.5\phi_y^2 K_o \\
& - 0.5(\phi_{\max} - \phi_E)\left[\phi_y K_o + (\phi_{\max} - \phi_y)R_p K_o - M_E\right] - (\phi_{\max} - \phi_E)M_E - 0.5\phi_E M_E \\
= \; & 0.5(\phi_{\max} - \phi_y)^2 R_p K_o + \phi_{\max}\phi_y K_o - \phi_y^2 K_o + 0.5\phi_y^2 K_o \\
& - 0.5\left\{\phi_{\max}\phi_y K_o + \phi_{\max}(\phi_{\max} - \phi_y)R_p K_o - \phi_{\max} M_E - \phi_E\left[\phi_y K_o + (\phi_{\max} - \phi_y)R_p K_o\right] + \phi_E M_E\right\} \\
& - \phi_{\max} M_E + \phi_E M_E - 0.5\phi_E M_E \\
= \; & 0.5(\phi_{\max} - \phi_y)^2 R_p K_o + \phi_{\max}\phi_y K_o - 0.5\phi_y^2 K_o - 0.5\phi_{\max}\phi_y K_o - 0.5\phi_{\max}(\phi_{\max} - \phi_y)R_p K_o \\
& + 0.5\phi_{\max} M_E + 0.5\phi_E\left[\phi_y K_o + (\phi_{\max} - \phi_y)R_p K_o\right] - \phi_{\max} M_E \\
= \; & 0.5(\phi_{\max} - \phi_y)R_p K_o(\phi_{\max} - \phi_y - \phi_{\max}) + 0.5\phi_{\max}\phi_y K_o - 0.5\phi_y^2 K_o - 0.5\phi_{\max} M_E \\
& + 0.5\phi_E\left[\phi_y K_o + (\phi_{\max} - \phi_y)R_p K_o\right] \\
= \; & -0.5\phi_y R_p K_o(\phi_{\max} - \phi_y) + 0.5\phi_{\max}\phi_y K_o - 0.5\phi_y^2 K_o - 0.5\phi_{\max}\left(\frac{M_u}{\phi_u}\right)\phi_E \\
& + 0.5\phi_E\left[\phi_y K_o + (\phi_{\max} - \phi_y)R_p K_o\right] \\
= \; & -0.5\phi_y R_p K_o(\phi_{\max} - \phi_y) + 0.5\phi_{\max}\phi_y K_o - 0.5\phi_y^2 K_o \\
& + 0.5\phi_E\left[\phi_y K_o + (\phi_{\max} - \phi_y)R_p K_o - \phi_{\max}\left(\frac{M_u}{\phi_u}\right)\right]
\end{aligned}
\qquad \text{(D-13)}
$$

Substituting Eq. (D-6) into Eq. (D-13):

$$
\begin{aligned}
& D_s + D_d \\
= \; & -0.5\phi_y R_p K_o(\phi_{\max} - \phi_y) + 0.5\phi_{\max}\phi_y K_o - 0.5\phi_y^2 K_o \\
& + 0.5\phi_E\left[\phi_y K_o + \phi_y R_p K_o(\mu_{\max} - 1) - \phi_y \mu_{\max}\left(\mu_u^{-1} K_o + (1 - \mu_u^{-1})R_p K_o\right)\right] \\
= \; & 0.5\phi_y K_o\left\{\phi_{\max} - R_p(\phi_{\max} - \phi_y) - \phi_y + \phi_E\left[1 + R_P(\mu_{\max} - 1) - \mu_{\max}\left(\mu_u^{-1} + (1 - \mu_u^{-1})R_p\right)\right]\right\}
\end{aligned}
\qquad \text{(C-14)}
$$

Substituting Eq. (D-7) into Eq. (D-14):

$$
\begin{aligned}
& D_s + D_d \\
= \; & 0.5\phi_u K_o\left\{(\phi_{\max} - \phi_y)(1 - R_p)\right. \\
& \left. + \frac{\phi_y\left[1 + (\mu_{\max} - 1)R_p - \phi_y \mu_{\max}^{-1}\right]}{R_p + (1 - R_p)\mu_u^{-1} - \mu_{\max}^{-\alpha}}\left(1 + R_p\mu_{\max} - R_p - \mu_{\max}\mu_u^{-1} - \mu_{\max}R_p + \mu_{\max}\mu_u^{-1}R_p\right)\right\}
\end{aligned}
$$

$$= 0.5\phi_y^2 K_o \left\{ (\mu_{\max}-1)(1-R_p) + \frac{\left[1+(\mu_{\max}-1)R_p - \phi_y \mu_{\max}^{-1}\right]}{R_p + (1-R_p)\mu_u^{-1} - \mu_{\max}^{-\alpha}} \left[(1-R_p) - \mu_{\max}\mu_u^{-1}(1-R_p)\right] \right\}$$

$$= 0.5\phi_y^2 K_o (1-R_p) \left\{ \mu_{\max} - 1 + \frac{\left[1+(\mu_{\max}-1)R_p - \phi_y \mu_{\max}^{-1}\right](1-\mu_{\max}\mu_u^{-1})}{R_p + (1-R_p)\mu_u^{-1} - \mu_{\max}^{-\alpha}} \right\}$$

$$= 0.5\phi_y^2 K_o (1-R_p) *$$

$$\left[\frac{\mu_{\max}R_p + (1-R_p)\mu_{\max}\mu_u^{-1} - \mu_{\max}^{1-\alpha} - R_p - (1-R_p)\mu_u^{-1} + \mu_{\max}^{-\alpha}}{+1+\mu_{\max}R_p - R_p - \phi_y\mu_{\max}^{-1} - \mu_{\max}\mu_u^{-1} - (\mu_{\max}-1)R_p\mu_{\max}\mu_u^{-1} + \phi_y\mu_u^{-1}} \right]$$
$$R_p + (1-R_p)\mu_u^{-1} - \mu_{\max}^{-\alpha}$$

$$= 0.5\phi_y^2 K_o (1-R_p) *$$

$$\left[\frac{\mu_{\max}R_p + \mu_{\max}\mu_u^{-1} - R_p\mu_{\max}\mu_u^{-1} - \mu_{\max}^{1-\alpha} - R_p - \mu_u^{-1} + R_p\mu_u^{-1} + \mu_{\max}^{-\alpha}}{+1+\mu_{\max}R_p - R_p - \phi_y\mu_{\max}^{-1} - \mu_{\max}\mu_u^{-1} - R_p\mu_{\max}^2\mu_u^{-1} + R_p\mu_{\max}\mu_u^{-1} + \phi_y\mu_u^{-1}} \right]$$
$$R_p + (1-R_p)\mu_u^{-1} - \mu_{\max}^{-\alpha}$$

$$= 0.5\phi_y^2 K_o (1-R_p) *$$

$$\left[\frac{2\mu_{\max}R_p - \mu_{\max}^{1-\alpha} - 2R_p - \mu_u^{-1} + R_p\mu_u^{-1} + \mu_{\max}^{-\alpha} + 1 - \phi_y\mu_{\max}^{-1} - \mu_{\max}^2 R_p\mu_u^{-1} + \phi_y\mu_u^{-1}}{R_p + (1-R_p)\mu_u^{-1} - \mu_{\max}^{-\alpha}} \right]$$

$$= 0.5\phi_y^2 K_o (1-R_p) *$$

$$\left[\frac{2R_p(\mu_{\max}-1) - \mu_{\max}^{-\alpha}(\mu_{\max}-1) - \mu_u^{-1}(1-R_p) + 1 - \phi_y\mu_{\max}^{-1} - \mu_{\max}^2 R_p\mu_u^{-1} + \phi_y\mu_u^{-1}}{R_p + (1-R_p)\mu_u^{-1} - \mu_{\max}^{-\alpha}} \right] \quad \text{(D-15)}$$

From Eqs. (D-1) and (D-15) the Bracci damage index with simple fatigue line assumption for modified Takeda hysteresis model is obtained as follows:

$$DI = \frac{D_s + D_d}{D_p}$$

$$= \frac{0.5\phi_y^2 K_o (1-R_p)}{0.5(1-R_p)K_o\phi_y^2(\mu_u - 1)} *$$

$$\left[\frac{2R_p(\mu_{\max}-1) - \mu_{\max}^{-\alpha}(\mu_{\max}-1) - \mu_u^{-1}(1-R_p) + 1 - \phi_y\mu_{\max}^{-1} - \mu_{\max}^2 R_p\mu_u^{-1} + \phi_y\mu_u^{-1}}{R_p + (1-R_p)\mu_u^{-1} - \mu_{\max}^{-\alpha}} \right]$$

$$= \frac{(\mu_{\max}-1)(2R_p-\mu_{\max}^{-\alpha})-\mu_u^{-1}(1-R_p)+1+\phi_y(\mu_u^{-1}-\mu_{\max}^{-1})-\mu_{\max}^2 R_p\mu_u^{-1}}{(\mu_u-1)[R_p+(1-R_p)\mu_u^{-1}-\mu_{\max}^{-\alpha}]} \quad \text{(D-16)}$$

Let $R_p = \alpha = 0.0$ the Bracci damage index for Elasto-plastic model is obtained from Eq. (D-16).

$$DI = \frac{(\mu_{\max}-1)(-1)-\mu_u^{-1}+1+\phi_y(\mu_u^{-1}-\mu_{\max}^{-1})}{(\mu_u-1)(\mu_u^{-1}-1)} = \frac{-\mu_{\max}+1-\mu_u^{-1}+1+\phi_y(\mu_u^{-1}-\mu_{\max}^{-1})}{(\mu_u-1)(\mu_u^{-1}-1)}$$

$$= \frac{2+(\phi_y-1)\mu_u^{-1}-\mu_{\max}+\phi_y\mu_{\max}^{-1}}{(\mu_u-1)(\mu_u^{-1}-1)} \quad \text{(D-17)}$$

For the Origin-centred bilinear hysteresis model:

Damage potential D_p for the modified Takeda and Origin-centred models is the same defined using Eq. (D-1). There is no inelastic permanent deformation damage D_d for the Origin-centred model as shown in Fig. D-1b.

$$D_s + D_d = D_s = A_{ACGO} - A_{OCG} \quad \text{(D-18)}$$

where

$$A_{ACGO} = 0.5(\phi_{\max}-\phi_y)^2 R_p K_o + (\phi_{\max}-\phi_y)\phi_y K_o + 0.5\phi_y^2 K_0 \quad \text{(D-19)}$$

$$A_{OCG} = 0.5\phi_{\max} M_{\max}$$

$$= 0.5\phi_{\max}(\phi_y K_o + \phi_{\max} R_p K_o - \phi_y R_p K_o) \quad \text{(D-20)}$$

Substituting Eqs. (D-19) and (D-20):

$$D_s + D_d = D_s = A_{ACGO} - A_{OCG}$$

$$= 0.5\phi_{\max}^2 R_p K_o - \phi_{\max}\phi_y R_p K_o + 0.5\phi_y^2 R_p K_o + \phi_{\max}\phi_y K_o - \phi_y^2 K_o + 0.5\phi_y^2 K_o$$

$$-0.5\phi_{\max}\phi_y K_o - 0.5\phi_{\max}^2 R_p K_o + 0.5\phi_{\max}\phi_y R_p K_o$$

$$= -0.5\phi_{\max}\phi_y R_p K_o + 0.5\phi_y^2 R_p K_o + 0.5\phi_{\max}\phi_y K_o - 0.5\phi_y^2 K_o$$

$$= 0.5K_o\phi_y(\phi_y R_p + \phi_{\max} - \phi_{\max} R_p - \phi_y) \quad \text{(D-21)}$$

The Bracci damage index with simple line fatigue failure assumption for Origin-centred hysteresis model can be obtained with Eq. (D-1) and (D-21) for potential damage and the strength damage respectively:

$$DI = \frac{D_s + D_d}{D_p} = \frac{0.5K_o\phi_y\left(\phi_y R_p + \phi_{\max} - \phi_{\max} R_p - \phi_y\right)}{0.5K_o\phi_y\left(1-R_p\right)\left(\phi_u - \phi_y\right)}$$

$$= \frac{\left(R_p - 1\right)\phi_y + \phi_{\max}\left(1-R_p\right)}{\left(1-R_p\right)\left(\phi_u - \phi_y\right)}$$

$$= \frac{\phi_{\max} - \phi_y}{\phi_u - \phi_y} = \frac{\mu_{\max} - 1}{\mu_u - 1} \qquad \text{(D-22)}$$

APPENDIX E
Derivation of the Bracci damage index for modified Takeda and Origin-Centred bilinear hysteresis models with transposed bilinear fatigue failure assumption

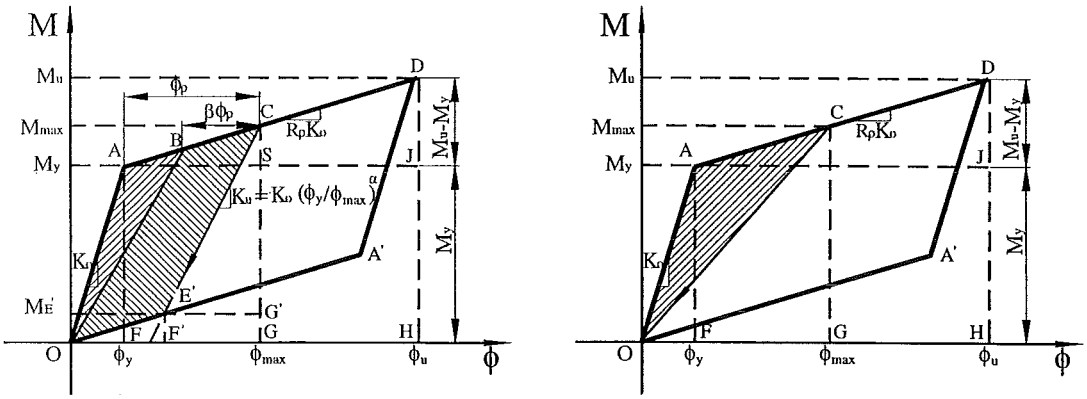

a) Modified Takeda hysteresis model

b) Origin-centred bilinear hysteresis model

Fig. E-1 The Bracci damage index for modified Takeda and Origin-centred bilinear hysteresis models with transposed bilinear fatigue failure assumption

For modified Takeda hysteresis model.

The damage potential is the quadrilateral area $A_{OADA'}$ shown in Fig. E-1, which is two times the triangle area A_{OAD} obtained from Eq. D-1 in Appedix-D:

$$D_p = 2A_{OAD}$$
$$= (1-R_p)K_o\phi_y^2(\mu_u - 1) \qquad \text{(E-1)}$$

where ϕ_y yielding curvature.

ϕ_u ultimate curvature capacity.

K_o initial stiffness.

R_p ratio of post yielding stiffness to initial stiffness.

μ_u ultimate curvature ductility capacity.

The coordinate for point E' shown in Fig. E-1a should be derived for calculation of the hatched area, i.e sum of the strength and deformation damage. The function for line EC has been derived in Appendix-D, which is shown again below for convenience.

$$M = K_o(\phi_y / \phi_{\max})^{\alpha}\left(\phi - \phi_{\max} + \frac{M_{\max}}{K_o(\phi_y / \phi_{\max})^{\alpha}}\right) \tag{E-2}$$

The function for line OA' of same slope as line AD is expressed by Eq. (E-3):

$$M = R_p K_o \phi \tag{E-3}$$

The coordinate $(M_{E'},\ \phi_{E'})$ at point E' should satisfy the two Eqs (E-2) and (E-3), hence

$$R_p K_o \phi_{E'} = K_o(\phi_y / \phi_{\max})^{\alpha}\left(\phi_{E'} - \phi_{\max} + \frac{M_{\max}}{K_o(\phi_y / \phi_{\max})^{\alpha}}\right)$$

$$\phi_{E'} = \frac{M_{\max} - \phi_{\max} K_o\left(\phi_y / \phi_{\max}\right)^{\alpha}}{K_o\left[R_p - \left(\phi_y / \phi_{\max}\right)^{\alpha}\right]} \tag{E-4}$$

Substituting $M_{\max} = K_o\phi_y + (\mu_{\max}\phi_y - \phi_y)R_p K_o = K_o\phi_y[1 + (\mu_{\max} - 1)R_p]$ (E-5)

and $\phi_{\max} = \mu_{\max}\phi_y$ (E-6)

into Eq. (E-4):

$$\phi_{E'} = \frac{\phi_y[1 + (\mu_{\max} - 1)R_p - \mu_{\max}^{1-\alpha}]}{(R_p - \mu_{\max}^{-\alpha})} \tag{E-7}$$

The strength and deformation damage is the hatched area $A_{OACE'}$:

$$D_s + D_d = A_{OACE'} = A_{OACG} - (A_{E'CG'} + A_{E'G'GF'} + A_{OE'F'}) \tag{E-8}$$

where $A_{OACG} = A_{ACS} + A_{ASGF} + A_{OAF}$

$$= 0.5(\phi_{\max} - \phi_y)R_p K_o(\phi_{\max} - \phi_y) + (\phi_{\max} - \phi_y)K_o\phi_y + 0.5\phi_y K_o\phi_y$$

$$= 0.5R_p K_o(\phi_{\max} - \phi_y)^2 + \phi_{\max}K_o\phi_y - \phi_y^2 K_o + 0.5K_o\phi_y^2$$

$$= 0.5R_p K_o(\phi_{\max} - \phi_y)^2 + \phi_{\max}K_o\phi_y - 0.5\phi_y^2 K_o \tag{E-9}$$

$$
\begin{aligned}
&A_{E'CG'} + A_{E'G'GF'} + A_{OE'F'} \\
&= 0.5(\phi_{\max} - \phi_{E'})(M_{\max} - M_{E'}) + (\phi_{\max} - \phi_{E'})M_{E'} + 0.5\phi_{E'}M_{E'} \\
&= (\phi_{\max} - \phi_{E'})(0.5M_{\max} - 0.5M_{E'} + M_{E'}) + 0.5\phi_{E'}M_{E'} \\
&= 0.5\phi_{\max}M_{\max} + 0.5\phi_{\max}M_{E'} - 0.5\phi_{E'}M_{\max} - 0.5\phi_{E'}M_{E'} + 0.5\phi_{E'}M_{E'} \\
&= 0.5\phi_{\max}M_{\max} + 0.5\phi_{\max}R_pK_o\phi_{E'} - 0.5\phi_{E'}M_{\max} \\
&= 0.5\phi_{\max}M_{\max} - 0.5\phi_{E'}(M_{\max} - \phi_{\max}R_pK_o)
\end{aligned} \tag{E-10}
$$

Substituting Eq. (E-5) and (E-6) into Eq. (E-10):

$$
\begin{aligned}
&A_{E'CG'} + A_{E'G'GF'} + A_{OE'F'} \\
&= 0.5\mu_{\max}\phi_yK_o\phi_y[1 + (\mu_{\max} - 1)R_p] - 0.5\phi_{E'}\{K_o\phi_y[1 + (\mu_{\max} - 1)R_p] - \mu_{\max}\phi_yR_pK_o\} \\
&= 0.5\mu_{\max}\phi_y^2\ K_o[1 + (\mu_{\max} - 1)R_p] - 0.5\phi_{E'}\{K_o\phi_y(1 + \mu_{\max}R_p - R_p - \mu_{\max}R_p)\} \\
&= 0.5\mu_{\max}\phi_y^2\ K_o[1 + (\mu_{\max} - 1)R_p] - 0.5\phi_{E'}K_o\phi_y(1 - R_p)
\end{aligned} \tag{E-11}
$$

Substituting Eqs. (E-9) and (E-11) into Eq. (E-8):

$$
\begin{aligned}
&D_s + D_d = A_{OACE'} = A_{OACG} - (A_{E'CG'} + A_{E'G'GF'} + A_{OE'F'}) \\
&= 0.5R_pK_o\phi_y^2(\mu_{\max} - 1)^2 + \phi_{\max}K_o\phi_y - 0.5\phi_y^2K_o \\
&- 0.5\mu_{\max}\phi_y^2\ K_o[1 + (\mu_{\max} - 1)R_p] + 0.5\phi_{E'}K_o\phi_y(1 - R_p)
\end{aligned} \tag{E-12}
$$

Substituting Eq. (E-7) into Eq. (E-12):

$$
\begin{aligned}
&D_s + D_d = A_{OACE'} = A_{OACG} - (A_{E'CG'} + A_{E'G'GF'} + A_{OE'F'}) \\
&= 0.5R_pK_o\phi_y^2(\mu_{\max} - 1)^2 + \mu_{\max}\phi_yK_o\phi_y - 0.5\phi_y^2K_o \\
&- 0.5\mu_{\max}\phi_y^2K_o[1 + (\mu_{\max} - 1)R_p] + 0.5K_o\phi_y(1 - R_p)\frac{\phi_y[1 + (\mu_{\max} - 1)R_p - \mu_{\max}^{1-\alpha}]}{(R_p - \mu_{\max}^{-\alpha})}
\end{aligned} \tag{E-13}
$$

Finally substituting Eqs. (E-1) and (E-13) into $DI = \dfrac{D_s + D_d}{D_p}$, the damage is obtained as follows:

$$DI = \frac{D_s + D_d}{K_o \phi_y^2 (1 - R_p)(\mu_u - 1)}$$

$$= \frac{0.5R_p(\mu_{\max} - 1)^2 + \mu_{\max} - 0.5 - 0.5\mu_{\max}\left[1 + (\mu_{\max} - 1)R_p\right]}{(1 - R_p)(\mu_u - 1)} + \frac{0.5 * \left[1 + (\mu_{\max} - 1)R_p - \mu_{\max}^{1-\alpha}\right]}{(R_p - \mu_{\max}^{-\alpha})(\mu_u - 1)}$$

$$= \frac{0.5R_p(\mu_{\max}^2 - 2\mu_{\max} + 1) + \mu_{\max} - 0.5 - 0.5\mu_{\max} - 0.5\mu_{\max}^2 R_p + 0.5\mu_{\max} R_p}{(1 - R_p)(\mu_u - 1)}$$

$$+ \frac{0.5 * \left[1 + (\mu_{\max} - 1)R_p - \mu_{\max}^{1-\alpha}\right]}{(R_p - \mu_{\max}^{-\alpha})(\mu_u - 1)}$$

$$= \frac{0.5R_p\mu_{\max}^2 - R_p\mu_{\max} + 0.5R_p + \mu_{\max} - 0.5 - 0.5\mu_{\max} - 0.5\mu_{\max}^2 R_p + 0.5\mu_{\max} R_p}{(1 - R_p)(\mu_u - 1)}$$

$$+ \frac{0.5 * \left[1 + (\mu_{\max} - 1)R_p - \mu_{\max}^{1-\alpha}\right]}{(R_p - \mu_{\max}^{-\alpha})(\mu_u - 1)}$$

$$= \frac{-0.5R_p\mu_{\max} + 0.5\mu_{\max} + 0.5R_p - 0.5}{(1 - R_p)(\mu_u - 1)} + \frac{0.5 * \left[1 + (\mu_{\max} - 1)R_p - \mu_{\max}^{1-\alpha}\right]}{(R_p - \mu_{\max}^{-\alpha})(\mu_u - 1)}$$

$$= \frac{0.5\mu_{\max}(1 - R_p) - 0.5(1 - R_p)}{(1 - R_p)(\mu_u - 1)} + \frac{0.5 * \left[1 + (\mu_{\max} - 1)R_p - \mu_{\max}^{1-\alpha}\right]}{(R_p - \mu_{\max}^{-\alpha})(\mu_u - 1)}$$

$$= \frac{0.5(\mu_{\max} - 1)}{\mu_u - 1} + \frac{0.5 * \left[1 + (\mu_{\max} - 1)R_p - \mu_{\max}^{1-\alpha}\right]}{(R_p - \mu_{\max}^{-\alpha})(\mu_u - 1)}$$

$$= \frac{0.5(\mu_{\max} - 1)(R_p - \mu_{\max}^{-\alpha}) + 0.5 + 0.5\mu_{\max} R_p - 0.5R_p - 0.5\mu_{\max}^{1-\alpha}}{(R_p - \mu_{\max}^{-\alpha})(\mu_u - 1)}$$

$$= \frac{0.5\mu_{\max} R_p - 0.5\mu_{\max}^{1-\alpha} - 0.5R_p + 0.5\mu_{\max}^{-\alpha} + 0.5 + 0.5\mu_{\max} R_p - 0.5R_p - 0.5\mu_{\max}^{1-\alpha}}{(R_p - \mu_{\max}^{-\alpha})(\mu_u - 1)}$$

$$= \frac{R_p\mu_{\max} - \mu_{\max}^{1-\alpha} + 0.5\mu_{\max}^{-\alpha} - R_p + 0.5}{(R_p - \mu_{\max}^{-\alpha})(\mu_u - 1)} \qquad \text{(E-14)}$$

Let $R_p = \alpha = 0.0$ the Bracci damage index for the Elasto-plastic hysteresis model is obtained from Eq. (E-14).

$$DI = \frac{\mu_{\max} - 1}{\mu_u - 1} \qquad \text{(E-15)}$$

Let $\alpha = 0.0$ the Bracci damage index for the Bilinear and Clough hysteresis models is obtained from Eq. (E-14).

$$DI = \frac{R_p\mu_{\max} - \mu_{\max}^{1-\alpha} + 0.5\mu_{\max}^{-\alpha} - R_p + 0.5}{(R_p - \mu_{\max}^{-\alpha})(\mu_u - 1)}$$

$$= \frac{R_p\mu_{\max} - \mu_{\max} - R_p + 1}{(R_p - 1)(\mu_u - 1)}$$

$$= \frac{\mu_{\max}(R_p - 1) - (R_p - 1)}{(R_p - 1)(\mu_u - 1)}$$

$$= \frac{\mu_{\max} - 1}{\mu_u - 1} \qquad \text{(E-16)}$$

For the Origin-centred bilinear hysteresis model:

Damage potential D_p for the modified Takeda and Origin-centred bilinear hysteresis models is the same defined using Eq. (E-1). There is no inelastic permanent deformation damage D_d for the origin-centred hysteresis model as shown in Fig. E-1b. The strength damage for the Origin-centred hysteresis model for the transposed bilinear and triangular fatigue failure curve is equal, defined by Eq. (D-21) in Appendix-D. Hence the Bracci damage index for the Origin-centred hysteresis model with the transposed bilinear fatigue failure curve assumption is obtained:

$$DI = \frac{D_s + D_d}{D_p} = \frac{D_s}{D_p}$$

$$= \frac{0.5K_o\phi_y(\phi_y R_p + \phi_{\max} - \phi_{\max}R_p - \phi_y)}{K_o\phi_y^2(1 - R_p)(\mu_u - 1)}$$

$$= \frac{0.5\phi_y(R_p + \mu_{\max} - \mu_{\max}R_p - 1)}{\phi_y(1 - R_p)(\mu_u - 1)}$$

$$= \frac{0.5[(1 - R_p)\mu_{\max} - (1 - R_p)]}{(1 - R_p)(\mu_u - 1)}$$

$$= \frac{0.5(\mu_{\max} - 1)}{\mu_u - 1} \qquad \text{(E-17)}$$

APPENDIX F

Storey shear V.S. storey displacement curves, lateral loading patterns and constrains for storey yield points of the 6-, 12- and 18-storey structures using the push over analysis

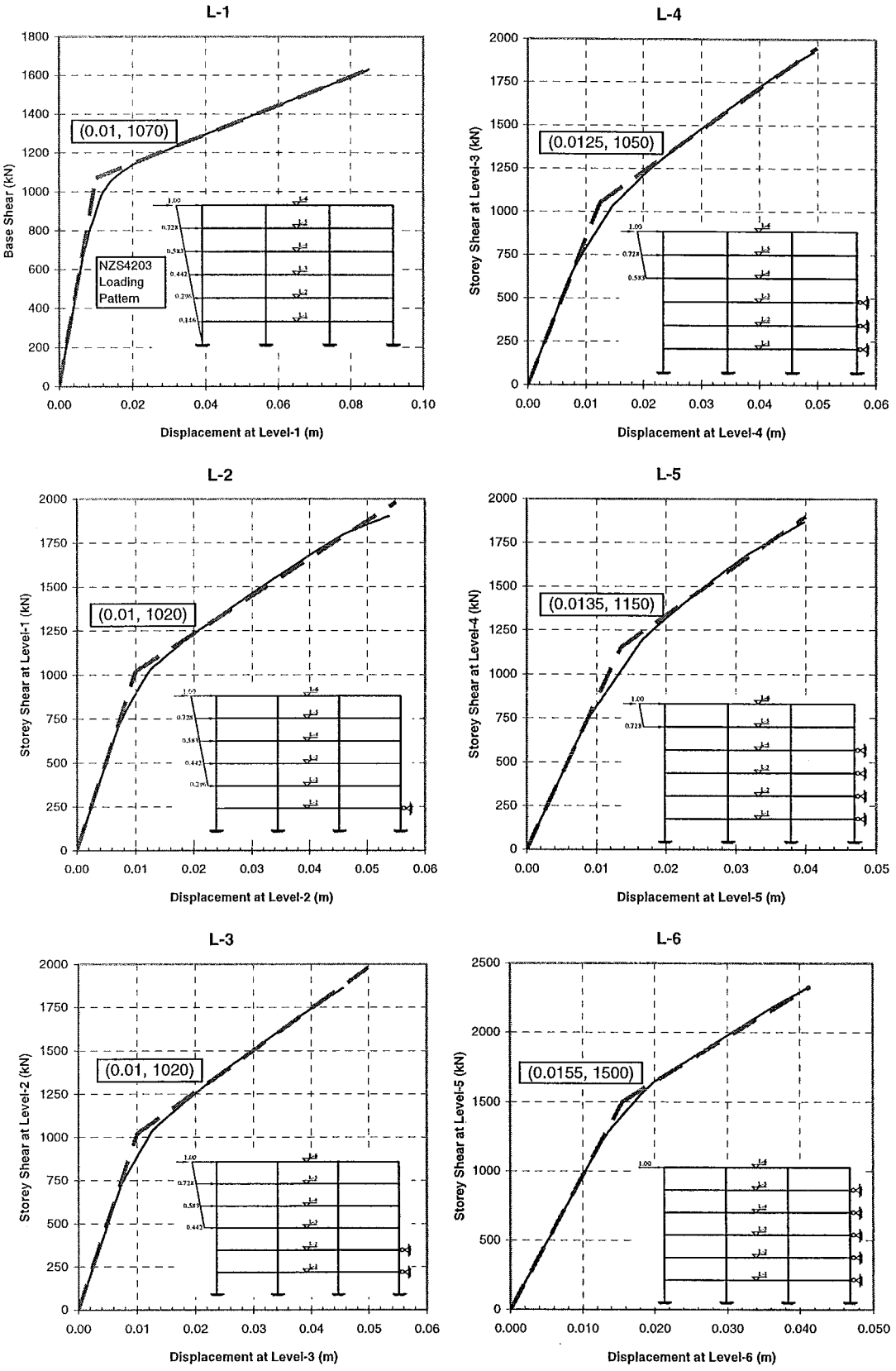

Fig. F-1 Storey shear V.S. storey displacement curves, lateral loading patterns and constrains for storey yield displacements of storeys 1~6 of 6 storey structure using the pushover analysis

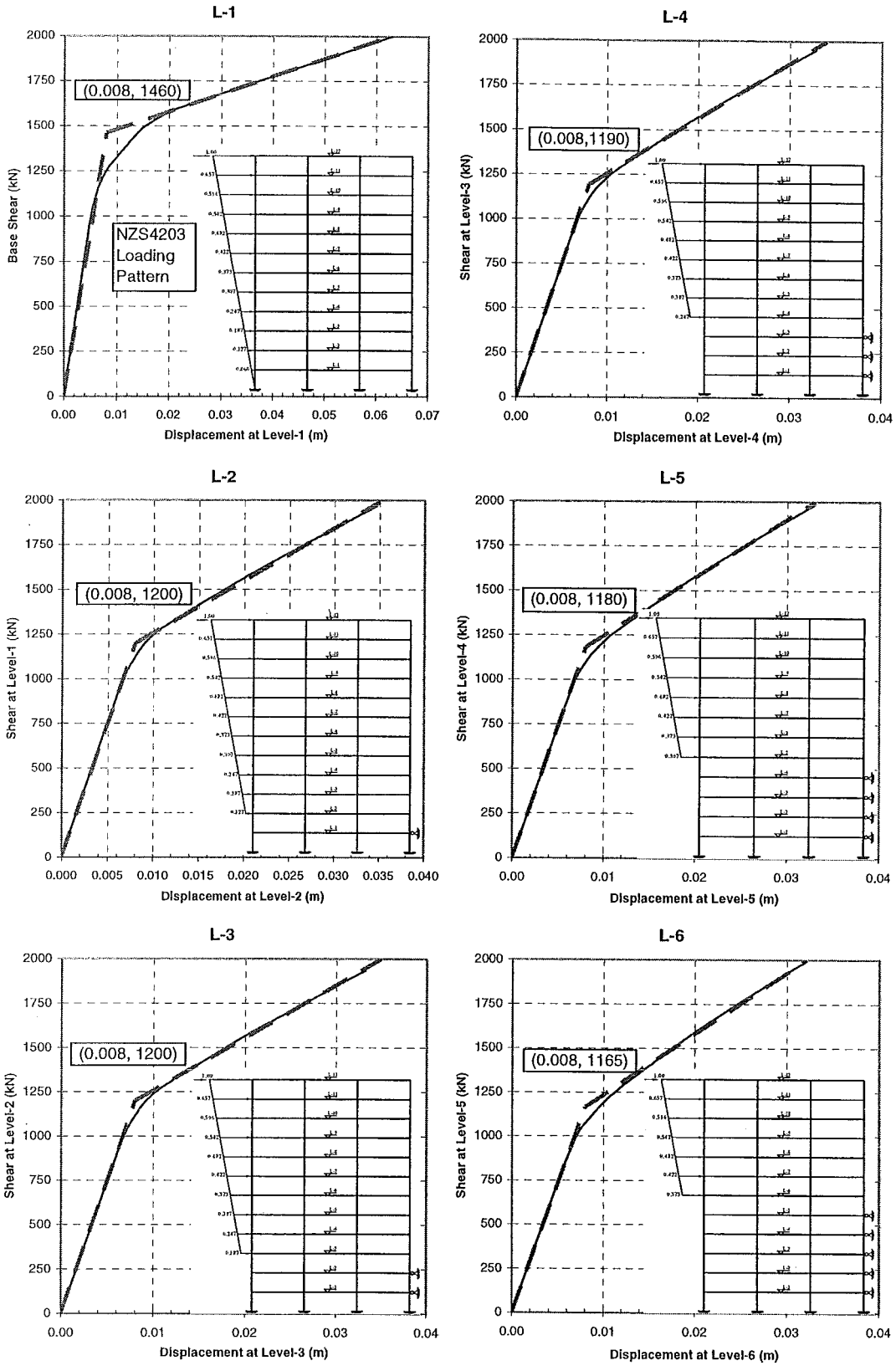

Fig. F-2 Storey shear V.S. storey displacement curves, lateral loading patterns and constrains for storey yield displacements of storeys 1~6 of 12 storey structure using the pushover analysis

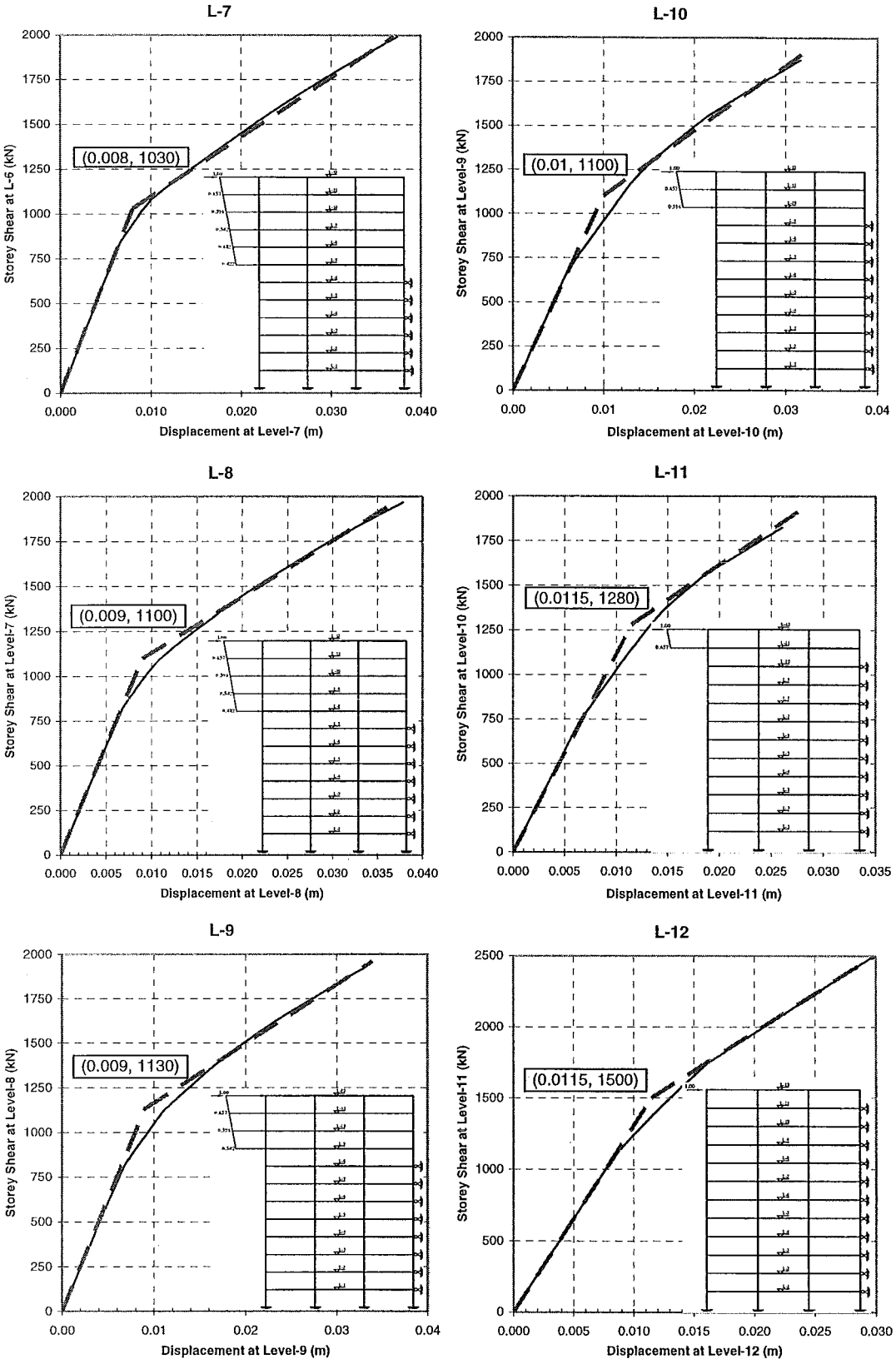

Fig. F-3 Storey shear V.S. storey displacement curves, lateral loading patterns and constrains for storey yield displacements of storeys 7~12 of 12 storey structure using the pushover analysis

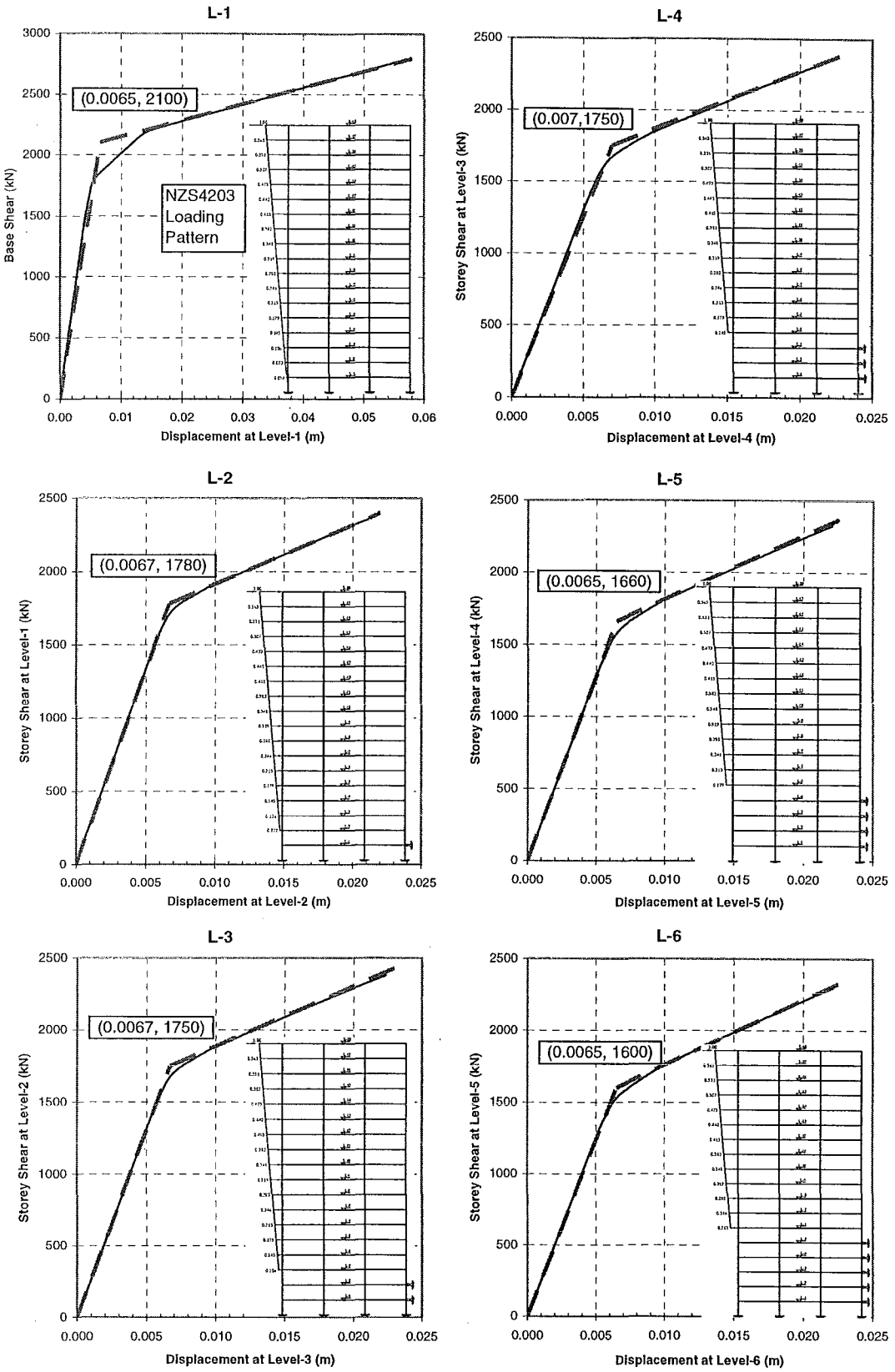

Fig. F-4 Storey shear V.S. storey displacement curves, lateral loading patterns and constrains for storey yield displacements of storeys 1~6 of 18 storey structure using the pushover analysis

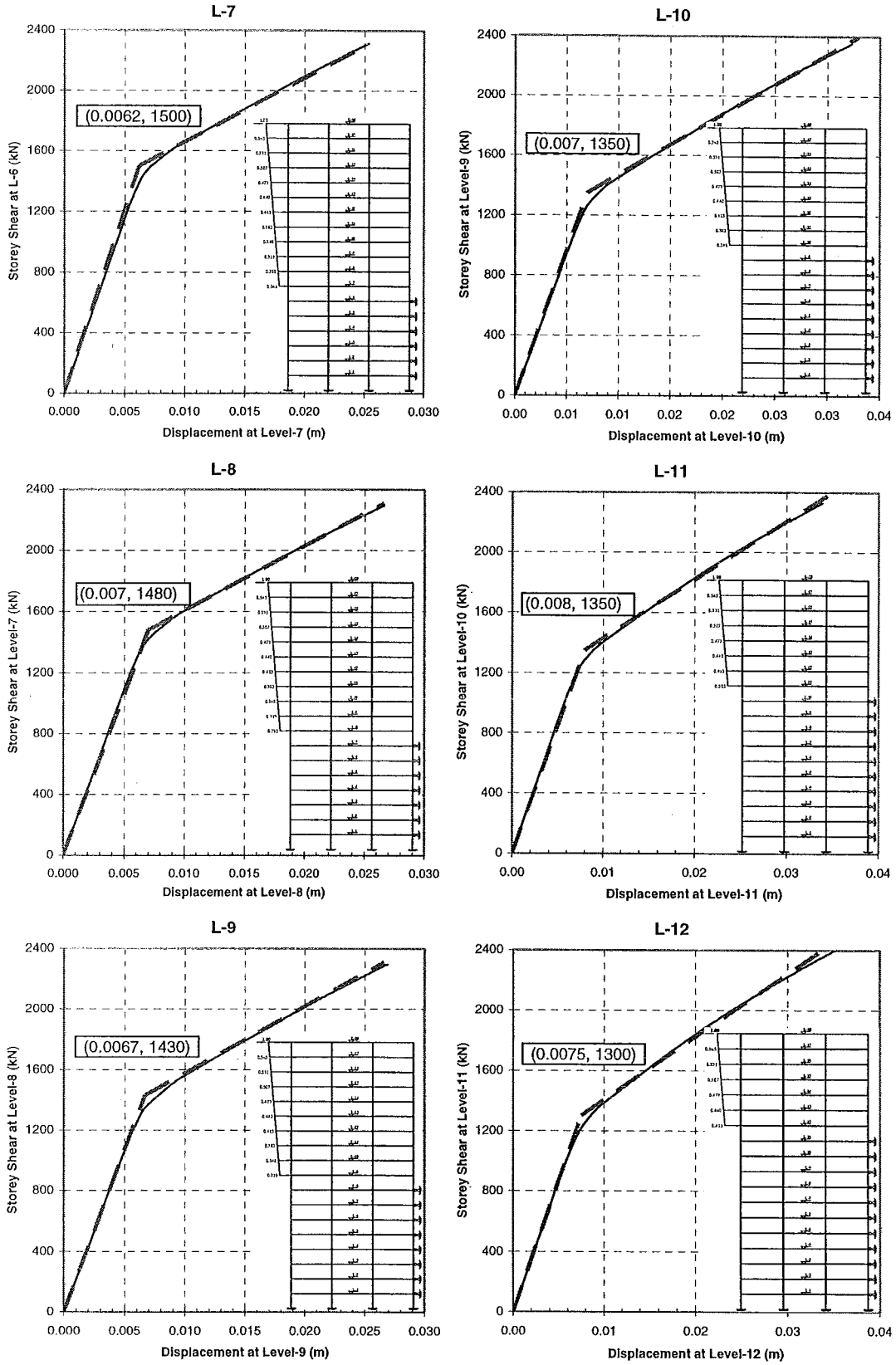

Fig. F-5 Storey shear V.S. storey displacement curves, lateral loading patterns and constrains for storey yield displacements of storeys 7~12 of 18 storey structure using the pushover analysis

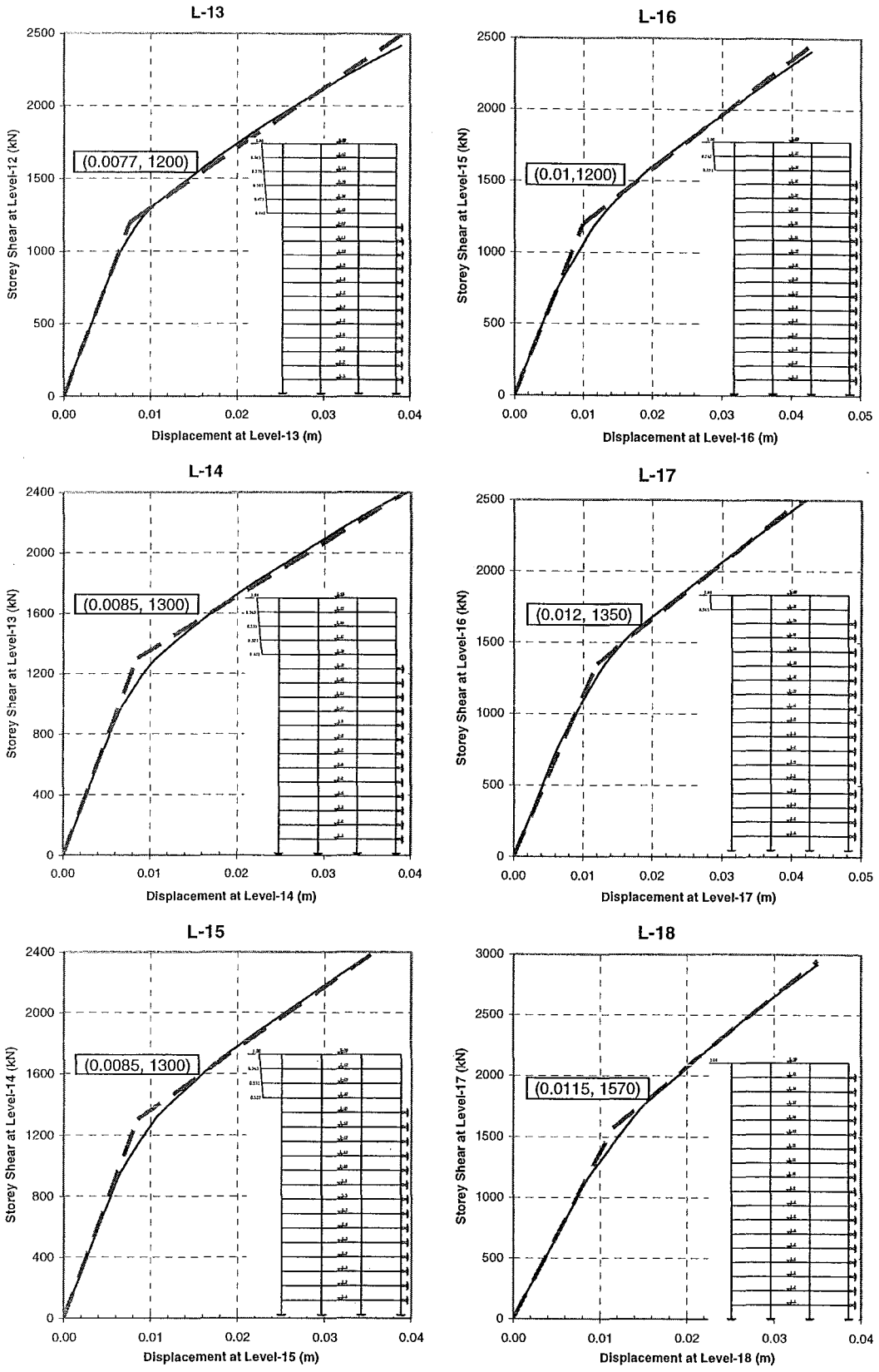

Fig. F-6 Storey shear V.S. storey displacement curves, lateral loading patterns and constrains for storey yield displacements of storeys 13~18 of 18 storey structure using the pushover analysis

APPENDIX G

Figures for overall structural and storey yield points of the three structures for the Carr & Tabuchi approach using each of the eight hysteresis models, and Tables G-1 to G-5

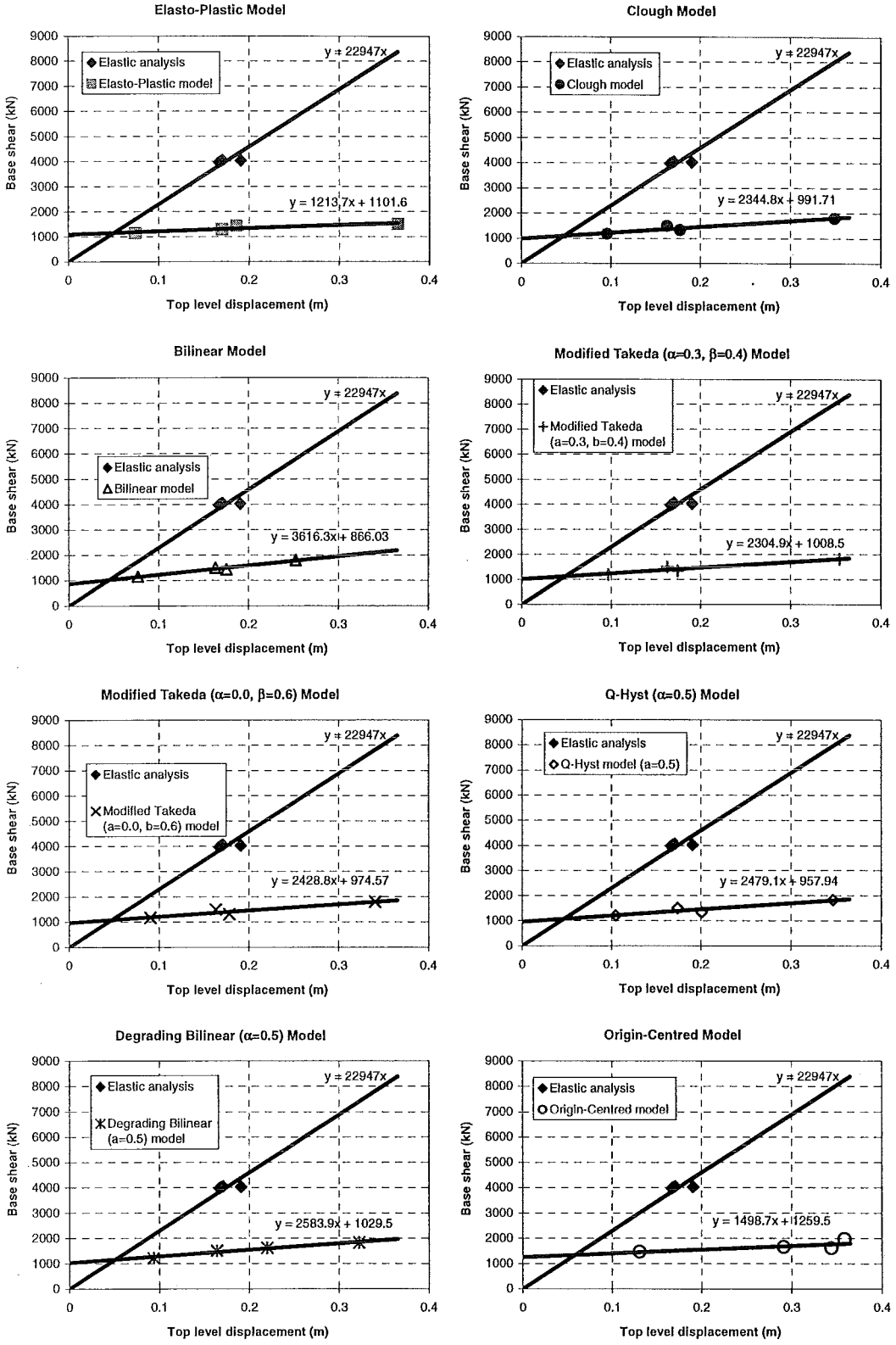

Fig. G-1 Overall structural yield point of 6 storey structure for Carr & Tabuchi method to the eight hysteresis models

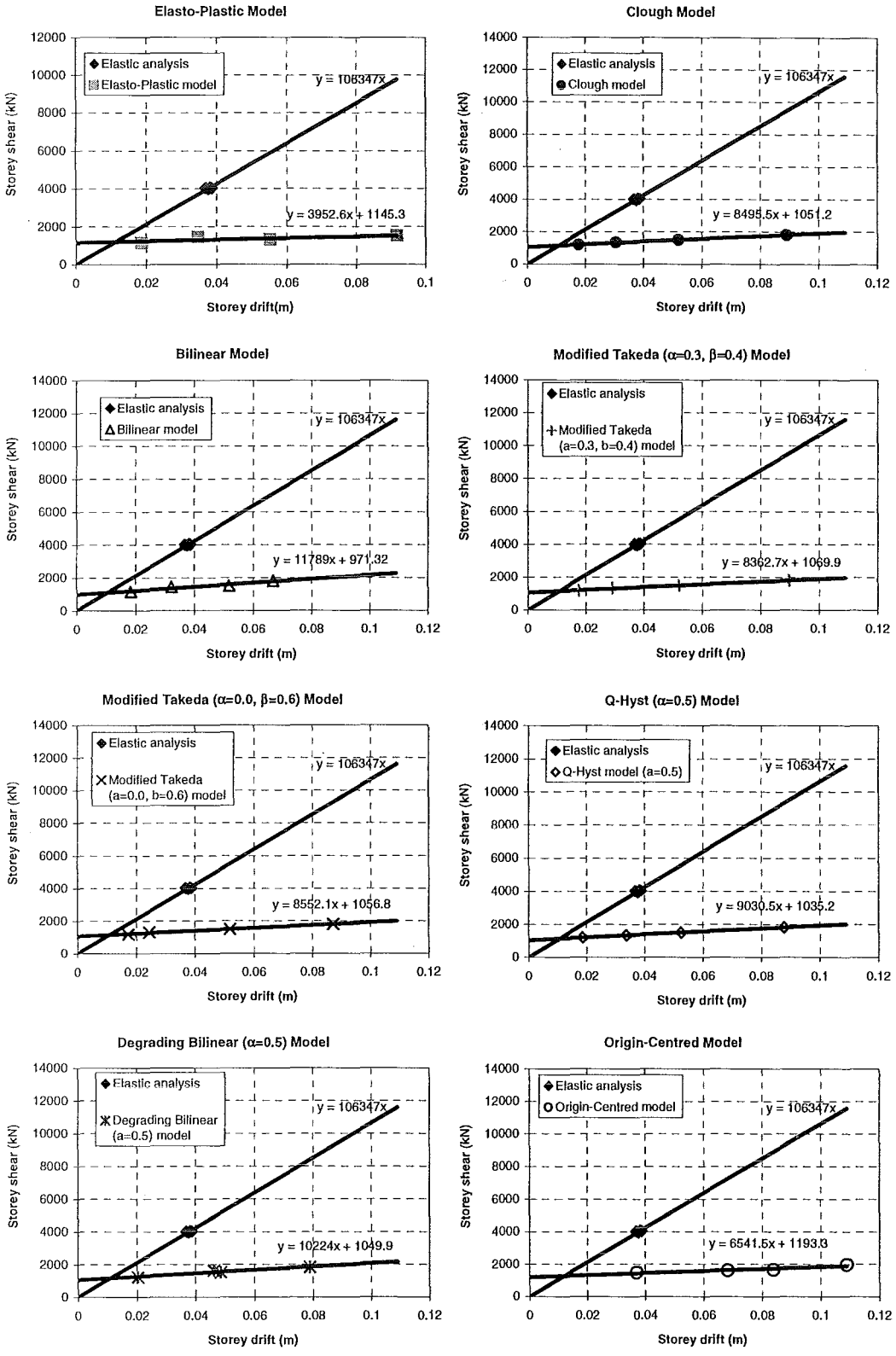

Fig. G-2 Storey yield point at level-1 of 6 storey structure for Carr & Tabuchi method to the eight hysteresis models

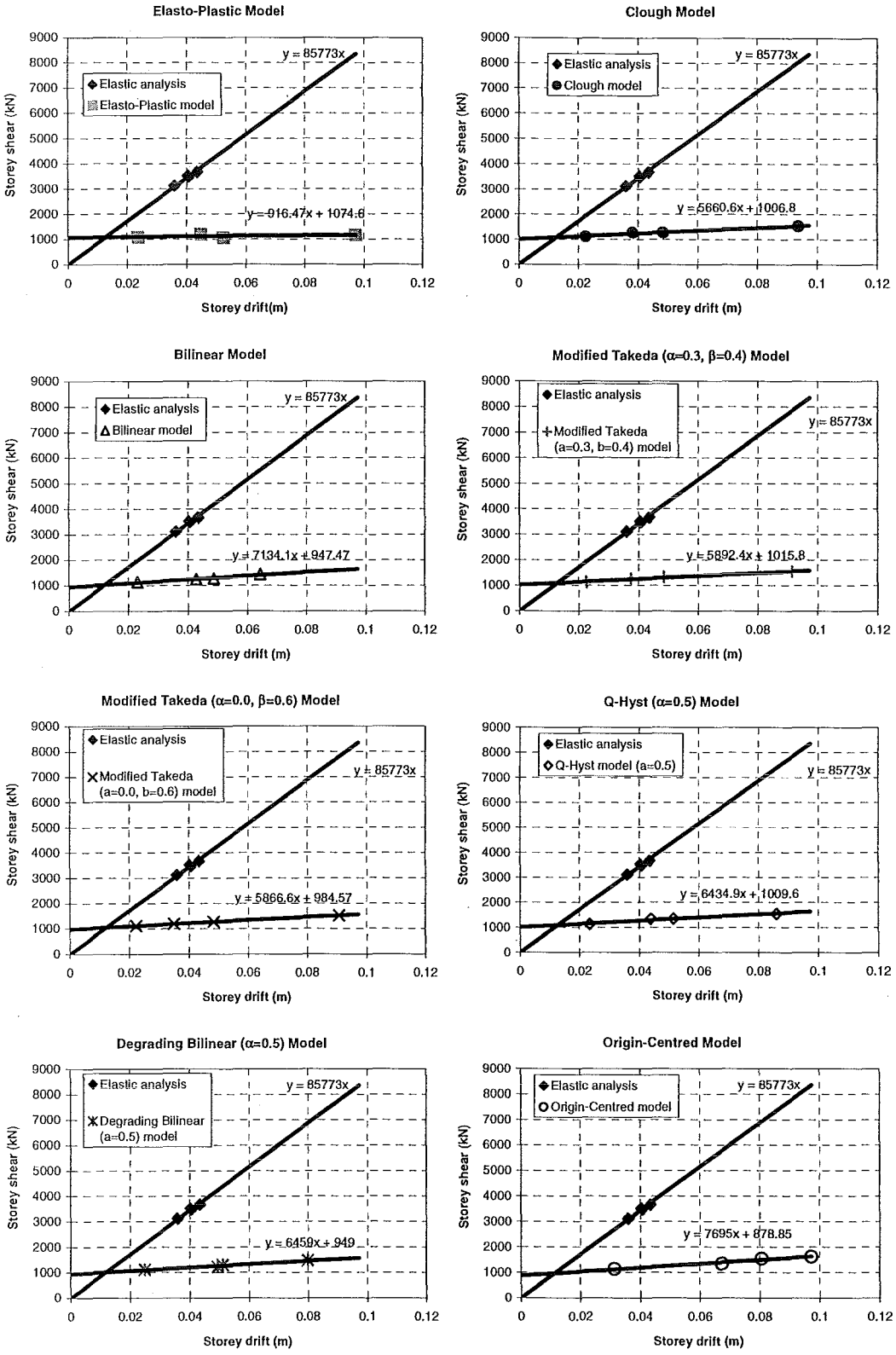

Fig. G-3 Storey yield point at level-2 of 6 storey structure for Carr & Tabuchi method to the eight hysteresis models

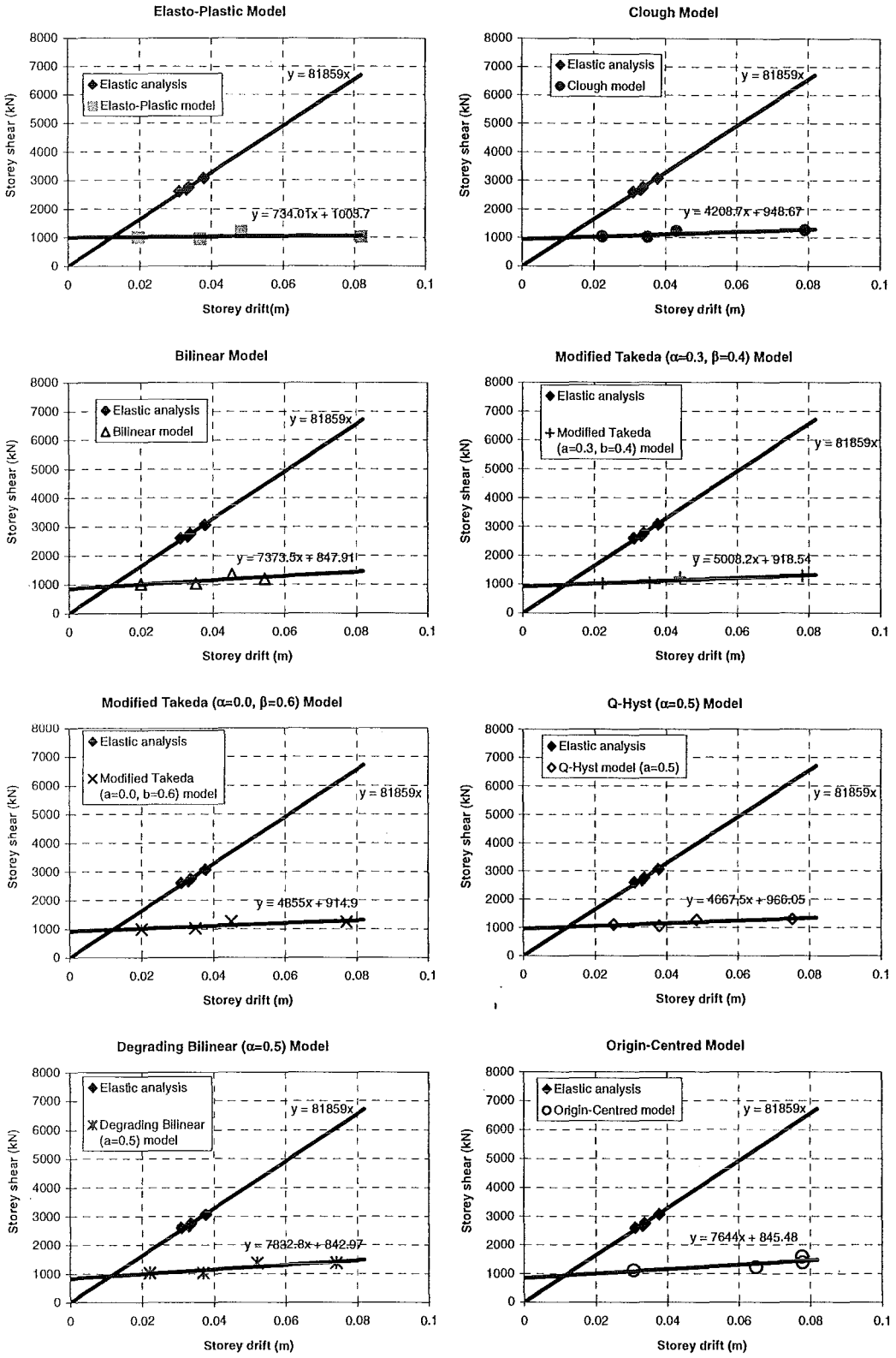

Fig. G-4 Storey yield point at level-3 of 6 storey structure for Carr & Tabuchi method to the eight hysteresis models

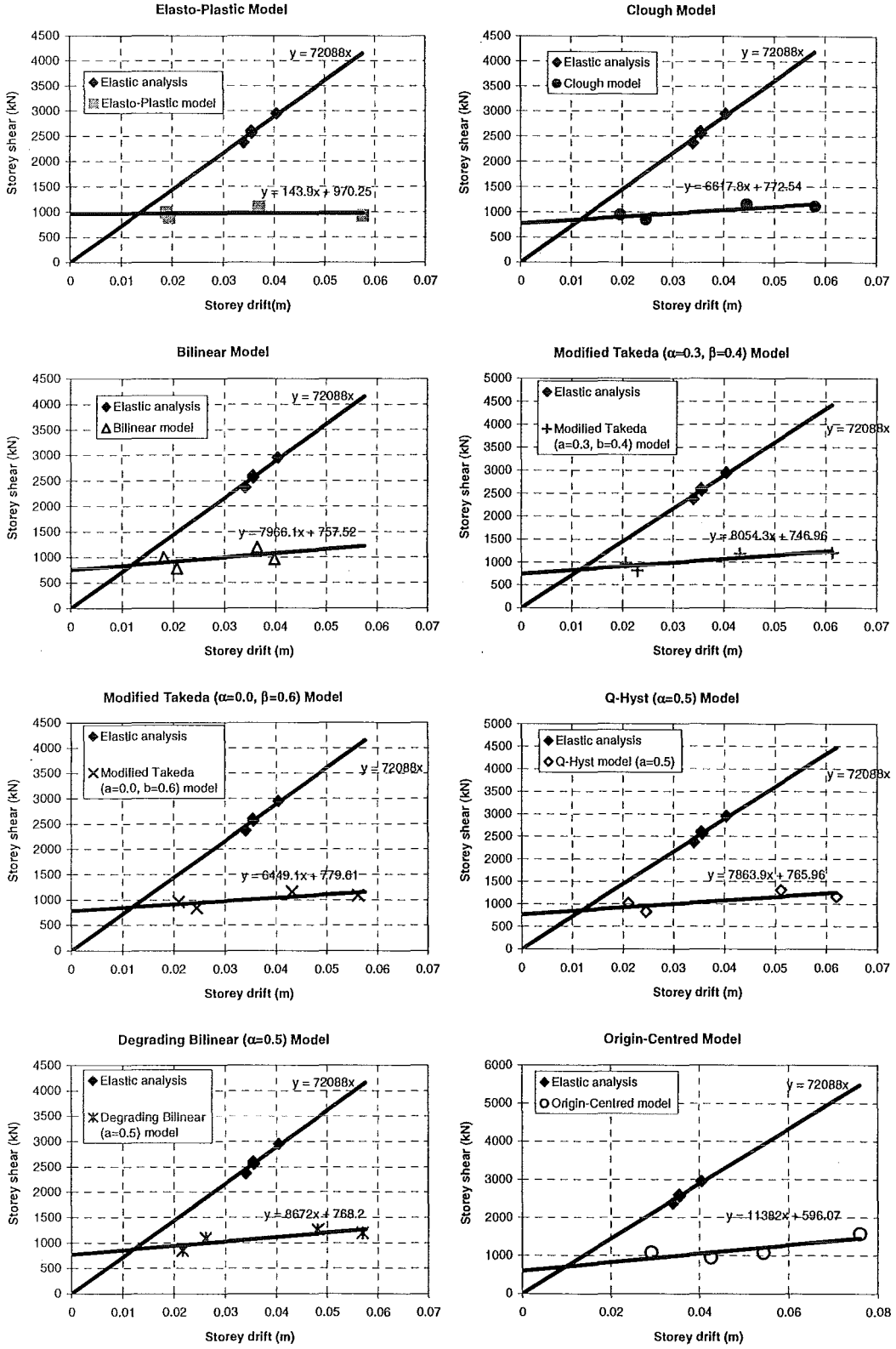

Fig. G-5 Storey yield point at level-4 of 6 storey structure for Carr & Tabuchi method to the eight hysteresis models

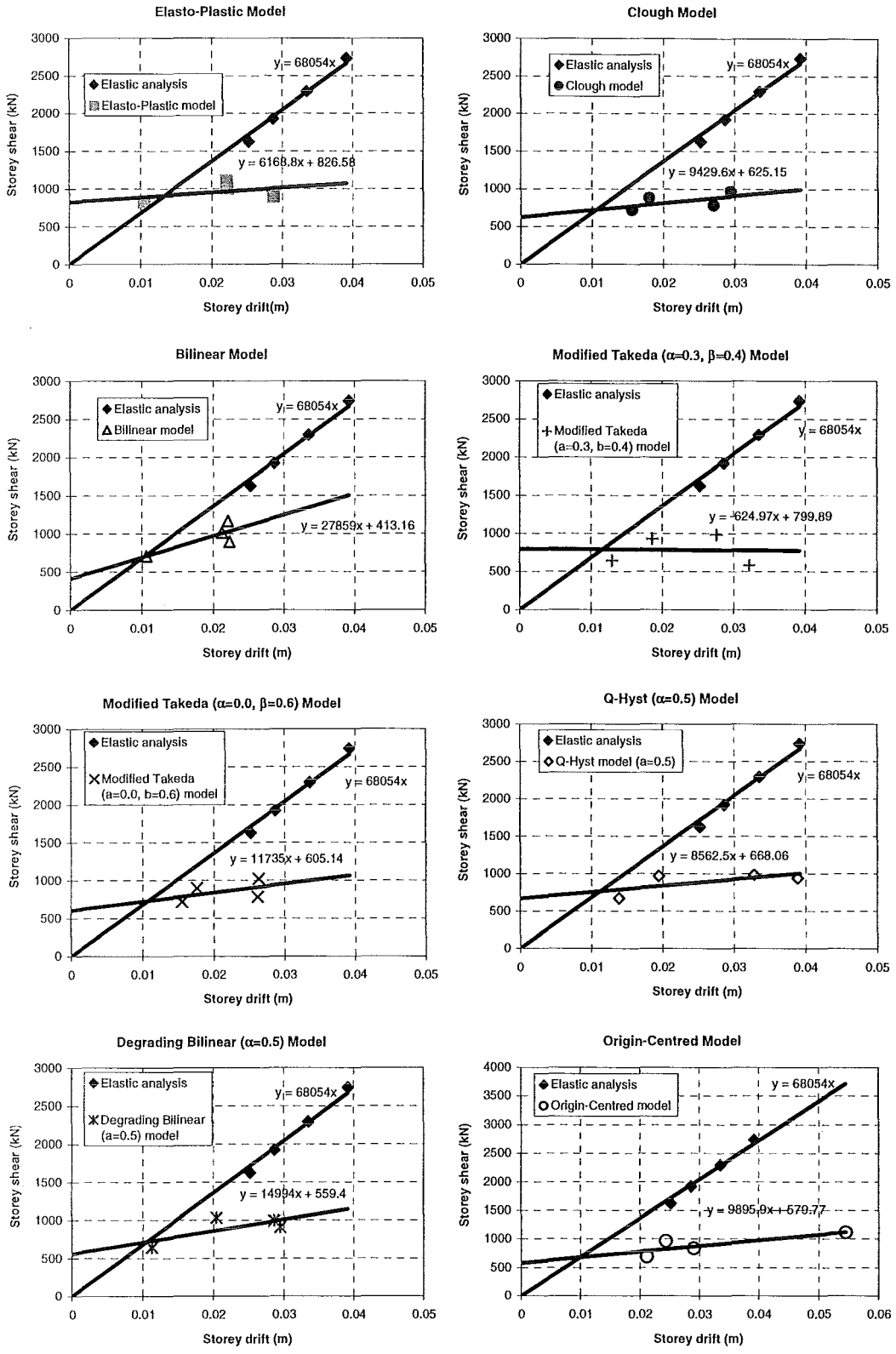

Fig. G-6 Storey yield point at level-5 of 6 storey structure for Carr & Tabuchi method to the eight hysteresis models

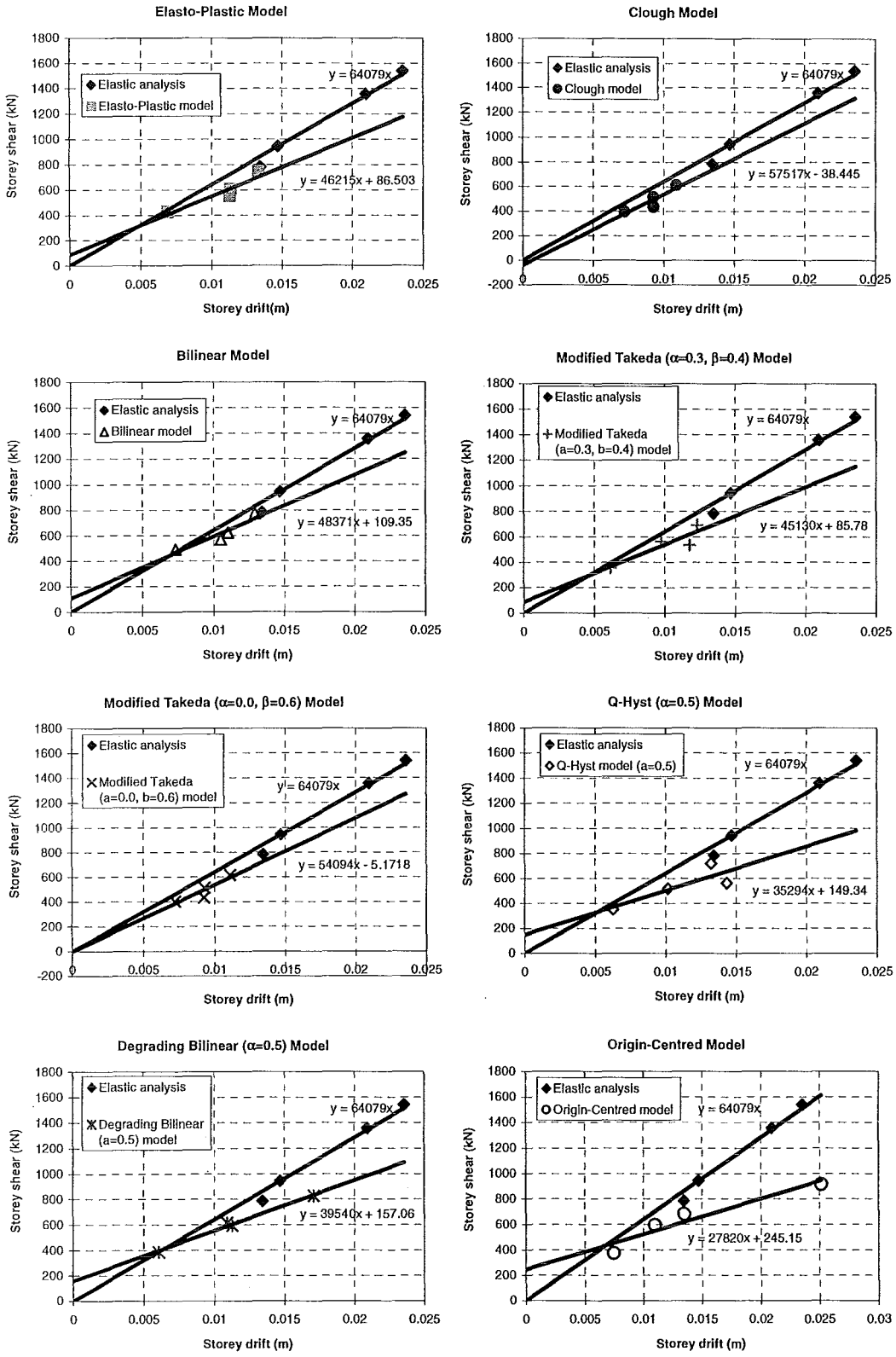

Fig. G-7 Storey yield point at level-6 of 6 storey structure for Carr & Tabuchi method to the eight hysteresis models

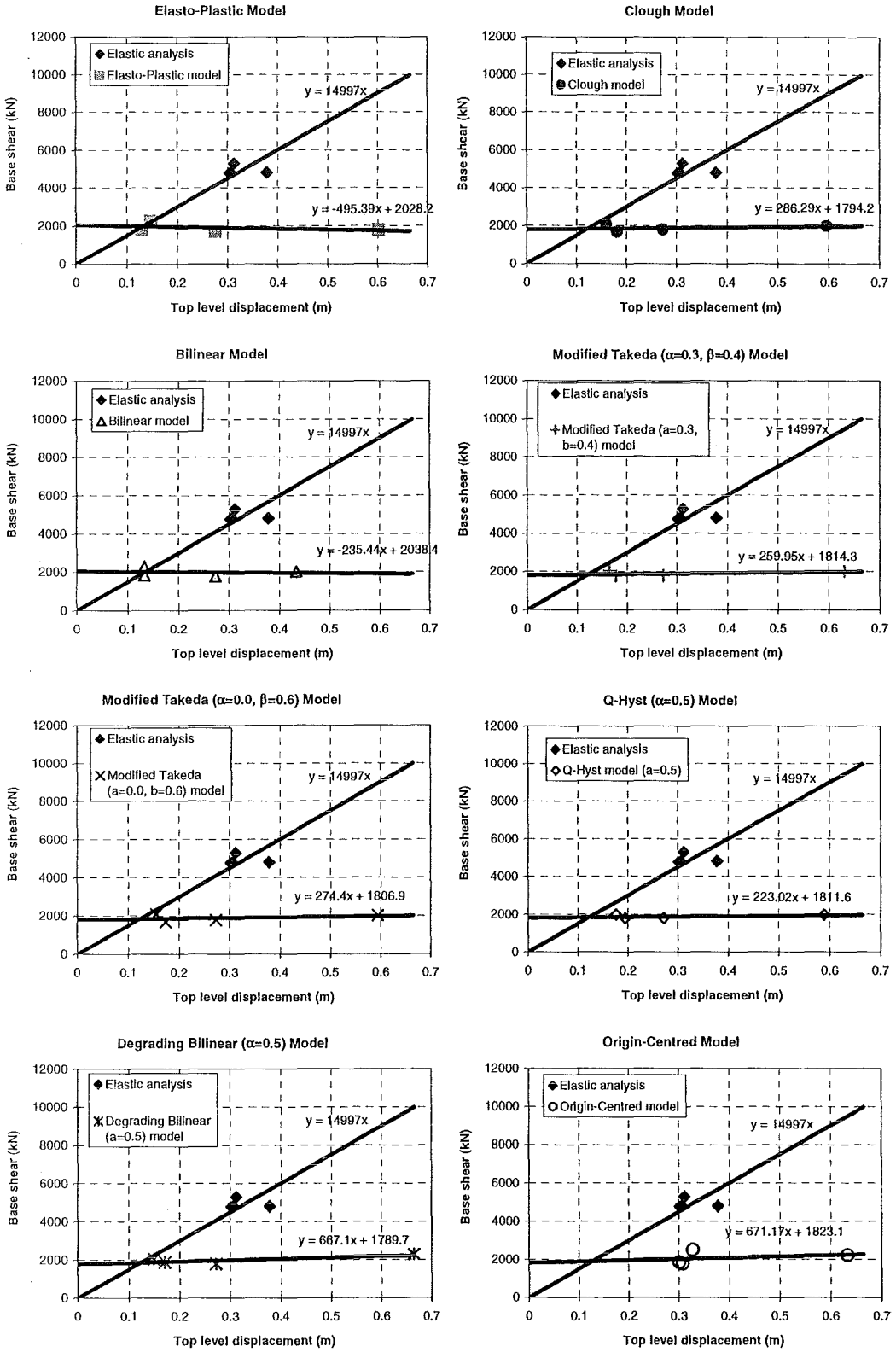

Fig. G-8 Overall structural yield point of 12 storey structure for Carr & Tabuchi method to the eight hysteresis models

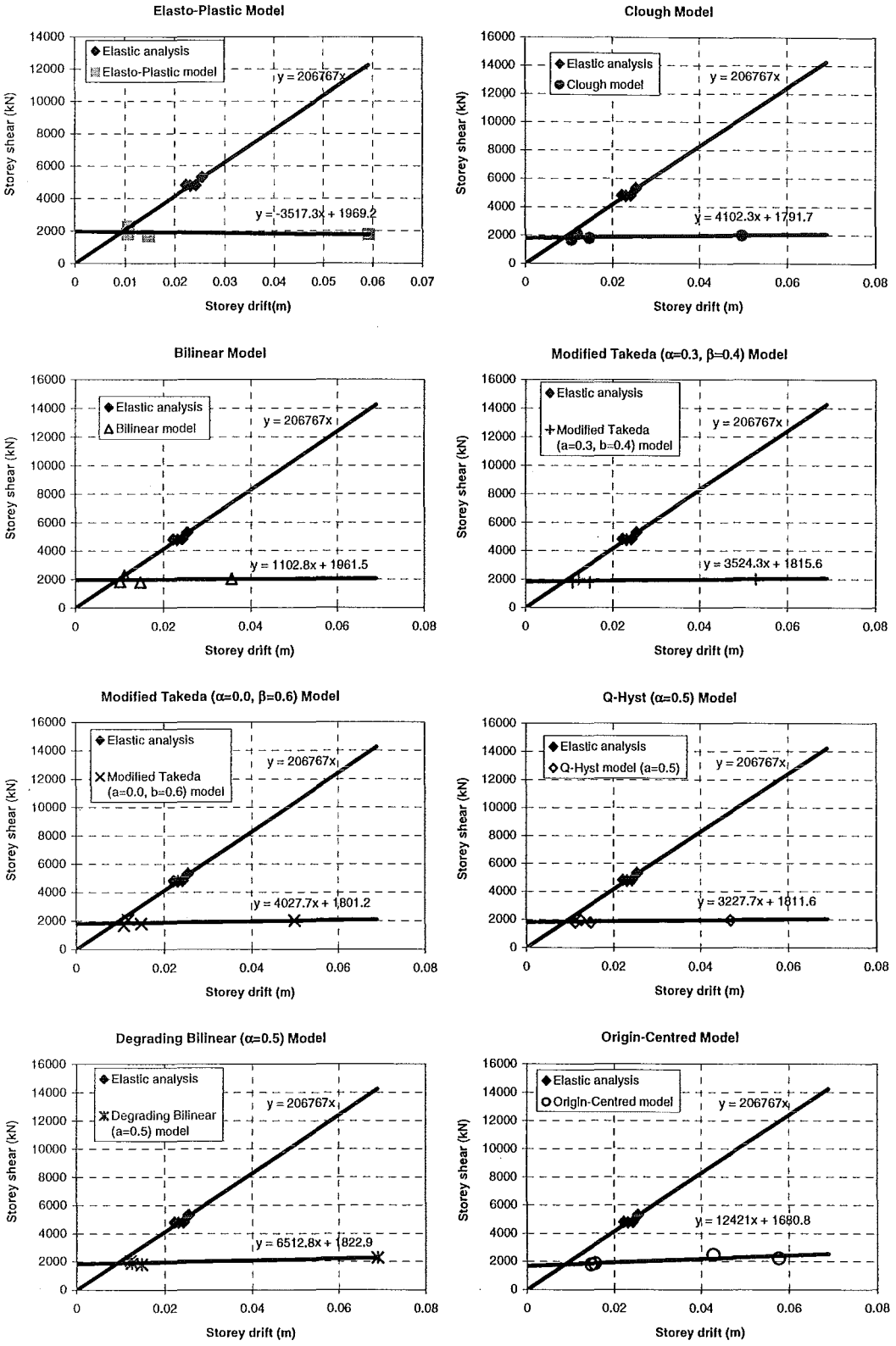

Fig. G-9 Storey yield point at level-1 of 12 storey structure for Carr & Tabuchi method to the eight hysteresis models

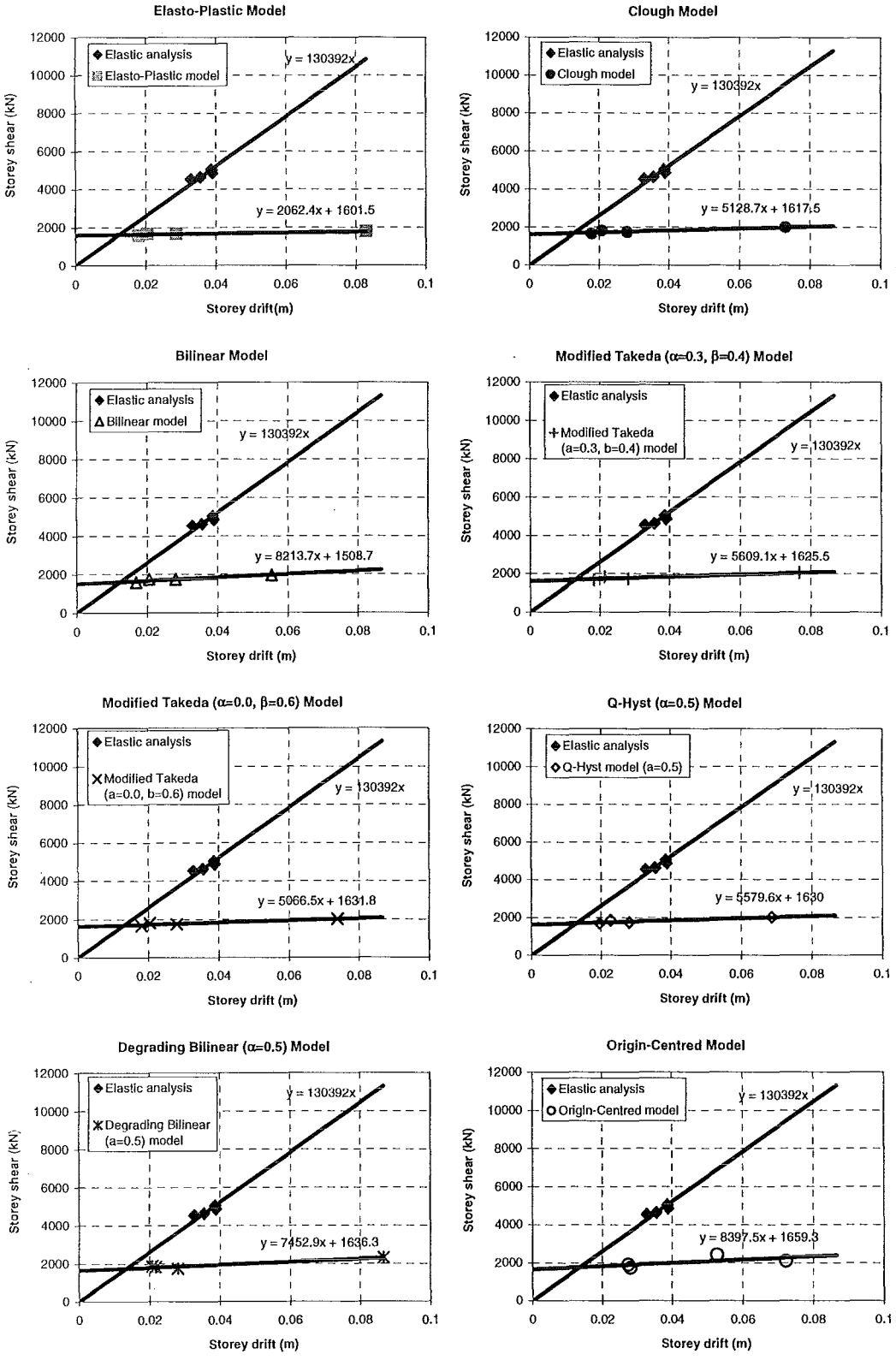

Fig. G-10 Storey yield point at level-2 of 12 storey structure for Carr & Tabuchi method to the eight hysteresis models

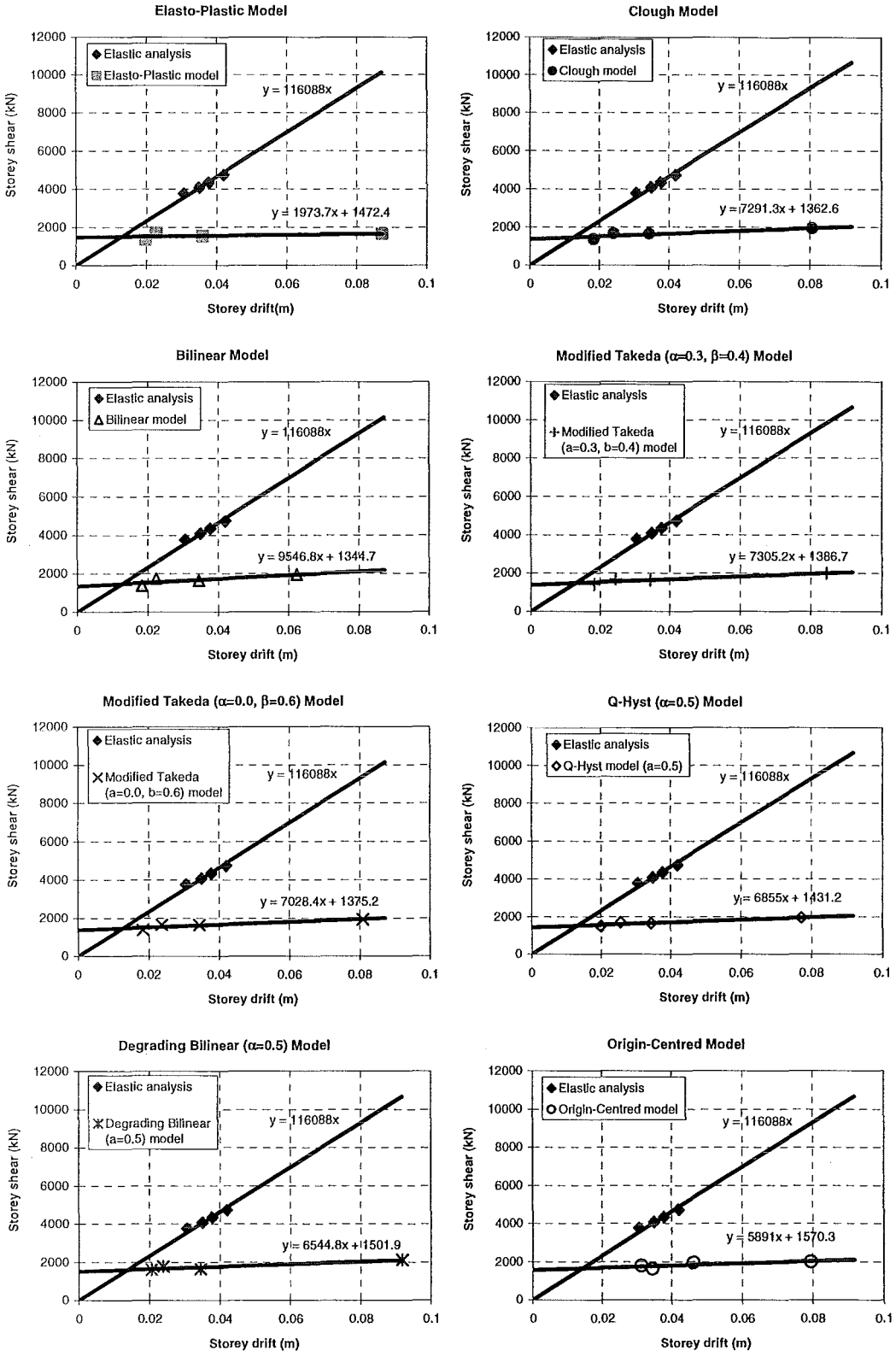

Fig. G-11 Storey yield point at level-3 of 12 storey structure for Carr & Tabuchi method to the eight hysteresis models

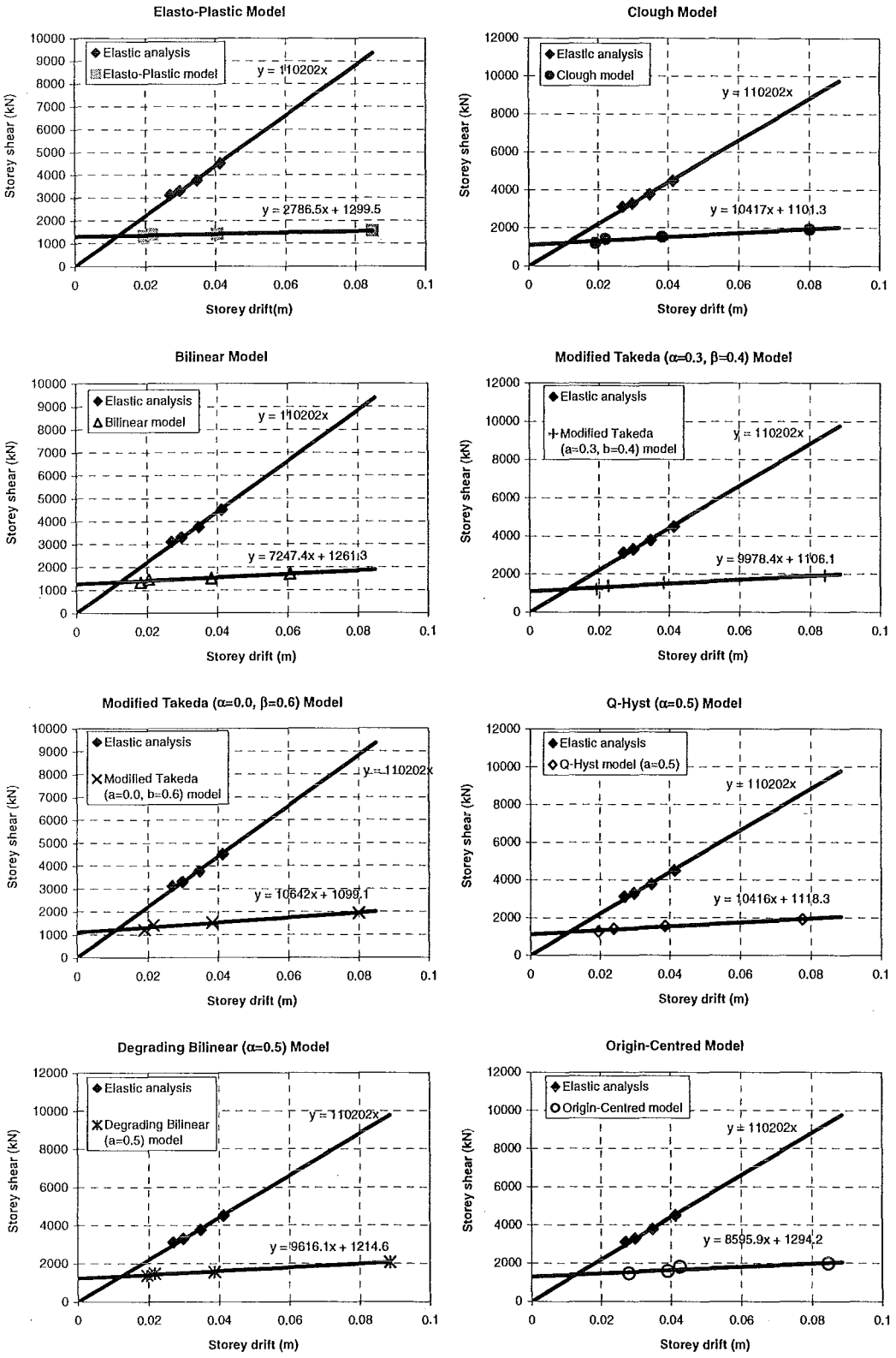

Fig. G-12 Storey yield point at level-4 of 12 storey structure for Carr & Tabuchi method to the eight hysteresis models

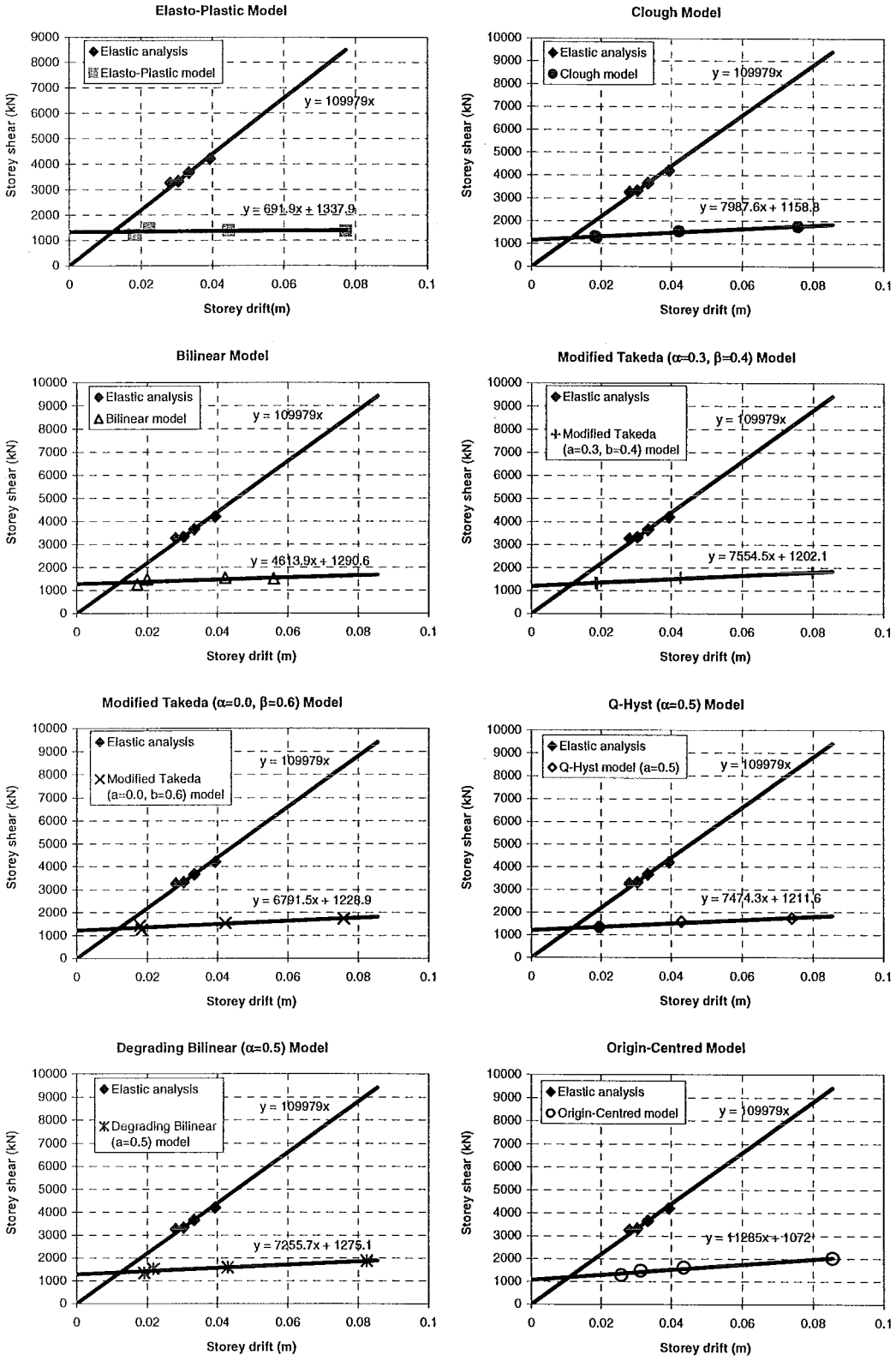

Fig. G-13 Storey yield point at level-5 of 12 storey structure for Carr & Tabuchi method to the eight hysteresis models

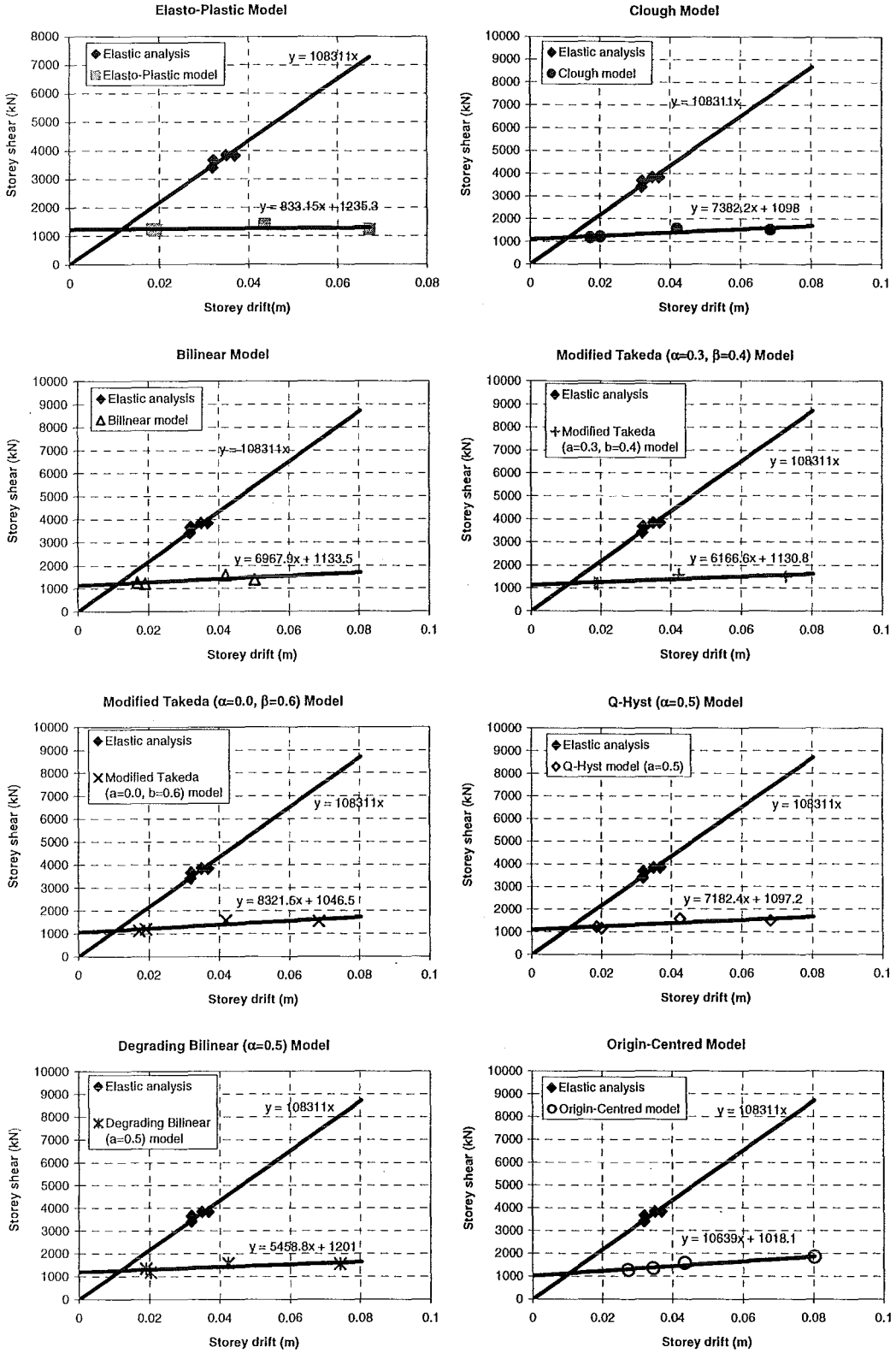

Fig. G-14 Storey yield point at level-6 of 12 storey structure for Carr & Tabuchi method to the eight hysteresis models

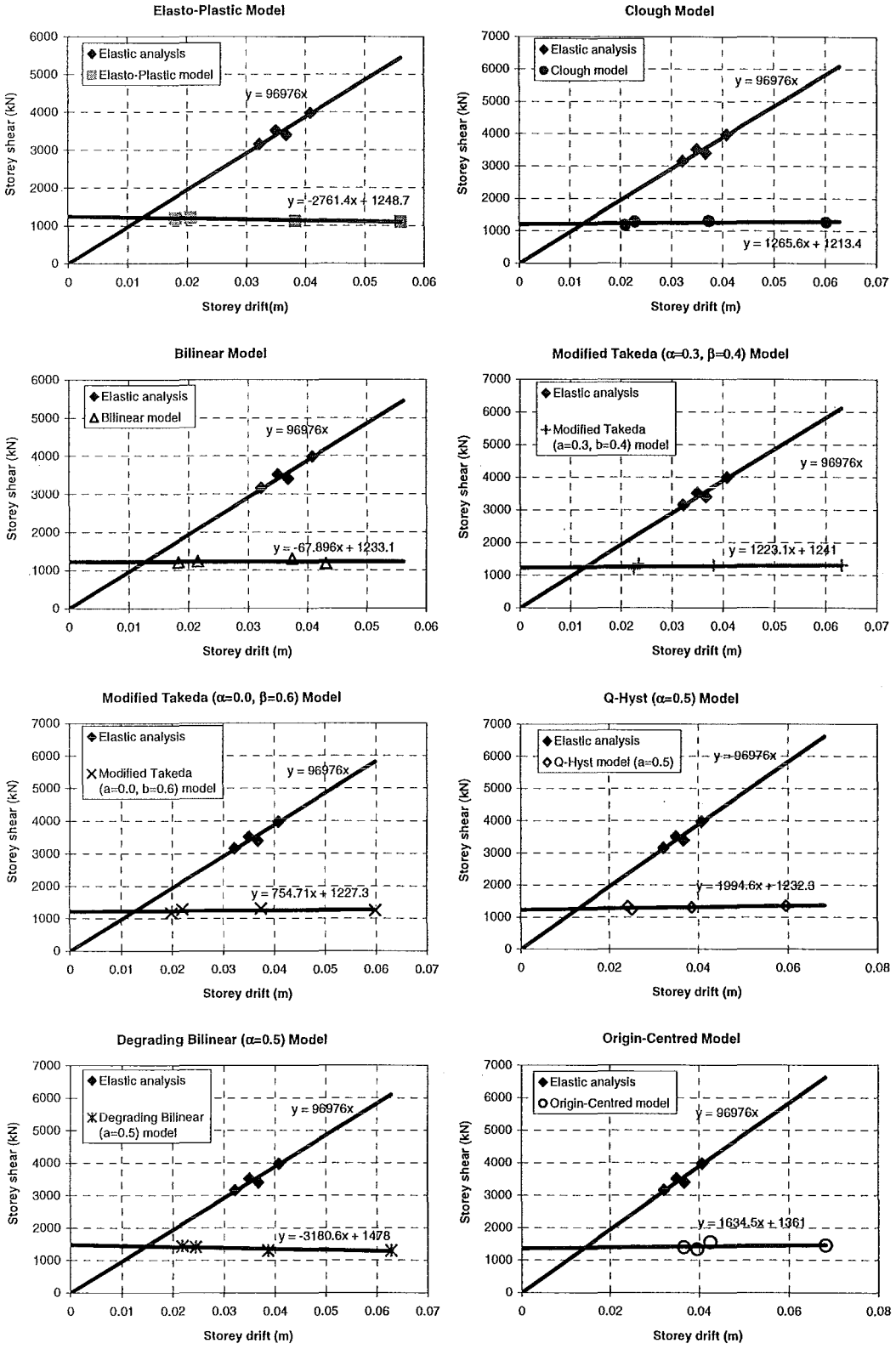

Fig. G-15 Storey yield point at level-7 of 12 storey structure for Carr & Tabuchi method to the eight hysteresis models

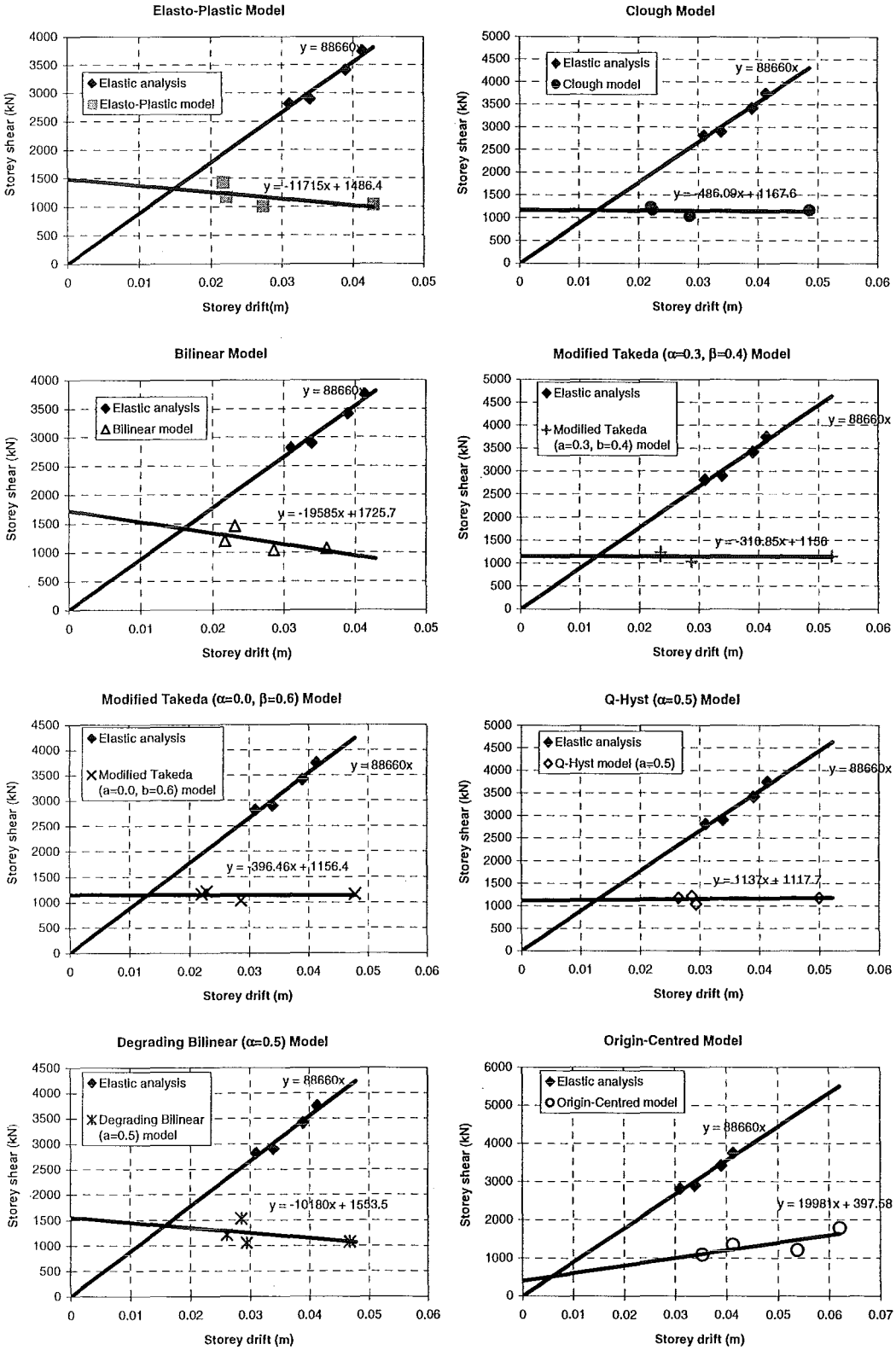

Fig. G-16 Storey yield point at level-8 of 12 storey structure for Carr & Tabuchi method to the eight hysteresis models

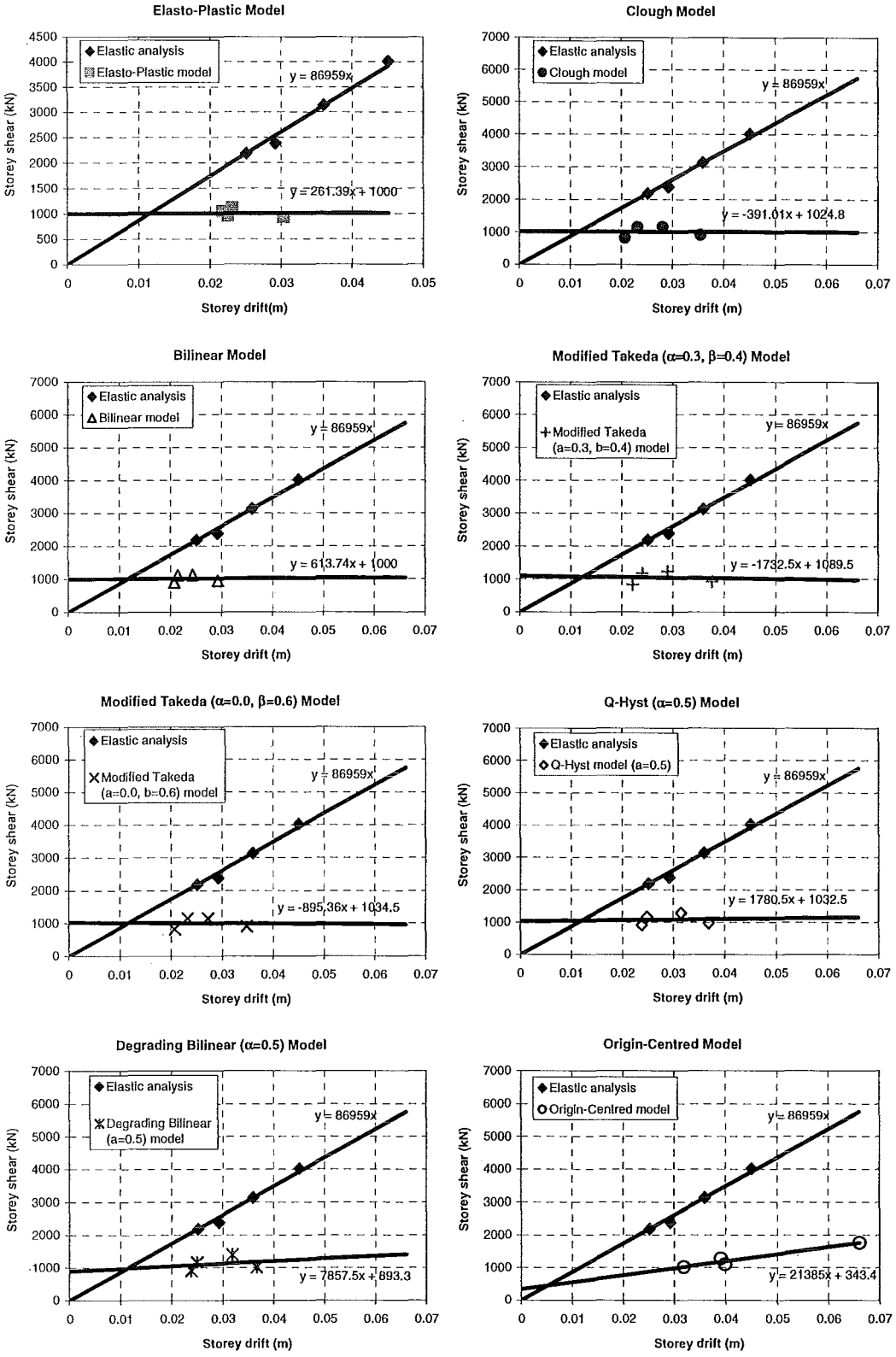

Fig. G-17 Storey yield point at level-9 of 12 storey structure for Carr & Tabuchi method to the eight hysteresis models

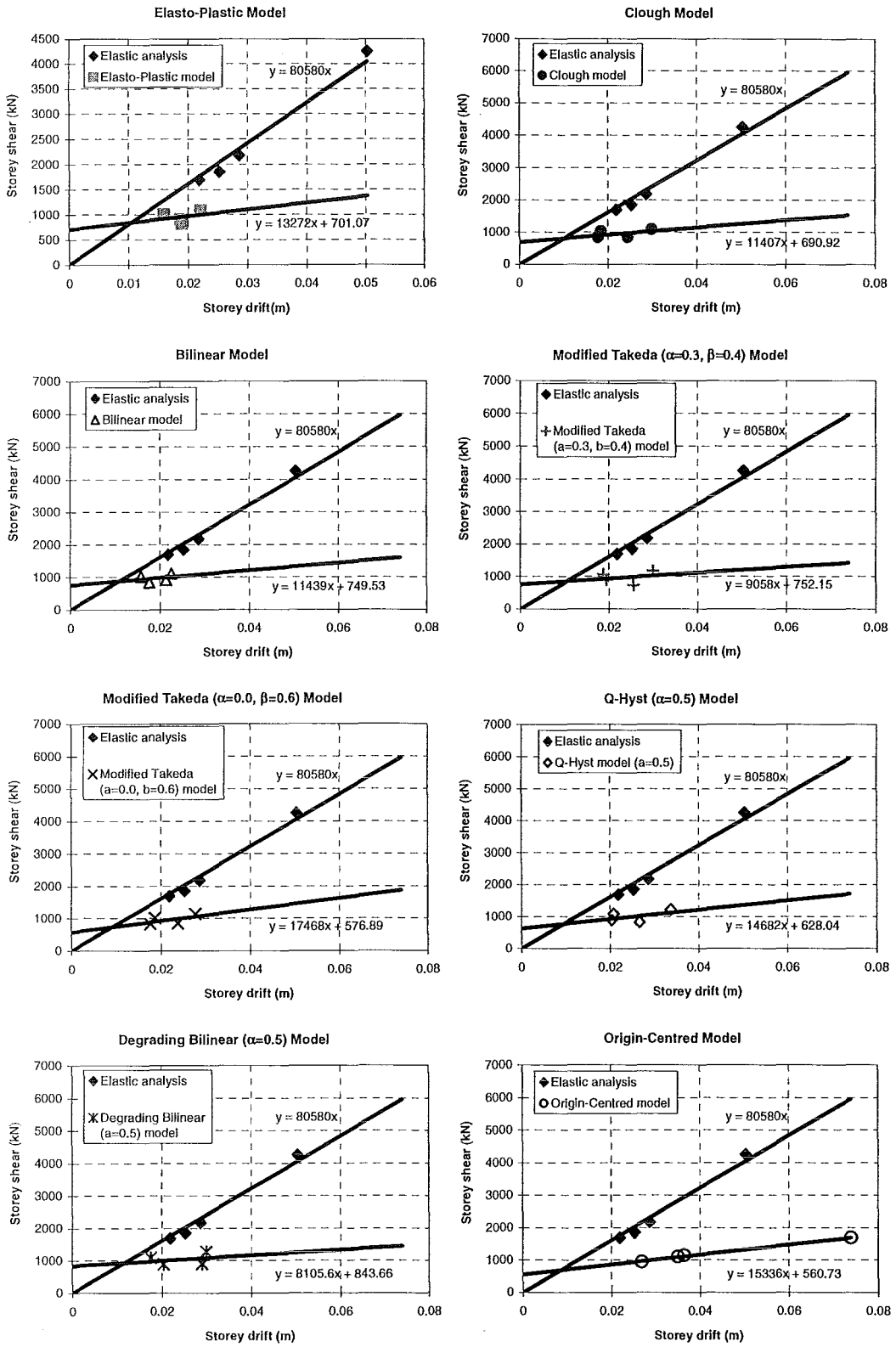

Fig. G-18 Storey yield point at level-10 of 12 storey structure for Carr & Tabuchi method to the eight hysteresis models

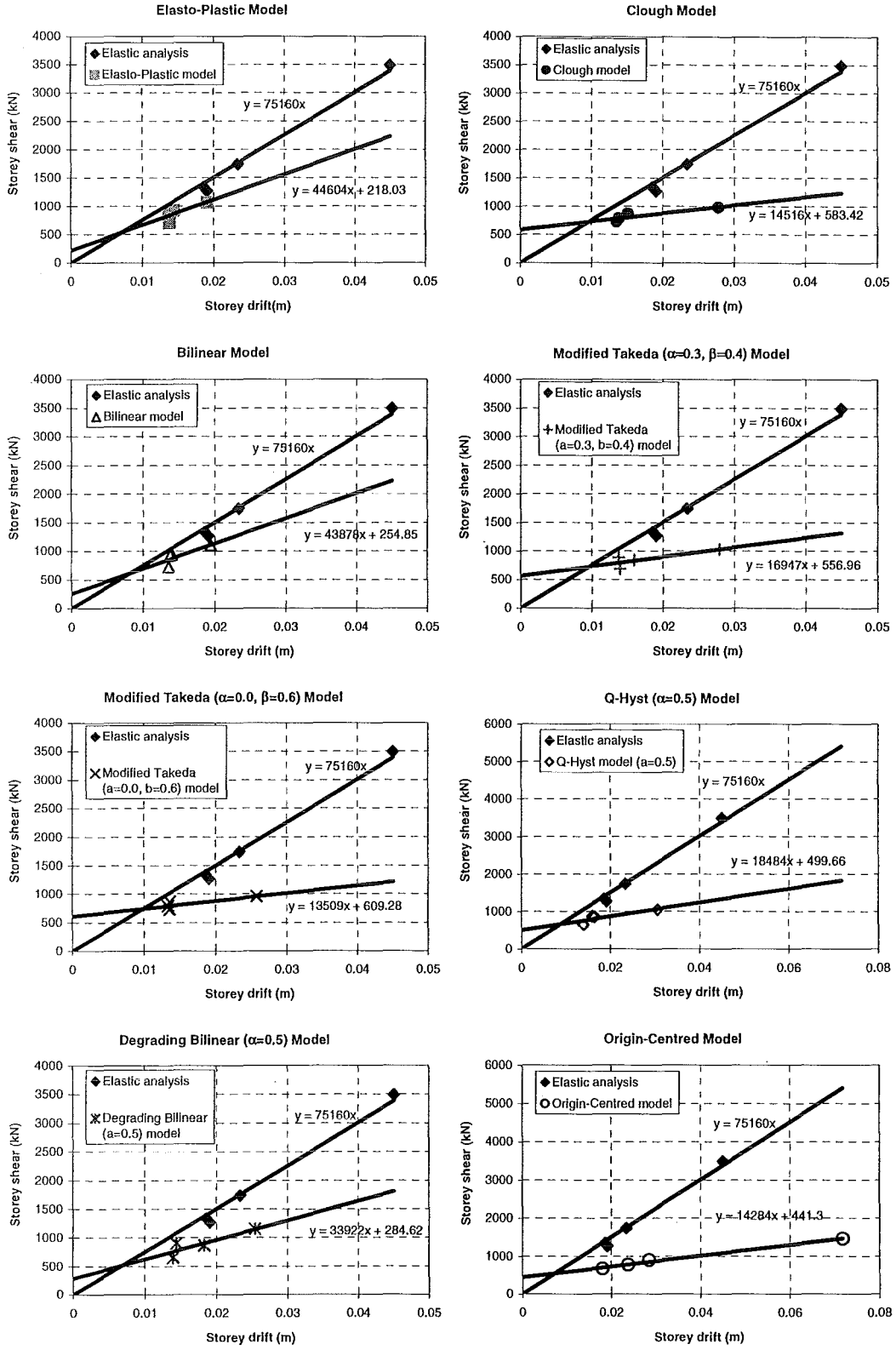

Fig. G-19 Storey yield point at level-11 of 12 storey structure for Carr & Tabuchi method to the eight hysteresis models

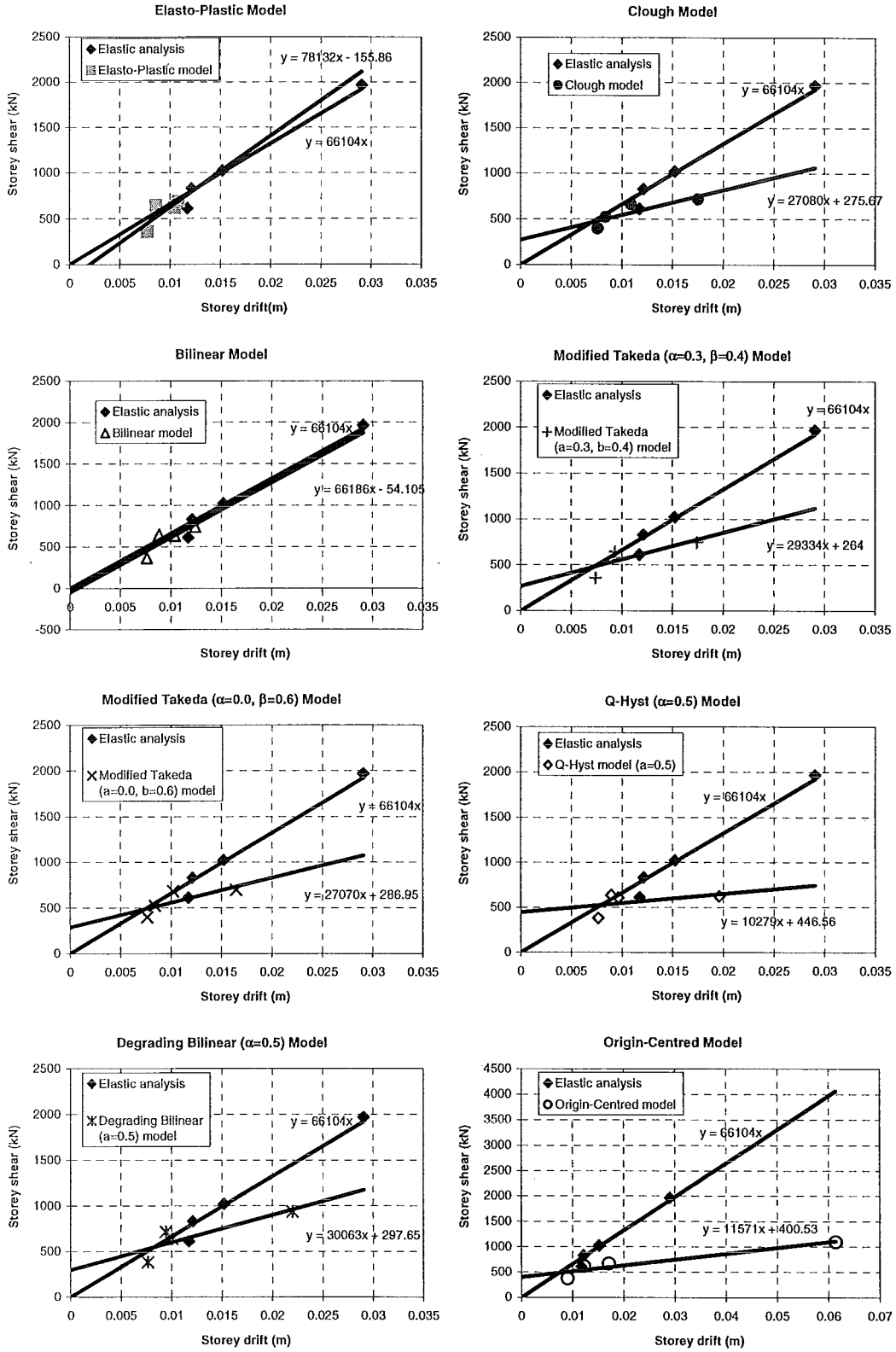

Fig. G-20 Storey yield point at level-12 of 12 storey structure for Carr & Tabuchi method to the eight hysteresis models

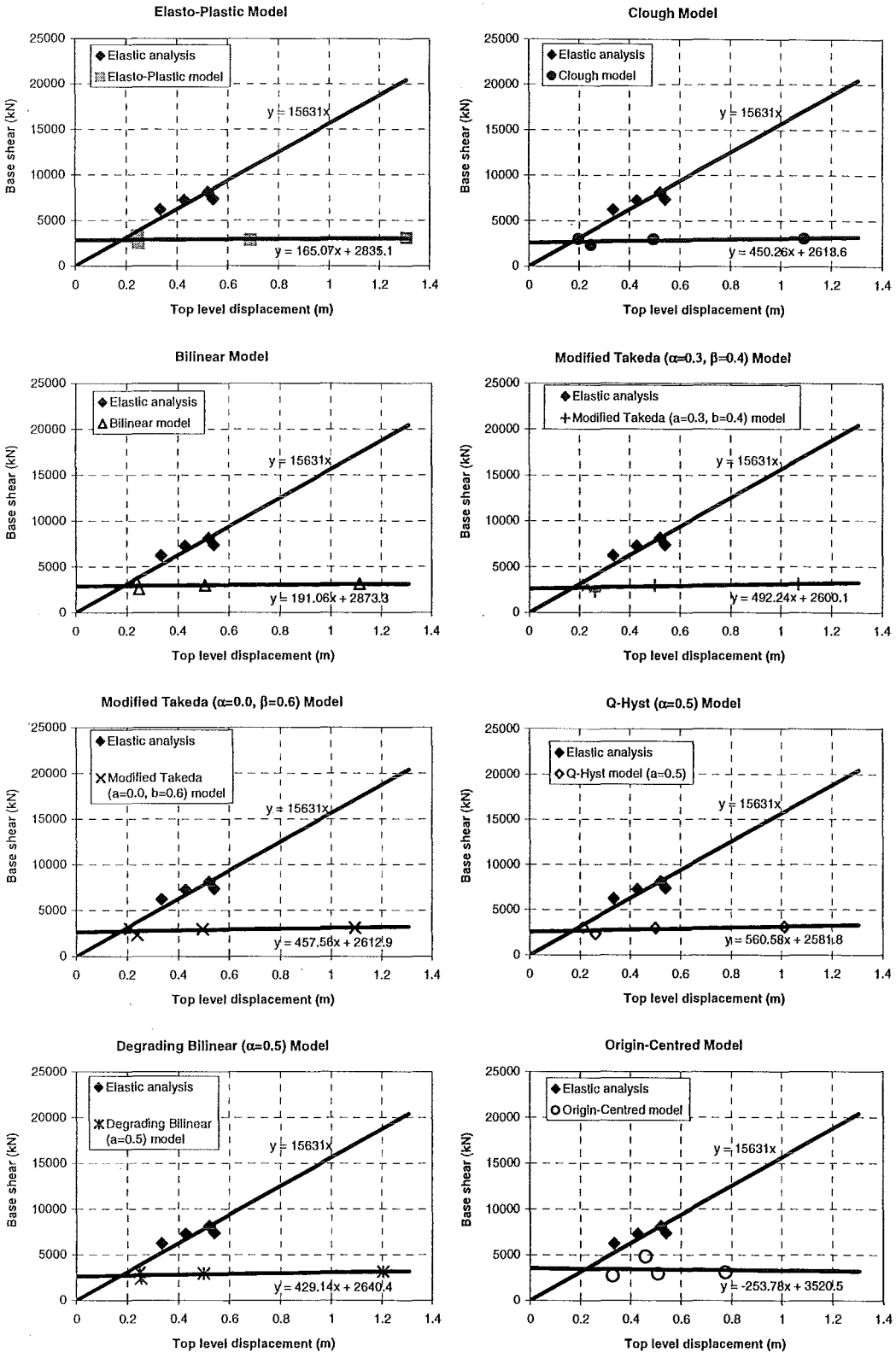

Fig. G-21 Overall structural yield point of 18 storey structure for Carr & Tabuchi method to the eight hysteresis models

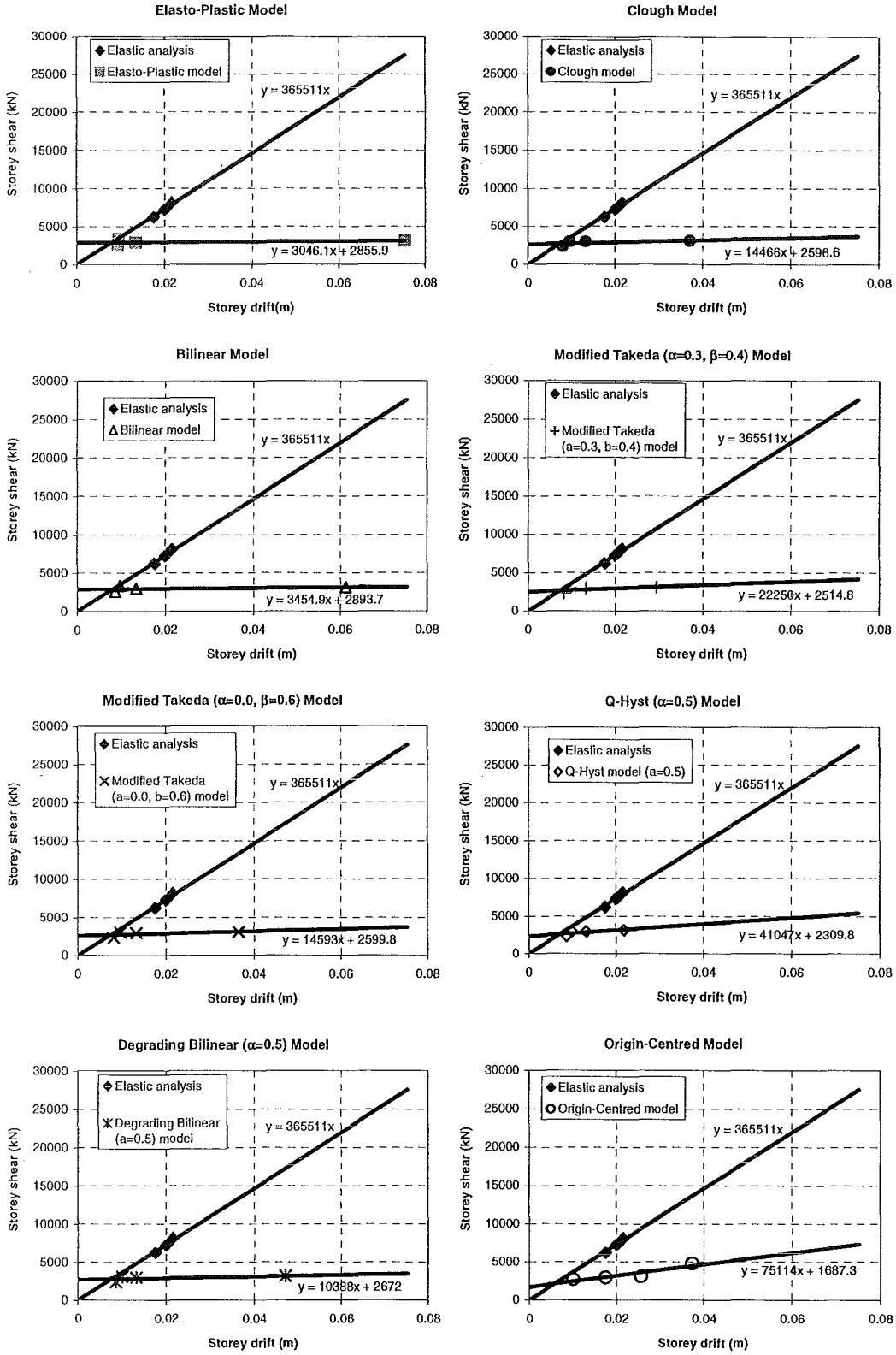

Fig. G-22 Storey yield point at level-1 of 18 storey structure for Carr & Tabuchi method to the eight hysteresis models

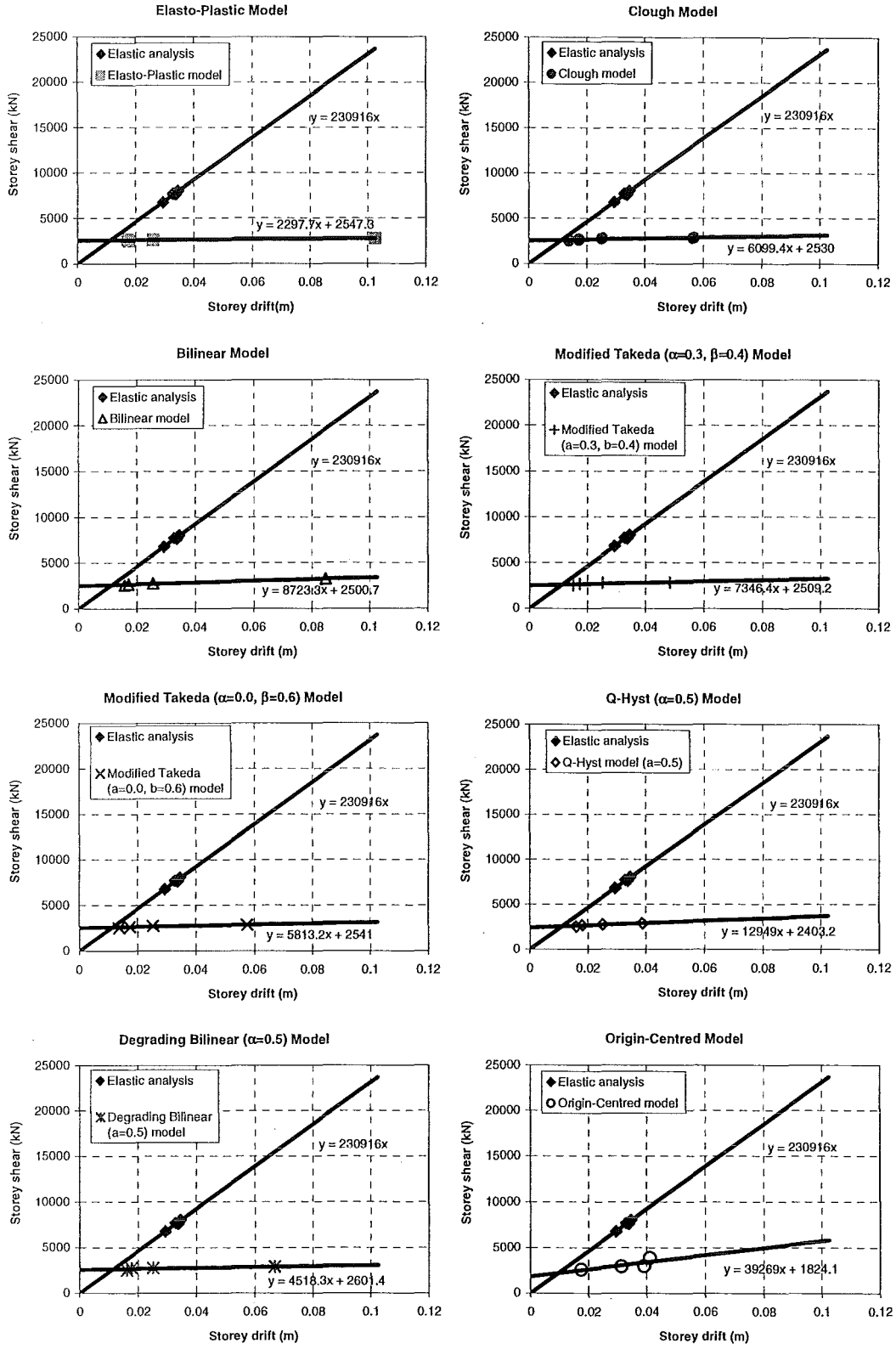

Fig. G-23 Storey yield point at level-2 of 18 storey structure for Carr & Tabuchi method to the eight hysteresis models

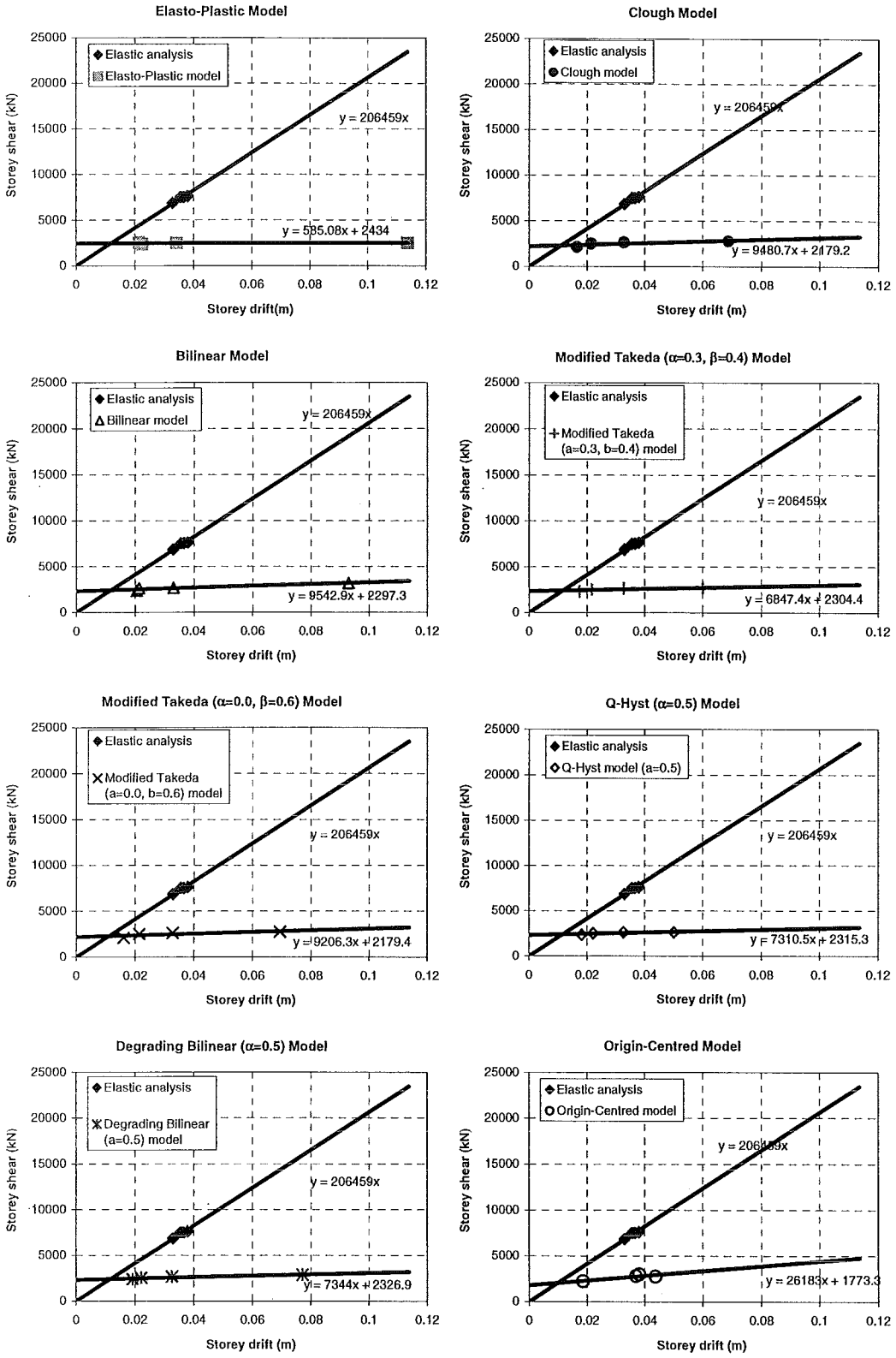

Fig. G-24 Storey yield point at level-3 of 18 storey structure for Carr & Tabuchi method to the eight hysteresis models

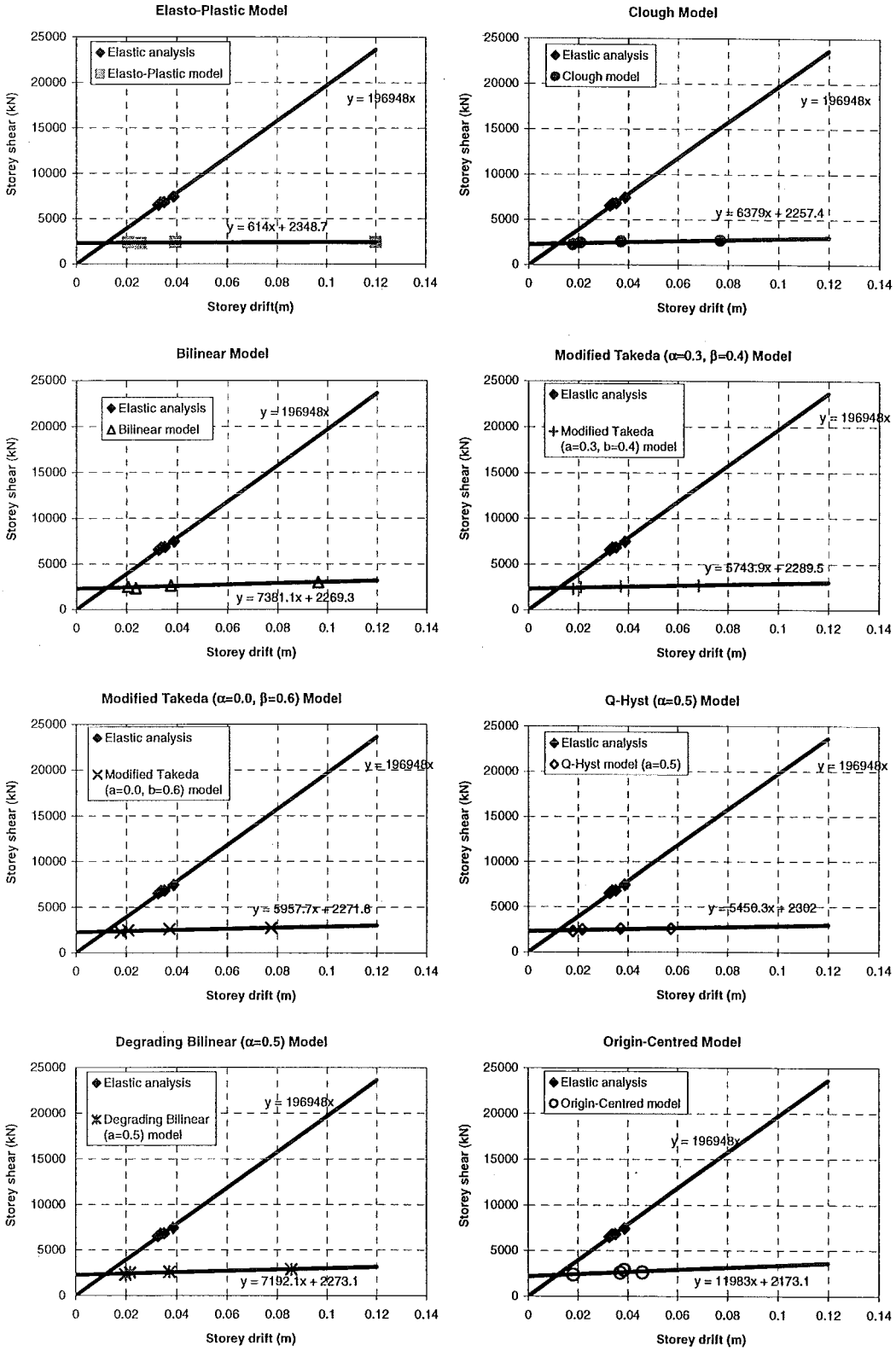

Fig. G-25 Storey yield point at level-4 of 18 storey structure for Carr & Tabuchi method to the eight hysteresis models

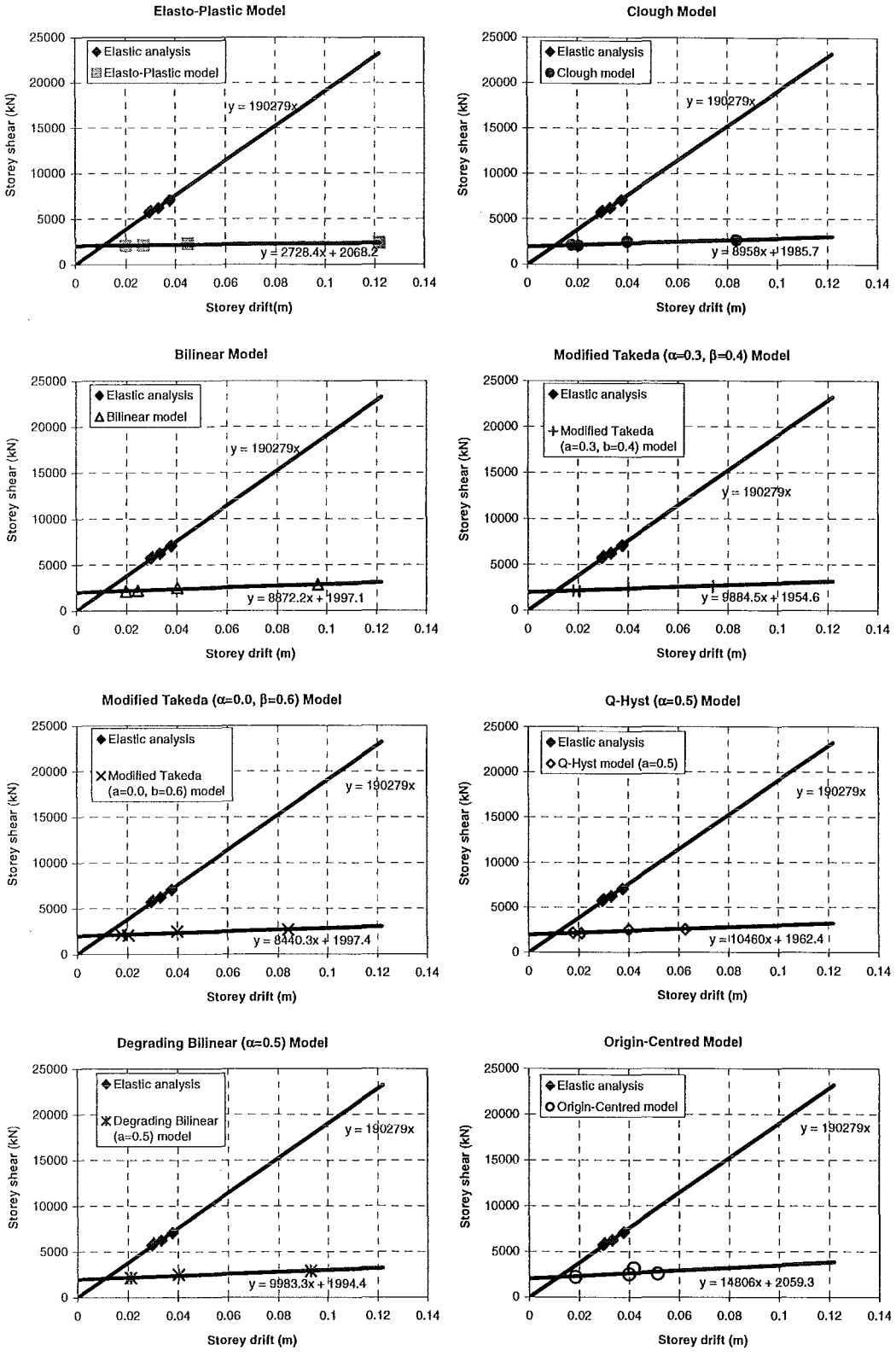

Fig. G-26 Storey yield point at level-5 of 18 storey structure for Carr & Tabuchi method to the eight hysteresis models

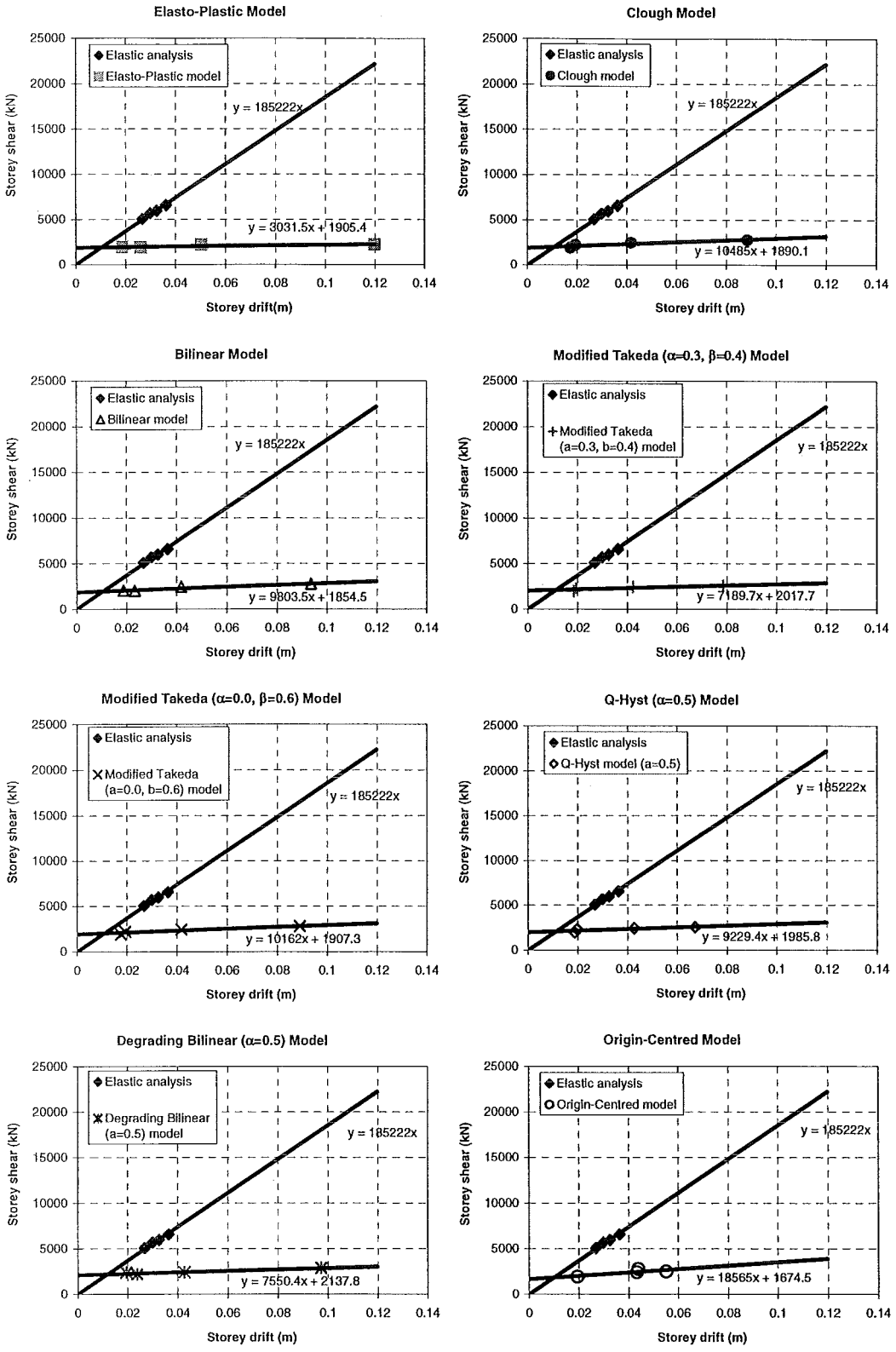

Fig. G-27 Storey yield point at level-6 of 18 storey structure for Carr & Tabuchi method to the eight hysteresis models

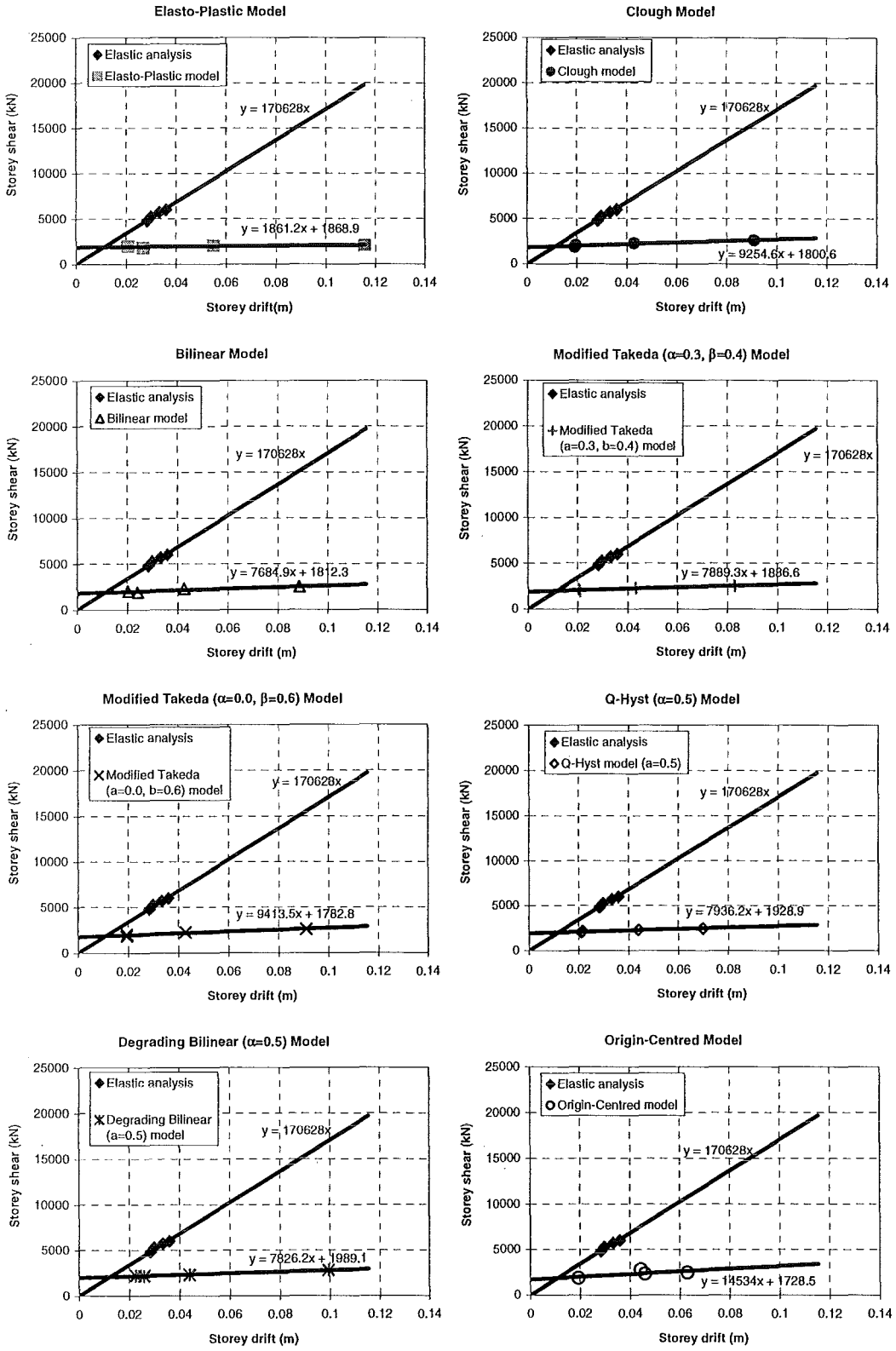

Fig. G-28 Storey yield point at level-7 of 18 storey structure for Carr & Tabuchi method to the eight hysteresis models

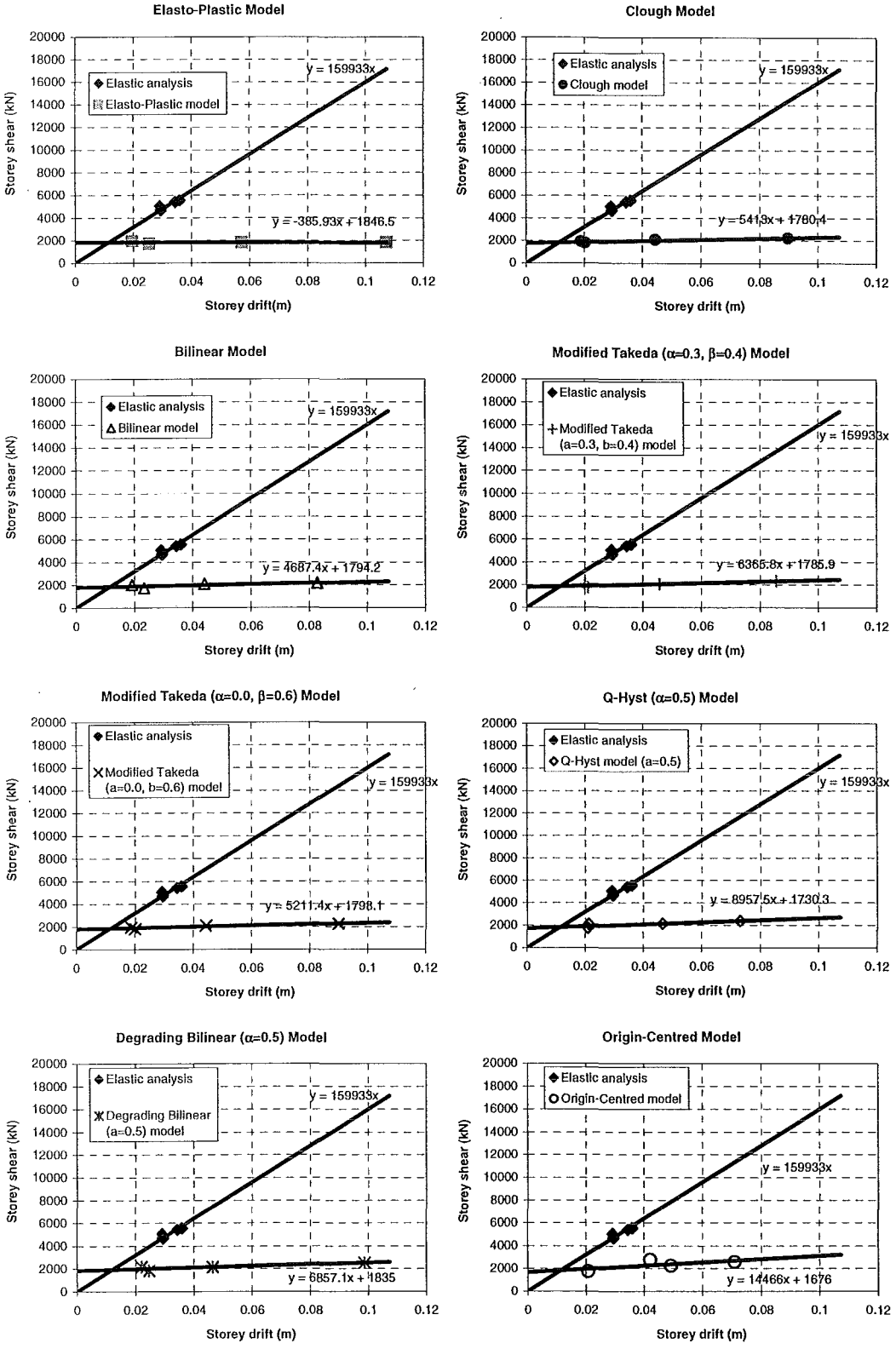

Fig. G-29 Storey yield point at level-8 of 18 storey structure for Carr & Tabuchi method to the eight hysteresis models

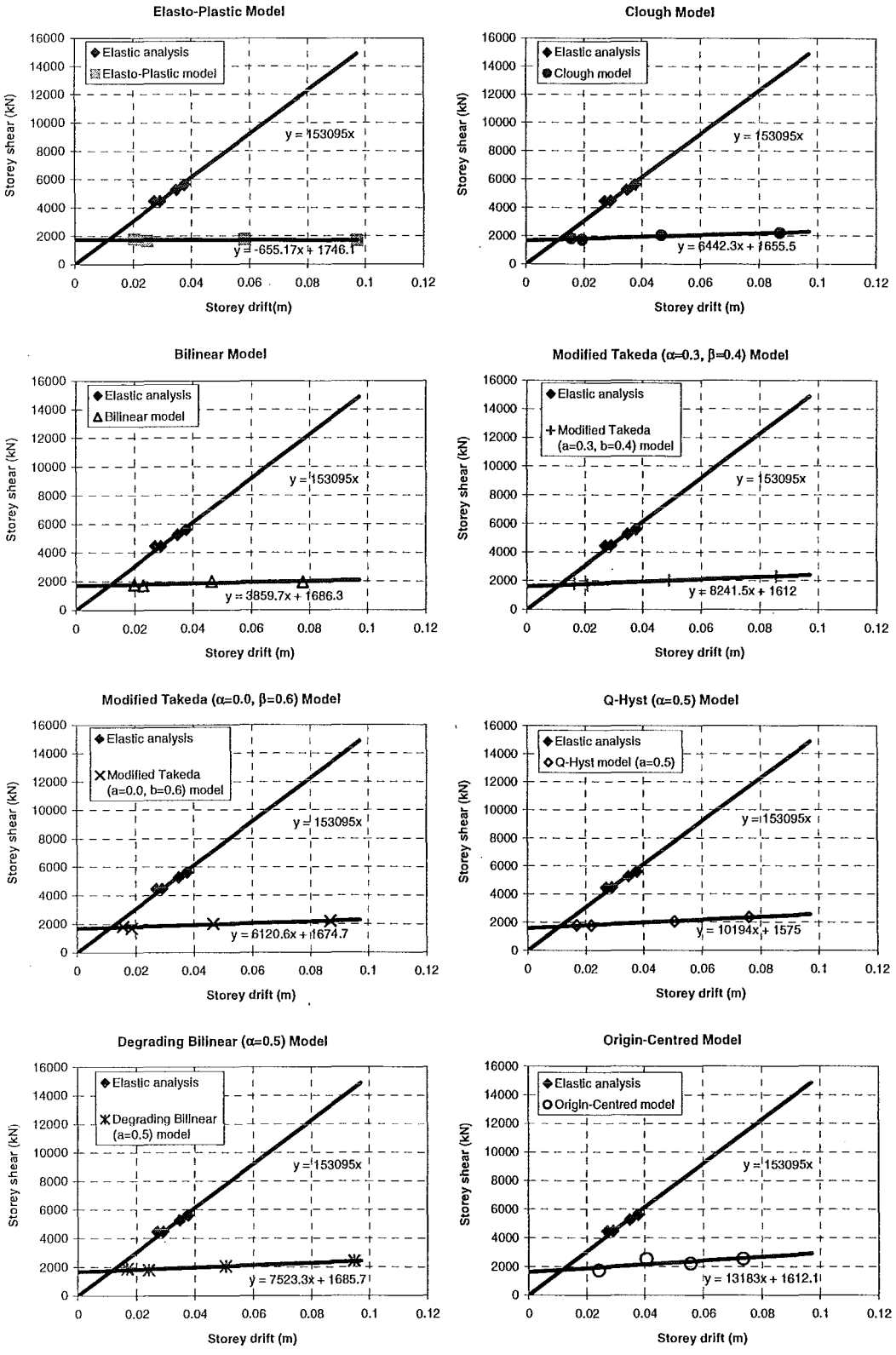

Fig. G-30 Storey yield point at level-9 of 18 storey structure for Carr & Tabuchi method to the eight hysteresis models

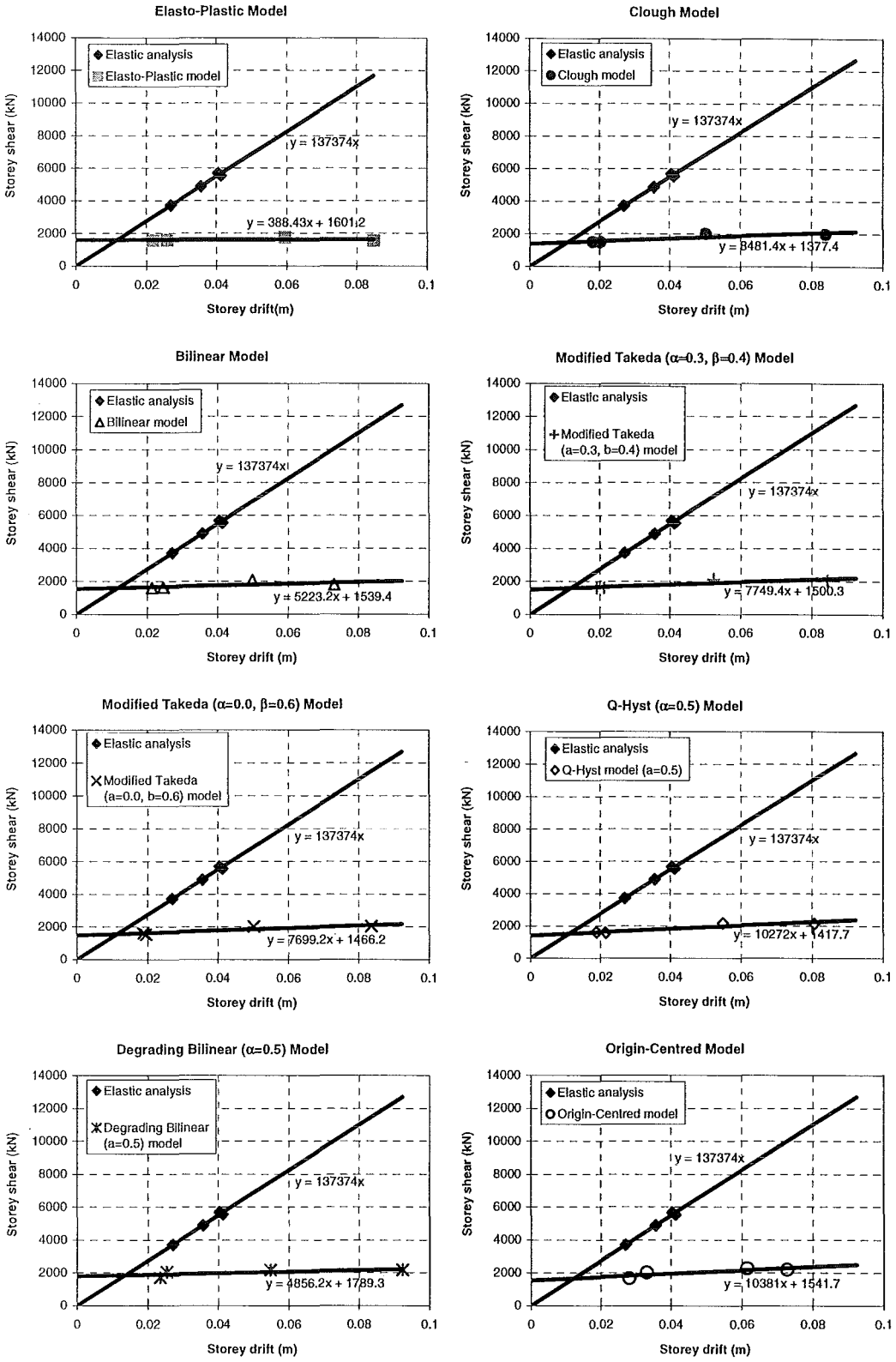

Fig. G-31 Storey yield point at level-10 of 18 storey structure for Carr & Tabuchi method to the eight hysteresis models

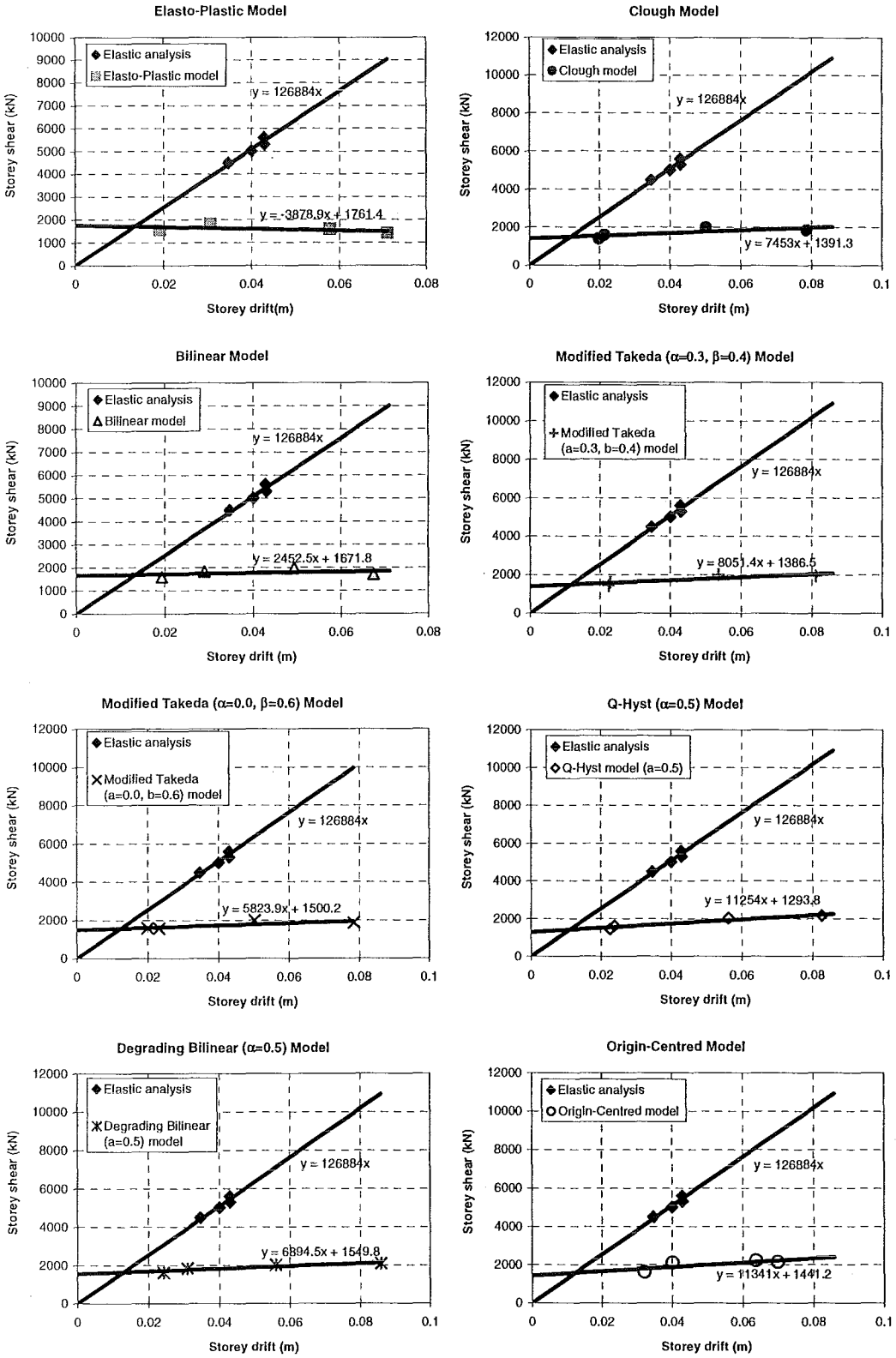

Fig. G-32 Storey yield point at level-11 of 18 storey structure for Carr & Tabuchi method to the eight hysteresis models

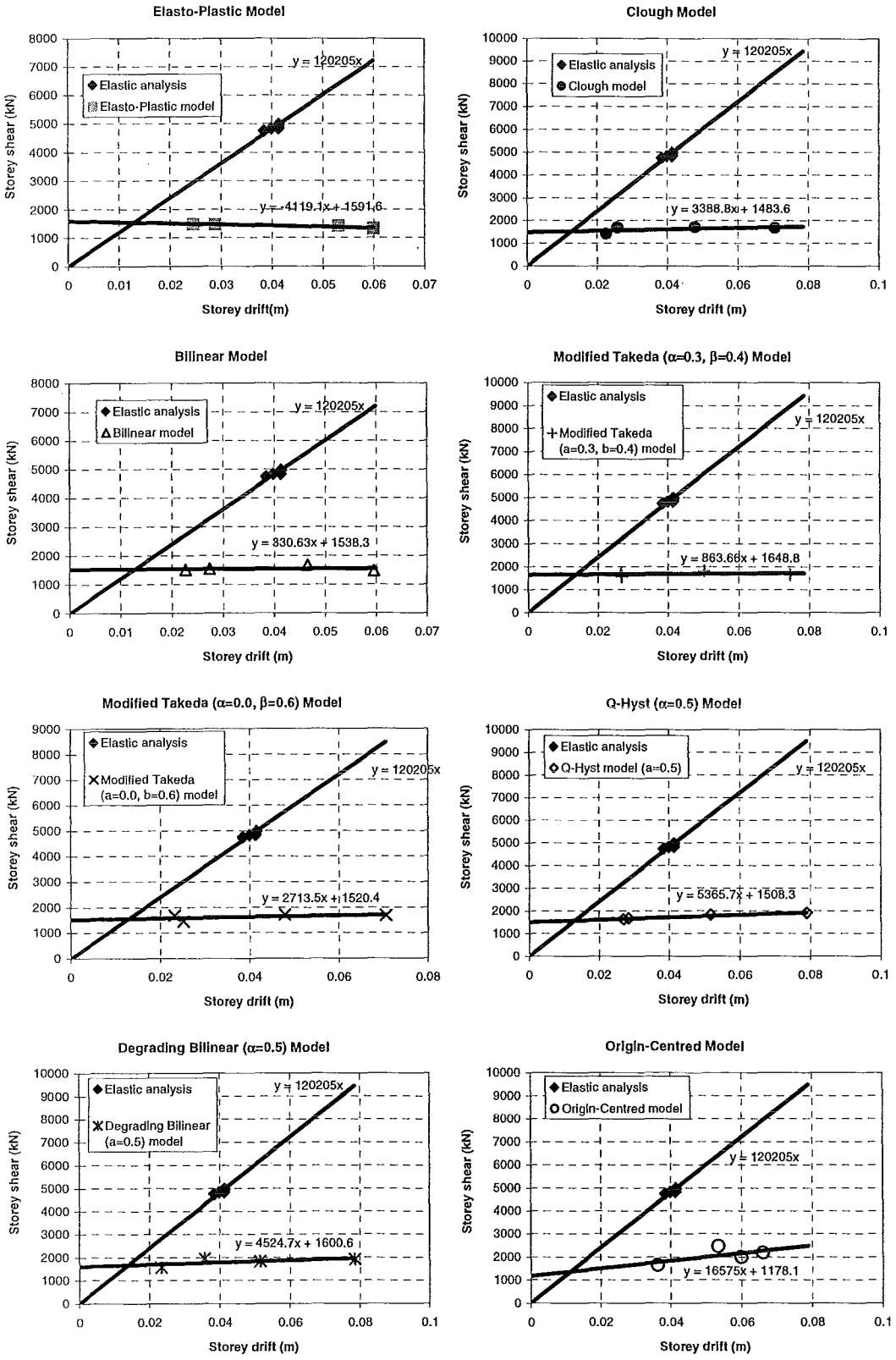

Fig. G-33 Storey yield point at level-12 of 18 storey structure for Carr & Tabuchi method to the eight hysteresis models

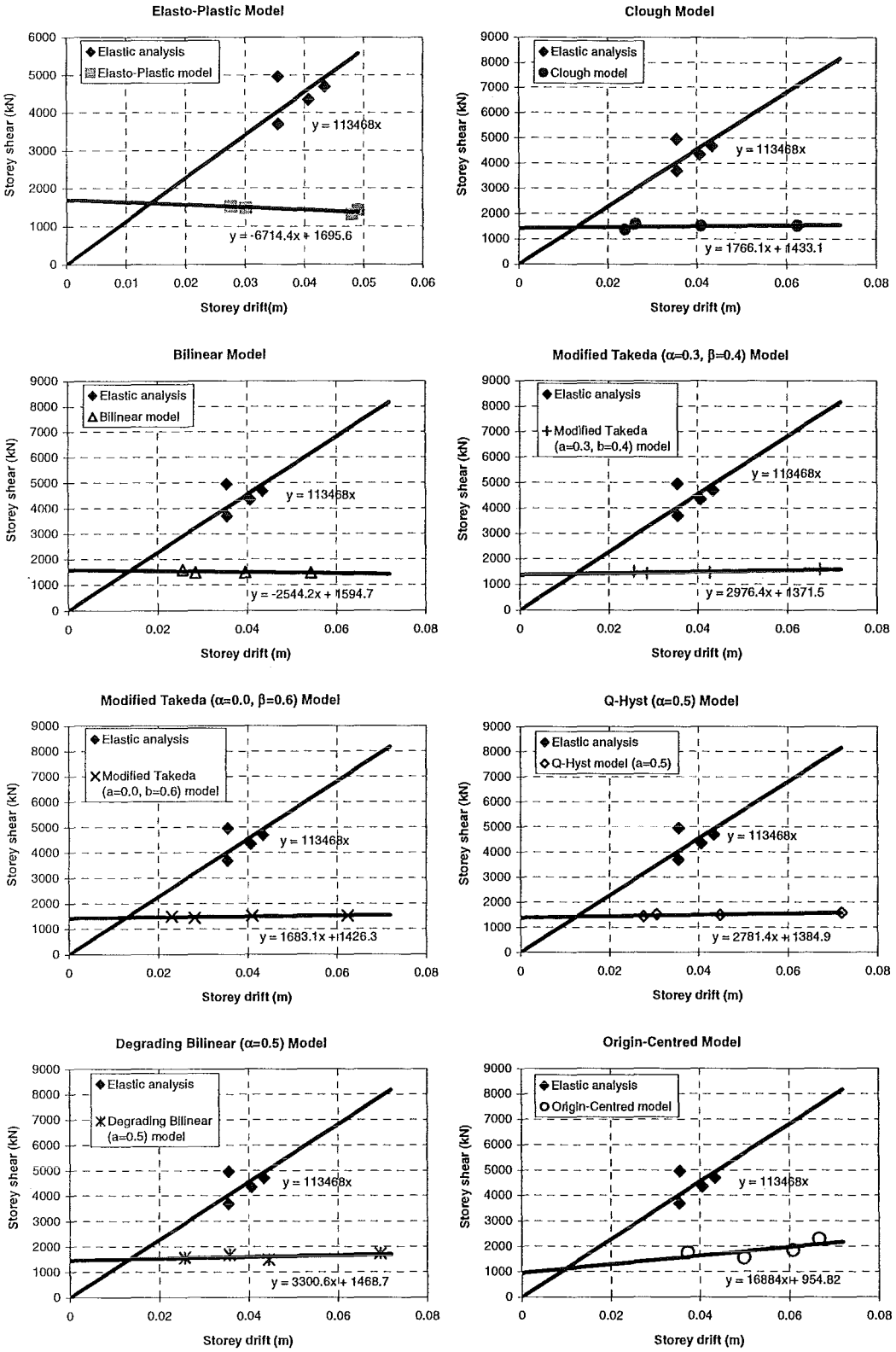

Fig. G-34 Storey yield point at level-13 of 18 storey structure for Carr & Tabuchi method to the eight hysteresis models

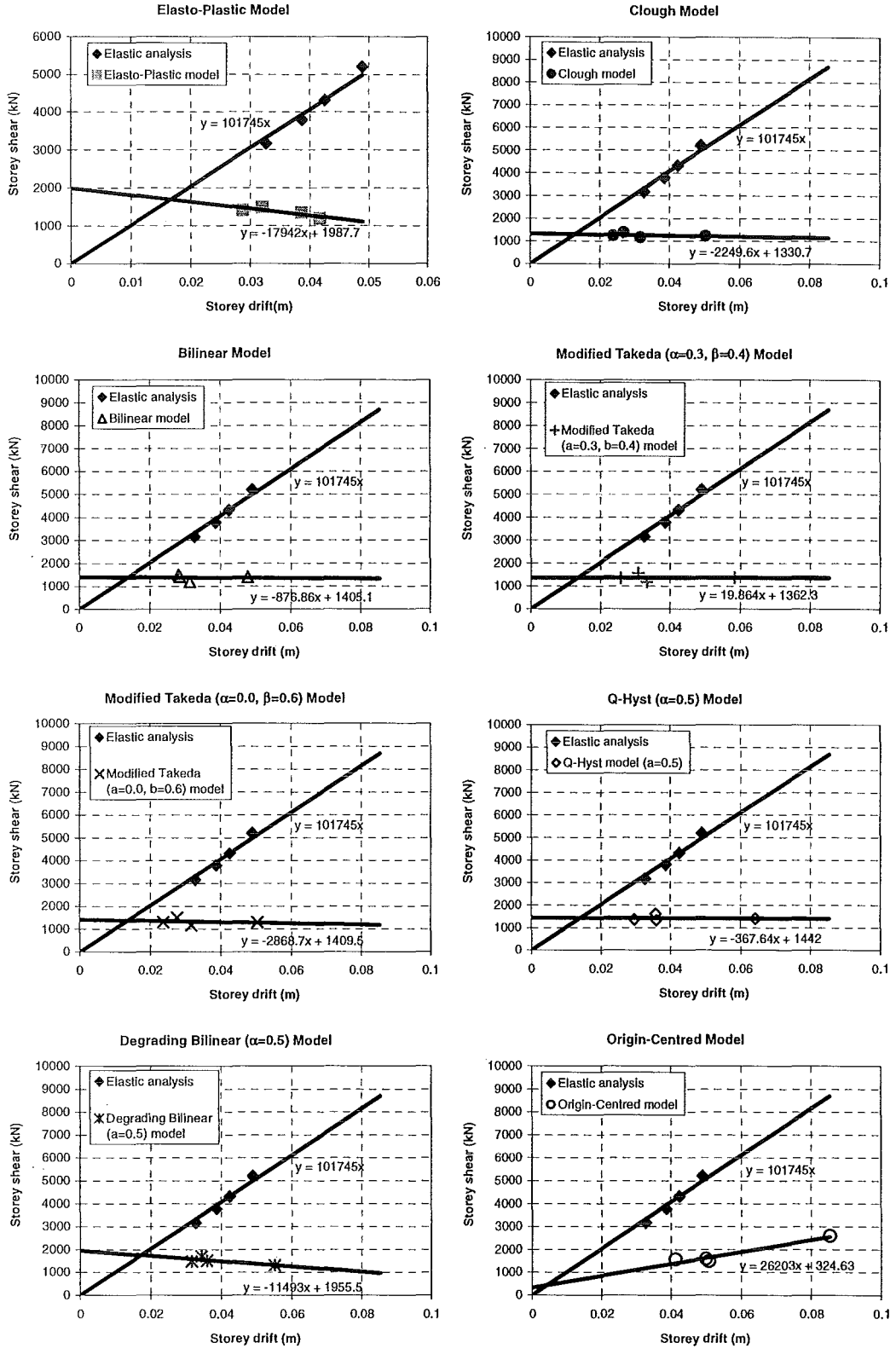

Fig. G-35 Storey yield point at level-14 of 18 storey structure for Carr & Tabuchi method to the eight hysteresis models

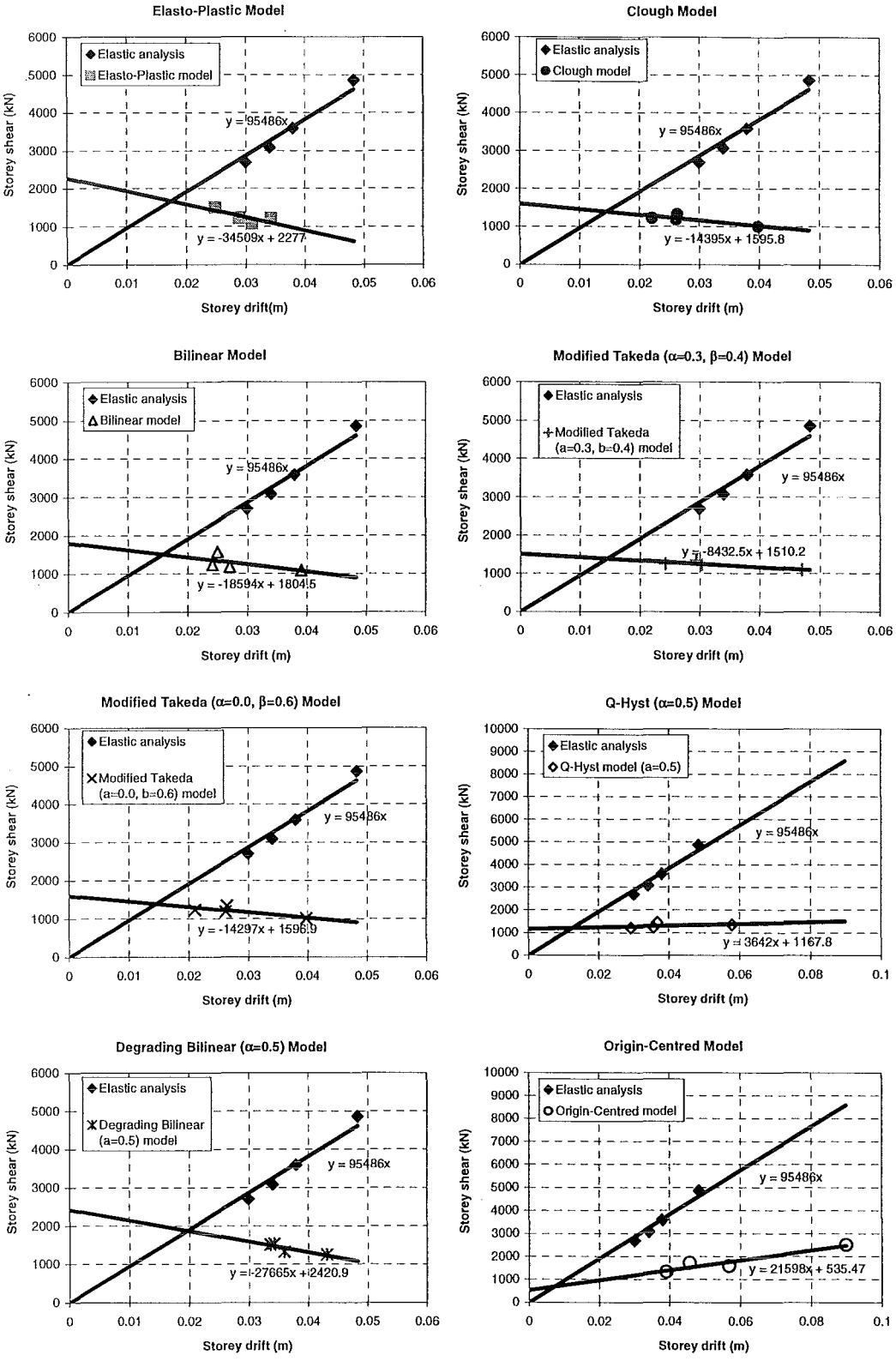

Fig. G-36 Storey yield point at level-15 of 18 storey structure for Carr & Tabuchi method to the eight hysteresis models

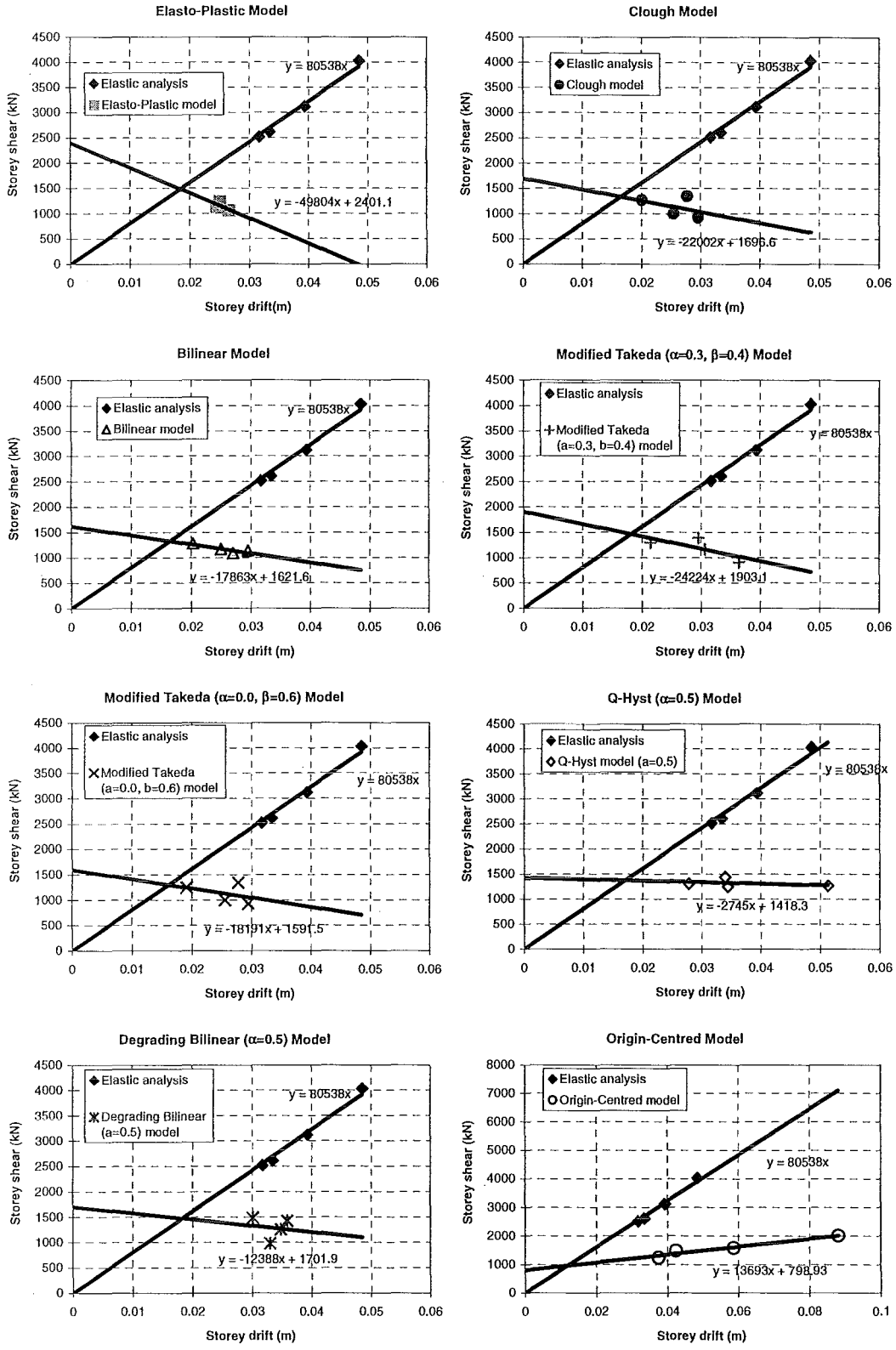

Fig. G-37 Storey yield point at level-16 of 18 storey structure for Carr & Tabuchi method to the eight hysteresis models

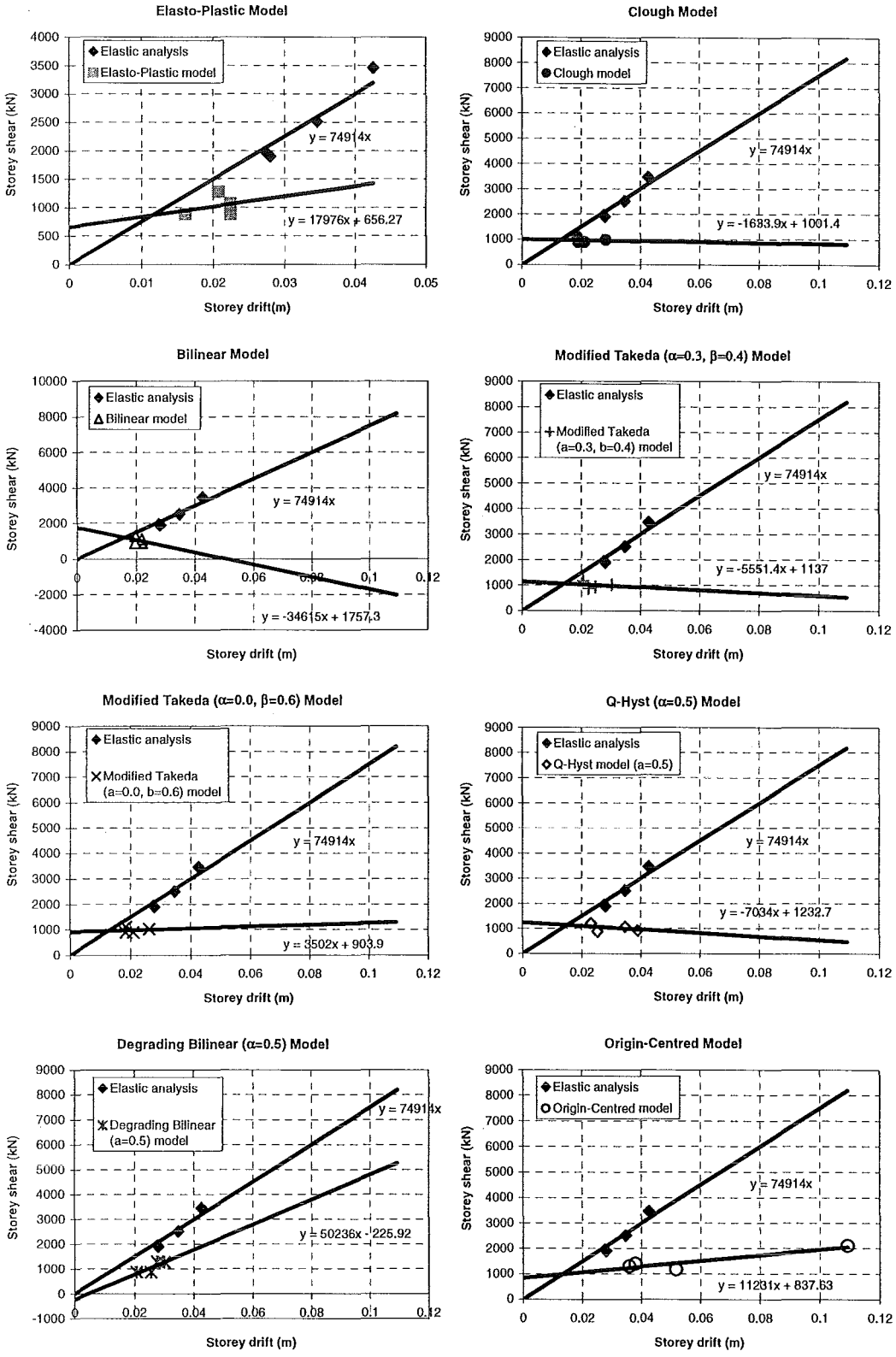

Fig. G-38 Storey yield point at level-17 of 18 storey structure for Carr & Tabuchi method to the eight hysteresis models

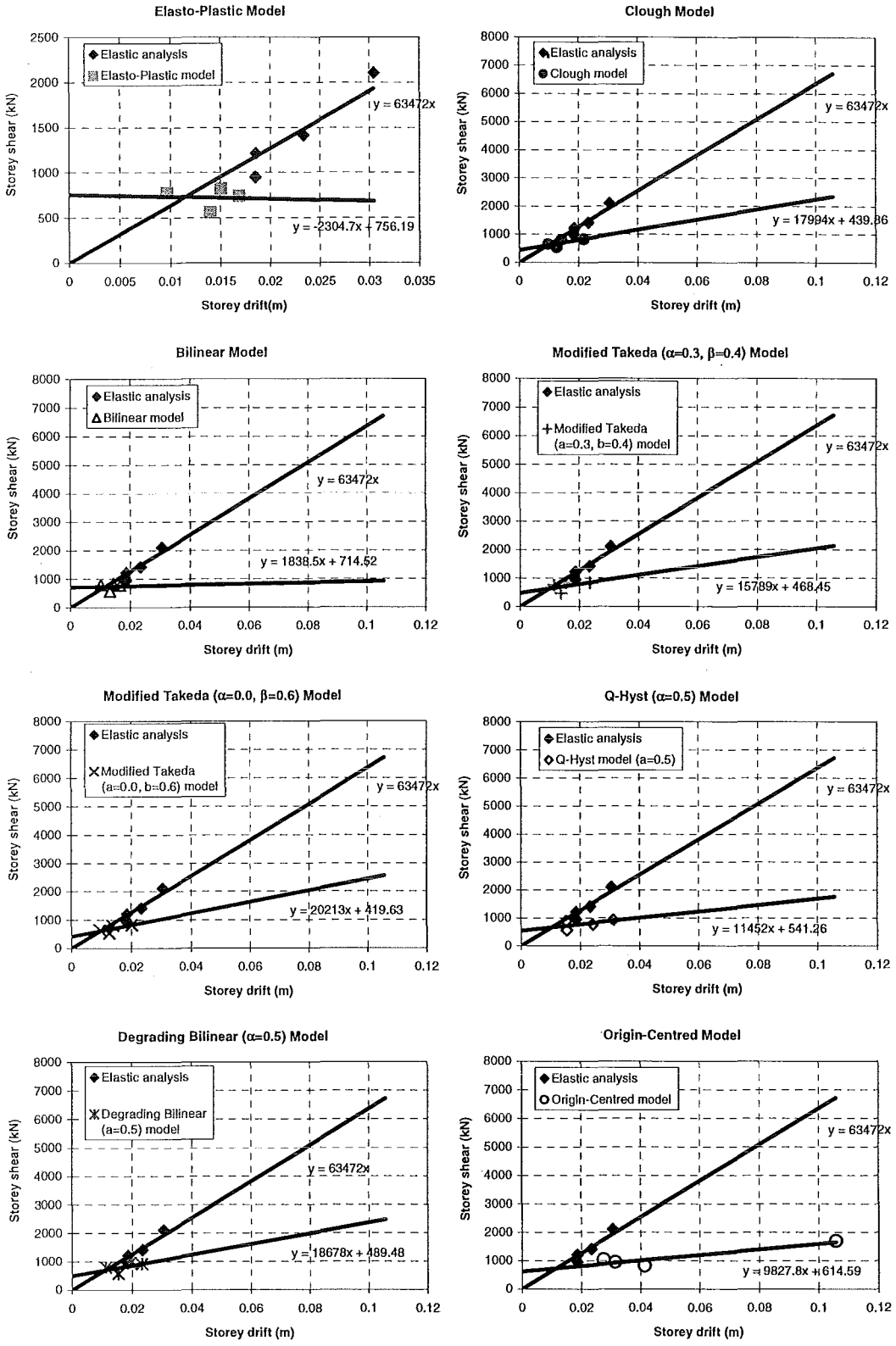

Fig. G-39 Storey yield point at level-18 of 18 storey structure for Carr & Tabuchi method to the eight hysteresis models

APPENDIX H
Figures for Chapter 8

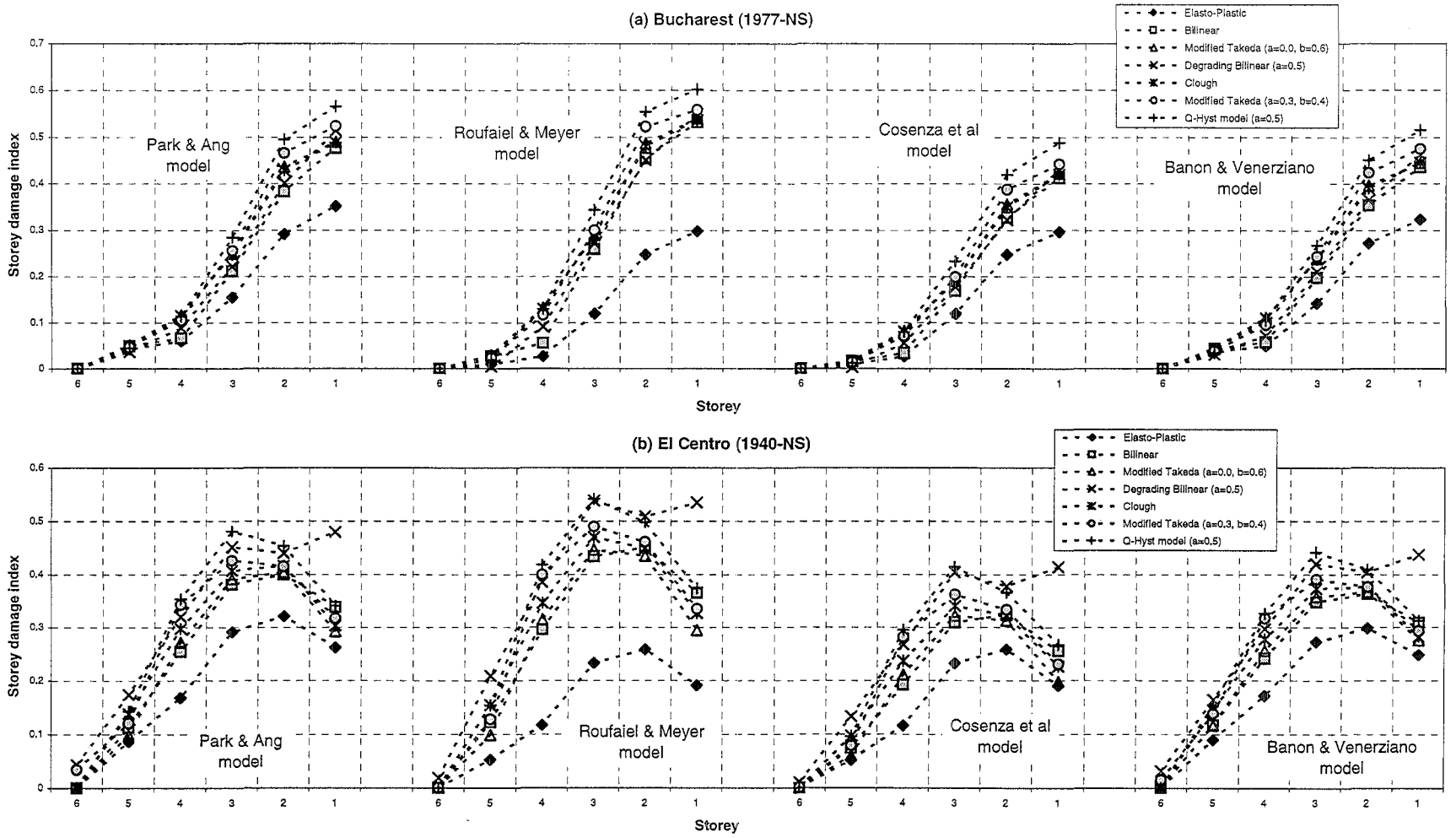

Fig. H-1 Distribution of storey damage indices to the seven hysteresis models for the four member damage models for the **6 storey structure** under the **Bucharest (1977-NS)** and **El Centro (1940-NS)** earthquakes

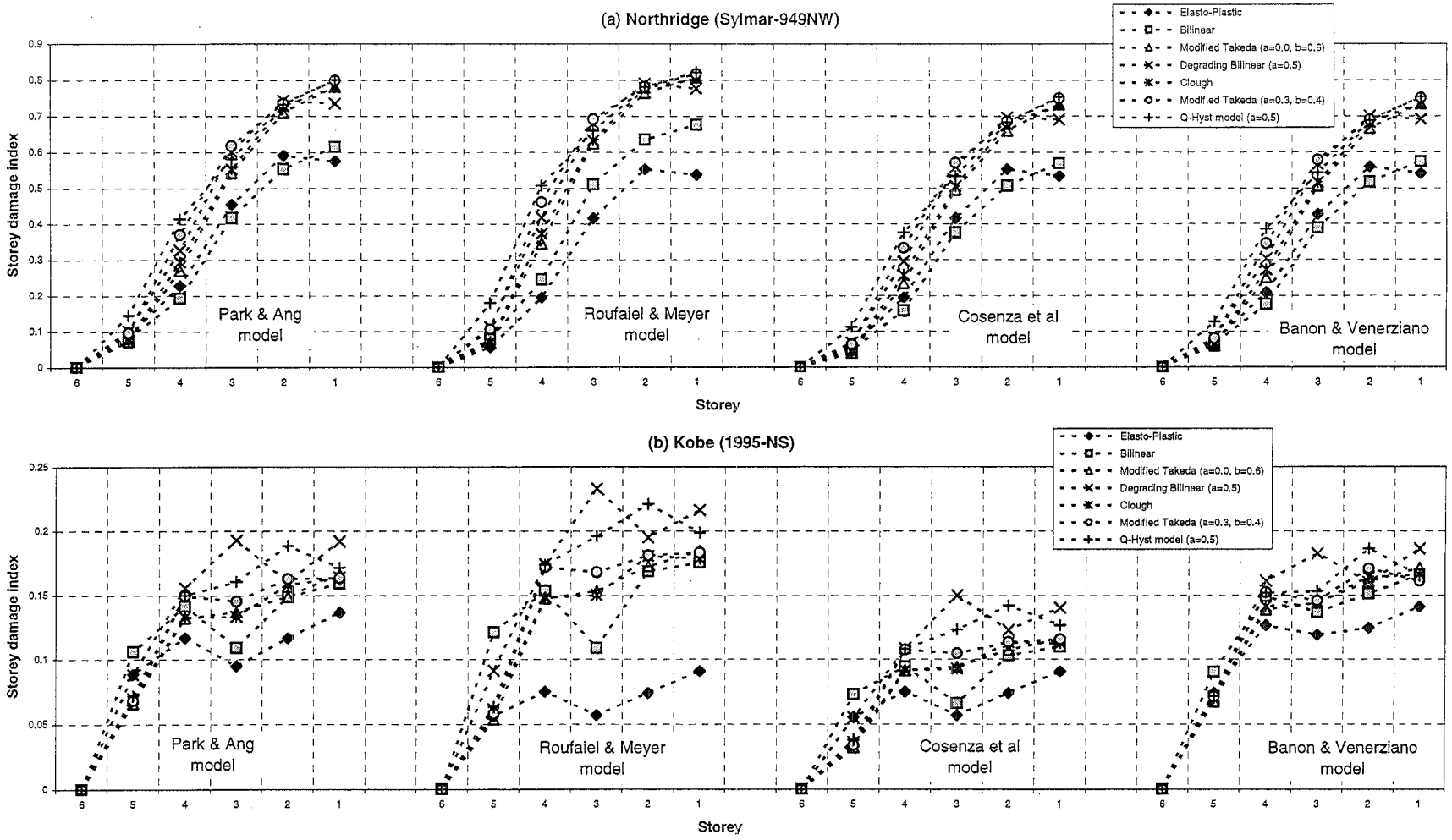

Fig. H-2 Distribution of storey damage indices to the seven hysteresis models for the four member damage models for the **6 storey structure** under the **Northridge (Sylmar-949NW)** and **Kobe (1995-NS)** earthquakes

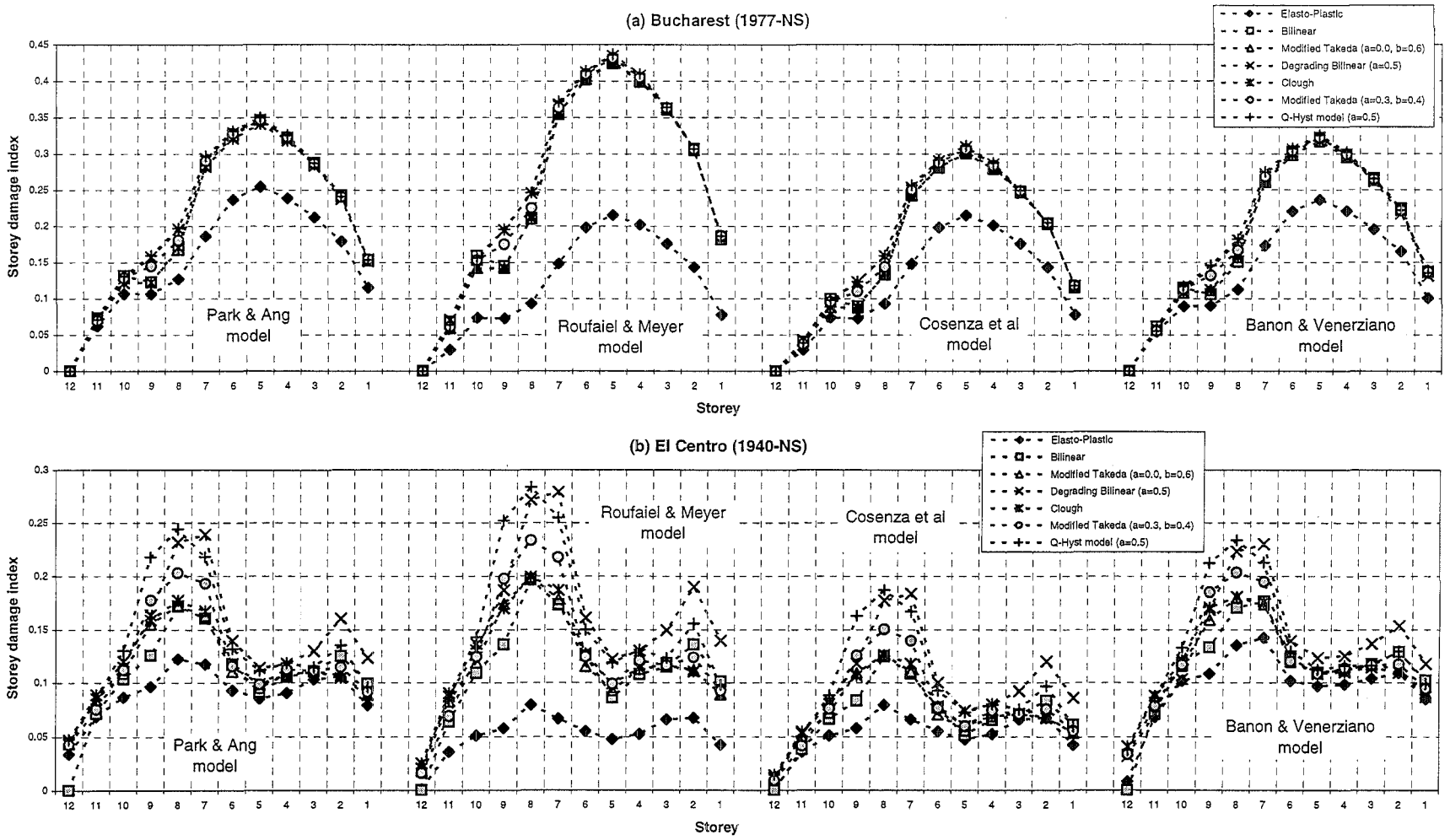

Fig. H-3 Distribution of storey damage indices to the seven hysteresis models for the four member damage models for the **12 storey structure** under the **Bucharest (1977-NS)** and **El Centro (1940-NS)** earthquakes

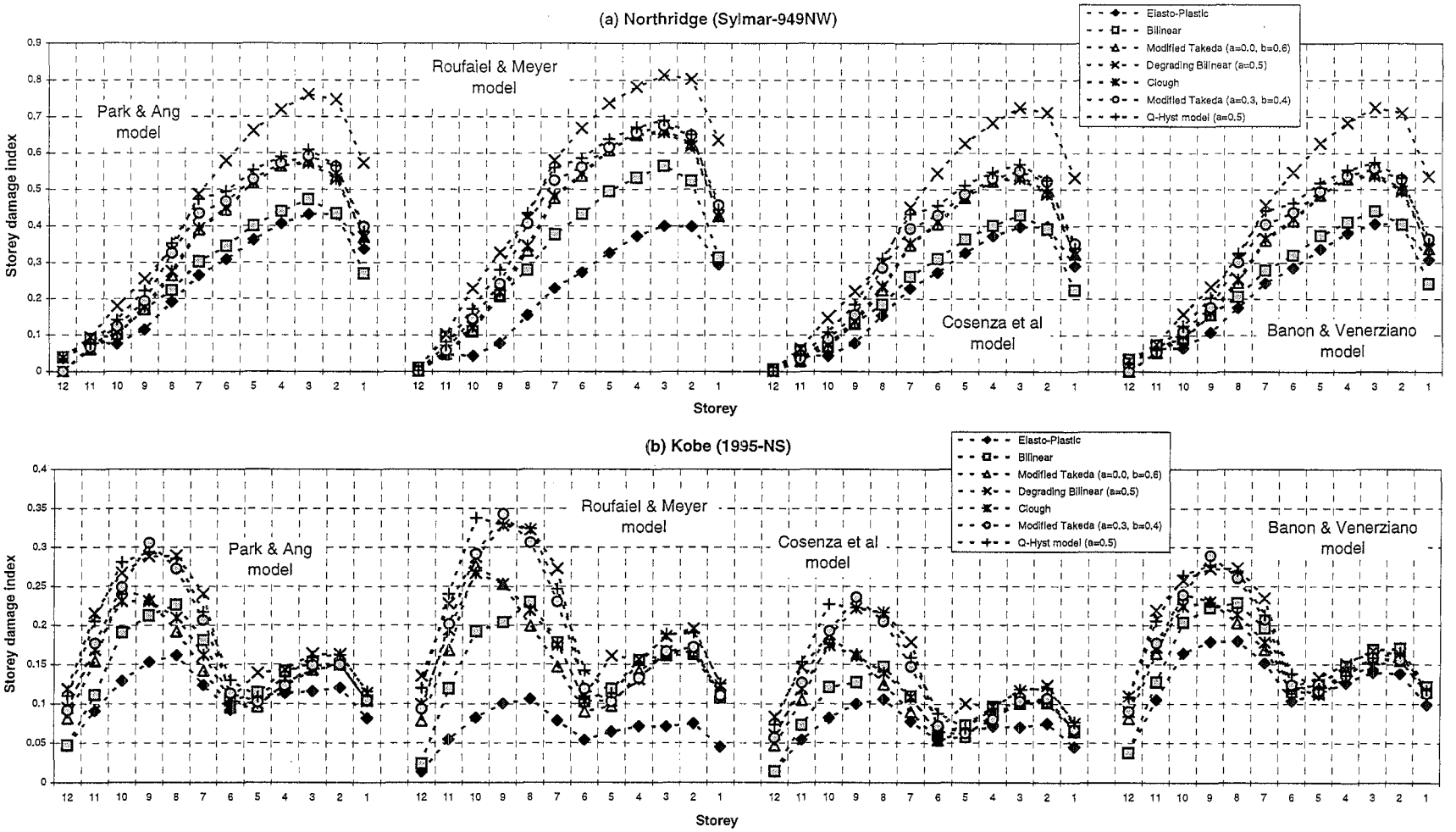

Fig. H-4 Distribution of storey damage indices to the seven hysteresis models for the four member damage models for the **12 storey structure** under the **Northridge (Sylmar-949NW)** and **Kobe (1995-NS)** earthquakes

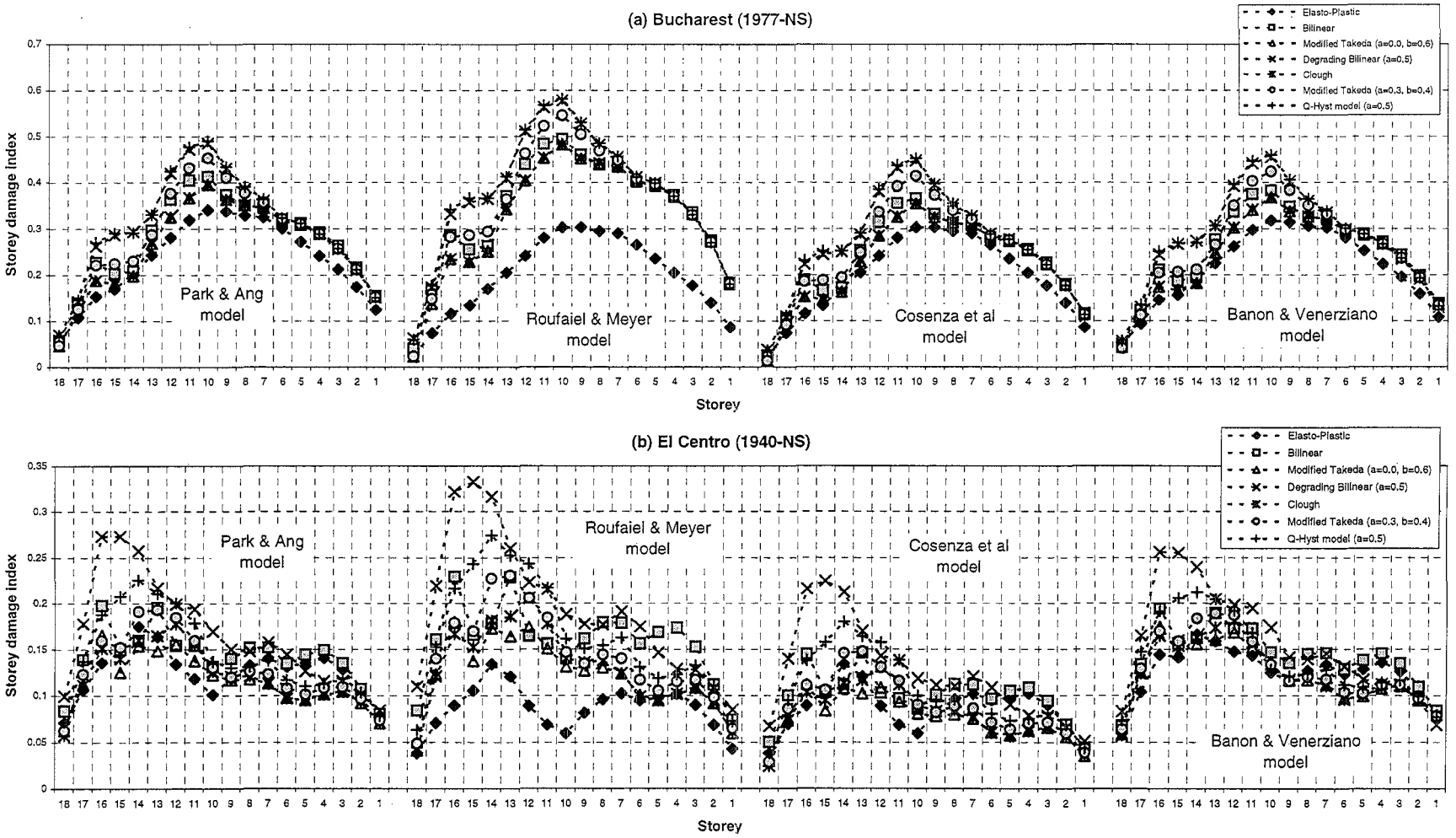

Fig. H-5 Distribution of storey damage indices to the seven hysteresis models for the four member damage models for the **18 storey structure** under the **Bucharest (1977-NS)** and **El Centro (1940-NS)** earthquakes

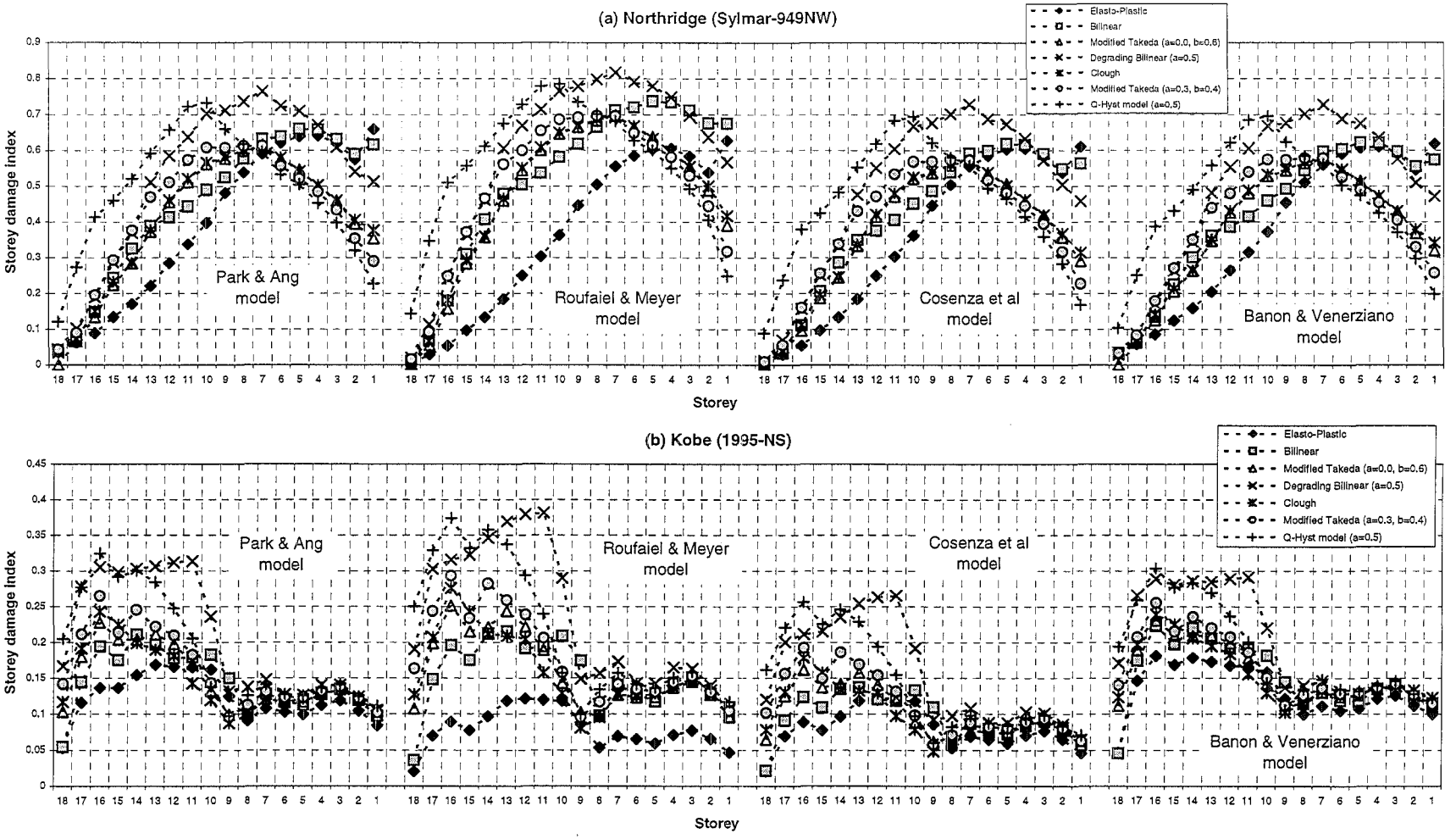

Fig. H-6 Distribution of storey damage indices to the seven hysteresis models for the four member damage models for the **18 storey structure** under the **Northridge (Sylmar-949NW)** and **Kobe (1995-NS)** earthquakes

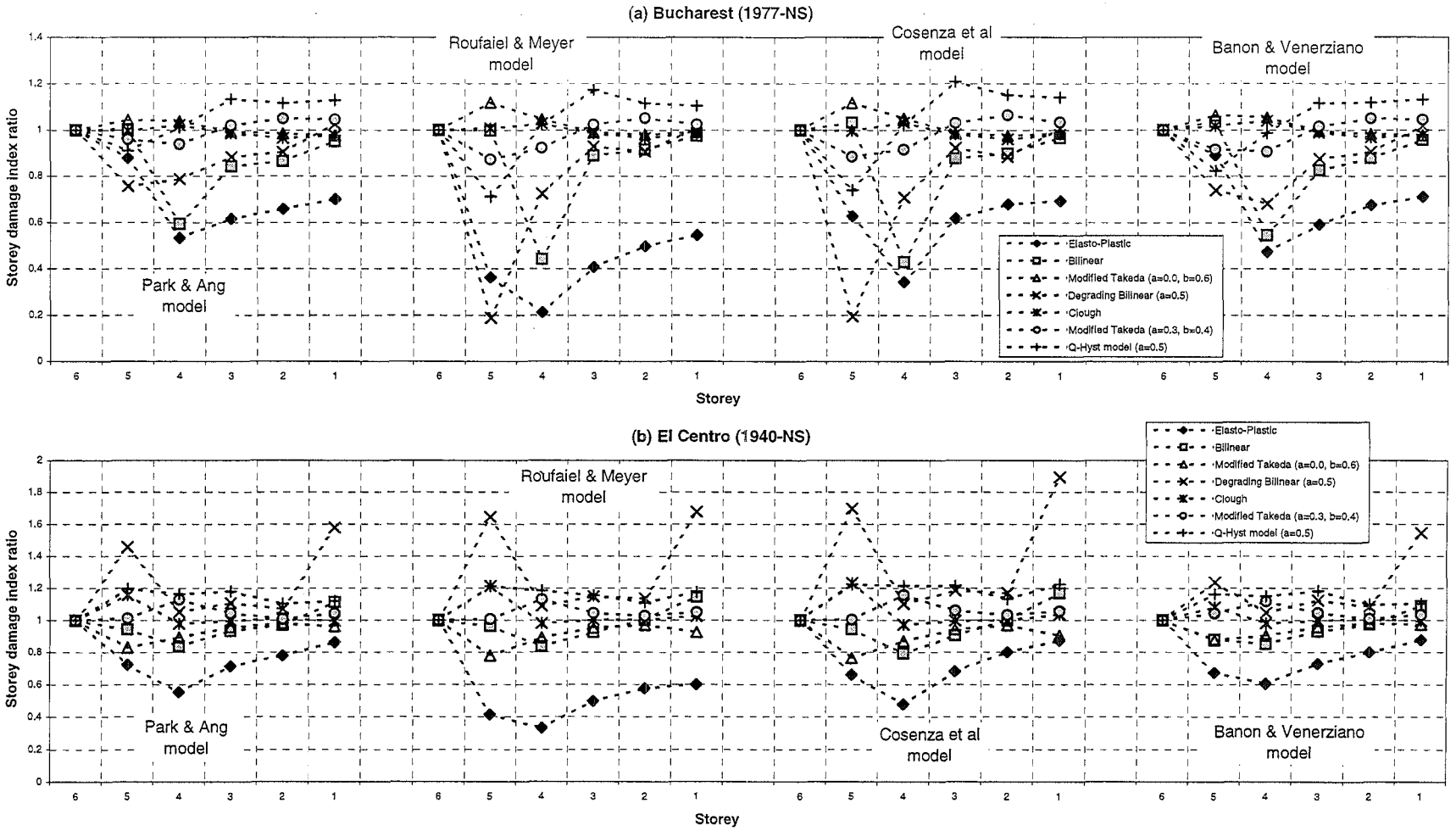

Fig. H-7 Distribution of ratios of storey damage indices for each of the seven hysteresis model to the average of those for the three hysteresis models for the **6 storey structure** under the **Bucharest (1977-NS)** and **El Centro (1940-NS)** earthquakes

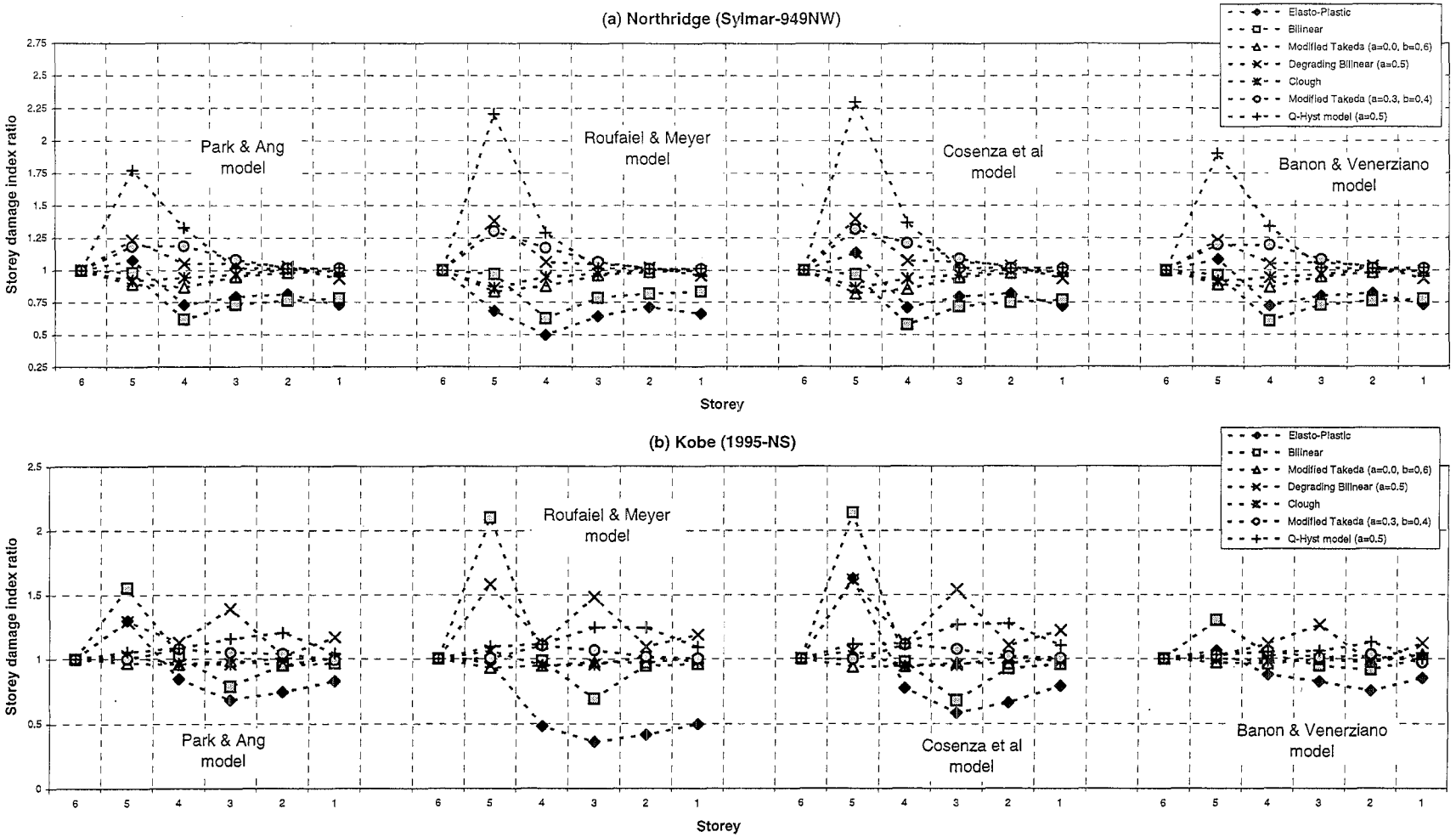

Fig. H-8 Distribution of ratios of storey damage indices for each of the seven hysteresis models to the average of those for the three hysteresis models for the **6 storey structure** under the **Northridge (Sylmar-949NW)** and **Kobe (1995-NS)** earthquakes

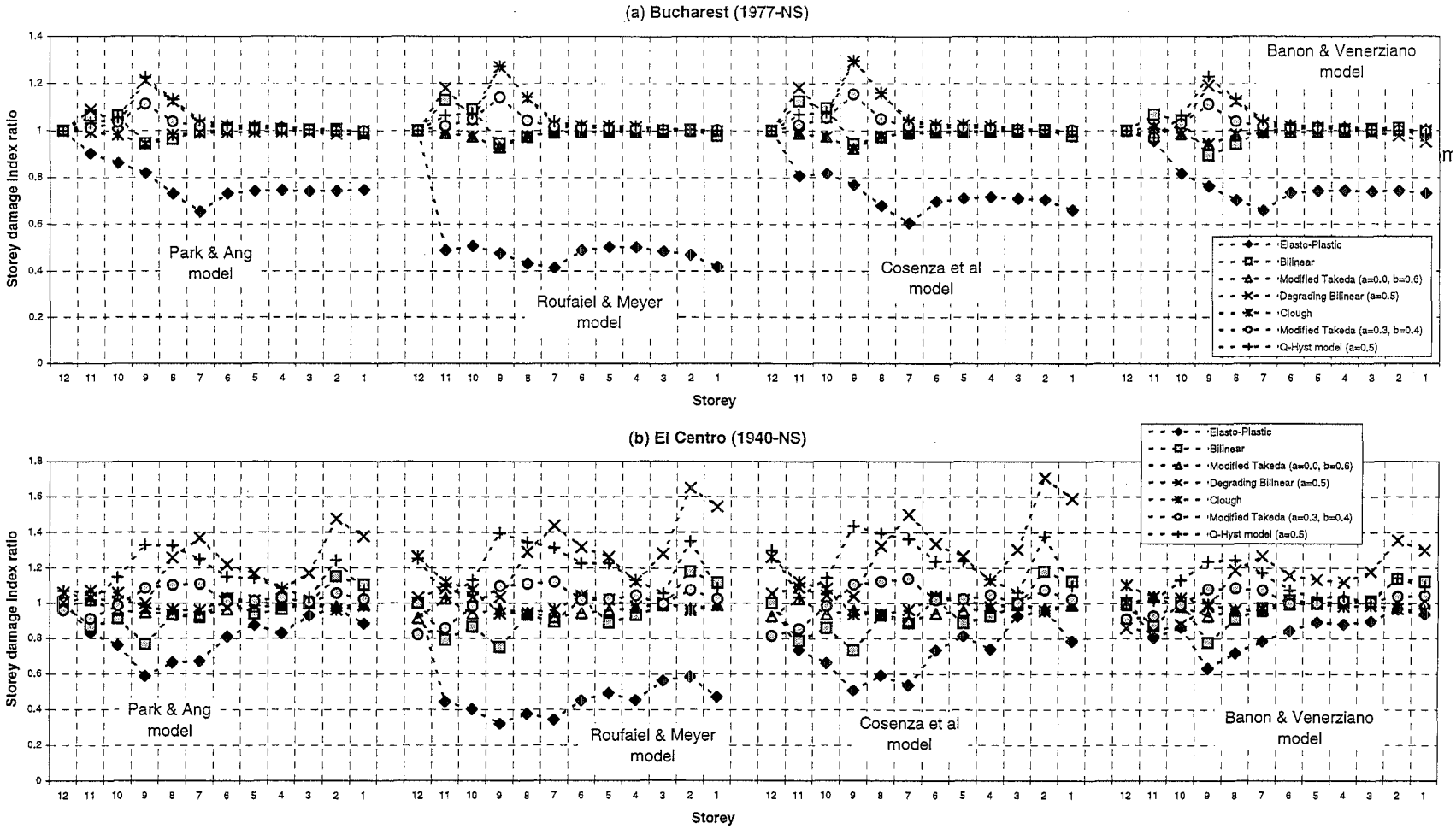

Fig. H-9 Distribution of ratios of storey damage indices for each of the seven hysteresis model to the average of those for the three hysteresis models for the **12 storey structure** under the **Bucharest (1977-NS)** and **El Centro (1940-NS)** earthquakes

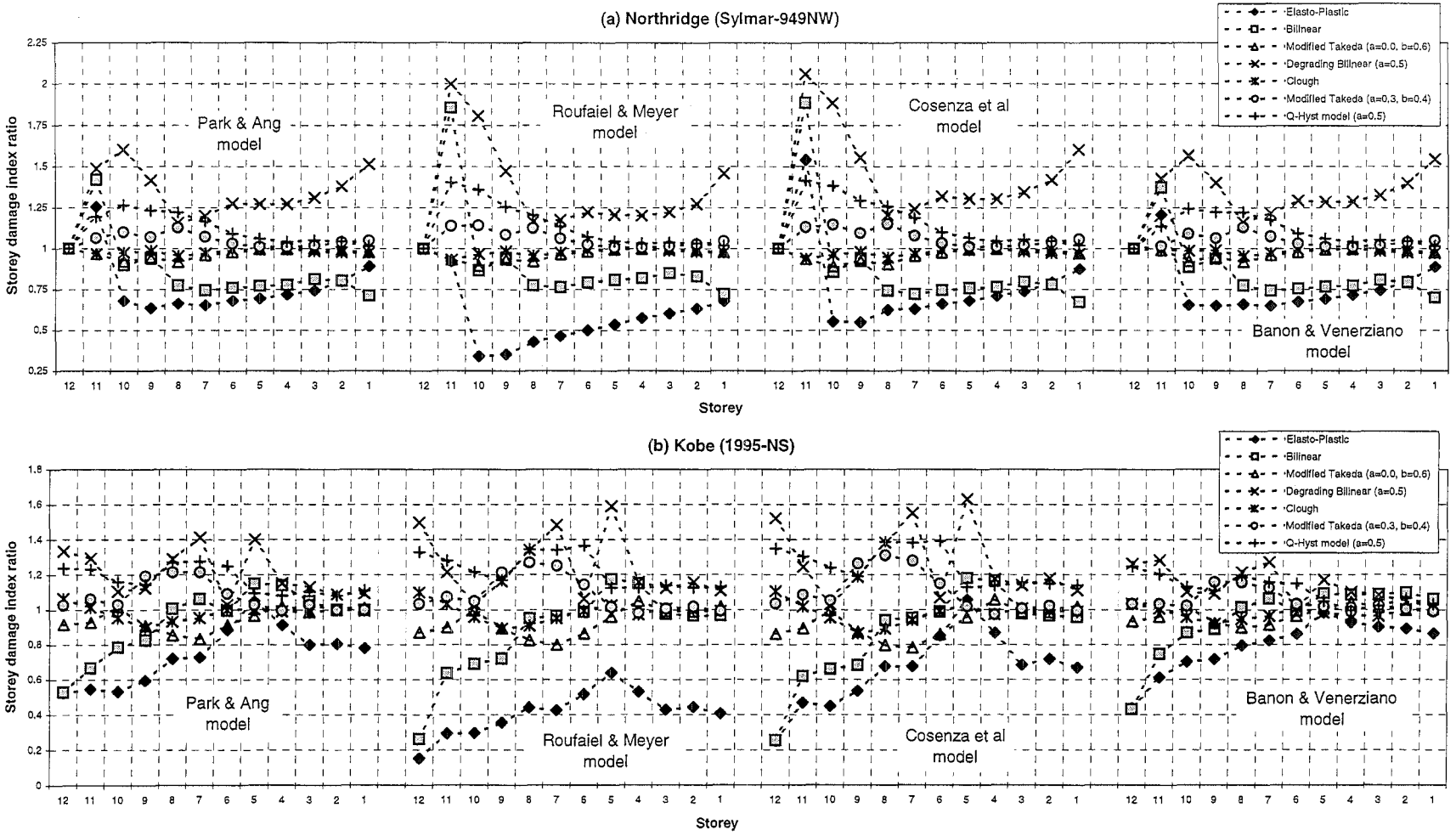

Fig. H-10 Distribution of ratios of storey damage indices for each of the seven hysteresis model to the average of those for the three hysteresis models for the **12 storey structure** under the **Northridge (Sylmar-949NW)** and **Kobe (1995-NS)** earthquakes

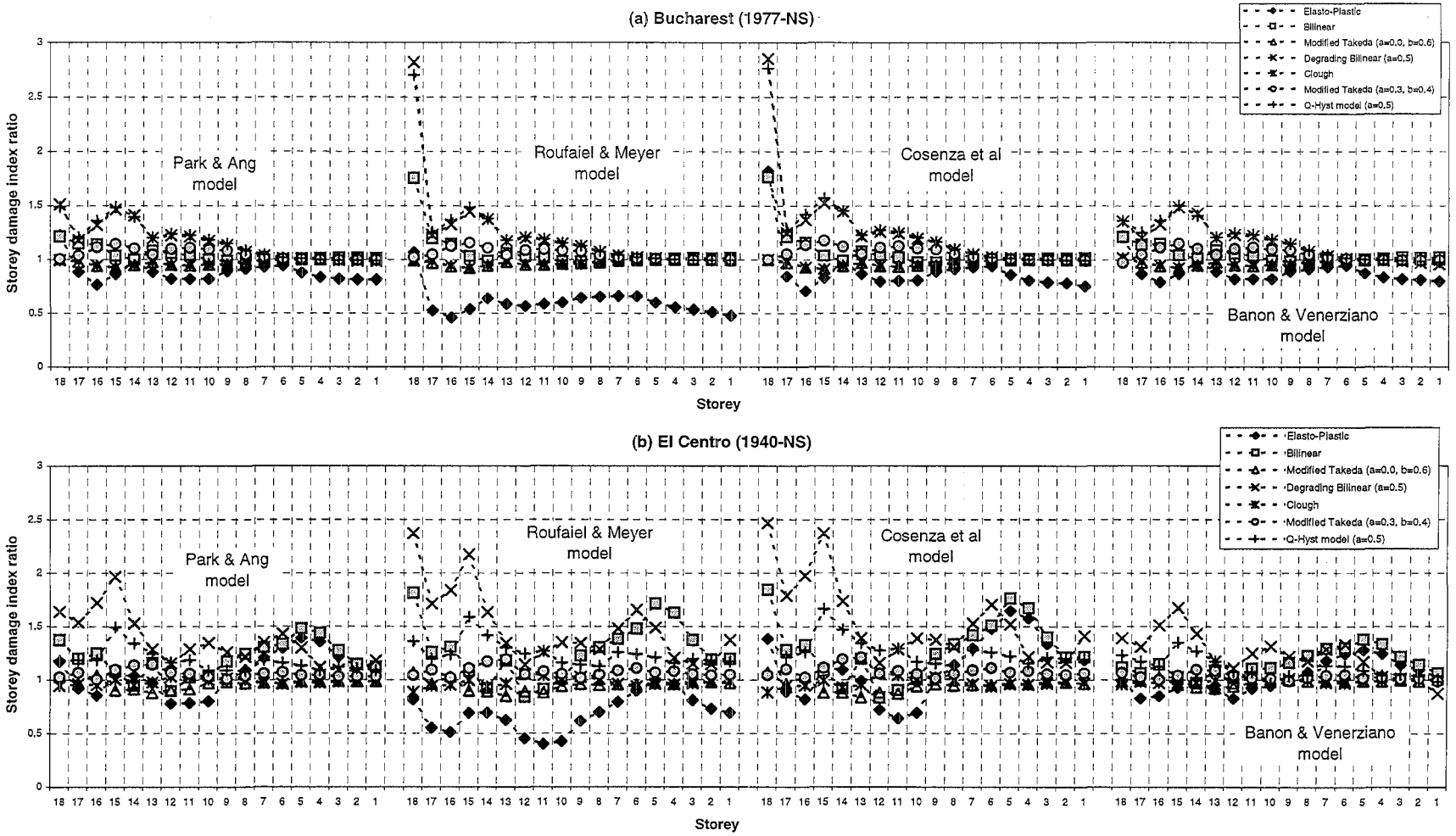

Fig. H-11 Distribution of ratios of storey damage indices for each of the seven hysteresis model to the average of those for the three hysteresis models for the **18 storey structure** under the **Bucharest (1977-NS)** and **El Centro (1940-NS)** earthquakes

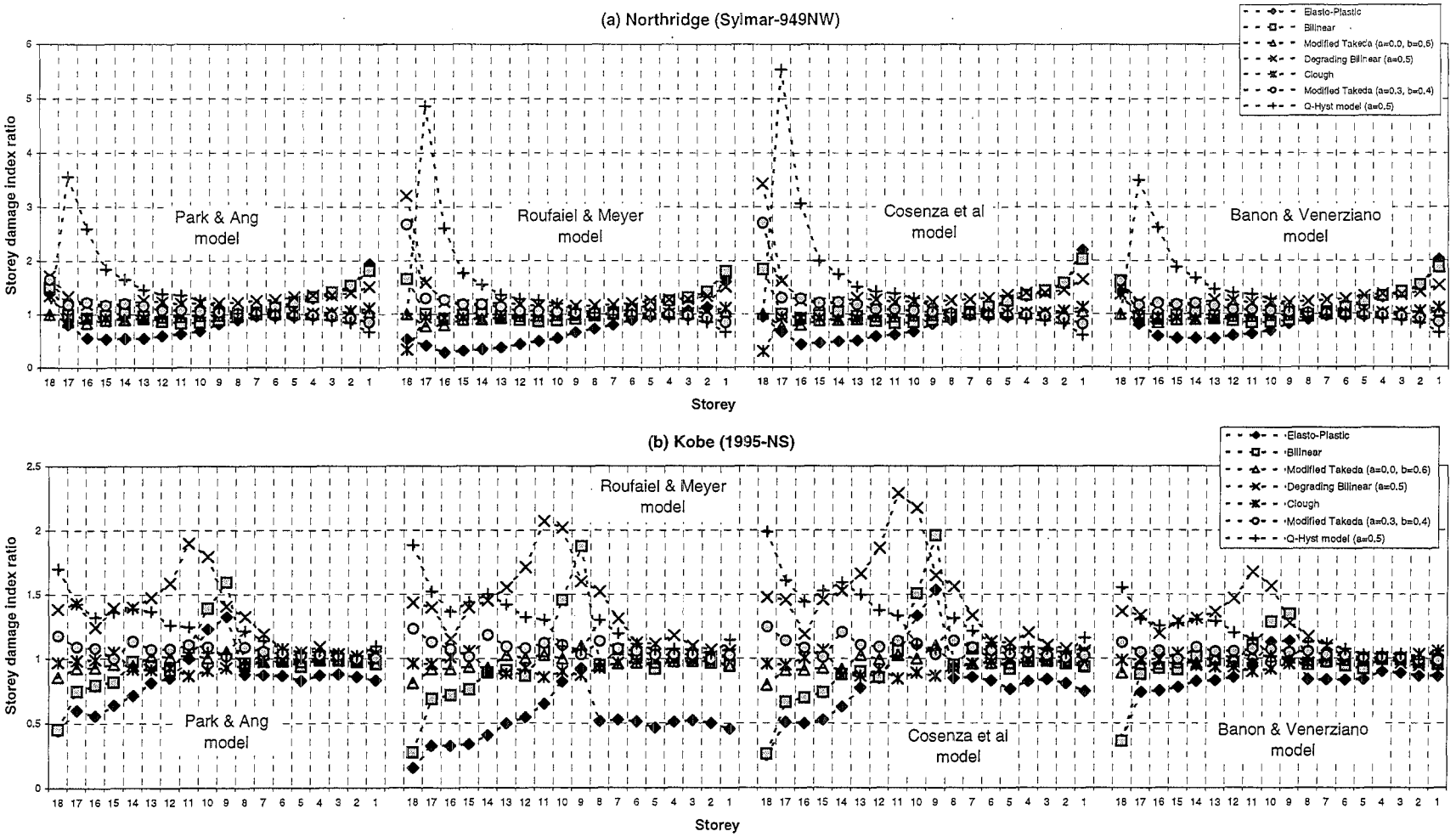

Fig. H-12 Distribution of ratios of storey damage indices for each of the seven hysteresis model to the average of those for the three hysteresis models for the **18 storey structure** under the **Northridge (Sylmar-949NW)** and **Kobe (1995-NS)** earthquakes

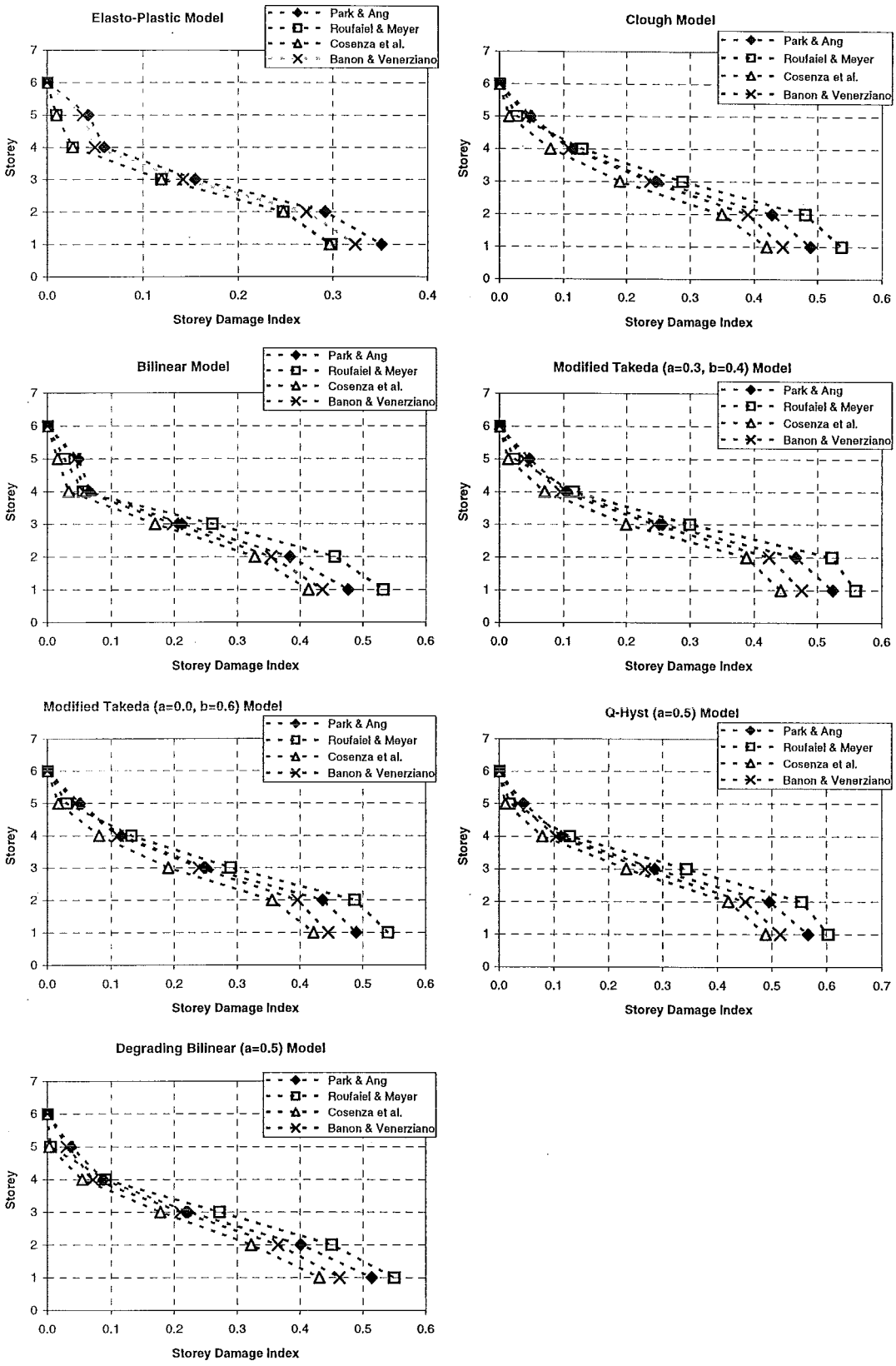

Fig. H-13 The distribution of storey damage index of the seven hysteresis models to the four damage models for the **6 storey structure** under the **Bucharest (1977-NS)** earthquake

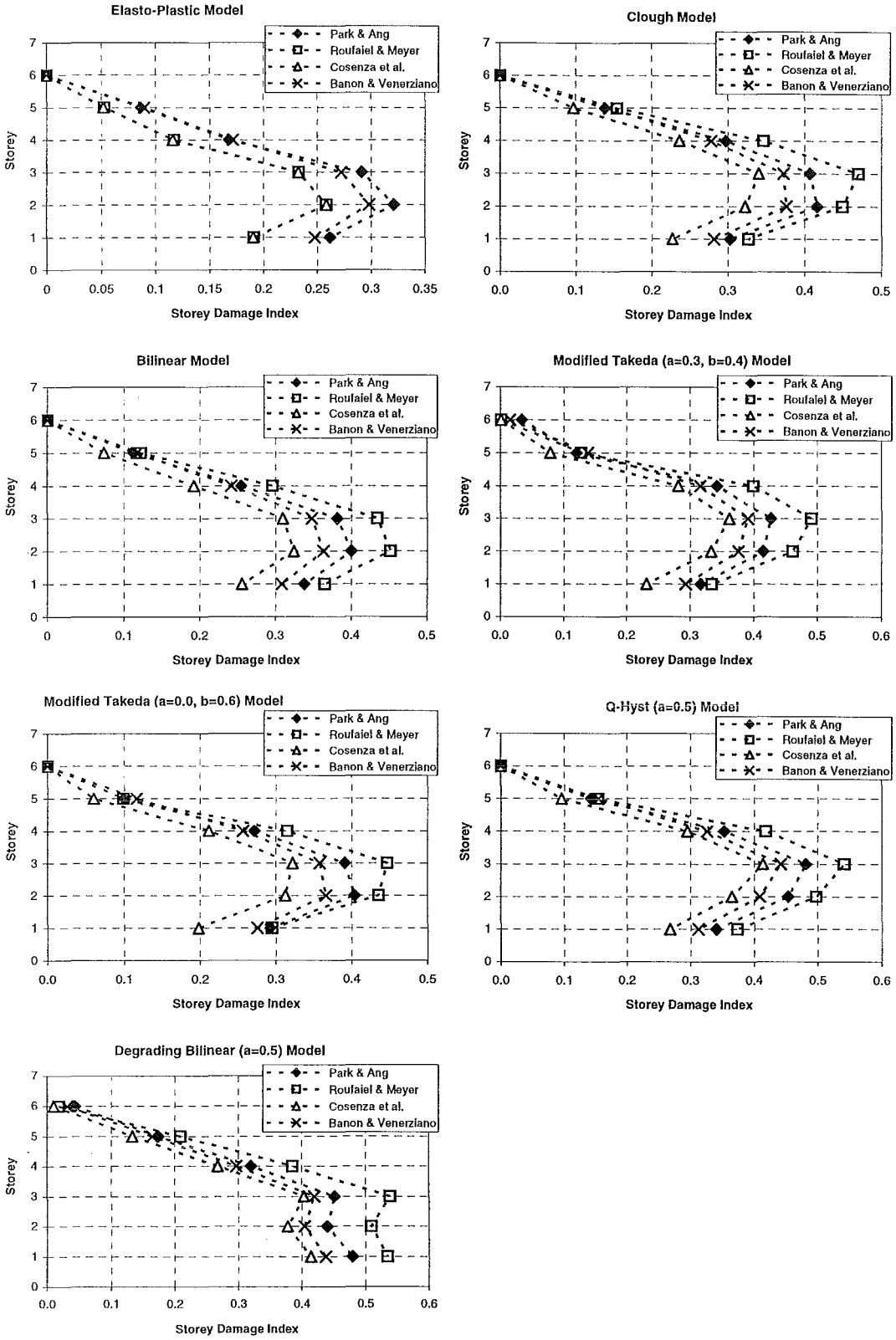

Fig. H-14 The distribution of storey damage index of the seven hysteresis models to the four damage models for the **6 storey structure** under the **El Centro (1940-NS)** earthquake

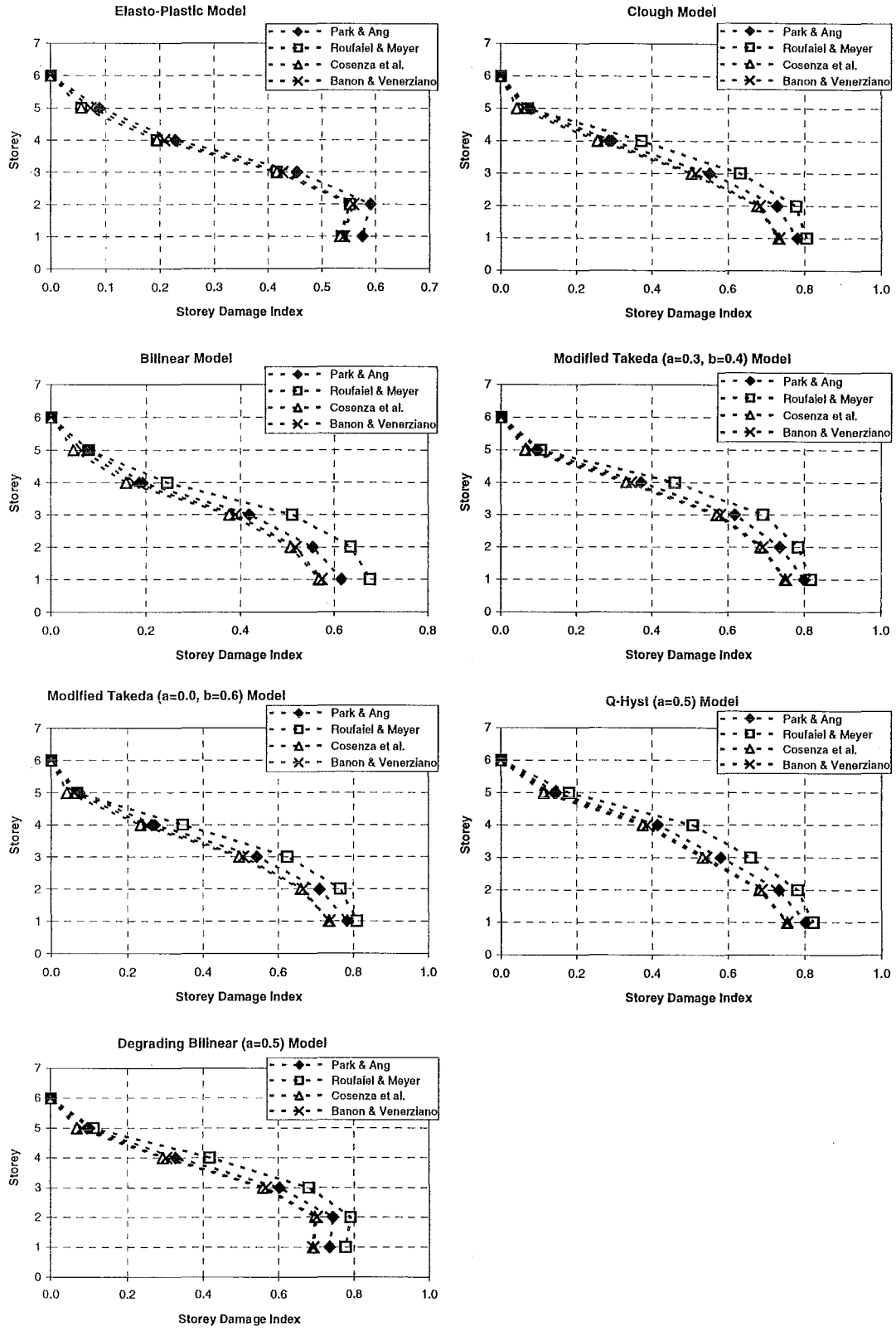

Fig. H-15 The distribution of storey damage index of the seven hysteresis models to the four damage models for the **6 storey structure** under the **Northridge (Sylmar-949NW)** earthquake

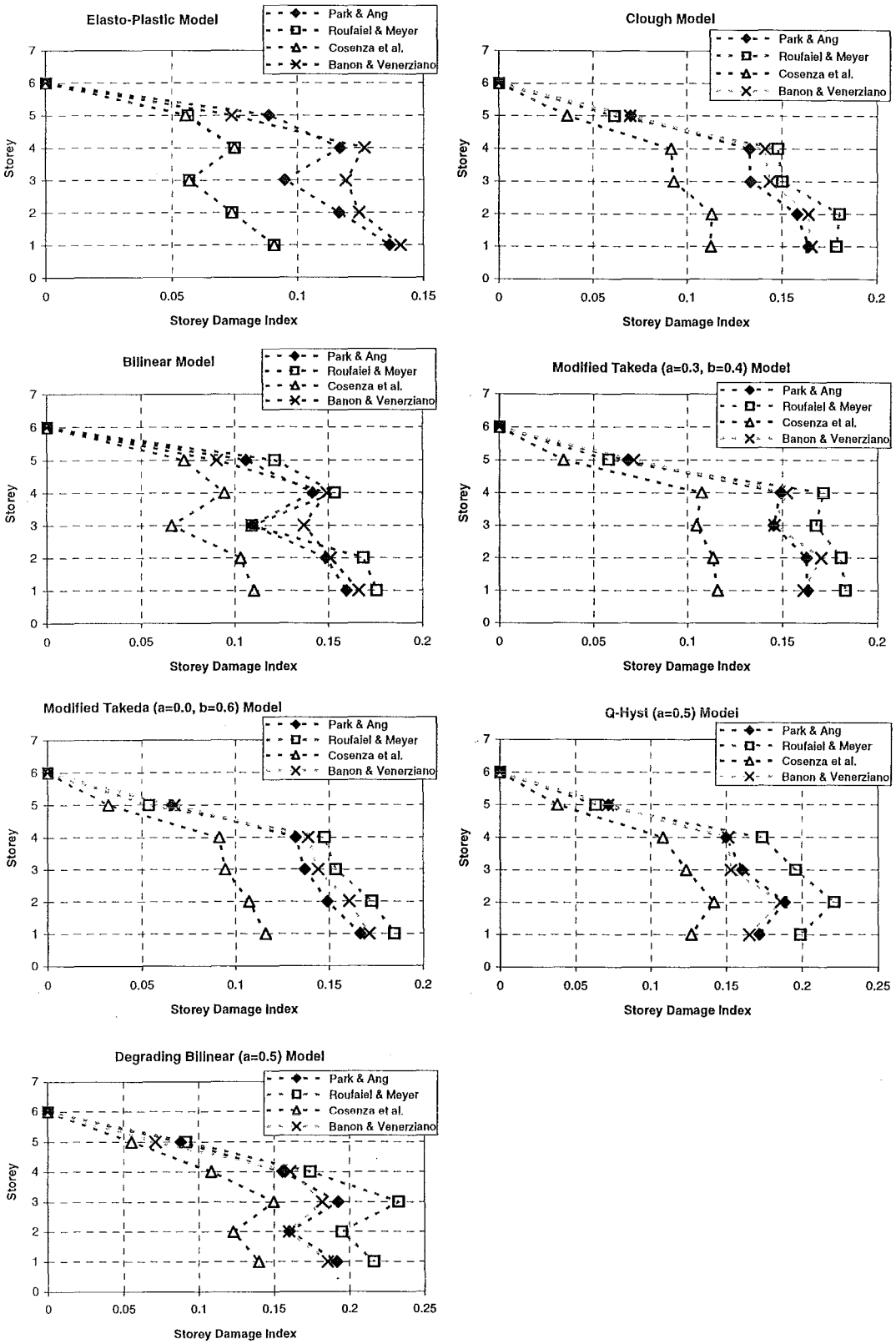

Fig. H-16 The distribution of storey damage index of the seven hysteresis models to the four damage models for the **6 storey structure** under the **Kobe (1995-NS)** earthquake

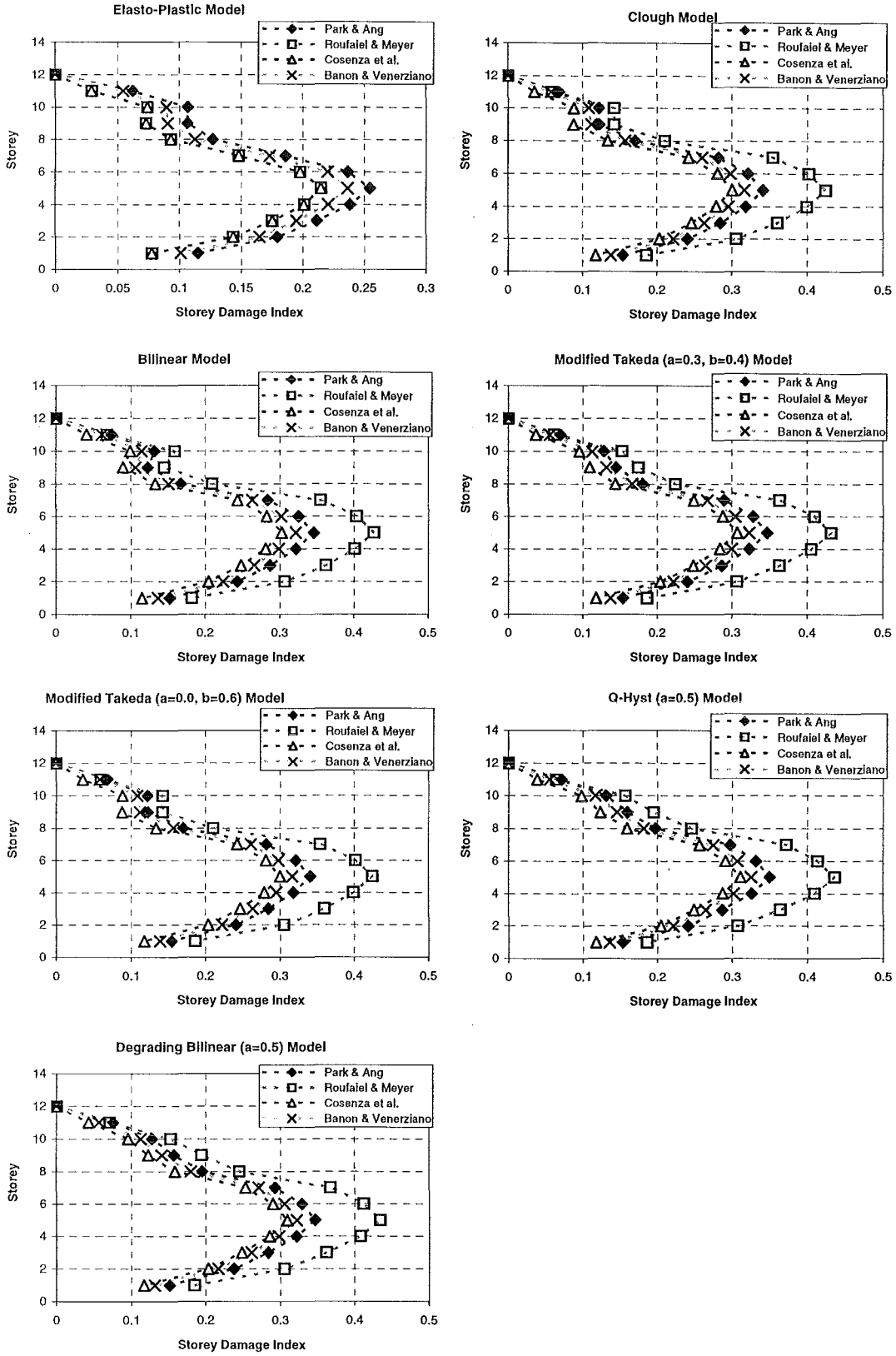

Fig. H-17 The distribution of storey damage index of the seven hysteresis models to the four damage models for the **12 storey structure** under the **Bucharest (1977-NS)** earthquake

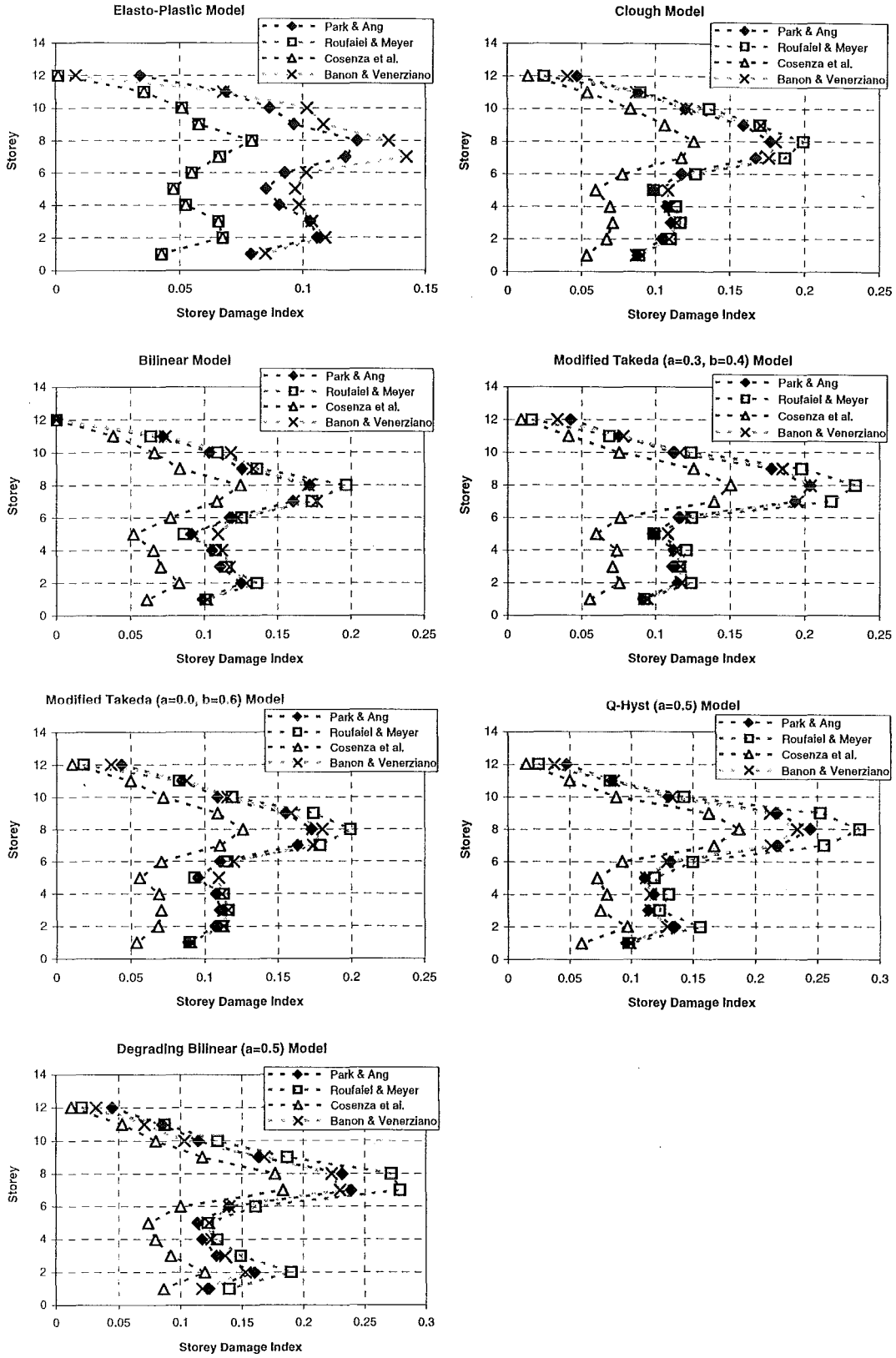

Fig. H-18 The distribution of storey damage index of the seven hysteresis models to the four damage models for the **12 storey structure** under the **El Centro (1940-NS)** earthquake

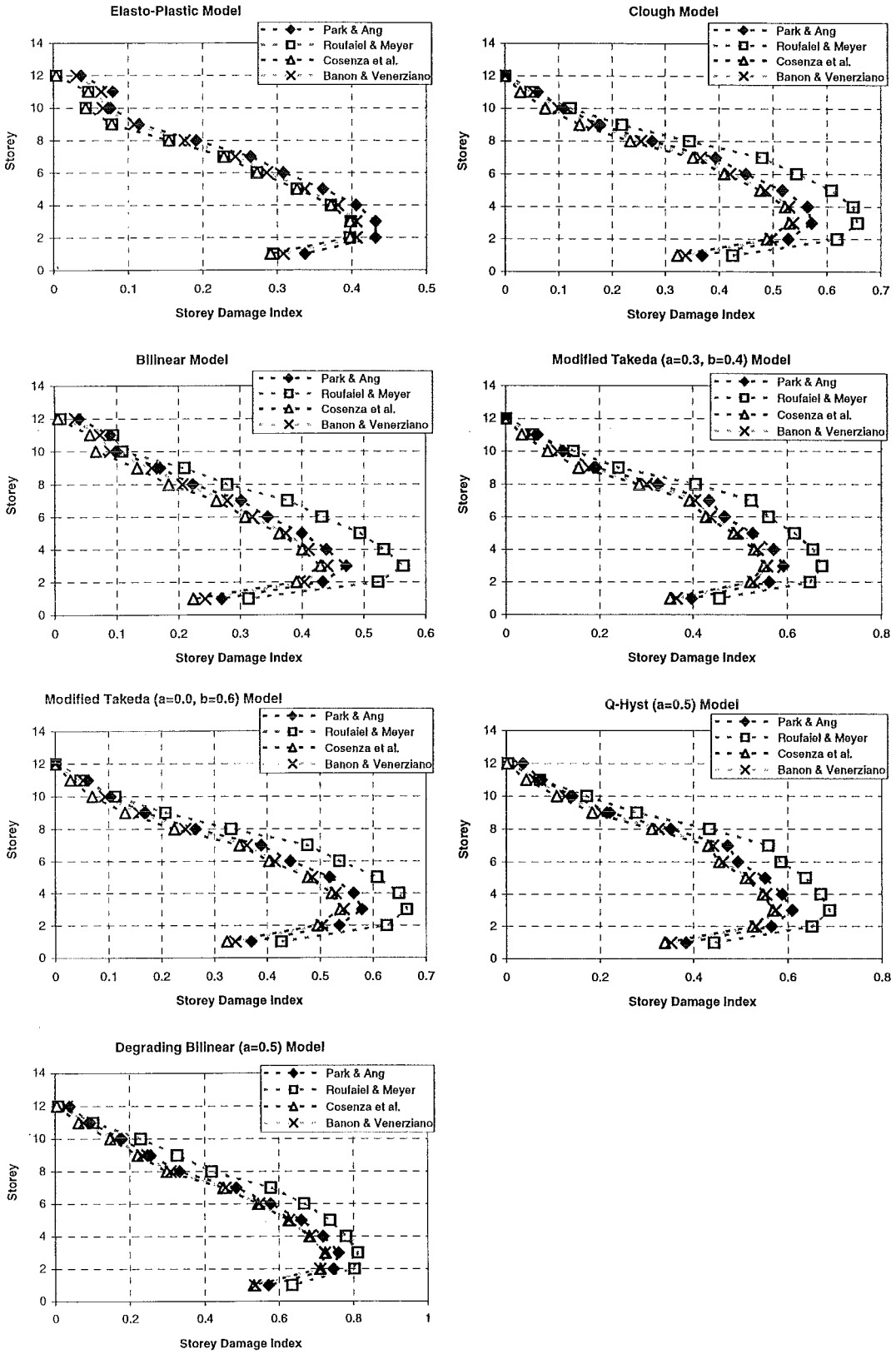

Fig. H-19 The distribution of storey damage index of the seven hysteresis models to the four damage models for the **12 storey structure** under the **Northridge (Sylmar-949NW)** earthquake

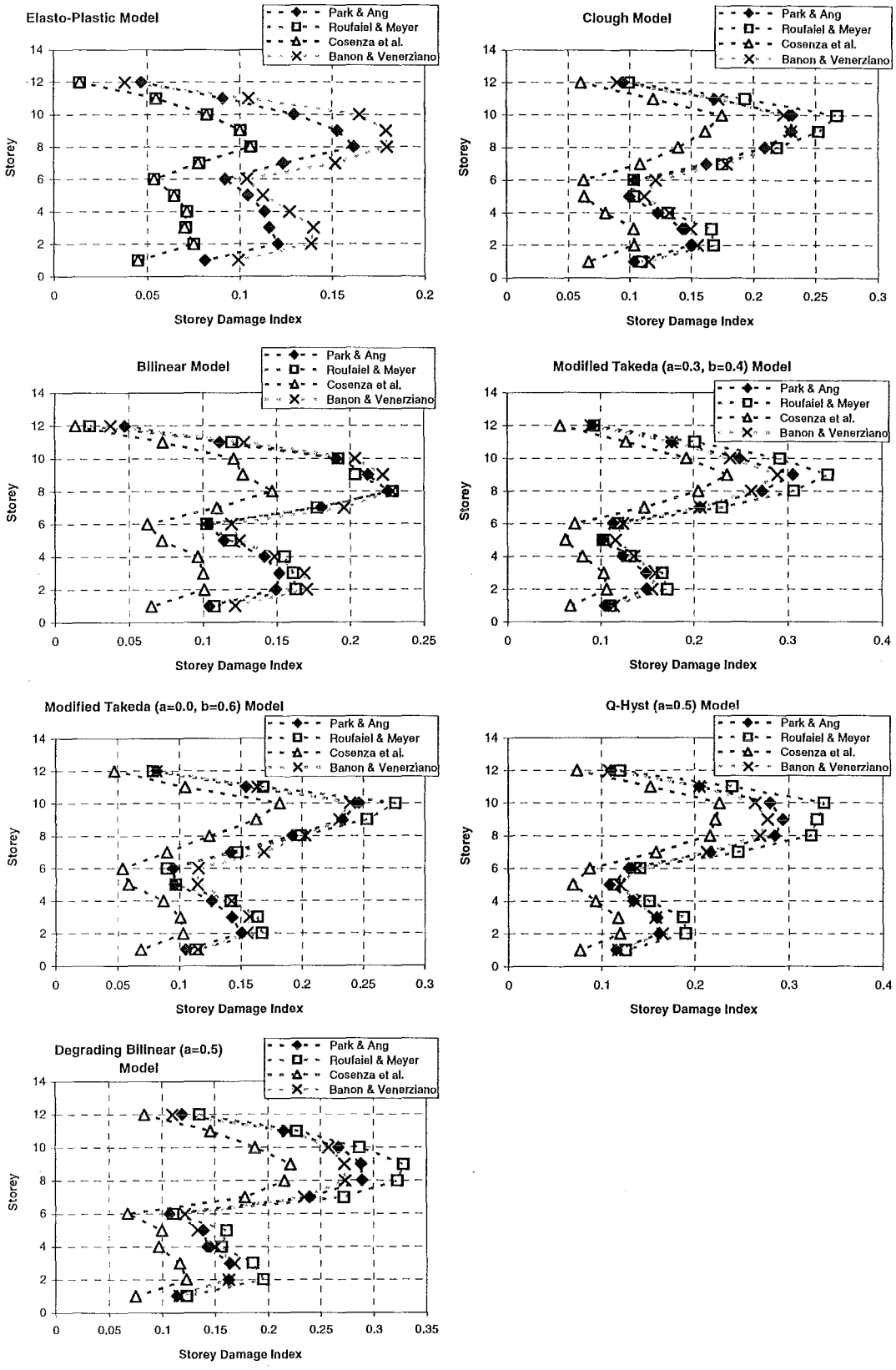

Fig. H-20 The distribution of storey damage index of the seven hysteresis models to the four damage models for the **12 storey structure** under the **Kobe (1995-NS)** earthquake

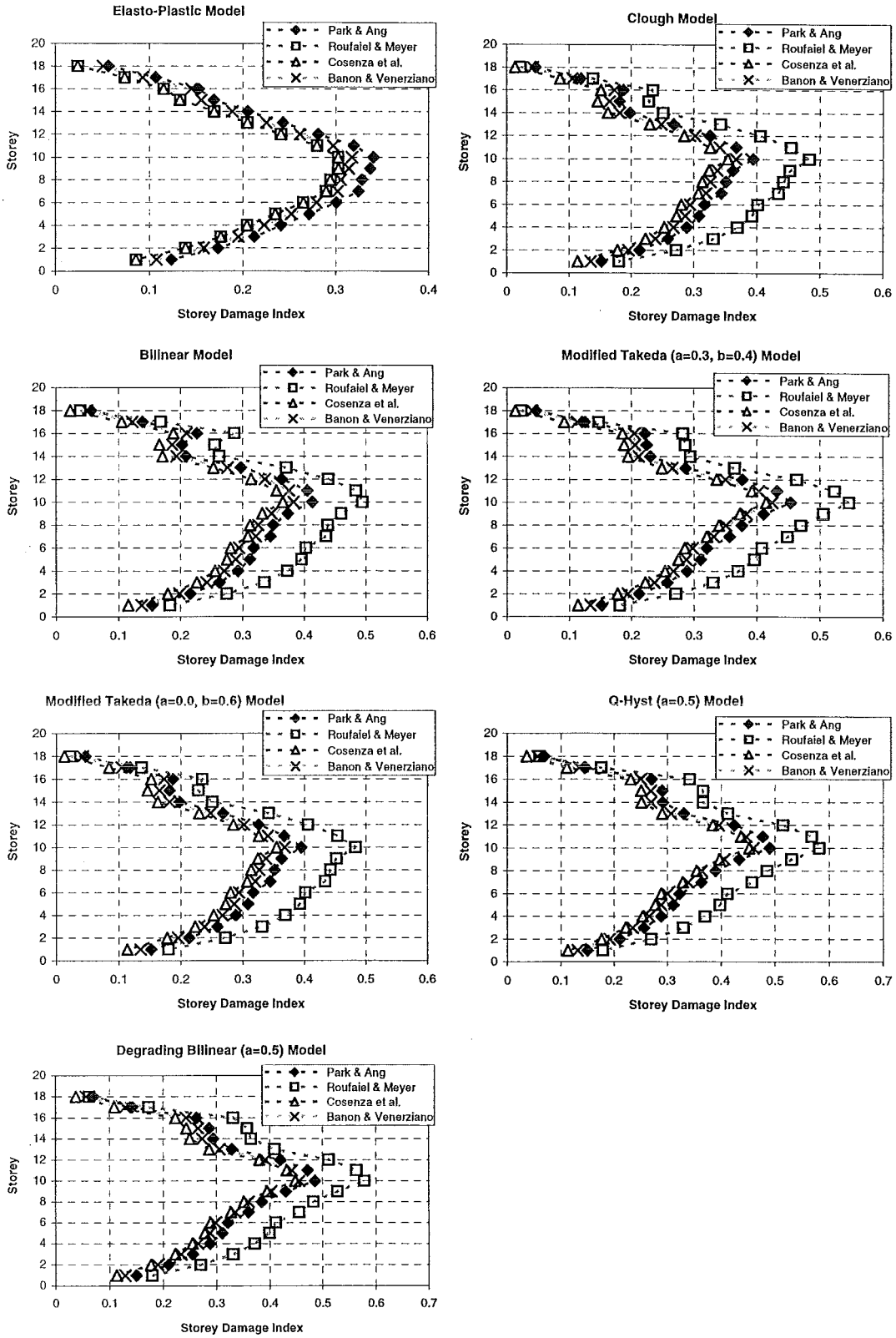

Fig. H-21 The distribution of storey damage index of the seven hysteresis models to the four damage models for the **18 storey structure** under the **Bucharest (1977-NS)** earthquake

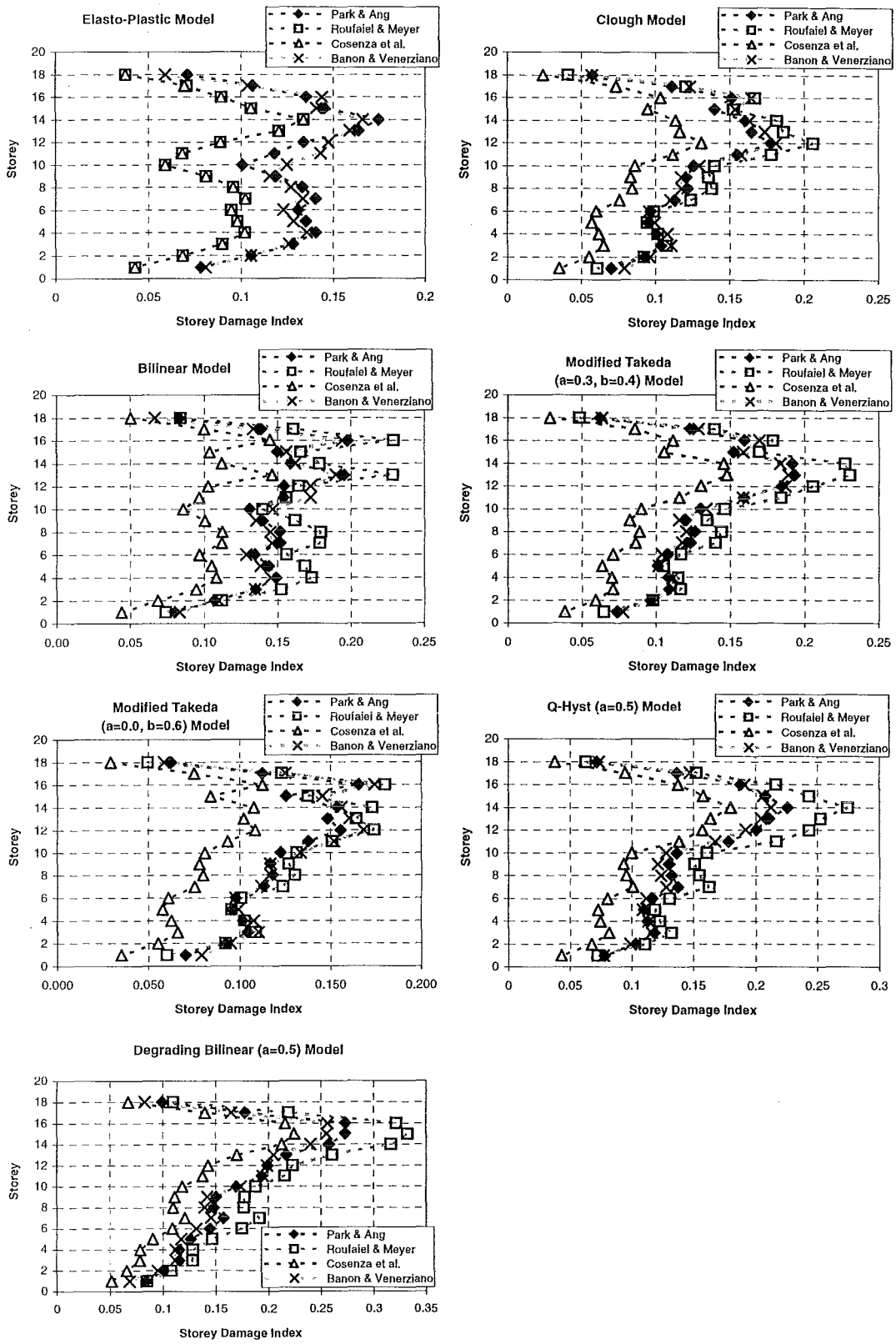

Fig. H-22 The distribution of storey damage index of the seven hysteresis models to the four damage models for the **18 storey structure** under the **El Centro (1940-NS)** earthquake

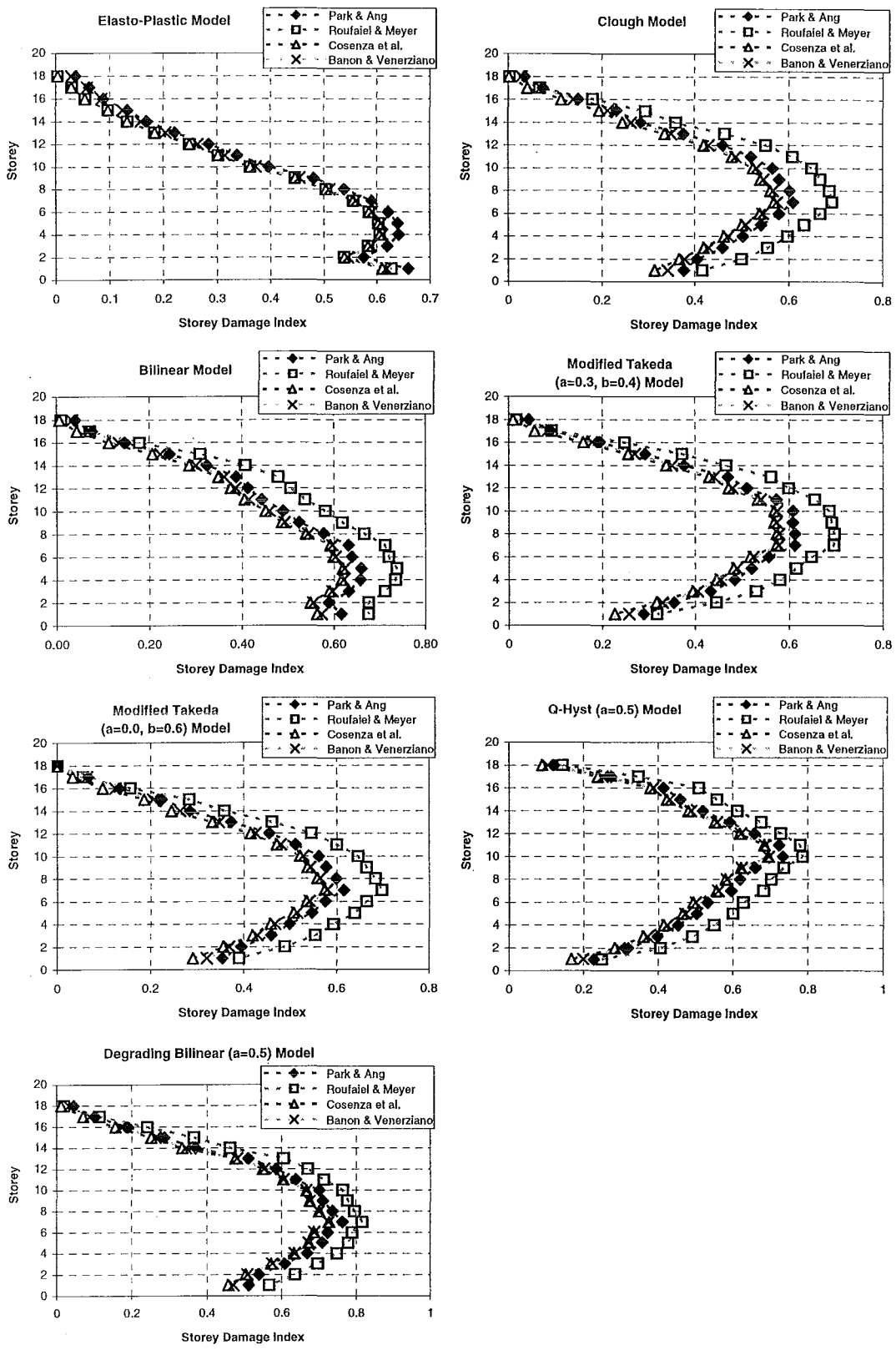

Fig. H-23 The distribution of storey damage index of the seven hysteresis models to the four damage models for the **18 storey structure** under the **Northridge (Sylmar-949NW)** earthquake

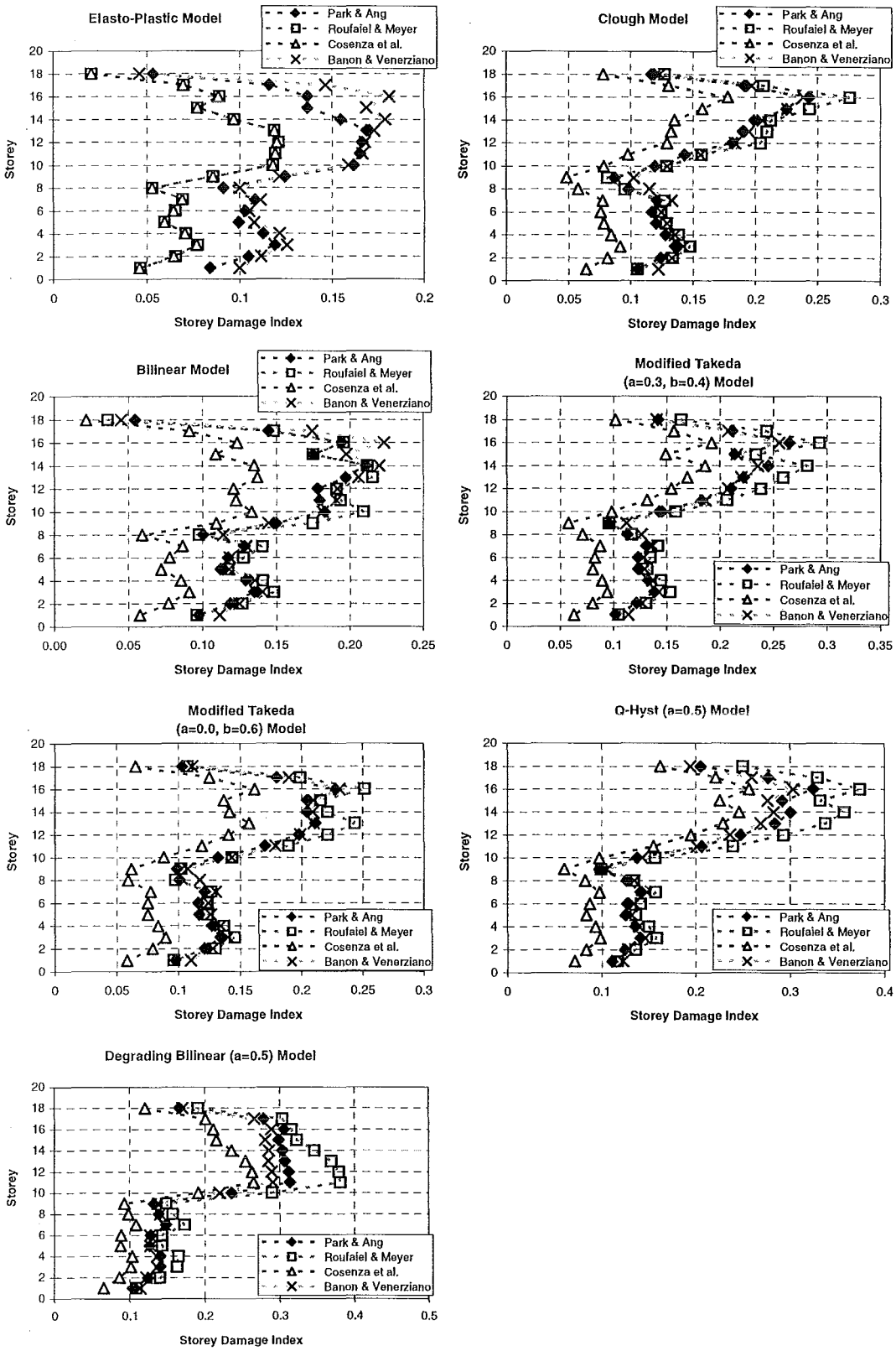

Fig. H-24 The distribution of storey damage index of the seven hysteresis models to the four damage models for the **18 storey structure** under the **Kobe (1995-NS)** earthquake

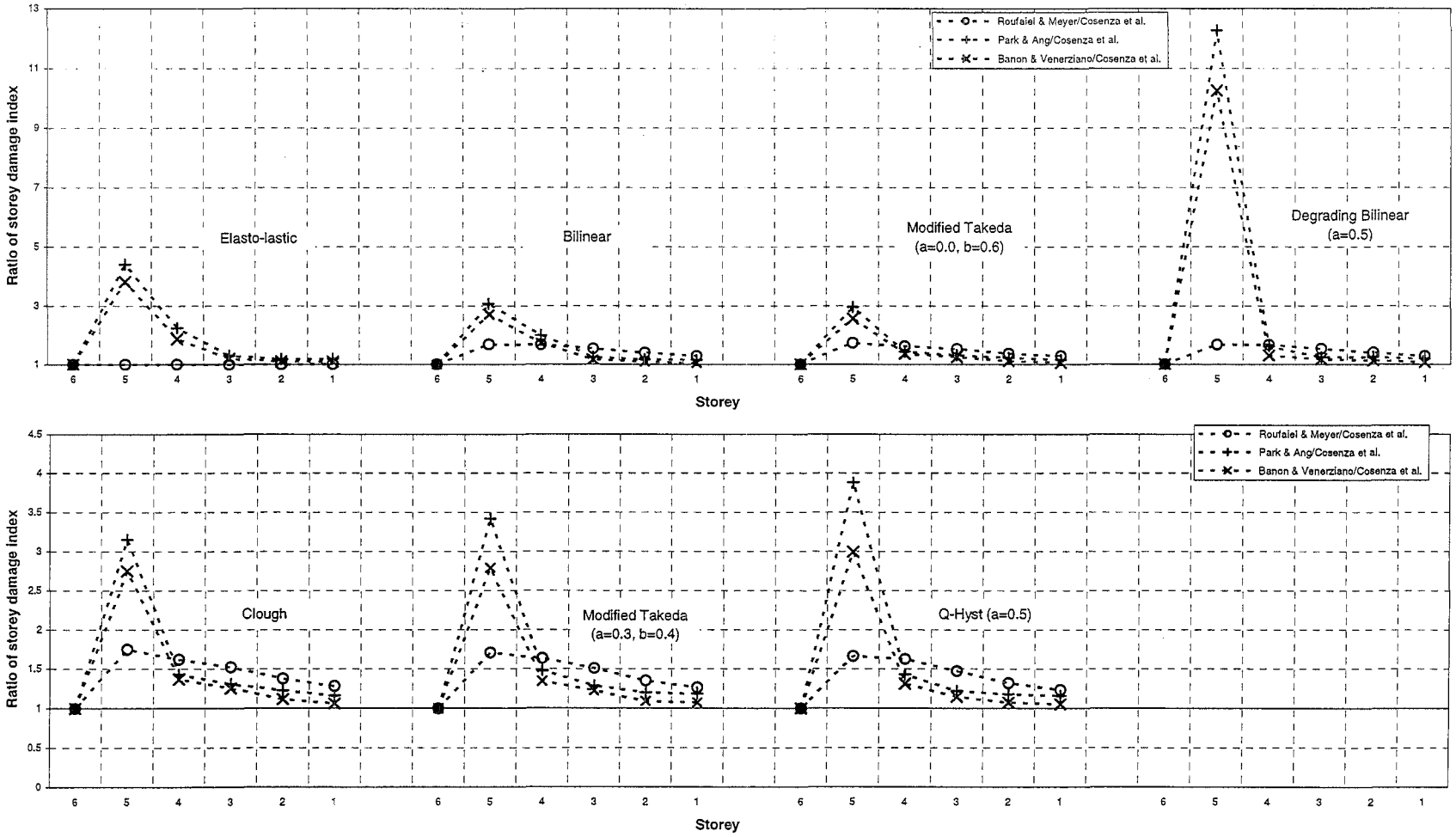

Fig. H-25 Distribution of ratios of storey damage indices for the Park & Ang, Roufaiel & Meyer and Banon & Venerziano member damage models to those for the Cosenza et al member damage model for the seven hysteresis models for the **6 storey structure** under the **Bucharest (1977-NS)** earthquake

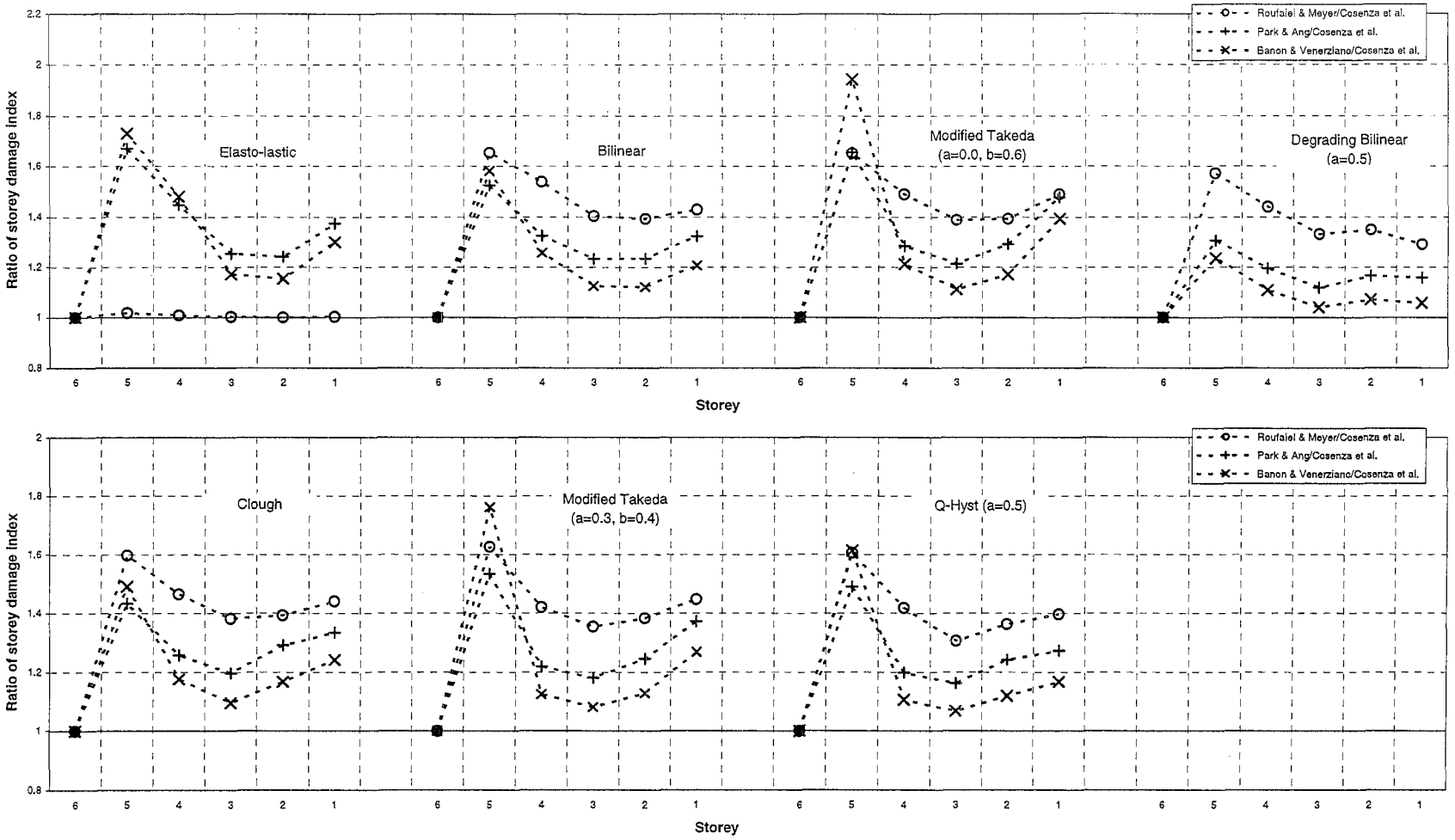

Fig. H -26 Distribution of ratios of storey damage indices for the Park & Ang, Roufaiel & Meyer and Banon & Venerziano member damage models to those for the Cosenza et al member damage model for the seven hysteresis models for the **6 storey structure** under the **El Centro (1940-NS)** earthquake

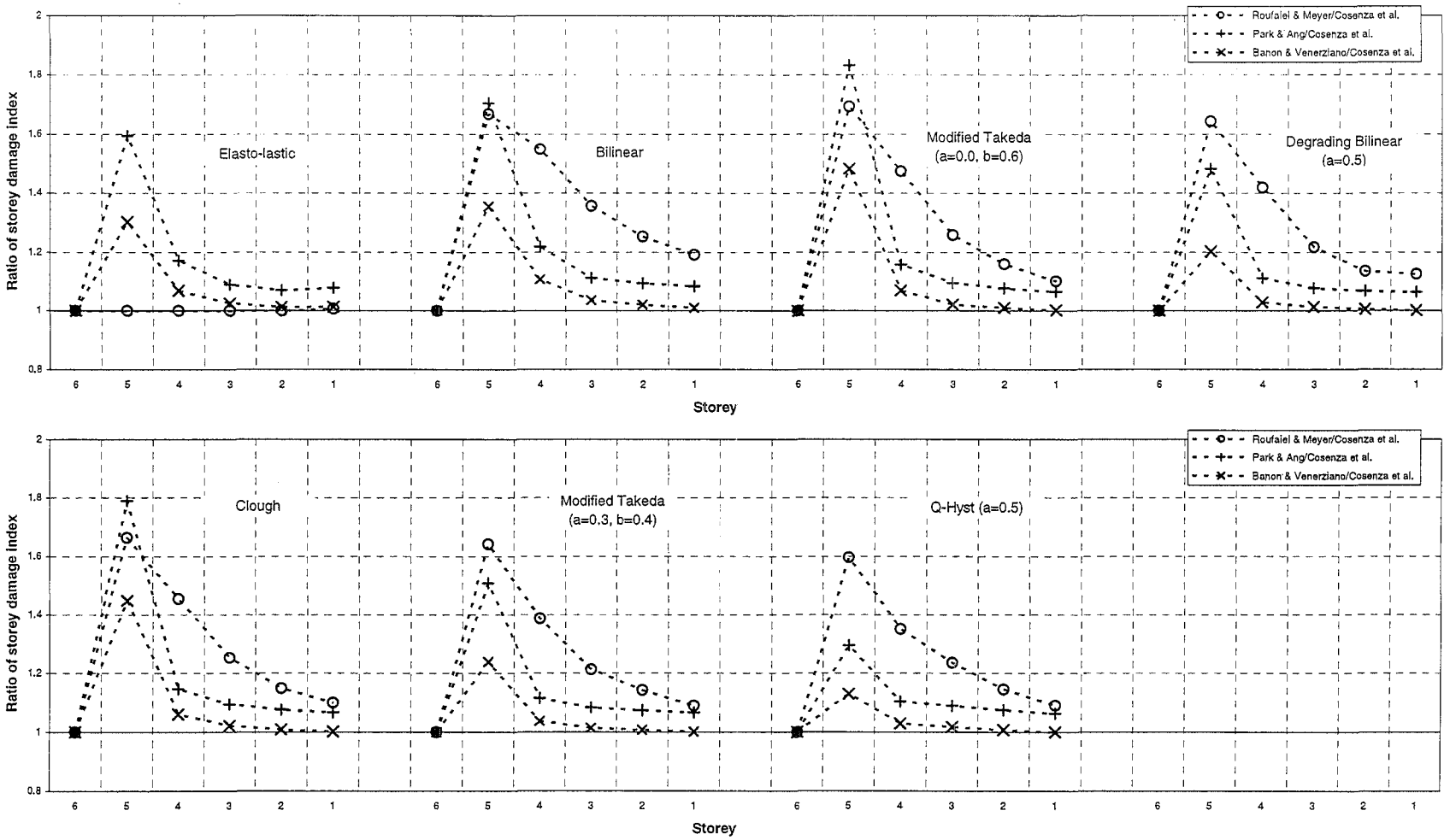

Fig. H -27 Distribution of ratios of storey damage indices for the Park & Ang, Roufaiel & Meyer and Banon & Venerziano member damage models to those for the Cosenza et al member damage model for the seven hysteresis models for the **6 storey structure** under the **Northridge (Sylmar-949NW)** earthquake

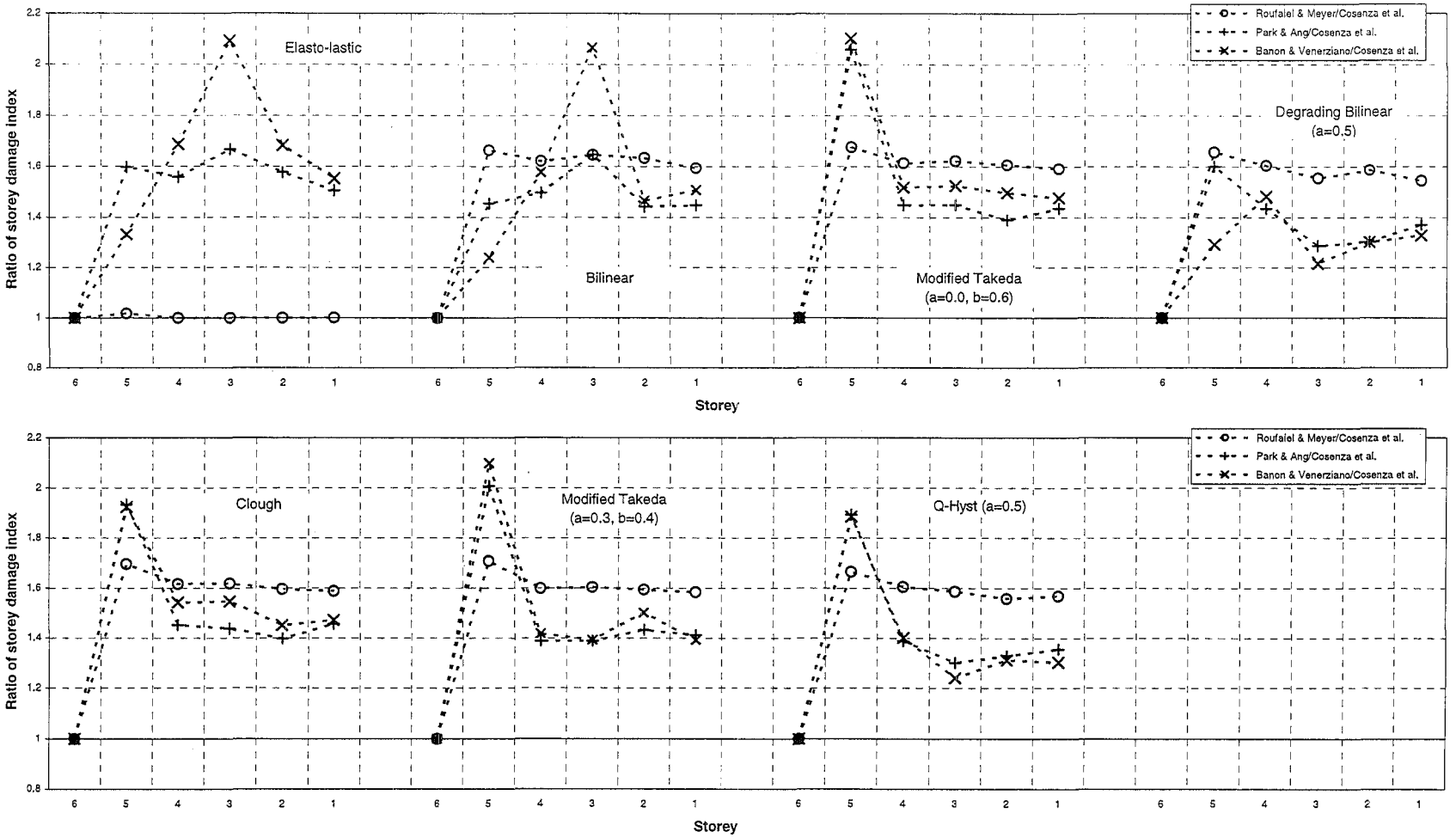

Fig. H -28 Distribution of ratios of storey damage indices for the Park & Ang, Roufaiel & Meyer and Banon & Venerziano member damage models to those for the Cosenza et al member damage model for the seven hysteresis models for the **6 storey structure** under the **Kobe (1995-NS)** earthquake

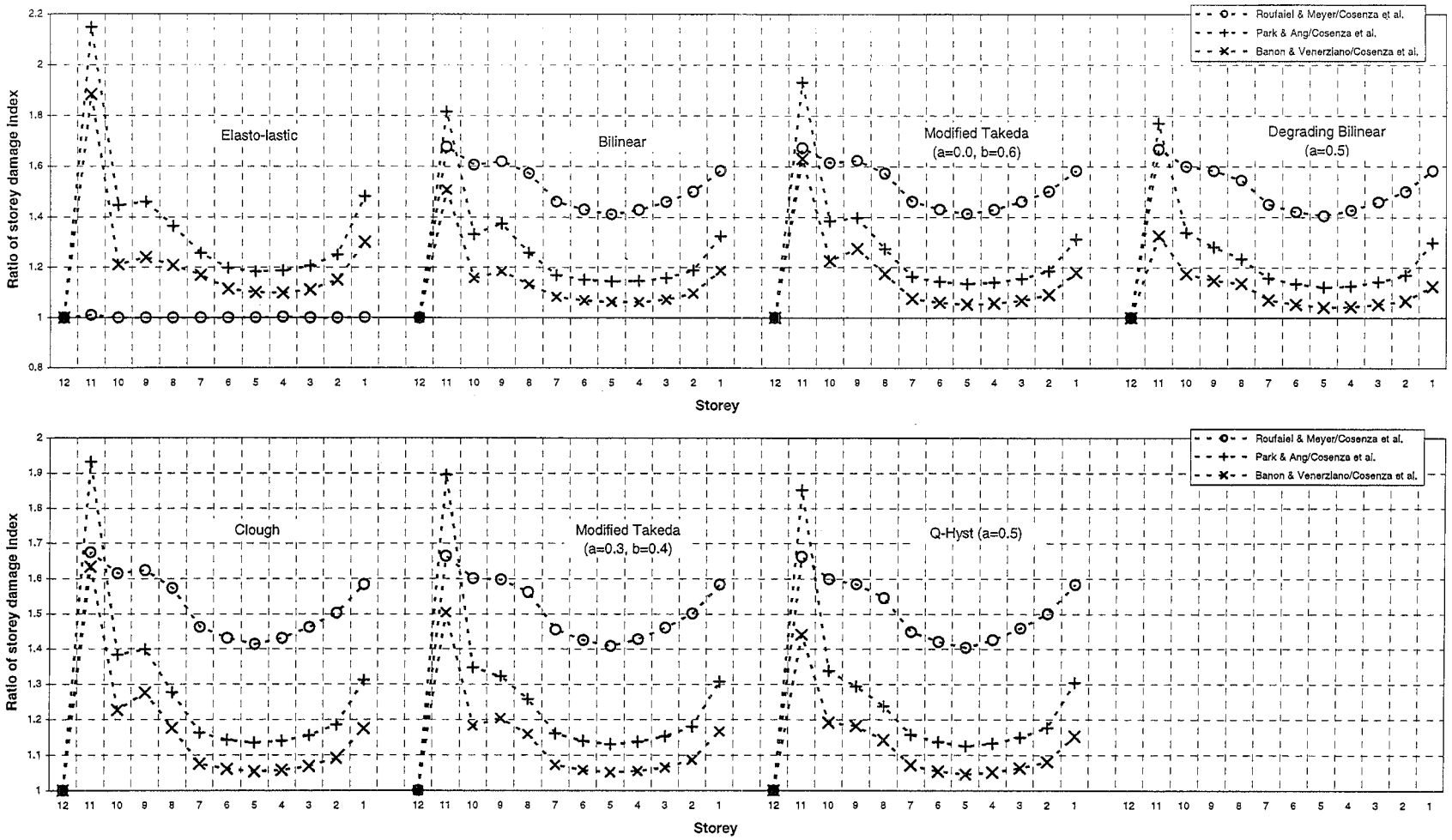

Fig. H -29 Distribution of ratios of storey damage indices for the Park & Ang, Roufaiel & Meyer and Banon & Venerziano member damage models to those for the Cosenza et al member damage model for the seven hysteresis models for the **12 storey structure** under the **Bucharest (1977-NS)** earthquake

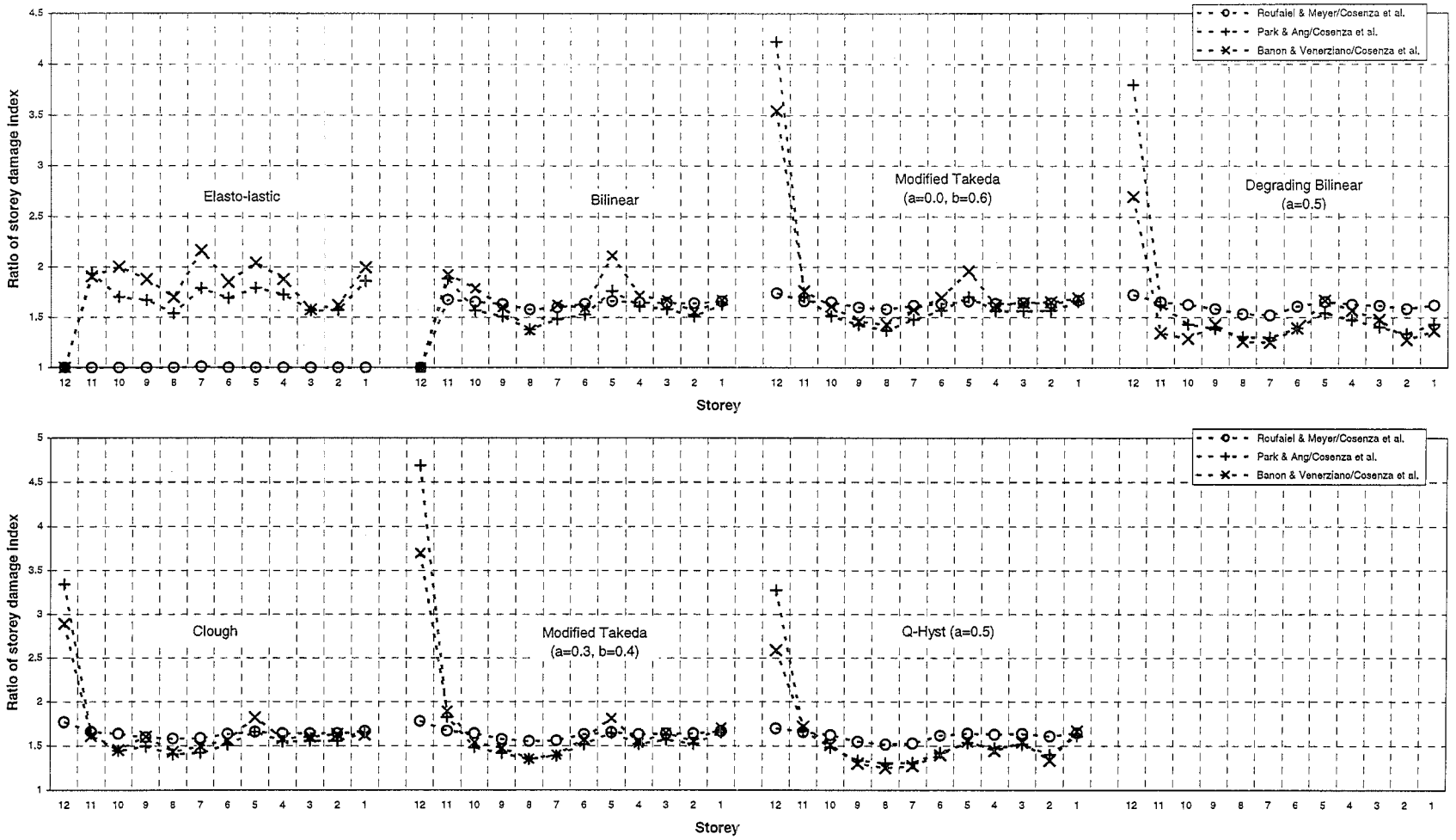

Fig. H -30 Distribution of ratios of storey damage indices for the Park & Ang, Roufaiel & Meyer and Banon & Venerziano member damage models to those for the Cosenza et al member damage model for the seven hysteresis models for the **12 storey structure** under the **El Centro (1940-NS)** earthquake

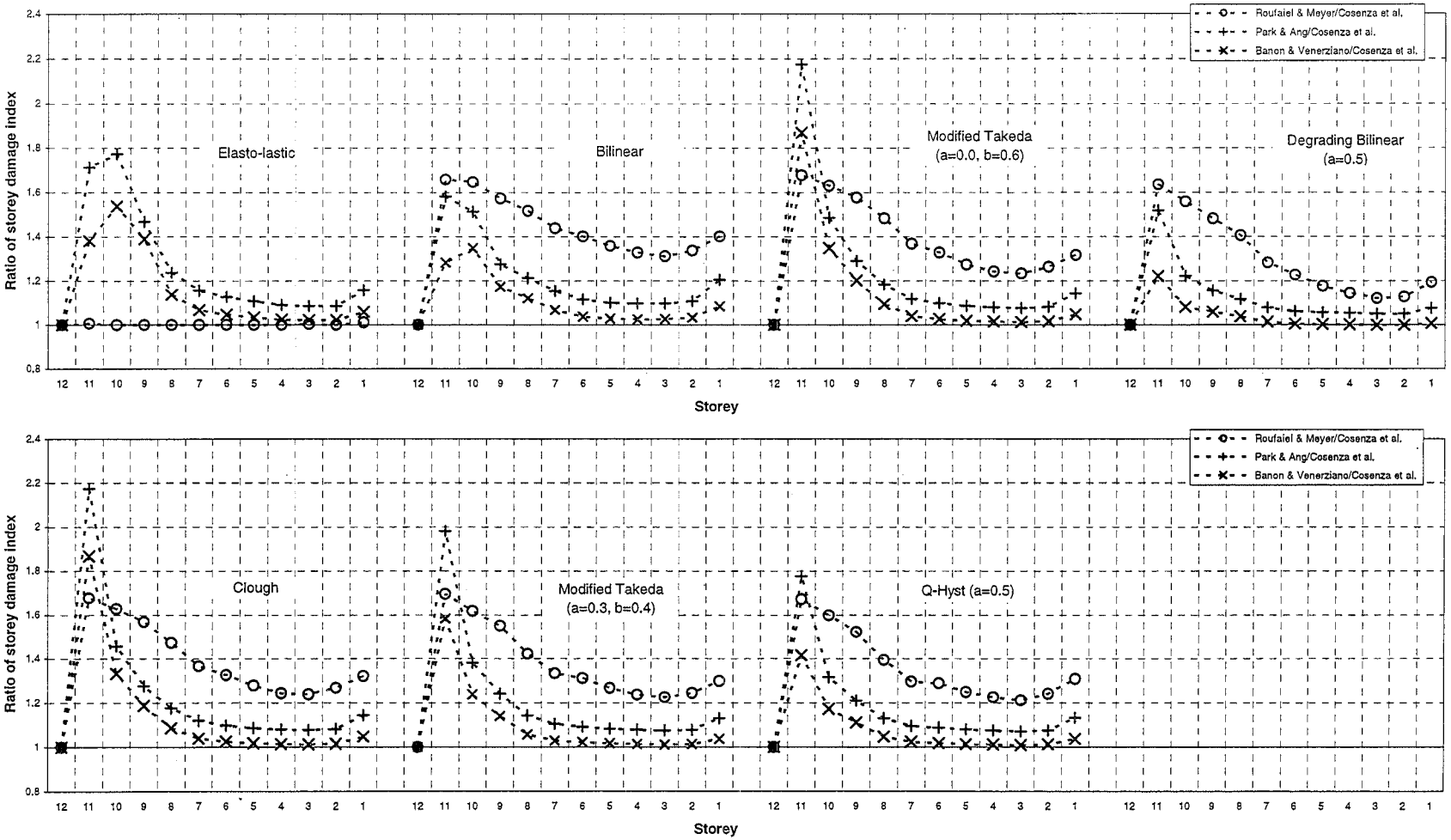

Fig. H -31 Distribution of ratios of storey damage indices for the Park & Ang, Roufaiel & Meyer and Banon & Venerziano member damage models to those for the Cosenza et al member damage model for the seven hysteresis models for the **12 storey structure** under the **Northridge (Sylmar-949NW)** earthquake

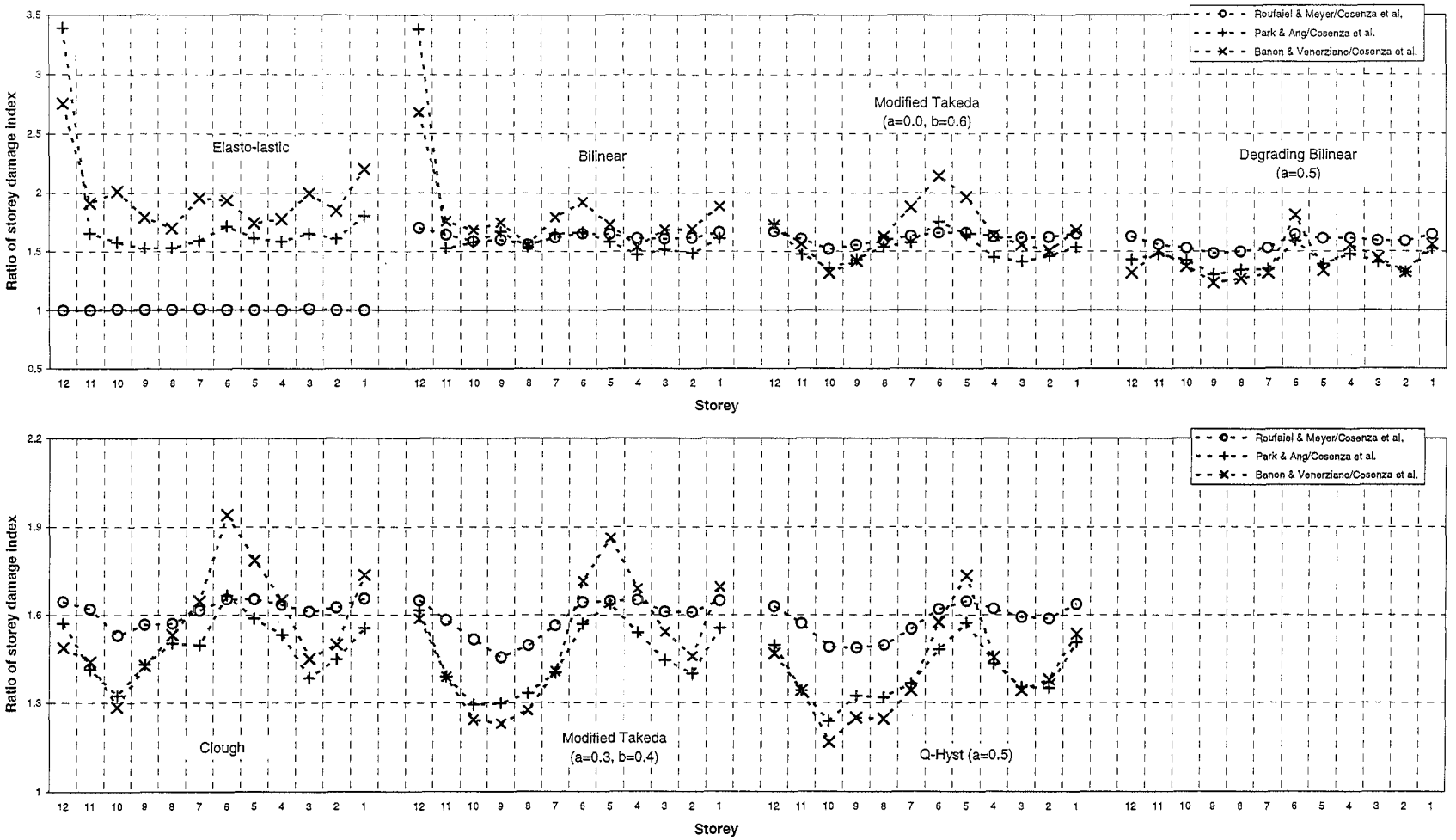

Fig. H -32 Distribution of ratios of storey damage indices for the Park & Ang, Roufaiel & Meyer and Banon & Venerziano member damage models to those for the Cosenza et al member damage model for the seven hysteresis models for the **12 storey structure** under the **Kobe (1995-NS)** earthquake

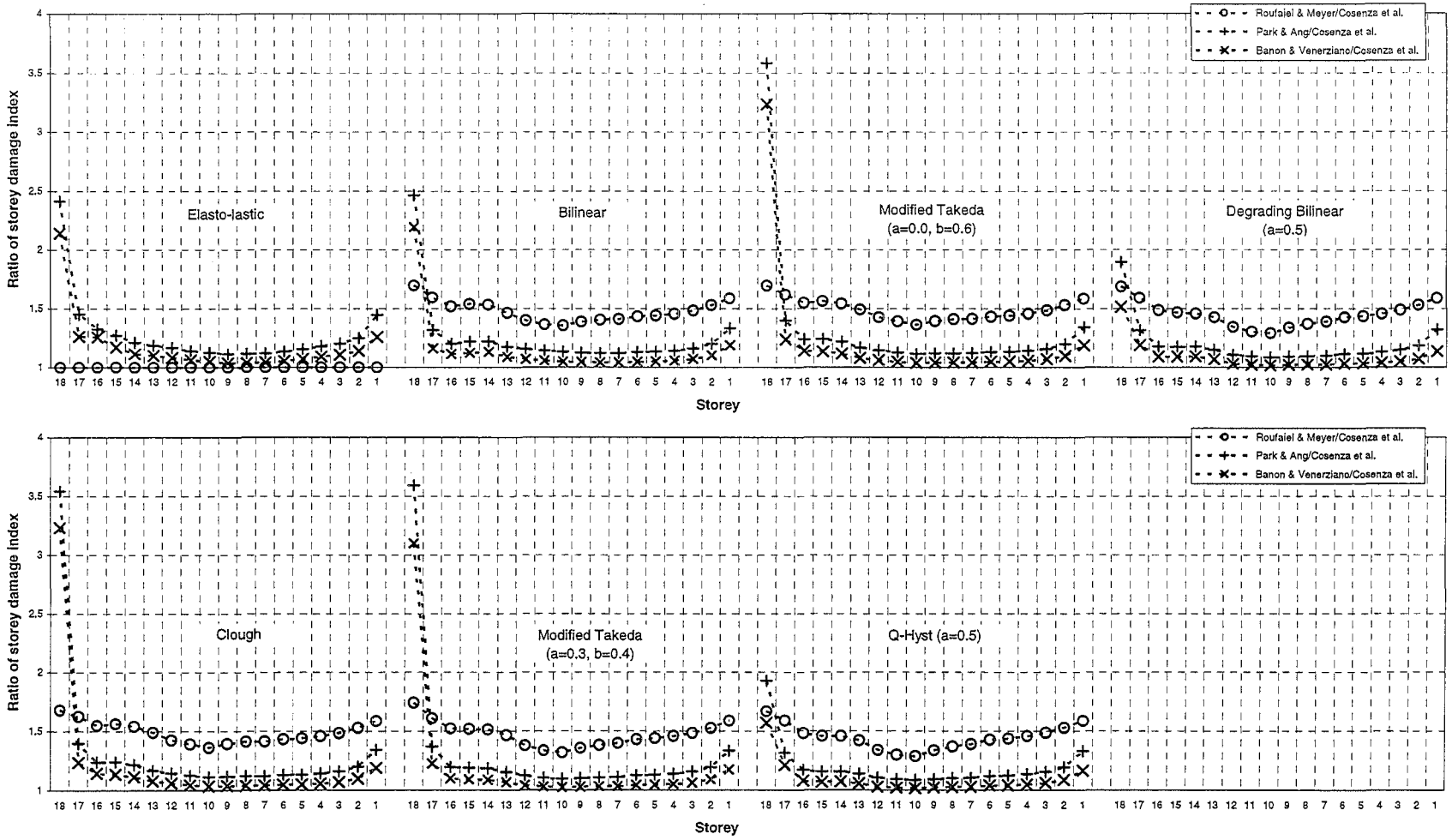

Fig. H -33 Distribution of ratios of storey damage indices for the Park & Ang, Roufaiel & Meyer and Banon & Venerziano member damage models to those for the Cosenza et al member damage model for the seven hysteresis models for the **18 storey structure** under the **Bucharest (1977-NS)** earthquake

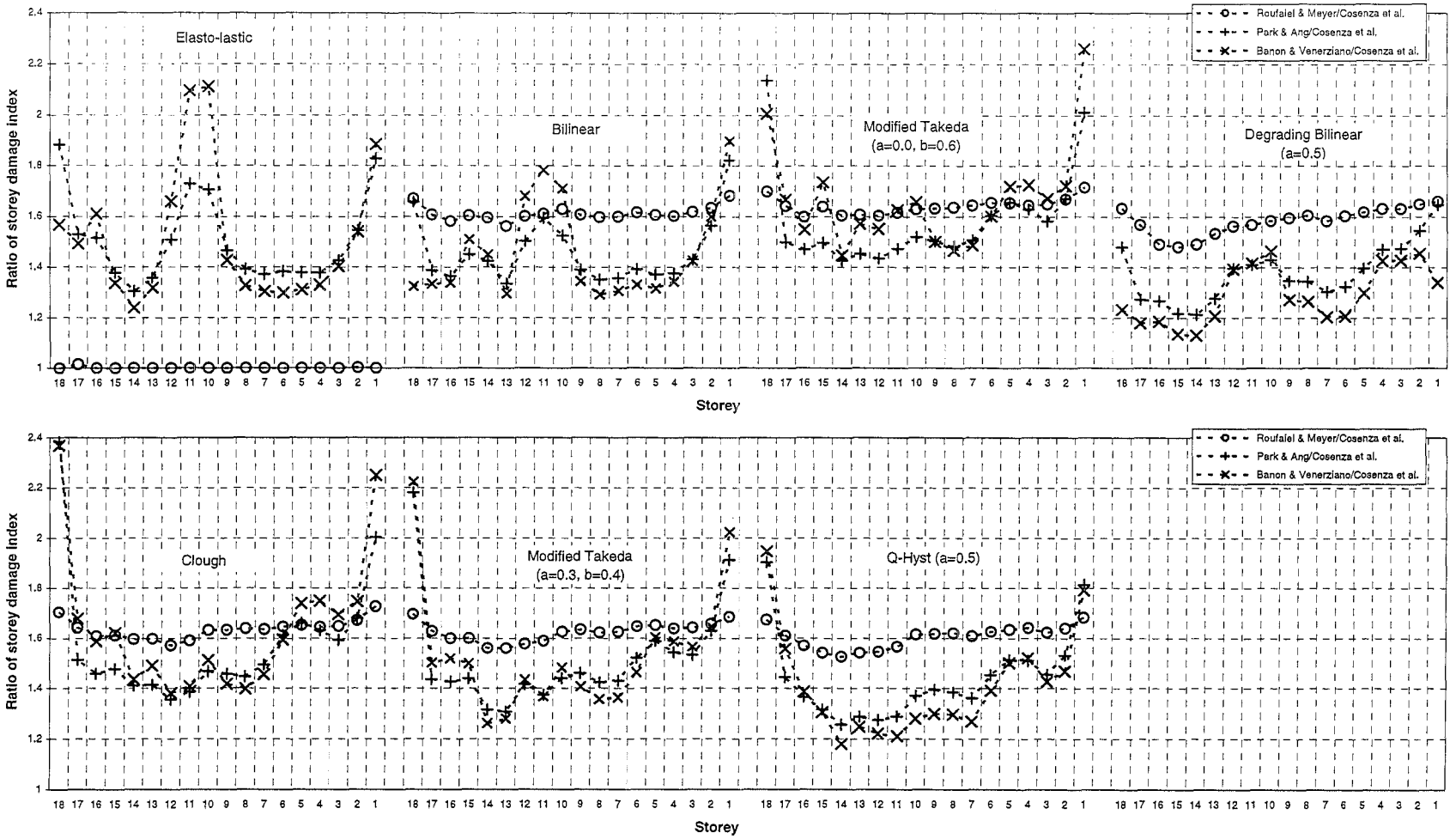

Fig. H -34 Distribution of ratios of storey damage indices for the Park & Ang, Roufaiel & Meyer and Banon & Venerziano member damage models to those for the Cosenza et al member damage model for the seven hysteresis models for the **18 storey structure** under the **El Centro (1940-NS)** earthquake

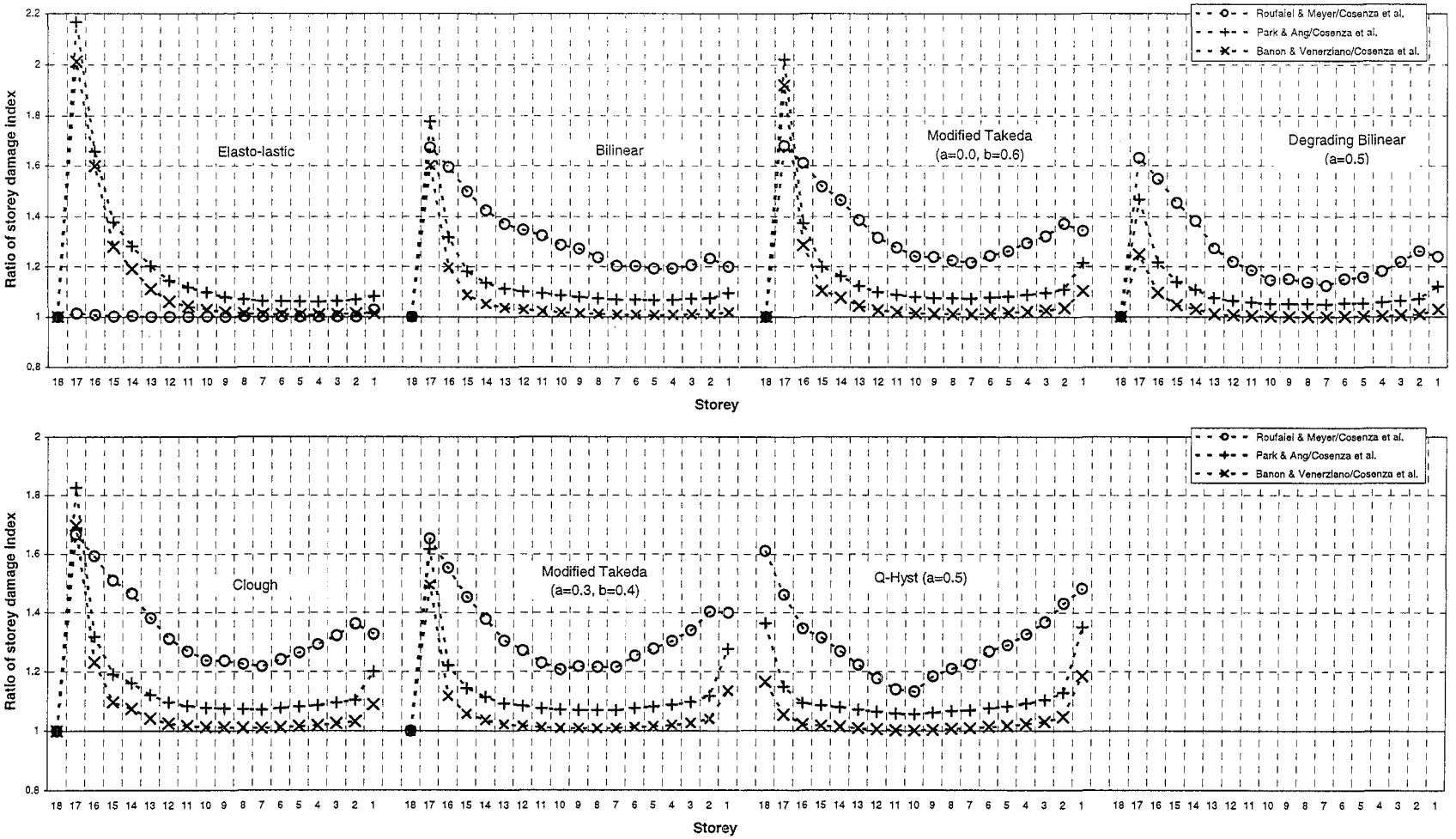

Fig. H -35 Distribution of ratios of storey damage indices for the Park & Ang, Roufaiel & Meyer and Banon & Venerziano member damage models to those for the Cosenza et al member damage model for the seven hysteresis models for the **18 storey structure** under the **Northridge (Sylmar-949NW)** earthquake

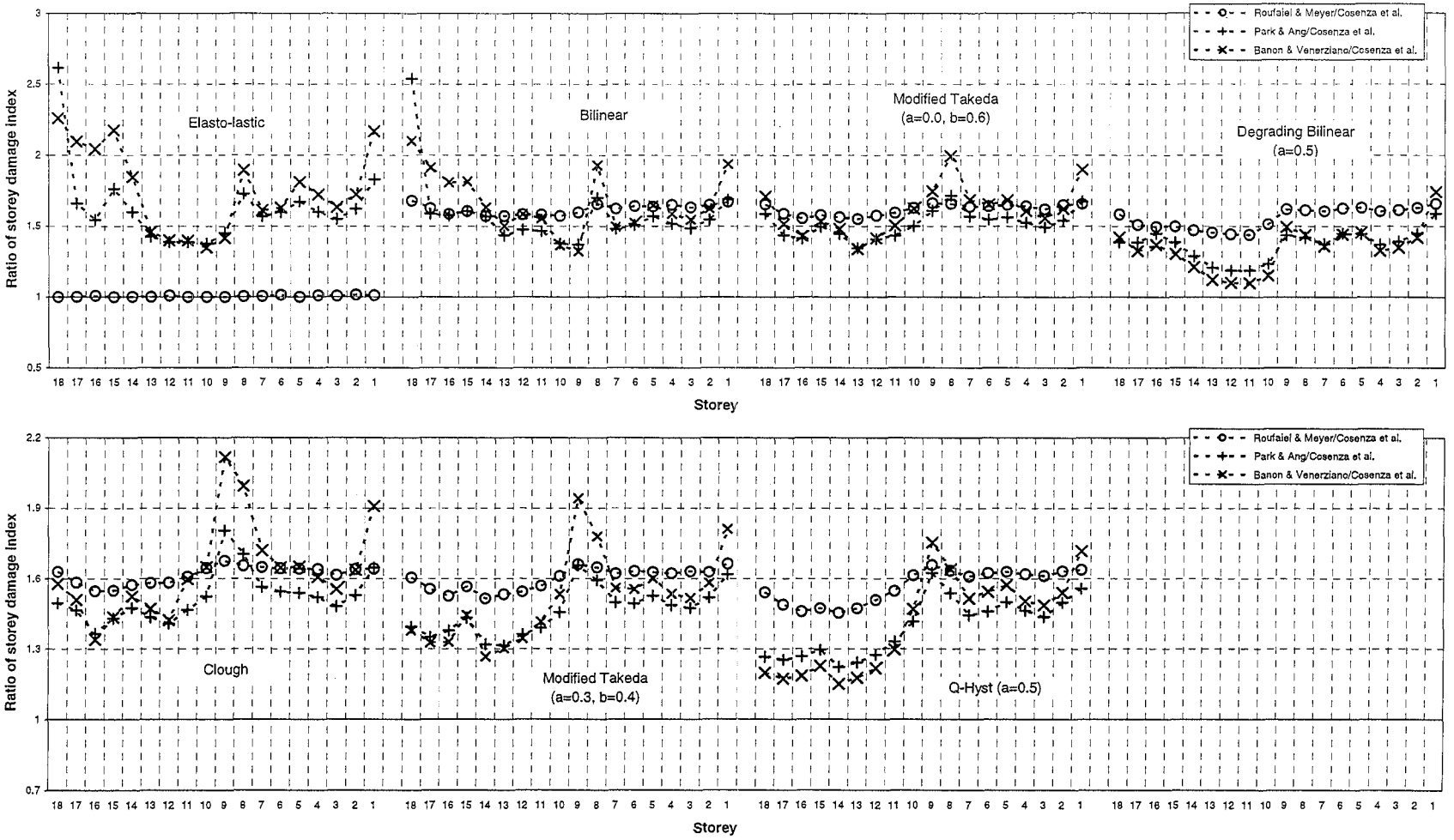

Fig. H -36 Distribution of ratios of storey damage indices for the Park & Ang, Roufaiel & Meyer and Banon & Venerziano member damage models to those for the Cosenza et al member damage model for the seven hysteresis models for the **18 storey structure** under the **Kobe (1995-NS)** earthquake

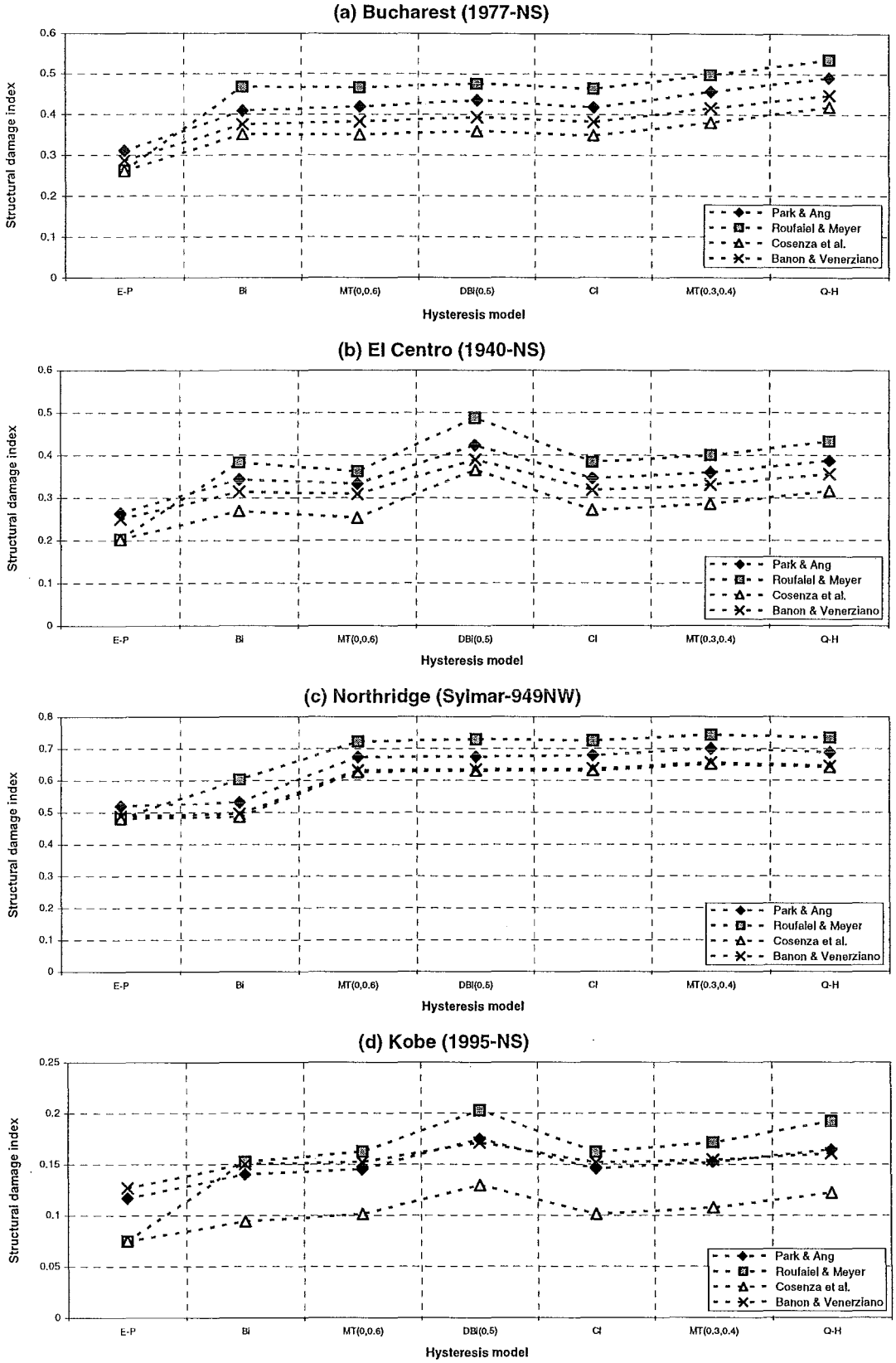

Fig. H-37 The overall structural damage indices (energy weighted average) for the four member damage models to the seven hysteresis models for the **6 storey structure** under the four excitations

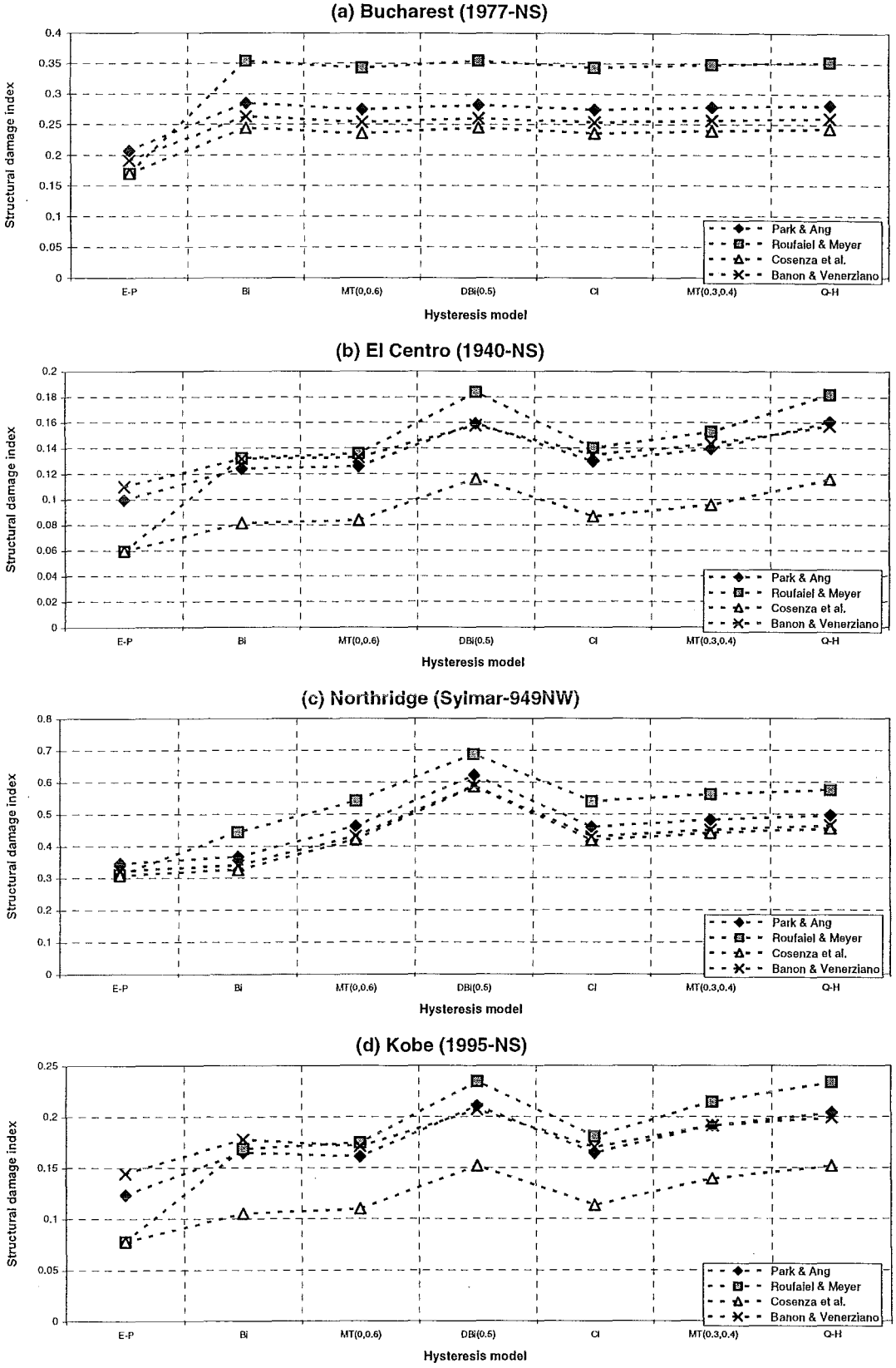

Fig. H-38 The overall structural damage indices (energy weighted average) for the four member damage models to the seven hysteresis models for the **12 storey structure** under the four excitations

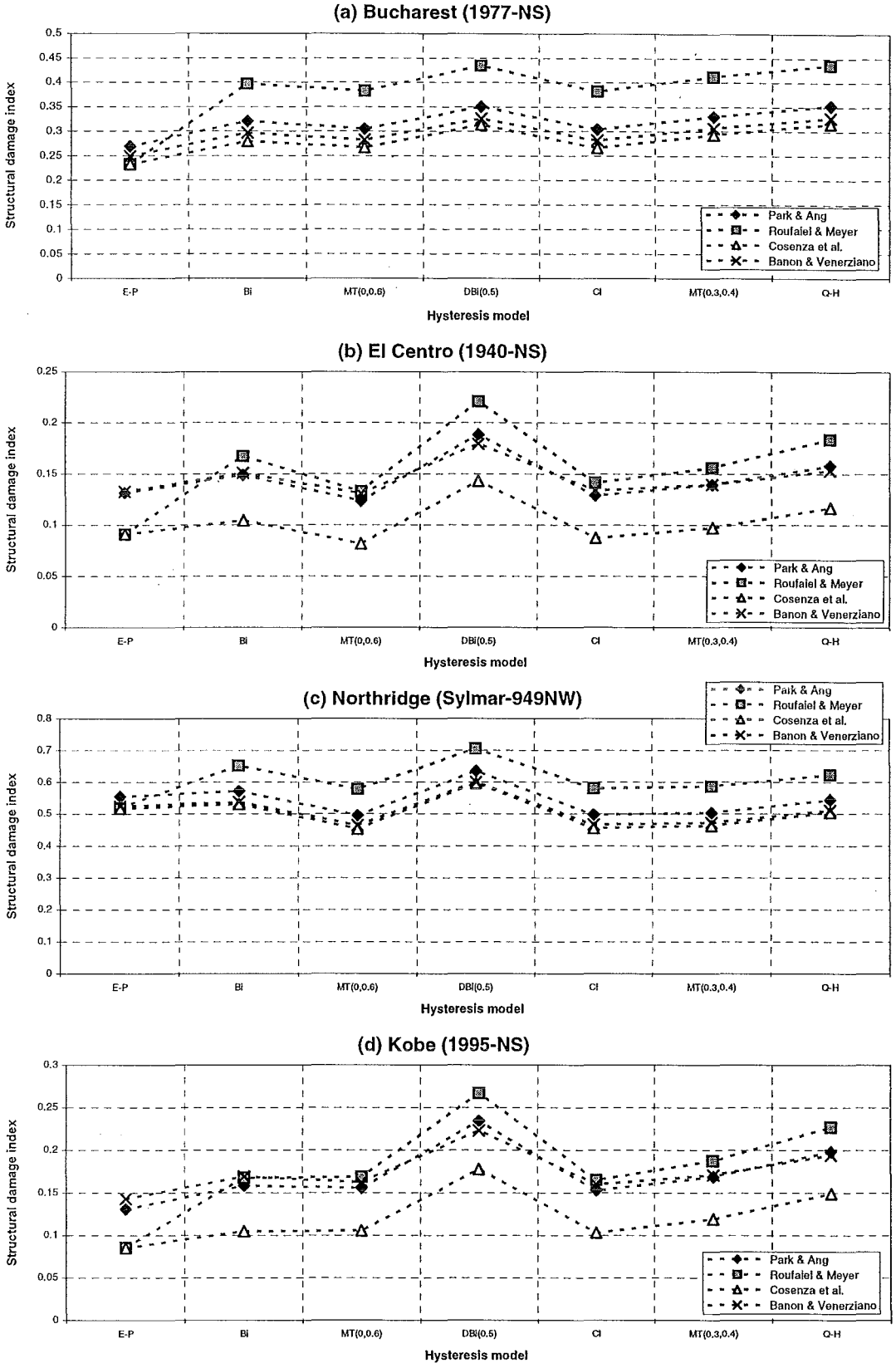

Fig. H-39 The overall structural damage indices (energy weighted average) for the four member damage models to the seven hysteresis models for the **18 storey structure** under the four excitations

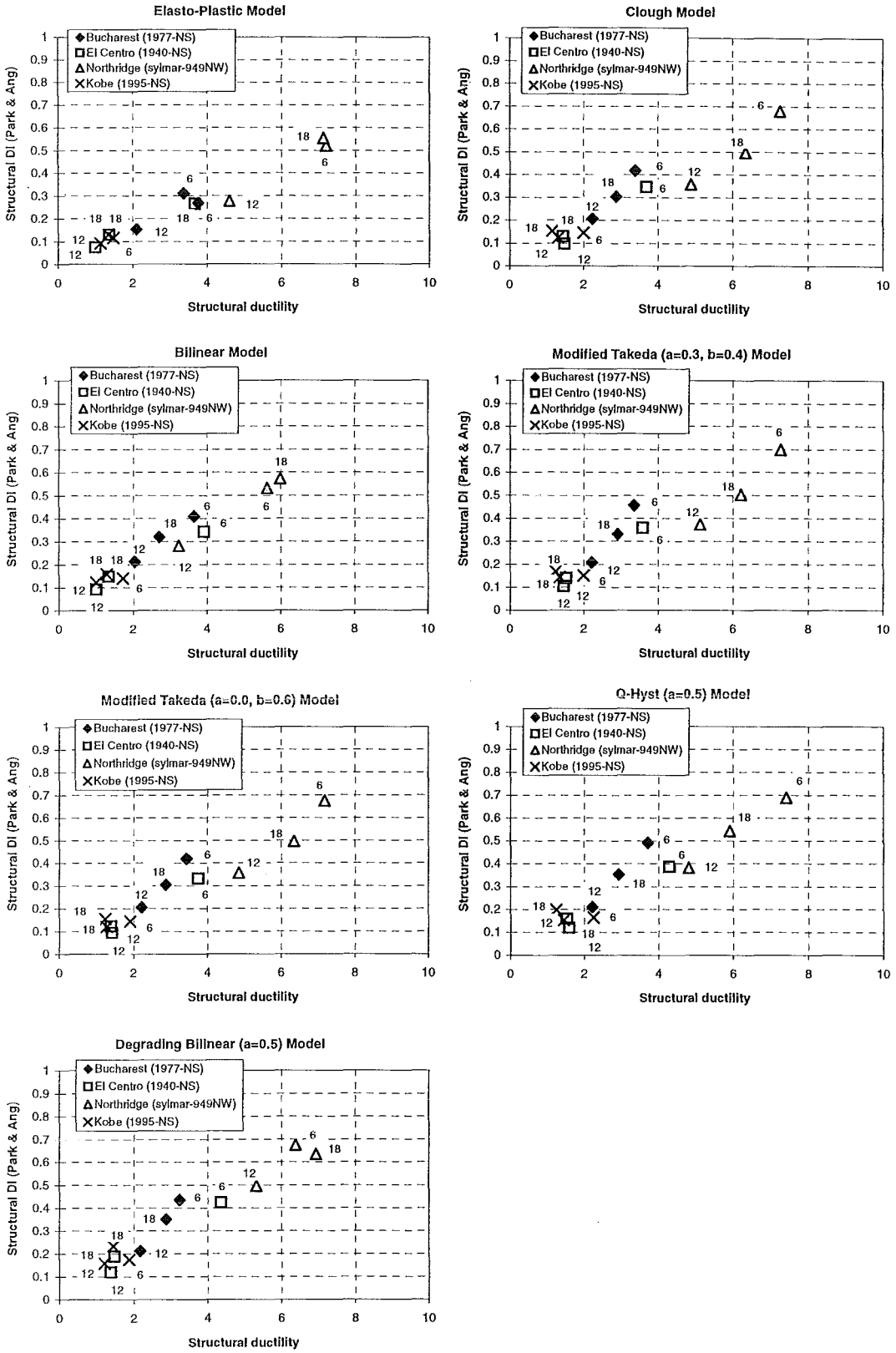

Fig. H-40 The relationship between structural damage indices for the Park & Ang member damage model and the maximum structural ductility of the three structures under the four excitations for the seven hysteresis models

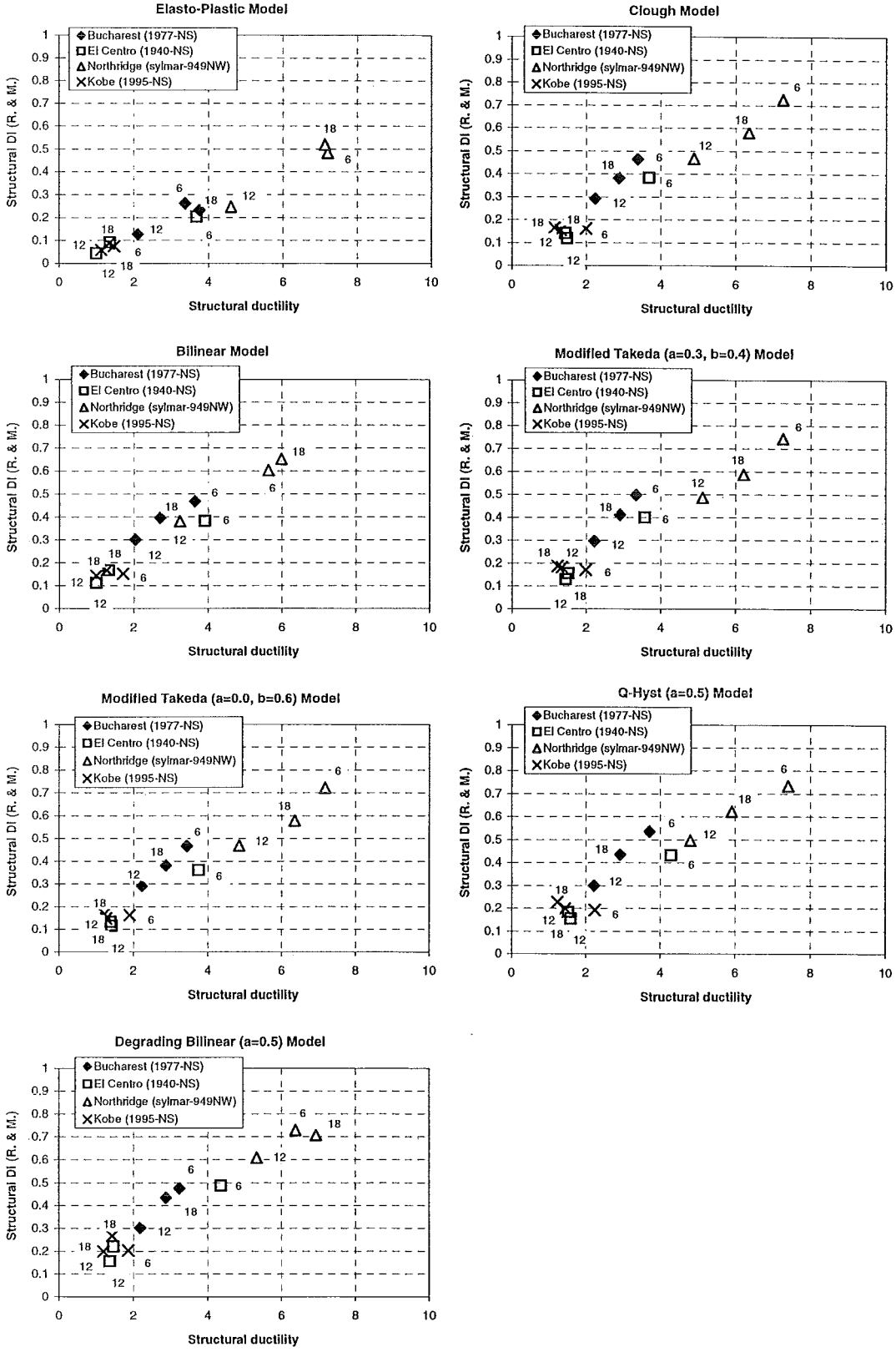

Fig. H-41 The relationship between structural damage indices for the Roufaiel & Meyer member damage model and the maximum structural ductility of the three structures under the four excitations for the seven hysteresis models

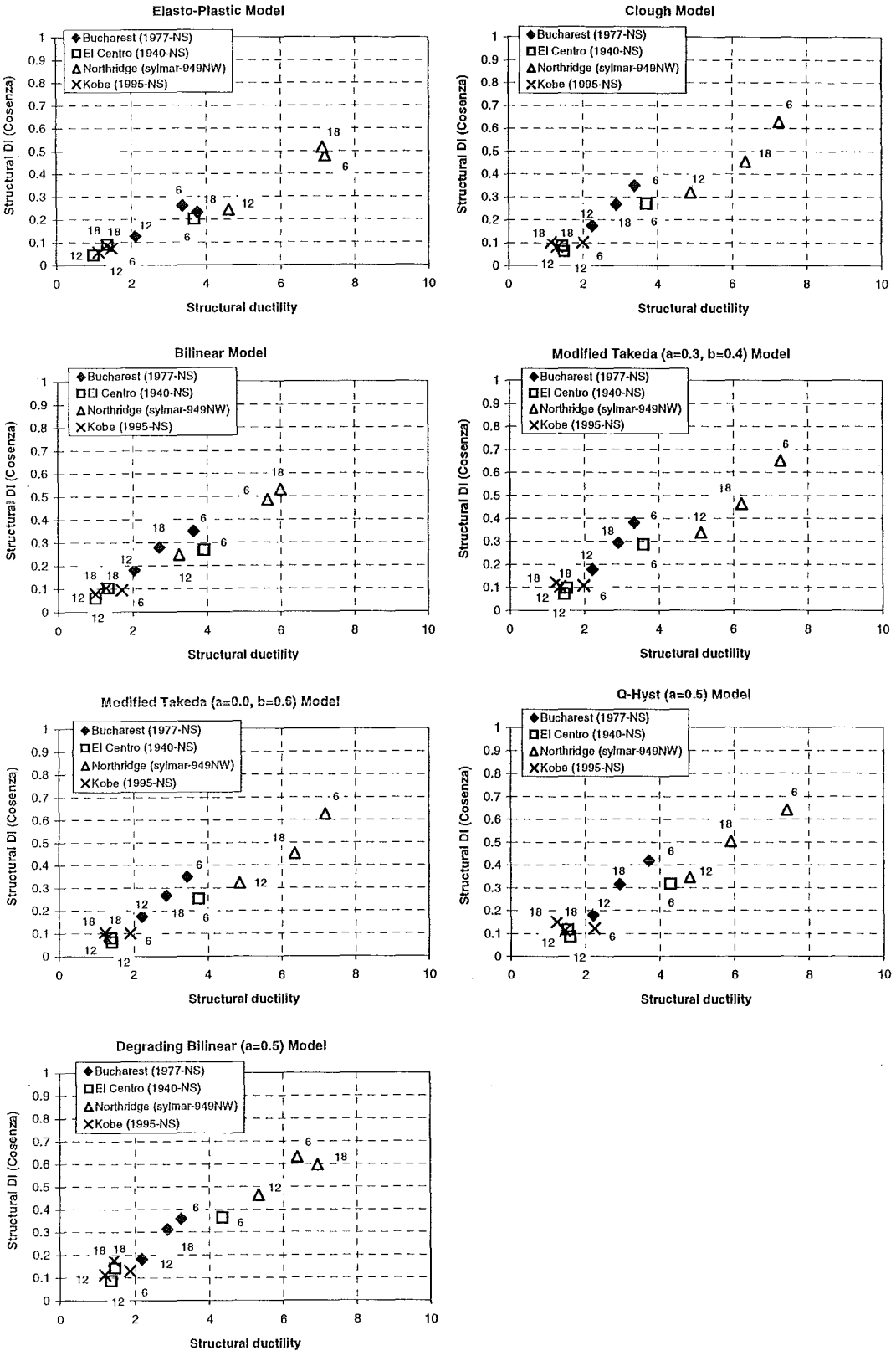

Fig. H-42 The relationship between structural damage indices for the Cosenza at al member damage model and the maximum structural ductility of the three structures under the four excitations for the seven hysteresis models

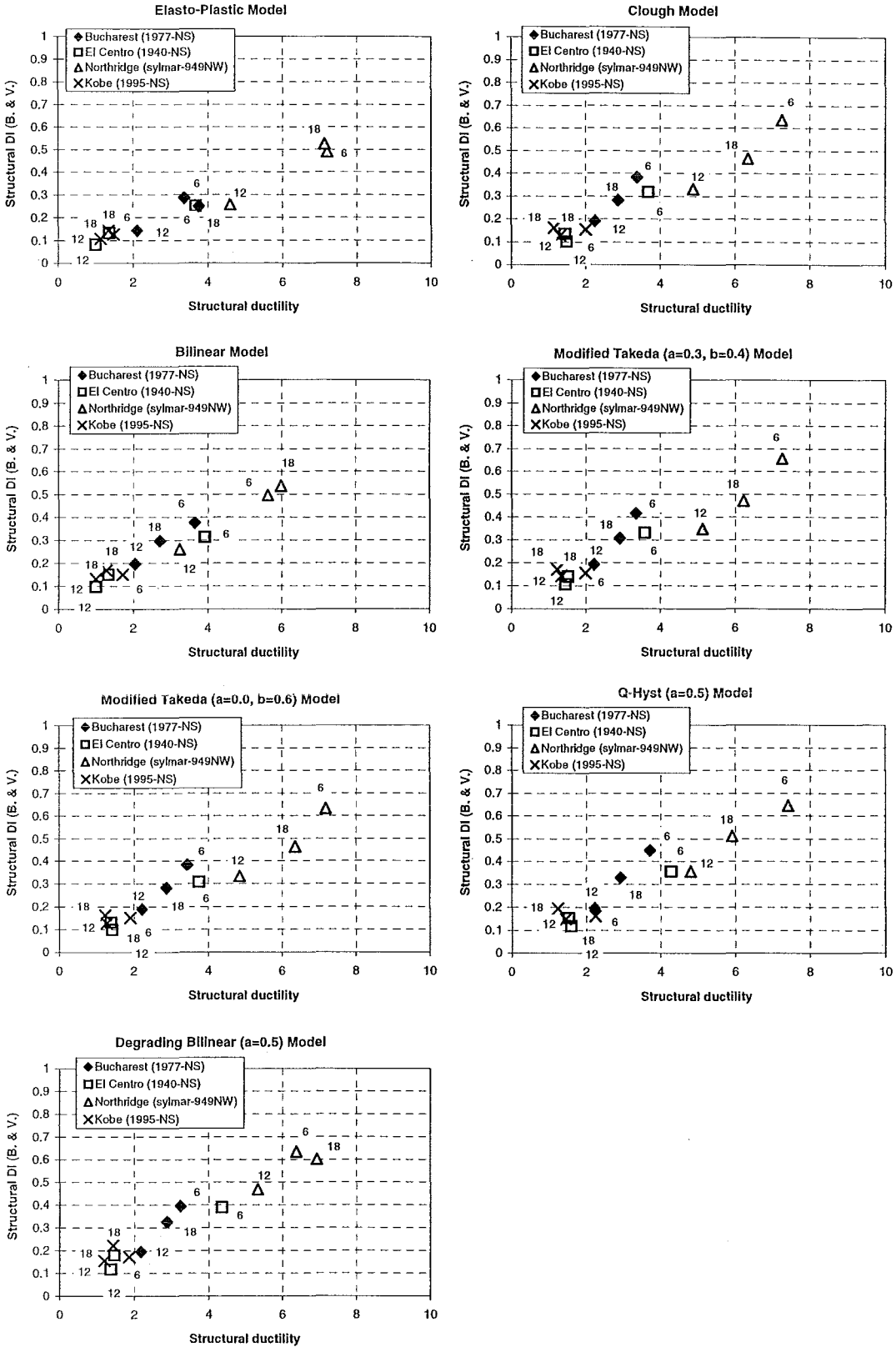

Fig. H-43 The relationship between structural damage indices for the Banon & Venerziano member damage model and the maximum structural ductility of the three structures under the four excitations for the seven hysteresis models

APPENDIX I
Modified Jury 6 storey ductile-framed structure model

General Data

Modulus of Elasticity, E = 25.0 GPa
Shear Modulus, G = 10.4 GPa

Section Properties

Member	Levels	Axial Area (m^2)	Shear Area (m^2)	Moment of Inertia (m^4)	Plastic Hinge Length (m)
Beams	1-3	0.105	0.105	0.003150	0.420
	4-6	0.0963	0.0963	0.002426	0.385
External Columns	0-3	0.1688	0.1688	0.002813	0.350*
	3-6	0.1519	0.1519	0.002050	-
Internal Columns	0-3	0.2269	0.2269	0.006100	0.385*
	3-6	0.1875	0.1875	0.004167	-

- Those values are only used for the first storey columns.

Length of Rigid End Block (m)

Beams: (symmetric values were used.)

Level	*Left Bay*		*Middle Bay*
	Left End	*Right End*	*Left End*
1-3	0.25	0.275	0.275
4-6	0.225	0.25	0.25

Columns:

Level	*Exterior and Interior Columns*	
	End-1	*End-2*
1	0.00	0.3
2-3	0.3	0.3
4	0.3	0.275
5-6	0.275	0.275

Additional Data

Bay Width = 5.5 metres
Storey Height = 3.35 metres
Total Structure Height = 20.1 metres
Column Interaction Type = Concrete Beam-Column Yield Interaction (See Fig. A –1)

Yield Interaction Data for First Storey Column: for definition of term see Fig. A–1

Column	*Pyc (kN)*	*Pb (kN)*	*Mb (kNm)*	*M1b (kNm)*	*M2b (kNm)*	*Mo (kNm)*	*Pyt (kN)*
Exterior	-6290	-3690	435	519	423	197	934
Interior	-8454	-5010	645	775	635	300	1255

Beam Yield Data

	Left Span				*Right Span*			
Level	*Left End Positive*	*Left End Negative*	*Right End Positive*	*Right End Negative*	*Left End Positive*	*Left End Negative*	*Right End Positive*	*Right End Negative*
1-3	262	-262	232	-232	232	-232	262	-262
4	173	-184	155	-155	155	-155	184	-173
5	115	-131	119	-115	115	-119	131	-115
6	115	-115	115	-115	115	-115	115	-115

Note: All the numbers are in *kNm*.

Beam Initial Fixed End Moments and Shears

Level	*Moment (kNm) Left End*	*Moment (kNm) Right End*	*Shear (kNm) Left End*	*Shear (kNm) Right End*
1-3	-40.04	-41.25	-48.33	48.33
4-6	-40.05	-41.68	-47.33	47.33

Note: Fig. A–2 depicts the positive sign conventions used in RUAUMOKO.

APPENDIX J
Modified Jury 12 storey ductile-framed structure model

General Data

Modulus of Elasticity, E	=	25.0	GPa
Shear Modulus, G	=	10.4	GPa

Section Properties

Member	Levels	Axial Area (m^2)	Shear Area (m^2)	Moment of Inertia (m^4)	Plastic Hinge Length (m)	Rigid End Block (m)
Beams	1-6	0.1800	0.1800	0.02382	0.63	0.400
	7-8	0.1700	0.1700	0.02017	0.595	0.375
	9-12	0.1600	0.1600	0.01689	0.56	0.338
External Columns	1-6	0.2906	0.2906	0.01455	0.543*	0.450
	7-8	0.2813	0.2813	0.01318	-	0.425
	9-12	0.2438	0.2438	0.008552	-	0.400
Internal Columns	1-6	0.4800	0.4800	0.02560	0.543*	0.450
	7-8	0.3942	0.3942	0.01727	-	0.425
	9-12	0.3417	0.3417	0.01297	-	0.400

- Those values are only used for the first storey columns.

Additional Data

Bay Width	=	9.2	metres
Storey Height	=	3.65	metres
Total Structure Height	=	43.8	metres
Column Interaction Type	=	Concrete Beam-Column Yield Interaction (See Fig. A –1)	

Yield Interaction Data for First Storey Column: for definition of term see Fig. A–1

Column	*Pyc (kN)*	*Pb (kN)*	*Mb (kNm)*	*M1b (kNm)*	*M2b (kNm)*	*Mo (kNm)*	*Pyt (kN)*
Exterior	-11152	-6075	1338	1531	1263	665	1930
Interior	-17888	-10920	1986	1986	2450	2038	2656

Beam Yield Data

	Left Span				*Right Span*			
Level	*Left End Positive*	*Left End Negative*	*Right End Positive*	*Right End Negative*	*Left End Positive*	*Left End Negative*	*Right End Positive*	*Right End Negative*
1	976	-976	893	-893	893	-893	976	-976
2-4	1142	-1142	1047	-1047	1047	-1047	1142	-1142
5-6	988	-988	887	-887	887	-887	988	-988
7-8	762	-833	714	-714	714	-714	762	-833
9-10	559	-631	547	-464	547	-464	559	-631
11	307	-369	381	-307	381	-307	307	-369
12	307	-307	307	-307	307	-307	307	-307

Note: All the numbers are in *kNm*.

Beam Initial Fixed End Moments and Shears

Level	*Moment (kNm) Left End*	*Moment (kNm) Right End*	*Shear (kNm) Left End*	*Shear (kNm) Right End*
1-6	-187.8	-186.3	-135.8	135.8
7-8	-188.4	-186.7	-133.4	133.4
9-12	-188.8	-187.2	-131.1	131.1

Note: Fig. A–2 depicts the positive sign conventions used in RUAUMOKO.

Appendix K
The contribution of β of 5% used for energy component in Park & Ang damage model

Park & And damage model:

$$DI = \frac{\mu_m}{\mu_u} + \frac{\beta}{M_y * \mu_u} \int dE \qquad \textbf{(K-1)}$$

Where β=0.05

Contribution of the energy component:

In order to demonstrate the contribution of energy component of the Park & Ang damage model to the member damage index, the numbers of cycles required for the member damage index to reach 1.0 is derived as shown as follows:

Assumption:
Member curvature ultimate ductility is $\mu_u = 30$.
Elasto-Plastic hysteresis model is applied.

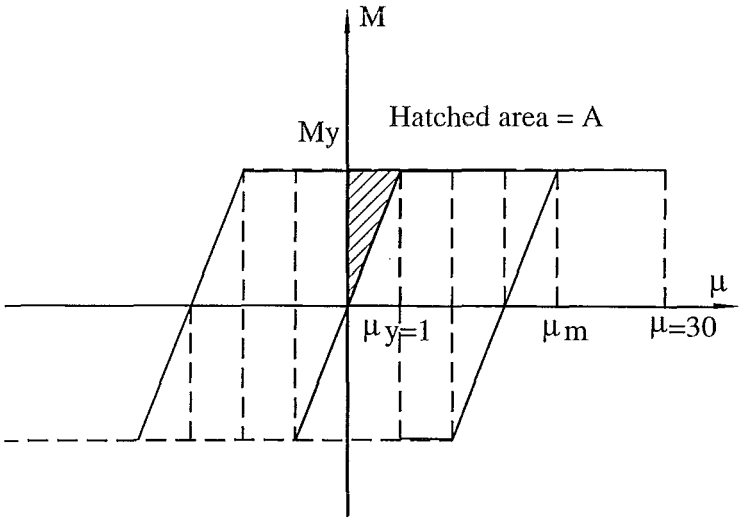

Fig. K-1 Elasto-Plastic hysteresis model for derivation of the number of cycles needed for Park & Ang member damage index reaching 1.0 for a given constant curvature ductility μ_m

The dissipated energy in the first quadrant A_I for μ_m is:

$$A_I = (2\mu_m - 1)A \qquad \textbf{(K-2)}$$

The dissipated energy in the second quadrant A_{II} for μ_m is:

$$A_{II} = (2(\mu_m - 1) - 1)A \quad \textbf{(K-3)}$$

The dissipated energy in the first and second quadrants A_{I+II} for μ_m is:

$$A_{I+II} = A_I + A_{II} = 8(\mu_m - 1)A \quad \textbf{(K-4)}$$

The contribution of the energy component to the member damage according per cycle to the Park & Ang is:

$$\frac{\beta}{F_y * \mu_u} \int dE = \frac{\beta * 8(\mu_m - 1)A}{60A} = 0.0067(\mu_m - 1) \quad \textbf{(K-5)}$$

The number of cycles N needed for the damage index to reach 1.0 is:

$$N = \frac{1.0 - (\mu_m / 30)}{0.0067(\mu_m - 1)} \quad \textbf{(K-6)}$$

The numbers of cycles required for the member damage index to reach 1.0 for specified maximum curvature ductility μ_m are shown in Table K-1 and the figure below:

Table K-1 The number of cycles needed for the member damage index to reach 1.0 versus the maximum curvature ductility

Maximum ductility μ_m	Number of cycles
2	139.3
4	43.1
8	15.6
10	11.1
15	**5.3**
16	4.6
20	2.6
24	1.3
25	**1.0**
26	0.8

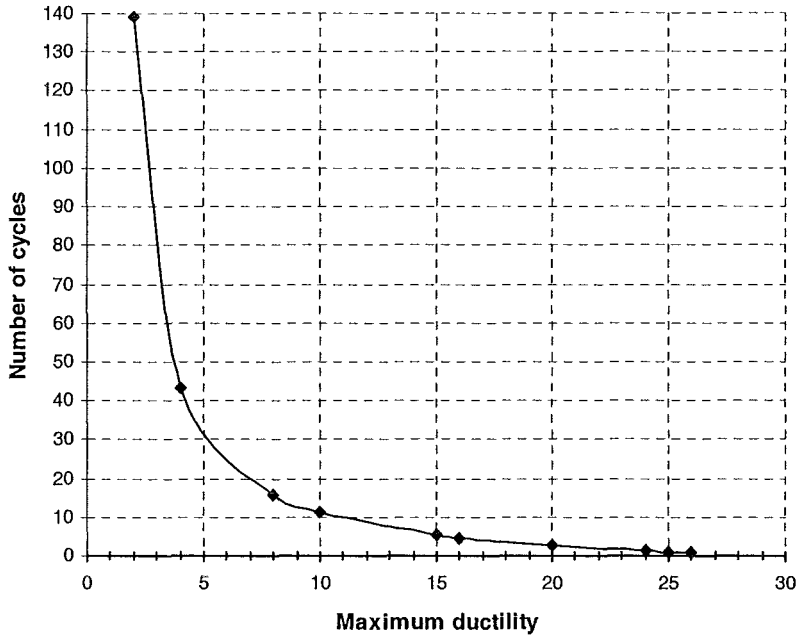

Fig. K-2 The number of cycles needed for the member damage index to reach 1.0 versus the maximum curvature ductility

For μ_m=25, only one cycle could make the member totally damaged as shown in the table K-1, according to Park & Ang. For μ_m>15, no more than five cycles are needed.

This shows that although the value of β at 5% appears to indicate a very small significance of the hysteretic energy, the accumulative effect of the hysteretic energy over several cycles of inelastic behaviour is very significant.